STUDY OF PARAMETERS OF THE MIXTURE AND HEAT GENERATION
OF THE DD15 DIESEL ENGINE OF THE SANDVIK LH514 LOADER
IN THE PROCESS OF USING ALTERNATIVE FUELS BASED ON RME

Michał BEMBENEK*, **Vasyl MELNYK****, **Yurii MOSORA****

**Department of Manufacturing Systems, Faculty of Mechanical Engineering and Robotics, AGH University of Krakow,
al. Adama Mickiewicza 30, 30-059 Kraków, Poland
**Ivano-Frankivsk National Technical University of Oil and Gas, 15 Karpatska St., Ivano-Frankivsk, Ukraine*

bembenek@agh.edu.pl, vasyl.melnyk@nung.edu.ua, yuramosora@gmail.com

Abstract: Today, there is a growing shortage of commercial motor fuels in the world. This is due to the tendency to regulate the extraction of hydrocarbons, which are the main raw materials for their production; and, therefore, to reduce the import of oil, alternative types of fuel for diesel engines based on oils and animal fats are becoming widespread today. In this regard, intensive work is underway to convert internal combustion engines to biofuel-based ones both in countries with limited fuel and energy resources and in highly developed countries that have the opportunity to purchase liquid energy carriers. Biodiesel fuel (biodiesel, PME, RME, FAME, EMAG, etc.) is an environmentally friendly type of biofuel obtained from vegetable and animal fats and used to replace petroleum diesel fuel. According to the results of modelling, in the process of using RME B100 biodiesel fuel, we found a reduction in nitrogen dioxide emissions by 21.5% and a reduction in soot emissions by 34.5%. This will positively affect the environmental performance of the Sandvik LH514 loader, which is especially relevant in closed environments such as mines. So, according to the results of studies of the operation of the DD15 engine of the Sandvik LH514 loader on commercial and RME B100 biodiesel fuel, it was established that the use of biodiesel fuel leads to a deterioration of the mixture, due to which heat generation is reduced and, as a result, fuel consumption increases and engine power decreases, but the aspect of environmental indicators constitutes the significant improvement demonstrated by the present work.

Key words: engine, alternative fuels, biodiesel, economy, spraying, mixing, heat release, consumption, power

1. INTRODUCTION

The use of alternative fuels in internal combustion engines (ICE) will lead to a change in the working process in the cylinders of the ICE, and this change may lead to a violation of the engine's operating mode, and a decrease in reliability and durability.

Therefore, the question of researching mixture and heat formation in DD15 diesel engines in the process of using RME B100 biodiesel fuel is relevant, and the results will help to eliminate or reduce negative factors that lead to the deterioration of technical and operational indicators of diesel engines.

Scientists [1–15] have conducted research on methods of reducing emissions of harmful substances and soot by diesel engines in the process of using commercial diesel fuel and biodiesel.

Thus, in Horibe et al. [1], the effect of reducing smoke after fuel injection due to changing the number of nozzle injection holes and injection pressure was established. The results showed that the smoke output of the six-hole, seven-hole and eight-hole nozzles was reduced. It has also been demonstrated in the literature [2–5] that additional fuel injection reduces soot emissions of various engine designs and at various operating points. Horibe et al. [6] investigate the effect of post-injection smoke reduction by changing numerous parameters: number of post-injections, post-injection time, injection pressure, main injection time, intake pressure, number of injection nozzle holes and combustion chamber shape. Eismarka et al. [7] found that fuel properties mainly affect parameters related to processes near the nozzle, such as ignition delay, flame separation distance and air intake by the atomiser. A comparative assessment of gasoline and diesel engine emissions was performed in the study of Benajes et al. [8], and the results show that the dual-mode fuel concept has the potential for implementation in vehicles. In Millo et al. [10], the geometry of the piston bottom of a diesel engine was optimised, which contributed to the improvement of wall flame development, better mixing of air with fuel, and reduction of soot emissions.

As we can see from the researches discussed above, scientists solve the problem of reducing the toxicity of a diesel engine by making changes to the design of parts of the power system, which is quite complicated and expensive.

Scientists [11–15] have also studied the advantages and disadvantages of biodiesel fuel and its effect on exhaust gas toxicity and engine performance.

Thus, in the studies of Tuan Hoang [11, 12], to improve the mixing process and reduce engine toxicity, biodiesel fuel was preheated to 105°C to achieve similarities in some physical properties and atomisation parameters compared to diesel fuel, but emissions did not decrease. Further, the effect of biodiesel on engine performance and emissions depending on the oil source is established in various studies [13–15], which have used castor oil biodiesel (CAB), coconut oil biodiesel (COB), waste cooking oil (WCB) and soybean oil biodiesel (SME).

As we can see from previous studies [11–15], the quality of fuel mixing in engine cylinders, as well as its economy and environmental friendliness, largely depends on the type

and quality of fuel, and biodiesel fuel B100 based on rapeseed oil (RME) was not studied in these researches.

There are also other studies in the literature [16–30] that are devoted to discussion of issues pertaining to the influence of mixing quality on heat generation processes in diesel engines.

In Jo et al. [16], the effect of injection pressure, nozzle hole diameter and oxygen concentration was investigated. The results show that the jet and the separation length at the 30° jet angle were smaller than at the 45° jet angle, regardless of the injection conditions and oxygen concentration. The development of innovative designs of the diesel piston chamber by Millo et al. [10] and Piano et al. [17] demonstrated a significant improvement in the development of the wall flame, which led to a decrease in fuel consumption and soot emissions from the engine. Jena et al. [18] found that fuel properties significantly affect engine combustion characteristics. In Sevostyanov et al. [19], new aspects of the global problem are considered, including that of increasing the efficiency of diesel engines during the time of their operation in partial and transient modes. The research made it possible to reveal the physical nature of complex hydrodynamic phenomena in diesel fuel equipment, which causes the appearance of intercycle instability of fuel supply in the working process of individual cylinders. In Li et al. [20], the opposed-piston two-stroke diesel engine developed in Abani et al. [21] was investigated. To solve the problems of non-uniformity of mixing and economy, a combustion system with lateral swirl is proposed in this work. Additionally, combustion parameters were optimised using sensitivity analysis and parameter normalisation methods.

In Huo et al. [22], a comprehensive study of the effect of piston design on scavenging and combustion in a two-stroke engine was carried out, and the results show how an optimised combustion chamber design improves combustion and achieves a balance between scavenging and combustion, as well as piston temperature control.

Yamauchi et al. [23] and Fuyuto et al. [24] found that the return flow of hot burnt gas surrounding the diesel flame is one of the factors reducing the separation length, that is, the distance from the nozzle exit to which the flame spreads. To visualise the phenomena occurring in the combustion chamber of the engine, Pastor et al. [25] propose the use of optical designs of engines.

Studies of fuel atomisation in the combustion chamber and its mixing with air are carried out in the literature [26–30]. Thus, in Yaqing Bo et al. [26], it was established that the influence of injection pressure on ignition at low temperatures is not systematic. Increasing the fuel temperature from 313 K to 353 K [27] affected atomisation, while increasing temperature also increased the spray cone angle and spray width. On the other side, the decrease in spray cone angle and spray width was evident due to the decrease in fuel density and viscosity. In Yin et al. [28], the results showed that the penetration length of biodiesel liquid was longer than that of diesel under the same injection conditions.

In the study of Raghu and Nallusamy [29], the characteristics of biodiesel fuel atomisation in the combustion chamber were optimised according to three factors: fuel injection pressure, fuel temperature and fuel type. According to the results, it is proved that due to the optimisation of these parameters, it is possible to achieve optimal conditions of heat release.

Yu et al. [30] investigated the internal flow in the nozzle and the macroscopic characteristics of diesel and biodiesel spraying using a proven numerical model and the scattering method. The results show that the mass flow rate of diesel is higher than that of biodiesel.

As can be inferred from the literature [16–30], the issue of the influence of mixing quality on heat generation processes in diesel engines has not been studied adequately, and the influence of biodiesel based on RME has not been studied.

Researches are available in the literature that examine the feasibility of a diesel engine running on hydrogenated vegetable oil (HVO) [31–33] and pure vegetable oil (PVO) [34, 35]. According to the results obtained [31–33], there was an increase in NOx and a decrease in solid particles, soot and carbon oxides in the emissions. According to the results of researches conducted by Espadafor et al. [34] and Chiaramonti and Prussi [35], a reduction in emissions of harmful substances, including SOx, was observed, which characterises this fuel as a good substitute for commercial diesel fuel. However, the various studies conducted in the relevant literature [31–35] do not reveal the process of mixture formation and heat release, which accordingly forms the basis of our research.

So, based on the results of the review of literary sources, we found that the process of mixture and heat formation and emissions of harmful components are affected by such factors as fuel spray pressure, fuel spray angle, the number of nozzle holes and the content of hydrogen and oxygen in the fuel. Given that the influence of biodiesel based on RME for these processes is poorly studied, this line of research is taken up in the present work.

2. MATERIALS AND METHODS

2.1. Methodology for modelling mixture formation in diesel engines

To conduct studies of the work process in the engine, when using RME B100 biodiesel fuel, there is a need to use methods of system analysis and comparison. System analysis makes it possible to analyse, using objective criteria of comparative efficiency, the influence of factors operating in the working volume of the engine on the engine's performance.

The method of comparing the influence of factors such as the fractional composition of the fuel, cetane number, auto-ignition delay period, density, viscosity, calorific value, etc. on work processes in internal combustion engines allows us to make assumptions about the validity of the accepted assumptions. However, based only on the data of such a comparison, it is impossible to unequivocally state that the same factor will have the same effect on the processes in the internal combustion engine, both when using standard fuels and when using alternative analogues. This follows from the fact that there are significant differences in the flow of work processes in internal combustion engines that use only base fuel or fuel with a variable fractional composition.

Analysis of the problems associated with the use of biodiesel fuel in automobile internal combustion engines showed that the efficiency of engine operation depends on the following:

- the ratio between low-boiling, medium and heavy fuel fractions, which significantly affects the nature of the working process in the cylinders;
- the relationship between the fuel supply parameters and gas distribution phases of the internal combustion engine;
- redistribution of the components of the heat balance due to a change in the characteristics of the heat supply;
- the nature and law of heat transfer in the thermodynamic cycle of an internal combustion engine operating on biodiesel fuel.

The method of direct analogy between the processes in an internal combustion engine operating on standard fuels with the working processes in an internal combustion engine in the case of using biodiesel fuel makes it possible to find such solutions that allow us to ensure acceptable characteristics of heat release, as well as preserve or reduce the thermal stress of the elements of the internal combustion engine, which will improve environmental indicators.

The method of physical modelling of work processes in internal combustion engines using biodiesel fuel will not only allow the determination of the adequacy of the mathematical model and the validity of the assumptions made in the work but also enable the efficiency, fuel economy, reliability and durability of the engine to be ensured.

Mathematical modelling of the working process in an internal combustion engine in the case of using biodiesel fuel will allow us to determine the nature of the flow processes in the engine cylinders, to determine the influence of fuel parameters on the nature of the working process and the thermodynamic efficiency of the engine as a whole, and to develop methods for calculating the working cycle of the engine.

In the implementation of the mathematical model, a modified Euler method was used, which has satisfactory convergence and gives fairly accurate results.

During the development of the research methodology of the work process in diesel engines using biodiesel fuel, the following areas were highlighted:

- analysis of the problem associated with the use of biodiesel fuel in diesel engines, as well as analysis of factors affecting the work process;
- establishment of the influence of biodiesel fuel on mixture formation in internal combustion engines using mathematical modelling;
- proposal of ways to improve the work process in the internal combustion engine when using biodiesel fuel.

When using the original system of equations, generally accepted assumptions are made: about the homogeneity of the thermodynamic system, about the validity of the Mendeleev-Clapeyron equation of state, and about the dependence of the properties of the working body on composition and temperature.

The main difficulty in calculating the work processes that take place in an internal combustion engine cylinder is the determination of the dynamics of heat release $dx/dFi = F(\varphi)$ for calculating the amount of added heat at each calculation step:

$$Q_x = \xi_a \cdot q_c \cdot H_u \cdot \frac{dx}{dF_i} \cdot \Delta F_i, \tag{1}$$

where Hu represents the lower heat of fuel combustion, *ΔFi* the calculated time step and ξ_a the factor accounting for heat loss due to incomplete combustion of fuel.

Nowadays, the Wiebe formula is widely used to calculate the rate of heat release, *dx/dFi*. However, its use for calculating working processes in diesel engines can be justified only if the fuel supply parameters will not change in the study, since the formula does not consider several determining physical processes. Wiebe's method is quite suitable for calculating the combustion process in gasoline and gas internal combustion engines.

The theoretically necessary amount of air for the combustion of 1 kg of fuel is determined from the equation of the combustion reactions of the elemental composition of the fuel:

$$l_0 = \frac{m_{air}}{0.21} \cdot \left(\frac{C}{12} + \frac{H}{4} + \frac{S}{32} - \frac{O}{32}\right), \tag{2}$$

where $m_{air} = 28.9$ is the molecular weight of air, and C, H, S and O represent the elementary mass composition of 1 kg of fuel.

We have implemented a modelling technique based on the works of Professor N.F. Razleitseva, which was later refined by A.S. Kuleshov. This method, with sufficient speed, allows consideration of the design features of the fuel equipment, the nature of injection, and the dynamics of the development of fuel jets, including the interaction of their products with walls of arbitrary shape and with each other.

In the refined model of heat release, as well as in the simplified one, four periods are distinguished, which differ in physical and chemical features and factors limiting the speed of the process:

- the self-ignition delay period;
- the outbreak start period;
- the period of controlled combustion in the fuel supply area after the flash;
- the period of diffusion combustion after the end of the fuel supply.

A model is conceptually described below, which additionally considers several significant factors, including the distribution of part of the fuel on the walls of the chamber in the piston, on the walls of the cylinder cover and on the cylinder mirror, and the conditions of fuel evaporation under the conditions of specific temperatures of these walls. Additionally, the model considers the influence of the tangential vortex, both on the free jet and on the wall flow formed by it. The conditions of the collision of a deformed jet vortex with a wall of arbitrary shape and the interaction of the wall flows of neighbouring jets with each other are considered.

The calculation of mixture formation and combustion is carried out in increments of 0.2° ... 1° rotation of the crankshaft.

The average fuel flow rate from the injector nozzle is given as the following:

$$U_{0m} = \frac{24 \cdot g_c \cdot n}{0.75 \cdot \rho_f \cdot d_c \cdot i_c \cdot \varphi_{di}}, \tag{3}$$

where qc indicates the cyclic fuel supply, n the crankshaft rotation frequency, ρf the fuel density, dc and ic the diameter and number of sprayer nozzles, respectively, and φdi the duration of injection.

The instantaneous flow rate of fuel from the nozzle atomiser $U_0 = U_{0m} \cdot d\sigma/d\varphi$, where dσ/dφ represents the dimensionless differential characteristic of injection.

The criterion M can be expressed as:

$$M = \mu_f^2 / (d_c \cdot \rho_f \cdot \sigma_f), \tag{4}$$

where μf represents the coefficient of dynamic viscosity of fuel at 323 K, and σf the coefficient of surface tension of fuel at 323 K.

The Weber criterion can be expressed as:

$$W_e = U_{0m}^2 \cdot \rho_f \cdot d_c / \sigma_f. \tag{5}$$

The criterion E can be expressed as:

$$E = \tau_S^2 \cdot \sigma_f / (\rho_f \cdot d_c^2), \tag{6}$$

where τ_S represents the time from the start of injection.

The simplex can be expressed as:

$$\rho = \rho_{air} / \rho_m, \tag{7}$$

where ρair represents air density at the end of the compression stroke.

Michał Bembenek, Vasyl Melnyk, Yurii Mosora
Study of Parameters of the Mixture and Heat Generation of the DD15 Diesel Engine of the Sandvik LH514 Loader in the Process of Using Alternative Fuels Based on RME

DOI 10.2478/ama-2024-0021

The average surface diameter of droplets (Sauter diameter), in micrometre, is given as:

$$d_{32} = 10^6 \cdot E_{32} \cdot d_c \cdot M^{0.0733}/(\rho \cdot W_e)^{0.266} \qquad (8)$$

where E_{32} indicates the empirical coefficient.

According to the model described above, in the main area of the jet development, each elementary portion of injected fuel moves in the axial core of the jet up to its top, where this portion is pushed to the periphery of the jet, decelerates sharply until the initial speed is completely lost, and fills the shell of the jet. Part of the mass of the elementary portion of the fuel is dispersed in the shell of the jet along the path of movement to the front.

2.2. Calculation scheme of the development of the fuel jet in the wall zone

The scheme of the development of the jet in the wall zone is presented in Fig. 1. During the impact of the front of the jet on the wall, a cone-shaped condensed fuel-gas layer (7) is formed on it within the spot, formed by the intersection of the cone of the jet with the surface of the wall. After the rapid formation of the jet front on the wall, the fuel will begin to spread beyond the initial spot. The high-speed axial flow of the jet, hitting the wall, compacts the wall layer and pushes its boundaries, and part of the flow moves above this layer to its periphery. The shape of the wall spot and the speed of its spreading in different directions depend on the angle of the jet meeting the wall and the influence of air turbulence.
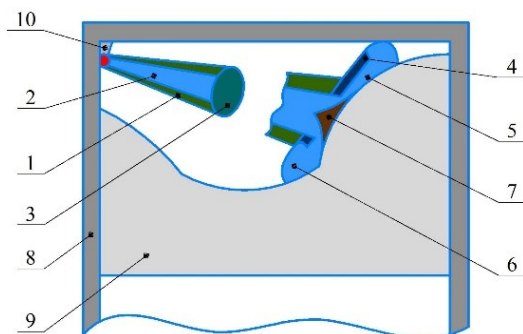
Fig. 1. Calculation scheme of the fuel jet of one injector hole: (1) rarefied shell of the jet; (2) compacted axial core; (3) compacted front; (4) rarefied PP shell; (5) compacted PP core; (6) the front line of the PP; (7) cone-shaped axial core PP; (8) cylinder; (9) piston; (10) nozzle

The advance of the fuel along the wall slows down compared to the free development of the jet due to the friction of the flow against the wall, the dissipation of the kinetic energy of the jet with drops reflected from the wall, etc. Additionally, the movement of the wall flow is affected by the air vortex in the combustion chamber, the intensity of which is given by the vortex number H.

The wall flow is heterogeneous in structure, density and temperature, which complicates the calculation of fuel evaporation. Therefore, it is advisable to distinguish three characteristic zones with averaged heat and mass transfer rates in the wall flow, as well as in the free jet.

The first zone is the cone formation of the axial core (7) on the wall, which is formed when the jet front is placed on the wall. In the future, the composition of this core would be continuously

updated due to new masses of fuel flying up to the wall. However, the total proportion of fuel in it changes little during the injection process.

The second zone is the wall layer of fuel, spreading beyond the initial spot (5). It can be considered as an analogue of an axial core in a free jet (2) in the main area of its development.

The third zone is a rarefied shell (4) above the wall layer, where part of the fuel slows down in the front (6) of the wall flow passes.

When the fuel spreads along the wall, and it spreads in all directions, the wall flow, which is also deformed by the vortex, may cross a characteristic boundary that separates zones with different conditions of fuel evaporation and combustion, for example, the transition from the side inclined to the horizontal surface of the bottom of the piston, the surface cylinder mirrors, etc. It is also possible to close the wall flow of neighbouring jets. In all these cases, the mass of fuel that has crossed the border is found from the solution of the geometric problem of the intersection of the oval formed by spots from the wall fuel flows.

If the calculated height of the front of the wall flow on the piston crest is greater than the height above the piston gap, then part of the fuel from the shell and core of the wall flow pops onto the cylinder head.

The study of the evaporation of atomised fuel in the combustion chamber and on the walls, as well as the calculation of the dynamics of heat release on different types of diesel fuel, is carried out using mathematical modelling. Heat supply is carried out according to a mixed scheme (Trinkler–Sabot cycle).

3. RESULTS AND DISCUSSION

3.1. Modelling of mixture and heat generation parameters in diesel engines during the use of diesel fuel

For modelling, we choose the DD15 engine of the Sandvik LH514 loader, whose brief characteristics are given in Tab. 1, using the Diesel-RK software complex.

The reference indicator for comparison will be the parameters obtained for the selected DD15 engine in the process of using commercial diesel fuel at full loads (n = 1,800 rpm).

According to the generally accepted description of the fuel jet (Fig. 1), it has a cone-shaped appearance and is denser in its central part than on the periphery. When the jet of fuel is evenly filled with drops, then on the image it is depicted in approximately one shade, or vice versa.

Tab. 1. Brief technical characteristics of the DD15 engine

| Parameter name	Units	Parameter value
Number of cylinders	-	V8
Cylinder diameter	mm	130
Piston stroke	mm	139
Number of nozzle holes	-	3
Torque	N·m	1,559–1,830 (1,200 rmp.)
Working volume	l	11.1
Engine power	kW	246–272 (1,800–2,100 RMP)
Application	-	Mining and automotive equipment

Fig. 2 shows the results of studies of diesel atomisation parameters that comply with DSTU 7687:2015 for the DD15 engine. According to the results of these studies (Fig. 2), the main proportion of fuel, 0.71, is located in the shell of the jet, which contributes to better mixing of fuel with air. In the core of the wall, there is 0.15 of fuel, which will spread over the walls and mix poorly with air.
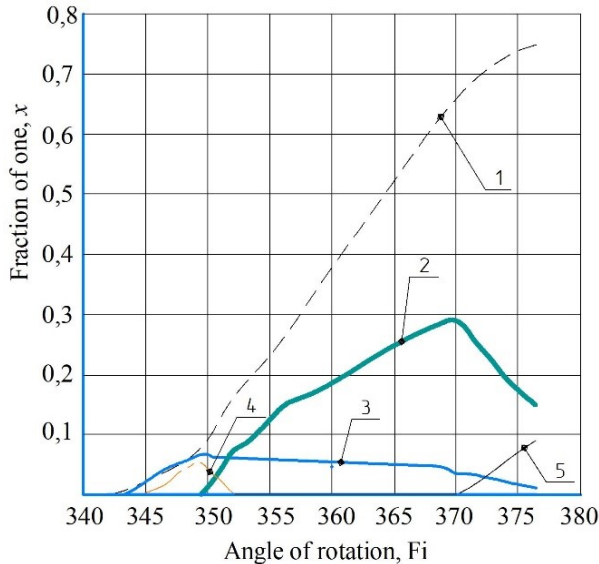
Fig. 2. Distribution of fuel by the spray torch zones of the DD15 engine of the Sandvik LH514 loader: (1) the proportion of fuel in the jet envelope; (2) the proportion of fuel in the wall core; (3) the proportion of fuel in the jet core; (4) the proportion of fuel in the front of the free jet; (5) the proportion of fuel in the intersection zones of wall flows

The rest of the fuel will be located in the core of the jet, the front of the free jet and the intersection zones of the wall flows, and will partially participate in the mixture formation and contribute to the mixing of the fuel–air mixture.
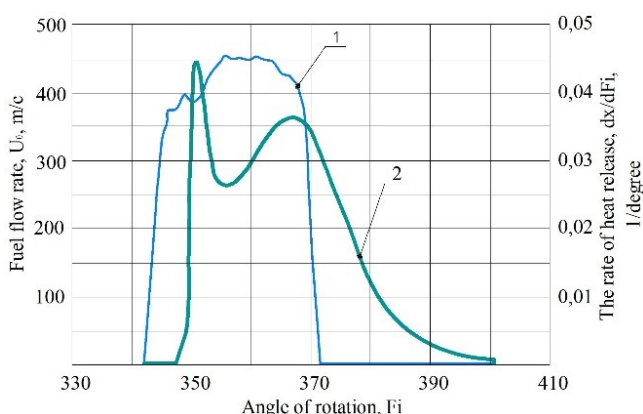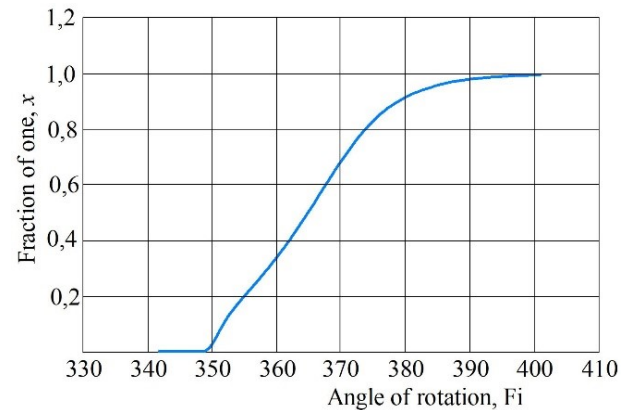

Fig. 3. Dependence of fuel flow rate U0 and heat release dx/dFi on the angle of rotation of the crankshaft of the DD15 engine of the Sandvik LH514 loader: (1) fuel flow rate; (2) rate of heat release

Fig. 3 graphically displays the dependence of the fuel flow rate and heat release parameters (U0 and dx/dFi, respectively) on the angle of rotation of the crankshaft for the DD15 engine of the Sandvik LH514 loader. As can be seen, the speed of fuel flow and heat release occurs instantaneously in a jump-like manner during

5°–7° of rotation of the crankshaft, which positively affects the power and economy of the engine.

The main part of heat release (Fig. 4) occurs at the angle of rotation of the crankshaft of 20°–25°, which is related to the previous graph since the speed of fuel flow and heat release occurs at this moment.

Fig. 4. Dependence of the share of heat release x on the angle of rotation of the crankshaft of the DD15 engine of the Sandvik LH514 loader

3.2. Modelling of mixture and heat generation in diesel engines during the use of biodiesel fuel

In the process of using RME B100 biodiesel, the characteristics of which are shown in Tab. 2, several indicators were obtained, as presented in Figs. 5–7.

However, considering the external characteristics of fuel jet spraying, the analysis of the obtained images showed that the use of RME B100 biodiesel leads to the following consequences:

– an increase in the average diameter of fuel drops;
– an increase in the range of the jet together with a decrease in its width;
– the assumption of a conical shape by the contour of the torch;
– the observation of an aggravation at its peak, from which it can be assumed that there is, to some extent, an overenrichment of the jet's core; and
– a decrease in the opening angle of the torch.

Tab. 2. Basic physical and chemical parameters of diesel fuel according to DSTU 7688:2015 and RME B100 biodiesel fuel

Indicator name	Units	Value for diesel fuel	Value for RME B100
Chemical composition:	%		
C		87	77
H		12.6	12.1
O		0.4	10.9
Sulphur content	%	0.001	0.0015
Lower heat of combustion	MJ/kg	42.5	39.45
Cetane number	-	51	54.4
Density at a temperature of 323 K	kg/m³	820–845	874
Saturated vapour pressure at a temperature of 481 K	bar	-	0.001
Molecular weight	kg/kmol	-	296

Michał Bembenek, Vasyl Melnyk, Yurii Mosora

DOI 10.2478/ama-2024-0021

Study of Parameters of the Mixture and Heat Generation of the DD15 Diesel Engine of the Sandvik LH514 Loader in the Process of Using Alternative Fuels Based on RME

All these listed factors lead to a worse distribution of fuel in the zones of the spray torch, as shown in Fig. 5. Only 63% of the fuel is in the jet shell, which leads to poor mixing of fuel with air. In the core of the wall, there is 13% of the fuel, which will spread over the walls and mix poorly with air.

The remaining 24% of the fuel will be in the core of the jet, the front of the free jet and the intersection zones of the wall flows, and will partially participate in the mixture formation.

Fig. 6 graphically displays the dependence of the fuel flow rate and heat release parameters (U0 and dx/dFi, respectively) on the angle of rotation of the crankshaft for the DD15 engine of the Sandvik LH514 loader in the process of using the RME B100.
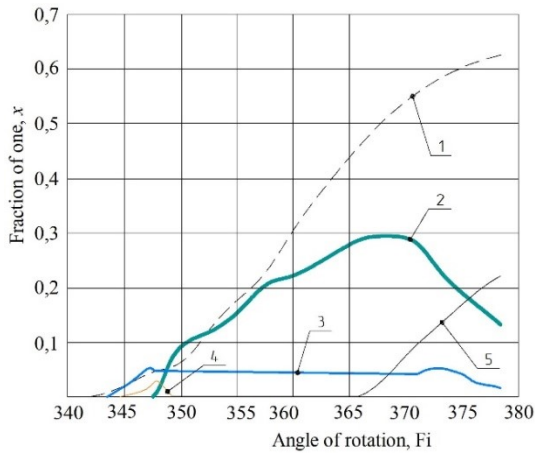
Fig. 5. Distribution of fuel in the zones of the spray torch during the operation of the DD15 engine of the Sandvik LH514 loader: (1) the proportion of fuel in the jet envelope; (2) the proportion of fuel in the wall core; (3) the proportion of fuel in the jet core; (4) the proportion of fuel in the front of the free jet; (5) the proportion of fuel in the intersection zones of wall flows
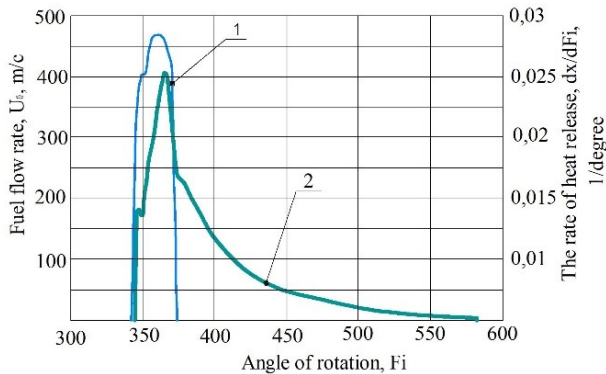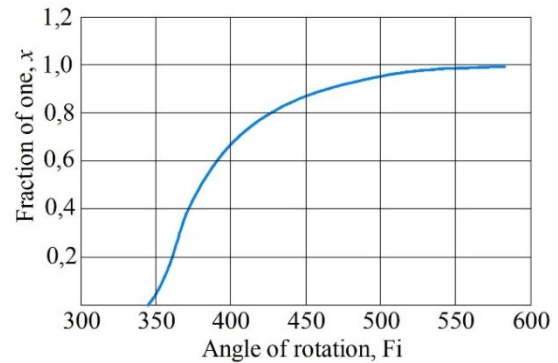

Fig. 6. Dependence of the rate of heat release dx/dFi and fuel leakage U0 on the angle of rotation of the crankshaft during the operation of the DD15 engine of the Sandvik LH514 loader on RME B100 biodiesel fuel: (1) fuel flow rate; (2) rate of heat release

As can be seen from Fig. 6, the speed of fuel flow and heat release occurs with a delay, by 8°–10° of rotation of the crankshaft, which will lead to an increase in fuel consumption and a decrease in engine power.

The main share of heat release of 80% (Fig. 7) occurs at the angle of rotation of the crankshaft of 102° relative to the bottom dead centre, which is related to the previous graph, since the speed of the fuel flow and release decreases.

We also modelled emissions of NO2 and soot from the DD15 engine of the Sandvik LH514 loader in the process of using diesel fuel and RME B100 biodiesel (Fig. 8).

Fig. 7. Dependence of the share of heat release x on the angle of rotation of the crankshaft during the operation of the DD15 engine of the Sandvik LH514 loader on RME B100 biodiesel fuel
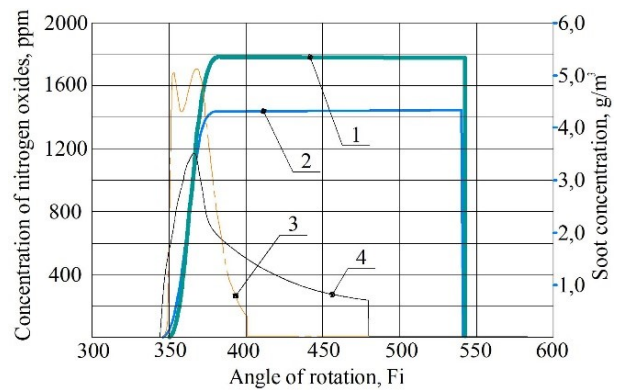
Fig. 8. Emissions of nitrogen oxides and soot from the DD15 engine of the Sandvik LH514 loader when running on diesel and RME B100 biodiesel: NO2 emissions (1) when using diesel fuel; (2) when using RME B100 biodiesel fuel; soot emissions (3) when using diesel fuel; (4) when using RME B100 biodiesel

Based on the simulation results demonstrated in Fig. 8, we may infer that we have managed, in the process of using RME B100 biodiesel fuel, to improve the environmental performance of the diesel engine. A reduction in nitrogen dioxide emissions by 21.5% and a reduction in soot emissions by 34.5% were obtained. This can be explained by a decrease in the combustion temperature of biodiesel fuel by 7% and a decrease in the carbon content of the fuel by 11.5%.

3. CONCLUSION

In the process of modelling the mixture and heat generation parameters using the Diesel-RK software complex during the use of RME B100 biodiesel fuel on the DD15 engine of the Sandvik LH514 loader, the presence of the following phenomena was established: an increase in the average diameter of fuel drops; a recorded increase in the long-range of the jet together with a decrease in its width; the assumption of a conical shape by the contour of the torch; the observation of an aggravation at its peak, from which it can be assumed that there is, to some extent, an over-enrichment of the jet's core; and a decrease in the opening

angle of the torch. The listed factors lead to a worse distribution of fuel in the zones of the spray torch. Only 63% of the fuel is in the jet shell, which leads to poor mixing of fuel with air. In the core of the wall, there is 13% of the fuel, which will spread over the walls and mix poorly with air. The remaining 24% of the fuel will be in the core of the jet, the front of the free jet and the intersection zones of the wall flows, and will partially participate in the mixture formation.

The use of RME B100 biodiesel leads to a delay in heat release by 8°–10° of crankshaft rotation, which in turn leads to a slight increase in fuel consumption and a decrease in engine power by 7%.

According to the results of mowing in the process of using RME B100 biodiesel fuel, we determined a decrease in nitrogen dioxide emissions by 21.5% and a decrease in soot emissions by 34.5%. This will positively affect the environmental performance of the Sandvik LH514 loader, which is especially relevant in closed environments such as mines.

So, according to the results of studies of the operation of the DD15 engine of the Sandvik LH514 loader on commercial and RME B100 biodiesel fuel, it was established that the use of biodiesel fuel leads to a deterioration of the mixture, due to which heat generation is reduced and, as a result, fuel consumption increases and engine power decreases, but the aspect of environmental indicators constitutes the significant improvement demonstrated by the present work.

Accordingly, in consideration of these results, further research should be directed at improving mixture formation in the process of using biodiesel fuel, and one of the options for accomplishing this would be improving the geometric shapes of the combustion chamber.

Also, in the future, our work will be oriented towards the study of the performance indicators of the diesel engine in the process of using biodiesel fuel based on rapeseed oil.

REFERENCES

1. Naoto H, Tatsuya K, Yuji M, Takashi S, Hiroshi K, Ishiyama T. Analysis of Mixture Formation Process in a Diesel Engine with Post Injection. SAE technical paper series. 2015. https://doi.org/10.4271/2015-01-1836
2. O'Connor J, Musculus M. In-Cylinder Mechanisms of Soot Reduction by Close-Coupled Post-Injections as Revealed by Imaging of Soot Luminosity and Planar Laser-Induced Soot Incandescence in a Heavy-Duty Diesel Engine. SAE International Journal of Engines. 2014 Apr 1;7(2):673–93.DOI:10.4271/2014-01-1255
3. Hessel R, Reitz RD, Musculus M, O'Connor J, Flowers D. A CFD Study of Post Injection Influences on Soot Formation and Oxidation under Diesel-Like Operating Conditions. SAE International Journal of Engines. 2014 Apr 1;7(2):694–713. DOI:10.4271/2014-01-1256
4. O'Connor J, Musculus M. Effects of exhaust gas recirculation and load on soot in a heavy-duty optical diesel engine with close-coupled post injections for high-efficiency combustion phasing. International Journal of Engine Research. 2013 Jul 24;15(4):421–43. DOI:10.1177/1468087413488767
5. O'Connor J, Musculus M. Post Injections for Soot Reduction in Diesel Engines: A Review of Current Understanding. SAE International Journal of Engines. 2013 Apr 8;6(1):400–21. DOI:10.4271/2013-01-0917
6. Naoto H, Tatsuya K, Takashi S, Wang H, Ishiyama T. Smoke Reduction Effects by Post Injection for Various Injection Parameters and Combustion Chamber Shapes in a Diesel Engine. SAE technical paper series. 2014 Oct 13. DOI:10.4271/2014-01-2634
7. Eismark J, Christensen M, Andersson M, Karlsson A, Denbratt I. Role of fuel properties and piston shape in influencing soot oxidation in heavy-duty low swirl diesel engine combustion. Fuel. 2019 Oct;254:115568. DOI: https://doi.org/10.1016/j.fuel.2019.05.151
8. Benajes J, García A, Monsalve-Serrano J, Lago Sari R. Fuel consumption and engine-out emissions estimations of a light-duty engine running in dual-mode RCCI/CDC with different fuels and driving cycles. Energy. 2018 Aug;157:19–30. DOI:10.1016/j.energy.2018.05.144
9. Rao L, Zhang Y, Kook S, Kim KS, Kweon CB. Morphology and internal structure of soot particles under the influence of jet–swirl and jet–jet interactions in a diesel combustion environment. Combustion and Flame. 2020 Apr;214:25–36. https://doi.org/10.1016/j.combustflame.2019.12.017
10. Millo F, Piano A, Roggio S, Pastor JV, Micó C, Lewiski F, et al. Mixture formation and combustion process analysis of an innovative diesel piston bowl design through the synergetic application of numerical and optical techniques. February 2022, Fuel, Volume 309. https://doi.org/10.1016/j.fuel.2021.122144
11. Hoang AT. Experimental study on spray and emission characteristics of a diesel engine fueled with preheated bio-oils and diesel fuel. Energy. 2019 Mar;171:795–808. https://doi.org/10.1016/j.energy.2019.01.076
12. Hoang AT. Waste heat recovery from diesel engines based on Organic Rankine Cycle. Applied Energy. 2018 Dec;231:138–66. https://doi.org/10.1016/j.apenergy.2018.09.022
13. Zareh P, Zare AA, Ghobadian B. Comparative assessment of performance and emission characteristics of castor, coconut and waste cooking based biodiesel as fuel in a diesel engine. Energy. 2017 Nov;139:883–94. https://doi.org/10.1016/j.energy.2017.08.040
14. Rakopoulos DC, Rakopoulos CD, Giakoumis EG, Papagiannakis RG, Kyritsis DC. Influence of properties of various common bio-fuels on the combustion and emission characteristics of high-speed DI (direct injection) diesel engine: Vegetable oil, bio-diesel, ethanol, n-butanol, diethyl ether. Energy. 2014 Aug;73:354–66. https://doi.org/10.1016/j.energy.2014.06.032
15. Mohamed Khaled Abdelrazek, Mohsen Mohamed Abdelaal, Ahmed Mustafa El-Nahas. Numerical simulation of a diesel engine performance powered by soybean biodiesel and diesel fuels. Beni-Suef University Journal of Basic and Applied Sciences. 2023 Jan 22;12(1). https://doi.org/10.1186/s43088-023-00349-w
16. Jo H, Ishikawa T, Naoto Horibe, Hayashi J, Hiroshi Kawanabe, Ishiyama T. Effect of Jet-Jet Angle on Combustion Process of Diesel Spray in an RCEM. SAE International Journal of Advances and Current Practices in Mobility. 2020 Sep 15;3(1):276–86. https://doi.org/10.4271/2020-01-2058
17. Piano A, Roggio S, Millo F, García A, Micó C, Lewiski F, et al. Numerical and optical soot characterization through 2-color pyrometry technique for an innovative diesel piston bowl design. Fuel. 2023 Feb 1;333:126347–7. https://doi.org/10.1016/j.fuel.2022.126347
18. Jena A, Akhilendra Pratap Singh, Avinash Kumar Ágarwal. Optical and computational investigations of the effect of Spray-Swirl interactions on autoignition and soot formation in a compression ignition engine fuelled by Diesel, dieseline and diesohol. Applied Energy. 2022 Oct 1;324:119677–7. https://doi.org/10.1016/j.apenergy.2022.119677
19. Sevostyanov SM, Melnyk ME, Vakarenko SV. Research of intercommunication of serve of fuel and mixtureform with working process in diesels during work on partial modes. Modern problems and ways of their solution in science, transport, production and education. Sworld. 2012 Dec 18-27:48-53.
20. Yang W, Li F, Ma F, Xu J. Numerical analysis of mixing and combustion characteristics of a lateral swirl combustion system in OP2S diesel engines. Proceedings of the Institution of Mechanical Engineers, Part D: Journal of Automobile Engineering. 2022 Sep 16;095440702211218. https://doi.org/10.1177/09544070221121874

21. Neerav A, Nagar N, Zermeno R, Chiang M, Thomas I. Developing a 55% BTE Commercial Heavy-Duty Opposed-Piston Engine without a Waste Heat Recovery System. SAE technical paper series. 2017 Mar 28. https://doi.org/10.4271/2017-01-0638

22. Huo M, Huang Y, Hofbauer P. Piston Design Impact on the Scavenging and Combustion in an Opposed-Piston, Opposed-Cylinder (OPOC) Two-Stroke Engine. SAE technical paper series. 2015 Apr 14. https://doi.org/10.4271/2015-01-1269

23. Yamauchi J, Dong P, Nishida K, Ogata Y. Effects of Hole Diameter and Injection Pressure on Fuel Spray and Its Evaporation Characteristics of Multi-Hole Nozzle for Diesel Engine. 2017 Oct 8. DOI:10.4271/2017-01-2305

24. Fuyuto T, Hattori Y, Yamashita H, Toda N, Mashida M. Set-off length reduction by backward flow of hot burned gas surrounding high-pressure diesel spray flame from multi-hole nozzle. International Journal of Engine Research. 2016 Jul 28;18(3):173–94. DOI:10.1177/1468087416640429.

25. Pastor J, Olmeda P, Javier Rodríguez Martín, Lewiski F. Methodology for Optical Engine Characterization by Means of the Combination of Experimental and Modeling Techniques. Applied sciences. 2018 Dec 11;8(12):2571–1. DOI:10.3390/app8122571

26. Bo Y, Liu F, Wu H, Li H, Shi Z. A numerical investigation of injection pressure effects on wall-impinging ignition at low-temperatures for heavy-duty diesel engine. Applied Thermal Engineering. 2021 Feb 1;184:116366–6.
https://doi.org/10.1016/j.applthermaleng.2020.116366

27. Srinivasan R, Raja G, Nallusamy N, Raghu P. Experimental study of mixture formation in biodiesel spray with preheated fuel International Journal of Applied Engineering Research. 2015 Mar; 10;19; 13687-13691.

28. Yin B, Ye Z, Jia H, Yu S, Deng WQ. Experimental Study on the Penetration of Diesel and Biodiesel Spray Liquid Emerging from an Equilateral Triangular Orifice under Evaporative Conditions. Journal of Thermal Science. 2022 Jan 22;31(5):1565–74.
https://doi.org/10.1007/s11630-022-1529-5

29. Raghu P, Nallusamy N, Spray characteristics of biodiesel fuel in constant volume chamber using multi-response optimization technique. Journal of Thermal Science, 2016, 25(6):581–588.

30. Yu S, Yin B, Jia H, Wen S, Li X, Yu J. Theoretical and experimental comparison of internal flow and spray characteristics between diesel and biodiesel. Fuel. 2017 Nov 1;208:20–9.
DOI:10.1016/j.fuel.2017.06.136

31. McCaffery C, Zhu H, Sabbir Ahmed CM, Canchola A, Chen JY, Li C, et al. Effects of hydrogenated vegetable oil (HVO) and HVO/biodiesel blends on the physicochemical and toxicological properties of emissions from an off-road heavy-duty diesel engine. Fuel. 2022 Sep;323:124283. https://doi.org/10.1016/j.fuel.2022.124283

32. Aatola H, Larmi M, Sarjovaara T, Mikkonen S. Hydrotreated Vegetable Oil (HVO) as a Renewable Diesel Fuel: Trade-off between NOx, Particulate Emission, and Fuel Consumption of a Heavy Duty Engine. SAE International Journal of Engines. 2008 Oct 6;1(1):1251–62. DOI:10.4271/2008-01-2500

33. Roque LFA, Berlini R, de Z, Coronado CJR, Pinto GM, Cintra AJA, et al. Experimental analysis and life cycle assessment of green diesel (HVO) in dual-fuel operation with bioethanol. 2023 Jan 1;389:135989–9. https://doi.org/10.1016/j.jclepro.2023.135989

34. Jiménez Espadafor F, Torres García M, Becerra Villanueva J, Moreno Gutiérrez J. The viability of pure vegetable oil as an alternative fuel for large ships. Transportation Research Part D: Transport and Environment. 2009 Oct;14(7):461–9.
https://doi.org/10.1016/j.trd.2009.05.005

35. Chiaramonti D, Prussi M. Pure vegetable oil for energy and transport. International Journal of Oil, Gas and Coal Technology. 2009;2(2):186. DOI: 10.1504/IJOGCT.2009.024886

Michał Bembenek: https://orcid.org/0000-0002-7665-8058

Vasyl Melnyk: https://orcid.org/0000-0002-5793-5486

Yurii Mosora: https://orcid.org/0000-0002-3192-7146

OPTIMAL SYSTEM OF 1-D SUBALGEBRAS AND CONSERVED QUANTITIES
OF A NONLINEAR WAVE EQUATION
IN THREE DIMENSIONS ARISING IN ENGINEERING PHYSICS

Oke Davies ADEYEMO*, Chaudry Masood KHALIQUE*

*Material Science, Innovation and Modelling Research Focus Area, Department of Mathematical Sciences, North-West University,
Mafikeng Campus, Private Bag X 2046, Mmabatho 2735, Republic of South Africa

adeyemodaviz@gmail.com, masood.khalique@nwu.ac.za

Abstract: The construction of explicit structures of conserved vectors plays diverse crucial roles in the study of nonlinear science inclusive of the fact that they are invoked in developing appropriate numerical schemes and for other mathematical analyses. Therefore, in this paper, we examine the conserved quantities of a nonlinear wave equation, existing in three dimensions, and highlight their applications in physical sciences. The robust technique of the Lie group theory of differential equations (DEs) is invoked to achieve analytic solutions to the equation. This technique is used in a systematic way to generate the Lie point symmetries of the equation under study. Consequently, an optimal system of one-dimensional (1-D) Lie subalgebras related to the equation is obtained. Thereafter, we engage the formal Lagrangian of the nonlinear wave equation in conjunction with various gained subalgebras to construct conservation laws of the equation under study using Ibragimov's theorem for conserved vectors.

Key words: A nonlinear wave equation in three dimensions, Lie group theory of differential equations, 1-D optimal system of subalgebras, formal Lagrangian, conserved vectors

1. INTRODUCTION

In recent years, intensive investigations have been diverted into nonlinear partial differential equations (NLPDEs) alongside their exact travelling wave solutions since many physical phenomena are represented using these NLPDEs. Nonlinearity is a captivating and enthralling element of nature. Scientists in their numbers have deemed it fit to contemplate nonlinear science as the most significant frontier for the fundamental comprehension of nature. Some of these models include a generalised system of three-dimensional variable-coefficient modified Kadomtsev–Petviashvili-Burgers-type equations in Gao's research [1], which has been examined in the present study. Adeyemo et al.'s research [2] studies the generalised advection-diffusion equation, which is a NLPDE in fluid mechanics, characterising the motion of buoyancy-propelled plumes in a bent-on absorptive medium. Moreover, in the study of Khalique and Adeyemo [3], a generalised Korteweg-de Vries-Zakharov-Kuznetsov equation was studied. This equation delineates mixtures of warm adiabatic fluid and hot isothermal fluid, as well as cold immobile background species applicable in fluid dynamics. The modified and generalised Zakharov-Kuznetsov model, which recounts the ion-acoustic drift solitary waves existing in a magnetoplasma with electron-positron-ion that are found in the primordial universe, was investigated in Du et al.'s study [4]. This equation was engaged in modelling ion-acoustic, dust-magneto-acoustic, quantum-dust-ion-acoustic and/or dust-ion-acoustic waves in one of the cosmic or laboratory dusty plasmas. Moreover, in Zhang et al.'s study [5], the vector bright solitons, as well as their interaction characteristics in the coupled Fokas-Lenells system modelling the femtosecond optical pulses in a birefringent optical fibre, were examined. In addition, the Boussinesq-Burgers-type system of equations that delineates shallow-water waves appearing close to lakes or ocean beaches was studied in Gao et al.'s research [6]; the list goes on and on, as can be seen in the literature [7–20].

It is revealed that no general and well-structured technique existed in gaining various exact travelling wave solutions of NLPDEs. However, various sound and efficient techniques have arisen lately to secure a lasting solution to this seemingly neverending problem.

In consequence, we present some of these techniques as $exp(-\Phi(\eta))$-expansion technique [18], Painlev´e expansion [19], bifurcation technique [20], ansatz technique [21], homotopy perturbation technique [22], extended homoclinic test approach [23], mapping and extended mapping technique [17], tanh-coth approach [24], generalised unified technique [25], Adomian decomposition approach [26], Cole-Hopf transformation approach [27], B¨acklund transformation [28], F-expansion technique [29], rational expansion technique [30], tan-cot method [31], Lie symmetry analysis [32, 33], Hirota technique [34], extended simplest equation method [35], Darboux transformation [36], the G'-expansion technique [37], tanh-function technique [38], Kudryashov technique [39], sine-Gordon equation expansion technique [40] and exponential function technique [41], to name a few.

There are a vast number of partial differential equations (DEs) that explicate nonlinear wave motion. One of them is the Kadomtsev–Petviashvili equation (KP) (usually abbreviated as KP, although we use the acronym KPSH for Kadomtsev–Petviashvili equation in the present case) existing in the field of mathematical physics. Moreover, it has been well-established that investigating

Oke Davies Adeyemo Chaudry Masood Khalique

Optimal System Of 1-D Subalgebras and Conserved Quantities of a Nonlinear Wave Equation in Three Dimensions Arising in Engineering Physics

diverse nonlinear phenomena in studying nonlinear waves is significant.

There are various versions of KPSH studied by many researchers. One among these is the Kadomtsev–Petviashvili equation in three dimensions, given as [42]:

$$(u_t + 6uu_x + u_{xxx})_x \pm 3u_{yy} \pm 3u_{zz} = 0 \qquad (1.1)$$

This equation can be traced back to the classic work carried out in 1970 by the Soviet physicists Kadomtsev and Petviashvili [43]. Eq. (1.1) models waves involved in a situation whereby water wavelength and water depth ratio is very small in the context of nonlinear restoring forces that are insubstantial. Besides, it is ascertained to be a generalised version of the Korteweg-de Vries (KdV) – an equation that was named after two Dutch mathematicians, namely Korteweg and De Vries [44]. On the analysis of Eq. (1.1), uux delineates the nonlinearity part of the wave equation and the last two terms portray diffractive divergence, while the highest term depicts weak dispersion [45]. The "±" sign attached to the last two terms relates to the positive or negative magnitude of dispersion. Since then, a good number of researchers have investigated Eq. (1.1) [e.g. 46–51]. Diverse studies carried out on the equation ranged from the achievement of Painlev´e analysis [48], construction of their closed-form multiple wave solutions [49] and the establishment of the stability property of their soliton [50] to the decision of their integrability features [51].

The (3+1)-dimensional generalised KPSH equation that reads [52]:

$$u_{tx} + u_{ty} + 3u_x u_{xy} + 3u_{xx} u_y + u_{xxxy} - u_{zz} = 0, \qquad (1.2)$$

was examined by the authors using Plu¨cker relation for determinants to gain one Wronskian solution to it. In addition, the Jacobi identity for determinants in the same work was implored to secure a Grammian solution. Moreover, multiple solitons as well as multiple singular solitons were also achieved for Eq. (1.2) in Wazwaz's research [53] by utilising a simplified structure of Hirota's technique. The investigations conducted in Wazwaz's research [53] revealed the prevalence of a contrast between their results and those gained in Ma et al.'s study [52] with regard to spatial variable z. Later, in the research of Wazwaz and El-Tantawy [54], a new form of the (3 + 1)-dimensional generalised KPSH Eq. (1.2) was introduced with the addition of utz, thus yielding

$$u_{tx} + u_{ty} + u_{tz} + 3u_x u_{xy} + 3u_{xx} u_y + u_{xxxy} - u_{zz} = 0. \ (1.3)$$

In their investigation, Wazwaz and El-Tantawy [54] made known the fact that the new term added significantly impacted the dispersion relations. Further, they implored Hirota's direct approach to decide multiple soliton solutions of the equation. Besides, Eq. (1.3) was studied in Liu et al.'s research [55], where its analytic solutions were achieved via Hirota's bilinear technique as well as an extended homoclinic test approach.

We contemplate a two-dimensional Kadomtsev–Petviashvili equation, expressed as [56, 57]:

$$u_{tx} - 6u^2 - 6uu_{xx} + u_{xxxx} + 3u_{yy} = 0. \qquad (1.4)$$

This version of the Kadomtsev–Petviashvili equation delineates the evolution of nonlinear together with long waves, possessive of small amplitude that slowly depends on its transverse coordinate. In deriving a completely integrable Eq. (1.4), the restriction that the waves be strictly one-dimensional was relaxed by Kadomtsev and Petviashvili [56, 58]. Besides, Eq. (1.4) delineates

the evolution of shallow-water waves given in terms of a quasi-one-dimensional, especially in the presence of negligible surface tension and viscose effect.

Eq. (1.4) has been invoked in modelling diverse natural occurrences ranging from tsunami wave that travels in a non-homogeneous domain, emerging at the ocean base, to the study of water waves [59]. Moreover, it also surfaced in the analysis of nonlinear ion-acoustic waves existent in a magnetised dusty plasma [60]. A variety of research output for Eq. (1.4) has been achieved over the past few years. Resultantly, travelling wave solutions in the studies of Borhanifar et al. [61] and Khan and Akbar [62] and rogue wave, as well as a pair of resonance stripe solitons in Zhang et al.'s study [63], have been achieved for Eq. (1.4). Khalique [64] carried out symmetry reductions of the equation and also derived its conserved currents. In Zhao and Ma [65], the Hirota bilinear structure of Eq. (1.4) was implored in gaining mixed lump-kink solutions via Maple software. Further, rational lump solutions alongside line soliton pairs were established for Eq. (1.4) by engaging exponential alongside positive quadratic functions [66].

In this work, we seek to investigate conservation laws of the Kadomtsev–Petviashvili-like equation in three dimensions, which we abbreviated as 3D-extKPLEq and expressed as [67].

$$u_{tx} + \tfrac{3}{2}u^3 u_x + \tfrac{3}{2}u^2 u_{xx} + 3uu_x^2 + 3u_x u_{xx} + u_{yy} + u_{zz} = 0. \qquad (1.5)$$

Eq. (1.5) was introduced as an extended Kadomtsev–Petviashvili-like equation through the use of a generalised bilinear DE. In their investigation, the bilinear representations in the Hirota sense were engaged by the authors alongside a certain transformation to derive Eq. (1.5). Moreover, based on generalised bilinear equation alongside Bell polynomial theories [68], the authors achieved 18 classes of rational solutions Eq. (1.5) through symbolic computation. Besides, Adeyemo and Khalique [69], in consonance with Lie symmetry reduction, utilised Kudryashov's technique to secure some closed-form solutions of Eq. (1.5). They also achieved a power series solution of the equation. Furthermore, Adeyemo and Khalique [70] went ahead to carry out a more detailed reduction process where various group-invariant solutions associated with the equation were calculated through the use of an optimal system of subalgebras. In consequence, various solutions that are noteworthy were obtained in the process.

However, this research work examines 3D-extKPLEq (1.5) explicitly through the use of the optimal system of subalgebras obtained from the Lie group technique to achieve various new conserved quantities of the equation. In plain terms, we state categorically that the work explicated in this study reveals a copious Lie group analysis of Eq. (1.5) where an optimal system is computed to obtain results, and for this reason the approach adopted in the present study may be adjudged novel. Thus, we organise the rest of this article in the following manner. In Section 2, we outline the methodical way of securing the Lie point symmetries via Lie group analysis of Eq. (1.5). We further calculate the Lie group transformation associated with the Lie point symmetries. Section 3 purveys the detailed steps taken in the construction of an optimal system of subalgebras using the computed symmetries. Section 4 furnishes us with the conservation laws of 3D-extKPLEq (1.5) by invoking Ibragimov's conserved vectors theorem via the associated formal Lagrangian. In addition, the applications of the obtained results in physical sciences are outlined. Later, the concluding remarks follow.

2. LIE GROUP ANALYSIS OF 3D-extKPLEq (1.5)

This section presents a systematic computation of the classical Lie symmetries of 3D-extKPLEq (1.5), which shall be used in the construction of an optimal system of one-dimensional Lie subalgebra. This, in turn, occasions the copious construction of conserved vectors related to the equation that is under study.

2.1 Determination of Lie point symmetries of Eq. (1.5)

The crucial step involved in the Lie symmetry technique [32, 33] is to determine the symmetry of NLPDEs. Thus, this subsection gives a detailed way of obtaining the infinitesimal generators of symmetries as well as geometric vector fields for the 3D-extKPLEq (1.5). Now, we examine an infinitesimal generator of Eq. (1.5) structured as

$$Q = \xi^1 \frac{\partial}{\partial t} + \xi^2 \frac{\partial}{\partial x} + \xi^3 \frac{\partial}{\partial y} + \xi^4 \frac{\partial}{\partial z} + \vartheta \frac{\partial}{\partial u},$$

with the coefficient functions ($\xi 1$, $\xi 2$, $\xi 3$, $\xi 4$, ϑ), all depending on (t, x, y, z, u).

Theorem 2.1 Let vector Q be the infinitesimal generators of the classical Lie point symmetry group of 3D-extKPLEq (1.5) where ξ^i, $i = 1,2,3,4$ and ϑ are smooth functions of (t, x, y, z, u); then, we generate solutions that are of the form [69, 70]:

$$\left.\begin{array}{l} \xi^1 = c_1 + \frac{3c_6 t}{2}, \xi^2 = \frac{1}{2}(2c_2 + c_6 x - c_4 y - c_8 z), \\ \xi^3 = c_3 + c_4 t + c_6 y - c_7 z, \\ \xi^4 = c_5 + c_8 t + c_7 y + c_6 z, \vartheta = -\frac{c_6 u}{2}. \end{array}\right\} \quad (2.6)$$

with $c_i s, \forall i = 1,2,3,4,5,7$ regarded as arbitrary constants of solution.

Proof Vector Q generates all the classical Lie point symmetries of Eq. (1.5) if the symmetry invariant condition given as

$$pr^{(2)}Q \begin{bmatrix} u_{tx} + \frac{3}{2}u^3 u_x + \frac{3}{2}u^2 u_{xx} \\ +3uu_x^2 + 3u_x u_{xx} + u_{yy} + u_{zz} \end{bmatrix} = 0, \quad (2.7)$$

anytime.

$$u_{tx} + \frac{3}{2}u^3 u_x + \frac{3}{2}u^2 u_{xx} + 3uu_x^2 + 3u_x u_{xx} + u_{yy} + u_{zz} = 0$$

holds in which $pr^{(2)}Q$ stands for the second prolongation of vector Q, and it is expressed as

$$pr^{(2)}Q = Q + \eta^t \partial_{u_t} + \eta^x \partial_{u_x} + \eta^{tx} \partial_{u_{tx}} + \eta^{xx} \partial_{u_{xx}} + \eta^{yy} \partial_{u_{yy}} + \eta^{zz} \partial_{u_{zz}}, \quad (2.8)$$

representing the coefficient functions in pr(2)Q and the total derivatives Di in Eq. (2.9), given too in general form as

$$\eta^i = D_i(\vartheta) - u_j D_i(\xi^j), \\ \eta^{ij} = D_j(\eta^i) - u_{ik}D_j(\xi^k), ijk = 1,2,3,4, \quad (2.9)$$

representing the coefficient functions in $pr^{(2)}Q$ and the total derivatives D_i in Eq. (2.9), given too in general form as

$$D_i = \frac{\partial}{\partial x^i} + u_i \frac{\partial}{\partial u} + u_{ij} \frac{\partial}{\partial u_j} + \cdots,$$

which can also be used for D_j. Thus, inserting the expanded form of relations Eq. (2.9) together with Eq. (2.8) into Eq. (2.7) gives a polynomial equation comprising diverse derivatives of u(t,

x, y, z) whose coefficients also include certain derivatives with regards to ξ^1, ξ^2, ξ^3, ξ^4 and ϑ. Equating the individual coefficients to zero, one can secure the complete set of determining equations:

$$\vartheta_{xu} = 0, \quad \xi_x^4 = 0, \quad \xi_x^3 = 0, \quad \xi_x^1 = 0, \quad \xi_y^1 = 0,$$
$$\xi_z^1 = 0, \quad \vartheta_{uu} = 0, \xi_u^4 = 0, n\xi_u^3 = 0,$$
$$\xi_u^2 = 0, \quad \xi_u^1 = 0, \quad \xi_z^3 + \xi_y^4 = 0,$$
$$2\xi_z^2 + \xi_t^4 = 0, \quad 2\xi_y^2 + \xi_t^3 = 0,$$
$$\xi_{xx}^2 - u\xi_x^2 - \vartheta = 0, \quad \vartheta_u - 2\xi_x^2 + \xi_t^1 = 0,$$
$$2\vartheta_{yu} + \xi_{yz}^4 - \xi_{yy}^3 = 0$$
$$2\xi_y^3 - \xi_x^2 - \xi_t^1 = 0, \quad 2\xi_z^4 - \xi_x^2 - \xi_t^1 = 0,$$
$$2\vartheta_{zu} - \xi_{zz}^4 - \xi_{yy}^4 = 0,$$
$$3\xi_x^2 u^2 - 3\xi_t^1 u^2 - 6\vartheta u - 6\vartheta_x + 2\xi_t^2 = 0,$$
$$3\vartheta_x u^3 + 3\vartheta_{xx} u^2 + 2\vartheta_{zz} + 2\vartheta_{yy} + 2\vartheta_{tx} = 0,$$
$$3\xi_t^1 u^3 + 9\vartheta u^2 - 3\xi_{tx}^1 u^2 + 6\vartheta_x u + 2\vartheta_{tu} + \xi_{tz}^4 + \xi_{ty}^3 = 0.$$

Thus, solving the system of equations via computer package, we arrive at the solutions given in Eq. (2.6) and so ends the proof of Theorem 2.1. In addition, Eq. (2.6) furnishes eight classical symmetries of 3D-extKPLEq (1.5) [69]. Therefore, we give a corollary:

Corollary 2.1 The classical Lie point infinitesimal projectable symmetries of Eq. (1.5) are computed as

$$\left.\begin{array}{l} Q_1 = \frac{\partial}{\partial t}, \quad Q_2 = \frac{\partial}{\partial x}, \quad Q_3 = \frac{\partial}{\partial y}, \\ Q_4 = \frac{\partial}{\partial z}, Q_5 = y\frac{\partial}{\partial z} - z\frac{\partial}{\partial y}, \\ Q_6 = 2t\frac{\partial}{\partial z} - z\frac{\partial}{\partial x}, Q_7 = 2t\frac{\partial}{\partial y} - y\frac{\partial}{\partial x}, \\ Q_8 = 3t\frac{\partial}{\partial t} + x\frac{\partial}{\partial x} + 2y\frac{\partial}{\partial y} + 2z\frac{\partial}{\partial z} - u\frac{\partial}{\partial u}. \end{array}\right\} \quad (2.11)$$

Hence, 3D-extKPLEq (1.5) admits an eight-dimensional vector space, which constitutes its Lie algebra G and whose basis is structured as $\{Q_1, Q_2, Q_3, \ldots, Q_8\}$.

2.2 Calculation of Lie group transformations of Eq. (1.5)

We contemplate the exponentiation of the vector fields Eq. (2.11) by computing the flow or one parameter group generated by Eq. (2.11) via the Lie equations [32, 33, 71]

$$\left.\begin{array}{l} \frac{d\bar{t}}{d\varepsilon} = \xi^1(\bar{t}, \bar{x}, \bar{y}, \bar{z}, \bar{u}), \quad \bar{t}|_{\dot{o}=0} = t, \\ \frac{d\bar{x}}{d\varepsilon} = \xi^2(\bar{t}, \bar{x}, \bar{y}, \bar{z}, \bar{u}), \quad \bar{x}|_{\dot{o}=0} = x, \\ \frac{d\bar{y}}{d\varepsilon} = \xi^3(\bar{t}, \bar{x}, \bar{y}, \bar{z}, \bar{u}), \quad \bar{y}|_{\dot{o}=0} = y, \\ \frac{d\bar{z}}{d\varepsilon} = \xi^4(\bar{t}, \bar{x}, \bar{y}, \bar{z}, \bar{u}), \quad \bar{z}|_{\dot{o}=0} = z, \\ \frac{d\bar{u}}{d\varepsilon} = (\bar{t}, \bar{x}, \bar{y}, \bar{z}, \bar{u}), \quad \bar{u}|_{\dot{o}=0} = u. \end{array}\right\}$$

Let us take, for instance, the rotation generator Q6, given as

$$Q_5 = y\frac{\partial}{\partial z} - z\frac{\partial}{\partial y}. \quad (2.12)$$

The associated Lie equations are:

$$\frac{d\bar{z}}{d\varepsilon} = \bar{y}, \quad (2.13)$$

$$\frac{d\bar{y}}{d\varepsilon} = -\bar{z}, \quad (2.14)$$

with the initial criteria $(t\dot{Z}, x\dot{Z}, y\dot{Z}, z\dot{Z}, u\dot{Z})|_{\epsilon=0} \to (t, x, y, z, u)$.
We first notice that

$$\frac{d^2\bar{z}}{d\varepsilon^2} = \frac{d\bar{y}}{d\varepsilon} = -\bar{z}. \tag{2.15}$$

Thus, we have a system of ordinary differential equations (ODEs). Now, from Eq. (2.15), we consider

$$\frac{d^2\bar{z}}{d\varepsilon^2} = -\bar{z}. \tag{2.16}$$

Solving the second-order ODE in Eq. (2.15) gives the trigonometric relation

$$\bar{z} = A\cos(\varepsilon) + B\sin(\varepsilon). \tag{2.17}$$

Applying the initial condition to Eq. (2.17) gives $z = A$. So, Eq. (2.17) becomes

$$\bar{z} = z\cos(\varepsilon) + B\sin(\varepsilon). \tag{2.18}$$

Now, solving the first-order ODE Eq. (2.15) in the same vein, we achieve

$$\overline{y} = B\cos(\varepsilon) - A\sin(\varepsilon) + C_0, \tag{2.19}$$

Application of the initial condition to Eq. (2.19) and taking integration constant C0 = 0 yields y = B. Therefore, Eqs (2.18) and (2.19) become, respectively,

$$\bar{z} = z\cos(\varepsilon) + y\sin(\varepsilon), \bar{y} = y\cos(\varepsilon) - z\sin(\varepsilon). \tag{2.20}$$

Hence, following the same procedure for other generators in Eq. (2.11), we achieve one parameter transformation group of 3D-extKPLEq (1.5). Thus, we arrive at a theorem to that effect, viz.:

Theorem 2.2 Let $T^i(t, x, y, z, u), i = 1,2,3,\cdots 8$ be the transformations group of one parameter $_\varepsilon$ generated by vectors $Q_1, Q_2, Q_3\ldots, Q_8$ in Eq. (2.11); then, for each of the vectors, we have accordingly

$$
\left.\begin{aligned}
&T^1_\varepsilon: (\tilde{t}, \tilde{x}, \tilde{y}, \tilde{z}, \tilde{u}) \to (t + \varepsilon_1, x, y, z, u),\\
&T^2_\varepsilon: (\tilde{t}, \tilde{x}, \tilde{y}, \tilde{z}, \tilde{u}) \to (t, x + \varepsilon_2, y, z, u),\\
&T^3_\varepsilon: (\tilde{t}, \tilde{x}, \tilde{y}, \tilde{z}, \tilde{u}) \to (t, x, y + \varepsilon_3, z, u),\\
&T^4_\varepsilon: (\tilde{t}, \tilde{x}, \tilde{y}, \tilde{z}, \tilde{u}) \to (t, x, y, z + \varepsilon_4, u),\\
&T^5_\varepsilon: (\tilde{t}, \tilde{x}, \tilde{y}, \tilde{z}, \tilde{u}) \to (t, x, y\cos(\varepsilon)\\
&\quad -z\sin(ò), z\cos(\varepsilon) + y\sin(\varepsilon), u),\\
&T^6_\varepsilon: (\tilde{t}, \tilde{x}, \tilde{y}, \tilde{z}, \tilde{u}) \to (t, x - t\varepsilon_6^2 - z\varepsilon_6, y, z + 2\varepsilon_6 t, u),\\
&T^7_\varepsilon: (\tilde{t}, \tilde{x}, \tilde{y}, \tilde{z}, \tilde{u}) \to (t, x - t\varepsilon_7^2 - y\varepsilon_7, y + 2\varepsilon_7 t, z, u),\\
&T^8_\varepsilon: (\tilde{t}, \tilde{x}, \tilde{y}, \tilde{z}, \tilde{u}) \to (te^{3\varepsilon_7}, xe^{ò_7}, ye^{2\varepsilon_7}, ze^{2\varepsilon_7}, ue^{-\varepsilon_7}),
\end{aligned}\right\}
$$

where $\varepsilon \in R$ is regarded as the group parameter.

Theorem 2.3 Hence, supposing that $u(t, x, y, z) = \Theta(t, x, y, z)$ satisfies 3D-extKPLEq (1.5), in the same vein, the functions given in the structure

$$
\left.\begin{aligned}
&u^1(t, x, y, z) = \Theta(t - \varepsilon_1, x, y, z),\\
&u^2(t, x, y, z) = \Theta(t, x - \varepsilon_2, y, z),\\
&u^3(t, x, y, z) = \Theta(t, x, y - \varepsilon_3,\\
&\quad z, u), u^4(t, x, y, z) = \Theta(t, x, y, z - \varepsilon_4),\\
&u^5(t, x, y, z) = \Theta(t, x, y\cos(\varepsilon)\\
&\quad +z\sin(ò), z\cos(\varepsilon) - y\sin(\varepsilon)),\\
&u^6(t, x, y, z) = e^{\varepsilon_6}\Theta(t, x + t\varepsilon_6^2 + z\varepsilon_6, y, z - 2\varepsilon_6 t),\\
&u^7(t, x, y, z) = \Theta(t, x + t\varepsilon_7^2 + y\varepsilon_7, y - 2\varepsilon_7 t, z),\\
&u^8(t, x, y, z) = e^{\varepsilon_7}\Theta(te^{3\varepsilon_7}, xe^{\varepsilon_7}, ye^{2\varepsilon_7}, ze^{2\varepsilon_7}),
\end{aligned}\right\}
$$

will do, where $u^i(t, x, y, z) = T^ò_i \cdot \Theta(t, x, y, z)$,

$i = 1,2,3,\ldots,8$ with $\epsilon \ll 1$ regarded as any positive real number.

3. OPTIMAL SYSTEM

Let us suppose that G is a Lie group with gl regarded as its Lie algebra. Then, for any element $H \in G$, we have an inner automorphism defined as Ha −→ HHaH−1 on the Lie group G. In addition, this automorphism of G influences an automorphism of Lie algebra gl. Therefore, the group of all these automorphisms constitutes a Lie group that is referred to as the adjoint group and we denote it as G^A. Now, for any arbitrary vectors $P, Q \in gl$, we can define $AdP(Q): Q \to [P, Q]$, which is a linear map and also an automorphism of gl referred to as the inner derivation of gl. Moreover, for all $P, Q \in gl$, the algebra of all inner derivations $AdP(Q)$ alongside Lie bracket $[AdP, AdQ] = Ad[P, Q]$ is regarded as a Lie algebra gl^A commonly referred to as the adjoint algebra of gl whereas gl^A is the Lie algebra of G^A. Therefore, two algebras in gl are said to be conjugate if there exists a transformation G^A that takes one subalgebra into the other. Hence, the collection of all pairwise non-conjugate q-dimensional subalgebras forms the optimal system of subalgebras of order q.

3.1 Optimal system of Lie subalgebra of 3D-extKPLEq (1.5)

In this subsection, the construction of optimal system one-dimensional subalgebras can be carried out by imploring a global matrix of the adjoint transformations as recommended by Ovsiannikov [32]. This task tends to help in determining a list (which we refer to as an optimal system) of conjugacy inequivalent subalgebras possessing the property that stipulates that any other subalgebra is equivalent to a unique list under some element of the adjoint representation. Consequently, we construct an optimal system of Lie subalgebra of 3D-extKPLEq (1.5). We begin with the adjoint action presented via the Lie series [33]

$$Ad(\exp(\varepsilon Q_i))Q_j = \sum_{n=0}^{\infty} \frac{\varepsilon^n}{n!}(adQ_i)(Q_j). \tag{3.21}$$

The commutator relations of the infinitesimal generators for 3D-extKPLEq (1.5) in Eq. (2.11) with the $(i; j)th$ entry in designating the Lie bracket $[Q_i, Q_j] = Q_iQ_j - Q_jQ_i$. Thus, we observe that Tab. 1 has zero elements in the diagonal, and it is thus said to be skew-symmetric. Besides, the generators $Q_1, Q_2, Q_3, \ldots, Q_8$ are linearly independent.

Tab. 1. Commutator table of the Lie algebra of 3D-extKPLEq (1.5) $[Q_i, Q_j]$

	Q_1	Q_2	Q_3	Q_4	Q_5	Q_6	Q_7	Q_8
Q_1	0	0	0	0	0	0	0	Q_1
Q_2	0	0	0	0	Q_3	0	$-Q_1$	$2Q_2$
Q_3	0	0	0	0	$-Q_2$	$-Q_1$	0	$2Q_3$
Q_4	0	0	0	0	0	$2Q_3$	$2Q_2$	$3Q_4$
Q_5	0	$-Q_3$	Q_2	0	0	Q_7	$-Q_6$	0
Q_6	0	0	Q_1	$-2Q_3$	Q_7	0	0	$-Q_6$
Q_7	0	Q_1	0	$-2Q_2$	$-Q_6$	0	0	$-Q_7$
Q_8	$-Q_1$	$-2Q_2$	$-2Q_3$	$-3Q_4$	0	Q_6	Q_7	0

From the commutator relations existent between vectors Eq. (2.11) and given in Tab. 1, these infinitesimal generators in Eq. (2.11) can be purveyed as a linear combination of Qi as

$$Q = \alpha_1 Q_1 + \alpha_2 Q_2 + \alpha_3 Q_3 + \alpha_4 Q_4 + \alpha_5 Q_5 \\ + \alpha_6 Q_6 + \alpha_7 Q_7 + \alpha_8 Q_8. \tag{3.22}$$

Next, we achieve the adjoint representation relations, as revealed in Tab. 2. Engaging the Olver approach [33], one can generate the adjoint representation of 3D-extKPLEq (1.5) via symbolic computation from the commutator relations with the aid of the secured vector fields.

3.1.1 Construction of general invariants

In order to achieve the optimal system of Lie algebra R^8, it is expedient to secure the invariants to aid the selection of the required representative elements. Using Tab. 1, one gains the needed matrix representations of Ad(Qi). In the foregoing, we will refer to Tab. 2 as follows, where

$\Delta_0 = Q_2\cos(\varepsilon_5) + Q_3\sin(\varepsilon_5), \Delta_1 = Q_3\cos(\varepsilon_5) - Q_2\sin(\varepsilon_5), \Delta_2 = Q_6\cos(\varepsilon_5) - Q_7\sin(\varepsilon_5), \Delta_3 = Q_6\sin(\varepsilon_5) + Q_7\cos(\varepsilon_5), \Delta_4 = Q_4 + 2\varepsilon_6 Q_3 - \varepsilon_6^2 Q_1,$

$\Delta_5 = Q_4 + 2\varepsilon_7 Q_2 - \varepsilon_7^2 Q_1,$
$\Delta_6 = Q_2 - \varepsilon_7 Q_1,$ and

$\Delta_7 = Q_3 - \varepsilon_6 Q_1.$

$$Ad_{\exp(\grave{o}Q)}(Q) = e^{-\varepsilon Q}Qe^{\varepsilon Q} \\ = \boxed{?}Q - \varepsilon[Q,Q] + \frac{1}{2!}\varepsilon^2[Q,[Q,Q]] - \cdots \\ = \boxed{?}(a_1 Q_1 + \cdots + a_n Q_n) - \varepsilon[b_1 Q_1 + \cdots \\ + b_n Q_n, a_1 Q_1 + \cdots + a_n Q_n] + O(\varepsilon^2) \\ = (a_1 Q_1 + \cdots + a_n Q_n) \\ - \grave{o}(\Theta_1 Q_1 + \cdots + \Theta_n Q_n) + O(\varepsilon^2), \tag{3.23}$$

with function $\Theta_i \equiv \Theta_i(\alpha_1,\ldots,\alpha_8,\beta_1,\ldots,\beta_8)$. We observe that the values of $\Theta_i, i = 1,\ldots,8$ can be achieved via the commutator table. On inserting the partial sums $Q = \sum_i^8 a_i Q_i$ as well as $Q = \sum_j^8 b_j Q_j$ in Eq. (3.23), we obtain Θ_i as

$$\Theta_1 = -\alpha_1\beta_8 + \alpha_2\beta_7 + \alpha_3\beta_6 - \alpha_6\beta_3 - \alpha_7\beta_2 + \alpha_8\beta_1, \\ \Theta_2 = -2\alpha_2\beta_8 + \alpha_3\beta_5 - 2\alpha_4\beta_7 - \alpha_5\beta_3 + 2\alpha_7\beta_4 + 2\alpha_8\beta_2, \\ \Theta_3 = -\alpha_2 b_5 - 2\alpha_3\beta_8 - 2\alpha_4\beta_6 + \alpha_5\beta_2 + 2\alpha_6\beta_4 + 2\alpha_8\beta_3, \\ \Theta_4 = -3\alpha_4\beta_8 + 3\alpha_8\beta_4, \Theta_5 = 0, \Theta_6 = \alpha_5\beta_7 + \alpha_6\beta_8 \\ -\alpha_7\beta_5 - \alpha_8\beta_6, \\ \Theta_7 = -\alpha_5\beta_6 + \alpha_6\beta_5 + \alpha_7\beta_8 - \alpha_8\beta_7, \Theta_8 = 0. \tag{3.24}$$

Tab. 2. Adjoint representation table of 3D-extKPLEq (1.5)

Ad	Q_1	Q_2	Q_3	Q_4	Q_5	Q_6	Q_7	Q_8
Q_1	Q_1	Q_2	Q_3	Q_4	Q_5	Q_6	Q_7	$Q_8 - \epsilon_1 Q_1$
Q_2	Q_1	Q_2	Q_3	Q_4	$Q_5 - \epsilon_2 Q_3$	Q_6	$Q_7 + \epsilon_2 Q_1$	$Q_8 - 2\epsilon_2 Q_2$
Q_3	Q_1	Q_2	Q_3	Q_4	$Q_5 + \epsilon_3 Q_2$	$Q_6 + \epsilon_3 Q_1$	Q_7	$Q_8 - 2\epsilon_3 Q_3$
Q_4	Q_1	Q_2	Q_3	Q_4	Q_5	$Q_6 - 2\epsilon_4 Q_3$	$Q_7 - 2\epsilon_4 Q_2$	$Q_8 - 3\epsilon_4 Q_4$
Q_5	Q_1	Δ_0	Δ_1	Q_4	Q_5	Δ_2	Δ_3	Q_8
Q_6	Q_1	Q_2	Δ_7	Δ_4	$Q_5 + \epsilon_6 Q_7$	Q_6	Q_7	$Q_8 + \epsilon_6 Q_6$
Q_7	Q_1	Δ_6	Q_3	Δ_5	$Q_5 - \epsilon_7 Q_6$	Q_6	Q_7	$Q_8 + \epsilon_7 Q_7$
Q_8	$e^{\epsilon_8}Q_1$	$e^{2\epsilon_8}Q_2$	$e^{2\epsilon_8}Q_3$	$e^{3\epsilon_8}Q_4$	Q_5	$e^{-\epsilon_8}Q_6$	$e^{-\epsilon_8}Q_7$	Q_8

Now, for any β_j, where $1 \le j \le 8$, it is required to have

$$0 = \Theta_1\frac{\partial\Phi}{\partial a_1} + \Theta_2\frac{\partial\Phi}{\partial a_2} + \Theta_3\frac{\partial\Phi}{\partial a_3} + \Theta_4\frac{\partial\Phi}{\partial a_4} + \Theta_5\frac{\partial\Phi}{\partial a_5} \\ + \Theta_6\frac{\partial\Phi}{\partial a_6} + \Theta_7\frac{\partial\Phi}{\partial a_7} + \Theta_8\frac{\partial\Phi}{\partial a_8}. \tag{3.25}$$

Thus, by equating the coefficients of all same powers of βj in Eq. (3.25), one achieves the needed eight DEs with regard to real-valued function invariant

$$\begin{aligned} b_1: \quad & a_8\frac{\partial\Phi}{\partial a_1} = 0, \\ b_2: \quad & -a_7\frac{\partial\Phi}{\partial a_1} + 2a_8\frac{\partial\Phi}{\partial a_2} + a_5\frac{\partial\Phi}{\partial a_3} = 0, \\ b_3: \quad & -a_6\frac{\partial\Phi}{\partial a_1} - a_5\frac{\partial\Phi}{\partial a_2} + 2a_8\frac{\partial\Phi}{\partial a_3} = 0, \\ b_4: \quad & 2a_7\frac{\partial\Phi}{\partial a_2} + 2a_6\frac{\partial\Phi}{\partial a_3} + 3a_8\frac{\partial\Phi}{\partial a_4} = 0, \\ b_5: \quad & a_3\frac{\partial\Phi}{\partial a_2} - a_2\frac{\partial\Phi}{\partial a_3} - a_7\frac{\partial\Phi}{\partial a_6} + a_6\frac{\partial\Phi}{\partial a_7} = 0, \\ b_6: \quad & a_3\frac{\partial\Phi}{\partial a_1} - 2a_4\frac{\partial\Phi}{\partial a_3} - a_8\frac{\partial\Phi}{\partial a_6} - a_5\frac{\partial\Phi}{\partial a_7} = 0, \\ b_7: \quad & a_2\frac{\partial\Phi}{\partial a_1} - 2a_4\frac{\partial\Phi}{\partial a_2} + a_5\frac{\partial\Phi}{\partial a_6} - a_8\frac{\partial\Phi}{\partial a_7} = 0, \\ b_8: \quad & -a_1\frac{\partial\Phi}{\partial a_1} - 2a_2\frac{\partial\Phi}{\partial a_2} - 2a_3\frac{\partial\Phi}{\partial a_3} - 3a_4\frac{\partial\Phi}{\partial a_4} \\ & + a_6\frac{\partial\Phi}{\partial a_6} + a_7\frac{\partial\Phi}{\partial a_7} = 0. \end{aligned} \tag{3.26}$$

On solving the system of equations displayed in Eq. (3.26), one secures the value of invariant Φ(α1, α2, α3, α4, α5, α6, α7, α8) = G(α5, α8), which is referred to as the general invariant function of Lie algebra R8. Here, function G is an arbitrary function depending on α5 and α8. In consequence, 3D-extKPLEq (1.5) has only two basic invariants.

3.1.2 Calculation of the adjoint matrix for Eq. (1.5)

Consider a linear map $F^\epsilon: h \mapsto h$ defined by $Q \mapsto Ad(exp(\varepsilon_i Q_i).Q)$ where $i = 1,2,3,\ldots,8$. The presentation of the matrix B_i^ε of $F_i^\varepsilon, i = 1,2,3,\ldots,8$ with regard to basis $\{Q_1, Q_2, Q_3, \ldots, Q_8\}$ [72] is given as:

$$B_1^{\varepsilon_1} = \begin{pmatrix} 1 & 0 & 0 & 0 & 0 & 0 & 0 & 0 \\ 0 & 1 & 0 & 0 & 0 & 0 & 0 & 0 \\ 0 & 0 & 1 & 0 & 0 & 0 & 0 & 0 \\ 0 & 0 & 0 & 1 & 0 & 0 & 0 & 0 \\ 0 & 0 & 0 & 0 & 1 & 0 & 0 & 0 \\ 0 & 0 & 0 & 0 & 0 & 1 & 0 & 0 \\ 0 & 0 & 0 & 0 & 0 & 0 & 1 & 0 \\ -\varepsilon_1 & 0 & 0 & 0 & 0 & 0 & 0 & 1 \end{pmatrix},$$

Oke Davies Adeyemo Chaudry Masood Khalique

DOI 10.2478/ama-2024-0022

Optimal System Of 1-D Subalgebras and Conserved Quantities of a Nonlinear Wave Equation in Three Dimensions Arising in Engineering Physics

$$B_2^{\varepsilon_2} = \begin{pmatrix} 1 & 0 & 0 & 0 & 0 & 0 & 0 & 0 \\ 0 & 1 & 0 & 0 & 0 & 0 & 0 & 0 \\ 0 & 0 & 1 & 0 & 0 & 0 & 0 & 0 \\ 0 & 0 & 0 & 1 & 0 & 0 & 0 & 0 \\ 0 & 0 & -\varepsilon_2 & 0 & 1 & 0 & 0 & 0 \\ 0 & 0 & 0 & 0 & 0 & 1 & 0 & 0 \\ \varepsilon_2 & 0 & 0 & 0 & 0 & 0 & 1 & 0 \\ 0 & -2\varepsilon_2 & 0 & 0 & 0 & 0 & 0 & 1 \end{pmatrix},$$

$$B_5^{\varepsilon_5} = \begin{pmatrix} 1 & 0 & 0 & 0 & 0 & 0 & 0 & 0 \\ 0 & \cos(\varepsilon_5) & \sin(\varepsilon_5) & 0 & 0 & 0 & 0 & 0 \\ 0 & -\sin(\varepsilon_5) & \cos(\varepsilon_5) & 0 & 0 & 0 & 0 & 0 \\ 0 & 0 & 0 & 1 & 0 & 0 & 0 & 0 \\ 0 & 0 & 0 & 0 & 1 & 0 & 0 & 0 \\ 0 & 0 & 0 & 0 & 0 & \cos(\varepsilon_5) & -\sin(\varepsilon_5) & 0 \\ 0 & 0 & 0 & 0 & 0 & \sin(\varepsilon_5) & \cos(\varepsilon_5) & 0 \\ 0 & 0 & 0 & 0 & 0 & 0 & 0 & 1 \end{pmatrix},$$

$$B_4^{\varepsilon_4} = \begin{pmatrix} 1 & 0 & 0 & 0 & 0 & 0 & 0 & 0 \\ 0 & 1 & 0 & 0 & 0 & 0 & 0 & 0 \\ 0 & 0 & 1 & 0 & 0 & 0 & 0 & 0 \\ 0 & 0 & 0 & 1 & 0 & 0 & 0 & 0 \\ 0 & 0 & 0 & 0 & 1 & 0 & 0 & 0 \\ 0 & 0 & -2\varepsilon_4 & 0 & 0 & 1 & 0 & 0 \\ 0 & -2\varepsilon_4 & 0 & 0 & 0 & 0 & 1 & 0 \\ 0 & 0 & 0 & -3\varepsilon_4 & 0 & 0 & 0 & 1 \end{pmatrix},$$

$$B_6^{\varepsilon_6} = \begin{pmatrix} 1 & 0 & 0 & 0 & 0 & 0 & 0 & 0 \\ 0 & 1 & 0 & 0 & 0 & 0 & 0 & 0 \\ -\varepsilon_6 & 0 & 1 & 0 & 0 & 0 & 0 & 0 \\ -\grave{o}_6^2 & 0 & 2\varepsilon_6 & 1 & 0 & 0 & 0 & 0 \\ 0 & 0 & 0 & 0 & 1 & 0 & \varepsilon_6 & 0 \\ 0 & 0 & 0 & 0 & 0 & 1 & 0 & 0 \\ 0 & 0 & 0 & 0 & 0 & 0 & 1 & 0 \\ 0 & 0 & 0 & 0 & 0 & \varepsilon_6 & 0 & 1 \end{pmatrix},$$

$$B_3^{\varepsilon_3} = \begin{pmatrix} 1 & 0 & 0 & 0 & 0 & 0 & 0 & 0 \\ 0 & 1 & 0 & 0 & 0 & 0 & 0 & 0 \\ 0 & 0 & 1 & 0 & 0 & 0 & 0 & 0 \\ 0 & 0 & 0 & 1 & 0 & 0 & 0 & 0 \\ 0 & \varepsilon_3 & 0 & 0 & 1 & 0 & 0 & 0 \\ \varepsilon_3 & 0 & 0 & 0 & 0 & 1 & 0 & 0 \\ 0 & 0 & 0 & 0 & 0 & 0 & 1 & 0 \\ 0 & 0 & -2\varepsilon_3 & 0 & 0 & 0 & 0 & 1 \end{pmatrix},$$

$$B_7^{\grave{o}_7} = \begin{pmatrix} 1 & 0 & 0 & 0 & 0 & 0 & 0 & 0 \\ -\varepsilon_7 & 1 & 0 & 0 & 0 & 0 & 0 & 0 \\ 0 & 0 & 1 & 0 & 0 & 0 & 0 & 0 \\ -\varepsilon_7^2 & 2\varepsilon_7 & 0 & 1 & 0 & 0 & 0 & 0 \\ 0 & 0 & 0 & 0 & 1 & -\varepsilon_7 & 0 & 0 \\ 0 & 0 & 0 & 0 & 0 & 1 & 0 & 0 \\ 0 & 0 & 0 & 0 & 0 & 0 & 1 & 0 \\ 0 & 0 & 0 & 0 & 0 & 0 & \varepsilon_7 & 1 \end{pmatrix},$$

$$B_8^{\varepsilon_8} = \begin{pmatrix} e^{\varepsilon_8} & 0 & 0 & 0 & 0 & 0 & 0 & 0 \\ 0 & e^{2v_8} & 0 & 0 & 0 & 0 & 0 & 0 \\ 0 & 0 & e^{2v_8} & 0 & 0 & 0 & 0 & 0 \\ 0 & 0 & 0 & e^{3\varepsilon_8} & 0 & 0 & 0 & 0 \\ 0 & 0 & 0 & 0 & 1 & 0 & 0 & 0 \\ 0 & 0 & 0 & 0 & 0 & e^{-\varepsilon_8} & 0 & 0 \\ 0 & 0 & 0 & 0 & 0 & 0 & e^{-\varepsilon_8} & 0 \\ 0 & 0 & 0 & 0 & 0 & 0 & 0 & 1 \end{pmatrix}.$$

Consequently, we obtained the global matrix associated with $B_i^{\grave{o}}$ of $F_i^{\varepsilon}, i = 1,2,3,\dots,8$

$$B^{\varepsilon} = \begin{pmatrix} e^{\varepsilon_8} & 0 & 0 & 0 & 0 & 0 & 0 & 0 \\ B_{21}^{\varepsilon} & e^{2\varepsilon_8}\cos(\varepsilon_5) & e^{2\varepsilon_8}\sin(\varepsilon_5) & 0 & 0 & 0 & 0 & 0 \\ B_{31}^{\varepsilon} & -e^{2\varepsilon_8}\sin(\varepsilon_5) & e^{2\varepsilon_8}\cos(\varepsilon_5) & 0 & 0 & 0 & 0 & 0 \\ B_{41}^{\varepsilon} & 2e^{2\varepsilon_8}\varepsilon_7 & 2e^{2\varepsilon_8}\varepsilon_6 & e^{3\varepsilon_8} & 0 & 0 & 0 & 0 \\ B_{51}^{\varepsilon} & B_{52}^{\varepsilon} & B_{53}^{\varepsilon} & 0 & 1 & -e^{-\varepsilon_8}\varepsilon_7 & e^{-\varepsilon_8}\varepsilon_6 & 0 \\ B_{61}^{\varepsilon} & B_{62}^{\varepsilon} & B_{63}^{\varepsilon} & 0 & 0 & e^{-\varepsilon_8}\cos(\varepsilon_5) & -e^{-\varepsilon_8}\sin(\varepsilon_5) & 0 \\ B_{71}^{\varepsilon} & B_{72}^{\varepsilon} & B_{73}^{\varepsilon} & 0 & 0 & e^{-\varepsilon_8}\sin(\grave{o}_5) & e^{-\varepsilon_8}\cos(\varepsilon_5) & 0 \\ B_{81}^{\varepsilon} & B_{82}^{\varepsilon} & B_{83}^{\varepsilon} & -3e^{3\varepsilon_8}\varepsilon_4 & 0 & e^{-\varepsilon_8}\varepsilon_6 & e^{-\varepsilon_8}\varepsilon_7 & 1 \end{pmatrix}$$

where

$B_{21}^{\varepsilon} = e^{\varepsilon_8}(-\sin(\varepsilon_5)\varepsilon_6 - \cos(\varepsilon_5)\varepsilon_7),$

$B_{31}^{\varepsilon} = e^{\varepsilon_8}(\sin(\varepsilon_5)v_7 - \cos(\varepsilon_5)\varepsilon_6)$

$B_{51}^{\varepsilon} = e^{\varepsilon_8}\begin{pmatrix}(\cos(\varepsilon_5)\varepsilon_2 - \sin(\varepsilon_5)\varepsilon_3)\varepsilon_6 \\ -(\sin(\varepsilon_5)\varepsilon_2 + \cos(\varepsilon_5)\varepsilon_3)\varepsilon_7\end{pmatrix}$

$B_{61}^{\varepsilon} = e^{\varepsilon_8}(\varepsilon_3 + 2\cos(\varepsilon_5)\varepsilon_4\varepsilon_6 - 2\sin(\varepsilon_5)\varepsilon_4\varepsilon_7),$

$B_{71}^{\varepsilon} = e^{\varepsilon_8}(\varepsilon_2 + 2\sin(\varepsilon_5)\varepsilon_4\varepsilon_6 + 2\cos(\varepsilon_5)\varepsilon_4\varepsilon_7)$

$B_{81}^{\varepsilon} = e^{\varepsilon_8}\begin{pmatrix}3\varepsilon_4\varepsilon_6^2 - \begin{pmatrix}-2\sin(\varepsilon_5)\varepsilon_2 \\ -2\cos(\varepsilon_5)\varepsilon_3\end{pmatrix}\varepsilon_6 + 3\varepsilon_4\varepsilon_7^2 \\ -\grave{o}_1 - \begin{pmatrix}2\sin(\varepsilon_5)\varepsilon_3 \\ -2\cos(\varepsilon_5)\varepsilon_2\end{pmatrix}\varepsilon_7\end{pmatrix},$

$B_{52}^{\varepsilon} = e^{2\varepsilon_8}(\sin(\varepsilon_5)\varepsilon_2 + \cos(\varepsilon_5)\varepsilon_3),$

$B_{82}^{\varepsilon} = e^{2\varepsilon_8}(-2\cos(\varepsilon_5)\varepsilon_2 + 2\sin(\varepsilon_5)\varepsilon_3 - 6\varepsilon_4\varepsilon_7),$

$B_{53}^{\varepsilon} = e^{2\varepsilon_8}(\sin(\varepsilon_5)\varepsilon_3 - \cos(\varepsilon_5)\varepsilon_2),$

$B_{83}^{\varepsilon} = e^{2\varepsilon_8}(-2\sin(\varepsilon_5)\varepsilon_2 - 2\cos(\varepsilon_5)\varepsilon_3 - 6\varepsilon_4\varepsilon_6),$

$B_{62}^{\varepsilon} = 2e^{2\varepsilon_8}\sin(\varepsilon_5)\varepsilon_4,$

$B_{72}^{\varepsilon} = -2e^{2\varepsilon_8}\cos(\varepsilon_5)\varepsilon_4, B_{63}^{\varepsilon} = -2e^{2\varepsilon_8}\cos(\varepsilon_5)\varepsilon_4,$

$B_{73}^{\varepsilon} = -2e^{2\varepsilon_8}\sin(\varepsilon_5)\varepsilon_4, B_{41}^{\varepsilon} = -e^{\varepsilon_8}(\varepsilon_6^2 + \varepsilon_7^2).$

3.1.3 Adjoint transformation equation

Here, we compute the adjoint transformation equation associated to 3D-extKPLEq (1.5). We present the adjoint transformation via the relation

$$(\tilde{a}_1, \tilde{a}_2, \cdots \tilde{a}_7, \tilde{a}_8) = (\alpha_1, \alpha_2, \cdots, \alpha_7, \alpha_8)B^\varepsilon, \qquad (3.27)$$

where

$Q = \sum_i^8 a_i Q_i$ and $Q = \sum_i^8 a_i Q_i$ are equivalent under the adjoint action and B^ε represents the universal adjoint matrix. Thus we have

$$\tilde{a}_1 = a_1 e^{\varepsilon_8} - a_4 e^{\varepsilon_8}(\varepsilon_6^2 + \varepsilon_7^2) - a_2 e^{\varepsilon_8}\begin{pmatrix}\varepsilon_6(\sin(\varepsilon_5)) \\ +\varepsilon_7\cos(\varepsilon_5)\end{pmatrix}$$

$$+a_3 e^{\varepsilon_8}(\varepsilon_7\sin(\varepsilon_5) - \varepsilon_6\cos(\varepsilon_5))$$

$$+a_5 e^{\grave{\partial}_8}\begin{pmatrix}\varepsilon_6(\varepsilon_2\cos(\varepsilon_5) - \varepsilon_3\sin(\varepsilon_5)) \\ -\varepsilon_7(\varepsilon_2\sin(\varepsilon_5) + \varepsilon_3\cos(\varepsilon_5))\end{pmatrix}$$

$$+a_7 e^{\varepsilon_8}(\varepsilon_2 + 2\varepsilon_4\varepsilon_6\sin(\varepsilon_5) + 2\varepsilon_4\varepsilon_7\cos(\varepsilon_5))$$

$$+a_6 e^{\varepsilon_8}(\varepsilon_3 - 2\varepsilon_4\varepsilon_7\sin(\varepsilon_5) + 2\varepsilon_4\varepsilon_6\cos(\varepsilon_5))$$

$$+a_8 e^{\varepsilon_8}(3\varepsilon_4\varepsilon_6^2 + 3\varepsilon_4\varepsilon_7^2 - \varepsilon_1 + \varepsilon_6 A - \varepsilon_7(2\varepsilon_3\sin(\varepsilon_5)$$

$$-2\varepsilon_2\cos(\varepsilon_5))),$$

$$A = (2\varepsilon_2\sin(\varepsilon_5) + 2\varepsilon_3\cos(\varepsilon_5))$$

$$\tilde{a}_2 = 2a_4 e^{2\varepsilon_8}\varepsilon_7 - a_3 e^{2\varepsilon_8}\sin(\varepsilon_5) + 2a_6 e^{2\varepsilon_8}\varepsilon_4\sin(\varepsilon_5)$$

$$+a_2 e^{2\varepsilon_8}\cos(\varepsilon_5) - 2a_7 e^{2\varepsilon_8}\grave{\partial}_4\cos(\varepsilon_5)$$

$$+a_5 e^{2\varepsilon_8}(\varepsilon_2\sin(\varepsilon_5) + \varepsilon_3\cos(\varepsilon_5))$$

$$+a_8 e^{2\varepsilon_8}(-6\varepsilon_4\varepsilon_7 + 2\varepsilon_3\sin(\varepsilon_5) - 2\varepsilon_2\cos(\varepsilon_5)),$$

$$\tilde{a}_3 = 2a_4 e^{2\varepsilon_8}\varepsilon_6 + a_2 e^{2\varepsilon_8}\sin(\varepsilon_5) - 2a_7 e^{2\varepsilon_8}\varepsilon_4\sin(\varepsilon_5)$$

$$+a_3 e^{2\varepsilon_8}\cos(\varepsilon_5) - 2a_6 e^{2\varepsilon_8}\varepsilon_4\cos(\varepsilon_5)$$

$$+a_5 e^{2\varepsilon_8}(\varepsilon_3\sin(\varepsilon_5) - \varepsilon_2\cos(\varepsilon_5))$$

$$+a_8 e^{2\varepsilon_8}(-6\varepsilon_4\varepsilon_6 - 2\varepsilon_2\sin(\varepsilon_5) - 2\varepsilon_3\cos(\varepsilon_5)),$$

$$\left.\begin{aligned}
&\tilde{a}_4 = a_4 e^{3\varepsilon_8} - 3a_8 e^{3\varepsilon_8}\grave{\partial}_4, \tilde{a}_5 = 0, \\
&\tilde{a}_6 = a_8 e^{-\varepsilon_8}\grave{\partial}_6 - a_5 e^{-\varepsilon_8}\grave{\partial}_7 \\
&+a_7 e^{-\varepsilon_8}\sin(\varepsilon_5) + a_6 e^{-\varepsilon_8}\cos(\varepsilon_5), \\
&\tilde{a}_7 = a_5 e^{-\varepsilon_8}\varepsilon_6 + a_8 e^{-\varepsilon_8}\varepsilon_7 \\
&-a_6(e^{-\varepsilon_8})\sin(\varepsilon_5) + a_7 e^{-\varepsilon_8}\cos(\varepsilon_5), \\
&\tilde{a}_8 = 0.
\end{aligned}\right\} \qquad (3.28)$$

Next, we engage the adjoint system in Eq. (3.28) in computing the one-dimensional subalgebra optimal system of 3D-extKPLEq (1.5).

3.1.4 Computation of 1-D subalgebra optimal system

Now, having secured the general invariant of 3D-extKPLEq (1.5) as $G(\alpha_5, \alpha_8)$ in a systematic way as earlier demonstrated, we calculate the optimal system of the equation using the invariant. We adopt the technique introduced in Hu et al.'s study [72] and so contemplate cases $\alpha_5 = 1, \alpha_8 = 1$ and $\alpha_5\alpha_8 = 0$ fundamentally on the bases of thesign of the invariants.

Case 1.

$\alpha_5 = 1, \alpha_8 = 1$

We choose based on this case, the representative element $Q = Q_5 + Q_8$.

On inserting the parameters $\tilde{\alpha}_i = 0, i = 1,2,3,4,6,7$ alongside $\tilde{\alpha}_i = 1, i = 5,8$ into the adjoint system in Eq. (3.28), we achieve the solution

$$\varepsilon_1 = a_1 - \frac{4}{15}a_4 a_6^2 - \frac{4}{15}a_4 a_7^2 - \frac{1}{5}a_2 a_6$$

$$+\frac{2}{5}a_2 a_7 + \frac{2}{5}a_3 a_6 + \frac{1}{5}a_3 a_7,$$

$$\varepsilon_2 = \frac{1}{5}a_3 - \frac{2}{15}a_6 a_4 - \frac{4}{15}a_7 a_4 + \frac{2}{5}a_2,$$

$$\varepsilon_3 = \frac{2}{15}a_7 a_4 - \frac{1}{5}a_2 - \frac{4}{15}a_6 a_4 + \frac{2}{5}a_3,$$

$$\varepsilon_4 = \frac{1}{3}a_4,$$

$$\varepsilon_6 = \frac{1}{2}a_6\sin(\varepsilon_5) - \frac{1}{2}a_7\cos(\varepsilon_5)$$

$$-\frac{1}{2}a_7\sin(\varepsilon_5) - \frac{1}{2}a_6\cos(\varepsilon_5),$$

$$\varepsilon_7 = \frac{1}{2}a_7\sin(\varepsilon_5) + \frac{1}{2}a_6\cos(\varepsilon_5)$$

$$+\frac{1}{2}a_6\sin(\varepsilon_5) - \frac{1}{2}a_7\cos(\varepsilon_5).$$

Case 2.

$\alpha_5\alpha_8 = 0$

In this case, we contemplate three different situations. These situations are treated in detail in the subsequent part of the research work.

Case 2.1.

$\alpha_5 = 0, \alpha_8 = 1$

We choose the representative element $Q = Q_8$. On substituting parametric values $\tilde{\alpha}_i = 0$ and $i = 1, 2, 3, \ldots, 7$ as well as $\tilde{\alpha}_8 = 1$ into the adjoint system in Eq. (3.28), we obtain the outcome

$$\varepsilon_1 = a_1 - \frac{1}{3}a_4 a_6^2 - \frac{1}{3}a_4 a_7^2 + \frac{1}{2}a_2 a_7 + \frac{1}{2}a_3 a_6,$$

$$\varepsilon_2 = \frac{1}{2}a_2 - \frac{1}{3}a_7 a_4, \varepsilon_3 = -\frac{1}{3}a_6 a_4 + \frac{1}{2}a_3,$$

$$\varepsilon_4 = \frac{1}{3}a_4, \varepsilon_6 = -a_7\sin(\varepsilon_5) - a_6\cos(\varepsilon_5),$$

$$\varepsilon_7 = a_6\sin(\varepsilon_5) - a_7\cos(\varepsilon_5).$$

Case 2.2.

$\alpha_5 = 1, \alpha_8 = 0$

In this subcase, we select the representative element $Q = Q_5$. On invoking parameters $\hat{\alpha}_i = 0$, $i = 1,2,3,4,6\ldots,8$ together with $\tilde{\alpha}_6 = 1$ into the adjoint system in Eq. (3.28), one secures

$$\varepsilon_2 = a_3 - 2a_6\varepsilon_4, \varepsilon_3 = -\frac{1}{a_6}(a_1 + a_7\varepsilon_2),$$

$$\varepsilon_4 = -\frac{1}{2a_6 a_4}(a_1 + a_7\varepsilon_2 - a_2 \boxed{?}_6), \varepsilon_4 = \frac{1}{3}a_4,$$

$$\varepsilon_6 = a_6\sin(\varepsilon_5) - a_7\cos(\varepsilon_5),$$

$$\varepsilon_7 = a_7\sin(\varepsilon_5) + a_6\cos(\varepsilon_5).$$

Case 2.3.

$\alpha_5 = 0, \alpha_8 = 0$

Here, we insert $\alpha_5 = 0$ and $\alpha_8 = 0$ into the system of partial differential equations elucidated in Eq. (3.26) and solve the resultant equations. So, we gain a new invariant function

$$\Phi(a_1, a_2, a_3, a_4, a_6, a_7) = H\left\{\sqrt[3]{a_4^2}(a_6^2 + a_7^2)\right\}.$$

Oke Davies Adeyemo Chaudry Masood Khalique

Optimal System Of 1-D Subalgebras and Conserved Quantities of a Nonlinear Wave Equation in Three Dimensions Arising in Engineering Physics

DOI 10.2478/ama-2024-0022

Thus, we engage the new invariants to find more subalgebras of Eq. (1.5) in detail.

Case 2.3.1

$a_4 \neq 0, a_6^2 = 1 - a_7^2$

We select the representative element $Q = Q_4 + Q_6 - Q_7$. If one substitutes parameters $\tilde{\alpha}_i = 0, i = 1, 2, 3, 6, 8$ together with $\tilde{\alpha}_i = 1, i = 4, 5, 7$ into the adjoint system in Eq. (3.28), one can achieve the solution

$$\varepsilon_3 = -\frac{1}{16a_4}\left(\begin{matrix} 4\sqrt{2}a_4a_6^4\varepsilon_4^2 + \sqrt{2}a_4a_2^2a_6^2 \\ +\sqrt{2}a_3^2a_4a_6^2 - 16a_3\varepsilon_4 \end{matrix}\right),$$

$$\varepsilon_5 = -\frac{1}{4}\pi, \varepsilon_6 = -\frac{1}{8}a_6{}^3(a_2 + a_3 - 2a_6\varepsilon_4),$$

$$\varepsilon_7 = -\frac{1}{8}a_6^3(a_2 - a_3 + 2a_6\varepsilon_4), \varepsilon_8 = ln\left(\frac{\sqrt{2}}{2}a_6\right).$$

Case 2.3.2.

$a_4 = 0, a_6^2 = 1 - a_7^2$

In this occurrence, we choose the representative element $Q = Q_6 - Q_7$. On substituting parametric values $\tilde{\alpha}_i = 0, i = 1, 2, 3, 4, 5, 8$ with $\tilde{\alpha}_6 = 1, \tilde{\alpha}_7 = -1$ into the adjoint system in Eq. (3.28), one then obtains a result that can be presented in the following manner:

$$\varepsilon_3 = -\frac{a_1}{a_6}, \varepsilon_4 = \frac{a_3}{2a_6},$$

$$\varepsilon_5 = \frac{1}{4}\pi, \varepsilon_8 = \ln\left(\frac{\sqrt{2}}{2}a_6\right).$$

Remark 3.1

We observe that other possible representatives from Case 2.3.2 have been obtained earlier, thereby contributing no additional subalgebra to the optimal system.

Next, we contemplate other possible cases (under Case 3) that can be secured by further scaling down on Q in Eq. (3.22) using the adjoint system in Eq. (3.28) in order to gain more subalgebras of 3D-extKPLEq (1.5).

Case 3.

$\boldsymbol{a_1 \neq 0, a_2 \neq 0, a_3 \neq 0}$

On scaling further vector Eq. (3.22), we select the representative element $Q = Q_1 + Q_2 + Q_3$.

Therefore, by inserting the parameters $\tilde{\alpha}_i = 0, i = 4,5,\ldots,8$ and $\tilde{\alpha}_i = 1, i = 1,2,3$ into the adjoint system in Eq. (3.28), we obtain

$$\varepsilon_5 = \arctan\left(\sqrt{\frac{(a_2+a_3)^2}{a_2^2+a_3^2}}\right),$$

$$\varepsilon_6 = \sqrt{\frac{2a_1^2}{a_2^2+a_3^2} - \left(\sqrt{\frac{2}{a_2^2+a_3^2}}\right)^{1/2}} - \varepsilon_7,$$

$$\varepsilon_8 = \frac{1}{2}\ln\left(\sqrt{\frac{2}{a_2^2+a_3^2}}\right).$$

Case 3.1.

$a_1 = 0, a_2 \neq 0, a_3 \neq 0$

Here, we examine two possibilities. When $\alpha_1 = 0, \alpha_2 > 0, \alpha_3 > 0$, we select optimal representative element $Q = Q_2 + Q_3$. So, on substituting parameters $\tilde{\alpha}_i = 0, i = 1,4,5,\ldots,8$ with $\tilde{\alpha}_i = 1, i = 1,2,3$ into the adjoint system in Eq. (3.28),

we gain the solution

$$\varepsilon_5 = \frac{1}{4}\pi, \varepsilon_6 = -\varepsilon_7, \varepsilon_8 = \frac{1}{2}\ln\left(\frac{\sqrt{2}}{a_2}\right).$$

Next, we consider when $\alpha_1 = 0, \alpha_2 < 0, \alpha_3 < 0$, and so we select the optimal representative element $Q = -Q_2 - Q_3$ then by inserting the appropriate parametric values of $\tilde{\alpha}$ in Eq. (3.28) as earlier demonstrated, which yields the result

$$\varepsilon_5 = \frac{1}{4}\pi, \varepsilon_6 = -\varepsilon_7, \varepsilon_8 = \frac{1}{4}\ln\left(\frac{2}{a_2^2}\right).$$

Case 3.2.

$a_1 \neq 0,$

Further, we investigate two possible cases. So with $\alpha_1 > 0, \alpha_2 > 0, \alpha_3 = 0$, we select the optimal representative element $Q = Q_1 + Q_2$. Thus, on invoking parameters $\hat{\alpha}_i = 0, i = 3,4,5,\ldots,8$ with $\tilde{\alpha}_i = 1, i = 1,2$ into the adjoint system in Eq. (3.28), we obtain the outcome

$$\varepsilon_5 = 0, \varepsilon_7 = \frac{1}{\sqrt[3]{a_2^2}}(a_1\sqrt{a_2} - a_2),$$

$$\varepsilon_8 = -\frac{1}{2}\ln(a_2).$$

Now, when $\alpha_1 < 0, \alpha_2 < 0, \alpha_3 = 0$, we choose the optimal representative element $Q = -Q_1 - Q_2$. Then, on engaging the appropriate parametric values of $\tilde{\alpha}$ in Eq. (3.28), we secure the solution

$$\varepsilon_5 = 0, \varepsilon_7 = \frac{a_1}{a_2} - \sqrt{\left|-\frac{1}{a_2}\right|}, \varepsilon_8 = \frac{1}{2}\ln\left(\left|-\frac{1}{a_2}\right|\right).$$

Case 3.3.

$a_1 \neq 0, a_2 = 0, a_3 \neq 0$

We explore here two possible situations. Therefore, for $\alpha_1 > 0, \alpha_2 = 0, \alpha_3 > 0$, we choose the optimal representative element $Q = Q_1 + Q_3$. Hence, on inserting parametric values $\hat{\alpha}_i = 0, i = 2,4,5,\ldots,8$ with $\hat{\alpha}_i = 1, i = 1,3$ into the adjoint system in Eq. (3.28), we achieve the result

$$\varepsilon_5 = \pi, \varepsilon_6 = -\frac{1}{a_3}\left(a_1 + a_3\left|-\frac{1}{a_3}\right|\right),$$

$$\varepsilon_8 = \frac{1}{2}\ln\left(\left|-\frac{1}{a_3}\right|\right).$$

Next, we take on $\alpha_1 < 0, \alpha_2 = 0, \alpha_3 < 0$ and select the optimal representative element $Q = -Q_1 - Q_3$. The substitution of the relevant parametric values of $\tilde{\alpha}$ in Eq. (3.28) purveyed the outcome

$$\varepsilon_5 = 0, \varepsilon_6 = \frac{a_1}{a_3} - a_3\sqrt{\left|-\frac{1}{a_3}\right|},$$

$$\varepsilon_8 = \frac{1}{2}\ln\left(\left|-\frac{1}{a_3}\right|\right).$$

Moreover, we further scale down and gain a single vector as part of the subalgebras of Eq. (1.5). On selecting representative element $Q = Q_1$ and solving Eq. (3.28) with adequate values of $\tilde{\alpha}$, we obtain $\partial_8 = -ln(\alpha_1)$. Engaging representative element $Q = Q_2$, and following the same process, we gain

$$\varepsilon_5 = \pi, \varepsilon_7 = 0, \varepsilon_8 = \frac{1}{2}\ln\left(-\frac{1}{a_2}\right),$$

Finally, by selecting the optimal representative element $Q = Q_3$ and solving the system in Eq. (3.28) for relevant parametric values of ã, one obtains the solution $\varepsilon_5 = \varepsilon_6 = 0$, and $\varepsilon_8 = -\frac{1}{2}\ln(a_3)$. In consequence, if we admit the discrete symmetry $(t, x, y, z, u) \mapsto (-t, -x, -y, -z, u)$, albeit not in the connected component of the identity of the full symmetry group that, for instance, maps $-Q_2 - Q_3$ to $Q_2 + Q_3$, we reduce the number of inequivalent subalgebras [33]. Thus, we arrive at the following theorem:

Theorem 3.1
The optimal system of one-dimensional Lie subalgebra for 3D-extKPLEq (1.5) comprises members listed as:

$$Q_1; \ Q_2; \ Q_3; \ Q_5 + Q_8; \ Q_2 + Q_3;$$
$$Q_6 - Q_7; Q_5; Q_8; Q_1 + Q_2 + Q_3; \cdot$$
$$Q_4 + Q_6 - Q_7; Q_1 + Q_2; Q_1 + Q_3$$

Remark 3.2
It is to be noted that the usual tradition is to invoke the subalgebras to obtain invariant solutions to the model under consideration but various invariant solutions associated with the subalgebras presented in Theorem 3.1 have been copiously explored, as can be seen in the study of Adeyemo and Khalique [70]. Thus, we do not consider using the subalgebras to find invariants anymore but to compute the conserved vectors related to the vectors in the subsequent part of the research paper. This is an interesting aspect of this study.

4. CONSERVATION LAWS OF 3D-extKPLEq (1.5)

In this section, we perform the computation of conserved vectors of Eq. (1.5) for the presented Lie subalgebras in Theorem 3.1 by exploiting Ibragimov's theorem [73, 74] for conserved quantities.

4.1 Formal Lagrangian and adjoint equation

Ibragimov [74] gave a new theorem on the conserved vectors of a DE. The theorem validates any system of DE whereby the number of the equation equals the number of dependent variables. In addition, the underlying theorem requires no existence of classical Lagrangian. Ibragimov's approach basically suggests that every infinitesimal generator is related to a conserved vector. Moreover, it is conceptualised based on adjoint equations for nonlinear DEs. We give a detailed outline of the theorem as follows:

Theorem 4.1
[74] We contemplate an NLPDE system whose adjoint is the system

$$\left.\Omega_\alpha^*(x, \Psi, \Theta, \Psi_{(1)}, \Theta_{(1)}, \cdots, \Psi_{(s)}, \Theta_{(s)}) \equiv \frac{\delta(\Theta^\beta \Omega_\beta)}{\delta \Psi^\alpha}\right\}$$
$$= 0 \qquad (4.29)$$

with $\alpha = 1, \ldots, p$ and $\beta = 1, \ldots, p$ for a system of p equations defined as

$$\Omega_\alpha(x, \Psi, \Psi_{(1)}, \Psi_{(2)}, \Psi_{(3)}, \cdots, \Psi_{(s)}) = 0, \qquad (4.30)$$

where $\Theta = \Theta(x)$ with q independent as well as p dependent variables given, respectively, as $x = (x^1, x^2, \cdots, x^q)$ and

$\Psi = (\Psi^1, \Psi^2, \cdots, \Psi^p)$, alongside the variational derivative popularly called the Euler-Lagrange operator, for each α.

Theorem 4.2
Let us suppose that a system of p of Eq. (4.30) is contemplated; then, the system of adjoint presented as Eq. (4.29) inherits the Lie point symmetries of Eq. (4.30), which implies that, if the system in Eq. (4.30) admits a group of point transformation with a generator given as $X = \xi^i \partial / \partial t + \eta \partial / \partial \Psi^\alpha$ such that the adjoint system in Eq. (4.29) admits operator X with an extension to the variables Θ^α via the relation

$$Y = \xi^i \frac{\partial}{\partial x^i} + \eta^\alpha \frac{\partial}{\partial \Psi^\alpha} + \eta_*^\alpha \frac{\partial}{\partial \Theta^\alpha} \qquad (4.31)$$

with suitably selected $\eta_*^\alpha = \eta_*^\alpha(x, \Psi, \Theta)$.

The functions ξ^i as well as η^α signify the infinitesimal generator coefficients that are depending on x alongside Ψ. We are aware that the coefficient η^α is given in Ibragimov's study [74] as

$$\eta^\alpha = -[\lambda^\alpha \Theta^\beta + \Theta^\alpha D_i(\xi^i)] \qquad (4.32)$$

where the computation of λ_β^α can be carried out by invoking the relation

$$Q(\Omega_\alpha) = \lambda_\beta^\alpha \Omega_\beta. \qquad (4.33)$$

In consequence, a conserved quantity for the system comprising both the equation and its adjoint is produced, with T^i possessing the conserved vectors' components $T = (T^1, \cdots, T^n)$, which we can decided by the relation

$$T^i = \xi^i \mathcal{L} + W^\alpha \frac{\delta \mathcal{L}}{\delta \Psi_i^\alpha} + \sum_{s \geq 1} D_{i_1} \ldots D_{i_s}(W^\alpha) \frac{\delta e \mathcal{L}}{\delta e \Psi_{ii_1 i_2 \ldots i_s}^a}, \qquad (4.34)$$
$$i = 1, \ldots, n$$

with formal Lagrangian L of system Ω and Ω_* together with Lie characteristic function W^α stated, respectively, as

$$\mathcal{L} = \Theta^\alpha \Omega_\alpha(x, \Psi, \Psi_{(1)}, \cdots, \Psi_{(s)}) \qquad (4.35)$$

and

$$W^\alpha = \eta^\alpha - \xi^j \Psi_j^\alpha, \alpha = 1, \cdots, p, j = 1, \cdots, q. \qquad (4.36)$$

Remark 4.1
We remark that a system of Eq. (4.30) is self-adjoint if the replacement Θ = Ψ in the system of adjoint Eq. (4.29) produces the same system as that of Eq. (4.30). For a more detailed understanding of the proof and more information on the results presented here, the reader is directed to refer to the studies of Ibragimov [73, 74].

4.1.1 Application of Ibragimov's theorem to derive conserved quantities

The interesting fact about the concept of engaging Ibragimov's theorem of conservation law is that, to every Lie point symmetry of a given DE, it is believed that there exists a unique conserved quantity. In consequence, we devote this subsection to secure conservation laws related to the underlying equation via Ibragimov's conserved theorem [2, 73–75]. Using the salient information provided in the given references, we have the theorem:

Theorem 4.3
The adjoint equation of 3D-extKPLEq (1.5) is expressed as

Oke Davies Adeyemo Chaudry Masood Khalique

Optimal System Of 1-D Subalgebras and Conserved Quantities of a Nonlinear Wave Equation in Three Dimensions Arising in Engineering Physics

DOI 10.2478/ama-2024-0022

$$\left.\begin{aligned} G^* &\equiv v_{tx} - \frac{3}{2}v_x u^3 + \frac{3}{2}v_{xx}u^2 + 3u_{xx}v_x \\ &+ 3u_x v_{xx} + v_{yy} + v_{zz} = 0 \end{aligned}\right\} \qquad (4.37)$$

and the formal Lagrangian given as

$$\mathcal{L} = vG \equiv v\begin{pmatrix} u_{tx} + \frac{3}{2}u_x u^3 + \frac{3}{2}u_{xx}u^2 + 3u_x^2 u \\ + 3u_x u_{xx} + u_{yy} + u_{zz} \end{pmatrix}, \qquad (4.38)$$

where

$$\left.\begin{aligned} G &= u_{tx} + \frac{3}{2}u_x u^3 + \frac{3}{2}u_{xx}u^2 + 3u_x^2 u \\ &+ 3u_x u_{xx} + u_{yy} + u_{zz}. \end{aligned}\right\} \qquad (4.39)$$

Proof

Suppose that we define the adjoint of Eq. (1.5) as [74]

$$\begin{aligned} G^* &= \frac{\delta}{\delta u}\left\{v\begin{pmatrix} u_{tx} + \frac{3}{2}u_x u^3 + \frac{3}{2}u_{xx}u^2 + 3u_x^2 u \\ + 3u_x u_{xx} + u_{yy} + u_{zz} \end{pmatrix}\right\} \\ &= \left[\frac{\partial}{\partial u} - D_x\frac{\partial}{\partial u_x} + D_x^2\frac{\partial}{\partial u_{xx}} + D_x D_t\frac{\partial}{\partial u_{xt}} \right. \\ &\quad \left. + D_y^2\frac{\partial}{\partial u_{yy}} + D_z^2\frac{\partial}{\partial u_{zz}}\right] \\ &\quad \times \left\{v\begin{pmatrix} \frac{3}{2}u_x u^3 + \frac{3}{2}u_{xx}u^2 + 3u_x^2 u + 3u_x u_{xx} \\ + u_{tx} + u_{yy} + u_{zz} \end{pmatrix}\right\} \\ &= v_{tx} - \frac{3}{2}v_x u^3 + \frac{3}{2}v_{xx}u^2 + 3u_{xx}v_x + 3u_x v_{xx} + v_{yy} + v_{zz} \\ &= 0. \end{aligned}$$

$$(4.40)$$

We are aware that we have introduced a new variable $v = v(t, x, y, z)$. In consonance with the approach adopted in Ibragimov's study [74], Eq. (1.5) alongside its adjoint Eq. (4.40) possesses a Lagrangian L presented in the structure L = vG as given in Theorem 4.3. We notice specifically that ∂L/δu = G^* whereas ∂L/δv = G. Now, all the symmetries Q₁, . . . , Q₈ as well as the Lie subalgebras computed in Section 3 are admitted by Eq. (1.5). Thus, the subalgebras of Eq. (1.5) are extended to the new variable $v(t, x, y, z)$, which implies that they become

$$Y = \xi^1\frac{\partial}{\partial t} + \xi^2\frac{\partial}{\partial x} + \xi^3\frac{\partial}{\partial y} + \xi^4\frac{\partial}{\partial z} + \eta\frac{\partial}{\partial u} + \eta^*\frac{\partial}{\partial v}, \qquad (4.41)$$

where

$$\begin{aligned} \eta^* &\equiv \eta^*(t, x, y, z, u, v) \\ &= -\left\{\begin{aligned} \lambda + D_t(\xi^1) + D_x(\xi^2) \\ + D_y(\xi^3) + D_z(\xi^4) \end{aligned}\right\}v. \end{aligned} \qquad (4.42)$$

We decide parameter λ via the relation

$$Q[2](G) = \lambda G \qquad (4.43)$$

with $Q^{[2]}$ denoting the generators that Eq. (2.11) prolonged to all of the various derivatives in Eq. (1.5), that is

$$\begin{aligned} Q^{[2]} &= Q + \zeta^x\frac{\partial}{\partial u_x} + \zeta^{tx}\frac{\partial}{\partial u_{tx}} + \zeta^{xx}\frac{\partial}{\partial u_{xx}} \\ &+ \zeta^{yy}\frac{\partial}{\partial u_{yy}} + \zeta^{zz}\frac{\partial}{\partial u_{zz}}. \end{aligned} \qquad (4.44)$$

In this case, the vector field

$$\left.\begin{aligned} Q &= \xi^1\,\partial/\partial t + \xi^2\,\partial/\partial x + \xi^3\,\partial/\partial y \\ &+ \xi^4\,\partial/\partial z + \eta\,\partial/\partial u \end{aligned}\right\}$$

and the functions $\xi^1, \xi^2, \cdots, \xi^4$ alongside η are depending on (t, x, y, z, u).

Moreover, coefficient functions $\zeta^x, \zeta^{tx}, \zeta^{xx}, \zeta^{yy}$ and ζ^{zz} are explicated through the formulae given as

$$\left.\begin{aligned} \zeta^x &= D_x(\eta) - u_t D_x(\xi^1) - u_x D_x(\xi^2) \\ &- u_y D_x(\xi^3) - u_z D_x(\xi^4), \\ \zeta^{tx} &= D_t(\zeta^x) - u_{tx}D_t(\xi^1) - u_{xx}D_t(\xi^2) \\ &- u_{xy}D_t(\xi^3) - u_{xz}D_t(\xi^4), \\ \zeta^{xx} &= D_x(\zeta^x) - u_{tx}D_x(\xi^1) - u_{xx}D_x(\xi^2) \\ &- u_{xy}D_x(\xi^3) - u_{xz}D_x(\xi^4), \\ \zeta^{yy} &= D_y(\zeta^y) - u_{ty}D_y(\xi^1) - u_{xy}D_y(\xi^2) \\ &- u_{yy}D_y(\xi^3) - u_{yz}D_y(\xi^4), \\ \zeta^{zz} &= D_z(\zeta^z) - u_{tz}D_z(\xi^1) - u_{xz}D_z(\xi^2) \\ &- u_{yz}D_z(\xi^3) - u_{zz}D_z(\xi^4), \end{aligned}\right\} \qquad (4.45)$$

where the total derivatives appearing in Eq. (4.45) are given as

$$\left.\begin{aligned} D_t &= \partial_t + u_t\,\partial_u + u_{tt}\,\partial_{ut} + u_{xt}\,\partial_{ux} + \cdots, \\ D_x &= \partial_x + u_x\,\partial_u + u_{xt}\,\partial_{ut} + u_{xx}\,\partial_{ux} + \cdots, \\ D_y &= \partial_y + u_y\,\partial_u + u_{ty}\,\partial_{ut} + u_{xy}\,\partial_{ux} + \cdots, \\ D_z &= \partial_z + u_z\,\partial_u + u_{tz}\,\partial_{ut} + u_{xz}\,\partial_{ux} + \cdots. \end{aligned}\right\} \qquad (4.46)$$

Readers are directed to the given references for acquiring an understanding of the detailed steps involved in the calculation of conserved vectors of NLPDEs via the considered technique. For instance, in the case of Lie subalgebra $Q_1, \cdots, Q_3$ and $Q_4 \equiv Q_5 + Q_8$ one can compute as follows:

Case $Q_1, \ldots, Q_3$

For the time translation symmetry $Q_1 = \partial/\partial t$, we have functions

$$\xi^1 = 1, \xi^2 = \xi^3 = \xi^4 = \eta = 0.$$

Therefore, one can easily observe that $\zeta^x = \zeta^{xx} = \zeta^{tx} = \zeta^{yy} = \zeta^{zz} = 0$.

Thus, we have

$Q^{[2]}(G) = 0G$, that is $\lambda = 0$.

Furthermore, from Eq. (4.42) we obtain $\eta^* = 0$, which makes the new subalgebra Eq. (2.11) to retain the structure of Q_1, that is $Y_1 = \partial/\partial t$. Resultant to the fact that the coefficients of the generators are all constants, the translation symmetries conserve their structures, and this leads us to the conclusion that $Y_2 = \partial/\partial x, Y_3 = \partial/\partial y$ and $Y_4 = \partial/\partial z$.

Case $Q_4 = Q_5 + Q_8$

$$\left.\begin{aligned} Q_4 &\equiv Q_5 + Q_8 = 3t\,\partial/\partial t + x\,\partial/\partial x \\ &+ (2y - z)\,\partial/\partial y + (y + 2z)\,\partial/\partial z - u\,\partial/\partial u \end{aligned}\right\},$$

where $\xi^1 = 3t, \xi^2 = x, \xi^3 = 2y - z, \xi^4 = y + 2z$ and $\eta = -u$. Thus, on engaging Eq. (4.45), the result of our calculation reveals

$$\begin{aligned} \zeta^x &= -2u_x, \ \zeta^{tx} = -5u_{tx}, \ \zeta^{xx} = -3u_{xx}, \\ \zeta^{yy} &= -2u_{yz} - 5u_{yy}, \ \zeta^{zz} = 2u_{yz} - 5u_{zz}. \end{aligned}$$

From Eqs (4.43)–(4.46), we have

$$Q_4^{[2]}(G) = \begin{pmatrix} -5u_{tx} - \frac{15}{2}u^2 u_{xx} - 15uu_x^2 - \frac{15}{2}u^3 u_x \\ -15u_x u_{xx} - 5u_{yy} - 5u_{zz} \end{pmatrix}$$

$$= -5\begin{pmatrix} u_{tx} + \frac{3}{2}u_x u^3 + \frac{3}{2}u_{xx}u^2 + 3u_x^2 u \\ +3u_x u_{xx} + u_{yy} + u_{zz} \end{pmatrix}$$

$$= -5G.$$

We can see then that $\lambda = -5$. In consequence

$$\eta^* = -\{-5 + D_t(3t) + D_x(x) + D_y(2y - z) \\ + D_z(y + 2z)\}v \\ = -3v.$$

Therefore, we arrive at the extended vector field

$$Y_4 = 3t\,\partial/\partial t + x\,\partial/\partial x + (2y - z)\,\partial/\partial y \\ + (y + 2z)\,\partial/\partial z - u\,\partial/\partial u - 5v\,\partial/\partial v$$

and the related characteristic function

$$W = -3tu_t - xu_x - (y + 2z)u_z - (2y - z)u_y - u.$$

On taking the same steps outlined above with the relation Eq. (4.34), one constructs the conserved vectors [2, 75] corresponding to the secured optimal system of 12 Lie subalgebras as subsequently presented:

$$T_1^t = \frac{3}{2}vu_x u^3 + \frac{3}{2}vu_{xx}u^2 + 3vuu_x^2 + vu_{zz} \\ + vu_{yy} + 3vu_x u_{xx} + \frac{1}{2}vu_{tx} + \frac{1}{2}u_t v_x,$$

$$T_1^x = \frac{3}{2}u_t v_x u^2 - \frac{3}{2}vu_t u^3 - \frac{3}{2}vu_{tx}u^2 \\ -3u_t u_x uv - 3u_x u_{tx}v - \frac{1}{2}u_{tt}v + 3u_t u_x v_x + \frac{1}{2}u_t v_t,$$
$$T_1^y = u_t v_y - u_{ty}v, \quad T_1^z = u_t v_z - u_{tz}v;$$

$$T_2^t = \frac{1}{2}u_x v_x - \frac{1}{2}u_{xx}v, \quad T_2^x = \frac{3}{2}u_x v_x u^2 \\ + u_{zz}v + u_{yy}v + \frac{1}{2}u_{tx}v + \frac{1}{2}v_t u_x + 3u_x^2 v_x,$$
$$T_2^y = u_x v_y - u_{xy}v, \quad T_2^z = u_x v_z - u_{xz}v;$$

$$T_3^t = \frac{1}{2}u_y v_x - \frac{1}{2}u_{xy}v,$$
$$T_3^x = -\frac{3}{2}u_y u^3 v + \frac{3}{2}u_y v_x u^2 - \frac{3}{2}u_{xy}u^2 v \\ -3u_x u_y uv - 3u_x u_{xy}v - \frac{1}{2}u_{ty}v + \frac{1}{2}v_t u_y \\ +3u_x u_y v_x,$$

$$T_3^y = \frac{3}{2}u_x u^3 v + \frac{3}{2}u_{xx}u^2 v + 3u_x^2 uv \\ + u_{zz}v + 3u_x u_{xx}v + u_{tx}v + u_y v_y,$$
$$T_3^z = u_y v_z - u_{yz}v;$$

$$T_8^y = 3yu_x u^3 v + 3yu_{xx}u^2 v + 6yu_x^2 uv + v_y u \\ +2yu_{zz}v - 3u_y v - 2zu_{yz}v - xu_{xy}v \\ +6yu_x u_{xx}v - 3tu_{ty}v + 2yu_{tx}v \\ +3tu_t v_y + xu_x v_y + 2zu_z v_y + 2yu_y v_y,$$

$$T_8^z = 3zu_x u^3 v + 3zu_{xx}u^2 v + 6zu_x^2 uv + v_z u \\ -3u_z v - 2yu_{yz}v + 2zu_{yy}v - xu_{xz}v \\ +6zu_x u_{xx}v - 3tu_{tz}v + 2zu_{tx}v \\ +3tu_t v_z + xu_x v_z + 2yu_y v_z + 2zu_z v_z;$$

$$T_9^t = \frac{3}{2}vu_x u^3 + \frac{3}{2}vu_{xx}u^2 + 3vu_x^2 u + vu_{zz} \\ + vu_{yy} + \frac{1}{2}u_y v_x + \frac{1}{2}u_x v_x - \frac{1}{2}vu_{xy} \\ - \frac{1}{2}vu_{xx} + 3vu_x u_{xx} + \frac{1}{2}v_x u_t + \frac{1}{2}vu_{tx},$$

$$T_9^y = \frac{3}{2}vu_x u^3 + \frac{3}{2}vu_{xx}u^2 + 3vu_x^2 u + vu_{zz} \\ +u_y v_y + v_y u_x - vu_{xy} + 3vu_x u_{xx} + v_y u_t \\ -vu_{ty} + vu_{tx}, \quad T_9^z = v_z u_y - vu_{yz} \\ +v_z u_x - vu_{xz} + v_z u_t - vu_{tz};$$

$$T_4^t = \frac{9}{2}tvu_x u^3 + \frac{9}{2}tvu_{xx}u^2 + 9tvu_x^2 u \\ + \frac{1}{2}v_x u + 3tvu_{zz} + 3tvu_{yy} - vu_x \\ + \frac{1}{2}yu_z v_x + zu_z v_x + yu_y v_x - \frac{1}{2}zu_y v_x \\ + \frac{1}{2}xu_x v_x - \frac{1}{2}yvu_{xz} - zvu_{xz} \\ -yvu_{xy} + \frac{1}{2}zvu_{xy} - \frac{1}{2}xvu_{xx} \\ +9tvu_x u_{xx} + \frac{3}{2}tv_x u_t + \frac{3}{2}tvu_{tx},$$

$$T_4^x = \frac{3}{2}zvu_y u^3 - \frac{3}{2}vu^4 - \frac{3}{2}yvu_z u^3 - 3zvu_z u^3 \\ -3yvu_y u^3 + \frac{3}{2}v_x u^3 - \frac{9}{2}tvu_t u^3 - 6vu_x u^2 \\ + \frac{3}{2}yu_z v_x u^2 + 3zu_z v_x u^2 + 3yu_y v_x u^2 \\ - \frac{3}{2}zu_y v_x u^2 + \frac{3}{2}xu_x v_x u^2 - \frac{3}{2}yvu_{xz}u^2 \\ -3zvu_{xz}u^2 - 3yvu_{xy}u^2 + \frac{3}{2}zvu_{xy}u^2 \\ + \frac{9}{2}tv_x u_t u^2 - \frac{9}{2}tvu_{tx}u^2 - 3yvu_z u_x u - 6zvu_z u_x u \\ -6yvu_y u_x u + 3zvu_y u_x u + 3u_x v_x u - 9tvu_x u_t u \\ + \frac{1}{2}v_t u - 6vu_x^2 + xvu_{zz} + xvu_{yy} + 3xu_x^2 v_x \\ +3yu_z u_x v_x + 6zu_z u_x v_x + 6yu_y u_x v_x \\ -3zu_y u_x v_x - 3yvu_x u_{xz} - 6zvu_x u_{xz} - 6yvu_x u_{xy} \\ +3zvu_x u_{xy} - 2vu_t + 9tu_x v_x u_t + \frac{1}{2}yu_z v_t + zu_z v_t \\ +yu_y v_t - \frac{1}{2}zu_y v_t + \frac{1}{2}xu_x v_t + \frac{3}{2}tu_t v_t - \frac{1}{2}yvu_{tz} \\ -zvu_{tz} - yvu_{ty} + \frac{1}{2}zvu_{ty} + \frac{1}{2}xvu_{tx} \\ -9tvu_x u_{tx} - \frac{3}{2}tvu_{tt},$$

$$T_4^y = 3yvu_x u^3 - \frac{3}{2}zvu_x u^3 + 3yvu_{xx}u^2 - \frac{3}{2}zvu_{xx}u^2 \\ +6yvu_x^2 u - 3zvu_x^2 u + v_y u - vu_z + 2yvu_{zz} - zvu_{zz} \\ -3vu_y + yu_z v_y + 2zu_z v_y + 2yu_y v_y - zu_y v_y - yvu_{yz} \\ -2zvu_{yz} + xv_y u_x - xvu_{xy} + 6yvu_x u_{xx} - 3zvu_x u_{xx} \\ +3tv_y u_t - 3tvu_{ty} + 2yvu_{tx} - zvu_{tx},$$

$$T_4^z = \frac{3}{2}yvu_x u^3 + 3zvu_x u^3 + \frac{3}{2}yvu_{xx}u^2 + 3zvu_{xx}u^2 \\ +3yvu_x^2 u + 6zvu_x^2 u + v_z u - 3vu_z + yu_z v_z + 2zu_z v_z \\ +vu_y + 2yv_z u_y - zv_z u_y - 2yvu_{yz} + zvu_{yz} + yvu_{yy} \\ +2zvu_{yy} + xv_z u_x - xvu_{xz} + 3yvu_x u_{xx} + 6zvu_x u_{xx} \\ +3tv_z u_t - 3tvu_{tz} + yvu_{tx} + 2zvu_{tx};$$

$$T_5^t = \frac{1}{2}u_x v_x - \frac{1}{2}u_{xy}v - \frac{1}{2}u_{xx}v + \frac{1}{2}u_y v_x,$$
$$T_5^x = \frac{3}{2}u_y v_x u^2 - \frac{3}{2}u_y u^3 v + \frac{3}{2}u_x v_x u^2 - \frac{3}{2}u_{xy}u^2 v \\ -3u_x u_y uv + u_{zz}v + u_{yy}vv - 3u_x u_{xy} - \frac{1}{2}u_{ty}v \\ + \frac{1}{2}u_{tx}v + \frac{1}{2}v_t u_x + \frac{1}{2}v_t u_y + 3u_x u_y v_x + 3u_x^2 v_x,$$

$$T_5^y = \frac{3}{2}u_x u^3 v + \frac{3}{2}u_{xx}u^2 v + 3u_x^2 uv + u_{zz}v \\ -u_{xy}v + 3u_x u_{xx}v + u_{tx}v + u_x v_y + u_y v_y,$$

Oke Davies Adeyemo Chaudry Masood Khalique

Optimal System Of 1-D Subalgebras and Conserved Quantities of a Nonlinear Wave Equation in Three Dimensions Arising in Engineering Physics

DOI 10.2478/ama-2024-0022

$$T_5^z = u_x v_z - u_{yz} v - u_{xz} v + u_y v_z;$$

$$\left.\begin{aligned} T_6^t &= t u_z v_x - t u_y v_x + \tfrac{1}{2} y u_x v_x - \tfrac{1}{2} z u_x v_x \\ &\quad - t v u_{xz} + t v u_{xy} - \tfrac{1}{2} y v u_{xx} + \tfrac{1}{2} z v u_{xx}, \end{aligned}\right\}$$

$$\left.\begin{aligned} T_6^x &= 3 t v u_y u^3 - 3 t v u_z u^3 + 3 t u_z v_x u^2 - 3 t u_y v_x u^2 \\ &\quad + \tfrac{3}{2} y u_x v_x u^2 + t u_z v_t - \tfrac{3}{2} z u_x v_x u^2 - 3 t v u_{xz} u^2 \\ &\quad + 3 t v u_{xy} u^2 - 6 t v u_z u_x u + 6 t v u_y u_x u - v u_z + y v u_{zz} \\ &\quad - z v u_{zz} + v u_y + y v u_{yy} - z v u_{yy} + 3 y u_x^2 v_x - 3 z u_x^2 v_x \\ &\quad + 6 t u_z u_x v_x - 6 t u_y u_x v_x - 6 t v u_x u_{xz} + 6 t v u_x u_{xy} - t u_y v_t \\ &\quad + \tfrac{1}{2} y u_x v_t - \tfrac{1}{2} z u_x v_t - t v u_{tz} + t v u_{ty} + \tfrac{1}{2} y v u_{tx} - \tfrac{1}{2} z v u_{tx}, \end{aligned}\right\}$$

$$\left.\begin{aligned} T_6^y &= y v v_y u_x - 3 t v u_x u^3 - 3 t v u_{xx} u^2 - 6 t v u_x^2 u \\ &\quad - 2 t v u_{zz} + 2 t u_z v_y - 2 t u_y v_y - 2 t v u_{yz} - v u_x \\ &\quad - z v_y u_x - y v u_{xy} + z v u_{xy} - 6 t v u_x u_{xx} - 2 t v u_{tx}, \end{aligned}\right\}$$

$$\left.\begin{aligned} T_6^z &= 3 t v u_x u^3 + 3 t v u_{xx} u^2 + 6 t v u_x^2 u + 2 t u_z v_z \\ &\quad - 2 t v_z u_y + 2 t v u_{yz} + 2 t v u_{yy} + v u_x + y v_z u_x \\ &\quad - z v_z u_x - y v u_{xz} + z v u_{xz} + 6 t v u_x u_{xx} + 2 t v u_{tx}; \end{aligned}\right\}$$

$$T_7^t = -\tfrac{1}{2} y u_{xz} v + \tfrac{1}{2} z u_{xy} v + \tfrac{1}{2} y u_z v_x - \tfrac{1}{2} z u_y v_x,$$

$$\left.\begin{aligned} T_7^x &= -\tfrac{3}{2} y u_z u^3 v + \tfrac{3}{2} z u_y u^3 v + \tfrac{3}{2} y u_z v_x u^2 - \tfrac{3}{2} z u_y v_x u^2 \\ &\quad - \tfrac{3}{2} y u_{xz} u^2 v + \tfrac{3}{2} z u_{xy} u^2 v - 3 y u_x u_z u v + 3 z u_x u_y u v \\ &\quad - 3 y u_x u_{xz} v + 3 z u_x u_{xy} v - \tfrac{1}{2} y u_{tz} v + \tfrac{1}{2} z u_{ty} v \\ &\quad + \tfrac{1}{2} y v_t u_z - \tfrac{1}{2} z v_t u_y + 3 y u_x u_z v_x - 3 z u_x u_y v_x, \end{aligned}\right\}$$

$$\left.\begin{aligned} T_7^y &= -\tfrac{3}{2} z u_x u^3 v - \tfrac{3}{2} z u_{xx} u^2 v - 3 z u_x^2 u v - u_z v - z u_{zz} v \\ &\quad - y u_{yz}v - 3 z u_x u_{xx} - z u_{tx} v + y u_z v_y - z u_y v_y, \end{aligned}\right\}$$

$$\left.\begin{aligned} T_7^z &= \tfrac{3}{2} y u_x u^3 v + \tfrac{3}{2} y u_{xx} u^2 v + 3 y u_x^2 u v \\ &\quad + u_y v + z u_{yz} v + y u_{yy} v + 3 y u_x u_{xx} v \\ &\quad + y u_{tx} v + y u_z v_z - z u_y v_z; \end{aligned}\right\}$$

$$\left.\begin{aligned} T_8^t &= \tfrac{9}{2} t u_x u^3 v + \tfrac{9}{2} t u_{xx} u^2 v + 9 t u_x^2 u v + \tfrac{1}{2} v_x u \\ &\quad + 3 t u_{zz} v + 3 t u_{yy} v - u_x v - z u_{xz} v - y u_{xy} v \\ &\quad - \tfrac{1}{2} x u_{xx} v + 9 t u_x u_{xx} v + \tfrac{3}{2} t u_{tx} v + \tfrac{3}{2} t u_t v_x \\ &\quad + y u_y v_x + z u_z v_x + \tfrac{1}{2} x u_x v_x, \end{aligned}\right\}$$

$$\left.\begin{aligned} T_8^x &= -\tfrac{3}{2} v u^4 - 3 z v u_z u^3 - 3 y v u_y u^3 + \tfrac{3}{2} v_x u^3 \\ &\quad - \tfrac{9}{2} t v u_t u^3 - 6 v u_x u^2 + 3 z u_z v_x u^2 + 3 y u_y v_x u^2 \\ &\quad + \tfrac{3}{2} x u_x v_x u^2 - 3 z v u_{xz} u^2 - 3 y v u_{xy} u^2 \\ &\quad + \tfrac{9}{2} t v_x u_t u^2 - \tfrac{9}{2} t v u_{tx} u^2 - 6 z v u_z u_x u \\ &\quad - 6 y v u_y u_x u + 3 u_x v_x u - 9 t v u_x u_t u + \tfrac{1}{2} v_t u \\ &\quad - 6 v u_x^2 + x v u_{zz} + x v u_{yy} + 3 x u_x^2 v_x + 6 z u_z u_x v_x \\ &\quad + 6 y u_y u_x v_x - 6 z v u_x u_{xz} - 6 y v u_x u_{xy} \\ &\quad - 2 v u_t + 9 t u_x v_x u_t + z u_z v_t + y u_y v_t \\ &\quad + \tfrac{1}{2} x u_x v_t + \tfrac{3}{2} t u_t v_t - z v u_{tz} - y v u_{ty} \\ &\quad + \tfrac{1}{2} x v u_{tx} - 9 t v u_x u_{tx} - \tfrac{3}{2} t v u_{tt}, \end{aligned}\right\}$$

$$\left.\begin{aligned} T_9^x &= \tfrac{3}{2} u_y v_x u^2 - \tfrac{3}{2} v u_y u^3 - \tfrac{3}{2} v u_t u^3 + \tfrac{3}{2} u_x v_x u^2 \\ &\quad - \tfrac{3}{2} v u_{xy} u^2 + \tfrac{3}{2} v_x u_t u^2 - \tfrac{3}{2} v u_{tx} u^2 - 3 v u_y u_x u \\ &\quad - 3 v u_x u_t u + v u_{zz} + v u_{yy} + 3 u_x^2 v_x + 3 u_y u_x v_x \\ &\quad - 3 v u_x u_{xy} + 3 u_x v_x u_t + \tfrac{1}{2} u_y v_t + \tfrac{1}{2} u_x v_t \\ &\quad + \tfrac{1}{2} u_t v_t - \tfrac{1}{2} v u_{ty} + \tfrac{1}{2} v u_{tx} - 3 v u_x u_{tx} - \tfrac{1}{2} v u_{tt}, \end{aligned}\right\}$$

$$\left.\begin{aligned} T_9^x &= \tfrac{3}{2} u_y v_x u^2 - \tfrac{3}{2} v u_y u^3 - \tfrac{3}{2} v u_t u^3 + \tfrac{3}{2} u_x v_x u^2 \\ &\quad - \tfrac{3}{2} v u_{xy} u^2 + \tfrac{3}{2} v_x u_t u^2 - \tfrac{3}{2} v u_{tx} u^2 - 3 v u_y u_x u \\ &\quad - 3 v u_x u_t u + v u_{zz} + v u_{yy} + 3 u_x^2 v_x + 3 u_y u_x v_x \\ &\quad - 3 v u_x u_{xy} + 3 u_x v_x u_t + \tfrac{1}{2} u_y v_t + \tfrac{1}{2} u_x v_t \\ &\quad + \tfrac{1}{2} u_t v_t - \tfrac{1}{2} v u_{ty} + \tfrac{1}{2} v u_{tx} - 3 v u_x u_{tx} - \tfrac{1}{2} v u_{tt}, \end{aligned}\right\}$$

$$\left.\begin{aligned} T_{10}^t &= t u_z v_x + \tfrac{1}{2} u_z v_x - t u_y v_x + \tfrac{1}{2} y u_x v_x \\ &\quad - \tfrac{1}{2} z u_x v_x - t v u_{xz} - \tfrac{1}{2} v u_{xz} + t v u_{xy} \\ &\quad - \tfrac{1}{2} y v u_{xx} + \tfrac{1}{2} z v u_{xx}, \; T_{10}^x = 3 t v u_y u^3 \\ &\quad - 3 t v u_z u^3 - \tfrac{3}{2} v u_z u^3 + 3 t u_z v_x u^2 \\ &\quad + \tfrac{3}{2} u_z v_x u^2 - 3 t u_y v_x u^2 + \tfrac{3}{2} y u_x v_x u^2 \\ &\quad - \tfrac{3}{2} z u_x v_x u^2 - 3 t v u_{xz} u^2 - \tfrac{3}{2} v u_{xz} u^2 \\ &\quad + 3 t v u_{xy} u^2 - 6 t v u_z u_x u - 3 v u_z u_x u \\ &\quad + 6 t v u_y u_x u - v u_z + y v u_{zz} - z v u_{zz} \\ &\quad + v u_y + y v u_{yy} - z v u_{yy} + 3 y u_x^2 v_x \\ &\quad - 3 z u_x^2 v_x + 6 t u_z u_x v_x + 3 u_z u_x v_x \\ &\quad - 6 t u_y u_x v_x - 6 t v u_x u_{xz} - 3 v u_x u_{xz} \\ &\quad + 6 t v u_x u_{xy} + t u_z v_t + \tfrac{1}{2} u_z v_t - t u_y v_t \\ &\quad + \tfrac{1}{2} y u_x v_t - \tfrac{1}{2} z u_x v_t - t v u_{tz} \\ &\quad - \tfrac{1}{2} v u_{tz} + t v u_{ty} + \tfrac{1}{2} y v u_{tx} - \tfrac{1}{2} z v u_{tx}, \end{aligned}\right\}$$

$$\left.\begin{aligned} T_{10}^x &= 2 t u_z v_y - 3 t v u_x u^3 - 3 t v u_{xx} u^2 \\ &\quad - 6 t v u_x^2 u - 2 t v u_{zz} + u_z v_y - 2 t u_y v_y \\ &\quad - 2 t v u_{yz} - v u_{yz} - v u_x + y v_y u_x - z v_y u_x \\ &\quad - y v u_{xy} + z v u_{xy} - 6 t v u_x u_{xx} - 2 t v u_{tx}, \end{aligned}\right\}$$

$$\left.\begin{aligned} T_{10}^z &= 3 t v u_x u^3 + \tfrac{3}{2} v u_x u^3 + 3 t v u_{xx} u^2 + \tfrac{3}{2} v u_{xx} u^2 \\ &\quad + 6 t v u_x^2 u + 3 v u_x^2 u + 2 t u_z v_z + u_z v_z - 2 t v_z u_y \\ &\quad + 2 t v u_{yz} + 2 t v u_{yy} + v u_{yy} + v u_x + y v_z u_x \\ &\quad - z v_z u_x - y v u_{xz} + z v u_{xz} + 6 t v u_x u_{xx} \\ &\quad + 3 v u_x u_{xx} + 2 t v u_{tx} + v u_{tx}; \end{aligned}\right\}$$

$$\left.\begin{aligned} T_{11}^t &= \tfrac{3}{2} u_x u^3 v + \tfrac{3}{2} u_{xx} u^2 v + 3 u_x^2 u v + u_{zz} v + u_{yy} v \\ &\quad - \tfrac{1}{2} u_{xx} v + 3 u_x u_{xx} v + \tfrac{1}{2} u_{tx} v + \tfrac{1}{2} u_t v_x + \tfrac{1}{2} u_x v_x, \end{aligned}\right\}$$

$$\left.\begin{aligned} T_{11}^x &= \tfrac{3}{2} u_x v_x u^2 - \tfrac{3}{2} u_t u^3 v + \tfrac{3}{2} u_t v_x u^2 - \tfrac{3}{2} u_{tx} u^2 v \\ &\quad - 3 u_t u_x u v + u_{zz} v + u_{yy} v + \tfrac{1}{2} u_{tx} v - 3 u_x u_{tx} v \\ &\quad - \tfrac{1}{2} u_{tt} v + 3 u_t u_x v_x + \tfrac{1}{2} v_t u_x + \tfrac{1}{2} u_t v_t + 3 u_x^2 v_x, \end{aligned}\right\}$$

$$\left.\begin{aligned} T_{11}^y &= u_x v_y - u_{xy} v - u_{ty} v + u_t v_y, \\ T_{11}^z &= u_x v_z - u_{xz} v - u_{tz} v + u_t v_z; \end{aligned}\right\}$$

$$T_{12}^t = \frac{3}{2}vu_x u^3 + \frac{3}{2}vu_{xx} u^2 + 3vu_x^2 u + vu_{zz} + vu_{yy}$$
$$+ \frac{1}{2}u_y v_x - \frac{1}{2}vu_{xy} + 3vu_x u_{xx} + \frac{1}{2}v_x u_t + \frac{1}{2}vu_{tx},$$

$$T_{12}^x = \frac{3}{2}v_x u_t u^2 - \frac{3}{2}vu_y u^3 - \frac{3}{2}vu_t u^3 + \frac{3}{2}u_y v_x u^2$$
$$- \frac{3}{2}vu_{xy} u^2 - \frac{3}{2}vu_{tx} u^2 - 3vu_y u_x u - 3vu_x u_t u$$
$$+ 3u_y u_x v_x - 3vu_x u_{xy} + 3u_x v_x u_t + \frac{1}{2}u_y v_t$$
$$+ \frac{1}{2}u_t v_t - \frac{1}{2}vu_{ty} - 3vu_x u_{tx} - \frac{1}{2}vu_{tt},$$

$$T_{12}^y = \frac{3}{2}vu_x u^3 + \frac{3}{2}vu_{xx} u^2 + 3vu_x^2 u + vu_{zz}$$
$$+ u_y v_y + 3vu_x u_{xx} + v_y u_t - vu_{ty} + vu_{tx},$$

$$T_{12}^z = v_z u_y - vu_{yz} + v_z u_t - vu_{tz}.$$

Remark 4.2

We observe that there is the possibility of obtaining solutions to the model 3D-extKPLEq (1.5) by exploring the double reduction method via the obtained conservation laws but our focus lies in generating the optimal system and using the same to calculate conserved vectors having applications in the fields of physical science.

4.2 Application of conserved quantities in physical sciences

Conservation laws [2, 75, 76], on the other hand, are a subject of pertinent engrossment in physics, inclusive of theoretical as well as quantum mechanics. This study investigates the conserved quantities of Eq. (1.5) where the results reveal that the model possesses conservation of momentum and energy. In isolated systems, physical quantities such as charge, mass, energy, and angular momentum along linear momentum are conserved. Conserved quantities can be invoked in carrying out integrability checks on DEs. In addition, we have among others the fact that conserved quantities play a key part in the establishment of existence as well as the uniqueness of solutions and linearisation mappings. They are also utilised in the global behaviour of solutions and stability analysis.

In addition, conserved quantities play a leading role in the evolution of numerical techniques. They also furnish a crucial starting point in securing non-locally related systems and potential variables. In particular, a conserved quantity is fundamental in the investigation of a given DE, which implies that it holds for any posed data, whether initial conditions, boundary conditions or both. Furthermore, the conservation laws' structure is such that it does not depend on coordinates, since it involves a contact transformation mapping one to the other.

Conservation law, which is otherwise called the law of conservation, in physics, refers to a principle that stipulates that a certain physical property (also referred to as a measurable quantity) within an isolated physical system remains unchanged over time. In classical physics, these types of laws are involved in governing energy, momentum, mass, angular momentum and electric charge. Moreover, in particle physics, various other conservation laws are applicable in relation to properties associated with subatomic particles that are interestingly invariant during the occurrence of interactions. One of the important functions attributable to conservation laws is the fact that they make it possible to make predictions concerning the macroscopic behaviour of a system without necessarily having to contemplate the microscopic details of the course of a chemical reaction or physical process [77].

Based on the understanding that energy and momentum are among the constituents of the physical quantities conserved by the obtained vectors, we provide some applications of these quantities.
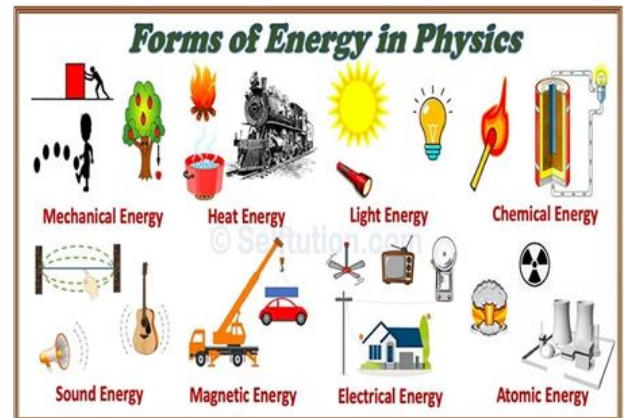
Fig. 1. Diagrammatic representation of various forms of energy in physics [78]

The law of conservation of energy reveals that energy can be neither created nor destroyed. However, its diverse forms (mechanical, kinetic, chemical, etc.) can be changed into others. It is to be noted that the sum of all forms of energy in an isolated system, therefore, remains unaltered. For instance, for a falling body, there is an existing constant amount of energy, although the form of the energy changes from one state to another, which is from potential to kinetic. Following the theory of relativity, mass and energy are revealed to be equivalent. Therefore, the rest of the mass of a body may be considered a form of potential energy, and part of this can later be converted into other forms of energy [78].

If one takes into cognizance all forms of energy (see Fig. 1), the total energy possessed by an isolated system always remains unchanged (constant). It is to be noted that all the forms of energy comply with the law of conservation of energy. Therefore, in summary, one can infer that the conservation of energy law explicates that in a closed system, that is, a system that is isolated from its surrounding environments, the total energy of a system is conserved. Therefore, in an isolated system such as the universe, if there exists a loss of energy in some part of the system, there must be a compensating gain of an equal amount of energy in some other part of the universe [79].

Furthermore, the application of the conservation law of momentum is significant concerning the solution of collision problems. We may take, for example, the operation of rockets, which showcases and exhibits the conservation of momentum: the increased forward momentum of the rocket is scientifically proven to be equal but opposite in sign to the involved momentum of the discharged exhaust gases.

Thus, one notices that the rocket fuel burns to push the exhaust gases downward, which consequently causes the rocket to be pushed upward. A rocket is a spacecraft or an aircraft vehicle that typically makes use of thrust generated by the rocket engine for its flight. A rocket is generally set in motion into outer space and this occasions various scientific researches as well as development applications. Rockets are kept running via some forms of fuel that is typically comprised of liquid hydrogen, hydrogen peroxide, liquid oxygen, hydrazine, and so on. The chemical confor-

Oke Davies Adeyemo Chaudry Masood Khalique
Optimal System Of 1-D Subalgebras and Conserved Quantities of a Nonlinear Wave Equation in Three Dimensions Arising in Engineering Physics

DOI 10.2478/ama-2024-0022

mation of the rocket fuels generates an enormous amount of energy that can assist the massive body of the vehicle to shoot straight up and also get launched into space.

In addition, the working mechanism of motorboats adopts the same principle; in this case, the water is pushed backwards, as a result of which the vehicle also gets pushed forward as part of the reaction so as to ensure momentum conservation [80].

In the case of real-life applications, we consider the example of a balloon, where it is observed that the particles of gas move rapidly, thus occasioning collisions with each other as well as the walls of the balloon. Although the particles themselves move slower and faster when they gain or lose momentum as they collide, the total momentum of the system is unaltered. The general law of physics is the conservation of momentum, and this stipulates that the value of momentum remains fixed in an isolated collection of objects. Alternatively, the conservation of momentum law can be delineated as a physical quantity that stays unaltered both before and after the collision of two or more objects that are present in a system. In more direct terms, this implies that, in the case of a collision between two or more bodies, the value of momentum before the collision and that which emerges after the collision are equal in magnitude [81].

More so, the conservation law of energy can be observed in the examples of energy transference that occur on a daily basis. An example is the use of flowing water for the generation of electricity. When water falls from an upper level, this provides an opportunity to productively tap into the conversion that can be facilitated of potential energy into another form of energy, namely kinetic energy. In turn, this energy is then utilised to rotate the turbine of a generator as the principle of function underlying a hydroelectric power plant's operation, resulting in the consequent generation of electricity.

5. CONCLUDING REMARKS

In this article, we investigated and discussed group invariance properties associated with a nonlinear wave Eq. (1.5) in three dimensions by invoking the Lie group theoretic technique, which gives eight Lie point symmetries. In addition, we presented infinitesimal generators, and Lie point symmetries along the corresponding optimal system of one-dimensional Lie subalgebras. Later, the conserved vectors associated to the Lie subalgebras obtained earlier were achieved via Ibragimov's conserved vectors theorem using the formal Lagrangian of the equation under study. It is undeniable that conservation laws are key ingredients in the deduction of the physical aspects of the model under study. As a result, some conservation laws that are well-known in physics, such as those pertaining to the conservation of energy and momentum, are derived in this study. In addition, applications of these quantities with regard to physics and mathematics are outlined. We declare here that, in addition to the fact that the presented formal calculations and analysis of results make the present study a more trustworthy source of referral, investigations carried out in this research work are more robust and comprehensive than those in Lu et al.'s study [67]. Having comprehensively explained the significance of the results achieved in this study, we declare confidently that they are going to be very useful in classical physics, other physical sciences and various engineering fields.

REFERENCES

1. Gao XY. Mathematical view with observational/experimental consideration on certain (2+1)-dimensional waves in the cosmic/laboratory dusty plasmas. Appl Math Lett. 2019;91:65–172.
2. Adeyemo OD, Motsepa T, Khalique CM. A study of the generalized nonlinear advection-diffusion equation arising in engineering sciences. Alex Eng J. 2022;61(1):185--194.
3. Khalique CM, Adeyemo OD. A study of (3+1)-dimensional generalized Korteweg-de Vries-Zakharov-Kuznetsov equation via Lie symmetry approach. Results Phys. 2020;18: 103197.
4. Du XX, Tian B, Qu QX, Yuan YQ, Zhao XH. Lie group analysis, solitons, self-adjointness and conservation laws of the modified Zakharov-Kuznetsov equation in an electron-positron-ion magnetoplasma. Chaos Solitons Fract., 2020;134:109709.
5. Zhang CR, Tian B, Qu QX, Liu L, Tian HY. Vector bright solitons and their interactions of the couple FokasLenells system in a birefringent optical fiber. Z. Angew Math Phys. 2020;71:1–19.
6. Gao XY, Guo YJ, Shan WR. Water-wave symbolic computation for the Earth, Enceladus and Titan: The higher-order Boussinesq-Burgers system, auto-and non-auto-Bcklund transformations. Appl Math Lett. 2020;104:106170.
7. Hussain A, Usman M, Al-Sinan BR, Osman WM. Symmetry analysis and closed-form invariant solutions of the nonlinear wave equations in elasticity using optimal system of Lie subalgebra. Chin J Phys. 2023;83:1–13.
8. Usman M, Hussain A, Zaman FD, Eldin SM. Group invariant solutions of wave propagation in phononic materials based on the reduced micromorphic model via optimal system of Lie subalgebra. Results Phys. 2023;48:106413.
9. Kumar S, Rani S. Invariance analysis, optimal system, closed-form solutions and dynamical wave structures of a (2+ 1)-dimensional dissipative long wave system. Phys Scr. 2021;96:125202.
10. Rani S, Kumar S, Kumar R. Invariance analysis for determining the closed-form solutions, optimal system, and various wave profiles for a (2+1)- dimensional weakly coupled B-Type Kadomtsev-Petviashvili equations. J Ocean Eng Sci. 2023;8:133–144.
11. Adeyemo OD, Khalique CM. Shock waves, periodic, topological kink and singular soliton solutions of a new generalized two dimensional nonlinear wave equation of engineering physics with applications in signal processing, electro-magnetism and complex media. Alex Eng J. 2023;73:751–769.
12. Akgül A, Ahmad A. Reproducing kernel method for Fangzhu's oscillator for water collection from air, Mathematical Methods in the Applied Sciences (2020).
13. Yusuf A, Sulaiman TA, Khalil EM, Bayram M, Ahmad H. Construction of multi-wave complexiton solutions of the Kadomtsev-Petviashvili equation via two efficient analyzing techniques. Results Phys., 2021;21:103775.
14. Kumar S, Niwas M, Wazwaz AM. Lie symmetry analysis, exact analytical solutions and dynamics of solitons for (2+1)-dimensional NNV equations. Phys Scr. 2020;95:095204.
15. Adeyemo OD, Khalique CM. Lie group theory, stability analysis with dispersion property, new soliton solutions and conserved quantities of 3D generalized nonlinear wave equation in liquid containing gas bubbles with applications in mechanics of fluids, biomedical sciences and cell biology. Commun Nonlinear Sci Numer Simul. 2023;123:107261.
16. Ablowitz MJ, Clarkson PA. Solitons, Nonlinear Evolution Equations and Inverse Scattering. Cambridge University Press; Cambridge, UK, 1991.
17. Zheng CL, Fang JP. New exact solutions and fractional patterns of generalized Broer-Kaup system via a mapping approach. Chaos Soliton Fract. 2006;27:1321–1327.
18. Akbar MA, Ali NHM. Solitary wave solutions of the fourth-order Boussinesq equation through the exp(−Φ(η))-expansion method. SpringerPlus. 2014;3:344.

19. Weiss J, Tabor M, Carnevale G. The Painl´ev´e property and a partial differen- tial equations with an essential singularity. Phys Lett A. 1985;109:205–208.

20. Zhang L, Khalique CM. Classification and bifurcation of a class of second- order ODEs and its application to nonlinear PDEs. Discrete Contin Dyn Syst - S. 2018;11:777–790.

21. Biswas A, Jawad AJM, Manrakhan WN. Optical solitons and complexitons of the Schr¨odinger-Hirota equation. Opt Laser Technol. 2012;44:2265–2269.

22. Chun C, Sakthivel R. Homotopy perturbation technique for solving two-point boundary value problems-comparison with other methods. Comput Phys Commun. 2010;181:1021–1024.

23. Darvishi MT, Najafi M. A modification of extended homoclinic test approach to solve the (3+1)-dimensional potential-YTSF equation. Chin Phys Lett. 2011;28:040202

24. Wazwaz AM. Traveling wave solution to (2+1)-dimensional nonlinear evolution equations. J Nat Sci Math. 2007;1:1–13.

25. Osman MS. One-soliton shaping and inelastic collision between double soli- tons in the fifth-order variable-coefficient Sawada-Kotera equation. Nonlinear Dynam. 2019;96:1491–1496.

26. Wazwaz AM. Partial Differential Equations. CRC Press; Boca Raton, Florida, USA, 2002.

27. Salas AH, Gomez CA. Application of the Cole-Hopf transformation for finding exact solutions to several forms of the seventh-order KdV equation. Math Probl Eng. 2010;2010.

28. Gu CH. Soliton Theory and Its Application. Zhejiang Science and Technology Press; Zhejiang, China, 1990.

29. Zhou Y, Wang M, Wang Y. Periodic wave solutions to a coupled KdV equations with variable coefficients. Phys Lett A. 2003;308:31–36.

30. Zeng X, Wang DS. A generalized extended rational expansion method and its application to (1+1)-dimensional dispersive long wave equation. Appl Math Comput. 2009;212:296–304.

31. Jawad AJM, Mirzazadeh M, Biswas A. Solitary wave solutions to nonlinear evolution equations in mathematical physics. Pramana. 2014;83:457–471.

32. Ovsiannikov LV. Group Analysis of Differential Equations. Academic Press; New York, USA, 1982.

33. Olver PJ. Applications of Lie Groups to Differential Equations. second ed., Springer-Verlag; Berlin, Germany, 1993.

34. Hirota R. The Direct Method in Soliton Theory. Cambridge University Press; Cambridge, UK, 2004.

35. Kudryashov NA, Loguinova NB. Extended simplest equation method for nonlinear differential equations. Appl Math Comput. 2008;205:396-402.

36. Matveev VB, Salle MA. Darboux Transformations and Solitons. Springer; New York, USA, 1991.

37. Wang M, Li X, Zhang J. The (Gj/G)−expansion method and travelling wave solutions for linear evolution equations in mathematical physics. Phys Lett A. 2005;24:1257–1268.

38. Wazwaz AM. The tanh method for generalized forms of nonlinear heat conduction and Burgers-Fisher equations. Appl Math Comput. 2005;169:321–338.

39. Kudryashov NA. Simplest equation method to look for exact solutions of non-linear differential equations. Chaos Solitons Fract. 2005;24:1217–1231

40. Chen Y, Yan Z. New exact solutions of (2+1)-dimensional Gardner equation via the new sine-Gordon equation expansion method. Chaos Solitons Fract. 2005;26:399–406.

41. He JH, Wu XH. Exp-function method for nonlinear wave equations. Chaos Solitons Fract. 2006;30:700–708.

42. Ma WX. Comment on the (3+1)-dimensional Kadomtsev-Petviashvili equations. Commun Nonlinear Sci Numer. Simulat. 2011;16:2663–2666.

43. Kadomtsev BB, Petviashvili VI. On the stability of solitary waves in weakly dispersing media. Sov Phys Dokl. 1970;192:753–756.

44. You F; Xia T, Chen D. Decomposition of the generalized KP, cKP and mKP and their exact solutions. Phys Lett A. 2008;372:3184–3194.

45. Kuznetsov EA, Turitsyn SK. Two- and three-dimensional solitons in weakly dispersive media. Zh Ebp Teor Fa. 1982;82:1457–1463.

46. Ablowitz MJ, Segur H. On the evolution of packets of water waves. J Fluid Mech. 1979;92:691–715.

47. Infeld E, Rowlands G. Three-dimensional stability of Korteweg-de Vries waves and solitons II. Acta Phys Polon A. 1979;56:329–332.

48. Xu G, Li Z. Symbolic computation of the Painlev´e test for nonlinear partial differential equations using Maple. Comput Phys Commun. 2004;161:65–75.

49. Ma WX, Fan E. Linear superposition principle applying to Hirota bilinear equations. Comput Math Appl. 2011;61: 950–959.

50. Senatorski A, Infeld E. Simulations of two-dimensional Kadomtsev-Petviashvili soliton dynamics in three-dimensional space. Phys Rev Lett. 1996;77:2855–2858.

51. Alagesan T, Uthayakumar A, Porsezian K. Painlev´e analysis and B¨acklund transformation for a three-dimensional Kadomtsev-Petviashvili equation. Chaos Soliton Fract. 1997;8:893–895.

52. Ma WX, Abdeljabbar A, Asaad MG. Wronskian and Grammian solutions to a (3+1)-dimensional generalized KP equation. Appl Math Comput. 2011;217:10016–10023.

53. Wazwaz AM. Multiple-soliton solutions for a (3 +1)-dimensional generalized KP equation. Commun Nonlinear Sci Numer Simulat. 2012;17:491–495.

54. Wazwaz AM, El-Tantawy SA. A new (3+1)-dimensional generalized Kadomtsev-Petviashvili equation. Nonlinear Dyn. 2016;84:1107–1112.

55. Liu JG, Tian Y, Zeng ZF. New exact periodic solitary-wave solutions for the new (3+1)-dimensional generalized Kadomtsev-Petviashvili equation in multi- temperature electron plasmas. AIP Adv. 2017;7:2158–3226.

56. Kadomtsev BB, Petviashvili VI. On the stability of solitary waves in weakly dispersive media. Sov Phys Dokl. 1970;15:539–541.

57. Gai L, Bilige S, Jie Y. The exact solutions and approximate analytic solutions of the (2+1)-dimensional KP equation based on symmetry method. Springer- Plus. 2016;5:1267.

58. Ebadi G, Fard NY, Bhrawy AH, Kumar S, Triki H, Yildirim A, Biswas A. Solitons and other solutions to the (3+1)-dimensional extended kadomtsev- petviashvili equation with power law nonlinearity. Rom Rep Phys. 2013;65:27–62.

59. Zakharov VE. Shock waves propagated on solitons on the surface of a fluid. Radiophys Quantum Electron. 1986;29:813–817.

60. Saha A, Pa N. Chatterjee P. Bifurcation and quasiperiodic behaviors of ion acoustic waves in magnetoplasmas with nonthermal electrons featuring tsallis distribution. Braz J Phys. 2015;45:325–333.

61. Borhanifar A, Jafari H, Karimi SA. New solitons and periodic solutions for the Kadomtsev-Petviashvili equation. J Nonlinear Sci Appl. 2008;1:224–229.

62. Khan K, Akbar MA. Exact traveling wave solutions of Kadomtsev-Petviashvili equation. J Egypt Math Soc. 2015;23: 278–281.

63. Zhang X, Chen Y, Tang X. Rogue wave and a pair of resonance stripe solitons to KP equation. Comput Math Appl. 2018;76:1938–1949.

64. Khalique CM. On the solutions and conservation laws of a coupled kadomtsev- petviashvili equation. J Appl Math. 2013;2013.

65. Zhao HQ, Ma WX. Mixed lump-kink solutions to the KP equation. Comput Math Appl. 2017;74:1399–1405.

66. Ma Z, Chen J, Fei J. Lump and line soliton pairs to a (2+1)-dimensional integrable Kadomtsev-Petviashvili equation. Comput Math Appl. 2018;76:1130–1138.

67. Lu¨ X, Ma WX, Zhou Y, Khalique CM. Rational solutions to an extended Kadomtsev-Petviashvili-like equation with symbolic computation. Comput Math Appl. 2016;71:1560–1567.

68. Ma WX. Bilinear equations, Bell polynomials and linear superposition principle. J Phys Conf Ser. 2013;411:2013.

69. Adeyemo OD, Khalique CM. Symmetry solutions and conserved quantities of an extended (1+3)-dimensional Kadomtsev-Petviashvili-like equation. Appl Math Inf Sci. 2021;15:1–12.

Oke Davies Adeyemo Chaudry Masood Khalique

DOI 10.2478/ama-2024-0022

Optimal System Of 1-D Subalgebras and Conserved Quantities of a Nonlinear Wave Equation in Three Dimensions Arising in Engineering Physics

70. Adeyemo OD, Khalique CM. Dynamics of soliton waves of group-invariant solutions through optimal system of an extended KP-like equation in higher dimensions with applications in medical sciences and mathematical physics. J Geom Phys. 2022;177:104502.

71. Ibragimov NH. CRC Handbook of Lie Group Analysis of Differential Equations. Vols 1–3, CRC Press; Boca Raton, Florida, 1994–1996.

72. Hu X, Li Y, Chen Y. A direct algorithm of one-dimensional optimal system for the group invariant solutions. J Math Phys. 2015;56:053504.

73. Ibragimov NH. Integrating factors, adjoint equations and Lagrangians. J Math Anal Appl. 2006;318:742–757.

74. Ibragimov NH. A new conservation theorem. J Math Anal Appl. 2007;333:311–328.

75. Khalique CM, Adeyemo OD. Closed-form solutions and conserved vectors of a generalized (3+1)-dimensional breaking soliton equation of engineering and nonlinear science. Mathematics. 2020;8:1692.

76. Anco SC. Generalization of Noethers theorem in modern form to non- variational partial differential equations. In: Recent progress and Modern Challenges in Applied Mathematics, Modeling and Computational Science. Fields Institute Communications. 2017;79:119--182.

77. Conservation laws: https://www.britannica.com/science/conservation-law

78. https://selftution.com/different-forms-or-types-of-energy-in-physics-and-examples-mechanical-potential-kinetic-heat-chemical-light-sound-magnetic- electrical-atomic-nuclear-thermal/

79. https://byjus.com/physics/law-of-conservation-of-energy/

80. https://studiousguy.com/conservation-of-momentum-examples/

81. https://sciencequery.com/laws-of-conservation-of-momentum/

82. https://www.usgs.gov/media/images/a-turbine-connected-a-generator- produces-power-inside-a-dam

83. https://www.usgs.gov/media/images/flow-water-produces-hydroelectricity

Oke Davies Adeyemo: https://orcid.org/0000-0002-8745-5387

Chaudry Masood Khalique: https://orcid.org/0000-0002-1986-4859

MATHEMATICAL ANALYSIS OF CHEMICALLY REACTING SPECIES AND RADIATION EFFECTS ON MHD FREE CONVECTIVE FLOW THROUGH A ROTATING POROUS MEDIUM

Pawan Kumar SHARMA* , Bhupendra Kumar SHARMA** , Anil KUMAR*

*Amity Institute of Applied Sciences, Amity University, Amity Road, Sector 125, Noida, Utter Pradesh – 201303, India
**Department of Mathematics, Birla Institute of Technology and Science, Pilani, Rajasthan – 333031, India

pksharma@amity.edu, bhupen_1402@yahoo.co.in, akumar35@amity.edu

Abstract: The present study deals with the effects of radiation and mass transfer on a laminar unsteady free convective flow of a viscous, incompressible, electrically conducting and chemically reacting fluid past a vertical surface in a rotating porous medium. It is assumed that the surface is rotating with angular velocity Ω. The governing mathematical equations are developed and solved by adopting complex variable notations and the analytical expressions for velocity, temperature and concentration fields are obtained. The effects of various parameters on mean primary velocity, mean secondary velocity, mean temperature, mean concentration, transient primary velocity, transient secondary velocity, transient temperature and transient concentration have been discussed and shown graphically. Further, the consequences of different parameters on rate of heat transfer coefficient (Nusselt number), rate of mass transfer coefficient (Sherwood number) and drag coefficient (mean skin-friction) are analysed. It is observed that the mean and transient primary velocities increase with the radiation parameter E, while reverse phenomena are observed for the Schmidt number, Sc, and the chemical reaction parameter, γ. The results may be useful in studying oil or gas and water movement through an oil or gas field reservoir, underground water migration, and the filtration and water purification processes.

Key words: porous medium; MHD; chemically reacting fluid, radiation, heat transfer, mass transfer

1. INTRODUCTION

In several trades of science and engineering, the impact of the chemical reaction along with the transfer of heat and mass is studied, since it has a significant practical importance among scientists and engineers. First of all, the combinatorial buoyancy effects were investigated, and we found that it imparts the naturalistic convective flows adjoining together with the upright and flat surfaces of the thermal and mass diffusion. In the realm of theoretical investigation, the dynamic interplay of magnetohydrodynamics and rotational forces unveils its enigmatic balance with a viscous, incompressible fluid cascading over a vertical plate ensconced within a porous medium [1–5]. The impact of the varying concentration and temperature of the surface extensively on the naturalistic convective flow for an upright flat surface was studied extensively. The flow model functions as a cooling agent at the surface, leading to a reduction in the concentration of the diffusing species at the boundary. The presence of an applied magnetic field, thermal radiation, porosity in the saturated porous medium, and a chemically reactive process all contribute to the gradual thinning of the boundary layer [6, 7]. The analysis of the thermal along with mass diffusion simultaneously was reported for the mixed type of convection flows via a perforated median. Increasing both the heat source parameter and the radiation quantity leads to a heightened concentration of temperature distribution. On the other hand, elevating one of the chemical reaction parameters causes a reduction in concentration throughout the entire fluid region. Manipulating the rotation parameter can decrease skin-friction, but it may worsen the Hall effect and ion slip

effect. Interestingly, augmenting the chemical reaction parameter results in a simultaneous increase in the mass transfer rate [8–11]. The impacts of varying temperature and concentration were found over the free convective stream flow in unsteady state condition passed on an upright surface with infinite length and static state of suction. The role of chemical reactions and activation energy holds immense significance in analysing the behaviour of fluid dynamics and its thermal characteristics [12–15]. The analysis delves into the application of fluid flow in various domains, including nuclear reactors, automobiles, manufacturing setups and electronic appliances. Specifically, when both the Darcy–Forchheimer and activation energy parameters are elevated, the velocity and concentration of the fluid decrease. This implies a delicate balance between these factors in the overall behaviour of the system under investigation. The impact of the heat along with mass transport on the blood flow model having two-phase has been represented and discussed in the analogous literature. Investigation is conducted into the dynamic behaviour of an unsteady flow of a viscous liquid subjected to an induced magnetic field while being controlled through uniform suction [16–19]. The nalysis addresses the thermal equation, radiation, and entropy rate in the thermodynamic system. These results provide valuable insights into the intricate interplay between the thermal and magnetic fields, entropy production, concentration and velocity. By approaching this complex problem in a unique way, the prevailing understanding into how different physical variables interact and influence the overall behaviour of the system under investigation was studied.

In the progressions containing higher temperatures, the transfer of heat through radiation along with the impact of convective

Pawan Kumar Sharma, Bhupendra Kumar Sharma, Anil Kumar
Mathematical Analysis of Chemically Reacting Species and Radiation Effects on MHD Free Convective Flow through a Rotating Porous Medium

DOI 10.2478/ama-2024-0023

heat transfer as well as mass transfer has a significant role in the designing and development of key equipment used in the fields, for instance gas turbines power generation plants, nuclear power plants and the numerous propulsive tactics used in the area of aerospace such as aircraft, satellites, space shuttles and missiles. The impacts of radiation were represented for the free convective stream flow over the hemi-infinite past porous surface along with the transfer of the mass. The numerical values of physical quantities, such as the local skin-friction coefficient, the local Nusselt number and the local Sherwood number, were also calculated in a clear and organised way [20–25]. The transfer of heat was evaluated under a thermally radiative medium, while the transfer of mass for an upright surface in the moving condition. The impacts of heat and mass transfer were explored on the free convective flow of a micropolar fluid adjacent to an infinite vertical porous plate [26–29]. The significance of this research extends to diverse fields such as geophysics, medicine, biology and any processes that benefit from a strong magnetic field in a low-density gas environment. The impact of the radiation along with the transfer of mass was also investigated over an isothermal upright surface under the two-dimensional flow. The introduction of coordinate and parametric transformations in the governing equations has revealed remarkable insights that have seldom been reported in the literature [30–32]. The investigation has yielded crucial findings, particularly concerning the impact of the Ergun number on various fluid types. Interestingly, the Ergun number has demonstrated its ability to reduce the velocity boundary layer of pseudo-plastic fluids, a highly desirable outcome. However, it has been observed to enhance the thermal boundary layer in these fluids. In contrast, for Newtonian and dilatant fluids, this effect has proven to be relatively insignificant. The unsteady convectional flow by means of the rotating perforated median with the radiational effect and periodic flux of heat was reported significantly [33, 34].

MHD is an important aspect in covering the mechanical properties of the liquid in the fluid dynamics and deals with the cooperation among the electrically conductive and electromagnetic fluids. The flows involved in the fluids that are a good conductor of the electricity subjected to the effect of the magnetic field have drawn the attention of various investigators due to their uses in astrophysics, geophysics, engineering applications and the control of aerodynamic boundary layer. The MHD free convective stream flows were assessed for a plate put at heat flux with oscillations of surface. The unsteady free convection flow of a viscous incompressible fluid delved through a highly porous medium, bounded by a vertical infinite moving plate, has been discussed by many researchers [35–39]. During the evaluation of the intricate interplay of thermal diffusion, chemical reaction and heat source, it is necessary to consider all of these as being under the influence of the Soret effect. The fluid is grey, absorbing and emitting, and yet non-scattering, adding complexity to the problem. This research sheds light on the complex dynamics of fluid flow through porous media, offering valuable implications for various practical applications and opening doors to further investigations in this captivating area of study. The transport of heat along with mass was clarified in the magneto-biofluid flow with Joule effect via a non-Darcian porous medium [40, 41].

Extensive investigations of the magnetohydrodynamic mixed convective stream flow passing through the upright flat surface were organised under the numerous applications of MHD flow through the porous type of medium. In a comprehensive investigation [42–46], the combined influences of Soret and Joule effects were thoroughly analysed on the magnetohydrodynamic mixed convective flow of an electrically conducting, incompressible and viscous fluid past an infinite vertical porous plate. The unique exploration provided valuable insights into the complex dynamics of MHD mixed convective flows, particularly in the presence of porous media and Hall effects. These findings are significant for various engineering applications, especially those involving heat and mass transfer phenomena. The state of the unsteady flow for free convective stream was represented under the thermal as well as mass diffusion in the environment of Hall impact. The influence of Hall current on the unsteady free convection flow of an electrically conducting, viscous incompressible fluid was explored [47–49]. The flow occurred past a fluctuating porous flat plate, with internal heat absorption/generation, and in the presence of foreign gases. The study considered various parameters, including the Hall current, the hydromagnetic parameter, the Grashoff number for heat transfer, the Grashoff number for mass transfer, the internal heat absorption/generation parameter, the transpiration parameter, the Schmidt parameter and the chemical reaction parameter. Overall, this investigation contributes valuable insights into the intricate interactions between Hall current, magnetic force, thermal buoyancy and heat generation/absorption, enriching our understanding of complex fluid dynamics and heat transfer phenomena. The effect of MHD on unsteady oscillatory Couette flow through porous media and the influence of the radiation and related chemical reactions were also investigated in an unsteady state magnetohydrodynamic free convection flow with the transfer of mass over a heated upright porous surface rooted in highly porous type of median [50, 51]. The unsteady natural oscillatory convective Couette flow was demonstrated via a variable perforated type of median with the effect of chemical species concentration [52, 53]. Under the presumption of varying permeability, the impact of related chemical reactions on the flow of micropolar fluid reported the replication of the microscopic effects owing to the local behaviour and micro-motion of the liquid particles. The influence of Joule heating on the steady two-dimensional flow of an incompressible micropolar fluid over a flat deformable sheet was investigated [54–56], with the investigation uncovering that the presence of second-order slip plays a constructive role in ensuring flow stability, during both the stretching and shrinking of the deformable surface. Overall, these insightful results contribute to our understanding of the interplay between Joule heating and micropolar fluid flow over deformable sheets, offering potential implications in diverse fields, ranging from engineering applications to scientific advancements. Recently, the impact of species chemical reactivity as well as the prevalence of radiation over the MHD flow through a relocating perpendicular perforated flat surface, together with that of the source of heat and suction, has been evaluated in the analogous research literature. The behaviour of a two-dimensional incompressible magnetohydrodynamic fluid flowing over a linear stretching sheet was investigated considering the effects of suction or injection and convective boundary conditions [57, 58]. To analyse the system, a scaling group transformation method was employed, which helps simplify the governing equations by revealing certain invariance properties. These studies contribute to a deeper understanding of the intricate fluid dynamics in the presence of magnetic fields and various boundary conditions, and the achieved agreement validates the reliability of the utilised numerical approach.

This research paper introduces a novel study of the combined effects of radiation and chemical reactions in a rotating porous medium. It investigates the impact of a magnetic field on unsteady state natural convective chemically reacted flow over an infinite

upright plate, considering a revolving condition with a permeable median. The inclusion of periodic thermal and mass diffusion at the upright surface adds complexity. The study employs a regular perturbation method to obtain investigational solutions for flow characteristics. The findings are presented graphically, providing a clear visualisation of the influence of different parameters on flow-related characteristics. This comprehensive analysis offers valuable insights into fluid dynamics and heat transfer in this unexplored scenario.

2. MATHEMATICAL FORMULATION

We considered the unsteady viscous incompressible flow through electrically conducting and chemically reacting the fluid by means of a foraminate median, inhabiting a hemi-infinite area of space confined by an upright endless foraminate plate in a revolving tract, when the temperature and mass flux of the plate area change with respect to the length of time. Now we assume the impact of radiations on an upright plate that is under a similar static magnetic field and suction velocity, which are exerted in a directional way that is vertical to the surface. An upright endless foraminate plane area revolving around a perpendicular axis of a vertical plane with the constant angular velocity Ω subjected to a viscous fluid embedded in porous medium is considered. At the z^* = 0 plane, a vertical porous plane is considered with the z^*-axis perpendicular to this plane. The x^*-axis is considered in a perpendicular upward direction while the y^*-axis is in the normal direction to the z^* = 0 plane. The stream flow is considered to be along with the plane z^* = 0. The schematic of flow configuration is given in Fig. 1. Now, considering the above assumptions, all the physical variable quantities, excluding the pressure 'p', are only the function of direction z^* and time t^*.
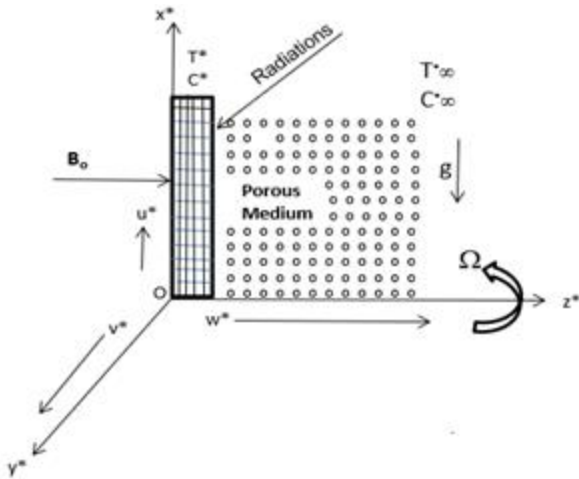
Fig. 1. Schematic of flow configuration

The mass and momentum conservation equations along with the transfer of energy in the revolving frame are specified below [50]:

$$\frac{\partial w^*}{\partial z^*} = 0, \tag{1}$$

$$\frac{\partial u^*}{\partial t^*} + w^*\frac{\partial u^*}{\partial z^*} - 2\Omega v^* = g\beta(T^* - T_\infty^*) + g\beta^/(C^* - C_\infty^*)$$
$$+\nu\frac{\partial^2 u^*}{\partial z^{*2}} - \frac{\nu\,u^*}{k^*} - \frac{(\vec{J}\times\vec{B})}{\rho}, \tag{2}$$

$$\frac{\partial v^*}{\partial t^*} + w^*\frac{\partial v^*}{\partial z^*} + 2\Omega u^* = \nu\frac{\partial^2 v^*}{\partial z^{*2}} - \frac{\nu v^*}{k^*} - \frac{(\vec{J}\times\vec{B})}{\rho}, \tag{3}$$

$$0 = -\frac{1}{\rho}\frac{\partial p^*}{\partial z^*} - \frac{\nu w^*}{k^*} - \frac{(\vec{J}\times\vec{B})}{\rho}, \tag{4}$$

where the terms of the right-hand side from Eq. (2) to Eq. (4) represent the occurrence of the Lorentz force attributable to the magnetic field '$\vec{B}$', which is specified by:

$$\vec{J}\times\vec{B} = \sigma(\vec{v}\times\vec{B})\times\vec{B} \tag{5}$$

Putting the value of Eq. (5) in Eqs (2)–(4), the resultant new forms of equations are given by:

$$\frac{\partial u^*}{\partial t^*} + w^*\frac{\partial u^*}{\partial z^*} - 2\Omega v^* = g\beta(T^* - T_\infty^*) + g\beta^/(C^* - C_\infty^*)$$
$$+\nu\frac{\partial^2 u^*}{\partial z^{*2}} - \frac{\nu\,u^*}{k^*} - \frac{\sigma B^2}{\rho}u^*, \tag{6}$$

$$\frac{\partial v^*}{\partial t^*} + w^*\frac{\partial v^*}{\partial z^*} + 2\Omega u^* = \nu\frac{\partial^2 v^*}{\partial z^{*2}} - \frac{\nu v^*}{k^*} - \frac{\sigma B^2}{\rho}v^*, \tag{7}$$

$$0 = -\frac{1}{\rho}\frac{\partial p^*}{\partial z^*} - \frac{\nu w^*}{k^*} - \frac{\sigma B^2}{\rho}w^*, \tag{8}$$

$$\frac{\partial T^*}{\partial t^*} + w^*\frac{\partial T^*}{\partial z^*} = \alpha\frac{\partial^2 T^8}{\partial z^{*2}} - \frac{1}{\rho C_p}\frac{\partial q_r^*}{\partial z^*}, \tag{9}$$

$$\frac{\partial C^*}{\partial t^*} + w^*\frac{\partial C^*}{\partial z^*} = D\frac{\partial^2 C^*}{\partial z^{*2}} - k_1(C^* - C_\infty^*). \tag{10}$$

The boundary conditions of the problem are as below:

$$\left.\begin{array}{l} z = 0\,.u^* = 0,\ v^* = 0,\ \frac{\partial T^*}{\partial z^*} = -\frac{q_w^*}{\kappa}(1 + \varepsilon e^{i\,\omega^*t^*}), \\ \frac{\partial C^*}{\partial z^*} = -\frac{m_w^*}{D}(1 + \varepsilon e^{i\,\omega^*t^*}) \\ z \to \infty: u^* \to 0, v^* \to 0, T^* \to T_\infty^*, C^* \to C_\infty^*. \end{array}\right\} \tag{11}$$

For the constant value of the suction, from Eq. (1), we obtain:

$$w = -w_0 \tag{12}$$

Assuming $u + iv = U$ with Eq. (12), Eqs (6) and (7) can be written as:

$$\frac{\partial U^*}{\partial t^*} - w_0\frac{\partial U^*}{\partial z^*} + 2i\Omega U^* = g\beta(T^* - T_\infty^*) + g\beta^/(C^* - C_\infty^*)$$
$$+\nu\frac{\partial^2 U^*}{\partial z^{*2}} - \frac{\nu U^*}{k^*} - \frac{\sigma B^2 U^*}{\rho} \tag{13}$$

Now, we introduce the dimensionless quantities, as the following:

$$z = \frac{w_0 z^*}{\nu}, U = \frac{U^*}{w_0},\ t = \frac{t^* w_0^2}{\nu},\ \omega = \frac{\nu\omega^*}{w_0^2},$$

$$\theta = \frac{\kappa(T^* - T_\infty^*)w_0}{q_w^*\nu}, k = \frac{w_0^2 k^*}{\nu^2}, \text{R(rotation parameter)} = \frac{\Omega\nu}{w_0^2},$$

$$\alpha \text{ (thermaldiffusivity)} = \frac{\kappa}{\rho C_p}, \text{Gr (Grash of number)} = \frac{g\beta q_w^* \nu^2}{w_0^4 \kappa},$$

Pr (Prandtal number) $= \frac{\nu}{\alpha}$, Gc (modified Grash of number) $=$

$\frac{g\beta^- m_w^* \nu^2}{w_0^4 D}$, Sc (Schmidt number) $= \frac{\nu}{D}$, E(radiationparameter)$=$

$\frac{4\nu I}{\rho C_p w_0^2}$, M(Hartmannnumber) $= \sqrt{\frac{\sigma B^2\nu}{\rho w_0^2}}$ and

γ (dimension less chemical reaction parameter) $= \frac{k_1\nu}{w_0^2}$.

The radiative heat flux, as ascertained in the study of Cogley et al. [59], can be expressed in the following form:

Pawan Kumar Sharma, Bhupendra Kumar Sharma, Anil Kumar
Mathematical Analysis of Chemically Reacting Species and Radiation Effects on MHD Free Convective Flow through a Rotating Porous Medium

DOI 10.2478/ama-2024-0023

$\frac{\partial q_r^*}{\partial z^*} = 4(T^* - T_\infty^*)I^*,$

$I^* = \int_0^\infty \kappa_{\lambda\omega} \frac{\partial e_{b\lambda}}{\partial T^*} d\lambda,$

where $\kappa_{\omega\lambda}$ is the absorption coefficient at the wall, $e_{b\lambda}$ is Planck's function.

Now, substituting the dimensionless quantities in Eqs (13), (9) and (10), the resultantly obtained dimensionless equations are:

$$\frac{\partial U}{\partial t} - \frac{\partial U}{\partial z} + 2i\,RU = Gr\,\theta + GcC + \frac{\partial^2 U}{\partial z^2} - \frac{U}{k} - M^2 U, \quad (14)$$

$$\frac{\partial \theta}{\partial t} - \frac{\partial \theta}{\partial z} = \frac{1}{Pr}\frac{\partial^2 \theta}{\partial z^2} \quad (15)$$

$$\frac{\partial C}{\partial t} - \frac{\partial C}{\partial z} = \frac{1}{Sc}\frac{\partial^2 C}{\partial z^2} - \gamma C, \quad (16)$$

and the corresponding boundary conditions of the problem embodied in Eq. (11) are mentioned by:

$$\left. \begin{array}{l} z = 0 : U = 0,\ \frac{\partial \theta}{\partial z} \\ \quad = -(1 + \varepsilon e^{i\omega t}), \frac{\partial C}{\partial z} \\ \quad = -(1 + \varepsilon e^{i\omega t}) \\ z \to \infty : U \to 0, \theta \to 0, C \to 0. \end{array} \right\} \quad (17)$$

2.1. Solution of the problem

Since the amplitude ε (< < 1) of the variation is extremely small, we accordingly consider the solutions of the problem in the following arrangement:

$$\left. \begin{array}{l} U(z,t) = U_0(z) + \varepsilon U_1(z)e^{i\omega t} + \ldots\ldots\ldots \\ \theta(z,t) = \theta_0(z) + \varepsilon \theta_1(z)e^{i\omega t} + \ldots\ldots\ldots \\ C(z,t) = C_0(z) + \varepsilon C_1(z)e^{i\omega t} + \ldots\ldots\ldots \end{array} \right\} \quad (18)$$

Substituting Eq. (18) in Eqs (14)–(16), and equating it to the coefficients of various powers of ε along with ignoring ε^2, ε^3 …, we thus obtain:

$$U_0'' + U_0' - 2iR\,U_0 - \frac{U_0}{k} - M^2 U_0 = -Gr\theta_0 - GcC_0, \quad (19)$$

$$U_1'' + U_1' - 2iR\,U_1 - i\omega\,U_1 - \frac{U_1}{k} - M^2 U_1 = -Gr\theta_1 - GcC_1, \quad (20)$$

$$\theta_0'' + Pr\,\theta_0' - E\,Pr\,\theta_0 = 0, \quad (21)$$

$$\theta_1'' + Pr\theta_1' - (E + i\omega)\theta_1 Pr\ 0\ . \quad (22)$$

$$C_0'' + Sc\,C_0' - \gamma Sc C_0 = 0, \quad (23)$$

$$C_1'' + Sc C_1' - i\omega\,Sc C_1 - \gamma Sc C_1 = 0\ . \quad (24)$$

The analogous boundary conditions Eq. (17) come in order to the following:

$$\left. \begin{array}{l} z = 0 : U_0 = 0, U_1 = 0, \frac{\partial \theta_0}{\partial z} = -1, \frac{\partial \theta_1}{\partial z} = -1, \frac{\partial C_0}{\partial z} = -1, \frac{\partial C_1}{\partial z} = -1, \\ z \to \infty : U_0 \to 0, U_1 \to 0, \theta_0 \to 0, \theta_1 \to 0, C_0 \to 0, C_1 \to 0. \end{array} \right\}$$
$$(25)$$

Solving Eqs (19)–(24) subject to the analogous boundary conditions expressed in Eq. (25), we obtain:

$$U_0(z) = a_3(e^{-a_1 z} - e^{-a_2 z}) + a_4(e^{-b_1 z} - e^{-a_2 z}) \quad (26)$$

$$U_1(z) = a_8(e^{-a_5 z} - e^{-a_7 z}) + a_9(e^{-a_6 z} - e^{-a_7 z}) \quad (27)$$

$$\theta_0(z) = \frac{1}{a_1} e^{-a_1 z}, \quad (28)$$

$$\theta_1(z) = \frac{1}{a_5} e^{-a_5 z}. \quad (29)$$

$$C_0(z) = \frac{1}{b_1} e^{-b_1 z}, \quad (30)$$

$$C_1(z) = \frac{1}{a_6} e^{-a_6 z}, \quad (31)$$

where,

$a_1 = \frac{1}{2}[Pr + \sqrt{Pr^2 + 4EPr}],$

$b_1 = \frac{1}{2}[Sc + \sqrt{Sc^2 + 4\gamma Sc}]$

$a_2 = \frac{1}{2}\left[1 + \sqrt{1 + 4(2iR + M^2 + \frac{1}{k})}\right]$

$a_3 = \frac{-Gr}{a_1(a_1^2 - a_1 - (2iR + M^2 + \frac{1}{k}))},$

$a_4 = \frac{-Gc}{b_1(b_1^2 - b_1 - (2iR + M^2 + \frac{1}{k}))},$

$a_5 = \frac{1}{2}[Pr + \sqrt{Pr^2 + 4Pr(E + i\omega)}]$

$a_6 = \frac{1}{2}[Sc + \sqrt{Sc^2 + 4i\omega Sc}]$

$a_7 = \frac{1}{2}\left[1 + \sqrt{1 + 4(2iR + i\omega) + \frac{4}{k} + 4M^2}\right]$

$a_8 = \frac{-Gr}{a_5(a_5^2 - a_5 - (2iR + i\omega + M^2 + \frac{1}{k}))},$

$a_9 = \frac{-Gc}{a_6(a_6^2 - a_6 - (2iR + i\omega + M^2 + \frac{1}{k}))}.$

2.2. Solution

2.2.1. Steady flow

By taking $U_0 = u_0 + iv_0$ in Eq. (26), and consequently allowing for the separation of real as well as imaginary portions, the average primary $\frac{u_0}{w_0}$ and mean secondary $\frac{v_0}{w_0}$ velocity fields are ascertained as the following:

$$\left. \begin{array}{l} \frac{u_0}{w_0} = e_3(e^{-a_1 z} - e^{-e_1 z}\cos e_2 z) - e_4 e^{-e_1 z}\sin e_2 z \\ + e_5(e^{-Scz} - e^{-e_1 z}\cos e_2 z) - e_6 e^{-e_1 z}\sin e_2 z \\ \frac{v_0}{w_0} = e_4(e^{-a_1 z} - e^{-e_1 z}\cos e_2 z) + e_3 e^{-e_1 z}\sin e_2 z \\ + e_6(e^{-Scz} - e^{-e_1 z}\cos e_2 z) + e_5 e^{-e_1 z}\sin e_2 z \end{array} \right\}, \quad (32)$$

2.2.2. Unsteady flow

Substituting the unsteady portions,

$U_1(z,t) = M_r + iM_i, C_1(z,t) = C_r + iC_i$ and $\theta_1(z,t) = T_r + iT_i$, respectively, in Eqs (27), (29) and (31), we obtain:

$$[U(z,t), \theta(z,t), C(z,t)] = [U_0(z), \theta_0(z)] + \varepsilon e^{i\omega t}[(M_r + iM_i), (T_r + iT_i), (C_r + iC_i]$$ (33)

The primary velocity, secondary velocity and temperature along with concentration areas in the components terms with fluctuation are given by:

$$\frac{u}{w_0}(z,t) = u_0 + \varepsilon(M_r \cos \omega t - M_i \sin \omega t)$$ (34)

$$\frac{v}{w_0}(z,t) = v_0 + \varepsilon(M_r \sin \omega t + M_i \cos \omega t)$$ (35)

$$\theta(z,t) = \theta_0 + \varepsilon(T_r \cos \omega t - T_i \sin \omega t)$$ (36)

$$C(z,t) = C_0 + \varepsilon(C_r \cos \omega t - C_i \sin \omega t)$$ (37)

Taking $\omega t = \frac{\pi}{2}$ in Eqs (34)–(37), we obtain the transient expressions for the primary velocity, secondary velocity and temperature, as well as the concentration, as the following:

$$\frac{u}{w_0}\left(z, \frac{\pi}{2\omega}\right) = u_0(z) - \varepsilon M_1(z),$$ (38)

$$\frac{v}{w_0}\left(z, \frac{\pi}{2\omega}\right) = v_0(z) + \varepsilon M_r(z),$$ (39)

$$\theta\left(z, \frac{\pi}{2\omega}\right) = \theta_0(z) - \varepsilon T_i(z).$$ (40)

$$C\left(z, \frac{\pi}{2\omega}\right) = C_0(z) - \varepsilon C_i(z).$$ (41)

where

$$M_r = e_{17}[e^{-e_7 z} \cos e_8 z - e^{-e_{11} z} \cos e_{12} z]$$
$$- e_{18}[-e^{-e_7 z} \sin e_8 z + e^{-e_{11} z} \sin e_{12} z]$$
$$+ e_{23}[e^{-e_9 z} \cos e_{10} z - e^{-e_{11} z} \cos e_{12} z] -$$
$$e_{24}[-e^{-e_9 z} \sin e_{10} z + e^{-e_{11} z} \sin e_{12} z]$$

$$M_i = e_{17}[-e^{-e_7 z} \sin e_8 z + e^{-e_{11} z} \sin e_{12} z]$$
$$+ e_{18}[e^{-e_7 z} \cos e_8 z - e^{-e_{11} z} \cos e_{12} z]$$
$$+ e_{23}[-e^{-e_9 z} \sin e_{10} z + e^{-e_{11} z} \sin e_{12} z] +$$
$$e_{24}[e^{-e_9 z} \cos e_{10} z - e^{-e_{11} z} \cos e_{12} z]$$

$$T_i = -\frac{e^{-e_7 z}}{e_7^2 + e_8^2}[-e_8 \cos e_8 z - e_7 \sin e_8 z]$$

$$C_i = \frac{e^{-e_9 z}}{e_9^2 + e_{10}^2}[-e_9 \sin e_{10} z - e_{10} \cos e_{10} z]$$

$$a_2 = e_1 + ie_2, a_3 = e_3 + ie_4, a_4 = e_5 + ie_6, a_5 = e_7 + ie_8,$$
$$a_6 = e_9 + ie_{10}, a_7 = e_{11} + ie_{12}, a_8 = e_{17} + ie_{18}, a_9$$
$$= e_{23} + ie_{24}$$

$$e_1 =$$
$$\frac{1}{2}\left[1 + \sqrt{\sqrt{[1 + 4(M^2 + \frac{1}{k})]^2 + 64R^2} \frac{[1+4(M^2+\frac{1}{k})]^2 - 64R^2}{[1+4(M^2+\frac{1}{k})]^2+64R^2}}\right]$$

$$e_2 = \frac{1}{2}\sqrt{\sqrt{[1 + 4(M^2 + \frac{1}{k})]^2 + 64R^2} \frac{16R[1+4(M^2+\frac{1}{k})]}{[1+4(M^2+\frac{1}{k})]^2+64R^2}}$$

$$e_3 = -\frac{Gr[a_1^3 - a_1^2 - (M^2 + \frac{1}{k})a_1]}{[a_1^3 - a_1^2 - (M^2 + \frac{1}{k})a_1]^2 + 4R^2 a_1^2}$$

$$e_4 = -\frac{2Ra_1 Gr}{[a_1^3 - a_1^2 - (M^2 + \frac{1}{k})a_1]^2 + 4R^2 a_1^2}$$

$$e_5 = -\frac{Gc[Sc^3 - Sc^2 - (M^2 + \frac{1}{k})Sc]}{[Sc^3 - Sc^2 - (M^2 + \frac{1}{k})Sc]^2 + 4R^2 Sc^2}$$

$$e_6 = -\frac{2RScGc}{[Sc^3 - Sc^2 - (M^2 + \frac{1}{k})Sc]^2 + 4R^2 Sc^2}$$

$$e_7 = \frac{1}{2}Pr + \sqrt{\sqrt{(Pr^2 + 4E Pr)^2 + 16\omega^2 Pr^2}}.$$

$$\frac{(Pr^2 + 4E Pr)^2 - 16\omega^2 Pr^2}{(Pr^2 + 4E Pr)^2 + 16\omega^2 Pr^2}$$

$$e_8 = \frac{1}{2}\sqrt{\sqrt{(Pr^2 + 4E Pr)^2 + 16\omega^2 Pr^2}}.$$

$$\frac{8 Pr \omega (Pr^2 + 4E Pr)}{(Pr^2 + 4E Pr)^2 + 16\omega^2 Pr^2}$$

$$e_9 = \frac{1}{2}\left[Sc + \sqrt{\sqrt{Sc^4 + 16\omega^2 Sc^2}}. \frac{Sc^4 - 16\omega^2 Sc^2}{Sc^4 + 16\omega^2 Sc^2}\right]$$

$$e_{10} = \frac{1}{2}\left[\sqrt{\sqrt{Sc^4 + 16\omega^2 Sc^2}}. \frac{8\omega Sc^3}{Sc^4 + 16\omega^2 Sc^2}\right]$$

$$e_{11} =$$
$$\frac{1}{2}\left[1 + \sqrt{\sqrt{(1 + \frac{4}{k} + 4M^2)^2 + (8R + 4\omega)^2}. \frac{(1+\frac{4}{k}+4M^2)^2 - (8R+4\omega)^2}{(1+\frac{4}{k}+4M^2)^2+(8R+4\omega)^2}}\right]$$

$$e_{12} =$$
$$\frac{1}{2}\left[\sqrt{\sqrt{(1 + \frac{4}{k} + 4M^2)^2 + (8R + 4\omega)^2}. \frac{2(1+\frac{4}{k}+4M^2)(8R+4\omega)}{(1+\frac{4}{k}+4M^2)^2+(8R+4\omega)^2}}\right]$$

$$e_{13} = e_7^2 - e_8^2 - e_7 - M^2 - \frac{1}{k}, e_{14} = 2e_7 e_8 - e_8 - 2R - \omega$$

$$e_{15} = e_7 e_{13} - e_8 e_{14}, e_{16} = e_8 e_{13} + e_7 e_{14}, e_{17} = -\frac{Gre_{15}}{e_{15}^2 + e_{16}^2}, e_{18} = \frac{Gre_{16}}{e_{15}^2 + e_{16}^2}$$

$$e_{19} = e_9^2 - e_{10}^2 - e_9 - M^2 - \frac{1}{k}, e_{20} = 2e_9 e_{10} - e_{10} - 2R - \omega$$

$$e_{21} = e_9 e_{19} - e_{10} e_{20}, e_{22} = e_{10} e_{19} - e_9 e_{20}, e_{23} = -\frac{Gce_{21}}{e_{21}^2 + e_{22}^2}, e_{24} = \frac{Gre_{22}}{e_{21}^2 + e_{22}^2}.$$

It is critical to understand the impact of the Grashoff numbers and magnetic field on mean skin-friction at $z = 0$ after learning about the mean flow velocity field, and the same is provided in the form:

$$\tau* = \mu\left(\frac{dU^*}{dz^*}\right)_{z*=0},$$ (42)

Further, in non-dimensional form, it is provided as follows:

$$\tau = \frac{\tau* v}{\mu w_0^2} = \left(\frac{\partial U}{\partial z}\right)_{z=0} = \left(\frac{\partial U_0}{\partial z}\right)_{z=0} + \varepsilon\left(\frac{\partial U_1}{\partial z}\right)_{z=0} e^{iwt}.$$ (43)

We denote the mean skin-friction by:

$$\tau_m = \left(\frac{du_0}{dz}\right)_{z=0}.$$ (44)

Now, after having ascertained the temperature field, we move on to examining how the rate of heat transfer is affected by ω. The Nusselt number can be used to calculate the rate of heat transfer.

$$Nu = -\frac{q_\omega^* v}{k w_0 (T^* - T_\infty^*)} = \left(\frac{\partial \theta}{\partial z}\right)_{z=0} = \left(\frac{\partial \theta_0}{\partial z}\right)_{z=0} + \varepsilon\left(\frac{\partial \theta_1}{\partial z}\right)_{z=0} e^{i\omega t}$$ (45)

Pawan Kumar Sharma, Bhupendra Kumar Sharma, Anil Kumar
Mathematical Analysis of Chemically Reacting Species and Radiation Effects on MHD Free Convective Flow through a Rotating Porous Medium

DOI 10.2478/ama-2024-0023

3. VALIDATION

To validate the findings of the present work vis-à-vis those of Sharma et al. [50] (while neglecting the rotation and radiation effect), a comparison of the velocity and transient temperature profiles is carried out, as indicated in Figs. 2 and 3. It is observed that there is good agreement between the present work and the previous research.
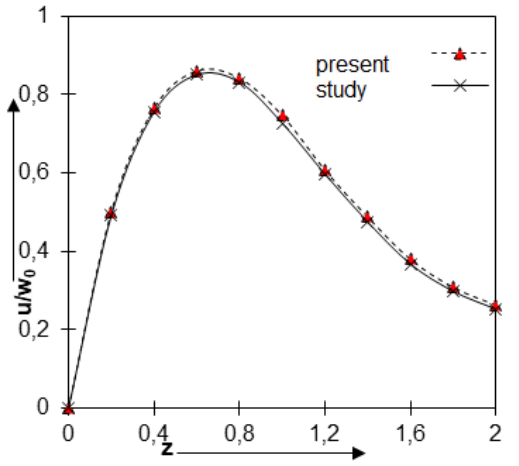
Fig. 2. Comparative analysis of mean primary velocity profile
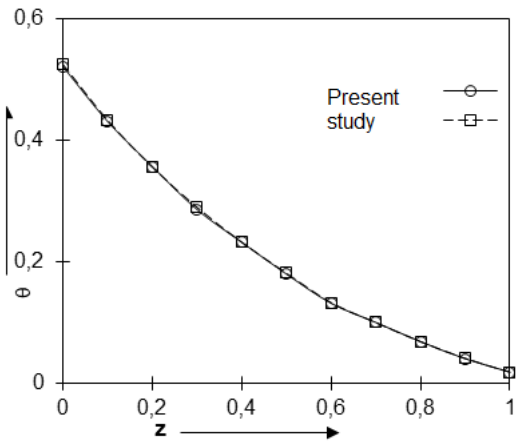
Fig. 3. Comparative analysis of transient temperature profiles

4. GRAPHICAL PRESNTATION AND DISCUSSION

After obtaining the various flow characteristics, the numerical calculations are made for the various numerical solutions of the thermal Grashoff number 'Gr', the solutal Grashoff number 'Gc', the Schmidt number 'Sc', the frequency ω, the permeability parameter k, the radiation parameter E and the Hartmann number (a magnetic field parameter) M. Approximately 0.71 is taken as the Prandtl, which, in the air, is designated at 20°C. The Schmidt numbers are considered in the study to show the utmost common diffusive chemical species present in the air. The values of the Schmidt number 'Sc' are 0.60 and 1.002 in the air, which represents the species H_2O and CO_2 in the air at 25°C and 1 atmospheric pressure. The values of various numbers such as Gc, Gr,

k, M, ω and E are determined based on the own judgement of the present researchers.
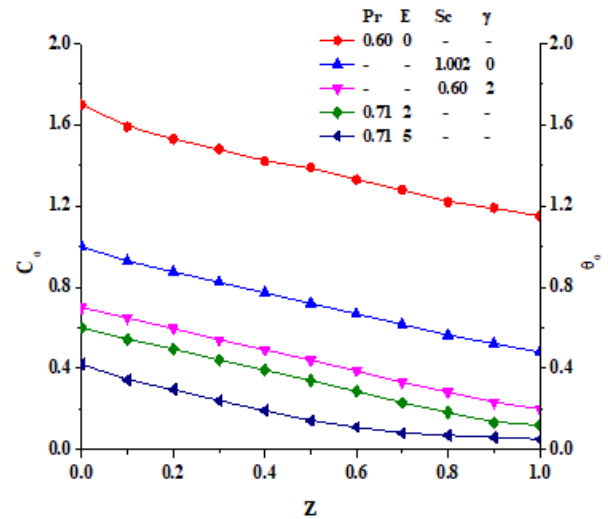
Fig. 4. Mean temperature and mean concentration profiles

It has been noted from Eq. (26) that the steady state portion of the average primary velocity value for its field is having a two-layer characteristic, and these two layers been acknowledged as the suction and thermal layers. The existence of the suction layer is because of the revolution and medium porousness, while the thermal layer exists because of an interplay of the thermal field generated by the radiation heat transfer and the velocity related to its field, as reported by Cogley et al. [59] and Xin et al. [60]; however, this interplay depends upon the Grashof number as well as the radiation parameters.

The profiles of the mean temperature as well as the mean concentration are represented in Fig. 4. It has been sighted that the mean temperature as well as the mean concentration decreases exponentially. The mean temperature reduces with the rise in the radiation-pertaining parameter E. From the quality point of view, the results are acceptable with some exceptions, since, due to the impact of the radiative heat transfer, the rate of energy transportation to the relevant fluid reduces with the reduction of the temperature of the fluid.

It has been perceived as well from Fig. 4 that the mean level of the concentration for the fluid decreases with the upturn in the Schmidt number, which indicates that the mass diffusivity increases the concentration level with steady rate. Moreover, it is also detected from Fig. 1 that there was a fall in the concentration under the impact of the parameter γ related to the chemical reaction. Similar trends can be observed in the researches of Sharma and Gandhi [61] and Li et al. [62].

The mean and transient primary velocities are presented in Figs. 5 and 7 for arbitrary values of the thermal Grashof number Gr = 2, the parameter related to permeability k = 0.5, the rotation parameter R = 2 and the Prandtl number Pr = 0.71 (air). The Grashof number 'Gc' is expressed by the ratio between the buoyancy force species and the hydrodynamic force due to viscosity. It has been observed that the mean and transient primary velocities rise significantly with an increase of the buoyancy force for species, and this phenomenon is in good agreement with the findings of Sharma et al. [63]. The mean and transient primary velocities are supposed to drop along with the upsurge of the parameter M of the magnetic field. This happens due to the use of the magnetic

field in the transverse direction, the consequence of which is the production of a resistive kind of force known as the Lorentz force. This is similar to a drag force, and it has a tendency to oppose the flow of fluid, together with a subsequent reduction in its velocity.
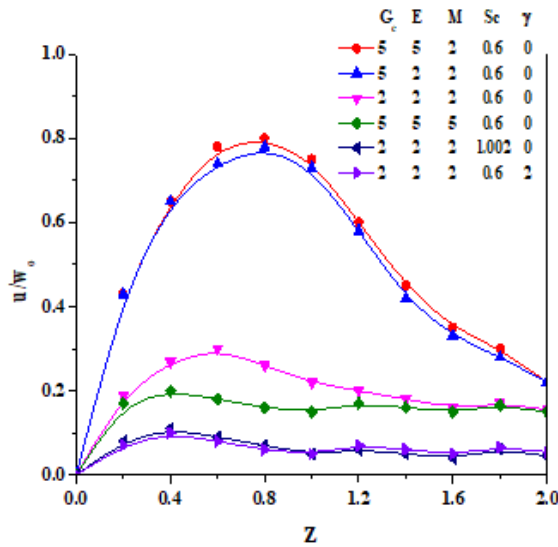
Fig. 5. Mean primary velocity profiles for Gr = 2, k = 0.5, R = 2 and Pr = 0.71
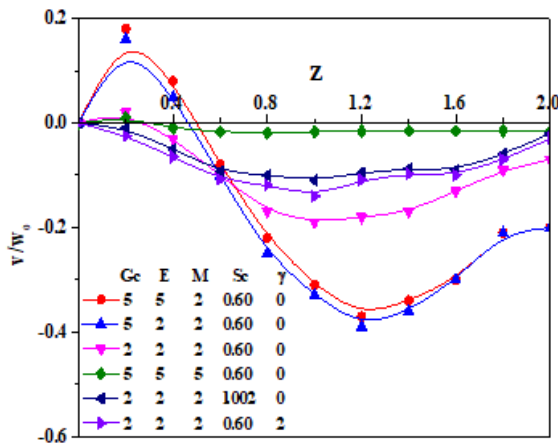
Fig. 6. Mean secondary velocity profiles for Gr = 2, k = 0.5, R = 2 and Pr = 0.71.

Fig. 6 demonstrates the variation of the profiles pertaining to the mean secondary velocity with the variation of the various parameters. It is seen that the mean secondary velocity rises both with increasing E and M. Interestingly, it has been found that the secondary velocity rises due to Gc close to the plate and then reduces remotely from the upright plate.

It is also observed that the mean secondary velocity falls under the effect of the Schmidt number 'Sc'. Interestingly, it is noted that the mean secondary velocity initially fall under the impact of the chemical reaction parameter γ, while a reverse impact is seen remotely from the plate. It has also been perceived that the mean and transient primary velocities become subject to upsurges with the radiation parameter E, while reverse phenomena are observed for the Schmidt number 'Sc' along with the chemical reaction parameter γ. Moreover, from Fig. 7, we infer that the transient primary velocity accelerates with frequency of oscillation ω.
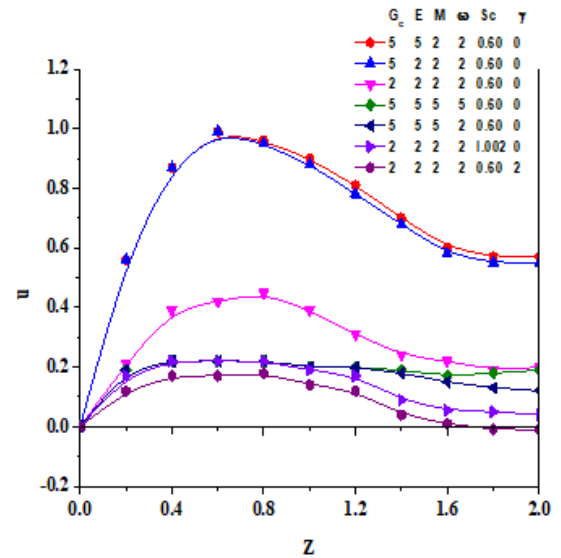
Fig. 7. Transient primary velocity profiles for Gr = 2, k = 0.5, ε = 2 and Pr = 0.71
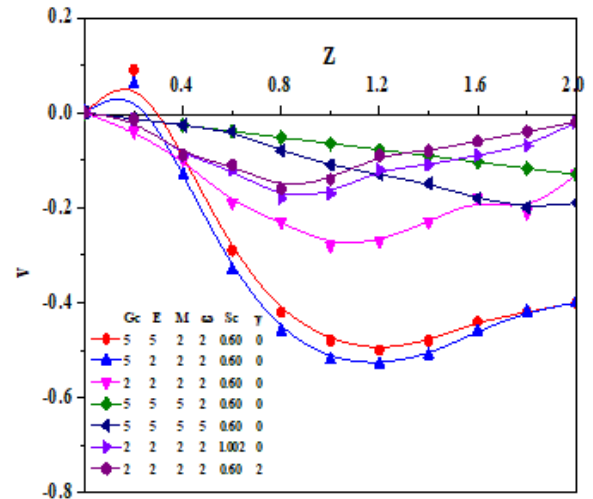
Fig. 8. Transient secondary velocity profiles for Gr = 2, k = 0.5, Pr = 0.71, R = 2 and ε = 2

Fig. 8 exhibits the variation of transient secondary velocity against span-wise coordinate z under the influence of Gc, E, M, ω and Sc. The transient secondary velocity accelerates with the parameter M related to the magnetic field and the Schmidt number 'Sc', whereas it falls under the effect of the radiation parameter E and the frequency of fluctuation ω. From Fig. 8, we observe that the transient secondary velocity underwent a rise owing to augmentation in the solutal's Grashof number 'Gc' near the plate, whereas a reverse effect was observed far away from the plate. Moreover, from Fig. 8, it is revealed that transient secondary velocity increases as rise occurs in the chemical reaction's parameter γ. This leads us to the understanding that the reduction in the chemical species directs towards a boost in the magnitude of the concentration field, and resultantly, there is an enhancement in the buoyancy impacts owing to the concentration gradients, which accelerates the fluid flow field.
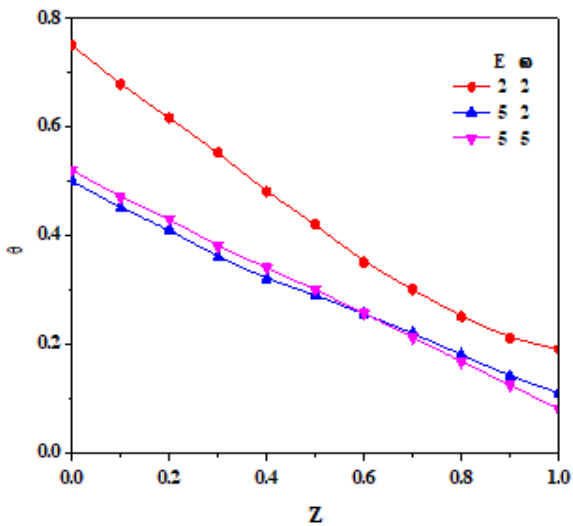
Fig. 9. Transient temperature profiles for Pr = 0.71 and ε = 0.2
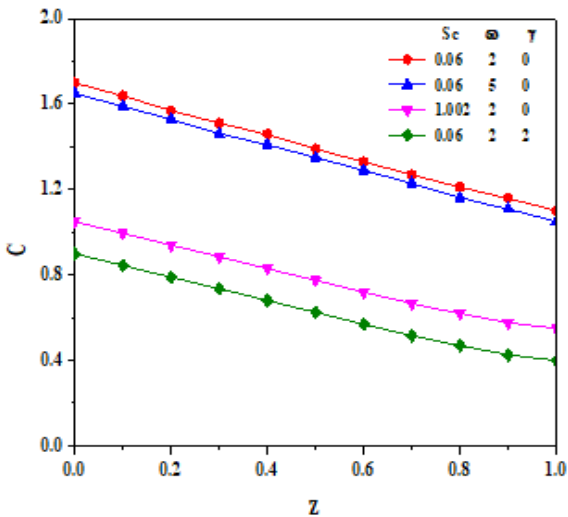
Fig. 10. Transient concentration profiles for ε = 0.2

A similar trend can be observed in previous studies in the literature [64–66]. The plot of the transient temperature profile for numerous values of radiation parameter as well as frequency of fluctuation is provided in Fig. 9. It is noticed that the transient temperature reduces along with the increase in the radiation parameter E, and this reduction is attributed to the fact that, under the existence of the thermal buoyancy force, the rise in the parameter E related to radiation guides towards the rise of the boundary layer concentration as well as towards the dropping of the rate of the heat flux. Further, it also ascertained that the temperature accelerated with the frequency of oscillation in the vicinage of the vertical surface, while it decelerated remotely from the plate.

Fig. 10 describes the impact of Schmidt number, frequency of fluctuation and the parameter γ related to chemical reaction on the transient concentrations. It is also ascertained from Fig. 7 that the transient concentration reduces with rising ω, γ and Sc. For the generative reaction $\gamma > 0$, while the reverse impact is detected, i.e. as soon as the reaction parameter rises, the concentration profiles become thicker, and accordingly, decreases take place in the transient concentration.

Tab. 1 illustrates the values of Nusselt number with frequency of fluctuations ω. It is observed that they behave similar to a cosine wave. Tab. 2 presents the values of mean skin-friction for different values of the magnetic field parameter M. It is observed that mean skin-friction decreases with increase in the magnetic field parameter M, for every value of the Schmidt number 'Sc'.

Tab. 1. Values of Nusselt number for ε = 0.2

ω	Nu for t = 2	Nu for t = 4	Nu for t = 6
0	−1.2	−1.2	−1.2
1	0.9167	0.8692	1.192
2	0.8692	0.9709	1.1687
3	1.192	1.1687	1.132
4	0.9709	0.8084	1.0848
5	0.8321	1.0816	1.0308
6	1.1687	1.0848	0.9744
7	1.0273	0.8074	0.92
8	0.8084	1.1668	0.8719
9	1.132	0.9744	0.8341
10	1.0816	0.8666	0.8095

Tab. 2. Values of τ_m (mean skin-friction) for Gr = 2, Gc = 2, E = 2, k = 0.5, Pr = 0.71 and γ = 2

M	Sc = 0.60	Sc = 0.78	Sc = 1.002
0	1.053428	0.917919	0.814144
2	0.753157	0.666109	0.597228
4	0.50047	0.448243	0.405931
6	0.367434	0.331293	0.301715
8	0.288942	0.261552	0.239024
10	0.237704	0.215728	0.197601
12	0.201763	0.183441	0.168304
14	0.175202	0.159506	0.146524
16	0.154792	0.14107	0.129711
18	0.138624	0.126439	0.116347
20	0.125506	0.114549	0.105471

5. CONCLUSIONS

Assuming the periodical thermal and mass diffusion at the upright surface, the investigational solutions are found for flow characteristics by following the regular perturbation method, and the impact of different parameters on flow-related characteristics are explained and depicted graphically. The results may be useful in studying oil or gas and water movement through an oil or gas field reservoir, underground water migration, and the filtration and water purification processes.

– The mean and transient primary velocities step-up significantly with the increase of the species buoyancy force, while a reverse response is observed for the magnetic field parameter M.

– It has also been noticed that the mean and transient primary velocities rise with the radiation parameter E, while reverse phenomena are observed for the Schmidt number 'Sc' and the parameter γ pertaining to chemical reaction.

– The temperature profile accelerated with frequency of oscillation near the plate, whereas it decelerated far away from plate.

− It has been observed that transient temperature falls with rise in the parameter related to radiation.
− The transient concentration drops with increasing ω, γ and Sc.

REFERENCES

1. Gebhart B, Pera L. The nature of vertical natural convection flow from the combined buoyancy effects-on thermal and mass diffusion. Int. J. Heat Mass Transfer. 1971; 14: 2024-2050 http://dx.doi.org/10.1016/0017-9310(71)90026-3.

2. Khanduri U, Sharma BK, Sharma M, Mishra NK, Saleem N. Sensitivity analysis of electroosmotic magnetohydrodynamics fluid flow through the curved stenosis artery with thrombosis by response surface optimization. Alexandria Engineering Journal, 2023: 75, 1-27. https://doi.org/10.1016/j.aej.2023.05.054.

3. Kodi R, Ganteda C, Dasore A, Kumar ML, Laxmaiah G, Hasan MA, Islam S, Razak A. Influence of MHD mixed convection flow for maxwell nanofluid through a vertical cone with porous material in the existence of variable heat conductivity and diffusion. Case Studies in Ther Engg. 2023; 44: 102875.

4. Veera Krishna M, Chamkha AJ. Hall and ion slip effects on magnetohydrodynamic convective rotating flow of Jeffreys fluid over an impulsively moving vertical plate embedded in a saturated porous medium with Ramped wall temperature. Numerical Methods for Partial Differential Equations. 2021; 37(3): 2150-2177. https://doi.org/10.1002/num varying concentratio.22670

5. Veera Krishna M. Hall and ion slip impacts on unsteady MHD free convective rotating flow of Jeffreys fluid with ramped wall temperature. Int. Commun in Heat and Mass Transf. 2020; 119: 107927. https://doi.org/10.1016/j.icheatmasstransfer.2020.104927

6. Hossain MA, Hussain S, Rees DAS. Influence of fluctuating surface temperature and concentration on natural convection flow from a vertical flat plate. J. of Appl. Math. and Mech. 2001; 81: 699-709. https://doi.org/10.1002/1521-4001(200110)81:10%3C699::AID-ZAMM699%3E3.0.CO;2-3

7. Sahoo SN, Rout PK, Dash GC. Unsteady MHD Flow through Porous Media with Temporal Variation in Temperature and Concentration at the Plate. Int. J. of Ambient Energy. 2022; 43(1): 7977-7986. https://doi.org/10.1080/01430750.2022.2086914

8. Sharma PK. Simultaneous thermal and mass diffusion on three-dimensional mixed convection flow through a porous medium. J. of Porous Media. 2005; 8(4): 419-427. doi:10.1615/JPorMedia.v8.i4.70.

9. Maatoug S, Babu HK, Deepthi VVL. Ghachem K, Raghunath K, Ganteda CK, Khan SU. Variable chemical species and thermo-diffusion Darcy-Forchheimer squeezed flow of Jeffrey nanofluid in horizontal channel with viscous dissipation effects. J. of the Indian Chem. Society. 2023; 100(1): 100831.

10. Deepthi VVL, Lashin MMA, Kumar NR, Raghunath K, Ali F, Oreijah M, Guedri K, Tag-ElDin ESM, Khan MI, Galal AM. Recent Development of Heat and Mass Transport in the Presence of Hall, Ion Slip and Thermo Diffusion in Radiative Second Grade Material: Application of Micromachines. *Micromachines.* 2022; *13*(10): 1566. https://doi.org/10.3390/mi13101566

11. Chu YM, Jakeer S, Reddy SRR, Rupa ML, Trabelsi Y, Khan MI, Hejazi HA, Makhdoum BM. Eldin S.M. Double diffusion effect on the bio-convective magnetized flow of tangent hyperbolic liquid by a stretched nano-material with Arrhenius Catalysts. Case Studies in Thermal Engg. 2023; 44: 102838. https://doi.org/10.1016/j.csite.2023.102838

12. Sharma BK, Sharma PK, Chaudhary RC. Effects of fluctuating surface temperature and concentration on unsteady convection flow past an infinite vertical plate with constant suction. Heat Transf. Res. 2009; 40(6): 505-519. doi: 10.1615/HeatTransRes.v40.i6.10.

13. Shuguang Li, Kodi R, Ayman A, Farhan A, Zaib A, Khan MI, Sayed M E & Puneeth V. Effects of activation energy and chemical reaction on unsteady MHD dissipative Darcy-Forchheimer squeezed flow of Casson fluid over horizontal channel. Sc. Report. 2023:13: 2666.

14. Bafakeeh OT, Raghunath K, Ali F, Khalid M, Tag-ElDin ESM, Oreijah M, Guedri K, Kheder NB, Khan MI. Hall Current and Soret Effects on Unsteady MHD Rotating Flow of Second-Grade Fluid through Porous Media under the Influences of Thermal Radiation and Chemical Reactions. *Catalysts.* 2022; *12*(10): 1233. https://doi.org/10.3390/catal12101233

15. Raghunath K, Mohanaramana R. Hall, Soret, and rotational effects on unsteady MHD rotating flow of a second-grade fluid through a porous medium in the presence of chemical reaction and aligned magnetic field. Int. Commun in Heat and Mass Transf. 2022; 137: 106287. https://doi.org/10.1016/j.icheatmasstransfer.2022.106287

16. Tripathi B, Sharma BK. Effect of variable viscosity on MHD inclined arterial blood flow with chemical reaction. Int. J. of Appl. Mech. and Engg. 2018; 23(3): 767–785. http://dx.doi.org/10.2478/ijame-2018-0042.

17. Tripathi B, Sharma BK. Influence of heat and mass transfer on two-phase blood flow with joule heating and variable viscosity in the presence of variable magnetic field. Int. J. of Comput. Method. 2020; 17(3): 1850139. https://doi.org/10.1142/S0219876218501396

18. Li S, Khan MI, Alzahrani F, Eldin SM. Heat and mass transport analysis in radiative time dependent flow in the presence of Ohmic heating and chemical reaction, viscous dissipation: An entropy modelling. Case Studies in Thermal Engg. 2023; 42: 102722. https://doi.org/10.1016/j.csite.2023.102722

19. Li S, Raghunath K, Alfaleh A, Ali F, Zaib A, Khan MI, Eldin SM, Puneeth V. Effects of activation energy and chemical reaction on unsteady MHD dissipative Darcy–Forchheimer squeezed flow of Casson fluid over horizontal channel. Scientific reports. 2023; 13: 2666. https://doi.org/10.1038/s41598-023-29702-w

20. Chamka AJ, Takhar HS, Soundalgekar VM. Radiation effects on free convection flow past a semi-infinite vertical plate with mass transfer. Chem. Engg. J. 2001; 84: 335-342. http://dx.doi.org/10.1016/S1385-8947(00)00378-8

21. Chamka AJ. Non-Darcy fully developed mixed convection in a porous medium channel with heat generation/absorption and hydromagnetic effects. Numer. Heat transfer. 1997; 32: 853-875. https://doi.org/10.1080/10407789708913911

22. Chamka AJ, Mujtaba M, Quadri A, Issac C. Thermal radiation effects on MHD forced convection flow adjacent to a non-isothermal wedge in the presence of heat source or sink. Heat Mass Transfer. 2003; 39: 305-312. https://doi.org/10.1007/s00231-002-0353-4.

23. Kumar YS, Hussain S, Raghunath K, Farhan A, Kamel G, Sayed M, Khan MI. Numerical analysis of magnetohydrodynamics Casson nanofluid flow with activation energy, Hall current and thermal radiation. Sc. Report. 2023:13: 4021.

24. Kodi R. Study of Heat and Mass Transfer of an Unsteady Magnetohydrodynamic Nanofluid Flow Past a Vertical Porous Plate in the Presence of Chemical Reaction, Radiation and Soret Effects. J. of Nanofluids. 2023; 12(3): 767-776(10). https://doi.org/10.1166/jon.2023.1965

25. Veera Krishna M, Jyothi K, Chamkha AJ. Heat and mass transfer on MHD flow of second-grade fluid through porous medium over a semi-infinite vertical stretching sheet. J. of Porous Media. 2020; 23(8): 751-765.10.1615/JPorMedia.2020023817.

26. Muthucumaraswamy R, Senthil Kumar G. Heat and mass transfer effects on moving vertical plate in the presence of thermal radiation. Theor. Appl. Mech. 2004; 31: 35-46. http://dx.doi.org/10.2298/TAM0401035M

27. Muthucumaraswamy R, Chandrakala P. Radiative heat and mass transfer effects on moving isothermal vertical plate in the presence of chemical reaction. Int. J. of Appl. Mech. and Engg. 2006; 11: 639-646.

28. http://www.ijame.uz.zgora.pl/ijame_files/archives/v11PDF/n3/639-646_Article_16.pdf.

sciendo

Pawan Kumar Sharma, Bhupendra Kumar Sharma, Anil Kumar   DOI 10.2478/ama-2024-0023
Mathematical Analysis of Chemically Reacting Species and Radiation Effects on MHD Free Convective Flow through a Rotating Porous Medium

29. Veera Krishna M, Jyothi K, Chamkha AJ. Heat and mass transfer on unsteady, magnetohydrodynamic, oscillatory flow of second-grade fluid through a porous medium between two vertical plates, under the influence of fluctuating heat source/sink, and chemical reaction. Int. J. of Fluid Mechanics Research. 2018; 45(5): 459-477. 10.1615/InterJFluidMechRes.2018024591.

30. Veera Krishna M, Anand PVS, Chamkha AJ. Heat and mass transfer on free convective flow of a micropolar fluid through a porous surface with inclined magnetic field and hall effects. Special topics & Reviews in the porous media: An Int. J. 2019; 10(3): 203-233. 10.1615/SpecialTopicsRevPorousMedia.2018026943.

31. Prasad VR, Reddy NB. Radiation and mass transfer effects on an unsteady MHD free convection flow past a heated vertical plate in a porous medium with viscous dissipation. Theoret. Appl. Mech. 2007; 34(2): 135-160. https://doi.org/10.2298/TAM0702135P.

32. Prasad VR, Reddy NB, Muthucumaraswamy R. Radiation and mass transfer effects on two-dimensional flow past an impulsively started infinite vertical plate. Int. J. of Therm. Science. 2007; 46(12): 1251-1258. http://dx.doi.org/10.1016/j.ijthermalsci.2007.01.004.

33. Baitharu AP, Sahoo SN, Dash GC. Numerical approach to non-Darcy mixed convective flow of non-Newtonian fluid on a vertical surface with varying surface temperature and heat source. Karabala Int. J. of Modern Sc. 2020; 6(3): 332-343. https://doi.org/10.33640/2405-609X.1753.

34. Krishna MV, Ahamad NA, Chamkha AJ. Numerical investigation on unsteady MHD convective rotating flow past an infinite vertical moving porous surface. Ain Shams Engg. J. 2021; 12(2): 2099-2109. https://doi.org/10.1016/j.asej.2020.10.013

35. Li S, Ali F, Zaib A, Loganathan K, Eldin SM, Khan MI. Bioconvection effect in the Carreau nanofluid with Cattaneo–Christov heat flux using stagnation point flow in the entropy generation: Micromachines level study. Open Physics. 2023; 21(1): 20220228. https://doi.org/10.1515/phys-2022-0228

36. Hossain MA, Das SK, Pop I. Heat transfer response of MHD free convection flow along a vertical plate to surface temperature oscillation. Int. J. Non-linear Mech. 1998; 33: 541-553. https://doi.org/10.1016/S0020-7462(96)00151-5

37. Reddy Vaddemani R, Kodi R, Mopuri O. Characteristics of MHD Casson fluid past an inclined vertical porous plate. Materialstoday: Proceedings. 2022; 49(5): 2136-2142. https://doi.org/10.1016/j.matpr.2021.08.328

38. Veera Krishna M, Chamkha AJ. Hall and ion slip effects on MHD rotating boundary layer flow of nanofluid past an infinite vertical plate embedded in a porous medium. Results in Physics. 2019; 15: 102652. https://doi.org/10.1016/j.rinp.2019.102652

39. Veera Krishna M. Hall and ion slip effects on radiative MHD rotating flow of Jeffreys fluid past an infinite vertical flat porous surface with ramped wall velocity and temperature. Int. Commun in Heat and Mass Transf. 2021; 126: 105399. https://doi.org/10.1016/j.icheatmasstransfer.2021.105399

40. Veera Krishna M, Chamkha AJ. Hall and ion slip effects on MHD rotating flow of elastico-viscous fluid through porous medium. Int. Commun in Heat and Mass Transf. 2020; 113: 104494. https://doi.org/10.1016/j.icheatmasstransfer.2020.104494

41. Sharma BK, Mishra A, Gupta S. Heat, and mass transfer in magneto-biofluid flow through a non-Darcian porous medium with joule effect. J. of Engg. Physics and Thermophys. 2013; 86(4): 766–774. http://dx.doi.org/10.1007/s10891-013-0893-0

42. Rout PK, Sahoo SN, Dash GC. Effect of Heat Source and Chemical Reaction on MHD Flow Past a Vertical Plate with Variable Temperature. J. of Naval Architec. and Marine Engg. 2016; 13(1): 101-110. https://doi.org/10.3329/jname.v13i1.23930

43. Aldoss TK, Al-Nimr A, Jarrah MA, Al-Sha'er BJ. Magnetohydrodynamic mixed convection from a vertical plate embedded in a porous medium. Numerical Heat Transfer Part A. 1995; 28(5): 635–645. https://doi.org/10.1080/10407789508913766.

44. Helmy KA. MHD unsteady free convection flow past a vertical porous plate. ZAMM. 1998; 78(4): 255–270. https://doi.org/10.1002/(SICI)1521-4001(199804)78:4%3C255::AID-ZAMM255%3E3.0.CO;2-V

45. Kim YJ. Unsteady MHD convective heat transfer past a semi-infinite vertical porous moving plate with variable suction. Int. J. of Engg. Sc. 2000; 38(8): 833–845. http://dx.doi.org/10.1016/S0020-7225(99)00063-4

46. Veera Krishna M, Swarnalathamma BV, Chamkha AJ. Investigations of Soret, Joule and Hall effects on MHD rotating mixed convective flow past an infinite vertical porous plate. J. of Ocean Engg. and Sc. 2019; 4(3): 263-275. https://doi.org/10.1016/j.joes.2019.05.002

47. Veera Krishna M, Ahamad NA, Chamkha AJ. Hall and ion slip effects on unsteady MHD free convective rotating flow through a saturated porous medium over an exponential accelerated plate. Alex. Engg. J. 2020; 59(2): 565-577. https://doi.org/10.1016/j.aej.2020.01.043

48. Takhar HS, Roy S, Nath G. Unsteady free convection flow over an infinite vertical porous plate due to the combined effects of thermal and mass diffusion, magnetic field and Hall currents. Heat and Mass Transfer. 2003; 39(10): 825–834. http://dx.doi.org/10.1007/s00231-003-0427-y

49. Raghunath K, Mohanaramana R, Nagesh G, Charankumar G, Khan SU, Khan MI. Hall and ion slip radiative flow of chemically reactive second grade through porous saturated space via perturbation approach. Waves in Random and Complex Media. 2022. https://doi.org/10.1080/17455030.2022.2108555.

50. 49. Kar M, Sahoo SN, Dash GC. Effect of the Hall Current and Chemical Reaction on   MHD Flow along an Accelerated Porous Flat Plate with Internal Heat Absorption/   Generation. J. of Enggg Physics and Thermophysics. 2014; 87(3): 624-634. https://doi.org/10.1007/s10891-014-1099-9

51. Sharma BK , Sharma PK and Chauhan SK. Effect of MHD on unsteady oscillatory Couette flow through porous media, Int. J. of Appl. Mech. and Engg., Poland, 2022, Vol (17),1, pp 188-202.

52. Choksi VG, Singh TR. A mathematical model of imbibition phenomenon in homogeneous porous media. Special topics & Reviews in the porous media: An Int. J. 2019; 10(1): 1-13. 10.1615/SpecialTopicsRevPorousMedia.2018021445

53. Jha BK, Isah BY, Uwanta IJ. Unsteady MDH free convective Couette flow between vertical porous plates with thermal radiation. J. of king Saud University-Science. 2015; 27(4): 338-348. https://doi.org/10.1016/j.jksus.2015.06.005

54. Kiranakumar HV, Thejas R, Naveen CS, Khan MI, Prasanna GD, Reddy S, Oreijah M, Guedri K, Bafakeeh OT, Jameel M. A review on electrical and gas-sensing properties of reduced graphene oxide-metal oxide nanocomposites. Biomass Conversion and Biorefinery. 2022. https://doi.org/10.1007/s13399-022-03258-7

55. Sharma BK, Singh AP, Yadav K, Chaudhary RC. Effects of chemical reaction on magneto-micropolar fluid flow from a radiative surface with variable permeability. Int.J. of Appl. Mech. and Engg. 2013; 18(3): 833–851. http://dx.doi.org/10.2478/ijame-2013-0050.

56. Sharma BK, Sharma P, Mishra N K, Fernandez-Gamiz U. Darcy-Forchheimer hybrid nanofluid flow over the rotating Riga disk in the presence of chemical reaction: Artificial neural network approach. Alexandria Engineering Journal, 2023: 76, 101-130. https://doi.org/10.1016/j.aej.2023.06.014.

57. Baitharu AP, Sahoo SN, Dash GC. Effect of Joule Heating on Steady MHD Convective Micropolar Fluid Flow over a Stretching/Shrinking Sheet with Slip. J. of Naval Architec. and Marine Engg. 2021; 18(2): 175-186. http://dx.doi.org/10.3329/jname.v18i2

58. Suresh P, Hari Krishan Y, Sreedhar Rao R, Janardhana Reddy PV. Effect of Chemical Reaction and Radiation on MHD Flow along a moving Vertical Porous Plate with Heat Source and Suction. Int. J. of Appl. Engg. Res. 2019; 14(4): 869-876. https://www.ripublication.com/ijaer19/ijaerv14n4_04.pdf

59. Mamatha SU, Renuka Devi RLV, Ahammad NA, Shah NA, Rao BM, Raju CSK, Khan MI, Guedri K. Multi-linear regression of triple diffusive convectively heated boundary layer flow with suction and injection: Lie group transformations. Int. J. of Modern Physics B. 2023; 37(1): 2350007. https://doi.org/10.1142/S0217979223500078

60. Cogley AC, Vinceti WG, Gilles SE. Differential approximation for radiation transfer in a nongray near equilibrium, AIAA Journal. 1968; 6: 551-553. https://doi.org/10.2514/3.4538

61. Xin X, Khan MI, Li S. Scheduling equal-length jobs with arbitrary sizes on uniform parallel batch machines. Open Mathematics. 2023; 21: 20220562. https://doi.org/10.1515/math-2022-0562

62. Sharma BK, Gandhi R. Combined effects of Joule heating and non-uniform heat source/sink on unsteady MHD mixed convective flow over a vertical stretching surface embedded stretching in a Darcy-Forchheimer porous medium. Propulsion and Power Research. 2022; 11(2): 276-292. https://doi.org/10.1016/j.jppr.2022.06.001

63. Li S, Puneeth V, Saeed AM, Singhal A, Al-Yarimi FAM, Eldin SM. Analysis of the Thomson and Troian velocity slip for the flow of ternary nanofluid past a stretching sheet. Scientific reports. 2023; 13: 2340. https://doi.org/10.1038/s41598-023-29485-0

64. Sharma PK, Sharma BK, Mishra NK, Rajesh H. Impact of Arrhenius activation energy on MHD nano-fluid flow past a stretching sheet with exponential heat source: A modified Buongiorno's model approach. Int. J. of Modern Physics B. 2023. https://doi.org/10.1142/S0217979223502843

65. Gandhi R, Sharma BK, Mishra NK, Al-Mdallal QM. Computer simulations of EMHD Casson nanofluid Flow of blood through an irregular stenotic permeable artery. App. of Koo-Kleinstreuer-Li Corr. Nanomaterials. 2023; 13: 652. https://doi.org/10.3390/ nano13040652

66. Jahanshahi H, Yao Q, Khan MI, Moroz I. Unified neural output-constrained control for space manipulator using tan-type barrier Lyapunov function. Adv. In Space Research. 2023; 71(9): 3712-3722. https://doi.org/10.1016/j.asr.2022.11.015

67. Liu Z, Li S, Sadaf T, Khan SU, Alzahrani F, Khan MI, Eldin SM. Numerical bio-convective assessment for rate type nanofluid influenced by Nield thermal constraints and distinct slip features. Case Studies in Thermal Engg. 2023; 44: 102821. https://doi.org/10.1016/j.csite.2023.102821

Pawan Kumar Sharma: https://orcid.org/0000-0001-5055-1159

Bhupendra Kumar Sharma: https://orcid.org/0000-0002-2051-9681

Anil Kumar: https://orcid.org/0000-0003-1681-0297

SELECTED RESEARCH ISSUES OF PROTOTYPE FLOATING SYSTEMS

Agnieszka DEREWOŃKO* , **Wiesław KRASOŃ***

*Faculty of Mechanical Engineering, Institute of Mechanics and Computational Engineering, Military University of Technology,
Sylwestra Kaliskiego Street 2, 00-908 Warsaw, Poland

agnes.derewonko@gmail.com, wieslaw.krason@wat.edu.pl

Abstract: The paper presents a solution that can be used as a temporary supplement to the existing infrastructure in cases of natural disasters, during structure or bridge repair, in military applications and in areas where it is necessary to provide a floating system crossing. The genesis of the proposed structure and its development, as well as examples of applications of the basic module, referred to as the river module – the floating cassette with the pneumatic pontoon – are presented. The original solutions, such as the bow–stern modules, designed using modern, light and durable materials acting as deflectors, are also described. Examples of the use of floating structures composed of identical/repeatable modules–cassettes are shown. The results of experimental tests of two prototype river modules sets are presented as a validation for numerical studies. Selected aspects of static, kinematic and dynamic analyses using finite element and multibody simulations are presented. The numerical simulation of the prototype floating bridge with an assessment of the impact of clearances and an estimation of the kinematic parameters of the floating ribbon with various configurations are described.

Key words: adjustable buoyancy, pneumatic pontoon, field tests, numerical analysis, finite element method, multibody simulation

1. INTRODUCTION

A pontoon bridge is a temporary structure for pedestrian and vehicle travel. A continuous deck is supported by floats. The maximum load it is able to transfer depends on the buoyancy of the floats. Pontoon bridges are used by both the army and civilians [1, 2]. In the military application, pontoon bridges are floating structures, in which the load-bearing elements are rigid, tight, metal tanks. To ensure the possibility of crossing for heavy objects, trucks or tanks, a sufficiently high buoyancy of floats is necessary. In addition, it is essential to provide an adequate number of people and equipment for mounting the floating bridge.

The objects of the discussed type are used mainly by the army for crossing water obstacles [3, 4]. Instances of their deployment are also found in civil applications; for instance, in emergency services and territorial defence units during natural disasters (flooding) for evacuating the population. They can also be used for the needs of local self-governments, among others when the possibility for the use of a fixed bridge becomes excluded owing to damage or destruction.

The unquestionable advantages of the pontoon bridge include its simplicity of construction and the possibility of combining different construction systems, depending on the type of water crossing. This solution allows the assembly of a pontoon bridge in various configurations [5].

The other advantage of the pontoon bridge is the possibility of using it regardless of the depth and length of the water crossing and various terrain conditions. However, the disadvantage that is associated with it is the large volume of floats required, and therefore, the need for a large storage area and a number of transport vehicles. The solution of the floating system presented here can help avoid a large part of these inconveniences.

The concept and development of the proposed mobile pontoon bridge with adjustable buoyancy have been presented in Refs. [6–9]. This type of construction results in the phenomenon that the deflection of the ribbon is partially offset by the buoyancy of water during the crossing of heavy objects such as tanks (Fig. 1).
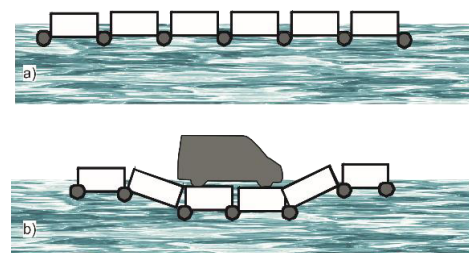
Fig. 1. Scheme of the deformation stages of a ribbon floating bridge: (a) unloaded, (b) loaded

The methodology of determining the buoyancy of a single module using the pneumatic carrier object (PCO) as well as the analysis of the stability of a single module has been presented in several previous papers [7–9]. The theoretical foundations of the vibration analysis of a multicomponent structure can be found in the studies of Xiang et al. [10], Liu [11] and Shao et al. [12]. Fragments of the kinematic and dynamic analyses carried out for the presented structure are illustrated in the studies of Derewońko et al. [7] and Krasoń and Sławek [8]. The experimental tests used to determine the strength of the complete bridge spans are discussed in Melcer's study [13], with this author having discussed selected aspects of the experimental strength tests of the prototype floating cassettes and innovative rod joints used to connect

cassette modules into a floating ribbon [9, 14–16]. The mobile pontoon bridge was transported on trailers of standard dimensions and installed in the desired location [9].

The floating systems studied in this work are composed of repeatable modules. Such an object is considered as a multiunit system with movable joints between the modules with assembly clearances. Experimental tests of complex, large-sized structures with clearance are difficult and expensive. Theoretical–analytical methods have some limitations due to geometrical nonlinearities determined by clearances. Therefore, simulation methods for tests using numerical analyses of multipart systems with clearances have been gradually improved. A typical approach to the research of complex multibody structures is multistage analysis as well as the analysis of selected parts of the complex structure. The original methodology of modelling as well as selected aspects of field tests, numerical finite element (FE) and multibody analysis of floating systems with constructional clearances are discussed in detail in the example of these prototype structures.

2. MOBILE PONTOON BRIDGE PROTOTYPE

The mobile pontoon bridge is classified as a "ribbon" floating bridge [7–9]. In terms of the static scheme, it is a continuous beam resting on a springy base. A scheme of the bridge without loading is shown in Fig. 1a. Deformation of the bridge caused by the force corresponding to the total weight (dead weight + load) of the conveyed vehicle is shown in Fig. 1b.

2.1. Design assumptions

A completed section of the mobile pontoon bridge is a river module performing a triple function: floating support, supporting structure and roadway. Requirements for this type of structure for military objects with the given parameters, e.g. MLC 70 class for wheeled vehicles and MLC 80 for tracked vehicles, were included in military standards, e.g. in the Polish NO-54-A203 [17] or in a trilateral agreement on a military bridge and crossing equipment concluded by the Federal Republic of Germany, the UK and the USA [3]. The MLC abbreviation is understood as a designation of a facility military load class in accordance with the NATO STANAG 2021 standardisation [4].

The mobile pontoon bridge can be developed by assembling individual modules in a desired configuration, the exemplary models of which, including models of vehicles being conveyed, are shown in Fig. 2.
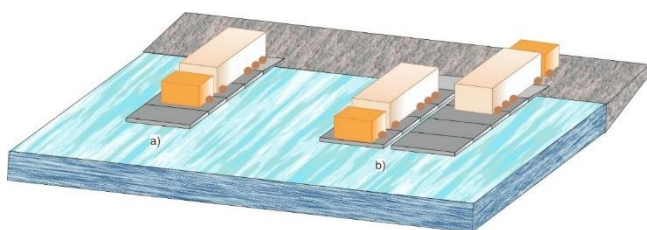
Fig. 2. Examples of a ribbon: **(a)** single, **(b)** double

Initial work on the design of the cassette pontoon bridge included simulation of a single-ribbon model composed of three

modules connected by mechanical locks under a moving load [9]. The vehicle was assumed to have the following characteristics, that is to say a weight of 4,000 kg, movement at a speed of 20 km/h along the track and in the direction presented in Fig. 3a, and the supporting of its weight by four wheels (Fig. 3b). The distance between the single tracks corresponded to the wheel spacing of the moving object.

When a vehicle with an assumed wheelbase exceeding the width of one module (i.e. an assumed wheelbase having a width greater than 2 m) was moving, the front wheels pressed on the modules, and differently from the pressing observed in the case of the rear wheels, thus causing deformations of different parts of the road surface in the adjacent modules. In Fig. 3a, a tracing of the wheels during the whole simulation of the vehicle movement is marked. On the other hand, Fig. 3b depicts the wheel tracing for the selected shorter-ride time interval.

The deformation of the cassette roadway surface in the selected time step under the pair of wheels (Sections 1 and 2 in Fig. 3a) in the direction of the repetitive module width is symbolically shown in Fig. 3c. The image of deformations of the roadway surface along the set of modules (in the vehicle-movement direction) under the front and rear wheels for the same time step is shown in the same way in Fig. 3d. This section is marked in Fig. 3a with the numbers 2 and 3.
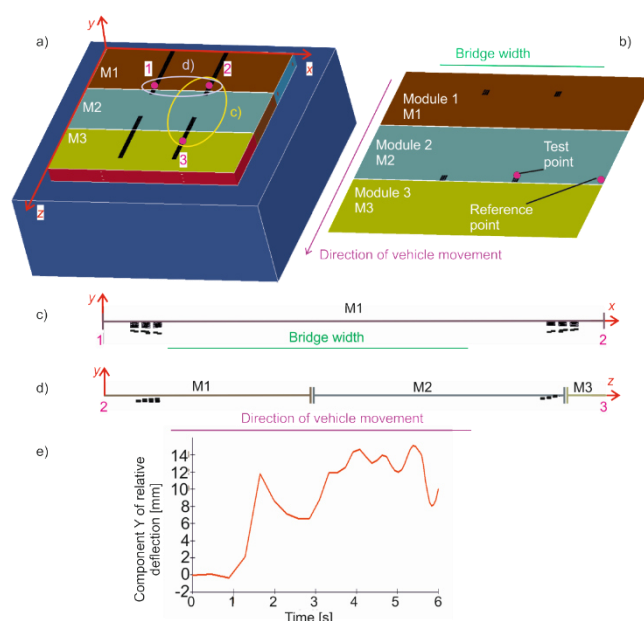
Fig. 3. Single-ribbon model: (a) vehicle motion track, (b) displacement registration points, (c) roadway deformation in the module width direction (O–X), (d) roadway deformation in the vehicle-movement direction (O–Z), (e) difference in vertical relative displacements (O–Y) determined in the test point and reference point (at module 2) as function of time

The relative deflection of the road surface caused by the wheel load, presented in the form of a graph in Fig. 3e, was obtained by referring the vertical displacement value Y of the node located on the roadway under the centre of a single wheel to the appropriate displacement of the node lying on the edge of the roadway.

2.2. River and bow–stern modules of a floating system

The main structural element of a single module is a closed metal cassette. Its required strength was ensured by the upper part, i.e. the roadway (Fig. 4a). The cassette is also a container for a PCO, constituting its basic protection, especially during transport, loading–unloading and launching–taking from water operations. In the opened position, the elastic pontoon (PCO) is folded inside the cassette (Fig. 4b).

In the lower part of the cassette, a movable bottom with a metal-composite structure was mounted. It can move downwardly under the pressure of the air-filled PCO. The return movement of the bottom was enabled by a set of 10 spring-telescopic mechanisms [6, 18, 19] placed symmetrically on both sides of the cassette (Fig. 4b), whereas the initial tension of the springs constituting the element of the telescope-spring mechanism allowed for tight closing of the cassette.

In the original version of the module structure, while opening the module, the deflector plate automatically extended from the side of the module stem (Fig. 4b) [9]. Such a construction of the cassette ensured the required strength and buoyancy, which allowed modules to be connected on water before filling the PCO with compressed air.

Fig. 4. Single prototype module – cassette with PCO: (a) in the closed position of the bottom plate – PCO without compressed air, (b) in the opened position of the bottom plate with PCO filled with compressed air. Designations: 1 – horizontal rod joints, 2 – cassette with roadway, 3 – vertical rod joints, 4 – module stem-deflector, 5 – bottom plate, 6 – elastic pontoon, and 7 – single telescopic mechanism

The cassettes were coupled by a set of mechanical locks [9, 14–16], which were vertical and horizontal rod joints (Fig. 4a). In addition, the connection of the cassettes on the road surface was carried out by the rotating arms [9]. The use of such side connections allowed for the immediate compilation of temporary crossings in the form of single-ribbon bridges of various lengths.

The bow–stern modules were unusual and innovative elements of the floating system equipment. Mounted at the bow and stern, they acted as deflectors, providing a streamlined shape, which reduced the resistance of the unit movement on the water. At the same time, they ensured user safety and increased the operational space of the system, which can be understood as an advantage in terms of facilitation of deck accessibility for the crew. From the side of the pressing water, the module surface was specially shaped (Fig. 5), which provided the proper direction of water streams flowing around the set of modules.

The use of unusual materials and innovative structures allowed for increasing the buoyancy of the entire set. A single bow–

stern module in the basic version with a load capacity of 18 kN could be folded into a set of two cassettes connected side by side [8, 9]. The structural solution of this sub-assembly allowed for the connection to the bow or the stern of the modules and determined the increase in the width of the module set deck by 1.2 m on each side. The connection with cassettes was made using the bow–stern horizontal rod joints (Fig. 5) that carried the main loads acting on those components. The top surface of the bow–stern module was inclined towards the cassette roadway, which formed an additional protection for the users of the floating object. The structure of the module enabled the assembly of protective barriers for the service crew.
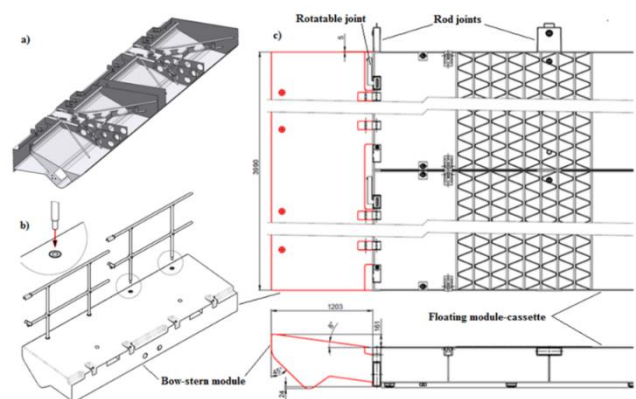
Fig. 5. Bow–stern modules: (a) internal space of module, (b) bow–stern module with protective barrier, (c) views of the floating system with two cassettes-river modules, joints and bow–stern overlays

The deflector designed in the unusual version of the cassette, used to properly direct the flow of water streams after opening the cassettes and filling the PCO, as well as for protecting the PCO from damage, was replaced with a system of expandable shutters (Fig. 6). This system was mainly used to reduce water resistance forces and eliminate ballistic threats. Due to the self-retracting mechanism, it was also possible to automatically roll up and fold the shutter system together with the movement of the bottom of the cassette.
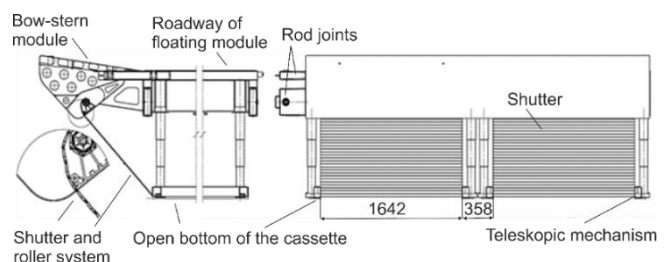
Fig. 6. Structure of roller shutter system in the basic version, mounted unilaterally on two river modules (in two views)

2.3. Example of mobile floating sets of individual modules as objects of research

The single floating module can also be used in the structure of a mobile floating ferry (Fig. 7) with its own roadway, consisting of 6 or 12 modules in various configurations [9]. Depending on the

required load space and load capacity, it was possible to combine different ferry variants.

The proposed solution allowed for building ferries in the 1×6 longitudinal configuration with a cargo space of 12 m $\times$ 6.3 m and a load capacity up to 480 kN and a parallel system 2×3 with a loading area of 12.7 m $\times$ 6 m and a load capacity up to 480 kN (Fig. 7).

The basic version is a fragment of a double ribbon with a length of 6 modules, which was a variant of the platform 2×6, i.e. a combination of 12 cassettes connected in 2 rows of 6 pieces each, with a loading space equal to 12.7 m $\times$ 12 m and a load capacity up to 960 kN. Additionally, with the use of two bow–stern modules, the operational space of each variant of a ferry increased the object roadway by 2.4 m.
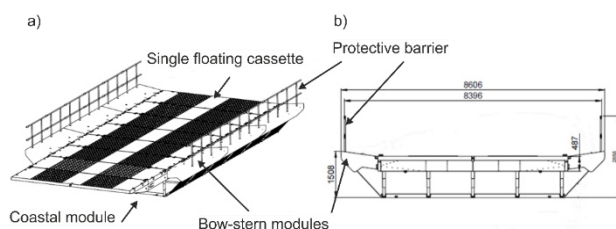
Fig. 7. Mobile floating platform in the 1×6 variant with the bow–stern modules and coastal modules in two views: (a) diagonal, (b) forehead view

3. EXPERIMENTAL TESTS OF TWO PROTOTYPE RIVER MODULES SETS

Experimental load tests of a prototype module were performed [9]. The research was carried out on a single-river module and a set of two connected cassette bridge pontoon modules.

The schedule of experimental tests of a single module and a set of two connected river modules included:

- an attempt to launch a single module with a closed bottom and register the value of its own immersion;
- the registration and evaluation of the operation of a single module on water in a closed state (without filling PCO with compressed air);
- the registration and evaluation of the process of filling a PCO before launching and after immersion in water;
- an assessment of the buoyancy and stability of the two-module set (after connecting the side locks and in the plane of the cassettes roadway), with the maximum filling of the PCOs;
- the observation and registration of the PCO-emptying process on water – an attempt to close the cassettes in water.

An experimental test of loading a two prototype river modules set, after filling a PCO with air, is shown in Fig. 8.

The test consisted of a sequential loading of the test modules with successive weights of appropriately selected masses of 1,000 kg or 1,600 kg. The maximum load value was 12.2 tonnes. The weights were set using a crane on the roadway of two connected river modules (Fig. 8).

The recording of module motion and the measurement of the set immersion were carried out using high-speed cameras to register the fast-changing phenomena. The results of the experimental test allowed assessment of the values of the changes in the dives, corresponding to the specific external loads, in individual loading sequences. The tests also allowed for the determination

of the load corresponding to the critical immersion of the ribbon when the plane of the module roadway was in the water surface plane.
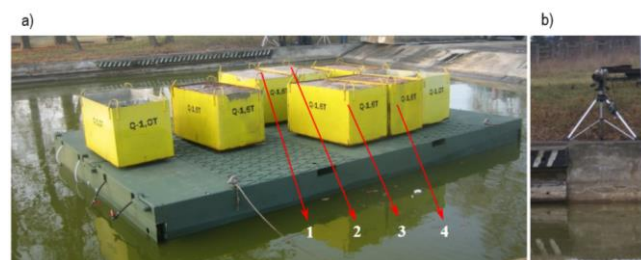
Fig. 8. Experimental load test of a set of two connected modules in WZI S.A. basin: (a) view after adding the last (8th) weight and obtaining the final load of 122 kN and (b) one of the cameras recording the field tests

Due to the limited memory of the cameras used (8 GBit), the recording time at full resolution and recording at 24 frames per second was approximately 4 min (231 s). The cameras were placed in perpendicular directions during the tests (Fig. 8b): one camera recorded the movement of the bow of the prototype pontoon assembly, and the other camera recorded the behaviour of the left side of the assembly. Based on the archived images of each camera, both the heights above the water surface of the centres, respectively the bow and the starboard side, as well as the inclination angles of the pontoon group in the transverse and longitudinal planes, were determined. Based on these results, it was possible to determine the displacements and angles used in the process of tuning the parameters of the numerical models and verifying the calculation results.

Based on the performed tests, it was found that the prototype river modules were characterised by high buoyancy and necessary stability. The tilt angles of the roadway, measured in the direction transverse to the set roadway axis and in the longitudinal direction, do not exceed 5°. Given the prevalence of a total external load of 12.2 kN, the modules' immersion in water was observed, with the result that the so-called "freeboard" was maintained, that is to say, there was a part of the module (measuring about 0.4 m) extending over the water surface (parameter H in Fig. 9). Thus, a large reserve of displacement of the two river modules assembled in such a way in the open configuration was obtained, with the PCO completely filled with air.

The graphs illustrating changes in the height value of the centre point of the right side, roadway and bow centres over the water level as a function of time are presented in Fig. 9a. These charts are a fragment of the full record of the changes in immersion during the sequential load process and correspond to the load phase of the module set with two, three and four weights (1–4 in Fig. 8).

The time interval from 178 s to 131 s corresponded to the load of the module set with four weights with a total weight of 64 kN. The value of the roadway centre height above the water plane varied between 660 mm and 720 mm. The average value of "freeboard" height H measured at the centre point of the roadway from the above range (marked with a square field with a blue background in Fig. 9a) was 690 mm.

The immersion V (Fig. 9b) of the cassette in the field test was determined according to the relationship:

$$V(t) = 1300 - H(t) \; [\text{mm}] \tag{1}$$

where the value of 1,300 mm is the structural dimension corresponding to the total height of the cassette and H(t) is the height of the "freeboard" measured at various points (Fig. 9b) of the cassette during the field test. The average value of the cassette immersion corresponding to the "freeboard" H = 690 mm was therefore V = 610 mm. This immersion value was used to tune and validate the numerical multibody model of the two cassettes presented in Sections 4 and 5.
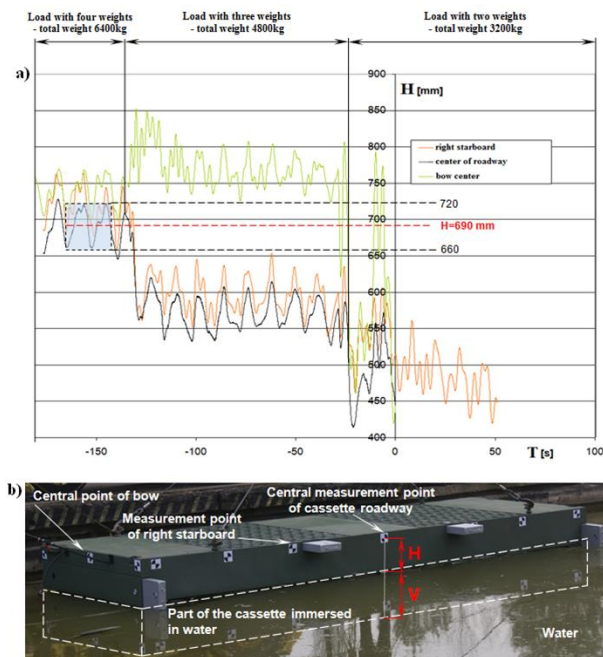
Fig. 9. Selected results of "freeboard" – the H measurement and the idea of immersion determination in a sequential load process during field tests: (a) changes in the value of the right starboard, roadway and bow centre's height over the water surface as a function of time during the loading process, (b) position of measurement points on the cassette and the view with an interpretation of the measurement parameters, H – height of the "freeboard" and the corresponding V – the immersion of the cassette

4. NUMERICAL STUDIES OF FLOATING SETS – VALIDATION TESTS

4.1. Methods of numerical simulations

Multibody system (MBS) and FE simulations were applied to selected aspects of the static, kinematic and dynamic analyses of the prototype floating bridge.

Newton and Euler equations (Newton's 2nd law and theorem related to rigid solid angular momentum change) as a relation (Eq. (2)) are often used to describe rigid body motion in MBS simulations.

$$m\dot{\boldsymbol{v}}_c = \boldsymbol{F}; \quad \dot{\boldsymbol{K}}_c = \boldsymbol{N}_c \tag{2}$$

Angular momentum vector components $\dot{\boldsymbol{K}}_c$ of the analysed object are defined in the following way:

$$\boldsymbol{K}_c = \boldsymbol{J}_c \boldsymbol{\omega} \tag{3}$$

where $\boldsymbol{\omega} = \begin{bmatrix} \omega_\xi & \omega_\eta & \omega_\zeta \end{bmatrix}^T$ and $\boldsymbol{v}_c = \begin{bmatrix} v_{cx} & v_{cy} & v_{cz} \end{bmatrix}^T = \begin{bmatrix} \dot{x}_c & \dot{y}_c & \dot{z}_c \end{bmatrix}^T$ is the generalised velocity of the centre C of the mass system.

In such a case, the solid motion equation takes the form (Eq. (4)):

$$\begin{bmatrix} m\boldsymbol{I} & 0 \\ 0 & \boldsymbol{J}_c \end{bmatrix} \begin{bmatrix} \dot{\boldsymbol{v}}_c \\ \dot{\boldsymbol{\omega}} \end{bmatrix} + \begin{bmatrix} 0 \\ \widetilde{\boldsymbol{\omega}} \boldsymbol{J}_c \boldsymbol{\omega} \end{bmatrix} = \begin{bmatrix} \boldsymbol{F} \\ \boldsymbol{N}_c \end{bmatrix} \tag{4}$$

where $\boldsymbol{J}_c$ represents the solid polar moment of inertia and N_c the moment of external forces (F) in relation to the center of mass C.

In the static FE tests for the developed numerical model of the mobile pontoon bridge with nonlinearities resulting from the contact phenomena and clearances, the analyses were conducted with the use of an iterative calculation algorithm. The algorithm in question is based on the Newton–Raphson scheme [20] and allows the analysis of the systems with a variable stiffness matrix resulting from the equilibrium state determined by equation Q = f(q), where Q represents the vector of external forces and q is a value of displacement corresponding to it.

4.2. Numericl MBS models

The research results were applied to build and validate numerical models of the experimentally tested set of two modules and models of single floating ribbons of various lengths and self-propelled floating platforms. Selected models used in numerical studies of module sets combined into floating platforms and into sections of the bridge ribbon are presented in Fig. 10.

The model shown in Fig. 10a was used in multivariate multibody analyses, in which load tests performed in field conditions were mapped. The model mapped the contact phenomena, friction in the locks joining the modules and a discrete influence of water represented by a set of springs with substitute stiffness determined based on the Winkler model.

Numerical models composed of rigid bodies (MBS models) or deformable bodies, respectively, represented by various FEs in the finite element method (FEM), were used in the verification tests and in the process of tuning the equivalent stiffness values and damping for the floating bridge multibody models. Rigid bodies mapping individual floating modules–cassettes (Figs. 10 and 12) in the MBS or deformable FEM models were connected with each other by means of movable constraints of the cylindrical joint type located in the plane of the bottom of the floating bridge set. The contact surfaces were mapped in the plane of the bridge roadway for the MBS and FEM numerical models considering assembly clearances (in the unloaded state) and appropriately selected structural damping. Spring-dampening elements were attached to the bottom of the models of individual cassettes (Figs. 10 and 12) for modelling the interaction of water with substitute parameters of stiffness (linear Winkler theory) and damping (Fig. 11) selected based on data recorded in field tests with a set of two cassettes (Fig. 10a).

Methods and procedures for determining stiffness and damping in mechanical problems are issues that were presented in scientific publications on modelling and simulation of dynamic problems, e.g. Refs. [8, 9, 21, 22]. The results of experimental tests recorded during field tests with a set of two prototype cassettes (presented in Section 3) were used for this purpose. The

work also used the comparative methodology of matching substitute values of stiffness and damping in numerical models, as explained below.
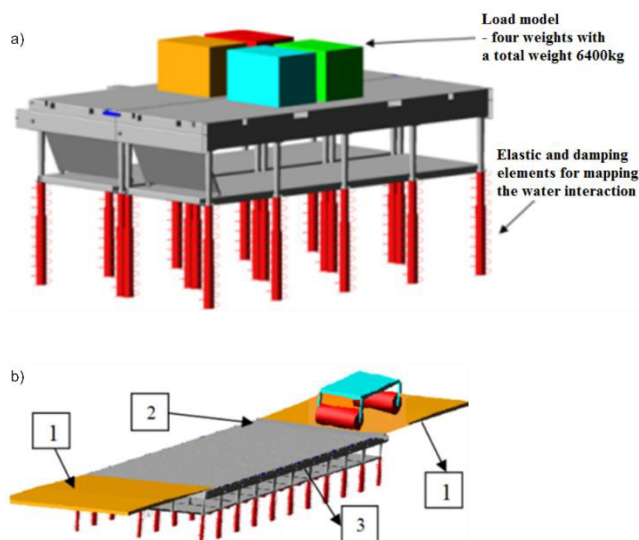
Fig. 10. Numerical rigid models of selected floating objects assembled from prototype modules: (a) multibody model of two floating modules set used in verification tests and for selection of substitute stiffness and damping values, (b) multibody model of single ribbon: 1 – coastal module, 2 – roadway, and 3 – river module

The diagrams of the changes in the maximum immersion of a two river modules set loaded at the same time with four weights as a function of time are shown in Fig. 11a. The average value of the immersion changes, referred to here as displacements of the central point of the cassette roadway and shown in Fig. 11a, was 610 mm. This value (V in Fig. 9b) corresponded to the average value of the "freeboard" height H = 690 mm measured at the central point of the cassette roadway during the field tests, as it is presented in Fig. 9a. A diagram of the change in the contact force in the pivot arm connecting the river modules in the plane of the roadway during the load test simulation is presented in Fig. 11b.
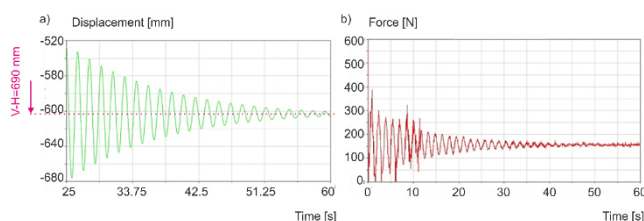
Fig. 11. Graphs of changes in kinematic and static parameters of the set after model's validation: (a) changes of displacements as a function of time, (b) changes of contact forces in the rotating arm connecting river modules during load test simulation

A three-dimensional multibody model of a single ribbon/platform, about 30 m long and 6 m wide (shown in Fig. 10b), was used in numerical studies conducted to ascertain the influence of the moved object's weight and position on kinematic and static parameters of the floating bridge section built of prototype modules connected by side locks.

Multiset numerical studies of the floating platform with coastal

modules were carried out. The set was loaded with the weight of the vehicle entering from the coastal module (1 in Fig. 10) and going to the platform external module (2 in Fig. 10) and moving along the platform at a constant speed of 1.5 m/s. In the initial variant P, only the self-weight of the floating structure including coastal modules (about 260 kN) was considered. In variant I, the total vehicle weight was 3.5 tonnes and in variant II, it was 10 tonnes.

5. NUMERICAL SIMULATION OF PROTOTYPE FLOATING BRIDGE

Numerical methods may be used even at the preliminary stage of the tests of the structures (Fig. 2). Due to the nature of the preliminary work, it is often necessary to perform verifying calculations repeatedly.

Multivariant load models, including time-varying models, inertial mapping of moving vehicles (multibody model – Fig. 12) and FE statics loads, were used in multivariant simulations under the influence of the size of clearances and various friction conditions.
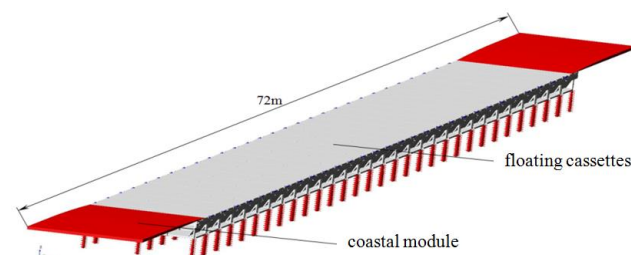
Fig. 12. Rigid body–MBS models of a single-ribbon type bridge for MB dynamics simulation

The model of the bridge section with the coast modules tested with the multibody method in the single-ribbon variant is shown in Fig. 12. The tested floating ribbon was composed of 30 prototype cassettes and two coast ramps. Each ramp was 6 m long and 6.25 m wide, corresponding with the dimensions for the bridge cassettes. Each ramp's mass was 6,000 kg. The end sections of both ramps were articulated with no translation displacement at the edges of the crossing (edge anchoring). The other end of the ramp rested on the roadway of the last mobile pontoon bridge ribbon cassette and was joined with it in a non-movable manner. The other end of the entry ramp was based on the road plate of the extreme cassette and the contact conditions along with the friction ones on the ribbon surface were defined. In the bridge model, three-dimensional connections between the individual cassettes of the set were mapped with the definitions of contact zones and assembly clearances corresponding to the nominal values provided for this type of structure.

In the static FE analysis, the floating ribbon was loaded in half of its length with a stationary lump representing various weights of the tracked vehicles being crossed: 100 kN, 250 kN, 500 kN and 700 kN. The dimensions of the body modelling the chassis of the tracked vehicle and the contour of the track in contact with the ribbon road were defined based on the STANAG standard [4], in accordance to the 50 MLC load class for tracked vehicles. In dynamic simulations, the solids modelling the tracked vehicle were given a constant speed of υ = 5 m/s. In this way, the movement of the transported vehicle was modelled in relation to the

road of the ribbon model compiled from the same floating cassettes, as given in Fig. 13. In individual variants of the dynamics analysis, identical weights of the vehicles were defined as in the statics analysis. In each considered variant, only a symmetrical passage along the longitudinal axis of the ribbon was defined (Fig. 13). Submersions and internal forces in the locks of such defined single-ribbon models were analysed.
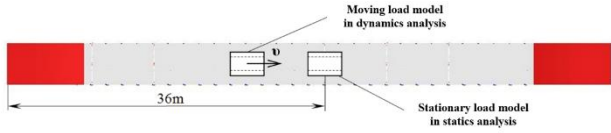

Fig. 13. The single-ribbon type model built from floating modules in the top view with models of stationary loads (statics analysis) and moving loads (dynamic analysis)

The changes in the floating ribbon's submersions recorded in the section corresponding to half the ribbon's length as a function of time during the runs of the vehicle with different weights – 100 kN, 250 kN, 500 kN and 700 kN – are summarised in Fig. 14. The maximum submersion values were determined as the differences in V displacements defining the initial and final positions of the cassette in the cross-section corresponding to half of the length of the floating ribbon in the individual load variants.

The results of the submersion numerically determined in the FE models of the floating ribbon (statics analysis) with results from the multibody tests – dynamic simulations – are compared in Tab. 1.

The maximum vertical displacements determined in the static analysis with FE models of the floating ribbon were greater by 9.9% and 0.9%, respectively, for loads of 250 kN and 500 kN, and lower by 4.2% for a load of 700 kN, than the maximum ribbon draft (submersion) determined in the dynamic analysis for analogous moving loads.
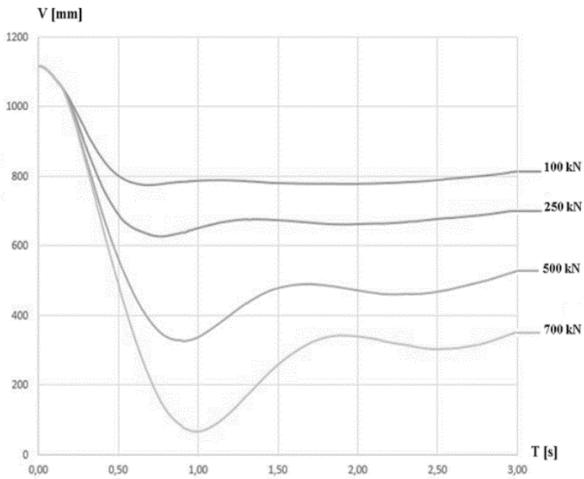
Fig. 14. Results of the MBS analysis: changes in vertical displacements of the cassette recorded in the middle of the ribbon length as a function of time during the runs of vehicle with different weights: 100 kN, 250 kN, 500 kN and 700 kN.

Prototype floating bridges with the maximum displacement (PCO is fully filled with air), in mixed and double ribbon systems,

may operate safely in crossings of vehicles with a weight of 1,000 kN (100 MLC according to the NATO classification [4]) moving at a speed of about 5 mps. The allowed load capacity of a single prototype ribbon was 700 kN (70 MLC).

Tab. 1. Comparison of results of numerically determined maximum submersion values in 3D models built of rigid and elastic bodies for various load values according to STANAG 2021 [4]

Load [kN]	Maximum submersion FE static analysis V [mm]	Maximum submersion MB dynamic analysis V [mm]	Relative differences $\left(\dfrac{\lvert V_{max}\rvert - \lvert V_{min}\rvert}{\lvert V_{min}\rvert}\right) \cdot 100\%$
250	500	455	9.9
500	687	681	0.9
700	823	858	4.2

6. CONCLUSIONS

The main original achievement of this work is the experimental and numerical research methodology established for testing the strength of multibody systems, which include modular floating systems. The work shows that the methodology can be used to test various floating systems in which, under the influence of moving loads, the assembly clearances change and the main part of them is formed without the clearances, the so-called "compact zone." This part of the modular floating object submerges the most because it absorbs all the loads from the moving object. An additional difficulty in static and dynamic tests of such systems, such as floating bridges, is the strong curvature and variable lengths of the compact zone depending on the weight of the objects being crossed. Moreover, a compact zone understood in this way is created directly under the vehicle being crossed. Its strong curvature results from the selection of clearances only in that part of the bridge that directly absorbs the loads from the vehicles being crossed. If the vehicle moves relative to the longitudinal axis of the floating bridge, the compact zone also moves with it. Correctly representing these phenomena in numerical simulations is a serious scientific challenge.

(1) The original achievements presented in the work are:
- a methodology for selecting substitute parameters – stiffness and damping – describing the multisegment model of the prototype bridge;
- verified based on experimental research, multimember models built of rigid bodies for MB simulation and results of dynamic analysis in models of floating bridges representing real crossing facilities;
- the possibility to determine the MLC classification of different variant floating bridges according to NATO STANAG military load standards, based on results of computer simulations.

(2) A river module with a movable bottom, with adjustable buoyancy, was characterised by a very good ratio of dead weight and usable carrying capacity to the working and transport volume.

(3) The structure in both the prototype and modernised version was tested in terms of strength and functionality. The verification tests of the assumptions, load capacity analyses and safety and strength in various operational states were carried out in laboratory tests and field tests as well as in computer analyses

with the use of advanced simulation techniques. The results obtained by numerical simulation were consistent to the experimental results.

(4) The structural modifications introduced in a single-river module allowed increasing of the range of potential applications of floating systems built on their basis. An increase in the structure susceptibility, as understood in this way, was confirmed. The possibility of building any configurations of ferries or floating bridges was proved.

(5) The bow–stern modules increased the operational space of the crew and the load capacity of the entire system and reduced the resistance of the set movement on water. The additional advantage of using the bow–stern modules was a roller shutter system, which, owing to the inclusion of a pneumatic carrier object filled with compressed air, can function as a ballistic protection as well as a protection against the occurrences of damages of various kinds.

(6) The repeatability of a single module and its ease of transport and operation make it possible to use it in many applications from the crossing of military vehicles (e.g. tanks), through replacement passes for trucks (e.g. providing materials for construction of a permanent bridge), to single-replacement ribbons for flooded roads and footbridges on suddenly enlarged watercourses.

(7) In the future, due to safety and functionality reasons, it is advisable to divide a PCO into at least three, independently assembled, chambers with a less complicated shape and a possibility of individual replacement in case of damage. External, high-strength joints of individual chambers would allow for creation of a coherent, multichamber pneumatic support body. The joints would be resistant to hydrostatic and hydrodynamic forces, external load and deformation of the bridge lines caused by them. The shape of a single chamber, similar to a rectangular prism, would limit the phenomenon of a number of internal tendons forming the walls of a PCO or would even eliminate the necessity for their use.

REFERENCES

1. Leqia He, Chiara Castoro, Angelo Aloisio, Zhiyong Zhang. Dynamic assessment. FE modelling and parametric updating of a butterfly-arch stress-ribbon pedestrian bridge. Struct Infrastruct Eng, 2021;18(7): 1064-1075.
2. Minwoo Chang, Sung Il Seo & Hyung Suk Mun. Running Safety and Behavior Tests for a Scaled-Down Railway Vehicle Crossing a Floating Bridge. KSCE J Civ Eng. 2020;24:1750–1762.
3. Hornbeck B, Kluck J, Connor R. Trilateral Design and Test Code for Military Bridging and Gap-Crossing Equipment. TARDEC BRIDGING 2005. http://www.dtic.mil/dtic/tr/fulltext/u2/a476390.pdf
4. STANAG 2021 Ed.8. Military Load Classification of Bridges, Ferries, Rafts and Vehicles. http://nso.nato.int/nso/nsdd/_CommonList.html]
5. Derewońko A, Krasoń W. Mobile pontoon bridge and floating systems, Special Interest Group A2 (Ports and Maritime) of the World Conference on Transport Research Society (WCTRS). Antwerpia conference proceedings. 3-4 May 2018.
6. EP2251255B1 2013. A sectional pontoon bridge. Military University of Technology.
7. Derewońko A, Kołodziejczyk D, Golczak K, Pneumatic Air Object Application in Design Of Water Crossing. Journal of KONES.2015; 19(4):155-161. DOI: 10.5604/12314005.1138333.
8. Krasoń W, Sławek P. Design and pre-testing of a mobile modular floating platform with adjustable displacement. Mechanik 2017;90(11). DOI: https://doi.org/10.17814/mechanik.2017.11.185
9. Krason W. Selected Problems of the Numerical Capacity Assessment for Floating Systems. Modelling in Engineering 2020: Applied Mechanics. Part of the Advances in Intelligent Systems and Computing book series (AISC, volume 1336), eBook ISBN978-3-030-68455-6. DOI https://doi.org/10.1007/978-3-030-68455-6pp. 168-180
10. Xiang X et al. Viscous damping modelling of floating bridge pontoons with heaving skirt and its impact on bridge girder bending moments. The 36th International Conference on Ocean, Offshore and Arctic Engineering. June 25-30. 2017. Trondheim Norway.
11. Jiachen Liu. Development of Vibration Base Health Monitoring in Bridge. Journal of Physics Conference Series 012021. September 2021. DOI:10.1088/1742-6596/2014/1/012021
12. Yanlin Shao, Xu Xiang, Jianyu Liu. Numerical Investigation of Wave-Frequency Pontoon Responses of a Floating Bridge Based on Model Test Results. Conference: Proceedings of the 38th International Conference on Ocean. Offshore and Arctic Engineering. June 2019. DOI:10.1115/OMAE2019-96545
13. Melcer J. Experimental Testing of a Bridge. Applied Mechanics and Materials. 2013; (486):333-340.
14. Krason W, Popławski A. Numerical research of the cassette bridge joint strength with mapping of stand for experimental tests. Cite as: AIP Conference Proceedings 2078, 020050 (2019). https://doi.org/10.1063/1.5092053, Published Online: 04 March 2019, 020050 pp. 1-6.
15. Krason W, Bogusz P. Strain research of side joints of floating bridge in lab bending test, Experimental Mechanics of Solids Materials Research Proceedings 12. 2019:96-103, Materials Research Forum LLC. https://doi.org/10.21741/9781644900215-14
16. Krason W, Bogusz P, Popławski A, Stankiewicz M. Selected aspects of stand tests of the floating prototype bridge connector. Experimental Mechanics of Solids Materials Research Proceedings 12. 2019:90-95. Materials Research Forum LLC. https://doi.org/ 10.21741/9781644900215-13
17. NO-54-A203: Mosty składane. Wymagania ogólne. http://g.ekspert.infor.pl/p/_dane/akty_pdf/U23/2001/22/186.pdf
18. Krason W, Kozłowski R, Derewońko A, Golczak K. Selected Aspects of Simulation of Multi-Module Mechanisms with the Use of Multibody Method. Journal of KONES.2012;19(1):207-214 DOI: 10.5604/12314005.1137359
19. EP2570551B1. A cassette of a floating bridge. 2012. Military University of Technology.
20. Zienkiewicz OC, Taylor L, Zhu JZ. The Finite Element Method: Its Basis and Fundamentals. Elsevier Butterworth-Heinemann. Berlin 2005.
21. Fengzong Gong, Fei Han, Yingjie Wang, Ye Xia. Bridge Damping Extraction Method from Vehicle–Bridge Interaction System Using Double-Beam Mode. Appl. Sci. 2021;11(21): 10304. https://doi.org/10.3390/app112110304
22. Lixia Peng, Zhiqiang Gao, Zhaoyang Ban, Feng Gao, Weiping Fu. Dynamic Tangential Contact Stiffness and Damping Model of the Solid–Liquid Interface. Machines.2022;10:804. https://doi.org/10.3390/machines10090804

Agnieszka Derewońko: https://orcid.org/0000-0002-6050-6359

Wiesław Krasoń: https://orcid.org/0000-0001-7242-648X

REDUCED GAIN PI/PID CONTROLLERS
FOR FOPTD/SOPTD PROCESSES UNDER LOAD DISTURBANCE

Andrzej BOŻEK* , **Leszek TRYBUS***

*Faculty of Electrical and Computer Engineering, Department of Computer and Control Engineering,
Rzeszow University of Technology, al. Powstańców Warszawy 12, 35-959 Rzeszów, Poland

abozek@prz.edu.pl, ltrybus@prz.edu.pl

Abstract: In practical applications, an engineer is sometimes expected to execute the step test for tuning the controller without waiting much for the steady-state or a low level of disturbances. Hence, knowing that the initial settings may not be quite reliable, he/she detunes the controller by reducing its gain as a precaution against possible poor behaviour of the closed-loop system. It is up to their experience to choose by how much to detune. Therefore, the development of a practically oriented approach that would assist the engineer to choose the degree of gain reduction is the goal of this paper. The approach assumes that process parameters are determined by the least-squares approximation of the step response. Accuracy of the approximation is evaluated by a relative approximation error involving integrals of the error and the process response itself. The SIMC tuning rules are applied to choose the initial controller settings. The approach relies on detecting by simulation the worst case that may happen when the step response is triggered at any time. Detuning nomograms specify by how much to reduce the initial gain for PI-FOPTD and PID-SOPTD designs, given the relative approximation error. Two long-lasting lab experiments involving temperature control identify a plant, verify the load disturbance model through multiple step tests and demonstrate usage of the approach in the closed-loop system.

Key words: load disturbance, process identification, controller tuning, SIMC, FOPTD, SOPTD

1. INTRODUCTION

Two types of disturbances are distinguished in industrial processes controlled by automation systems. The first one affects the state of the process, similar to the control input, whereas the other one only corrupts the output. Examples of the first type include disturbances of the load, fluctuations of raw material composition, power supply and ambient temperature usually jointly called a load disturbance [1,2]. Measurement noise dependent on transducer data, electromagnetic interference, and grounding quality is the other type. The load disturbance affects the process at low frequencies (LF), whereas the measurement noise interferes at high ones.

To suppress the effect of the disturbances, a process controller, typically PI or PID, must be reasonably well tuned, which in industrial practice is done experimentally by means of the step response or relay feedback [3]. In the case of the former, the parameters of the process are identified from the response and used to calculate controller settings. A steady-state and low level of disturbance, particularly the load disturbance, are the conditions required to obtain a trustworthy response and reliable parameters. The use of parameters acquired from a response triggered not at suitable conditions may lead to unreliable settings and poor behaviour of the closed-loop system.

However, in industrial applications, it is difficult to know whether the process to be identified is in a steady-state or not disturbed. In addition, waiting for such a steady-state can be cumbersome for a process with a long time constant or delay [4]. Therefore, an engineer has to sometimes execute the test when-

ever technology permits, without much waiting. Nevertheless, as a precaution, he/she does not apply the initial settings directly but detunes the controller by reducing its gain. The degree by how much to detune is determined by the rule of thumb.

Therefore, the purpose of this paper is to develop a practically oriented approach that will determine to what extent to reduce the gain in controller settings obtained from the response triggered at any time of process operation. A relative difference between the response and its least-squares approximation is the basic data for reducing the gain. SIMC tuning rules are applied to calculate the settings [2,5].

To justify the solutions used in the approach, we begin with a review of related work on process identification and SIMC tuning.

1.1. Process identification for load disturbance

A tutorial review of identification methods dealing with measurement noise and load disturbance is presented in Ref. [4]. In the presence of a general form of measurement noise, such as coloured noise, the least-squares solutions do not give unbiased parameter estimates [6]. To solve the bias problem, the instrumental variable (IV) method that adjusts the estimates in a few stages can be applied [7]. As far as the load disturbance is concerned, the problem of using the step response data while the output is not initially in a steady-state may be overcome by including the initial state and its derivatives into the identified parameters, yet assuming no load disturbance [8]. If, besides the initial conditions, the output is corrupted by measurement noise, the IV method can be applied [9].

sciendo

DOI 10.2478/ama-2024-0025

acta mechanica et automatica, vol.18 no.2 (2024)
Special Issue "Modern Trends in Automation and Robotics in tribute to Professor Tadeusz Kaczorek"

If the load disturbance description is known a priori, then the output may be decomposed into perturbed and unperturbed components, so as to obtain unbiased parameters of the process while estimating the dynamics of the disturbance response [10]. For example, a period of the perturbed component may be detected in this way [11]. No prior information is required if the perturbed component is treated as a dynamic parameter for estimation. A recursive least-squares algorithm is needed in such a case [12]. The perturbed component can also be estimated by correlation analysis [13].

Finally, no knowledge on the initial conditions or the load disturbance description is required if curve-fitting algorithms with quasi-Newton iterations are applied [6,7]. Both open and closed loops can be handled in this way, as demonstrated in Ref. [14] for an industrial application. In the case of overdamped systems with delay, each curve fitting iteration consists of two stages in which process parameters and the delay are estimated separately [15,16].

An approach is also proposed to calculate the process gain first from a steady-state change and then the time constant along with process delay in the second stage [17]. Good performance is reported for indirect identification of continuous delay systems based on discrete-time models [18]. Efficient identification from a low-quality step response by means of regularised least-squares is recommended in Ref. [19].

1.2. SIMC tuning rules

The selection of PI and PID tuning rules is another relevant issue. Note that to evaluate by how much the controller should be detuned, some quantification of the closed-loop behaviour is needed. Indicators of such behaviour include settling time, overshoot, peak time, IAE [20] or ITAE [21] integral, and relative delay margin [22]. However, among a large number of tuning rules collected in Ref. [23], only a fraction expresses controller settings not only in terms of process parameters, but also by a design specification related to the closed-loop behaviour.

The idea of using a desired closed-loop time constant to design a discrete controller was first introduced in Ref. [24], where this time constant was denoted by λ. Later, the approach was adapted to the internal model control (IMC) and PID controller [25]. In the case of the first- or second-order-plus-time-delay processes, i.e. FOPTD or SOPTD, the so-called SIMC tuning rules [2,5,26] express PI and PID settings in terms of the process parameters and the desired λ. This enables an engineer to choose how aggressive the controller should be. Due to simplicity, the SIMC rules have been widely approved in industrial practice [2]. Naturally, if due to disturbances, the identified parameters are unreliable, the value of λ must be increased to avoid poor closed-loop behaviour.

Performance of the SIMC rules for set-point and load disturbance responses can be assessed using the IAE, leading to some modification of the approach [26]. Minimisation of the IAE also enables to apply other closed-loop indicators for design. This is demonstrated in Ref. [27], where a weighted average of the IAEs for set-point and load disturbance responses is minimised subject to sensitivity constraints. A similar approach is used in Ref. [28] to improve disturbance rejection, but without applying the pole-zero cancellation of the original SIMC.

1.3. Outline of the approach

The development is based on a long uninterrupted MATLAB simulation of FOPTD and SOPTD disturbed processes, where step responses are continuously triggered one after another. Load disturbance is simulated by a low-pass filter driven by white noise. Measurement noise is treated as filtered out noise [29].

By repeating the simulation for different process delays, final nomograms specify the degree of reducing the gain for PI-FOPTD and PID-SOPTD designs in terms of a relative approximation error of the step response. Practical usage of the approach is demonstrated in a dedicated lab set up enabling repeatable tests in a long time period. The set up involves a temperature control plant, similar to the one in Ref. [30], whose dynamics can be well approximated by the FOPTD model. The load disturbance model is also verified from the tests.

The paper is organised as follows. The next section introduces normalised FOPTD and SOPTD process models affected by low-frequency load disturbance. The single, long simulation consists of multiple (5,000) up–down step tests resulting in 10,000 responses approximated by the curve fitting. Accuracy of the approximation is determined by a relative approximation error defined as the ratio of two integrals over time of the response. The first one integrates absolute estimation error and the second one involves the process response itself.

SIMC settings for PI-FOPTD and PID-SOPTD are given in Section 3 by taking the desired closed-loop time constant equal to the process delay [5]. Having the settings, the expected closed-loop behaviour can be inferred by calculation of the gain margin [31].

Controller settings and the corresponding gain margins are evaluated in Section 4 for each of the simulated responses. A minimum margin represents most inconvenient behaviour of the closed-loop system (worst case). This also enables to detect the maximum error for which the SIMC rules do not yet lead to instability. A worst case plant stabilised by means of an IMC-based PID controller is also considered in Ref. [32].

The difference between the nominal gain margin and the minimum margin determined above indicates by how much the design margin should be increased to avoid poor behaviour. In turn, that difference is converted in Section 5 into the corresponding reduction factor of the controller gain, expressed by respective nomograms for PI-FOPTD and PID-SOPTD designs.

The approach is verified in Section 6 by two long lab experiments, one for open loop and the other for closed loop, involving a heating resistor kept in open air. As in the MATLAB simulation, each experiment consists of multiple up–down step responses triggered in the presence of load disturbances. The time constant of the low-pass filter as a disturbance model is evaluated to justify the value used in the earlier sections.

2. PROCESS MODEL AND IDENTIFICATION

2.1. Process and load disturbance

A simulated process given in Fig. 1(a) is considered, where u denotes the control input, y the output and l the load disturbance interfering at LFs. High frequency (HF) measurement noise m is dropped from the simulation, although in the lab experiment, the

filtered m increases the effect of l. The following transfer functions

$$G_{\text{FOPTD}}(s) = \frac{k}{Ts+1} e^{-\tau s}, \quad G_{\text{SOPTD}}(s) = \frac{k}{(Ts+1)^2} e^{-\tau s} \quad (1)$$

represent the FOPTD and SOPTD process models (with different values of the parameters $k, T,$ and τ). Due to the double time constant in SOPTD, the two models are consistent in terms of the parameter set $\{k, T, \tau\}$. Different time constants for SOPTD are not considered as they would require much longer control input to get identified values reasonably close to true ones.

Settling times can be expressed as $4T + \tau$ and $6T + \tau$, respectively, or $5T$ and $7T$ for $\tau \leq T$. In practice, due to the disturbance, the step response is recorded for somewhat a longer time to be sure about the settling. Therefore, here, we take the double step-response settling time, i.e. $10T$ for FOPTD and $14T$ for SOPTD, as the identification time horizon.
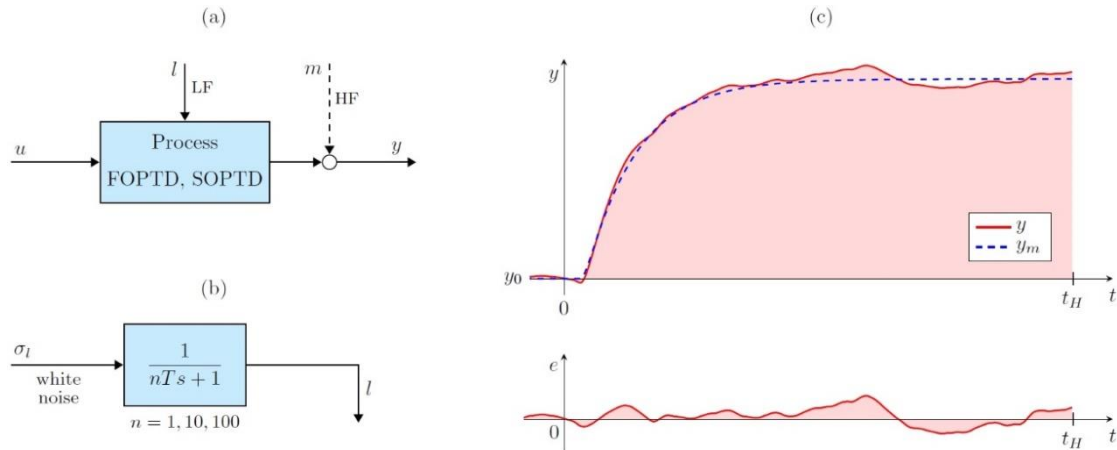
Fig. 1. (a) Process model, (b) load disturbance model, (c) step responses of the process y and model y_m, estimation error e
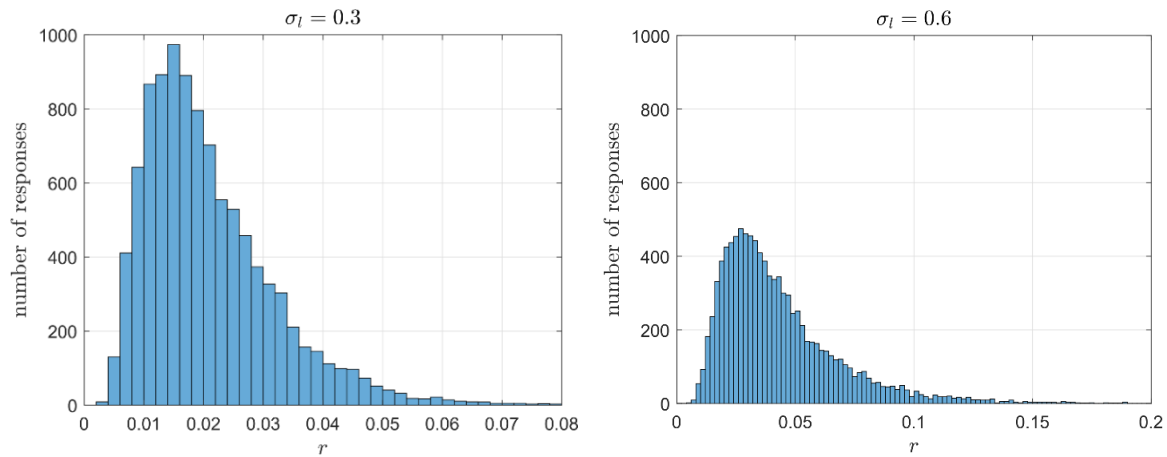
Fig. 2. Number of step responses in terms of the relative approximation error r
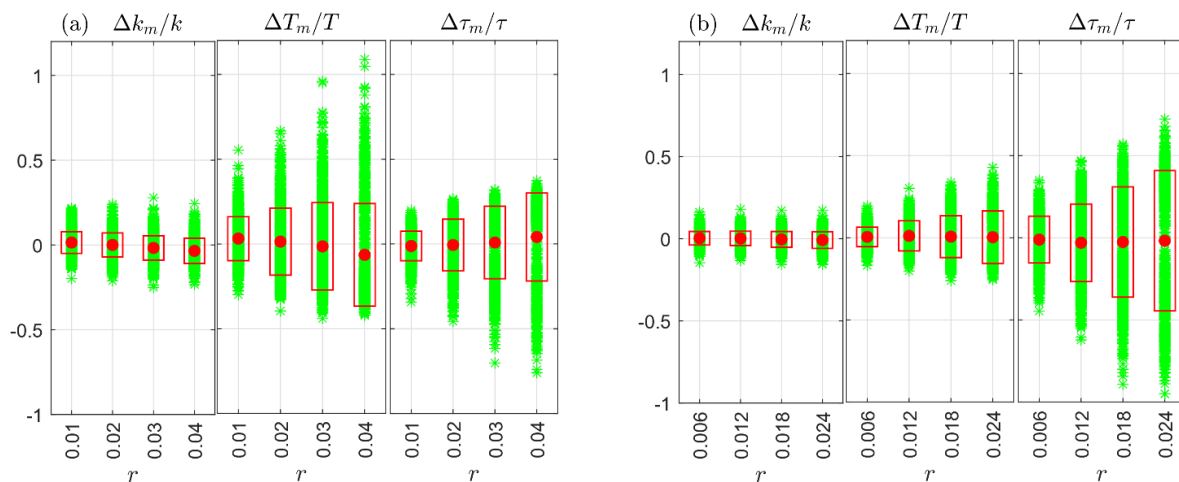
Fig. 3. Relative deviations of the parameter estimates for (a) FOPTD, $\sigma_l = 0.3$, (b) SOPTD, $\sigma_l = 0.15$

The LF load disturbance l is generated by the low-pass filter shown in Fig. 1(b), with the time constant n-times longer than the process. The results presented in the following sections refer to $n = 10$. Although it would be more appropriate to call the $n = 1$ case a "medium frequency" and not LF, it is left in the study for comparison. The level of l is adjusted by means of the standard deviation σ_l of the white noise driving the filter. A sample step response y of the disturbed process is shown in Fig. 1(c), where t_H denotes the identification time horizon.

2.2. Relative approximation error

The least-squares curve fitting the MATLAB lsqcurvefit function is used for identification, since the autoregressive arx and the instrumental variable iv4 cannot deal with the load disturbance [6,7]. Let $\{k_\mathrm{m}, T_\mathrm{m}, \tau_\mathrm{m}\}$ denote the parameter estimates of the identified model, y_m its step response and $e = y - y_\mathrm{m}$ the estimation error. The integrals

$$Y = \int_0^{t_\mathrm{H}} |y(t) - y_0|\mathrm{d}t, \ E = \int_0^{t_\mathrm{H}} |e(t)|\mathrm{d}t, \quad (2a)$$

representing the shaded areas in Fig. 1(c) determine the ratio

$$r = \frac{E}{Y} \quad (2b)$$

treated as an indicator to what extent the response is deformed by the load disturbance. The ratio, termed here a relative approximation error, is a basic data for detuning.

Realistic values of r for which parameter deviations from true values are not too large are below 0.05 for FOPTD and 0.03 for SOPTD. Larger deviations may cause instability of the closed-loop system tuned according to the SIMC rules [5] or excessive sluggishness in the case of the detuned controller (Section 5). Hence, trustworthy SOPTD responses require a smaller level of the load disturbance. If r of a particular real response turns out too high, it may be reduced in the next response by increasing the input step (if technology permits).

2.3. Simulation methodology and parameter estimates

Consider a continuously operating real process that can be tested any time by a step response. Meanwhile, the process can be perturbed by the load disturbance to a varying degree. An equivalent of such a process is implemented here in the form of a long uninterrupted simulation involving either the FOPTD or the SOPTD model, with the disturbance generated as shown in Fig. 1(b). During this simulation, step responses are triggered one after another, characterised by their own relative approximation error (2b). It turns out that about 10,000 tests are needed in the simulation to get histograms of r with fairly repeatable shape (see Fig. 2).

The results presented in the paper refer to the normalised time-constant-scaled process model, i.e. for $k = 1$, $T = 1$, and τ in the typical interval $[0.1, 1]$ (e.g. Ref. [31]). Some figures refer to $\tau = 0.32$ (middle of the decade). If T_m and τ_m are raw estimates of the parameters, then $\tau = \tau_m / T_m$.

Two histograms of the number of responses in terms of the error r for basic and twice increased standard deviation σ_l of the load disturbance are shown in Fig. 2 for FOPTD. Increase of σ_l extends the range of r while decreasing the maximum.

Roughly comparable deviations of the parameter estimates from true values are shown as bar graphs in Figs. 3(a) and (b) for FOPTD and SOPTD, respectively. Naturally, the deviations grow with the relative error r. Dots in the middle of the bars are means, and rectangle heights denote two standard deviations. The ranges $r = 0.04$ for FOPTD and 0.024 for SOPTD correspond to the load disturbance deviations $\sigma_l = 0.3$ and 0.15. This indicates that a similar degree of confidence in the SOPTD model as in the FOPTD requires a significantly lower disturbance level.

3. GAIN MARGIN FOR SIMC-BASED PI AND PID

Suppose for the time being that no load disturbance affects the process. The popular SIMC tuning rules used here express PI and PID settings in terms of the parameters $\{k, T, \tau\}$ and a desired closed-loop time constant λ [2,5].

Consider first the FOPTD process in Eq. (1) for which the PI controller

$$G_\mathrm{PI}(s) = k_p \left(1 + \frac{1}{T_I s}\right) \quad (3a)$$

suffices. Given the desired λ, the SIMC rules are as follows

$$k_P = \frac{1}{k}\frac{T}{\lambda + \tau}, \quad T_I = T. \quad (3b)$$

Skogestad in Ref. [5] recommends

$$\lambda = \tau \quad (4)$$

to get a tight response, whereas $\lambda = 1.5\tau$ provides a smoother response and $\lambda = 0.5\tau$ a more aggressive one. Some reduction of T_I for the large time constant T improves the reaction to the load disturbance [5,27]. However, we remain with the recommended Eq. (4) to preserve simplicity.

For Eq. (4), the rules become

$$k_P = \frac{1}{k}\frac{T}{2\tau}, \quad T_I = T \quad (5)$$

and the open-loop transfer function for $G_\mathrm{FOPTD}(s)$ obtains the simple form

$$G_\mathrm{open}(s) = G_\mathrm{PI}(s)G_\mathrm{FOPTD}(s) = \frac{1}{2\tau s}e^{-\tau s} \quad (6)$$

due to pole-zero cancellation. Since the plant model is not known exactly, the cancellation is not perfect. Therefore, some reduction of the gain k_P is needed to avoid possible oscillations (Section 5).

Gain margin $\mathrm{GM} = 1/|G_\mathrm{open}(j\omega_\mathrm{GM})|$ is determined by the frequency ω_GM obtained from the angle condition $\angle G_\mathrm{open}(j\omega_\mathrm{GM}) = -\pi$. In the case of Eq. (6), we have $\angle G_\mathrm{open}(j\omega_\mathrm{GM}) = -\pi/2 - \tau\omega_{GM}$, which yields

$$\omega_\mathrm{GM} = \frac{1}{\tau}\frac{\pi}{2} \ \text{and} \ |G_\mathrm{open}(j\omega_\mathrm{GM})| = \frac{1}{\pi}. \quad (7)$$

So, for the PI-FOPTD design, we get

$$\mathrm{GM} = \pi. \quad (8a)$$

Gain margin expressed in decibels will also be used, so

$$\mathrm{GM_{dB}} = 9.94 \ \mathrm{dB} \cong 10 \ \mathrm{dB}. \quad (8b)$$

For the SOPTD process in Eq. (1) and the PID controller,

$$G_\mathrm{PID}(s) = k_p \left(1 + \frac{1}{T_I s} + T_D s\right) \quad (9a)$$

the SIMC rules have the form [2,5]

$$k_P = \frac{1}{k}\frac{2T}{\lambda+\tau}, \quad T_I = 2T, \quad T_D = \frac{T_I}{4}. \tag{9b}$$

Then the controller becomes

$$G_{\text{PID}}(s) = k_P \frac{(Ts+1)^2}{2Ts}, \tag{10a}$$

where for the recommended $\lambda = \tau$, we get

$$k_P = \frac{1}{k}\frac{T}{\tau} \tag{10b}$$

and the transfer function $G_{\text{open}}(s) = G_{\text{PID}}(s)G_{\text{SOPTD}}(s)$ retains the form Eq. (6), so the margin GM or GM_{dB} is the same as before.

4. GAIN MARGINS FOR THE IDENTIFIED MODELS

4.1. Gain margin and relative approximation error

Let $\{k_m, T_m, \tau\}$ denote parameter estimates obtained from one of the disturbed responses characterised by a relative approximation error r in Eq. (2b). In the case of the PI-FOPTD design, we have

$$k_P = \frac{1}{k_m}\frac{T_m}{2\tau_m}, \quad T_I = T_m \tag{11}$$

from Eq. (5). Since the simulated process is given in the normalised form $e^{-\tau s}/(s+1)$ (Section 2), the open-loop transfer function becomes

$$G_{\text{open}}(s) = k_P \frac{T_I s+1}{T_I s}\frac{1}{s+1}e^{-\tau s}. \tag{12}$$

The angle condition $\angle G_{\text{open}}(j\omega_{GM}) = -\pi$ results in the equation

$$\frac{\pi}{2} + \text{arctg}(T_I\omega_{\text{GM}}) - \text{arctg}\,\omega_{\text{GM}} - \tau_m\omega_{\text{GM}} = 0 \tag{13a}$$

for the frequency ω_{GM}. After solving Eq. (13a), the corresponding gain margin is calculated as

$$\text{GM} = \frac{T_I\omega_{\text{GM}}}{k_P}\sqrt{\frac{\omega_{\text{GM}}^2+1}{(T_I\omega_{\text{GM}})^2+1}}. \tag{13b}$$

The bar graph in Fig. 4 presents the margin GM_{dB} in terms of the relative error r. Each bar consists of 1,000 points. Although the means are close to 10 dB, there are cases with quite small or even negative margins. The approximating parabolic curve $\text{GM}_{\text{dB,m}}(r, \tau = 0.32)$ specifies the minimum value of the margin in terms of the relative error. The minimum is defined here as three standard deviations below the mean. So, a few outliers in Fig. 4 are left out. From the controller's viewpoint, $\text{GM}_{\text{dB,m}}$ indicates the worst case among the step responses having the same relative error r. The value of $\text{GM}_{\text{dB,m}}$ is used in the next section to determine the degree of detuning.

Note that besides the main curve (continuous line) in Fig. 4 obtained for $n = 10$ in the low-pass filter of Fig. 1(b), there are also two other curves corresponding to the filters with $n = 1$ and 100. These two curves are fairly close to the main one. This confirms that the low-pass filter with $n = 10$ can be an appropriate model of the load disturbance interfering at LFs.
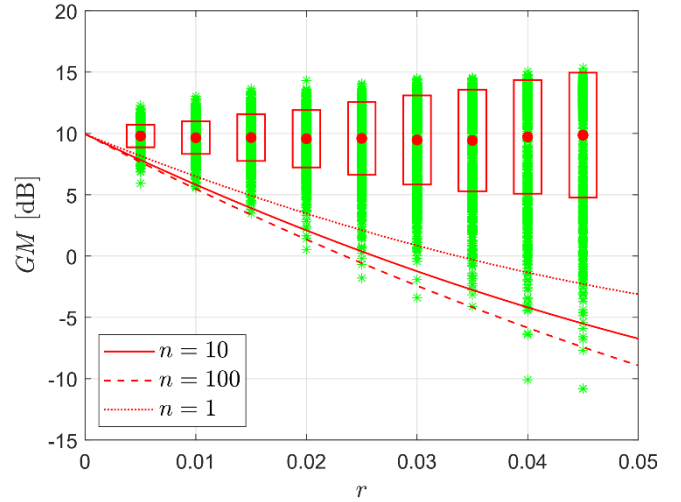
Fig. 4. PI-FOPTD gain margin as a function of the relative approximation error r for $\tau = 0.32$

4.2. Stability limit

By repeating the simulation and calculations for other delays $\tau \in [0.1, 1]$, a few functions $\text{GM}_{\text{dB,m}}(r, \tau)$ of the minimum gain margin shown in Fig. 5 are obtained. Increase of τ reduces the slope of the plots. Note that for $\tau < 0.56$, there exists a certain $r_{\max}$ for which $\text{GM}_{\text{dB,m}}$ becomes zero, which means stability limit. Hence for

$$r > r_{\max,} \tag{14}$$

detuning the controller becomes a necessity. The stability limit function $r_{\max}(\tau)$ is shown in Fig. 6. As seen, $r_{\max}$ increases with τ, which indicates more favourable conditions for identification.

Similar plots $\text{GM}_{\text{dB,m}}(r, \tau)$ and the function $r_{\max}(\tau)$ can be obtained for the PID-SOPTD design. About two times smaller values of $r_{\max}$ for PID-SOPTD in Fig. 6 translate into more demanding conditions for the step tests, i.e. lower level of the load disturbance.
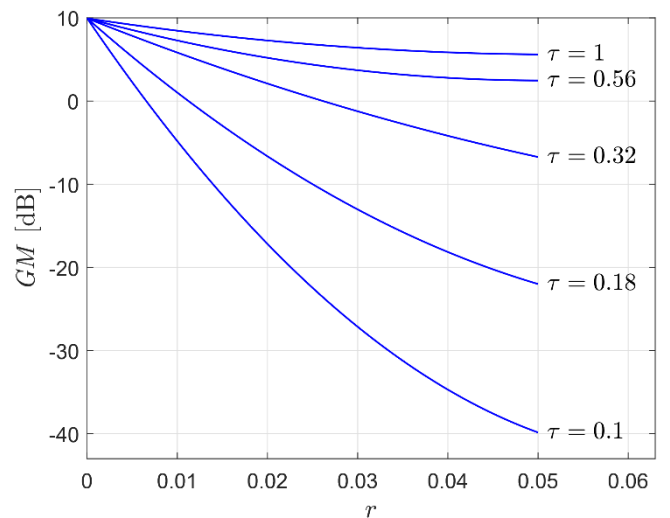
Fig. 5. PI-FOPTD minimum gain margin. $\text{GM}_{\text{dB,m}}$ as a function of r

![sciendo logo] **sciendo**

DOI 10.2478/ama-2024-0025

acta mechanica et automatica, vol.18 no.2 (2024)
Special Issue "Modern Trends in Automation and Robotics in tribute to Professor Tadeusz Kaczorek"
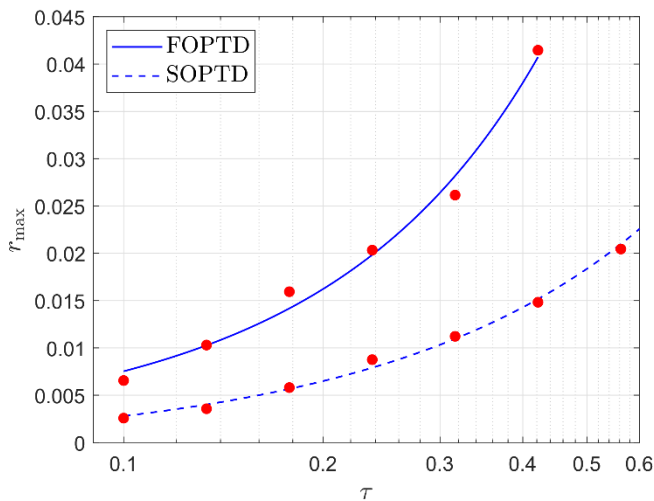
Fig. 6. Relative approximation error $r_{\max}$ for stability limit

5. REDUCTION OF THE CONTROLLER GAIN

While gain margins above $\mathrm{GM}_{\mathrm{dB,m}} \cong 10$ dB (Fig. 4) can be accepted since they indicate aperiodic responses, the ones below 10 dB rather not due to possible overshoots, oscillatory transients or even instability. The plots $\mathrm{GM}_{\mathrm{dB,m}}$ developed earlier determine the minimum margin that may occur for a particular relative approximation error r.

To avoid poor behaviour due to the insufficient gain margin, the design margin should be moved up by the difference between the desired nominal value $\mathrm{GM}_{\mathrm{dB}}$ and the worst case minimum value $\mathrm{GM}_{\mathrm{dB,m}}$. This can be done by replacing k_P in Eq. (11) by κk_P, where $\kappa \leq 1$ is the detuning factor.

Before the reduction, we have

$$G_{\mathrm{open}}(s) = k_P G'_{\mathrm{open}}(s) \tag{15}$$

with

$$\mathrm{GM}_{\mathrm{dB,m}} = 20 \log_{10} \frac{1}{k_P |G'_{\mathrm{open}}(j\omega_{\mathrm{GM}})|}. \tag{16}$$

The reduction is supposed to restore the nominal gain margin $\mathrm{GM}_{\mathrm{dB}}$, so

$$\mathrm{GM}_{\mathrm{dB}} = 20 \log_{10} \frac{1}{\kappa k_P |G'_{\mathrm{open}}(j\omega_{\mathrm{GM}})|}. \tag{17}$$

Subtracting Eq. (17) from Eq. (16) gives

$$\mathrm{GM}_{\mathrm{dB,m}} - \mathrm{GM}_{\mathrm{dB}} = 20 \log_{10} \kappa, \tag{18}$$

hence

$$\kappa = 10^{(\mathrm{GM}_{\mathrm{dB,m}} - \mathrm{GM}_{\mathrm{dB}})/20}. \tag{19}$$

The nomogram of the gain reduction factor κ in terms of the relative approximation error r and process delay τ is shown in Fig. 7(a) for PI-FOPTD. The value of κ decreases with r and increases with τ. Dots indicate $r_{\max}$, i.e. the stability limit from Fig. 6, where κ equals $1/\pi \cong 0.32$ according to Eq. (8a). Thus, having r and τ for a particular step response, one can read out κ from the nomogram and reduce the initial controller gain.
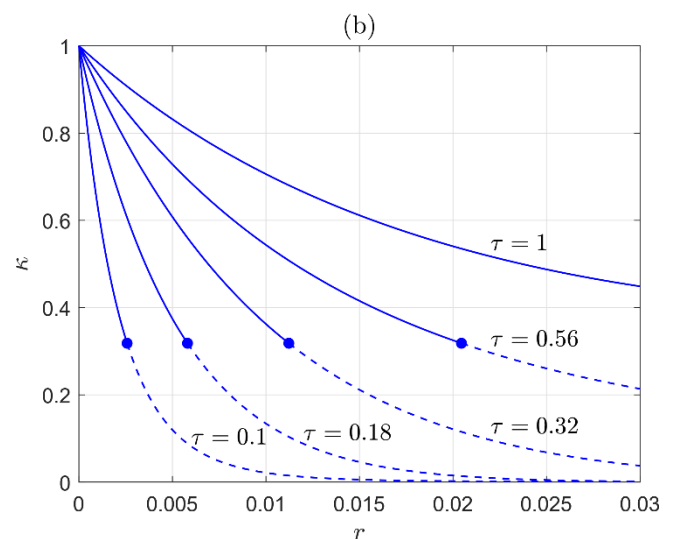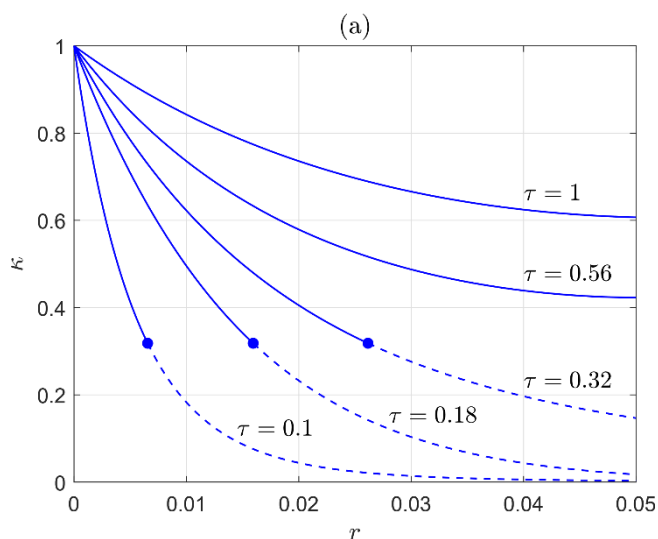
Fig. 7. Gain reduction factor κ of SIMC-based design for: (a) PI-FOPTD, (b) PID-SOPTD

The analogous nomogram for PID-SOPTD is given in Fig. 7(b) with a smaller range of the relative error r. At the first glance, for small r, both PI and PID could be applied. However, a more careful comparison of the nomograms reveals that the reduction factor κ for PID-SOPTD is much smaller than for PI-FOPTD. For instance, if $\tau = 0.32$, the error $r = 0.01$ yields $\kappa = 0.36$ for PID-SOPTD and 0.62 for PI-FOPTD. Only for very small r, the difference becomes negligible. This is another explanation why PI is most often preferred over PID in process control.

The nomograms determine the reduction factor κ also beyond the stability limit, i.e. for $r > r_{\max}$. However, since the proposed approach is worst-case-based, some of the closed-loop responses may turn out excessively sluggish for large r. In particular, it refers to the cases where the gain margins $\mathrm{GM}_{\mathrm{dB}}$ are above the nominal 10 dB (see Fig. 4), which indicates slow responses. Reduction of the gain makes them even slower. Unfortunately, for any disturbed step test, the gain margin is not known as to whether it is above or below 10 dB. Therefore, to avoid too slug-

gish responses, we recommend to accept only such step tests that satisfy the condition

$$r < r_{\max}, \tag{20}$$

with $r_{\max}$ given in Fig. 6. This excludes the tests with too large an approximation error.

The proposed approach is summarised in the form of a natural algorithm in Fig. 8. From the recorded step response, the model parameters, the time-scaled delay τ and the relative approximation error r are first obtained. The parameter $r_{\max}$ is then determined from the nomogram in Fig. 6. If the condition $r < r_{\max}$ is met, controller settings are given by the SIMC rules, followed by the gain reduction according to one of the nomograms in Fig. 7. Otherwise, if possible, the step response is repeated for an increased control step. If not, an engineer must wait for more favourable process conditions. The smooth closed-loop response is expected after completing the procedure.
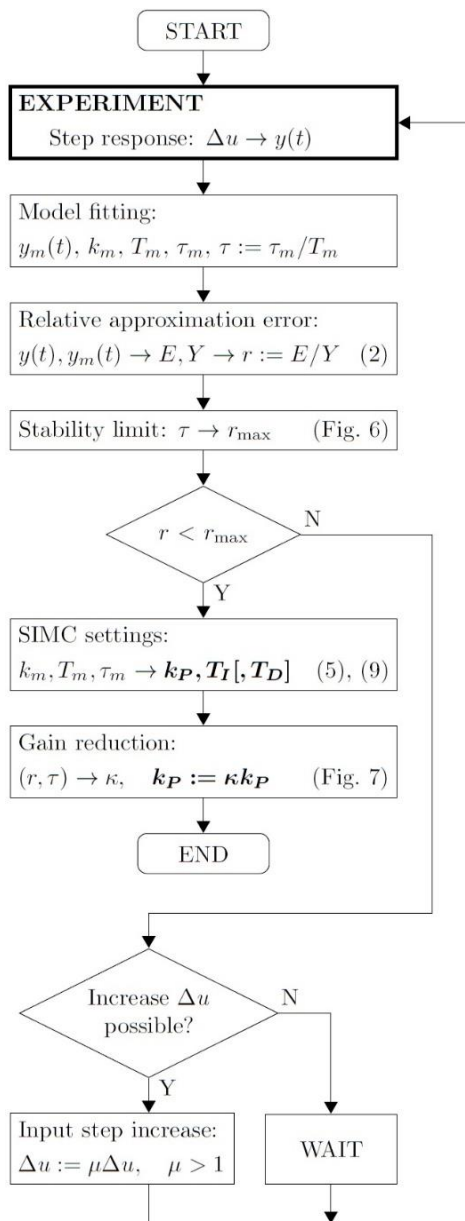
Fig. 8. Algorithm for tuning the controller from a disturbed step response

6. LAB EXPERIMENT

6.1. Equipment set up and operation

A simple lab set up (Fig. 9) has been assembled to demonstrate the proposed approach in two long experiments, one for open loop and the other for closed loop, involving repeatable tests under varying load disturbances. The set up involves a heating resistor kept in open air, Pt100 temperature sensor, transducer, PWM switch and an embedded system board connected to PC running MATLAB. The embedded system filters the measurements, works as the temperature controller, generates a PWM output signal and supervises the whole operation. Ambient temperature drift (daily cycle) is treated as a slowly varying load disturbance, although unexpected jumps caused, e.g. by opening the door or window, also happen for time to time. The basic open-loop experiment consists of 50 uninterrupted up-down step tests (100 responses in total) triggered automatically by the embedded system. The system continuously records the temperature in a file sent to the PC for identification. A second-order Butterworth filter with 10 s time constant is applied for measurement of the noise rejection.

For a nominal PWM = 25%, the resistor temperature is about 76 °C. After increasing the PWM to 27%, the temperature is recorded for 30 min, which is the t_H time in the integrals Eq. (2a). Such a modest 2% increase may correspond to technological restrictions in an industrial case. After waiting for 30 min, the input is decreased back to 25% and the down-response recorded again. Two up-down temperature changes of the plant and the models are shown in Fig. 10 to clarify the tests. The model output stops at the t_H time of Eq. (2a) followed by waiting. The whole experiment takes 100 h. The average up-down temperature change is 2.7 °C.

6.2. Verification of the disturbance model

Verification that the low-pass filter driven by white noise (Fig. 1(b)) can be a suitable model of the load disturbance is one of the objectives of the open-loop experiment. The verification involves three steps:

- Execution of 50 up-down tests with identification of the parameters $\{k_m, T_m, \tau_m\}$ by means of lsqcurvefit.
- Evaluation of the averages $\{\bar{k}, \bar{T}, \bar{\tau}\}$ treated as parameters of the plant for additional simulation.
- Selection of the low-pass filter parameters $\{n, \sigma_l\}$ to get a similar frequency spectrum of the real and simulated plants.

Histograms of the identified parameters are presented in Fig. 11. Parameter averages are the following

$$\bar{k} = 1.37\,°C/PWM_\%, \quad \bar{T} = 230\,s, \quad \bar{\tau} = 67\,s. \tag{21}$$

To verify the load disturbance model, the multiplier n in the filter time constant $n\bar{T}$ and the standard deviation σ_l of the white noise are determined by adjusting the simulated frequency spectrum to the real one by using FFT [33]. The resulting estimates are

$$n^* = 32, \quad \sigma_l^* = 10\,PWM_\% \tag{22}$$

(σ_l^* in control units).

The two spectra after adjustment of the disturbance model are shown in Fig. 12(a), where peaks represent odd harmonics of the up-down changes. The spectra practically overlap which confirms that the transfer function $1/(n^*\bar{T}s + 1)$ driven by white noise with the standard deviation σ_l^* models the load disturbance in the experiment quite well. Change of n would increase $(n > n^*)$ or decrease $(n < n^*)$ the slope of the simulated spectrum. Improper value of the standard deviation σ_l moves this spectrum up or down (Fig. 12(b)). The frequency range 0–1 mHz corresponds to harmonic components with periods above 1,000 s covering 4 time constants $\bar{T}$ $(4\bar{T} = 920)$. A rather large value of n^* is obtained here, so half a decade over $n = 10$ used before may be a hint for simulation of other processes subject to load disturbance.

6.3. Controller design and closed loop

The histogram of the distribution of r for the 100 recorded step responses is shown in Fig. 13a. Out of the responses, six have not passed the acceptance test, Eq. (20). Exemplary data from one of the accepted responses consist of the FOPTD parameters $k_m = 1.37\,°C/PWM_\%$, $T_m = 266\,s$, $\tau_m = 66.8\,s$ and the integrals $Y = 81.8\,°C \cdot s$, $E = 1.24\,°C \cdot s$ in Eq. (2a). So, we have the normalised delay $\tau = \tau_m/T_m = 0.296$ and the relative approximation error $r = E/Y = 0.0152$ $(r_{max} = 0.026$ from Fig. 6). The SIMC rules Eq. (11) give the initial PI settings $k_P = 1.23$ and $T_I = 226$. Having r and τ, the value of the gain reduction factor κ read out from Fig. 7a is 0.48 (after some interpolation). Hence, the controller gain is reduced to $\kappa k_P = 0.592$.
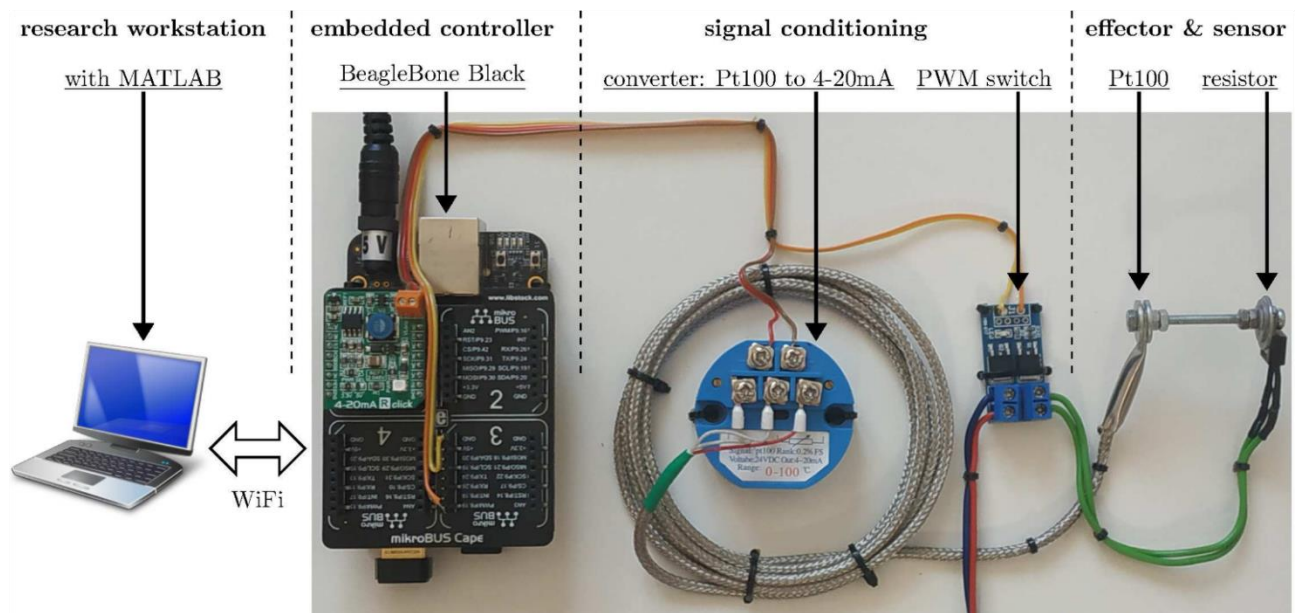
Fig. 9. Equipment set up
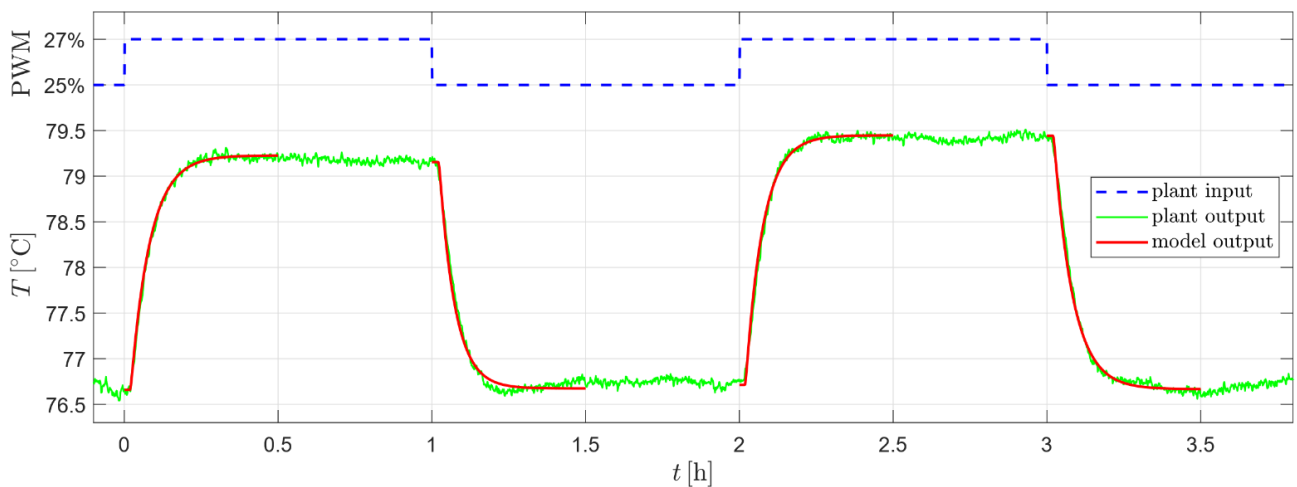
Fig. 10. Two exemplary up-down step responses
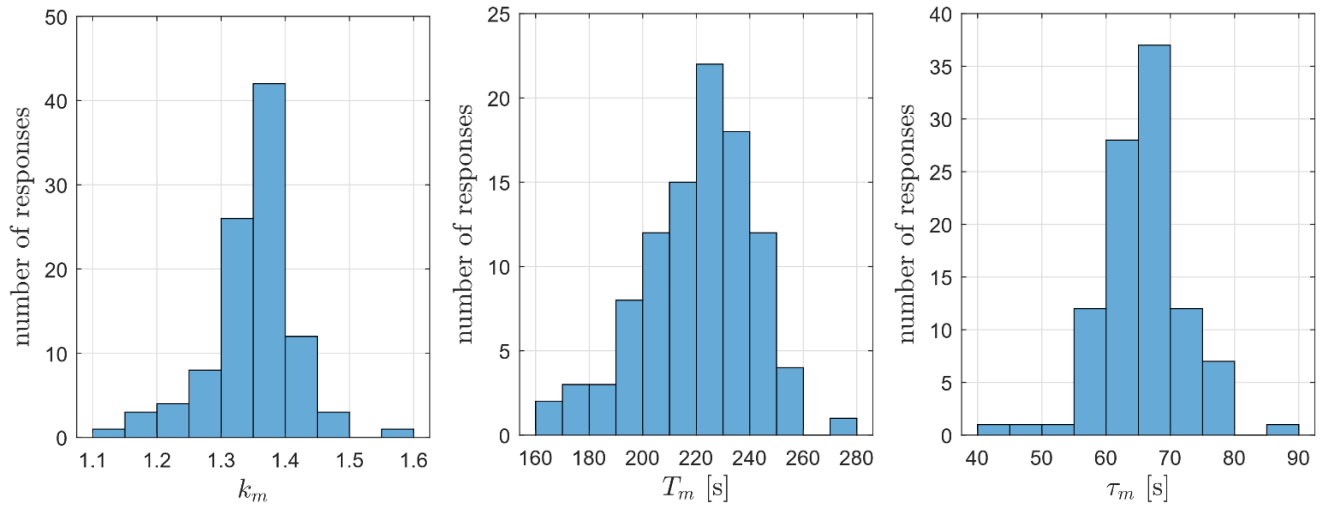
Fig. 11. Histograms of the identified parameters
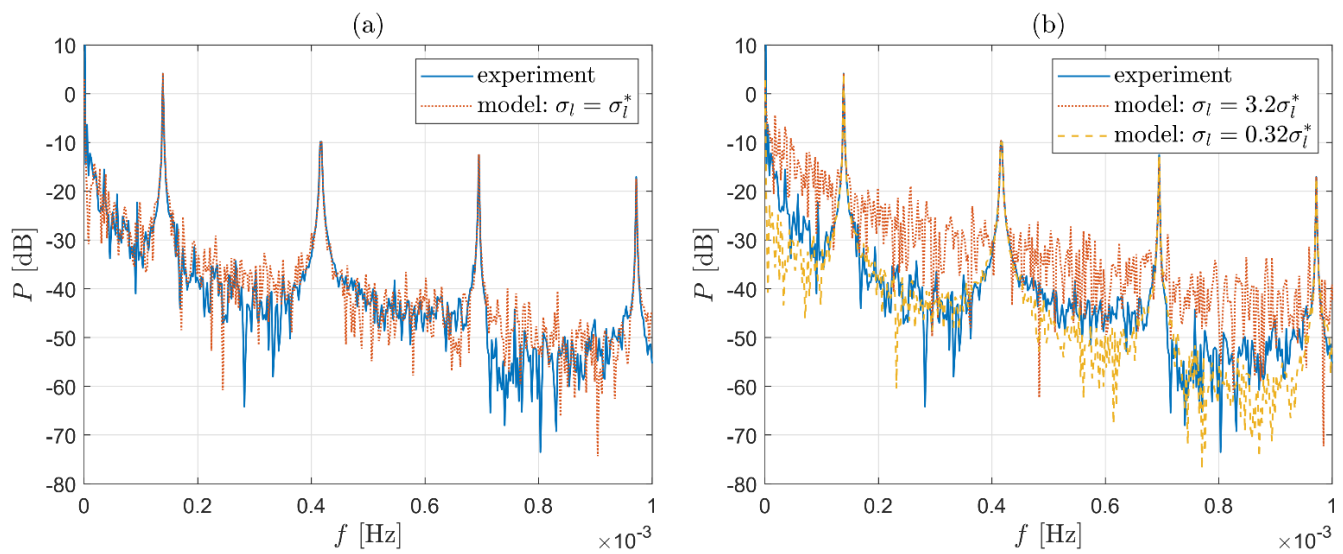
Fig. 12. Frequency spectra of the real and simulated plant outputs: (a) after adjustment of the disturbance model, (b) for improper standard deviation σ_l
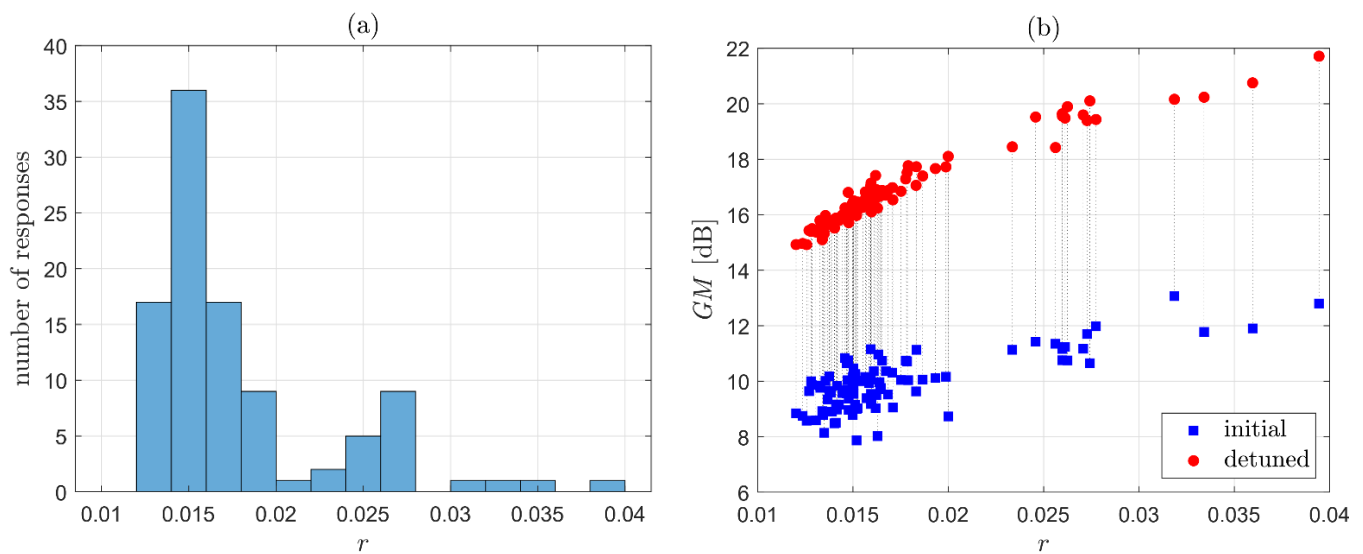
Fig. 13. (a) Number of step responses in terms of the relative error r, (b) gain margins for the initial and detuned settings
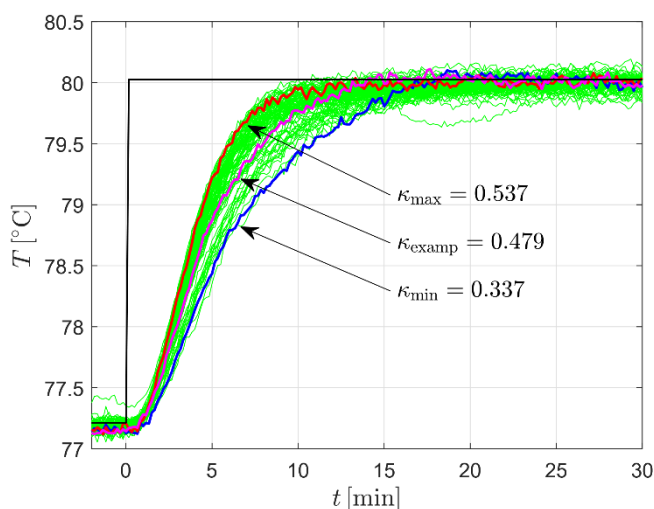
Fig. 14. Detuned closed-loop responses

The resulting closed-loop responses of the real plant recorded in the second experiment are shown in Fig. 14 for the 80 °C setpoint. The case for κ_{examp} relates to the exemplary calculations given above. The responses are smooth and settle down in a fairly similar time. The reduction factor assumes values from $\kappa_{\mathrm{min}} = 0.337$ to $\kappa_{\mathrm{max}} = 0.537$. Note that κ_{min} is close to the stability limit $1/\pi \cong 0.318$.

By taking the average parameters in Eq. (21) as plant data, one can check how the gain margins look like before and after the reduction. Lower squares in Fig. 13(b) represent the initial margins. Some of them are below the nominal 10 dB. The reduction increases the margins by 5–8 dB depending on the relative error r.

The presented results are obtained for rather a small input step $\Delta \mathrm{PWM} = 2\%$ to reflect technological restrictions. A larger step would decrease values of the error r thus, increasing the reduction factor κ. For $\Delta \mathrm{PWM} = 5\%$ the values of r do not exceed 0.012, giving $\kappa_{\mathrm{min}} = 0.568$ and $\kappa_{\mathrm{max}} = 0.863$.

The PID controller for the SOPTD model is not implemented since due to the smaller r_{max} (Fig. 6), too many step tests do not pass the acceptance condition in Eq. (20). Besides, the reduction factor κ is much smaller.

Finally, we explain why the identified $n^* = 32$ for the low-pass filter has not been used, although possible in this particular case. In a practical situation, an engineer only knows that the load disturbance interferes at lower frequencies in relation to process dynamics, but does not know exactly how much. Therefore, the approach with $n = 10$, justified by the similar plots in Fig. 4, seems an appropriate solution.

7. CONCLUSIONS

Due to technological restrictions, the step response required for controller tuning is sometimes triggered when the process is not in a steady-state or is subject to major load disturbance. This means that the parameter estimates obtained from the response and corresponding controller settings are not quite reliable. Hence, to avoid possible poor behaviour of the closed-loop system, the settings must be detuned, typically by reducing the gain. It is up to the engineer's experience to decide by how much to reduce.

FOPTD and SOPTD processes have been considered with the load disturbance modeled by a low-pass filter driven by white noise. Process parameters are determined by the least-squares curve fitting, so the estimation error of the response indicates to what extent the process is not in a steady-state or disturbed. Relative approximation error relates the error to the step response and is a basic data for reducing the gain.

SIMC rules have been applied to tune PI and PID controllers for FOPTD and SOPTD, respectively, taking process delay as the recommended closed-loop time constant. By repeating the tests in a long, uninterrupted simulation, the case with the lowest gain margin is detected and used subsequently for detuning. Final nomograms specify by how much to reduce the initial controller gain given a relative approximation error and process delay. So contribution of this paper rests in the precise evaluation of the gain reduction to assist the engineer.

Low-frequency load disturbance model has been verified in a simple, yet long, lab experiment with multiple step tests.

The MATLAB lsqcurvefit function has been used for identification. Ultimately however, the approach is supposed to be transferred from the embedded system board into a PLC-based process control equipment [34]. In such a case, a corresponding code may be written in structure text language of IEC 61131-3 standard [35] applying the two-stage curve-fitting algorithm from [15,16] for identification.

Research on the controller retuning directly in a closed-loop system subject to load disturbance is left for future work.

REFERENCES

1. Åström KJ, Murray RM. Feedback Systems: An Introduction for Scientists and Engineers. Princeton: Princeton University Press; 2008.
2. Seborg DE, Edgar TF, Mellichamp DA, Doyle FJ. Process Dynamics and Control, 4th Edition. New York: Wiley; 2016.
3. Åström KJ, Hägglund T. Advanced PID Control. Research. Triangle Park; 2005.
4. Liu T, Wang QG, Huang HP. A tutorial review on process identification from step or relay feedback test. Journal of Process Control. 2013; 23(10):1597-1623.
5. Skogestad S. Simple analytic rules for model reduction and PID controller tuning. Journal of Process Control. 2003; 13(4):291-309.
6. Ljung L. System Identification: Theory for the User, 2nd Edition. New York: Prentice Hall; 1999.
7. Söderström T, Stoica P. System Identification, 2nd Edition. New York: Prentice Hall; 2001.
8. Ahmed S., Huang B, Shah SL. Novel identification method from step response. Control Engineering Practice. 2007; 15(5):545-556.
9. Ahmed S, Huang B, Shah SL. Identification from step responses with transient initial conditions. Journal of Process Control. 2008; 18(2):121-130.
10. Liu T, Huang B, Qin SJ. Bias-eliminated subspace model identification under time-varying deterministic type load disturbance. Journal of Process Control. 2015; 25:41-49.
11. Hou J, Liu T, Wang QG. Recursive subspace identification subject to relatively slow time-varying load disturbance. International Journal of Control. 2017; 91(3):622-638.
12. Dong S., Liu T, Wang W, Bao J, Cao Y. Identification of discrete-time output error model for industrial processes with time delay subject to load disturbance. Journal of Process Control. 2017; 50:40-55.
13. Li LJ, Dong TT, Zhang S, Zhang XX, Yang SP. Time-delay identification in dynamic processes with disturbance via correlation analysis. Control Engineering Practice. 2017; 62:92-101.

14. Kon J, Yamashita Y, Tanaka T, Tashiro A, Daiguji M. Practical application of model identification based on ARX models with transfer functions. Control Engineering Practice. 2013; 21(2):195-203.
15. Hwang SH, Lai ST. Use of two-stage least-squares algorithms for identification of continuous systems with time delay based on pulse responses. Automatica. 2004; 40 (9):1561-1568.
16. Yan R, Liu T, Chen F, Dong S. Gradient-based step response identification of overdamped processes with time delay. Systems Science & Control Engineering. 2015; 3(1):504-513.
17. RamVD, Chidambaram M. On-line controller tuning for critically damped SOPTD systems. Chemical Engineering Communications. 2014; 202(1):48-58.
18. Du YY, Tsai JS, Patil H, Shieh LS, Chen Y. Indirect identification of continuous-time delay systems from step responses. Applied Mathematical Modelling. 2011; 35(2):594-611.
19. Liu Q, Shang C, Huang D. Efficient low-order system identification from low-quality step response data with rank-constrained optimization. Control Engineering Practice. 2021; 107:104671.
20. Jin Q, Liu Q, Huang B. Control Design for Disturbance Rejection in the Presence of Uncertain Delays. IEEE Transactions on Automation Science and Engineering. 2017; 14(4):1570-1581.
21. Sung SW, Lee J, Lee IB. Process Identification and PID Control. Wiley-IEEE Pres. 2009.
22. Sun L, Xue W, Li D, Zhu H, Su Z. Quantitative tuning of active disturbance rejection controller for FOPTD model with application to power plant control. IEEE Transactions on Industrial Electronics. 2022; 69(1):805-815.
23. O'Dwyer A. Handbook of PI and PID Controller Tuning Rules, 3rd Edition. Imperial College Press; 2009.
24. Dahlin EB. Designing and tuning digital controllers. Instruments and Control Systems. 1968; 41(6):77-83.
25. Rivera DE, Morari M, Skogestad S. Internal model control: PID controller design. Industrial & Engineering Chemistry Process Design and Development. 1986; 25(1):252-265.
26. Veronesi M, Visioli A. Performance Assessment and Retuning of PID Controllers. Industrial & Engineering Chemistry Research. 2009; 48(5):2616-2623.
27. Grimholt C, Skogestad S. Optimal PI and PID control of first-order plus delay processes and evaluation of the original and improved SIMC rules. Journal of Process Control. 2018; 70:36–46.
28. Veronesi M, Visioli A. Improving lambda tuning of PI controllers for load disturbance rejection. In Proceedings of the 26th IEEE International Conference on Emerging Technologies and Factory Automation (ETFA); 2021; 1-6.
29. Hägglund T. A unified discussion on signal filtering in PID control. Control Engineering Practice. 2013; 21(8):994-1006.
30. Oliveira PM, Hedengren JD. An APMonitor temperature lab PID control experiment for undergraduate students. In Proceedings of the 24th IEEE International Conference on Emerging Technologies and Factory Automation (ETFA). 2019; 790-797.
31. Veronesi M, Visioli A. On the Selection of Lambda in Lambda Tuning for PI(D) Controllers. IFAC-PapersOnLine. 2020; 53(2):4599-4604.
32. Saxena S, Hote YV. Stabilization of perturbed system via IMC: An application to load frequency control. Control Engineering Practice. 2017; 64:61-73.
33. Pintelon R, Schoukens J. System Identification: A Frequency Domain Approach, 2nd Edition. Wiley; 2012.
34. Rzońca D, Sadolewski J, Stec A, Świder Z, Trybus B, Trybus L. Developing a multiplatform control environment. Journal of Automation, Mobile Robotics and Intelligent Systems. 2019; 13(4):73-84.
35. EN 61131-3, Programmable controllers – Part 3: Programming languages (IEC 61131-3:2013), International Standard; 2013.

Andrzej Bożek: https://orcid.org/0000-0003-3015-7474

Leszek Trybus: https://orcid.org/0000-0002-1415-3679

ASSESSMENT OF PARAMETERS OF THE VIBRATION-BASED ENERGY HARVESTING SYSTEM LOCATED IN THE MICRO-POWER GENERATOR

Andrzej KOSZEWNIK*

Faculty of Mechanical Engineering, Bialystok University of Technology, Wiejska 45C Street, 15-351 Białystok, Poland

a.koszewnik@pb.edu.pl

Abstract: This article presents the optimisation process of some key parameters such as the size of the macro-fibre composite (MFC) and the optimal impedance load matching the piezoelectric harvester located in the prototype of the micro-power generator to enhance the vibration-based energy harvesting effect. For this, the distributed parameter model of this structure, including MFCs of the 8514 P2, 5628 P2 and 8528 P2 types, with a homogenous material in the piezoelectric fibre layer was determined. The numerical analysis of the FEM model of the flexure strip with piezo-composite indicated that the highest amplitude of voltage >7 V is generated by the proposed device with the piezo of the 8528 P2 type, while the lowest amplitude (close to 1.1 V) was noted for the piezo of the 8514 P2 type. Experiments were carried out on the laboratory stand to verify the obtained results. In addition, it was shown that the power output of the real EH system with the piezo of the MFC 8528 type, connecting with the matched resistive load (R = 120 kΩ), led to a significant increase in the value of the generating voltage up to 500 mW versus EH system with the piezo of 8514 P2 and 5628 P2 types. Finally, the effectiveness of this system was found to be close to 33% for the EH system with the piezo of the 8528 P2 type.

Key words: macro-fibre composite, homogenised material, micro-piezo generator, vibration-based energy harvesting system

1. INTRODUCTION

Energy harvesting is defined as the direct conversion of unused ambient energy, such as mechanical, thermal and solar, to electrical energy. The most popular and generally known energy harvesting methods in civil infrastructure are solar panels or wind turbines, which powers electronic devices with a high power demand. Another approach is using vibration-based energy harvesters that utilise vibrations of a mechanical structure or ambient vibrations that can be used to power small-scale sensors and actuators of a low power demand.

Numerous methods of converting mechanical motions to electric energy from a technical point of view, such as piezoelectric [1–3], electrostatic [4], and magnetostrictive or electromagnetic energy [5], can be found in the literature. Among them, piezoelectric generators is the most efficient in such applications due to their simple structure and the high robustness to external/internal electromagnetic waves. In addition, the effectiveness of this type of generator can be improved by modifying the piezoelectric materials, changing the stress direction, or altering the electrode pattern. Unfortunately, apart from these advantages, piezoelectric generators have numerous disadvantages, such as depolarisation, poor coupling in the piezo-film and poor adhesion between the polyvinylidene fluoride (PVDF) film and electrode material [6,7].

A group of researchers, with Morita as a leader, showed that electromagnetic energy harvester generators have a high energy density and they can be fabricated without any difficulties [8]. Compared to piezoelectric generators, smart materials and external voltage sources are not needed for electromagnetic genera-

tors. Hence, Nicoleti pointed out that electromagnetic harvesters represent a low-cost solution with the possibility of operating without any contact with the vibrating structure [9]. Similar to piezo generators, electromagnetic generators also have numerous disadvantages, one of which is the fact of being affected by electromagnetic waves, which will pose some difficulties when integrating with MEMS [10].

Smart materials are not needed for electrostatic generators, and they are also compatible with MEMS [11]. The advantages of electrostatic generators are presented in an article written by Roundy [12], who pointed out that using the out-of-plane gap-closing convert method will yield the highest potential capacitance, and the interaction between the two planes makes them easy to stick together. Other advantages of this method are described in articles [13,14] written by Li et al., who showed that an electrostatic MEMS energy harvester with a novel non-uniform comb or impact-based frequency up-conversion can enhance the power output generated by this device. Similar results were also obtained in a previous study [15] where an electrect-based Vibration Energy Harveters (e-VEH) device with the frequency up-conversion was used.

Electrostatic generators are widely used in many applications because of the advantageous properties of the piezo-patch strips and piezo-stacks [16–20]. Here is an example of such an application in structural health monitoring (SHM): [21] Pakrashi et al assessed the leak localisation in water pipes using piezo-patches and investigated several pipes with different widths of leak to propose and calibrate a leak index based on the monitoring voltage from a piezoelectric energy harvester (PEH) and the power spectrum of the output signal generated from particular PVDF piezoelectric transducers. Similar experiments have been carried

Andrzej Koszewnik
Assessment of Parameters of the Vibration-Based Energy Harvesting System Located in the Micro-Power Generator

DOI 10.2478/ama-2024-0026

out for bridge monitoring under operational conditions via Pb-zirconate titanate (PZT) patches [18,22,23] or the damage identification metric for smart beams with macro-fibre composite (MFC) elements to support SHM [24]. Ambroziak et al. [25] used piezoelectric energy harvesting systems for monitoring the propulsion system of Vertical Take-off Landing Unmanned Aerial Vehicle (VTOL UAV) in their study, where they investigated healthy and damaged propulsion systems and proposed a methodology for quickly detecting the failure of the UAV propulsion system.

As mentioned earlier, piezoelectric energy harvesting systems are also used to improve the effectiveness of systems, especially in a low frequency range. Pan et al. designed a hybrid energy harvester [26] that can generate an output power close to 70 µW. A similar study was done by Yang et al. who used a rail-borne PEH to collect energy from random railway vibrations [27]. They also demonstrated that the output power peaks from the system at the first two resonance frequencies are close to 10 mW. In another study [28], Wu et al. proposed a while-drilling energy harvesting device as a continuous power supply for downhole instruments during the drilling procedure. The designed device can obtain the best energy harvest performance with a peak voltage of 20–40 V and with the thickness of piezo-strips of 1.2–1.4 mm. Kan et al. [29] developed a PEH excited by an axially pushed wedge cam. The proposed rotary energy harvester is characterised by the simultaneous realisation of unidirectional deformation and limited amplitude for piezoelectric vibrations. Under the optimum matching parameters, the proposed harvester generated a maximum power of 10 mW. Ju et al. [30] proposed an energy harvester that consists of spherical proof mass in an aluminium housing and a piezoelectric cantilever beam fabricated by attaching metal blocks at the free end of an MFC beam. The obtained experimental results indicated that the proposed harvester based on an indirect impact enhanced the energy harvesting effect by obtaining an average power output of 964 µW by 3 g acceleration at 18 Hz.

The effectiveness of the energy harvesting system for cantilever beam structures can be also enhanced by considering the broadband effect. For example, Zhou et al. [31] used a novel multi-mode intermediate beam with a tip mass called a "dynamic magnifier". The results of in this study showed that the amplitude of the voltage generated by the proposed harvester in a low frequency range significantly increased in comparison to the conventional energy harvesting system. Similar results were obtained in a study by Caban et al. [32], where an energy harvesting system was located on a diesel engine suspension.

Other devices that produced more amount of energy are piezo generators equipped with piezo-stacks. For example, Peng et al. [33] indicated that this kind of generator can produce an instantaneous peak power of 300 mW. Similarly, Wen et al. [34] designed a piezoelectric generator with an integrated multistage force application. The experimental results showed that a high-peak power output of 50 mW can be obtained from the proposed device when connected with a properly matched resistive load.

Regardless of the type of piezoelectric generators, their effectiveness, especially in a low frequency range, can be enhanced by connecting them with storing units containing supercapacitors or the synchronised switch harvester on inductor (SSHI) circuit [35–39]. For example, Selleri et al. [40] described a system composed of an ionic liquid-based supercapacitor and a PZT disc. The charging process of the aforementioned supercapacitor, which lasted 2 h, lighted an LED for 120 s. Similarly, Koszewnik et al. [41] used an SSHI circuit in a beam-slider structure with an MFC composite to obtain an amplitude of voltage output of >20 V.

Taking the presented peer review into account, this study focuses on overcoming the problem of generating voltage from vibration-based systems with a low amplitude. To this end, the micro-power piezoelectric generator with MFC films attached to the host structure is designed and tested. In addition, in the proposed generator, the MFC made of a homogenised material in the active layer of the piezo is considered to show a novelty in the power range of some low-energy sensors. This article is organised as follows. The electromechanical model of the piezo harvester located on the considered mechanical structure in physical and modal coordinates is described in Section 2. In Section 3, the computational models of all structures with a homogenous model of MFC, which is also a core novelty of this study, is presented. Next, in Section 4, experimental investigations for three different host structures of the generator with MFC films of the 8514 P2, 5628 P2 and 8528 P2 types are presented and described. In addition, the effectiveness of the proposed energy harvesting system is assessed in this section. Section 5 concludes the main findings of this work.

2. ELECTROMECHANICAL MODEL OF THE ENERGY PIEZO HARVESTER LOCATED IN THE PROTOTYPE OF THE MICRO-POWER GENERATOR

In this section, a brief description of an electromechanical model distributed parameters of a flexure strip with a piezo-patch being part of the proposed prototype of the micro-power generator is analysed. To this end, the fixed–fixed glass fibre beam, being the host structure of the generator, is equipped with one piezo-strip harvester MFC including a single active layer, two Kapton layers and two electrode layers. As a result, a smart structure of the generator is designed, shown in Fig. 1. The parameters of the host beam, as well as the piezo adjusted to its structure, are listed in Tab. 1.
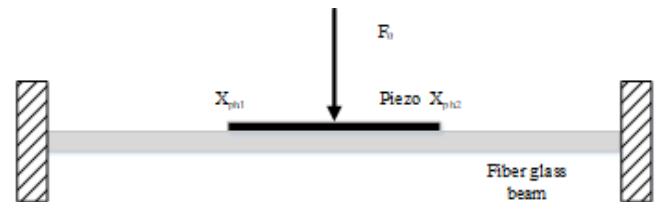

Fig. 1. Simplified model of a fixed–fixed beam with the piezo-strip

As can be seen in Fig. 1, a fixed–fixed beam representing the flexure strip of a micro-power generator with an integrated harvester is excited to vibration by force F_0 deriving in a real structure from the vibration shaker by the pusher and the cross-amplifying mechanism. The mentioned piezo-composite of the length of L_P, the width of w_P and the thickness t_P of the whole MFC, integrated with the host structure at the position x_{PH1}, x_{PH2}, was used to measure voltage from the vibration structure.

Then, the general equation of the transverse vibration of such excited part of the generator can be expressed as follows:

$$[E_F I_F + E_P I_P(H(x - x_{PH2}) - H(x - x_{PH1}))]\frac{\partial^4 w(x,t)}{\partial x^4} +$$
$$[m_F + m_P(H(x - x_{PH2}) - H(x - x_{PH1}))]\frac{\partial^2 w(x,t)}{\partial t^2} + \quad (1)$$
$$-\Gamma V(t)\left[\frac{d\,\partial(x - x_{PH2})}{dx} - \frac{d\,\partial(x - x_{PH1})}{dx}\right] = F_0\delta(x - x_0)$$

where: E_F is Young's modulus of the flexure strip of the generator, E_P is Young modulus of the piezo-composite harvester element, I_F is the inertia moment of the flexure strip, I_P is the inertia moment of the piezo-composite harvester element, m_F is the mass per unit length of the flexure strip, m_P is the mass per unit length of the piezo-composite harvester, $H(x)$ is the Heaviside function, $\delta(x)$ is the Dirac function along the longitudinal direction, $V(t)$ is the voltage flowing through the external resistive load R, F_0 is the force obtained from the pusher and the cross-amplifying mechanism of the micro-power generator, $x_{\_PH1}$ is the initial location of the piezo-patch harvester on the host structure, $x_{\_PH2}$ is the ending location of the piezo-patch and Γ is the electromechanical coupling factor.

Tab. 1. Parameters of the host structure and three different piezo-patch composites MFC 5628, MFC 8514 and MFC 8528 [15]

Mechanical parameters						
Fibre glass						
Length [mm]	Width [mm]	Length [mm]				
L_F 140	w_F 38	t_F 15				
Young's modulus (GPa)	Poisson's ratio (-)	Density [kg/m3]				
E_F 80	v_F 0.22	ρ_F 2,600				
Piezo-composite MFC						
Young's modulus (GPa)	Poisson's ratio (-)		Piezo-charge coeff. (pC/N)	Relative permittivity (-)		
E_x 31.6	v_{xy} 0.4		d_{31} −173	ε_r^T 2,253		
E_y 17.1	v_{yz} 0.2		d_{32} −150			
E_z 9.5	v_{xz} 0.4		d_{33} 325			
Geometrical parameters						
Overall length [mm]		Overall width [mm]	Active length [mm]	Active width [mm]	Thick. of PZT fibre layer [μm]	Thick. of electrode layer [μm]	Thick. of Kapton layer [μm]
	103		31 85	28	180	25	30
L_p	103	w_P	17 85	18	180	25	30
	67		31 56	28	180	25	30

MFC, macro-fibre composite; PZT, Pb-zirconate titanate.

The piezoelectric element used in the generator requires considering the approach from the electrical point of view. For this, the electrical charge accumulated at its electrodes can be calculated over the whole surface area in the following form:

$$Q = \int_{x\_PH1}^{x\_PH2}(d_{31}E_P\overline{\delta}_P + \varepsilon_{33}E_3)w_P dx \qquad (2)$$

where ε_{33} is the permittivity at constant stress, $\overline{\delta}_P$ is the bending strain along the middle surface of the piezo layer and E_3 is the electric field.

Next, applying Ohm's law, the current flowing through the load resistor R, connected to the MFC, can be expressed as follows:

$$i(t) = \frac{V(t)}{R} = \frac{dQ}{dt} = \frac{d}{dt}\left[\int_{x\_PH1}^{x\_PH2}(d_{31}E_P\overline{\delta}_P + \varepsilon_{33}E_3)w_P dx\right]$$

where R is the resistive load applied to the system.

Taking Eq. (3) into account, it can be seen that the current $i(t)$ is strongly associated with strains of the piezoelectric harvester and the electrical field applied to its electrodes. This resulted in the fact that the electrical circuit of the system can be obtained by substituting the electric field $E_3 = -V(t)/t_P$ and the strain $\overline{\delta}_{PH} = -t_c\frac{\partial^2 w}{\partial x^2}$ in the following form [16]:

$$C_p\frac{dV(t)}{dt} + \frac{V(t)}{R} + \Gamma\left[\int_{x\_PH1}^{x\_PH2}\frac{\partial^3 w(x,t)}{\partial x^2\,\partial t}dx\right] = 0 \qquad (4)$$

where C_p is the capacitance of the piezo-patch harvester $C_p = \frac{\varepsilon_{33}w_P L_P}{t_P}$

Both equations Eqs (1) and (4) refer to distributed electro-elastic model parameters of the piezo-patch harvester integrated to a 1D mechanical structure in physical coordinates. However, from the energy harvesting point of view, it should be analysed in modal coordinates. For this purpose, vertical displacement of the beam as a host structure is represented as multiplication of an absolutely and uniformly convergent series of the eigenfunctions in the following form:

$$w(x,t) = \sum_{n=1}^{\infty}\varphi_n(x)\eta_n(t) \qquad (5)$$

where $\varphi_n(x)$ is the mass normalised eigenfunction (mode shapes), $\eta_n(t)$ is the modal time response of the system for n-th mode.

The considered structure represents the fixed–fixed beam. As it was applied, the eigenvectors of this structure, after considering the boundary coordinates, given in Eq. (6), and split by geometric and time variables, can be expressed as given in the following equation [7]:

$$w(0,t) = 0 \qquad w(L_F,t) = 0$$
$$\left.\frac{\partial w(x,t)}{\partial x}\right|_{x=0} = 0 \qquad \left.\frac{\partial w(x,t)}{\partial x}\right|_{x=L_F} = 0 \qquad (6)$$

$$\phi_n(x) = \left(\cosh(\lambda_n L_F) - \cos(\lambda_n L_F)\right)\left(\cosh\left(\frac{\lambda_n}{L_F}\right)x - \cos\left(\frac{\lambda_n}{L_F}\right)x\right) +$$
$$-\left(\sinh(\lambda_n L_F) + \sin(\lambda_n L_F)\right)\left(\sinh\left(\frac{\lambda_n}{L_F}\right)x + \sin\left(\frac{\lambda_n}{L_F}\right)x\right) \qquad (7)$$

where $\lambda_n = \frac{(2n+1)\pi}{2\cdot L_F}$ for n = 1,2. λ_n is the frequency parameter of an undamped host structure.

Substituting Eq. (7) into Eq. (1) leads to solving the eigenvalue problem of the smart beam for short circuit conditions. Then, the natural frequency ωn of the structure, with no piezoelectric patch for the n-th mode, can be presented in the following form:

$$\omega_n = \lambda_n^2\sqrt{\frac{E_F I_F}{m_F L_F^4}} \qquad (8)$$

where LF is the length of the flexure strip of the micro-power generator.

Andrzej Koszewnik
Assessment of Parameters of the Vibration-Based Energy Harvesting System Located in the Micro-Power Generator

DOI 10.2478/ama-2024-0026

Taking account of the modal analysis procedure of the 1D structure with a piezo harvester adjusted to its surface by using support, an electromechanical coupled ordinary differential equation for the modal time response η_n can be expressed as follows [7]:

$$\frac{d^2\eta_n(t)}{dt^2} + 2\xi_n\omega_n\frac{d\eta_n(t)}{dt} + \omega^2{}_n\eta_n(t) + \tilde{\Gamma}_n V(t) = f_n(t)\delta(x - x_0) \tag{9}$$

where ξ_n is the modal damping ratio, $f_n(t)$ is the modal force applied to the structure.

As a result, the modal electromechanical coupling term $\tilde{\Gamma}_n$ can be presented as follows:

$$\tilde{\Gamma}_n = -E_P d_{31} w_P t_c \int_{x\_PH1}^{x\_PH2}\frac{d^2\varphi_n(x)}{dx^2}dx = -E_P d_{31} w_P t_c \frac{d\varphi_n(x)}{dx}\bigg|_{x\_PH1}^{x\_PH2} \tag{10}$$

The obtained modal electromechanical coupling term given by Eq. (10) and the vertical deflection from Eq. (7) put into Eq. (4) lead to modifying the electrical circuit equation in the following form:

$$\boldsymbol{C_p\frac{dV(t)}{dt} + \frac{V(t)}{R} - \sum_{n=1}^{\infty}\tilde{\Gamma}_n\frac{d\eta_n(t)}{dt} = 0} \tag{11}$$

The performed considerations of the tested structure with different active areas of the integrated piezo-patch harvester for modal coordinates allow to assess the voltage generated by the piezo as well as the effectiveness of the proposed Energy Harvester (EH) system located in the micro-power generator.

3. PROTOTYPE OF THE MICRO-POWER GENERATOR

The proposed micro-power generator with an EH system located on the flexure strip is shown in Fig. 2. It consists of a telescoping rod (1), cover (2), body case (3), cross-amplifying mechanism (8), flexure strip (5) and MFC piezo-strip (9). All elements, apart from the telescoping rod, were printed using a 3D printer and PLA filament wire of 1.75 mm diameter developed by Fiberlogy company. In addition, from the mechanical point of view, bearing balls are used to eliminate frication in the cross-amplifying mechanism.
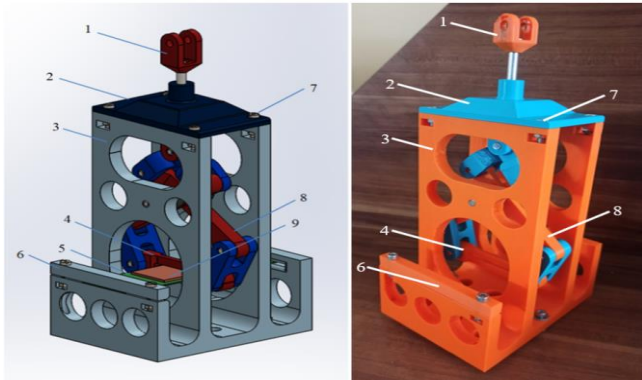
Fig. 2. Numerical model and prototype of the piezoelectric generator

3.1. Finite Element Model (FE) of the piezo generator and numerical results

The process of assessing parameters of the energy harvesting system in the micro-piezo generator is described in this section. In addition, the numerical calculations of the micro-piezo generator, including the flexure strip of a length of 140 mm, a width of 38 mm and a thickness of 1 mm and three different piezo-patch harvesters (MFC 5628, MFC 8514 and MFC 8528), are made.

To determine the parameters of the energy harvesting system located in the micro-piezo generator, the finite element (FE) model of the whole generator designed in Ansys is used. Taking this into account, the flexure strip structure made from glass fibre is modelled using an 8-node coupled-brick element Solid186, while the MFC element is discretised by using the representantive volume elements (RVE) technique [24,43]. Then, according to this method, the piezoelectric fibre layer with a homogenised material is modelled using a Solid 226-node coupled brick element, while the electrode and Kapton layers of the harvester are modelled using an 8-node coupled-brick element, Solid186. As a result, the computational model of the considered structure is determined, shown in Fig. 3b, where the thickness of the adhesive layer (<15 μm) is omitted.
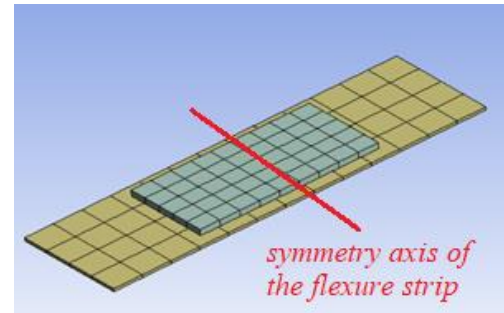
(a)

(b)

symmetry axis of the flexure strip
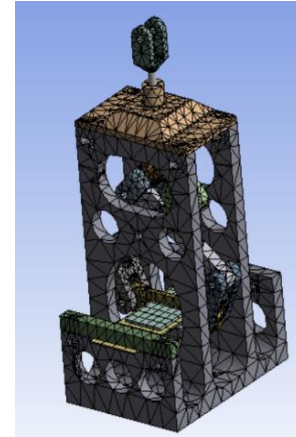
Fig. 3. Computational model (a) of the whole micro-piezo generator, (b) the flexure strip with piezo

Next, the behaviour of the flexure strip with the piezo element is analysed in the frequency domain. For this, a modal analysis of the FEM model of the proposed generator is performed in the limited frequency range of 1–300 Hz.
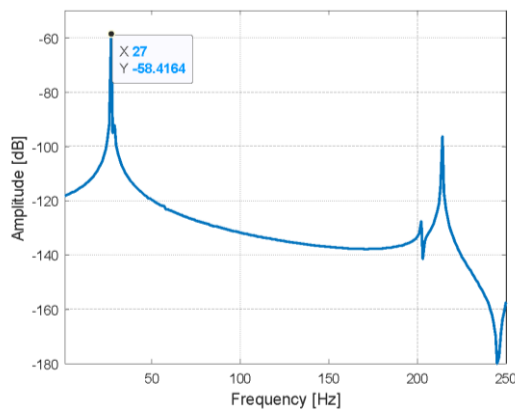
Fig. 4. Frequency response function of the FEM model of the flexure strip with chosen piezo-strip of type MFC 8514 P2
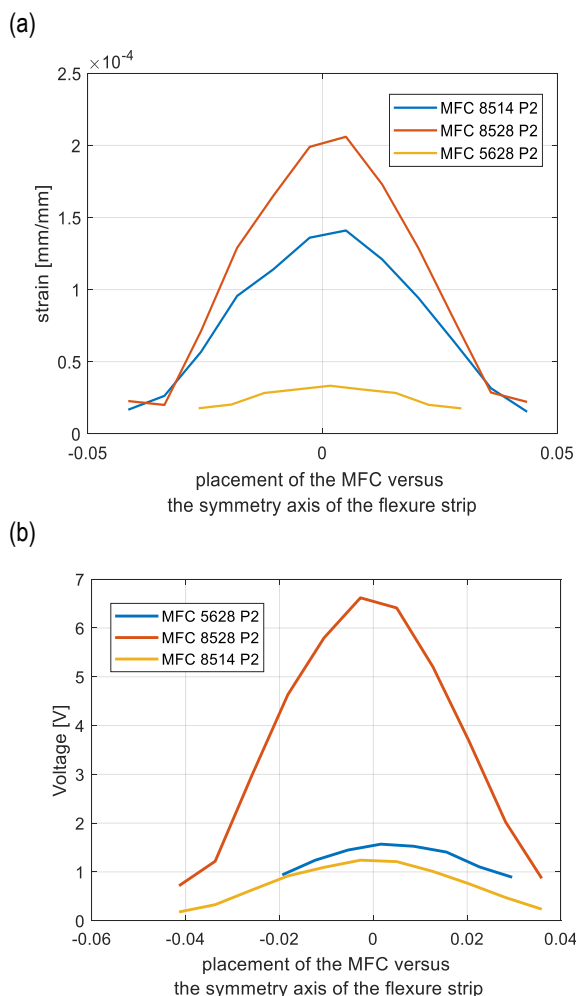
(a)

(b)

Fig. 5. Comparison of (a) strain distribution and (b) voltage generated by MFCs versus the symmetry axis of the flexure strip

Observing the determined amplitude plot of the flexure strip with a piezo-composite presented in Fig. 4, it can be noticed that this system should effectively work in the first resonance, where the amplitude peak is the highest. In the case of exciting the system to vibration with the second natural frequency, it can be supposed that the effectiveness of this system significantly decreases due to a smaller amplitude of strains of the piezo-composite. This behaviour allows to conclude that further analysis of this micro-piezo generator should be considered in the narrow frequency range, not exceeding 30 Hz.

Next, a harmonic analysis of this generator is performed to assess the parameters of the energy harvesting system located on the flexure strip according to Eq. (11). To do this, the computational models of the flexure strip with three different piezo-strips were excited to vibration by applying a sinusoidal excitation with a frequency close to the first natural frequency. The obtained results from the "Piezo and Mems Toolbox" (see Fig. 5) show that the size of the piezo-composite is a significant parameter that influences the values of strains, amplitude voltage output, as well as the effectiveness of the EH system.

As shown in Fig. 5b, the use of the piezo harvester with the highest active area (MFC 8528) leads to the generation of the highest amplitude strains and, consequently, the highest amplitude of voltages. In the case of using piezo-composites with the same length and twice shorter width (MFC 8514), smaller strains can be observed on the surface of this element and lower amplitudes of voltage generated by this element. A different effect is achieved for the piezo generator with the piezo-composite of the MFC 5628 type. In this case, shortening the length of the piezo-strip elements by the same width leads to generating a slightly higher voltage amplitude than that in the case of the piezo of the MFC 8514 type. This effect is due to the emergence of slightly higher strains in the longitudinal direction of this piezo.

4. EXPERIMENTAL SETUP

The process of the parameter assessment of the energy harvesting system located in the piezoelectric generator was carried out on the lab stand, as shown in Fig. 6, to verify the numerical results.

a)
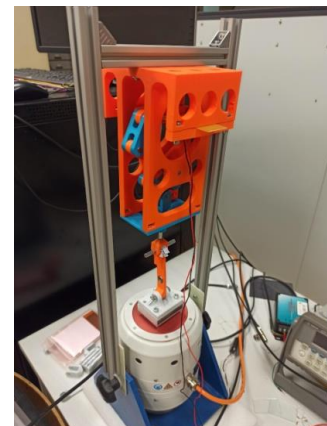
(b)
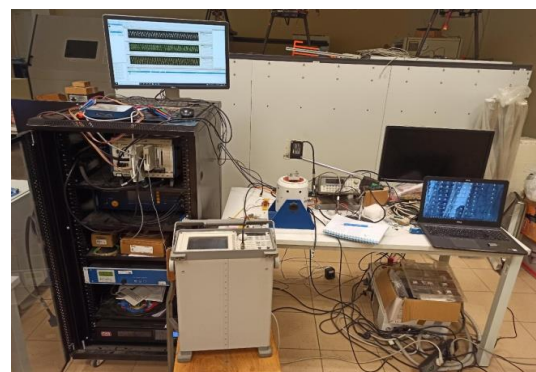
Fig. 6. View of (a) the micro-piezo generator placed on the vibration shaker Tira TV 51110-M, (b) the whole lab stand with the retrofitted equipment

Andrzej Koszewnik
Assessment of Parameters of the Vibration-Based Energy Harvesting System Located in the Micro-Power Generator

DOI 10.2478/ama-2024-0026

To do this, three different MFCs of 8514 P2, MFC 5628 P2 and MFC 8528 P2 types composed of two Kapton layers, two epoxy layers and one PZT fibre layer were chosen for an experimental test, where each of them was attached to the fibreglass beam with an adhesive epoxy layer of the Uhu plus type. The parameters of the host structure are listed in Tab. 1.

(a)

(b)

(c)
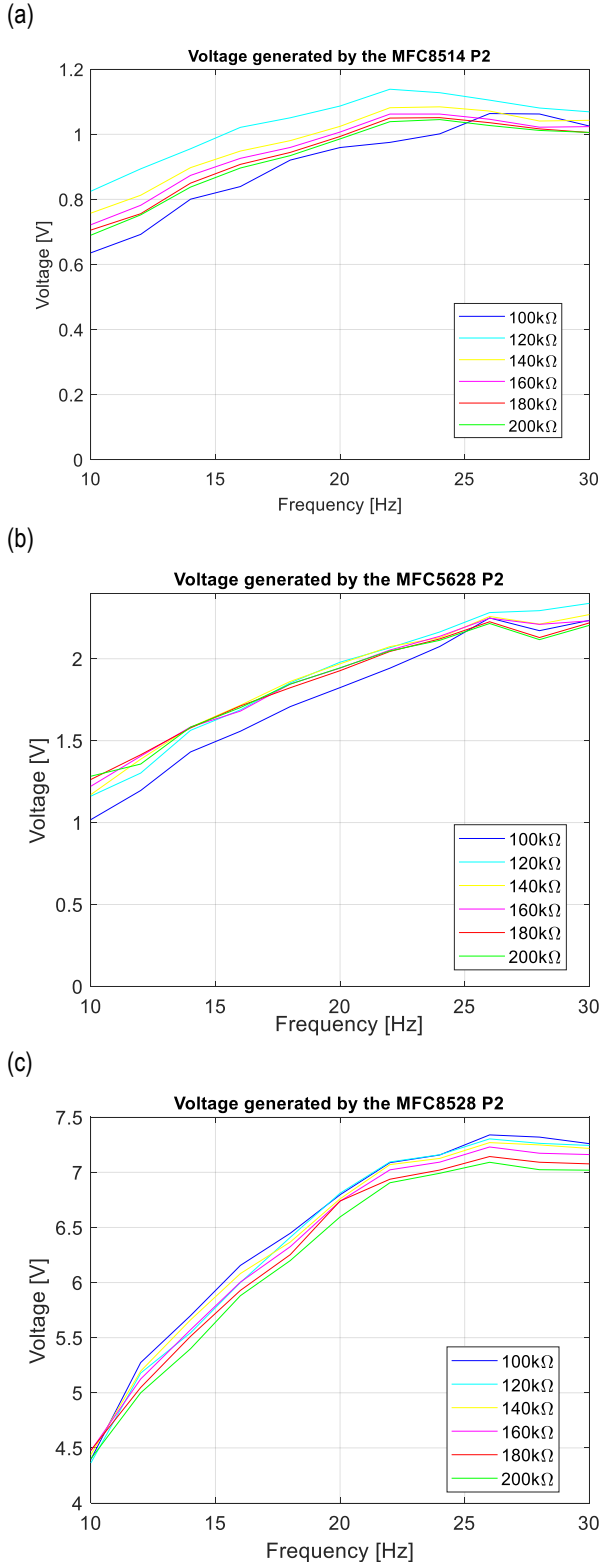
Fig. 7. Comparison of voltage generated by the real EH system with MFC of types (a) 8514 P2, (b) 5628 P2, (c) 8528 P2 by connecting them with resistive load in the range 100–200 kΩ

In addition, the lab stand was retrofitted into the system acquisition data National Instrument PXI used to measure the voltage generated by the EH system, as well as a laser displacement sensor LQ10A65PUA (Turck) to monitor the base acceleration. The lab stand, presented in Fig. 6, was also equipped with the signal generator Agilent and the vibration shaker TV51110-M with a BAA 120 amplifier (developed by Tira) to introduce a signal excitation.

In the first step, the experimental tests were carried out to measure the base acceleration and assess the power of the excitation signal. For this, an excitation signal in the form of a sinusoidal signal with an amplitude of 2 V and the frequency changing within the range of 10–30 Hz with a step of 1 Hz was generated from the signal analyser and later applied to the vibration shaker by an amplifier dedicated for this device. The displacement signal measured and recorded by using a laser sensor, which was placed in the distance of 4 mm from the vibrating base, was used to determine the value of the base acceleration (10 mm/s2–0.01 g) to ensure proper working of the proposed generator.

Next, the experimental tests were focused on matching the optimal impedance load connected to the EH system. For this, the optimisation process of the load resistance connected to the piezo was performed for six different resistive loads within the range of 100–200 kΩ with a step of 20 kΩ, as well as for three different types of MFC elements. The obtained results are shown in Fig. 7.

Fig. 7 indicates that the highest voltage is achieved for the matched resistance load equal to 120 kΩ. As a result, this impedance load can be called an optimal resistive load. Further analysis of the presented plots showed that the active area of the MFC significantly affected the amplitude of the voltage generated by the vibration-based energy harvesting system. This behaviour is shown in Fig. 7c, where using a piezo-strip with the highest active area generates the highest voltage amplitudes, which are close to 7.3 V. The inverse effect is achieved for the energy harvesting system with the piezo of the MFC 8514 P2 type, where a smaller width of this smart element leads to generating a voltage signal with the amplitude of only 1.1 V.

Next, the experimental tests were conducted to check how the frequency excitation influences the amplitude voltage generated by each piezo-composite attached to the flexure strip. For this, an experimental test was carried out for three different MFCs, where each of them was excited to vibration by applying a sinusoidal signal in the form of u(t) = 2sin(wt), with the frequency changing within the range of 10–30 Hz, and the resistive load was in the range of 100–300 kΩ.
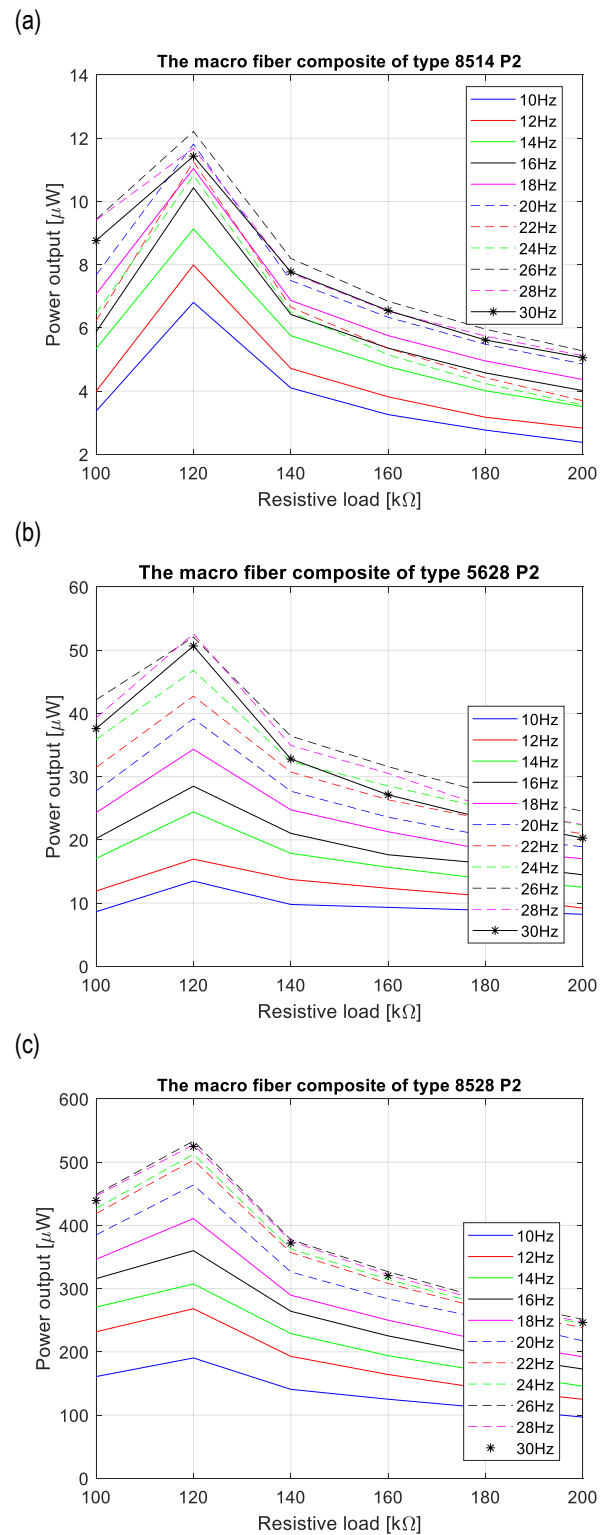
(a)

(b)

(a)

(c)

(b)
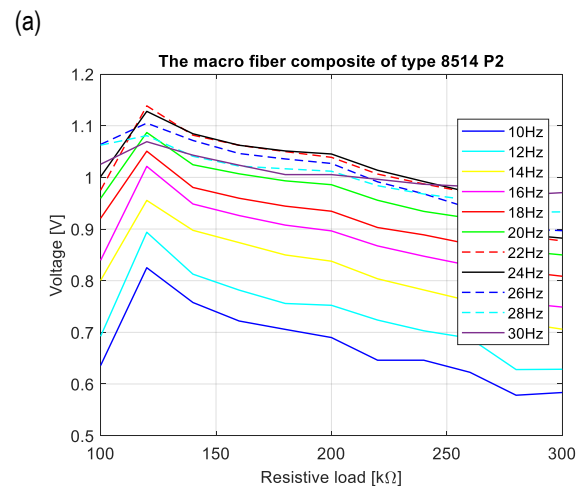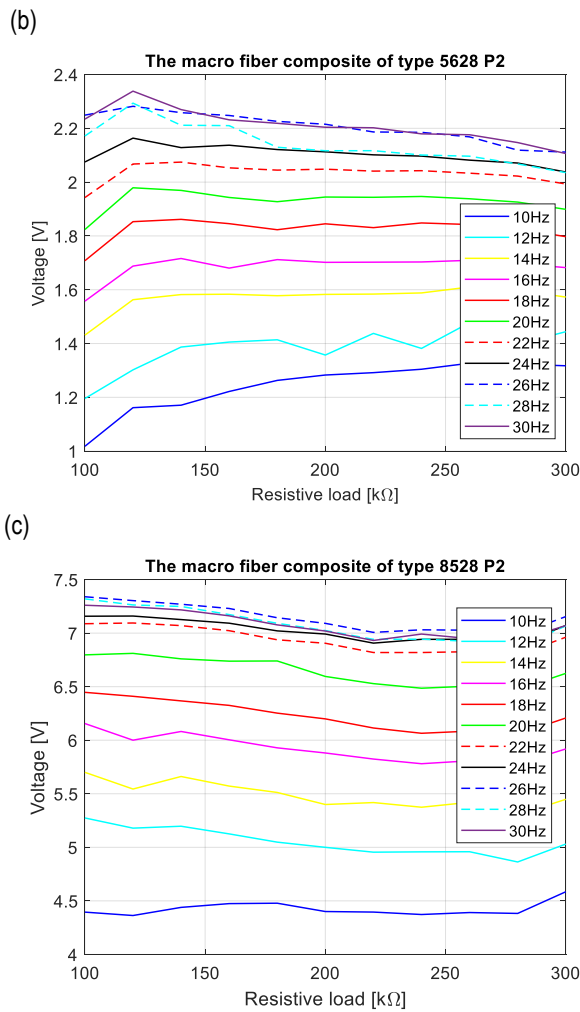
Fig. 8. Comparison of voltage generated by a real EH system with MFC of types (a) 8514 P2, (b) 5628 P2, (c) 8528 P2 excited to vibration with a frequency within the range of 10–30 Hz versus the resistive load

(c)

Fig. 9. Comparison of the power output generated by the EH system with an MFC of types (a) 8514 P2, (b) 5628 P2, (c) 8528 P2 excited to vibration with a frequency within the range of 10–30 Hz versus the resistive load

The results presented in Fig. 8 indicated that the highest voltage amplitude for each piezo-composite is generated for the micro-generator connected to the optimal resistive load set at 120 kΩ. This effect is shown in Fig. 8a and 8c, where an increase in the resistive load >120 kΩ for each considered excitation frequency led to a decrease in the voltage generated by the EH systems. Different results can be observed during the analysis of the energy harvesting with the piezo-composite of the MFC 5628 P2 type, where the amplitudes of voltages generated by this system were almost constant. This was due to smaller strains of the piezo of the 5628 P2 type, especially on the opposite edges.

Other experimental tests were carried out to check the power output generated by each considered piezo versus the load resistance connected to the piezo by various frequencies of excitation changing within the range of 10–30 Hz. The results presented in Fig. 9 indicate that the highest power output, which equals 0.5 mW, was achieved for the highest piezo of the MFC 8528 P2 type, while the lowest power output (12 µW) was achieved for the piezo-strip with the same length but twice the lowest width. As a result, it can be concluded that the width of the piezo-strip composite significantly affects the power output generated by the proposed micro-generator.

The last step of the experimental setup was to calculate the effectiveness of energy harvesting systems for three considered piezo-composites. To do this, firstly, the root mean square values for the obtained voltage output and excitation signals were calculated, and secondly, the power of these signals was determined.

$$\eta = \frac{P_{out}}{P_{in}} \cdot 100\% \qquad (15)$$

where $P_{out} = RMS(V_{out})^2 = \frac{1}{N}\sum_{i=1}^{N}V_{out}^2$ is the power of the output voltage signal from the piezo harvester, $P_{in} = RMS(u)^2 = \frac{1}{N}\sum_{i=1}^{N}u^2$ is the power of the excitation harmonic signal.

(a)

(b)

(c)
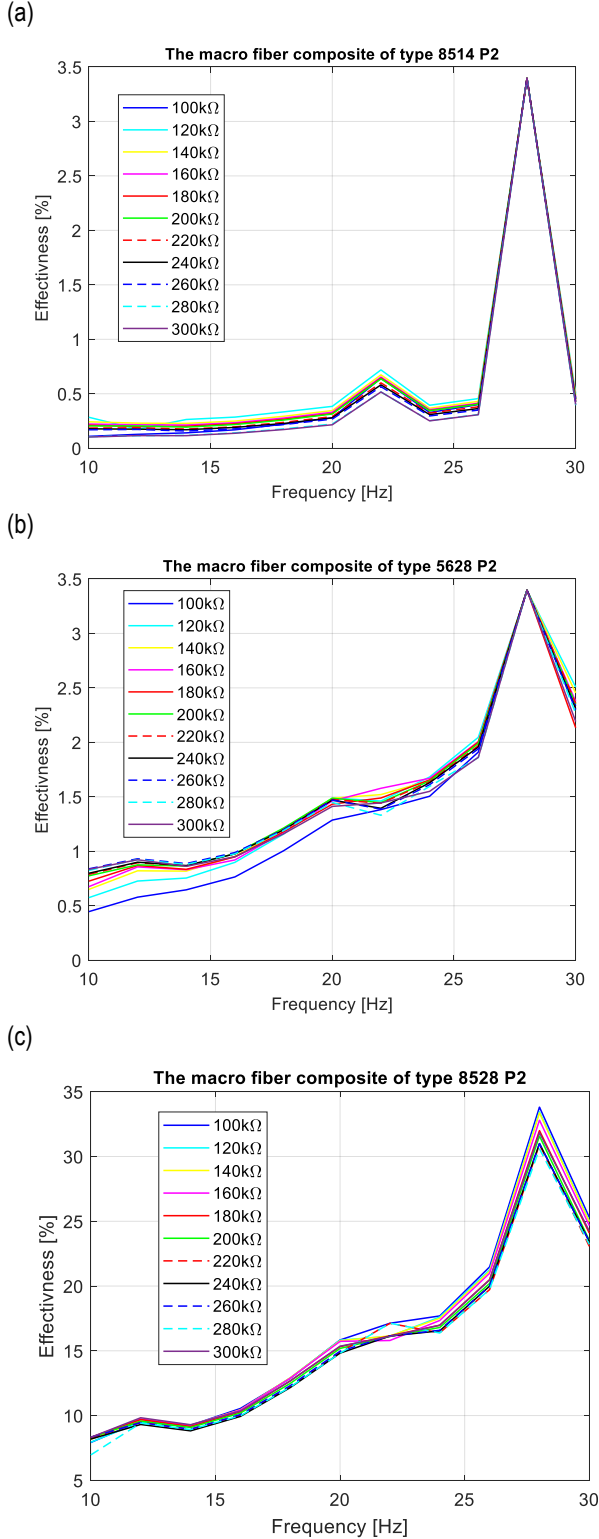
Fig. 10. Comparison of the effectiveness of a real EH system with a MFC of types (a) 8514 P2, (b) 5628 P2, (c) 8528 P2 by connecting them with the resistive load within the range of 100–300 kΩ

The obtained results presented in Fig. 10 indicated that the active area of the MFC attached to the flexure strip, as well as matched the resistive load of the energy harvesting system, plays an important role in enhancing the piezo generator efficiency. It is especially true for systems working at the resonance frequency, as well as around this frequency, where using the piezo-strip of the 8528 P2 type leads to increasing the effectiveness almost ten times (from 3.4% up to 33%). As a result, taking account of the results presented in other studies [30,33,34], it can be concluded that the proposed micro-power generator working with a frequency of 28 Hz can be a more useful device to power small electrical sensors with a low power demand, for example, to support the SHM system.

5. SUMMARY AND CONCLUSIONS

In this study, the effectiveness of the energy harvesting system located in the prototype of a micro-power generator for piezo-composites with different active areas was analysed. To this end, an FE model of the flexure strip with three different piezo-composites located symmetrically versus transverse axis of the flexure strip were analysed. The results obtained from numerical calculations (see Fig. 5) indicated that the proposed micro-generator with the piezo-composite of the 8528 type generates the highest amplitude of voltage, which is close to 7 V, while the voltage values are significantly lower for two other MFCs. This is due to the change in local strains of a particular piezo, which is >0.2 µm/mm for MFC 8528, while in the other case, it is <0.15 µm/mm.

Experimental tests of the EH system carried out on the lab stand, as shown in Fig. 6, for a real mechanical structure of the generator verified the numerical results. Again, the highest amplitudes of the voltage generated by the micro-piezo generator (see Fig. 7) were obtained for MFC 8528 P2, while the lowest values - for the piezo-composite with the same length but twice shorter width. As it was mentioned previously, the decrease in the voltage generated by the piezo of the 8514 P2 type is due to smaller local changes of the piezo strains.

In addition, the experimental tests were performed to determine the optimal resistive load, output power and effectiveness of the considered EH systems. The results presented in Fig. 8 show that the highest voltage amplitude for each piezo-composite was achieved by connecting the composite with the resistance load equal to R = 120 kΩ, further called the optimal resistive load, as well as by the frequency excitation close to the first natural frequency (fexc = 28 Hz). A similar effect was achieved by analysing the power output generated by particular piezo-composites. In this case again, the highest power value, close to 0.5 mW, was obtained for the piezo of the 8528 type. In other cases, the power generated by the EH system with the piezo-strip 5628 P2 and 8514 P2 types significantly decreased up to 50 µW and 12 µW, respectively, decreasing the effectiveness of the proposed micro-power generator from 33% to only 3.4% (see Fig. 10).

In sum, the obtained numerical and experimental results indicated that increasing the chosen geometrical parameters of the piezo-composite, such as length and width, leads to a significant increase in the voltage generated by the EH system. Therefore, the considered micro-piezo generator, when connected with a storing unit containing the optimal impedance load and a super-capacitor, can be used to power small electrical devices with a low

power demand. Hence, the current study filled the gap in the state of the art associated with the energy harvesting system with a homogenised material in the active layer of the MFC.

REFERENCES

1. Bradai S, Naifar S, Viehweger C, Kanoun O, Litak G. Nonlinear analysis of electrodynamics broadband energy harvester. European Physical Journal. Special Topics. 2015; 224: 2919-2927.

2. Chen Y, Yan Z. Nonlinear analysis of axially loaded piezoelectric energy harvesters with flexoelectricity. International Journal of Mechanical Science. 2020;173:105473.

3. Wang L, Yuan FG. Vibration energy harvesting by magnetostrictive material. Smart Mater Structures. 2008; 17(4).

4. Wei Ch, Jing X. A comprehensive review on vibration energy harvesting: Modelling and realization. Renewable and Sustinable Energy Reviews. 2017; 74: 1-18.

5. Dey S, Roy D, Patra S, Santra T. Performance of a modified magnetostrictive energy harvester in mechanical vibration. Heliyon. 2019; 5 (1).

6. Lei W, Yuang FG. Vibration energy harvesting by magnetostrictive material. Smart Material Structures. 2008; 17(4): 045009.

7. Lee CS, Joo J, Han S, Lee JH, Koh SK. Poly (vinylidene fluoride) transducers with highly conducting poly (3,4-ethylendioxythiopene) electrodes. Synthetic Metal 2005; 152(1-3): 49-52.

8. Morita T. Miniature piezoelectric motors, Sensors and Actuators. A: Physical. 2003: 103(3): 291-300.

9. Nicoletti R, de Araujo MVV. Electromagnetic harvester for lateral vibration in rotating machines. Mechanical Systems and Signal Processing. 2015:(52-53):685-699.

10. Wang I. Vibration Energy Harvesting by Magnetostractive Material for Powering Wireless Sensors. 2007. Doctoral Thesis.

11. Ouro-Koura H, Sotoudeh Z, Tichy JA, Borca-Tascius DA. Effectiveness of energy transfer versus mixing entropy in coupled mechanical-electrical oscillatiors. Energies. 2022;15:6105.

12. Roundy S, Wright PK, Rabaey J. A study of low level vibrations as a power source for wireless sensors node. Computer Comunications. 2013; 26(11): 1131:1144.

13. Li J, Ouro-Koura H, Arnow H, Nowbahari A, Galarza M, Obispo M, Tong X, Azadmehr M, Hella MM, Tichy JA, Borca-Tascius DA. A Novel comb design for enhanced power and bandwidth in electrostatic MEMS energy converters. IEEE 36th International Conference on Micro Electro Mechanical Systems (MEMS). DOI: 10.1109/MEMS49605.2023.10052590

14. Li J, Tichy J, Borca-Tascius DA. A predictive model for electrostatic energy harvesters with impact-based frequency up-conversion, Journal of Micromechanics and Microengineering. 2020; 30(12): 125012.

15. Li J, Ouro-Koura H, Arnow H, Nowbahari A, Galarza M, Obispo M, Tong X, Azadmehr M, Halvorsen E, Hella MM, Tichy JA, Borca-Tascius DA. Broadband Vibration-based Energy harvesting for Wireless Sensor Applications using Frequency Up-conversion. Sensors. 2023; 23(11): 5296.

16. Koszewnik A, Oldziej D. Performance assessment of an energy harvesting system located on a copter. European Physical Journa., Special Topics. 2019; 228: 1677–1692.

17. Koszewnik A. Analytical Modeling and Experimental Validation of an Energy Harvesting System for the Smart Plate with an Integrated Piezo-Harvester. Sensors. 2019; 19(4): 812.

18. Cahill P, Hazra B, Karoumi R, Mathewson A, Pakrashi V. Vibration energy harvesting based monitoring of an operational bridge undergoing forced vibration and train passage. Mechanical Systems and Signal Processing. 2018; 106: 265–283.

19. Na WS, Baek J. Piezoelectric Impedance-Based Non-Destructive Testing Method for Possible Identification of Composite Debonding Depth. Micromachines 2019, 10: 621.

20. O'Leary K, Pakrashi V, Kelliher D. Optimization of composite material tower for offshore wind turbine structures. Renewable Energy. 2019; 140: 928–942.

21. Okosun F, Cahill P, Hazra B, Pakrashi V. Vibration-based leak detection and monitoring of water pipes using output-only piezoelectric sensors. European Physical Journal Special Topics. 2019; 228: 1659–1675.

22. Koszewnik A. Experimental validation of equivalent circuit modeling of the piezo-stripe harvester attached to the SFSF rectangular plate. Acta Mechanica et Automatica. 2020; 14(1): 8-15.

23. Cahill P, Ni Nuallain NA, Jackson N, Mathewson A, Karoumi R, Pakrashi V. Energy Harvesting from Train-Induced Response in Bridges. Journal of. Bridge Engineering 2014; 19: 04014034.

24. Koszewnik A, Lesniewski K, Pakrashi V. Numerical Analysis and Experimental Verification of Damage Identification Metrics for Smart Beam with MFC elements to support structural health monitoring. Sensors. 2021; 21(20): 6796.

25. Ambroziak L, Ołdziej D, Koszewnik A. Multirotor Motor Failure Detection with Piezo Sensor. Sensors. 2023; 23(2): 1048.

26. Yang F, Gao M, Wang P, Zuo J, Dai J, Cong J. Efficient piezoelectric harvester for random broadband vibration of rail. Energy. 2021; 218: 119559.

27. Zheng J, Dou B, Li Z, Wu T, Tian H, Cui G. Design and Analysis of a While-Drilling Energy-Harvesting Device Based on Piezoelectric Effect. Energies. 2020; 14(5): 1266.

28. Wu Z, Xu Q. Design and Development of a Novel Two-Directional Energy Harvester with Single Piezoelectric Stack. IEEE Transaction and Industrial Electronics. 2021; 68: 1290–1298.

29. Kan J, Zhang M, Wang S, Zhang Z, Zhu Y, Wang J. A cantilevered piezoelectric energy harvester excited by an axially pushed wedge cam using repulsive magnets for rotary motion. Smart Material and Structures. 2021; 30: 065009.

30. Ju S, Ji Ch-H. Impact-based piezoelectric energy harvester. Applied Energy. 2018; 214: 139-151.

31. Zhou W, Penamalli GR, Zuo L. An efficient vibration energy harvester with a multi-mode dynamic magnifier. Smart Materials and Structures. 2012; 21: 015014.

32. Caban J, Litak G, Ambrozkiewicz B, Wolszczak P, Gardynski L, Stączek P. Impact-based piezoelectric energy harvesting system excited from diesel engine suspension. Applied Computer Science. 2020; 16(3): 16-29.

33. Peng Y, Xu Z, Wang, M, Li Z, Peng J, Luo J, Xie S, Pu H, Yang Z. Investigation of frequency-up conversion effect on the performance improvement of stack-based piezoelectric generators. Renewable Energy. 2021; 172: 551–563.

34. Wen S, Xu Q. Design of a Novel Piezoelectric Energy Harvester Based on Integrated Multistage Force Amplification Frame. IEEE/ASME Transaction Mechatronics. 2019; 24: 1228–1237.

35. Hwang GT et al. Self-powered wireless sensor node enabled by an aerosol-deposited PZT flexible energy harvester. Advanced Energy Materials. 2016; 6(13): 1-9.

36. Ramadoss A, Saravanakumar B, Lee SW, Kim YS, Kim SJ, Wang ZL. Piezoelectric-driven self-charging supercapacitor power cell. ACS Nano. 2015; 9(4): 4337-4345.

37. Gilshteyn EP et al. Flexible self-powered piezo-supercapacitor system for wearable electronics. Nanotechnology. 2018; 29(32): 1-14.

38. Pu X, Hu W, Wang ZL. Toward wearable self-charging power systems: the integration of energy-harvesting and storage devices. Small. 2018; 14(1): 1-19.

39. Zhao H, Wei X, Zhong Y, Wang P. A direction Self-tuning two-dimensional piezoelectric vibration energy harvester. Sensors. 2020; 20(77): 1–13.

40. Selleri G, Poli F, Neri R, Gasperini L, Gualandii Ch, Soavi F, Fabiani D. Energy harvesting and storage with ceramic piezoelectric transducers coupled with an ionic liquid-based supercapacitor. Journal of Energy Storage. 2023;60:106660.

41. Koszewnik A. The influence of a slider gap in the beam-slider structure with an MFC element on energy harvesting from the system: experimental case. Acta Mechanicca. 2021;232: 819-833.
42. Ma Y, Wang J, Lic Ch, Fu X. A micro-power generator based on Two Piezoelectric MFC Films. Crystals. 2021; 11(8): 861.
43. Hu K, Li H. Large deformation mechanical modeling with bilinear stiffness for Macro-Fiber Composite bimorph based on extending mixing rules. Journal of Intelligent Material Systems and Structures. 2020; 1-13. DOI:10.1177/1045389X20951257

.

Andrzej Koszewnik: https://orcid.org/0000-0001-6430-6007

HOMOTOPY PERTURBATION METHOD WITH TREFFTZ FUNCTIONS AND SIMCENTER STAR-CCM+ USED FOR THE ANALYSIS OF FLOW BOILING HEAT TRANSFER

Anna PAWIŃSKA*, Artur PIASECKI, Norbert DADAS***,
Sylwia HOŻEJOWSKA****, Magdalena PIASECKA*******

*,****Faculty of Management and Computer Modelling, Kielce University of Technology,
Al.Tysiąclecia Państwa Polskiego 7, 25-314 Kielce, Poland
**Faculty of Environmental Engineering, Geomatics and Renewable Energy, Kielce University of Technology,
Al.Tysiąclecia Państwa Polskiego 7, 25-314 Kielce, Poland
,** Faculty of Mechatronics and Mechanical Engineering, Kielce University of Technology,
Al. Tysiąclecia Państwa Polskiego 7, 25-314 Kielce, Poland

a.pawinska@tu.kielce.pl, apiasecki@tu.kielce.pl, ndadas@tu.kielce.pl,
ztpsf@tu.kielce.pl, tmpmj@tu.kielce.pl

Abstract: This work presents experimental and numerical studies of heat transfer during cooling fluid flow in a group of five minichannels 1 mm deep. The main purpose was to determine the heat transfer coefficient on the contact surface between the fluid and the heated wall of the selected minichannel at subcooled boiling. The temperature distribution on the outer surface of the heated plate was measured by means of an infrared camera. Thermal and flow parameters were monitored by an appropriate data-acquisition system. The test section was placed horizontally with fluid flowing above the heated wall. The HFE-649, HFE-7100 and HFE-7200 working fluids were examined in the experiments. Simcenter STAR-CCM+ software was used for numerical analysis of heat transfer in the test section. Furthermore, a simplified two-dimensional (2D) model was proposed that designates subcooled boiling heat transfer during fluid flow in a central minichannel. The heat-transfer process in the heated plate and the working fluid was described using indicated partial differential equations with appropriate boundary conditions. The solution to the proposed system of equations led to the solving of two more inverse Cauchy-type problems. The classical Trefftz method (TM) and the homotopy perturbation method (HPM) combined with the TM allowed for obtaining temperature distributions in the heater and the fluid and consequently, the heat transfer coefficient at the heater–fluid interface from the Robin boundary condition. Comparison of the results from numerical simulation due to Simcenter STAR-CCM+ showed similar temperature distributions at the heated surface. The calculated heat transfer coefficients, by HPM and Simcenter STAR-CCM+, were validated using the 1D approach. Furthermore, the results from simulations in Simcenter STAR-CCM+ in the form of local temperatures of the heater were confronted with experimental data for comparison. Similar results were achieved.

Key words: heat transfer, minichannel, subcooled boiling, homotopy perturbation method, Trefftz method, Simcenter STAR-CCM+

1. INTRODUCTION

Various technical difficulties also arise as technology continues to develop and new technologies are constantly being introduced. One of the major challenges facing scientific and industrial institutions worldwide is cooling smaller and smaller electronic components while improving their capabilities and functionality. Designing small-sized, energy-efficient, effective and environmentally friendly refrigerant-based heat exchangers with a set of channels has become a priority in the industrial domain. Although high heat fluxes in miniaturised devices are commonly managed by intensifying heat transfer in the minichannels, the process is not fully understood. It requires innovative experimental studies, new mathematical models and computational methods that also include computational fluid dynamics (CFD) simulations.

It should be underlined that although important accomplishments have been made in the investigation of micro-scale flow boiling over the last two decades, most aspects related to heat transfer still remain unclear. Tibirica and Ribatski [1] provided a wide review of the literature on micro-scale and mini-scale flow boiling. The authors focussed on the transition from macro-scale to micro-scale, the heat transfer coefficient, critical heat flux, the pressure drop, flow patterns and the void fraction. The general characteristics of the experiments carried out by the researchers were provided. The presented results covered the data of investigations, with the test section having small-dimensional channels, which were tested for single channels and for a larger number of channels, including sets of channels. One of the conclusions was that the heat transfer coefficient achieved in the minichannel system is still not clear in the literature, and additional innovative studies are, therefore, necessary to investigate local phenomena. Such results would be useful for the development of mechanistic and predictive methods concerning micro and minichannel heat exchangers.

In Ref. [2], the flow boiling pressure drop and the flow patterns of R-600a in a multi-port horizontal extruded tube, with five rectangular channels and two rectangular/circular profiles, were studied. The average hydraulic diameter of the channels was 1.47

mm. The influence of mass flux and vapour quality on pressure drop was investigated, and the recorded two-phase flow patterns were analysed. The main results indicate the dependence of pressure drop on both mass and heat fluxes. The authors observed that the friction pressure gradient increased with increasing mass flux and vapour quality. The influence of heat flux on the frictional pressure drop was also noted.

Investigations on the boiling characteristics in the minichannel heat sink are described in Ref. [3]. The counter-flow interconnected minichannels were developed in the test section. Two minichannel heat sink configurations were used. The co-current minichannel structure size, with channel width of 1 mm, height of 4 mm, length of 30 mm and wall thickness of 1 mm was produced in the first version of the test section. The other construction differs from the first one, taking into account the width of the connected trench, which was 0.5 mm and the spacing equal to 4.5 mm. The results were related to heat transfer coefficients, pressure drop, two-phase flow patterns and temperature uniformity under various experimental conditions. The authors noted that with an increase in mass flux, the flow boiling performance is better than that of a low mass flux. Their explanation was that the connected groove could be effectively activated and mixing could be triggered. Among other findings, it was stated that increasing the supercooling can delay the boiling instability and increase the sensible heat of the fluid, which improves heat transfer performance. The authors also observed that the connected grooves in the test section cause the mixing of fluids between adjacent channels with reverse flow.

Flow boiling in three parallel minichannels with a common inlet and outlet area was studied in Ref. [4]. The internal dimensions of the minichannels were 0.25 mm wide, 0.50 mm deep and 32 mm long, whereas the wall between the channels was 0.25 mm wide. The minichannels were covered with a transparent cover, which allowed observation of flow structures. The authors focussed on examining the synchronisation between flow distributions in minichannels. This problem was analysed in the local area due to the analysis of the two-phase flow images and was also based on the process of synchronisation between inlet and outlet pressure fluctuations. The processes were investigated with the use of cross-recurrence plots. To recognise the similarity of flow patterns within the minichannels, the analysis of pixel brightness changes inside the minichannels was performed. The results revealed that the processes of synchronisation have a negative impact on water input and outlet temperature and inlet and outlet pressure oscillations. It was noticed that during synchronisation, a high amplitude of oscillations of temperature and pressure occurred. The authors stated that it was caused by reverse flow.

Numerical analyses of specific design solutions for minichannel devices have been the subject of an increasing number of research works. In Ref. [5] was showed the results of the CFD simulation using the COMSOL software. This software was used to simulate the convective heat exchange problem during forced water flow through the zone with the minichannel section. From the simulations, the local temperature of the fluid and that of the wall of the minichannel were calculated. Minichannels with a fixed length of 37.8 mm and a width of 1.615 mm had a height of 3.41 mm, 6.82 mm, 10.21 mm or 12.7 mm. As a result, local values of the Nusselt number were determined. The simulation was carried out for five different values of the Reynolds number. The fluid flow field and temperature distribution were also visualised. The frictional effects and the associated flow resistances were also analysed for various dimensions of the minichannel system.

In Ref. [6], the authors performed CFD modelling and a numerical analysis of fluid flow and heat transfer in a minichannel heat exchanger using Simcenter STAR-CCM+ software. The results of the numerical simulations were confronted with the data from the experiments. The main parameters that were measured during the experiments included the temperature distribution of the heater achieved by infrared thermography. The analyses covered the working fluid comprising two fluids (FC-72 and HFE-7100), the heater material (Haynes-230 alloy, aluminium and copper), the spatial orientation of the test section (vertical with fluid upflow and horizontal with fluid flow above the heater) and the number of minichannels (7, 9, 11 and 15). The calculations helped to indicate which parameters tested in terms of heat transfer turned out to be the most effective. Furthermore, a mesh dependency analysis was performed based on the grid convergence index to ensure the convergence stability of the numerical simulations.

Experimental data describing heat transfer during flow boiling in minichannels are needed to validate the results from numerical simulations. For more than two decades, the authors of this work performed calculations using various methods such as the simple 1D method [7], the 2D method described in this work and using the commercial software STAR-CCM+ [6] and ADINA [8].

This paper proposes two approaches to analyse the heat transfer in a test section with five rectangular minichannels and determine heat transfer coefficients at the heated plate–cooling fluid interface. The first approach used computational methods with Trefftz functions. A mathematical model was proposed in which the temperatures of the heated plate and all refrigerants were assumed to satisfy the Poisson and Fourier–Kirchhoff equations, respectively. The boundary conditions for both equations considered the results of experimental measurements. Determining the continuous temperature distributions of the heating plate and refrigerant leads to solving two inverse Cauchy-type problems in two contacting areas with different geometrical and physical parameters. Inverse problems belong to ill-posed problems [9], in which measurement uncertainties make the solution unstable. Inverse and ill-posed problems have been the subject of many works [10–13], and an overview of methods for solving Cauchy problems is given in Ref. [14]. For example, in Refs. [15–22], the Trefftz method (TM) or its modifications were used to solve direct and inverse problems that occur in engineering problems. In the TM (first described by Trefftz in 1926) [23], the unknown solution of a linear partial differential equation is approximated by a linear combination of functions (Trefftz functions or T-functions) that exactly satisfy the given differential equation. The coefficients of the linear combination are determined by minimising the error function that describes the mean square error between the approximate solution and the adopted boundary conditions. Trefftz functions combined with other methods, for example, Picard's method [22], radial functions [24] or homotopy perturbation method (HPM) [16, 20 and 21], are also used to solve non-linear differential equations.

This work uses two methods based on Trefftz functions for numerical calculations: the classical TM and a hybrid method that combines the HPM with Trefftz functions. Both methods use harmonic polynomials and are not limited by the number and type of boundary conditions. This greatly simplifies the calculations and makes these methods suitable methods for solving direct and inverse problems found in engineering. In the proposed approach, the solution to the differential equation (describing the heater temperature) was approximated by a finite sum of functions that

are linear combinations of the Trefftz functions. In the HPM, the unknown fluid temperature, the satisfying energy equation, is expressed as an infinite series of functions converging to the exact solution. The heat transfer coefficient at the heating plate–refrigerant interface was determined from the Robin boundary condition. The second approach used the CFD program, Simcenter STAR-CCM+. Numerical methods in CFD are designed to solve systems of nonlinear differential equations. The literature provides a good overview of mathematical models and numerical calculations for heat exchangers of various designs, as, for example, in the works [25–31]. The numerical simulation results were compared with those from methods based on Trefftz functions. Similar temperature distributions in the heated plate and heat transfer coefficients were obtained. The one-dimensional approach allowed for the validation of heat transfer coefficients obtained based on methods with Trefftz functions and from Simcenter STAR-CCM+ simulations.

2. EXPERIMENTS AND RESEARCH METHODOLOGY

2.1. Experimental rig

The experimental investigation was conducted in the own experimental set up. A view of the experimental rig is shown in Fig. 1 while its schematic diagram is shown in Fig. 2.

Fig. 1. A view of the experimental rig

In the main loop for the boiling process examination, the cooling fluid, i.e. HFE-649 (Novec-649 3M™ Novec™ [32]), HFE-7100 (3M™ Novec™ 7100 Engineered Fluid [33]) and HFE-7200 (3M™ Novec™ 7200 Engineered Fluid [34]), flows. Hydrofluoroethers (HFEs) are more environmentally friendly and, like fluorocarbon (FC), have zero (or close to zero) ozone-depletion potential (ODP). The significant difference, however, is a much lower global warming potential (GWP). According to the manufacturer [35], the FC-72 or FC-770 has more than 5,000 GWP, while the HFE fluids have the GWP even several times lower. For example, HFE-649, HFE-7000, HFE-7100 and HFE-7200 have a GWP of 1, 530, 320 and 55, respectively. Furthermore, FC fluids have a long atmospheric lifetime (ALR) and HFE-649, HFE-7000, HFE-7100 and HFE-7200 have ALRs of 0.014, 4.9, 4.1 and 0.77 years, respectively.

The main flow loop, besides the most important part, i.e. the test section, consists of the following elements: a circular pump (gear type, Tuthill), heat exchanger and pressure regulator. The most important set-up elements for the flow, pressure and temperature control and measurement are: mass flow meter (Coriolis type, Endress+Hauser), pressure meters (Endress+Hauser) and K-type thermoelements (Czaki Thermo-Product).

The data and image acquisition system includes an infrared camera A655SC FLIR (nominal accuracy ±2 °C or ±2% at measuring temperature range), a PC and two data acquisition stations (I/OTech DaqLab2005 and MCC SC-1608G) and a high-speed video camera (SP-5000M-CXP2, JAI). A lighting system consisting of LEDs (four LED panels of 50 W each) was applied to illuminate the flow of the working fluid along the minichannels. The power supply and control system consisted of a power supply, an ammeter and a voltmeter.
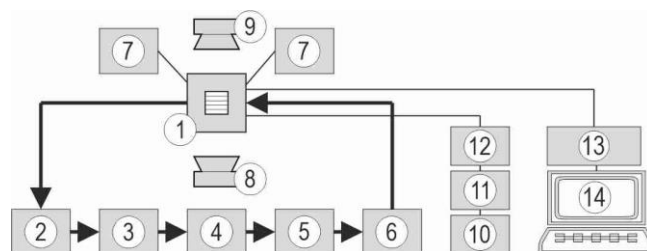

Fig. 2. A schematic diagram of the experimental rig – 1: test section, 2: heat exchanger, 3: compensation tank, 4: filter, 5: gear pump, 6: Coriolis mass flow meter, 7: pressure sensor, 8: infrared camera, 9: a high-speed video camera, 10: power supply system, 11: voltmeter, 12 -ammeter, 13: data acquisition station, 14: PC computer
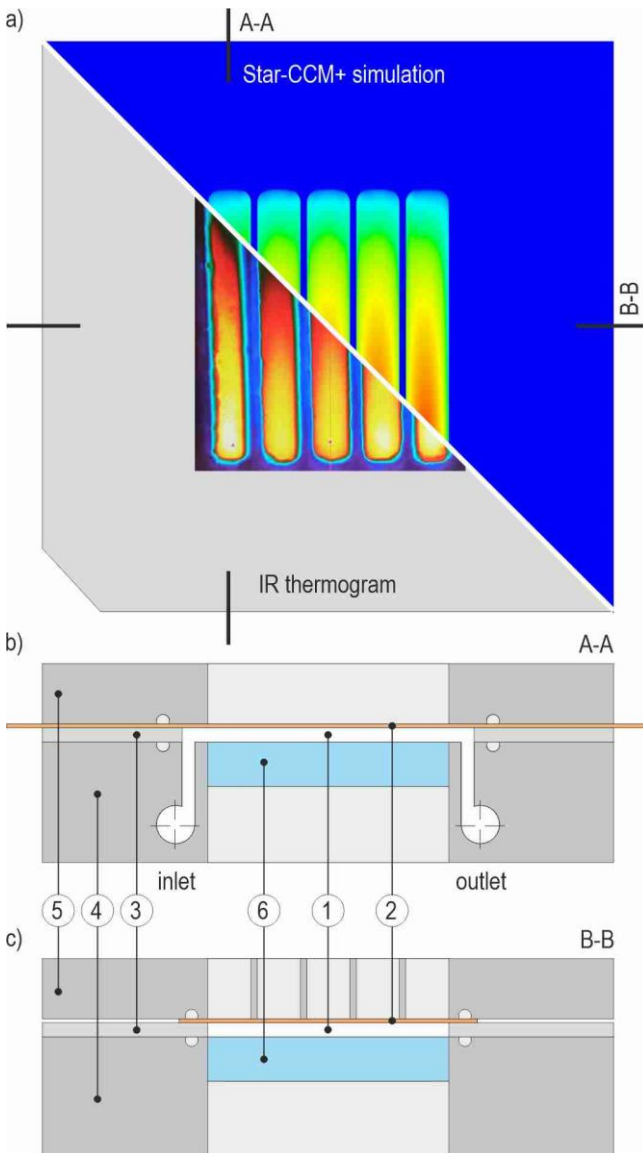
2.2. Test section

The essential part of the experimental set up was the test section with a group of five parallel minichannels of rectangular cross-sections, each of pre-set depth 1 mm and width 6 mm, while their lengths taken into consideration are 43 mm. The schematic diagrams of the test section are shown in Fig. 3. The test section was placed horizontally with the fluid flowing above the heated wall. The heating element for the working fluid that flowed laminarly along the minichannels was a thin alloy plate stretched between two metal parts. This 0.1-mm-thick plate designated Haynes-230 is made of a high-temperature Ni–Cr–W–Mo alloy. The heater was powered by a heat source (the inverter welder acts as a regulated power supply) and was resistively heated, supplying heat to the fluid flowing in minichannels. The temperature distribution on the outer surface of the heated plate was measured by means of an infrared camera. Example thermograms on an outer side of the heated plate captured by an infrared camera are shown in Fig. 3a. It should be explained that a plate surface was coated with black paint of known emissivity (0.97). Example distributions of the temperature as a result of numerical computations based on experimental data are also shown in a half-image illustrated in Fig. 3a. Furthermore, a high-speed camera allowed recording flow structures through a transparent glass, which constitutes the opposite wall to the heated plate. Sensors of K-type thermoelements and pressure meters were mounted at the inlet and outlet of the minichannels.

Table 1 summarises the basic geometrical data of the test section. These data were used for calculations using methods with Trefftz functions and implemented into the Simcenter STAR-CCM+ program.

sciendo

Anna Pawińska, Artur Piasecki, Norbert Dadas, Sylwia Hożejowska, Magdalena Piasecka
Homotopy Perturbation Method with Trefftz Functions and Simcenter STAR-CCM+ used for the Analysis of Flow Boiling Heat Transfer

DOI 10.2478/ama-2024-0027

Tab. 1. Basic geometrical data of the test section

Basic geometrical data of the test section	Value (unit)
Number of minichannels in the test section	5
Length of the minichannels*	0.043 (m)
Thickness of the heated plate	0.0001 (m)
Depth of the minichannels	0.001 (m)
Width of a singular minichannel	0.006 (m)

*The length over which the temperature measurement is measured due to an infrared camera

Fig. 3. Schematic diagram of the test section: (a) front view, (b) longitudinal section, (c) cross section; 1: minichannel, 2: heated plate, 3: Teflon spacer, 4: channel body, 5: front cover, 6: glass plate

2.3. Research methodology

A research pre-procedure is needed to ensure stabilisation of the set crucial experimental parameters. In this pre-procedure, the degassing of the fluid should be first ensured while it was circulating in a closed flow loop. Then, the initial temperature, pressure and flow parameters are set and stabilised during work-

ing fluid circulation. During the regular experimental series, there is a smooth increase in the current intensity supplied to the heated wall of the minichannels. The gradually increased heating power resulted in an increase in the temperature of the minichannel wall, and thus the cooling fluid in the minichannels is gradually heated along its flow. Sequentially, the values of pressure, temperature and mass flow of the working fluid and current supplied to the heated plate are collected in a 1-s interval, whereas single images of thermograms are captured by an infrared camera. Flow structures are simultaneously observed and recorded by a high-speed video camera.

According to the physical interpretation of the heat-transfer mechanism that occurs during the fluid flow, the experimental set up can be characterised as follows:

- After degassing and stabilising the experimental conditions, the subcooled liquid flows laminarly into an asymmetrically heated minichannel;
- In the beginning, when the heat flux increases, the heat transfer between the heating plate and the liquid proceeds via the single-phase forced convection;
- Further in the experiment, the increase in the heat flux results in boiling incipience in the minichannel, and subcooled boiling starts;
- When the heat flux continues to increase, nucleate boiling is in progress in the minichannel.

It should be underlined that the range of parameters characterising the selected series indicates that the data under analyses belong to the single-phase forced convection and the start of the subcooled
boiling region.

3. COMPUTATIONAL METHODS

3.1. Methods based on Trefftz functions

The 2D temperature distributions of the heated plate and cooling fluids were calculated with the classical TM and a hybrid method combining the HPM with the TM, respectively. This approach, which is a modification of that described in Ref. [36] considers two dimensions: one in the flow direction (x) and the other perpendicular to the flow (y) that relates to the thickness of the heated plate thickness δ_G and the minichannel depth δ_M.

The heat-transfer process in the heated plate, where $0 < x < H, 0 < y < \delta_G$, is assumed to be characterised by the Poisson equation, [36]

$$\lambda_G \left(\frac{\partial^2 T_G}{\partial x^2} + \frac{\partial^2 T_G}{\partial y^2} \right) = -q_V \qquad (1)$$

where H: length of the minichannel, T_G: temperature of the heated plate, λ_G: thermal conductivity of the heated plate and q_V: heat flux supplied to the heated plate.

For Eq. (1), the temperature distribution at the plate's edge (T_{IR}) is known from infrared camera measurements. The remaining three edges (not in contact with the fluid) are insulated. The fluid flow in the minichannel is assumed to be laminar, with the velocity vector having one non-zero component $w(y)$ parallel to the flow direction. The fluid temperature for $0 < x < H, \delta_G < y < \delta_G + \delta_M$ satisfies the energy equation in the form:

$$\lambda_f \left(\frac{\partial^2 T_f}{\partial x^2} + \frac{\partial^2 T_f}{\partial y^2} \right) = \rho_f c_{p,f} w(y) \frac{\partial T_f}{\partial x} \tag{2}$$

where T_f: temperature of the fluid, λ_f: thermal conductivity of the liquid, ρ_f: density of the liquid and $c_{p,f}$: specific heat capacity of the liquid.

In Eq. (2), the temperatures of the fluid T_f and the heated plate at the fluid–plate contact surface are assumed to be equal, and that the fluid temperatures at the inlet $T_{f,in}$ and outlet $T_{f,out}$ of the minichannel are known. The boundary conditions adopted for Eqs (1) and (2) are shown in Table 2.

Tab. 2. Boundary conditions for the heated plate and the fluid

Section	Boundary conditions
Wall: $y = 0, 0 < x < H$	$T_G = T_{IR}$ $\frac{\partial T_G}{\partial y} = 0$
Wall: $x = 0, x = H, 0 < y < \delta_G$	$\frac{\partial T_G}{\partial x} = 0$
Contact wall: $y = \delta_G, 0 < x < H$	$T_f = T_G$
Inlet: $x = 0, \delta_G < y < \delta_G + \delta_M$	$T_f = T_{f,in}$
Outlet: $x = H, \delta_G < y < \delta_G + \delta_M$	$T_f = T_{f,out}$

Knowing the fluid and plate temperature allows for calculating the heat transfer coefficient from the formula:

$$\alpha(x) = \frac{-\lambda_G \frac{\partial T_G}{\partial y}(x, \delta_G)}{T_G(x, \delta_G) - T_{f,ave}(x)} \tag{3}$$

where: $T_{f,ave}$ is the average fluid temperature in the minichannel, calculated as in Ref. [36].

First, using the TM, the 2D temperature distribution of the heated plate was determined according to Ref. [36]. Then, the HPM with the TM was used to find the fluid temperature following the scheme below [20, 21].

In the HPM, differential Eq. (2) is written to distinguish two operators L (linear) and N (nonlinear), i.e.

$$LT_f = NT_f \tag{4}$$

For further calculations, it is assumed that

$$LT_f = \lambda_f \left(\frac{\partial^2 T_f}{\partial x^2} + \frac{\partial^2 T_f}{\partial y^2} \right) \tag{5}$$

$$NT_f = \rho_f c_{p,f} w(y) \frac{\partial T_f}{\partial x} \tag{6}$$

In the HPM, function $h(x, y, p)$ dependent inter alia on parameter $0 \le p \le 1$ satisfies the following equation:

$$(1 - p)[L(h) - L(u_0)] + p[L(h) - N(h)] = 0 \tag{7}$$

where u_0 denotes the initial approximation of the solution to Eq. (2).

Note that substituting p=1 in Eq. (7), Eq. (2) is obtained. Expanding the function $h(x, y, p)$ into a Taylor series about p, the solution to Eq. (2) can be written as follows:

$$T_f(x, y) = \lim_{p \to 1} h(x, y, p) = \sum_{i=0}^{\infty} h_i(x, y) \tag{8}$$

where $h_i(x, y) = \frac{1}{i!} \frac{\partial^i h(x, y, 1)}{\partial p^i}$.

Finally, the solution is approximated with a Taylor series truncated to M+1 components, i.e.

$$T_f(x, y) \approx \sum_{i=0}^{M} h_i(x, y) \tag{9}$$

By substituting Eq. (9) into Eq. (7) and equating the coefficients with successive powers of p, we obtain a system of equations containing the functions $h_i(x, y)$ as in Ref. [20]. We determine the functions $h_i(x, y)$ using the TM. The resulting fluid temperature approximately satisfies both Eq. (2) and the boundary conditions. The convergence of the solution obtained by the HPM, in the case of partial differential equations, has been proven, for example, in Ref. [37]. In practice, satisfactory results have already been obtained with three or four components of series (9), and the assumptions on the initial approximation u_0 can be weaker – it can be any function.

The experimental data used in calculations with the methods employing Trefftz functions and in Simcenter STAR-CCM+ are presented in Tabs. 3 and 4. In Tab. 3, the physical properties of the solids composed of the main elements of the test section are listed. Furthermore, in Tab. 4, the main physical properties of the working fluids and experimental parameters are shown.

Tab. 3. Physical properties of the solids composed of the main elements of the test section

Element of the test section				
Parameter/physical property	Haynes 230	Glass	Teflon	Aluminium
Density (kg·m^{-3})	8,970	2,500	2,160	2,702
Specific heat of the liquid (J·kg^{-1}·K^{-1})	400	840	702	903
Thermal conductivity (W·m^{-1}·K^{-1})	10.07	1.4	0.21	237

3.2. Numerical simulations in Simcenter STAR-CCM+

Numerical calculations were performed using Simcenter STAR-CCM+, version 2020.2.1 Build 15.05.010. This program let one perform calculations related to heat transfer, change of state of matter, fluid flow or mixing of different substances. After assuming the model of the test section and implementation, the data shown in Tabs. 3 and .4 into program, a desktop computer with an Intel Core i9 CPU (24 cores) and 256 GB of RAM clock speed at 3.50 GHz helped provide simulations.

4. RESULTS

4.1. Simulations due to Simcenter STAR-CCM+ and validation with experimental data

The temperature distribution in the test section as the results of numerical computations due to Simcenter STAR-CCM+ is shown in Fig. 4, respectively, for experiments with the fluids: HFE-649 (Fig. 4a,b), HFE-7100 (Fig. 4c) and HFE-7200 (Fig. 4d). In this figure, the computational grids assumed for numerical simulations are additionally enlarged to indicate more details in Fig. 4b.

Anna Pawińska, Artur Piasecki, Norbert Dadas, Sylwia Hożejowska, Magdalena Piasecka
Homotopy Perturbation Method with Trefftz Functions and Simcenter STAR-CCM+ used for the Analysis of Flow Boiling Heat Transfer

DOI 10.2478/ama-2024-0027

Tab. 4. Main physical properties of the working fluids and experimental parameters

Physical properties of the working fluids			
Physical property	HFE-7200	HFE-7100	HFE-649
Density (kg·m^{-3})	1,430	1,532	1,510
Dynamic viscosity (Pa·s)	0.00061	0.00061	0.00057
Specific heat of the liquid (J·kg^{-1}·K^{-1})	1,214	1,118	1,183
Thermal conductivity (W·m^{-1}·K^{-1})	0.068	0.069	0.069
Experimental parameters			
Fluid temperature at the inlet (°C)	16.2	16.60	13.8
Fluid temperature at the outlet (°C)	23.1	23.70	18.6
Temperature of an ambient air (°C)	24.5	21.5	18.7
Absolute pressure at the outlet (Pa)	94,503	106,045	109,471
Atmospheric pressure (Pa)	97,143	94,921	94,654
Mass flow rate of the fluid (kg/s)	0.00575	0.00580	0.00583
Heat flux supplied to the heater (W)	99.54	95.54	83.29

The velocity distribution in the fluid due to STAR-CCM+, shown in the longitudinal section of the central minichannels, based on the data from the experiment with HFE-649 are presented in Fig. 5. Additionally, computational grids are illustrated in enlarged sections of the inlet (left side) and the outlet (right side) of this figure.

For validation of the results from numerical simulations performed in Simcenter STAR-CCM+, the temperature of the heated plate on the outer surface that contacts ambient air was compared to the results known from the infrared thermography measurement. Figure 6 shows the dependence of the temperatures on the outer surface of the heated plate obtained from simulations and experimentation as a function of the distance from the minichannel inlet.

When the heater temperature vs the distance from the inlet was examined, a gradual increase in the temperature of the heated plate was observed with the increase in the distance in both relationships.

For a more detailed comparison, Tab. 5 shows the values of the mean relative differences (MRD) between the outer surface of the heated plate calculated by Simcenter STAR-CCM+ and measurements carried out by the infrared camera during the experiments.

Furthermore, the maximum absolute differences (MADs) were determined from the following formula:

$$MAD = \max|f - g| \tag{10}$$

where f and g are functions.

The MAD values are also listed in Tab. 5.

When analysing the local temperatures of the outer surface of the heated plate obtained from numerical calculations in Simcenter STAR-CCM+ with the data obtained from the experiments shown in Fig. 6, it was stated that no significant disparities can be observed. The temperature distributions are very similar in both cases. Furthermore, the MRD between the results do not

exceed 3% and the MAD do not exceed 3°C (only for HFE-7200, the maximum value of the MAD is equal to 3.93°C).
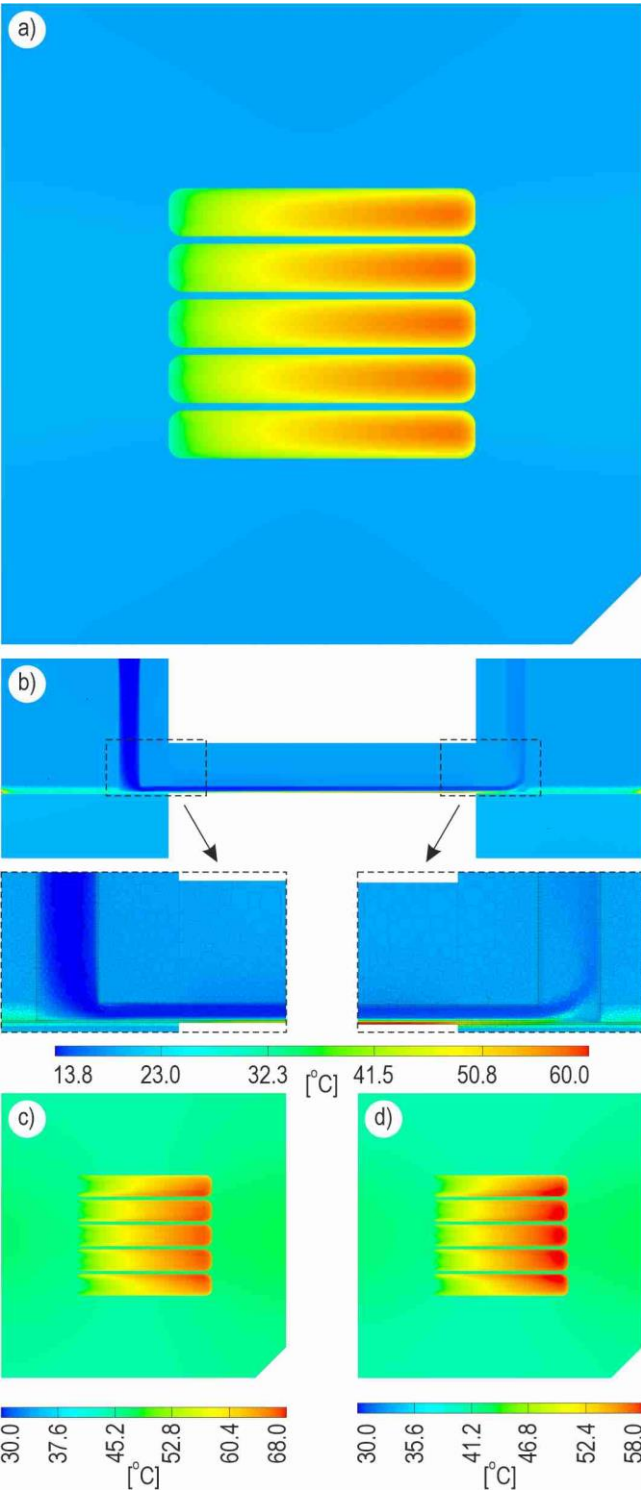
Fig. 4. Temperature distribution in the test section as the results of numerical computations in Simcenter STAR-CCM+, for experiments with fluids: HFE-649 (a,b), HFE-7100 (c) and HFE-7200 (d); (a) view on the side with the heated plate, (b) longitudinal section of the central minichannel; computational grids are visible in enlarged sections of the inlet (left side) and the outlet (right side)

Tab. 5. The MRD and MAD values determined on the basis of the Simcenter STAR-CCM+ results and the data from the experiments

Compared results	MRD (%)	MAD (°C)
HFE-649		
Temperature of an outer surface of the heated plate obtained by an infrared camera and by Simcenter STAR-CCM+	1.59	2.39
HFE-7100		
Temperature of on outer surface of the heated plate obtained by an infrared camera and by Simcenter STAR-CCM+	2.82	3.93
HFE-7200		
Temperature of the outer surface of the heated plate obtained by an infrared camera and by Simcenter STAR-CCM+	2.28	2.57

MAD, maximum absolute difference; MRD, mean relative differences.
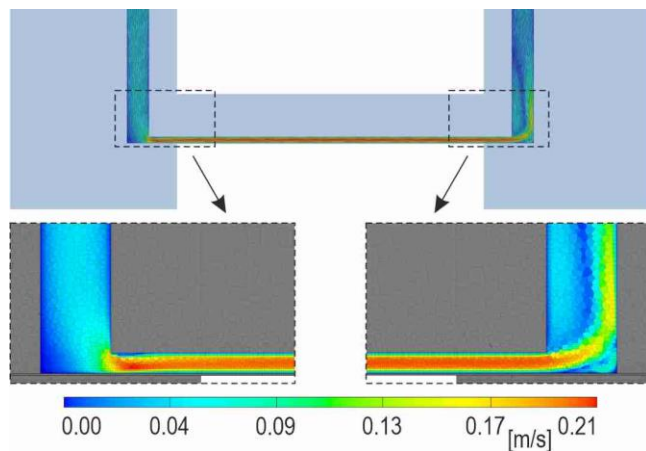
Fig. 5. Velocity distribution in the fluid obtained from numerical calculations by Simcenter STAR-CCM+ in the longitudinal section of the central minichannel based on the data from the experiment with HFE-649; computational grids are visible in enlarged sections of the inlet (left side) and the outlet (right side)

4.2. Simcenter STAR-CCM+ vs HPM and TM

The TM was used to determine the temperature of the heated plate at the contact surface with the working fluids. Moreover, the results from numerical simulation in the Simcenter STAR-CCM+, in the form of temperature plots at the heated plate-fluid interface, were also obtained and shown for comparison. The local heat transfer coefficients were also determined according to the proposed calculation methods. A 1D approach based on Fourier's law was utilised to validate the heat transfer coefficient results derived from the TM and the HPM with TM. According to Ref. [38], the local heat transfer coefficients were calculated from the following formula:

$$\alpha_{1D}(x) = \frac{q_V}{T_G(x,\delta_G) - T_{f,lin}(x) - q_V \delta_G \lambda_G^{-1}} \quad (11)$$

where $T_{f,lin}$ is the linearly changing fluid temperature from the inlet temperature to the outlet temperature.

The results of calculations based on the experimental data are presented against the distance from the minichannel inlet as follows:

– in Fig. 7, as the temperature of the contact heated plate – fluid surface according to the calculations using the TM and by Simcenter STAR-CCM+;
– in Fig. 8, as the heat transfer coefficient according to the calculations using the HPM with the TM and by Simcenter STAR-CCM+.
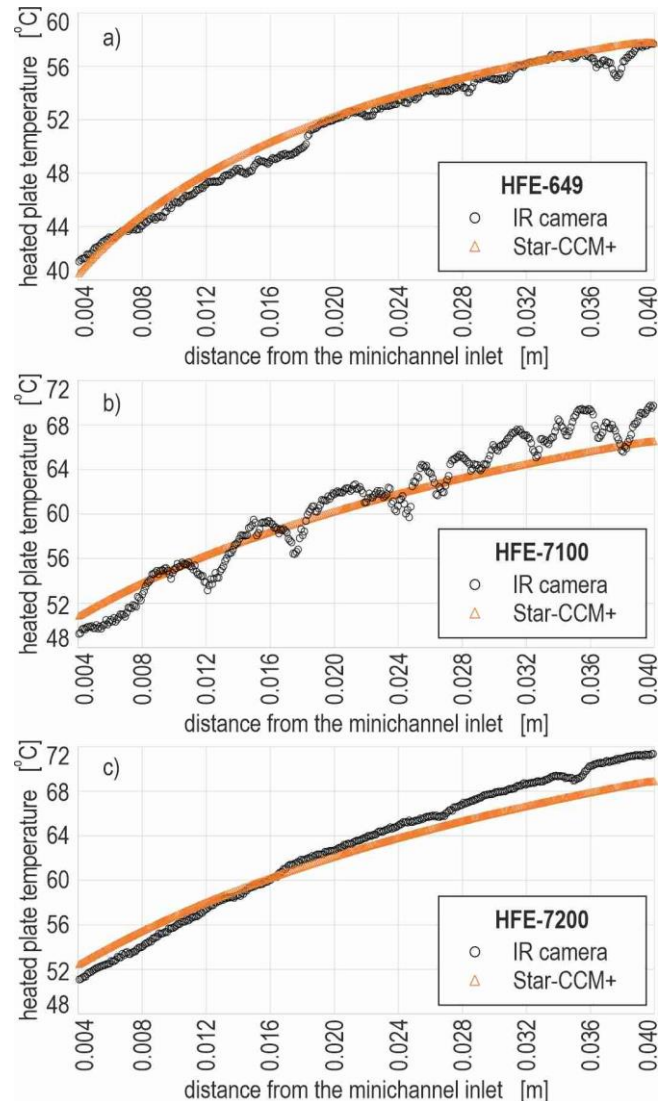
Fig. 6. Temperature of the heated plate on the outer surface contacting ambient air from the calculation performed in Simcenter STAR-CCM+ and obtained from the measurement due to an infrared camera, both as a function of the distance from the minichannel inlet

To compare the results from numerical simulations and calculations with the use of TM and the 1D approach, the differences in form of MAD and the maximum average relative differences (MARD) were determined.

MARD was defined by the following formula

$$\mathrm{MARD} = \max \left(\frac{\|f-g\|}{\|f\|}, \frac{\|f-g\|}{\|g\|} \right) \quad (12)$$

where: $\| \ \|$ means L 2 norm.

Anna Pawińska, Artur Piasecki, Norbert Dadas, Sylwia Hożejowska, Magdalena Piasecka
Homotopy Perturbation Method with Trefftz Functions and Simcenter STAR-CCM+ used for the Analysis of Flow Boiling Heat Transfer

DOI 10.2478/ama-2024-0027

Tables 6 and 7 show the fluids MARD and MAD values for the fluids under consideration and related to the contact surface temperatures and the calculated heat transfer coefficients.

The analysis of the temperature results shows that numerical simulations in Simcenter STAR-CCM+ yield similar results to those obtained from the experiment (Fig. 6) and methods based on Trefftz functions (Fig. 7) and the 1D approach. For both methods, i.e. the TM and simulations in Simcenter STAR-CCM+, similar temperature distribution patterns are observed, with minor differences in their values.

A comparative analysis of the results obtained from the two methods was carried out, the effects of which are shown in Fig. 7 and listed in Tab. 6. The MARD and MAD values determined between the temperature values at the plate–fluid interface, determined with the help of TM and the Simcenter STAR-CCM+ are listed in Tab. 6 The MARD values appear to be slight and are in the range 1.4%–2.28%. Furthermore, MAD values do not exceed 3 °C.
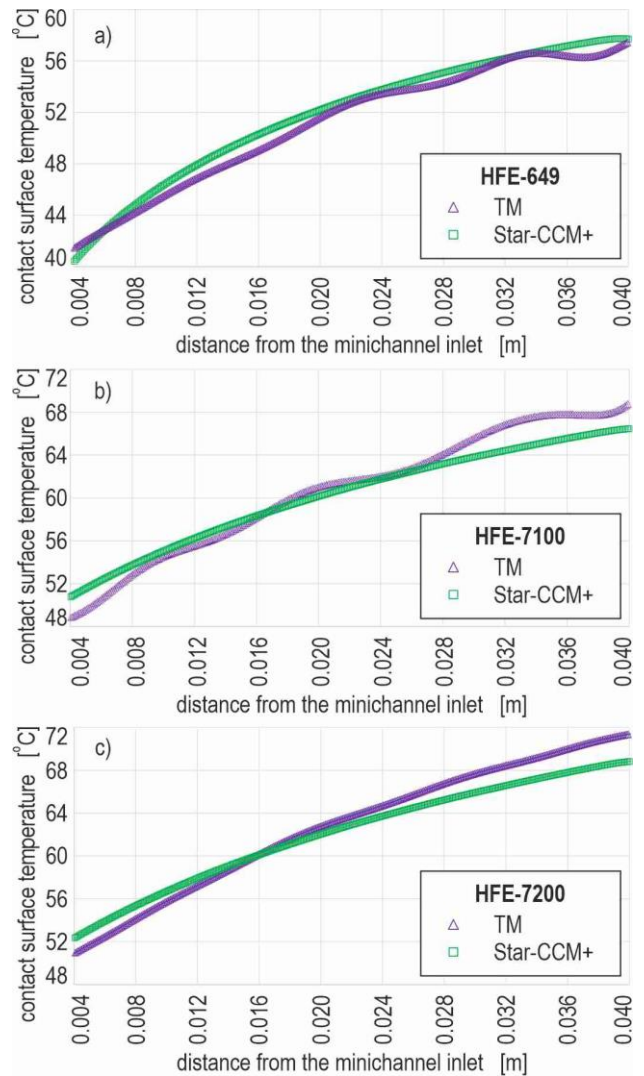
Fig. 7. Temperature of the contact heated plate-fluid surface according to the calculations using the TM and due to Simcenter STAR-CCM+ as a function of the distance from the minichannel inlet. TM, Trefftz method
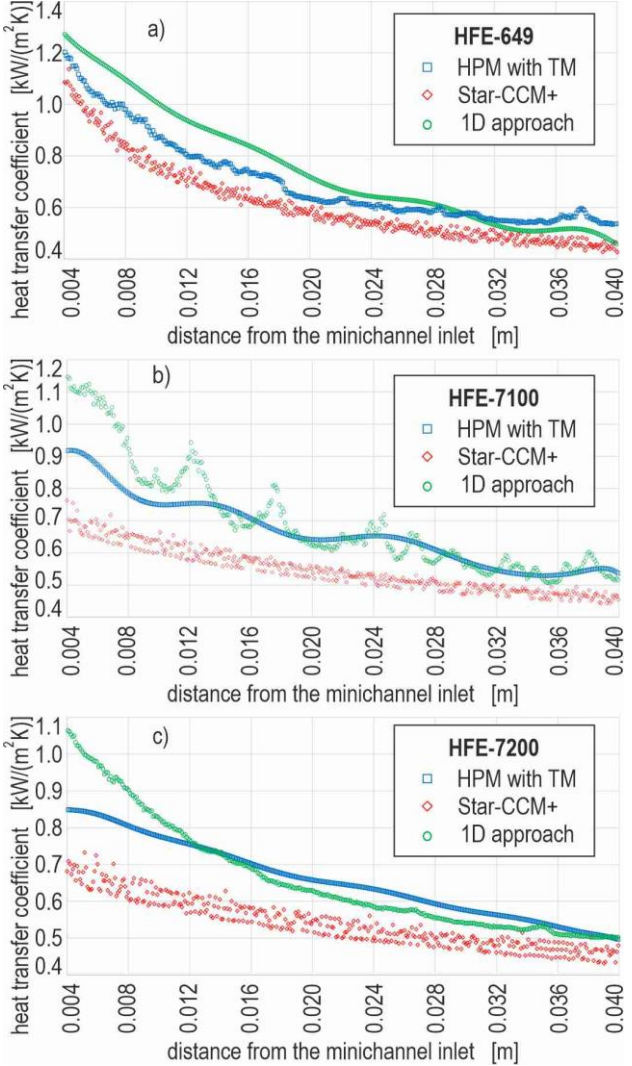
Fig. 8. Heat transfer coefficient according to the calculations using the HPM with the TM, Simcenter STAR-CCM+ and the 1D approach as a function of the distance from the minichannel inlet. HPM, homotopy perturbation method; TM, Trefftz method

Tab. 6. The MARD and the MAD values for calculated contact surface temperature

Compared results	MARD [%]	MAD [°C]
HFE-649		
Contact surface temperature from calculations by the TM and Simcenter STAR-CCM+	1.40	2.81
HFE-7100		
Contact surface temperature from calculations by the TM and Simcenter STAR-CCM+	2.28	2.81
HFE-7200		
Contact surface temperature from calculations by the TM and Simcenter STAR-CCM+	2.20	2.48

Tab. 7. The MARD and the MAD values between heat transfer coefficient values calculated from the proposed mathematical methods

Compared results	MARD [%]	MAD [W/(m²K)]]
HFE-649		
Heat transfer coefficient obtained by the HPM with the TM and Simcenter STAR-CCM+	25.07	251.68
Heat transfer coefficient obtained by the HPM with the TM and 1D approach	21.64	131.08
Heat transfer coefficient obtained by the Simcenter STAR-CCM+ and 1D approach	14.26	128.29
HFE-7100		
Heat transfer coefficient obtained by the HPM with the TM and Simcenter STAR-CCM+	22.26	223.63
Heat transfer coefficient obtained by the HPM with the TM and 1D approach	11.03	227.95
Heat transfer coefficient obtained by the Simcenter STAR-CCM+ and 1D approach	32.34	451.58
HFE-7200		
Heat transfer coefficient obtained by the HPM with the TM and Simcenter STAR-CCM+	22.80	174.98
Heat transfer coefficient obtained by the HPM with the TM and 1D approach	9.43	227.17
Heat transfer coefficient obtained by the Simcenter STAR-CCM+ and 1D approach	27.31	387.81

The primary purpose of the HPM combined with the application of the TM was to determine the heat transfer coefficient. Analysis of the results in Fig. 8 shows that the coefficient takes the highest values at the minichannel inlet while the lowest values at the outlet. According to the dependences, it was noticed that the heat transfer coefficient decreases with distance from the minichannel inlet. Similar plots were achieved with respect to the results obtained from HPM with the TM compared to the results resulting from the Simcenter STAR-CCM+ simulations and the 1D approach. Furthermore, for the results obtained by the presented calculation methods, the MARDs are in the range 9.43%–32.34% and the MAD did not exceed 451.58 W/(m2K) (see Tab. 7).

Generally, it was stated that the high agreement between the experimental results and those obtained with the TM and 1D approach allows for the validation of the CFD model.

When the heat transfer coefficient values determined from the combination of the HPM with the TM, Simcenter STAR-CCM+ and 1D approach were analysed, it was noticed that similar heat results were achieved. The highest value of the calculated difference between the heat transfer coefficients (262.68 W/(m2K)) according to both computational approaches occurred near the channel inlet. It could also be underlined that the same relationship was obtained between the heat transfer coefficient and the distance from the minichannel inlet. With increasing distance from the inlet, the heat transfer coefficient decreased not dependently on the type of a cooling fluid.

5. CONCLUSIONS

The main aim was to develop an effective method to identify the heat transfer coefficient at the heater–working fluid interface during its flow in a minichannel. Numerical studies of heat transfer were based on experimental data concerning cooling fluid flow in a group of five 1-mm deep minichannels. The selected data from the experimental series relate the single-phase forced convection and the start of subcooled boiling. A two-dimensional mathematical model was developed, which assumed steady state heat transfer in the test section. The 1D approach allowed for the validation of heat transfer coefficients determined according to the Trefftz functions and numerical calculation in CFD.

Two methods based on Trefftz functions, i.e. the classical TM and the HPM, were used to determine the temperature of the heated plate and the fluid. The advantage of the methods based on Trefftz functions used in the work is the simple mathematical apparatus. It was sufficient to use a small number of Trefftz functions and a few iterations to obtain satisfactory results. Methods based on Trefftz functions were compared with the results obtained with commercial CFD software, Simcenter STAR-CCM+ and the 1D approach.

The main findings from the analysis of the results are as follows.

- the temperature distribution on the heated plate obtained from numerical simulations was consistent with the temperature distribution achieved experimentally and determined by the TM. The MRD do not exceed 3% and the MAD was below 4°C. The high agreement between the experimental results and those obtained with the TM allows for the validation of the CFD model;
- the comparison between the heat transfer coefficients, calculated by the presented calculations methods gave satisfactory results;
- the use of combination of the HPM with the TM and Simcenter STAR-CCM+ yielded similar heat transfer coefficient values; the most significant differences reaching 251.68 W/(m2K) were observed near the minichannel inlet;
- from computational approaches, a similar plot of heat transfer coefficient variation as a function of distance from the minichannel inlet was obtained – the coefficient was found decreasing.

Comparison of the results obtained with the two presented calculation methods, i.e. simulation by CFD and methods with Trefftz functions, is the forte of this work. The 1D approach based on Fourier's law was utilised to validate the heat transfer coefficient results derived from the hybrid method HPM with TM and numerical simulations in Simcenter STAR-CCM+. It should be noted that the presented calculations are based on experimental data. Furthermore, comparison of the results by the Simcenter STAR-CCM+ program with experimental measurements made it possible to validate the model adopted in this program. As a result of the validation of the aforementioned model, further studies including other refrigerants could allow for reduction of the experimental part in favour of numerical simulations. Both steady-state and time-dependent problems will be considered, and the CFD software will also be used for their analysis.

Nomenclature:
c_p – specific heat capacity, J/(kg K)
f, g – functions
H – length of the minichannel, m
h – function
HPM – homotopy perturbation method
L – linear operator

M	–	number of terms in Taylor series
MAD	–	maximum absolute difference
$MARD$	–	maximum average relative difference
MRD	–	mean relative differences
N	–	nonlinear operator
p	–	parameter
q_V	–	volumetric heat flux, W/m3
T	–	temperature, K
TM	–	Trefftz method
u_0	–	initial approximation of the solution
w	–	velocity, m/s
x	–	coordinate in the direction of flow, m
y	–	coordinate in the direction perpendicular to the flow and width of the partitions, m

Greek letters:

α	–	heat transfer coefficient, W/(m2 K)
δ	–	thickness, depth, m
λ	–	thermal conductivity, W/(m K)
ρ	–	density, kg/m3

Subscripts:

ave	–	average
f	–	fluid
G	–	heated plate
in	–	inlet
IR	–	infrared camera
lin	–	linear
M	–	minichannel
out	–	outlet
$1D$	–	one dimension

REFERENCES

1. Tibirica CB, Ribatski G. Flow boiling in micro-scale channels - Synthesized literature review. International Journal of Refrigeration. 2013;36(2): 301-324. https://doi.org/10.1016/j.ijrefrig.2012.11.019

2. Da Silva PF, de Oliveira JD, Copetti JB, Macagnan MH, Cardoso EM. Flow boiling pressure drop and flow patterns of R-600a in a multiport minichannels. International Journal of Refrigeration. 2023;148: 13-24. http://doi.org/10.1016/j.ijrefrig.2023.01.001

3. Wang D, Wang D, Hong F, Xu J, Zhanga C. Experimental study on flow boiling characteristics of R-1233zd(E) of counter-flow interconnected minichannel heat sink. International Journal of Heat and Mass Transfer. 2023;215(124481):1-19.
https://doi.org/10.1016/j.ijheatmasstransfer.2023.124481

4. Rafałko G, Grzybowski H, Dzienis P, Zaborowska I, Mosdorf R, Litak G. Recurrence analysis of phase distribution changes during boiling flow in parallel minichannels. The European Physical Journal Special Topics. 2023;232: 201-207. https://doi.org/10.1140/epjs/s11734-022-00741-0

5. Saghir MZ, Alhajaj Z. Optimum multi-mini-channels height for heat enhancement under forced convection condition. Energies. 2021;14(7020):1-13. https://doi.org/10.3390/en14217020

6. Piasecka M, Piasecki A, Dadas N. Experimental Study and CFD Modeling of Fluid Flow and Heat Transfer Characteristics in a Mini-channel Heat Sink Using Simcenter STAR-CCM+ Software. Energies. 2022;15(536):1-20. https://doi.org/10.3390/en15020536

7. Piasecka M, Strąk K. Influence of the Surface Enhancement on the Heat Transfer in a Minichannel. Heat Transfer Engineering. 2019;40(13-14): 1162-1175.
https://doi.org/10.1080/01457632.2018.1457264

8. Piasecka M, Maciejewska B, Łabędzki P. Heat Transfer Coefficient Determination during FC-72 Flow in a Minichannel Heat Sink Using the Trefftz Functions and ADINA Software. Energies. 2020;13(6647): 1-25. https://doi.org/10.3390/en13246647

9. Hadamard J. Sur les Problèmes aux Dérivées Partielles et Leur Signification Physique. Princet. Univ. Bull. 1902;13: 49–52.

10. Kurpisz K, Nowak AJ. Inverse Thermal Problems. Southampton, UK and Boston: Computational Mechanics Publications; 1995.

11. Bakushinskii A, Goncharsky A. Ill-Posed Problems:Theory and Applications. Dordrecht: Kluwer; 1995.

12. Tikhonov AN, Goncharsky AV, Stepanov VV, Yagola AG. Numerical Methods for the Solution of Ill-Posed Problems. London: Kluwer Academic; 1990.

13. Lesnic D. Inverse Problems with Applications in Science and Engineering. New York: Chapman and Hall/CRC; 2021. https://doi.org/10.1201/9780429400629

14. Belgacem Ben F, El Fekih H. On Cauchy's Problem: I. A Variational Steklov-Poincar´e Theory. Inverse Problems. 2005;21:1915–1936. https://doi.org/10.1088/0266-5611/21/6/008

15. Ciałkowski MJ, Frąckowiak A, Grysa K. Solution of a stationary inverse heat conduction problems by means of Trefftz non-continuous method. International Journal of Heat and Mass Transfer. 2007;50: 2170-2181.
https://doi.org/10.1016/j.ijheatmasstransfer.2006.11.030

16. Maciąg A, Grysa K. Temperature dependent thermal conductivity determination and source identification for nonlinear heat conduction by means of the Trefftz and Homotopy perturbation methods. International Journal of Heat and Mass Transfer. 2016;100: 627-633. https://doi.org/10.1016/j.ijheatmasstransfer.2016.04.103

17. Ciałkowski MJ, Grysa K. A sequential and global method of solving an inverse problem of heat conduction equation. Journal of Theoretical and Applied Mechanics. 2010;48(1): 111-134.

18. Liu CS. A modified collocation Trefftz method for the inverse Cauchy problem of Laplace equation. Engineering Analysis with Boundary Elements. 2008;32(9):778-785.
https://doi.org/10.1016/j.enganabound.2007.12.002

19. Qin QH. The Trefftz Finite and Boundary Element Method. Southampton: WIT Press; 2000.

20. Grysa K, Maciąg A. Homotopy perturbation method and Trefftz functions in the source function identification. Singapore: AP-COM&ISCM, 2013 Dec 11-14.

21. Hożejowska S. Homotopy perturbation method combined with Trefftz method in numerical identification of liquid temperature in flow boiling. Journal of Theoretical and Applied Mechanics. 2015;53(4): 969-980. https://doi.org/10.15632/jtam-pl.53.4.969

22. Maciąg A, Pawińska A. The solution of nonlinear direct and inverse problems for beam by means of the Trefftz functions. European Journal of Mechanics - A/Solids. 2022;92:1-6.
https://doi.org/10.1016/j.euromechsol.2021.104476

23. Trefftz E. Ein Gegenstück zum Ritzschen Verfahren. 2 Int. Kongress für Technische Mechanik. 1926: 131-137.

24. Hożejowska S, Hożejowski L, Piasecka M. Radial basis functions in mathematical modelling of flow boiling in minichannels. EPJ Web of Conferences. 2017;143(02037):1-5.

25. Zhao X, Li JM, Riffat SB. Numerical study of a novel counter-flow heat and mass exchanger for dew point evaporative cooling. Applied Thermal Engineering. 2008;28:1942-1951.
https://doi.org/10.1016/j.applthermaleng.2007.12.006

26. Zibart A, Kenig EY. Numerical investigation of conjugate heat transfer in a pillow-plate heat exchanger. International Journal of Heat and Mass Transfer. 2021;165(120567):1-17.
https://doi.org/10.1016/j.ijheatmasstransfer.2020.120567

27. Gorobets V, Trokhaniak V, Bohdan Y, Antypov I. Numerical Modeling of Heat Transfer and Hydrodynamics in Compact Shifted Arrangement Small Diameter Tube Bundles. Journal of Applied and Computational Mechanics. 2021;7(1):292-301.
https://doi.org/10.22055/jacm.2020.31007.1855

28. Lee W-J, Jeong JH. Development of a numerical analysis model for a multi-port minichannel heat exchanger considering a two-phase flow distribution in the header. Part I: Numerical modelling. International Journal of Heat and Mass Transfer. 2019;138: 1264-128 https://doi.org/10.1016/j.ijheatmasstransfer.2019.04.100

29. Adam A, Han D, He W, Chen J. Numerical analysis of cross-flow plate type indirect evaporative cooler: Modeling and parametric analysis. Applied Thermal Engineering. 2021;185(116379):1-13. https://doi.org/10.1016/j.applthermaleng.2020.116379

30. Ayli E, Bayer O, Aradag S. Experimental investigation and CFD analysis of rectangular profile FINS in a square channel for forced convection regimes. International Journal of Thermal Sciences. 2016;109: 279-290. https://doi.org/10.1016/j.ijthermalsci.2016.06.021

31. Mu Y-T, Chen L, He Y-L, Tao W-Q. Numerical study on temperature uniformity in a novel mini-channel heat sink with different flow field configurations. International Journal of Heat and Mass Transfer. 2015;85: 147-157
https://doi.org/10.1016/j.ijheatmasstransfer.2015.01.093

32. https://www.3m.com/3M/en_US/p/d/b5005005025/

33. https://www.3m.com/3M/en_US/p/d/b40044867/

34. https://www.3m.com/3M/en_US/p/d/b40045142/

35. https://www.3m.com/

36. Piasecka M, Hożejowska S, Maciejewska B, Pawińska A. Time-dependent heat transfer calculations with Trefftz and Picard methods for flow boiling in a mini-channel heat sink. Energies. 2021;14: 1-24. https://doi.org/10.3390/en14071832

37. Biazar J, Ghazvini H. Convergence of the homotopy perturbation method for partial differential equations. Nonlinear Analysis: Real World Applications. 2009;10: 2633-2640.
https://doi.org/10.1016/j.nonrwa.2008.07.002

38. Piasecka M, Strąk K. Characteristics of Refrigerant Boiling Heat Transfer in Rectangular Mini-Channels during Various Flow Orientations. Energies. 2021;14(4891):1-29.
https://doi.org/10.3390/en14164891

Anna Pawińska: https://orcid.org/0000-0002-1949-9433

Artur Piasecki: https://orcid.org/0009-0002-7870-5951

Norbert Dadas: https://orcid.org/0000-0001-9241-6158

Sylwia Hożejowska: https://orcid.org/0000-0003-2558-5132

Magdalena Piasecka: https://orcid.org/0000-0003-3696-6213

TESTING THE THERMAL PROPERTIES OF THE INSULATING STRUCTURES OF A FLIGHT DATA RECORDER

Andrzej J. PANAS*, Robert SZCZEPANIAK, Anna KRUPIŃSKA*,
Krzysztof ŁĘCZYCKI*, Mirosław NOWAKOWSKI***

*Air Force Institute of Technology, Księcia Bolesława Street No. 6, 01-494 Warszawa, Poland,
**Department of Aviation, Polish Air Force University, Dywizjonu 303 Street No. 35, 08-530 Dęblin, Poland

andrzej.panas@itwl.pl, r.szczepaniak@law.mil.pl, anna.krupinska@itwl.pl
krzysztof.leczycki@itwl.pl, miroslaw.nowakowski@itwl.pl

Abstract: This paper deals with the problems faced during the research on the insulating structures used in the thermal shielding of flight recorders. These structures are characterised by specific properties determined by, among other aspects, their porosity. The complex and coupled heat-exchange phenomena occurring under the operating conditions of the recorders, and in numerous cases combined with mass exchange, require dedicated test methods. The paper characterises the origin of the research problem, presents a methodology for comprehensive testing of the thermal propertiesand uses the example of determining the insulating properties of the Promalight microporous structure ®-1000R. The authors focussed on thermal diffusivity tests performed by means of the oscillatory excitation method. The measurements were conducted on a test stand to determine the effect the type of gas filling had on the porous structure and the pore filling gaspressure effect on the temperature characteristics of apparent thermal diffusivity. The authors also conducted research on the structure's resistance to direct flame exposure. The analysis of the obtained results enable recognition and characterisation of the key phenomena of heat and mass transfer; the numerical results exert a significant influence on their application.

Key words: aerogel insulating structures, thermal–physical properties, thermal diffusivity, Smoluchowski–Knudsen effect,
complex thermal analysis, ablation

1. INTRODUCTION

Due to the diversity and stringency of the requirements to be met by flight recorders [6, 10, 14], the very choice of materials for their construction requires a comprehensive approach. For this reason, the evaluation of material properties cannot be limited to the analysis of only selected characteristics, but should take into account all of them along with possible cross-correlations. This includes thermophysical parameters, which by themselves do not characterize the structure holistically. Instead of merely determining properties such as thermal conductivity, heat capacity, etc. special focus should be made on determining properties in the context of the totality of the heat-transfer and the mass-transport phenomena. The very testing procedures and the reliability and representativeness of the obtained results are important aspects here. In fact, the restrictive requirements for the thermal protection of the recorder enforce the use of modern materials rather than material structures. A simple construction and operation problem is becoming a fundamental issue. This problem is underlined by the question whether it is possible at all to describe the properties in terms of the classical parameters of the steady state and unsteady heat-conduction equations [5, 8, 11].

The present paper concerns the study of the fire-resistant microporous structure of Promalight®-1000R [7]. In this case, the complexity of heat-exchange phenomena, the coupling of mechanisms and the possibility of mass-exchange phenomena, for example in the form of phase transformations, determine the need for complex measurements with complementary results to determine individual properties or characteristics. Apart from the appropriate organisation of the overall study [22], in this case, it is essential to maintain as high a temperature resolution as possible [19]. High thermal resolution means that subsequent data points are obtained in such small temperature ranges that the averaging typical for experimental studies does not distort the temperature dependence of the measured parameter. With a low measurement resolution, a distorted image of the temperature characteristics is obtained in the ranges of its non-linearity, which applies, for example, to thermograms in the area of phase transitions. In this case, it is difficult to compare the test data with different parameters at different temperature resolutions. Difficulties also concern the conversion of thermal diffusivity into thermal conductivity, typical for thermophysical research, using the indirect measurement method [12, 13, 19].

According to the requirements of ED 112 norm [6], the recorder should "withstand" the environmental effects of a flame of 1,100 ˚C and a heat flux delivered to the walls of no less than 150 kW·mm^{-2} for at least 20 min in a high-temperature test. In a low-temperature test, the unit is subjected to an ambient temperature of 200 ˚C for 10 h. However, performing a set of measurements over such a large temperature range with all the requirements of complementary testing is extremely difficult. As a whole, however, it is essential to keep the interior with electronic

modules at a temperature not exceeding 130 ˚C. The examined microporous material is being considered in the context of internal insulation. Thus, while developing a test methodology with a different type of thermal protection for the recorders – using phase-change materials – this temperature range was the focus of attention for the research project tasks. The entire study included weight measurements, thermogravimetric (TG), microcalorimetric, i.e. dynamic scanning calorimetry (DSC) and heat diffusion tests by the oscillatory excitation method, as well as tests of the pre-fabricated product's resistance to a direct flame exposure.

2. MATERIAL STRUCTURES IN EXPERIMENTAL THERMOPHYSICAL RESEARCH

Due to the generally accepted standards for most test methods investigating material properties, also thermo-physical properties, the obtained measurement results are generally reduced to basic defining relationships, such as Fourier's law of heat conduction [26]. This is not entirely correct, for even in the case of a homogeneous solid, the expression of the Fourier–Kirchoff equation

$$\rho \; c_p \frac{\partial \; T}{\partial \tau} \;=\; \nabla \cdot \left(\bar{\lambda} \nabla T \right) \;+\; q_V \tag{1}$$

from a theoretical point of view makes it impossible to apply the formula commonly used in experimental practice [5, 21] for the determination of thermal conductivity of form

$$\lambda(T) = \rho(T) \; a(T) \; c_p(T) \tag{2}$$

While maintaining a high temperature resolution, this approximation is acceptable. However, in the case of heterogeneous materials, there is a problem of determining the resultant properties. For scalar parameters, the homogenisation relationships take form [9]

$$c_p = \sum_i g_i c_{p,i}, \quad \rho = \sum_i r_i (\rho_i)_{p,T} \tag{3}$$

However, in the case of thermal conductivity only for a steady state and simple parallel or series assembly geometries, the relationship becomes complicated to form:

$$\lambda_{cd,series} \;=\; \left[\sum_i r_i (\lambda_{pr,i})^{-1} \right]^{-1} \;,\; \lambda_{cd,parallel} = \sum_i r_i \lambda_{pr,i} \tag{4}$$

Geometrically complex systems, including porous structures, require much more complex formulations [2, 23]. In addition, heat transfer phenomena, i.e. convection and radiation, are the rule for porous structures. The following compound formula [5] should be treated with great caution, due to the coupling between mechanisms and the tensor-like general nature of thermal conductivity:

$$\lambda_{apparent} = \lambda_{cd} + \lambda_{cv} + \lambda_r, \quad \lambda_{cd} = f(\lambda_{cd,i}, \; r_i; i = 1,\ldots, \; n) \tag{5}$$

according to which the contributions of individual phenomena are additive.

The heterogeneity of the structure, its irregularity, the problem of anisotropy and the couplings that cause the behaviour of the physical system to differ from those anticipated by the defining laws do not end the problems. An additional difficulty arises from the need to take into account first-order phase transformation phenomena, which cannot be included as an input to the specific heat. The situation is somewhat bettered by both the statistical scattering of the experimental data the instrumental averaging of results under differential approximations [19]. This provides a basis for interpreting the results of measurements of classical thermo-physical parameters in terms of one of the following relationships:

$$a = \frac{\lambda}{\rho c_p} \quad vs. \quad a(T, p, \ldots) = \frac{\lambda(T,p,\ldots)}{\rho(T,p,\ldots) \; c_p(T,p,\ldots)}$$

$$vs. \quad a(T, p, \ldots) = \frac{\lambda(T,p,\ldots)}{\rho(T,p,\ldots) \left[\frac{\partial h(T,p,\ldots)}{\partial T} \right]_p} \tag{6}$$

However, it is important to emphasize the need for caution when interpreting experimental data and the need to describe them accurately. In particular, a precise distinction must be made between effective and apparent properties. In analogy to proposals [4, 16], the parameters that are shaped when only one physical mechanism is present should be considered as resultant. Apparent properties refer to the contributions of other processes, e.g. the contribution of convection or radiation to heat transfer with a diffusive description.

Due to the limited framework of this paper, the above methodological considerations do not provide an introduction to an in-depth analysis of the experimental results characterised below. They do, however, justify the need to present the results in an extended form – not only as the final result of a measurement under heat-stabilised conditions, as recommended by many thermal analysis textbooks [25], but also with a description of the process of obtaining the final result.

3. EXPERIMENTAL STUDIES

The concept of comprehensive research includes not only the idea of joint evaluation of the results obtained, but also the interdependence of the measurement procedures (Fig. 1). Maintaining the appropriate order of research and the joint use of data determined at a given stage has both methodological and practical justification. When using the indirect method of determining thermal conductivity [11, 12], it is calculated from the density, specific heat and thermal diffusivity data according to relation (2). From a practical point of view, it is recommended to first conduct microcalorimetric tests and then other measurements with thermogravimetric tests. During the TG test, the thermal resistance of the sample material can be determined, among others, based on the revealed phase-transition temperature or decomposition temperature. This, in turn, allows for the proper determination of the temperature range of the remaining tests. However, it is crucial to be able to jointly evaluate the obtained thermograms to properly determine the properties of the tested material.

Weight, thermogravimetric, microcalorimetric, flame resistance and heat diffusion characterised by effective/apparent thermal diffusivity tests were carried out as part of this project. While investigating the thermal diffusivity two factors shaping the behaviour of the porous structure were taken into account, namely temperature variation and pressure variation of the gas filling the pores. The object of research was the microporous structure of Promalight®-1000R high-temperature insulation. According to the manufacturer [7], it is an opaque glass fibre-reinforced colloidal (pyrogenic) silica blend with an open pore structure. Selected data from the product information sheet are shown in Tab. 1. Based on

Andrzej J. Panas, Robert Szczepaniak, Anna Krupińska, Krzysztof Łęczycki, Mirosław Nowakowski
Testing the Thermal Properties of the Insulating Structures of a Flight Data Recorder

DOI 10.2478/ama-2024-0028

data on the effective density of the structure (Tab. 1) and the literature value of the silica density given at 2,650 kg·m⁻³, the porosity of the material can be estimated at approximately 90%. Samples for testing were prepared from a flat panel, approximately 10 mm thick.

Tab. 1. Material properties of Promalight®-1000R [7]

ρ = 320 kg·m⁻³ (default for RT)				
t (°C)	200	400	600	800
λ (W·m⁻¹·K⁻¹)	0.022	0.024	0.029	0.039
c_p (J·g⁻¹·K⁻¹)	0.92	1.00	1.04	1.04

RT, room temperature.
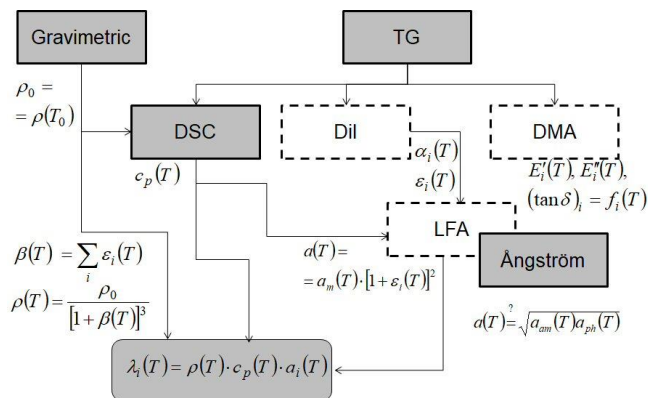
Fig. 1. Schematic diagram of the interdependence of the individual thermo-physical property tests, highlighting measurements not performed (dashed line) as part of the implementation of this project.DMA, dynamic thermomechanical analysis; DSC, differential scanning calorimetry; TG, thermogravimetry

3.1. Flame resistance tests

Due to a high demand for this type of material (which resists degradation during a prolonged operation at elevated temperatures [27, 29, 30]), an attempt was made to determine the effect of flame action on the material structure by measuring the temperature at the rear surface. The samples prepared for testing were cylindrical in shape with a diameter of approximately 50 mm and a thickness of approximately 10 mm. The tests were conducted on a test stand, designed by the authors. The test duration equalled 180 s. The sample was mounted on a fireproof board made of plasterboard. A Ceresit high-temperature filler was used for the gap between the sample and the casing, with a resistance temperature of up to 1,500 °C. J-type thermocouples (t_{s1} – t_{s3}) were used to measure the temperature of the rear surface. The temperature was recorded using National Instruments' SCB (Shielded Comparator Block) instrument and LabVIEW software. The temperature of the ablation surface (exposed to a flame) of the tested sample was measured using a pyrometer (Optris, CT model), along with a head equipped with a laser indicator of the measurement place. For control purposes, the temperature field distribution of the rear surface was also measured using an FLIR i60 thermal imaging camera (t_{th}). Also, a single value of this temperature was read out over a specified period of time. A detailed

measurement methodology is presented in Ref.[28].

The obtained result ofthe temperature measurements is given in Fig. 2. The authors also illustrate the distribution of the rear surface temperature field at intervals according to the scale in the picture (Fig. 2). Each measurement made on the rear surface of the sample using the thermal imaging camera is placed at the cross-mark position (Fig. 2) on the temperature diagram and indicated with a red dot (nine measurement points in total). The measurements from the thermocouples indicate a temperature of about 65 °C (for thermocouples) after about 180 s of measurement similar to the thermal camera measurement of 68 °C. The nature of the temperature increase qualitatively is very similar for all readings for both the thermocouples and the measurement from the thermal imaging camera, according to the temperature field distribution in the thermal camera image. Visual inspection of the flame-exposed surface did not reveal any significant damage or loss of sample weight. Only traces of soot were visible on the surface.
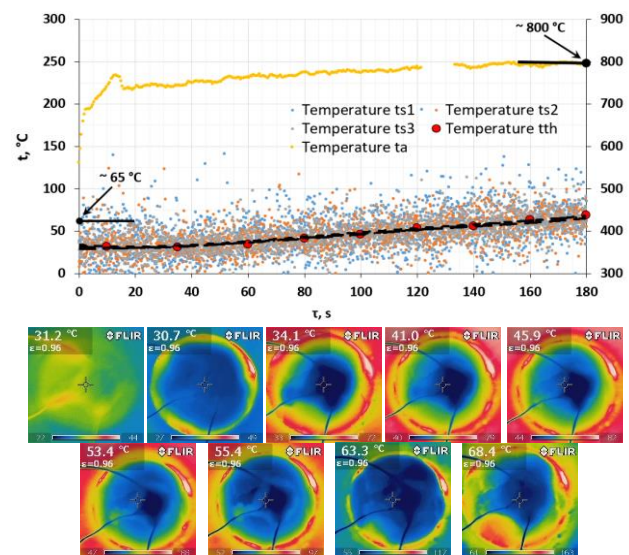
Fig. 2. Diagram with the course of temperature changes on the surface of the tested specimen exposed to the flame (ta – from remote measurements) and on the opposite surface (ts – from thermocouples, tth – IR (infrared) camera), as well as temperature distributions at selected moments on the opposite surface.

3.2. Weight measurements and thermogravimetric analysis

A Mettler Toledo AT 262 analytical balance was used to determine the mass of the test samples. The scale has a resolution of 0.01 mg and a declared accuracy of 0.02 mg. On the basis of the results of weighing control samples of approximately 15 cm³, the density was determined as 316±10 kg·m⁻³. The high measurement inaccuracy is mainly due to the measurement error of the thickness of the material panel, which is quite brittle and is subject to the pressure of the measuring tool.

A Netzsch TG 209 F3 Tarsus thermobalance was used to carry out the thermogravimetric tests. The measuring range of the thermobalance covers the temperature range from room temperature (RT) up to 1,000 °C, with the resolution equal to 0.1 μg, the maximum weight range of 2,000 mg, the rates of temperature change range from 0.001 °C/min to 100 °C/min and the capacity

of a standard alumina capsule equal to 85 μl. For the measurements, a 14.48 mg sample of crushed material was prepared and pressed with a punch in an open vessel. The first two of the three tests performed immediately one after another were carried out in the range from RT to approximately 130 °C with a declared temperature change rate of 5 K·min^{-1}. The declared rate of change of the temperature of the third measurement up to 550 °C was 10 K·min^{-1}. The findings of the TG tests are presented in Fig. 3.
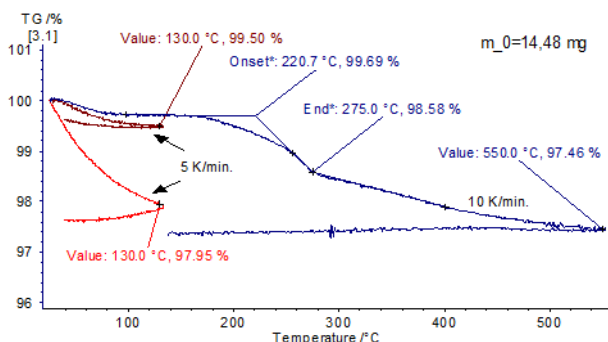
Fig. 3. TG (thermogravimetric) test results – changes in test sample weight as a function of temperature.

The resulting density measurement is consistent with the manufacturer's data. An analysis of the thermograms of the low-temperature TG test shows a likely effect of moisture release. Moisture adsorption in the ambient atmosphere (at room conditions) is typical for porous structures. As the temperature increases in the TG test, water evaporates continuously, which causes a weight loss of several percent. Due to the high enthalpy of water evaporation, even small changes in mass may have significant changes visible in the thermograms of other tests, especially microcalorimetric investigations.This may be reflected in the results of the other tests. High-temperature measurement shows the effect of releasing another component at temperatures >200 °C. The type of substance was not identified and the performed differential differential thermogravimetry (DTG) analysis is too inaccurate to determine any other details based on it. However, the indicated onset (beginning of the transformation/decomposition) temperature of 220.7 °C indicates the macromolecular nature of the additive.

3.3. Microcalorimetric measurements

DSC i.e. microcalorimetric measurements were performed using a Pyris 1 power-compensated scanning microcalorimeter from Perkin-Elmer with a temperature range of −30 °C to 600 °C and RT to 710 °C, a declared accuracy of enthalpy and specific heat determination of ± 2% and a capacity of a typical DSC vessel of 25 μl. The three-curve method [12, 13, 15] was used to determine the specific heat, with a proprietary temperature variation programme [18] used in the study. With the latter, it is possible to obtain reliable results of specific heat measurement for both heating and cooling DSC measurement steps – the so-called linear ramps of constant temperature change rate.

As in the previous case, the test sample with an initial mass of 10.17 mg was subjected to several cycles of thermal forcing. A comparison between the results obtained with the first heating cycle and the results obtained in a subsequent measurement,

after the sample condition had stabilised, is shown in Fig. 3. An analysis of the results confirms a supposition that moisture absorption has a fairly large effect on material properties, at least on the metrological scale. The increased specific heat values are related to enthalpy changes due to water release. These effects subside with subsequent cycles of thermal forcing. The results of a repeated measurement show more than a satisfactory agreement with the manufacturer's data in the comparative temperature range (>200 °C). They also confirm the transformation effect observed in TG studies at approximately 230 °C.

Direct test results of specific heat are not very suitable for calculation purposes. For the representation of the temperature characteristics and possible conversions, the numerical data were therefore processed using splain function approximation procedures [17]. Splain functions allow the irregularity of the waveforms to be reproduced for essentially any continuity class. The result of the approximation in a graphical form is shown in Fig. 4.
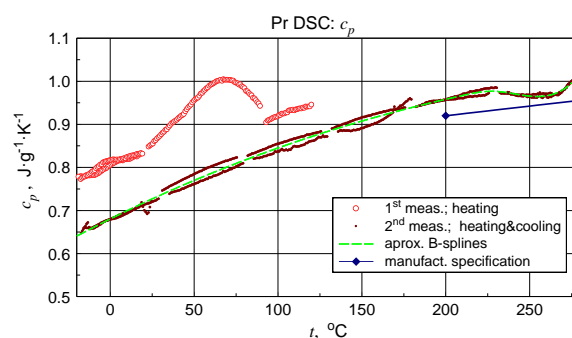

Fig. 4. Results of DSC (differential scanning calorimetry) measurements in the form of specific heat values determined for successive heating segments (measurement 1) or heating and cooling together (measurement 2).

3.4. Heat diffusion tests by temperature oscillation

Both in terms of the applicability of the results and in terms of cognitive aspects, research on heat diffusion is key to the project. Although the oscillatory excitation method used in this research, developed in Ref. [1] and subjected to multiple modifications [3], is to determine the thermal diffusivity and conductivity of the material under investigation, both the scale of the phenomena that can be investigated and the research possibilities are much larger. Particularly when using linear sweep procedures for the temperature range [20], the possibilities for interpreting the resulting signal recordings are greatly expanded. From a metrological point of view, it is also important to be able to achieve a high temperature resolution [19].

The ambient atmosphere test stand and test procedures are described in Ref. [20] where the method modification was presented. The measurement system allows thermal diffusivity to be measured within the range of −30 °C to 60 C and of−5 °C to 110 °C ,depending on the used coolant and the configuration of the measurement head. In this particular case, the authors used a different test stand, adapted for testing under conditions reduced to technical vacuum and increased to approximately the pressure of 15 bar. This system was developed in connection with the study of thermal phenomena accompanying the absorption of hydrogen by metallic powder deposits [21]. Fig. 5 illustrates a component assembly of the pressure system measuring head. The main

reason for separating the tests between the two systems is the difficulty in separating the effect of temperature changes from the effect of pressure changes in the pressure system.
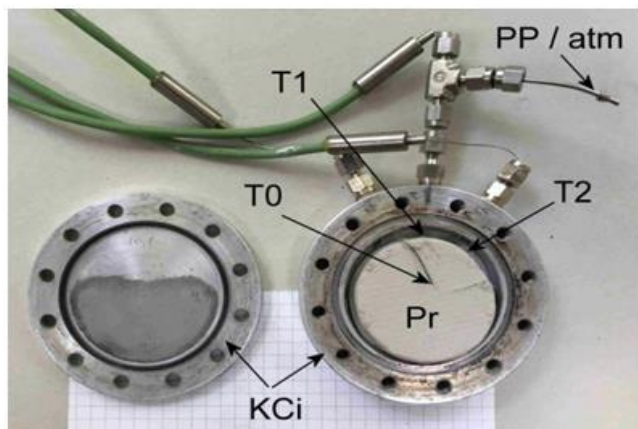

Fig. 5. Photograph of the measuring chamber (KCi) of the pressure system for thermal diffusivity measurement with the test sample (Pr), 0.5 mm K-type sheathed thermocouples (T0, T1, T2) and the marked connection point of the vacuum pump/gas tubes (PP)

The results of the behaviour of the microporous structure under varying temperature conditions with repeated thermal forcing are shown in Figs. 6 and 7. The illustrations contain the determined thermal diffusivity values of the so-called amplitude and phase. For the measurements, a thermal forcing with a period of 60 s or 120 s and an amplitude of about 1 K was used. Due to the limitations of the present study, the authors will limit the characterisation of the differences between these values to the information that the two values should be equal, provided the model conditions are maintained without a heat loss [1, 3, 20].However, it can be emphasised that the Angstrom method is well conditioned metrologically. If there are deviations from the adiabaticity of the sample, the thermal diffusivity value is still between the calculated thermal diffusivity values: amplitude and phase.So, when there are heat losses from the edge of the sample, the actual value under model conditions is included between the higher phase and lower amplitude values [1, 12]. Not only do the boundary heat losses cause the discrepancy in results,they can also be caused by phase transformations not taken into account in the basic model. In the case under consideration, the observed divergence effect is probably due to the release of moisture from the porous structure under investigation. The phenomenon is intensified when the temperature rises. Due to the decreasing vapour pressure and as a result of dehumidification, the effect weakens with a decreasing temperature. It is also observed becoming less intense in subsequent cycles (Fig. 6). Drying the sample stabilises its response to temperature forcing (Fig. 7). The overall results are consistent with the TG and DSC findings.

Clearly, the properties of the porous structure are shaped by the properties of the matrix (the structure's core material) and the filling. The influence of the type and pressure of the filling gas on the determined thermal diffusivity values is illustrated by the test results shown in Figs. 8 and 9. The tests were performed with an oscillation period of 60 s and similar amplitude parameters of the external oscillatory forcing as in the previous case. The gases used for filling, namely helium and dehydrated nitrogen, differ significantly in their thermal conductivity values under standard

conditions. The difference reaches one order of magnitude. However, the thermal conductivity as well as other thermodynamic parameters of nitrogen are similar to those of atmospheric air. In order to avoid effects related to moisture sorption, the sample was first degassed and then the temperature level of the oscillation (test temperature) was set to approximately 18 °C. Under these conditions, the discrepancies in amplitude and phase values did not exceed the level featured in Fig. 7 and the geometric mean values of each pair– amplitude value, phase value [1, 20] – were chosen to present the results.
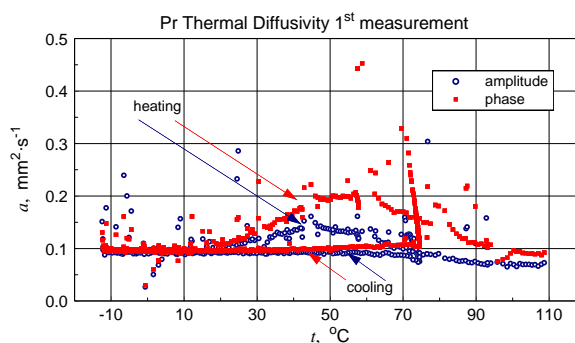
Fig. 6. Amplitude and phase values of the thermal diffusivity of the tested structure as a function of temperature for the first two temperature forcing cycles (open system)
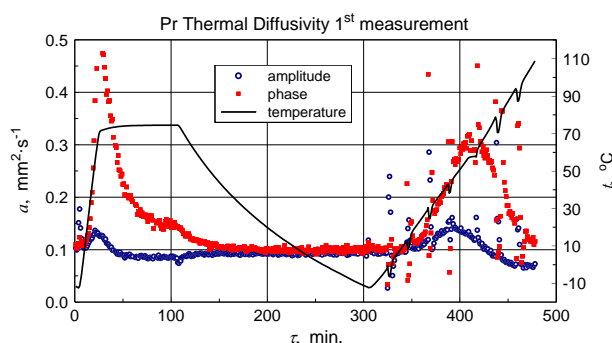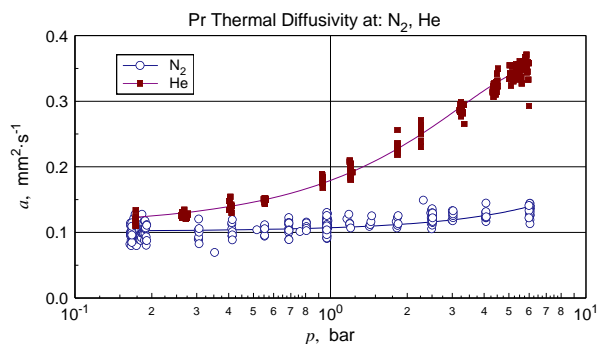

Fig. 7. Results of thermal diffusivity tests during the first temperature forcing cycles in comparison with the force-time characteristics
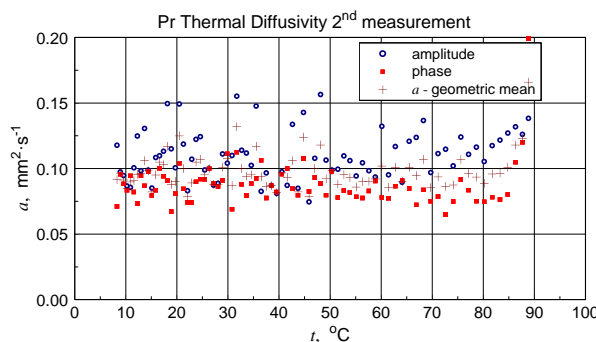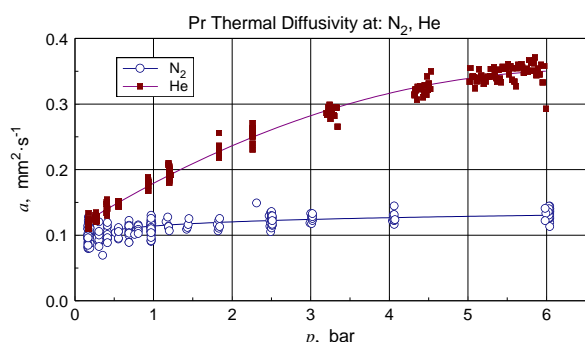

Fig. 8. Effective thermal diffusivity from measurements performed on thermally stabilised specimen – without moisture-releasing effects

Fig. 9. Geometric mean amplitude and phase values of thermal diffusivity obtained in pressure tests at a constant temperature of approximately 18 ˚C

Fig. 10. Representation of test results in the pressure chamber with a logarithmic scale of the abscissa axis

Both figures clearly illustrate both the pressure dependence of the calculated thermal diffusivity values and the quantitative differences for the compared filling gases. At pressures close to normal conditions, the test results for nitrogen filling are consistent with those obtained in an open system for the same reference temperature. With an increase in pressure from approximately 0.15 bar to 6 bar, the calculated diffusivity values for the He filling increased approximately three times and for N2 merely by approximately 40%. It can, therefore, be considered that the conductivity properties of the matrix (base) are similar to those of nitrogen and are far inferior to those of helium. The data illustrated in Fig. 10 show asymptotic convergence with decreasing filling pressures. The relationship can form the basis for an extrapolative determination of the properties of the microporous structure itself. Taking into account the measurement results obtained in an open system, the value of the design diffusivity for this structure can be determined to be approximately $9.5 \cdot 10^{-8} m^2 \cdot s^{-1}$.

3.5. Analysis of the experimental data

In addition to each individual characterisation of the research results, it is important to emphasise their compatibility. This applies primarily not only to the effects of moisture sorption found with high probability, but also to the irregularity of the thermograms around 230 ˚C. These phenomena, as well as the results of the influence of the atmosphere filling the open micro pore structure, should be taken into account both when presenting the test results and when developing representative characteristics.

From the point of view of the formation of the properties of the investigated microporous structure, the results of the tests in the pressure chamber are important. In this case, it is worth noting the relationships shown in Fig. 9 in the context of the contribution of gas thermal conductivity, in accordance with relationship [24]

$$\lambda_g = \frac{1}{3}\rho_g \, c_V w \, l \qquad (6)$$

which determines the thermal conductivity of the undiluted gas. Since the density of a gas is inversely proportional to pressure and the mean free path is directly proportional to pressure [24],

$$l = \frac{2\mu}{p}\sqrt{\frac{\pi \, R \, T}{8}} \qquad (7)$$

the thermal conductivity should not depend on the pressure. The thermal conductivity decreases with pressure merely in diluted gases, which is referred to as the Smoluchowski–Knudsen effect. In a porous structure, gas dilution is considered in terms of the ratio of the mean free path to the characteristic dimension of the object, in this case, the dimension of a single pore. In the transitional area, defined by the following Knudsen number values:

$$0{,}1 < \mathrm{Kn} < 10; \quad \mathrm{Kn} = \frac{l}{L} \qquad (8)$$

Thermal conductivity values change smoothly and the effect of this can be seen in the results of the thermal diffusivity measurements illustrated in Figs. 8 and 9 in view of relation (2). If the microstructure distribution were characterised by monodispersity, meaning equal pore dimensions, the above relationships canbe used to estimate the characteristic pore dimension. Due to the polydispersity of the examined structure, topological fuzziness is superimposed on the transitional range of the physical model and the issue of evaluating the characteristic dimensions becomes significantly complicated. Nevertheless, one aspect that does not need to be considered is the matter of estimating the minimum distances between the elements of the microstructure. The failure of the design values of thermal diffusivity to stabilise at a constant level along with an increase in pressure means that, for some part of the structure, the investigated heat transport phenomena in the gas phase still remain in the transient range.

As mentioned earlier, great care must be taken when determining representative characteristics, as well as when using the results of heat diffusion tests to determine the resultant or apparent thermal conductivity. However, since the effect of gas density on mass proportions of the homogenisation relationship on cp (3) is negligible, and also the contributions of the gas phase to the resultant density ρ (3) are small, one may attempt to determine representative temperature relationships of the three key parameters characterising transient heat transfer for the thermally non-stabilised state: specific heat, thermal diffusivity and thermal conductivity. The results of the relevant calculations are shown in Tab. 2. To determine the value of the apparent thermal conductivity expressed by relationship (2), a constant density value of 316 $kg \cdot m^{-3}$, the numerical values of the approximation characteristic of the specific heat (see Fig.4) and the linear regression relationship of mean geometric diffusivity results from Fig. 7 have been used.

Tab. 2. Computational temperature characteristics of the thermo-physical properties of the Promalight®-1000R microstructure for the thermally stabilised state

t (°C)	c_p(J·g^{-1}·K^{-1})	a(mm^2·s^{-1})	λ(mW·m^{-1}·K^{-1})
0	0.681	0.0968	20.8
20	0.718	0.0967	21.9
40	0.753	0.0965	23.0
60	0.786	0.0964	23.9
80	0.817	0.0960	24.8
100	0.845	0.0960	25.7
120	0.872	0.0959	26.4

4. CONCLUSIONS

In the light of the detailed conclusions presented in this paper and the results of the development of the measurement data, it is a truism to claim that they all prove the need for comprehensive testing even when attention is focussed on one selected material characteristic. This is because the complementarity of research results allows for proper identification and evaluation of possible off-model phenomena and effects. This is particularly relevant for material structures.

From a methodological point of view, the issue of the correct choice of a method for determining a given property is also important, especially when the property in question cannot be reduced to the category of a real property but is determined in an indirect manner. In this case, it refers to thermal conductivity. It is also necessary to properly present the result of the research, highlighting possible effects conditioned by structural heterogeneity or complexity and coupling of phenomena. In defining representative characteristics, it is appropriate to define the reference condition.

When summarising the test results of the insulating microporous structure of Promalight®-1,000R, it can be concluded that they are largely in line with the manufacturer's declaration (see Tabs. 1 and 2). The research itself, however, provides a pretext for evaluating the used methods and procedures, later exploited for other tasks of the project. It is also interesting to confirm the previously demonstrated capabilities of the oscillatory excitation method and the pressure measurement system [21] for research beyond the strict boundaries of practical applications.

NOMENCLATURE

a	thermal diffusivity (m^2·s^{-1})/(mm^2·s^{-1})		Subscripts
c_p	specific heat (J·g^{-1}·K^{-1})	0	initial state / RT
h	specific enthalpy (J·kg^{-1})	a	front surface temperature
g	mass share (/%)	am	Amplitude
Kn	Knudsen number	cd	conduction
l	average free path (m)	cv	convection
L	characteristic dimension (m)	g	gas
m	weight (kg)	i	component indication
p	pressure (bar)	p	constant pressure
q	heat related to unit mass (J·kg^{-1})	ph	phase

r	volume share (•/%)	r	radiation
R	individual gas constant (J·g^{-1}·K^{-1})	s1-	rear surface temperature
		s3	from thermocouples
T	temperature (K)	th	rear surface from IR camera
t	temperature (°C)		
u	specific internal energy (J·kg^{-1})		Abbreviations
V	volume (m^3)	Dil	Dilatometry
w	average velocity of the gas molecule (m·s^{-1})	DMA	Dynamic Thermomechanical Analysis
α	linear thermal expansion (K^{-1})	DSC	Differential Scanning Calorimetry
ε	relative expansion i.e. relative length change (/mm·m^{-1})	DTG	Differential Thermogravimetry
λ	thermal conductivity (W·m^{-1}·K^{-1})	LFA	Laser Flash Analysis
μ	dynamic viscosity (Pa·s)	RT	Room Temperature
ρ	density (kg·m^{-3})	TG	Thermogravimetry
τ	time (s)		

REFERENCES

1. Ångström AJ. Neue Methode, das Warmeleitungsvermogen der Korper zu Bestimmen. Annalen der Physic und Chemie. 1861;114:513-530.
2. Ariaki N, Tang DW, Makino A, Hashimoto M, Sano T. Transient Characteristics of Thermal Conduction in Dispersed Composites. Int JThermophys. 1998;19(1):1239-1251.
3. Belling JM, Unsworth J. Modified Ångström's method for measurement of thermal diffusivity of materials with low conductivity. Rev.Sci.Instrum. 1987;58(6):997-1002
4. Dagan G. Effective, equivalent and apparent properties of heterogeneous media. H. Aref and J.W. Philips (eds.), Mechanics for a New Millenium, Kluwer Academic Publishers, 2001; 473-486
5. Ebert HP, Braxmeier S, Reichenauer G, Hemberger F, Lied F, Weinrich D, Fricke M. Intercomparison of Thermal Conductivity Measurements on a Nanoporous Organic Aerogel. Int. J. Thermophys. 2021;42(21):1-18.
6. EuroCAE ED 112. Minimum operational performance specification for crash protected airborne recorder systems, Revision A September 1. 2013.
7. Etex Industry. Promat Technical Data Sheet. Promalight®. 2022. Available from:www.promat-industry.com
8. Goual MS, Bali A, Quéneudec M. Effective thermal conductivity of clayey aerated concrete in the dry state: experimental results and modeling. J. Phys. D, Applied Physics. 1999;32:3041-3046.
9. Grimvall G. Thermophysical Properties of Materials. Amsterdam: Elsevier Science Publish-ers B.V.; 1986. p.347
10. Jakielaszek Z, Panas AJ, Nowakowski M, Klemba T, Fikus B. Evaluation of numerical modeling application for the crash test planning of the catastrophic Flight Data Recorder. J. Mar. Eng.Technol. 2017;16(4):319-325
11. Kanit T, N'Guyen F, Forest S, Jeulin D, Reed M, Singleton S. Apparent and effective physical properties of heterogenous materials: Representativity of samples of two materials from food industry. Comput Methods Appl Mech Engi, 2006;195:3960 – 3982.
12. Maglić KD, Cezairliyan A, Peletsky VE (Eds).Compendium of Thermophysical Property Measurement Methods. Volume 1: Survey of Measurement Techniques. New York: Plenum Press. 1984.

13. Maglić KD, Cezairliyan A, Peletsky VE. Compendium of Thermophysical Property Measurement Methods. 1992 Vol. 2: Recommended measurement Techniques and Practices. New York: Plenum Press 1992,

14. NO-16-A200. Wojskowe statki powietrzne, Pokładowe rejestratory katastroficzne, Wymagania i badania [Military aircraft, On-board catastrophic recorders, Requirements and tests] 2006.

15. McNaughton JL, Mortimer CT. Differential Scanning Calorimetry. IRS. Physical Chemistry Series 2 Vol.10. London: Butterworths; Norwalk: reprinted by Perkin-Elmer Corp. 1975; 44.

16. Ostoja-Starzewski M. Mechanics of Random Media. Warszawa: Military University of Technology 2017.

17. Panas AJ. B-spline approximation of DSC data of specific heat of NiAl and NiCr alloys. Arch Thermod. 2003;24:47–65.

18. Panas AJ, Panas D. DSC investigation of binary iron-nickel alloys. High Temp. – High Press 2009;38(1):63-78.

19. Panas AJ. Comparative-Complementary Investigations of Thermophysical Properties – High Thermal Resolution Procedures In Practice. Zmeskal, O. et al. (eds). Thermophysics. Brno University of Technology. Faculty of Chemistry. 2010; 218-235.

20. Panas AJ. IR Support of Thermophysical Property Investigation. Medical and Advanced Technology Materials Study. Prakash, R.V. (Ed.). Infrared Thermography. InTech (Rijeka). 2012;65-90.

21. Panas AJ, Fikus B, Płatek P, Kunce I, Dyjak S, Michalska-Domanska M, Witek K, Kuziora P, Olejarczyk A, Jaroszewicz L, Polański M. Pressurised-cell test stand with oscillating heating for investigation heat transfer phenomena in metal hydride beds. Int. J. Hydrogen Energy. 2016;41:16974-16983.

22. Panas AJ, Błaszczyk J, Dudziński A, Figur K, Foltyńska A, Krupińska A, Nowakowski M. Badania wpływu temperatury na zmiany właściwości cieplnych i mechanicznych osnowy lotniczego konstrukcyjnego materiału kompozytowego. Mechanika w lotnictwie ML-XVII. tom II. Warszawa: PTMTS 2016.

23. Pietrak K, Wiśniewski ST. A review of models for effective thermal conductivity of composite materials. J Pow Technol. 2015;95(1): 14-24.

24. Reif F. Fizyka statystyczna. Warszawa: PWN. 1971; 394.

25. Wendlandt WW. Thermal Analysis. 3rd ed. New York: John Willey & Sons. 1986; 815.

26. Wiśniewski S, Wiśniewski T. Wymiana ciepła. Warszawa:WNT. 2000; 445.

27. Friedrich K, Fakirov S, Zhang Z. Czigány T. Discontinuous basalt fibre-reinforced hybrid composite. Polymer composites: from nano- to macro scale. 2005;309-328.

28. Szczepaniak R, Kozun G, Przybylek P, Komorek A, Krzyzak A, Woroniak G. The effect of the application of a powder additive of a phase change material on the ablative properties of a hybrid composite. Compos Struct. 2021;256:113041.
https://doi.org/10.1016/j.compstruct.2020.113041

29. Krzyżak A, Kucharczyk W, Gąska J, Szczepaniak R. Ablative test of composites with epoxy resin and expanded perlite. Compos Struct. 2018;202:978-987.
https://doi.org/10.1016/j.compstruct.2018.05.018

30. Przybyłek P, Komorek A, Szczepaniak R. The Influence of Metal Reinforcement upon the Ablative Properties of Multi-Layered Composites.Adv SciTechnol Res J. 2023;17(2).

Andrzej J. Panas: https://orcid.org/0000-0002-5497-5845

Robert Szczepaniak: https://orcid.org/0000-0003-3838-548X

Anna Krupińska: https://orcid.org/0000-0002-0130-6445

Krzysztof Łęczycki: https://orcid.org//0000-0003-3934-0902

Mirosław Nowakowski: https://orcid.org/0000-0001-6438-5235

STUDY OF CONTACT ALGORITHMS INFLUENCING SPECIMEN RESPONSE IN NUMERICAL SIMULATION OF DYNAMIC COMPRESSION TEST

Paweł BARANOWSKI*[ORCID], Krzysztof DAMAZIAK*[ORCID]

*Military University of Technology, Faculty of Mechanical Engineering, Institute of Mechanics and Computational Engineering,
2 Gen. S. Kaliskiego Street, 00-908 Warsaw, Poland

pawel.baranowski@wat.edu.pl, krzysztof.damaziak@wat.edu.pl

Abstract: This paper demonstrates the importance of a proper contact algorithm selection when a constitutive model is correlated and validated, especially in the case of brittle materials. A parametric study is carried out to study the influence of contact parameters on the outcomes of the numerical simulations of a dynamic compression test. The split Hopkinson pressure bar (SHPB) model is developed, and sandstone rock is considered as a representative material having considerably different properties compared to SHPB bars. The finite element method (FEM) and smoothed particle hydrodynamics (SPH) were used to simulate specimen behaviour using a LS-Dyna solver. Two contact types based on the penalty method are analysed: nodes to surface (FEM and SPH) and surface to surface (FEM only). Furthermore, three approaches of contact stiffness calculation are used for each contact type. The waveform data and failure patterns are then compared among all simulated cases and the corresponding experimental outcomes. It is found that the soft constraint stiffness (*SOFT = 1*) provides the best outcomes, especially in the case of one-way contact, and is nearly insensitive to stiffness scaling parameters. By contrast, standard (*SOFT = 0*) and segment-based (*SOFT =2*) approaches require a substantial effort in adjusting the stiffness scaling parameters to obtain satisfactory results. This paper provides valuable guidance for correlating and validating parameters of constitutive models for rock and other brittle materials in the SHPB test.

Key words: JH-2 constitutive model, sandstone, rock, SHPB, LS-DYNA

1. INTRODUCTION

Brittle materials, such as concrete, rocks or ceramics, have been extensively studied over the last years (1-11) (1, 2, 11, 3–10). In the case of dynamic problems, two main loadings scenarios can be distinguished: blast and dynamic impacts. The scholars mainly investigate the engineering structures of various applications made of these materials using experimental techniques (12–16). However, over the last two or three decades the numerical modelling has been found to be very effective in supporting the laboratory and field tests (17–21). The credibility of the computational simulations depends on an efficient numerical model that provides a reproduction of a simulated phenomenon as close as possible to the real-world data.

One of the basic experiments to investigate the dynamic brittle material properties is the split Hopkinson pressure bar (SHPB) test, which generates a high strain rate compression loading (22, 23). The mechanical properties of various types of brittle materials have been widely investigated using the SHPB setup. These studies include rocks (24–26), concrete (10, 27, 28), glass (29) or ceramics (30). Considering the complexity of the dynamic conditions to which the tested material is subjected, numerical methods are extremely useful for providing better insights in the material behaviour and associated failure processes during the SHPB test. However, a high-fidelity constitutive modelling and a validated numerical model are needed to provide information that will be useful for the understanding of material failure phenomena. Notably, the SHPB setup is a first-choice experiment to be reproduced

using numerical tools to correlate the selected constitutive model in dynamic conditions, which is then used in subsequent simulations of a material subjected to complex dynamic loadings such as blasts or impacts. The selected constants of a constitutive model, usually responsible for strength enhancement and damage, are modified and adjusted until a proper correlation with failure pattern of the specimen (31–34) waveform data, consisting of stress vs. strain curve and/or transmitted and reflected pulses (23, 35, 36), is achieved. Certainly, physical properties of the material described using specific constants of the constitutive model affect the results. However, other elements can also drastically influence the response of a discretised material specimen, among which the mesh properties and simulations parameters should be mentioned. These data are usually described in the referenced papers; however, many of the studies do not show detailed information about the numerical models in terms of the contact modelling as the sample-bar interface conditions can heavily affect obtained results, a situation similar to the case of real-world tests. General information regarding contact type or friction properties is not enough since the numerical procedures responsible for contact calculations can have a drastic impact on the numerical simulation outcomes.

Compared with previous studies of SHPB numerical simulations of concrete, rock or other brittle materials (23, 31, 40, 41, 32–39), the scientific and novel aspect of this paper includes a detailed presentation of contact parameters' effect on the brittle specimen response in the SHPB numerical simulations. Thus, the presented paper aims to fill the abovementioned gap between the correlation of constitutive model parameters and verification of

other aspects of numerical modelling, including especially contact definition. Due to the interlinks mentioned above, the lack of such information raises questions about the validity of the derived constitutive parameters. The numerical simulations are based on the SHPB methodology presented earlier (27, 42). During experimental tests a lubricant and polyester foil were used between the specimen and the bars to minimise friction; thus, it was neglected both in calculations and theoretical problem description. To make conclusions more general, two different numerical techniques are used for the study: Finite Element Method (FEM) and Smoothed Particle Hydrodynamics (SPH). Both methods are utilised to simulate rock behaviour, but from the point of view of the algorithms describing a continuum, these methods are completely different (see Sections 2.2 and 2.3). For the both methods, the Johnson–Holmquist ceramics (JH-2) model proposed by Timothy Johnson and Gordon Holmquist (4, 8, 43–50) was used, which has been widely adopted to simulate various dynamic loading problems (4, 7, 43–48). The parameters have been determined for a selected sandstone using a methodology presented in previous papers (42, 51). The model was validated under various stress conditions using the simulations of single-elemental tests, SHPB test, drop-weight impact tests, blast tests and projectile impact tests. The results of these simulations are not included in this study and they will be available in a forthcoming publication (52). The present study mainly aimed to demonstrate a need to correlate both constitutive model and contact procedure parameters, because both of these have a significant impact on the obtained numerical results.

The remainder of this article is structured as follows. In Section 2, the problem is formulated and the numerical modelling, including theoretical backgrounds of the FEM and SPH methods, contact definitions and constitutive model parameters as well as simulated cases, are described; Section 3 presents the study's results and their discussion, where the waveform data and failure patterns are analysed for different contact parameters; and Section 4 presents the conclusions.

2. PROBLEM DESCRIPTION

The SHPB setup is a very popular experimental test used to evaluate mechanical properties of materials under dynamic conditions and it is widely used in correlation and/or validation of the selected constitutive model for simulated material. Therefore, the authors decided to investigate the problem of the contact parameters' influence on the results based on this setup to highlight the importance of not restricting the tuning-up to parameters of the constitutive model only. The numerical studies are conducted using the commercially available explicit LS-Dyna code. The choice was made based on the popularity of this particular code among researchers modelling SHPB tests. At the same time, contact procedures implemented in LS-Dyna are representative of the algorithms used in a majority of software packages based on FEM that are named as a numerical simulation tool in articles presenting investigations on rock-like materials. Especially, contact procedure steering parameters are typical (although they can have different names).

This section also contains a short description of the numerical techniques underlying the presented research. Since the theory of these techniques is well-known, the authors provide only the brief, vital information, supported by widely accepted references.

2.1. SHPB setup and model definition

To achieve this goal, a representative numerical model of the real-world SHPB setup was developed. In the actual SHPB apparatus, the following main components can be distinguished: an air gun system; incident, transmitted and striker bars; velocity measurement system; and data acquisition system. The three bars were made of steel C45 and had diameters of 40.0 mm. During tests, a lubricant and polyester foil were used to minimise friction between the bars and the specimen as much as possible. The effectiveness of this concept has already been demonstrated in previous studies (42, 53).

In all simulated cases, it was decided to model a full 3D SHPB setup with the correspondent conditions with the experiments, with the following assumptions:

- The simulated test procedure is highly dynamic in its nature; thus, the analyses were conducted within time domain (transient analyses) using explicit time integration scheme with the implementation of an explicit LS-Dyna commercial hydrocode with multiparallel processing (MPP) (54–57).

- Only the bars with the specimen inserted between them were assumed while developing the finite element (FE) model based on the experimental setup. The other components were not included in the numerical modelling. Furthermore, to initialise a stress wave in the incident bar, a pressure load corresponding to the incident wave from the experiments was applied.

- The bars were represented using fully integrated hexagonal elements with a mesh size of 1.0 mm at the bar ends interacting with the specimen, while a larger element size was adopted for the remaining parts of the incident and transmission bars.

- As stated before, the specimen was modelled using two approaches: FEM and SPH. For both methods, the same grid size was considered, i.e. the average size of FE and the distance between the particles equal to 1.0 mm.

- The friction plays a significant role in FE predictions of the material response in SHPB tests. However, frictionless interaction was assumed between the bars and the specimen since polyester foil and lubricant were used in the SHPB experiments.
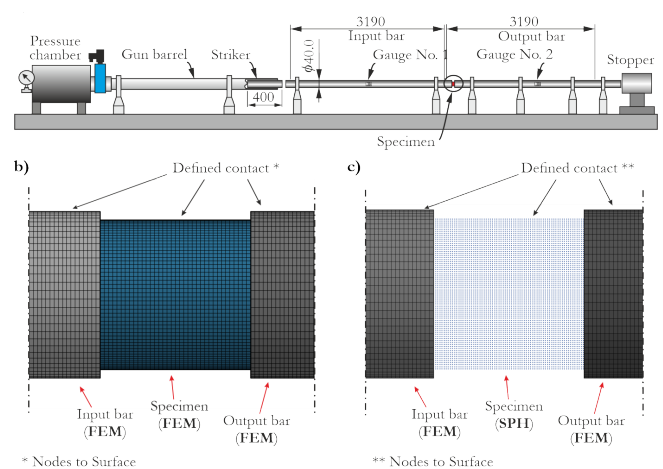

Fig. 1. (a) Scheme of the experimental SHPB setup and corresponding numerical model with (b) FEM specimen ann (c) SPH specimen

Paweł Baranowski, Krzysztof Damaziak
Study of Contact Algorithms Influencing Specimen Response in Numerical Simulation of Dynamic Compression Test

DOI 10.2478/ama-2024-0029

The laboratory setup and corresponding numerical models with Lagrangian and SPH representations of the specimen are presented in Fig. 1.

2.2. FEM modelling

In the field of solid mechanics, displacement-based FEM is currently the most widely used tool for solving Partial Differential Equations (PDEs). This comes from a few features characterising this method and the fact that its development was parallel in time with the rapid growth of computer hardware capabilities. The very basic idea of the method, which is to change PDE into a system of linear equations, allows us to adopt linear algebra techniques to obtain an approximate solution to the given problem. Easy algorithmising of linear algebra routines allowed development of robust and very efficient software packages. Increasingly easier access to hardware capable of handling real-live problems made this technique the most popular tool for engineering analysis. The FEM, as a very mature and popular method, has an extraordinarily rich bibliography. Starting with the classic work of Zienkiewicz (58), one can also mention the detailed lecture by Bathe (59), and many others (60–62). The governing equation of displacement FEM is the weak form of the minimum total potential energy principle:

$$\delta\Pi = \int_\Omega \delta\varepsilon^T \sigma d\Omega - \int_\Omega \delta\mathbf{u}^T \mathbf{b} d\Omega$$
$$\int_\Gamma \delta\mathbf{u}^T \mathbf{F} \, d\Gamma + \int_\Omega \rho \delta\mathbf{u}^T \ddot{\mathbf{u}} d\Omega = 0 \qquad (1)$$

where Ω denotes the volume of the body, Γ the surface of the body, F the vector of external forces acting on a body, u the displacement vector, b the vector of mass forces (acting on specific volume), σ the stress tensor, ε the strain tensor and Π the total energy of a body.

The solution of Eq. (1) indicates that one must find the displacement vector of all nodes (deformed shape of a body) fulfilling the equation. To solve the equation using FEM, the domain Ω (body of interest) is divided into subdomains (elements), connected to each other at corners (nodes). The movement of each corner within the subdomain is related to the movement of other corners via known, predefined, functions (shape functions). All these steps follow the idea of the Ritz method (63) and are required to approximate the integra-differential equation Eq. (2) by the system of algebraic equations that can be presented in matrix form as follows:

$$\mathbf{M\ddot{u}} + \mathbf{D\dot{u}} + \mathbf{Ku} = \mathbf{F}$$

where M denotes the mass matrix, D the damping matrix and K the stiffness matrix.

Time integration of Eq. (2) is conducted using the central difference method utilising the following differential operators:

$$\ddot{\mathbf{u}}^n = \frac{1}{\Delta t^n}(\dot{\mathbf{u}}^{n+1} - \dot{\mathbf{u}}^{n-1}) \qquad (3)$$

$$\dot{\mathbf{u}}^{n+\frac{1}{2}} = \frac{1}{\Delta t_{n+\frac{1}{2}}}(\mathbf{u}^{n+1} - \mathbf{u}^n) \qquad (4)$$

In the central difference method only a diagonal matrix of mass is inverted, which is one of the major advantages of this method.

2.3. SPH modelling

Despite its popularity, FEM has its limitations. Loss of material continuity, multi-scaling, large distortion of elements and high gradients variation are on the top of such difficulties. Therefore, new methods capable of overcoming these problems are constantly sought and developed. One such new method, or rather family of methods, is the meshless approach. As the name suggests, the biggest advantage of these methods is a lack of mesh. Probably the oldest of the meshless methods is SPH.

SPH is a meshfree method that originated in 1977 for astrophysics applications. A detailed description of SPH is shown in the study of Gingold and Monaghan (64), as well as in the study of Liu and Gu (65) and that of Liu and Liu (66), to mention the most popular sources. In short, description of continuum with the SPH uses conservation equations of mass, momentum end internal energy as the governing equations:

$$\frac{d\rho}{dt} = -\rho\frac{\partial v_i}{\partial x_i}; \quad \frac{dv_i}{dt} = \frac{1}{\rho}\frac{\partial \sigma_{ij}}{\partial x_j}; \quad \frac{dE}{dt} = \frac{\sigma_{ij}}{\rho}\frac{\partial v_i}{\partial x_j} \qquad (5)$$

where s denotes stress, v velocity, ij indexes of components and E internal energy.

Eqs. (5) are solved by interpolation of a given value of function <f> (i.e., density, velocity, energy, etc.) in a given point based on the known value of this function in surrounding points (particles) using the following formula:

$$< \mathrm{f} > (\mathbf{x}_p) = \sum_{q=1}^N \mathrm{f}(\mathbf{x}_q)\mathrm{W}(\mathbf{x}_p - \mathbf{x}_q, h) \; \Delta V_q \qquad (6)$$

where <f> denotes the function, x the vector defining particle position, p,q the indexes denoting different particles, W the kernel function and h the maximum distance between particles (smoothing length). Application of Eq. (6) to the laws of conservation leads to the following set of equations that constitute the set of basic equations used to model continuum with SPH:

$$\frac{\partial \rho_p}{\partial t} = \sum_{q=1}^N m_q v_{pq}\frac{\partial W_{pq}}{\partial x_p},$$
$$\frac{\partial v_p}{\partial t} = \sum_{q=1}^N m_q\left(\frac{\sigma_p}{\rho_p^2} + \frac{\sigma_q}{\rho_q^2}\right)\frac{\partial W_{pq}}{\partial x_p}, \qquad (7)$$
$$\frac{\partial E_p}{\partial t} = \sum_{q=1}^N m_q\frac{\sigma_p\sigma_q}{\rho_p\rho_q}v_{pq}\frac{\partial W_{pq}}{\partial x_p}.$$

where *m* denotes the mass of particle and *N* the number of particles within smoothing length.

In the presented simulations, the Lagrangian type of kernel W was used (i.e., representation of the function is formulated in material coordinates and thus the number of particles within the support domain is constant). Furthermore, the bulk viscosity coefficients were set as *Q1* = 1.5 and *Q2* = 1.0, since default values for the artificial bulk viscosity are not appropriate when SPH particles are used in such dynamic problems as the SHPB compression test (67, 68).

2.4. Constitutive modelling

The bars were assumed to have elastic properties of steel with the following properties: E_{steel} = 210 GPa, v_{steel} = 0.3 and ρ_{steel} = 7,850 kg/m3. The sandstone rock was simulated using the JH-2 model with the parameters determined using single-element tests, followed by structural simulations of quasi-static and dynamic tests characterised by different loading conditions and stress

state complexities. The results of these simulations are not included in this study and they will be available in a forthcoming publication (52). The JH-2 parameters that were determined for the sandstone are presented in Tab. 1.

Tab. 1. Material properties for the JH-2 constitutive model for sandstone

Parameter	Value	Unit
Density, ρ	2350.0	kg/m³
Poison's ratio, v	0.21	-
Bulk modulus, K_1	3735.6	MPa
Shear modulus, G	2686.0	MPa
Elastic modulus, E	6500.0	MPa
Hugoniot elastic limit, HEL	1982.0	MPa
HEL pressure, P_{HEL}	1374.0	MPa
Maximum tensile strength*, T	8.0	MPa
Intact strength coefficient, A	0.71	-
Fractured strength coefficient, B	0.30	-
Strain rate coefficient, C	0.022	-
Intact strength exponent, N	0.55	-
Fractured strength exponent, M	0.40	-
Bulk factor, β	1.0	-
Damage coefficient, D_1	0.002	-
Damage coefficient, D_2	1.20	-
Pressure coefficient 2, K_2	9000.0	MPa
Pressure coefficient 3, K_3	22000.0	MPa
Maximum normalised fracture strength, σ^*_{max}	0.25	-

*Value should be adjusted based on mesh size.

2.5. Contact modelling

Numerical procedures responsible for resolving the so-called contact problem work independently of the procedures responsible for finding a solution for the governing problem of a given numerical method (e.g., in case of FEM, displacement field fulfilling principle of minimum potential energy and thus state of equilibrium between external and internal forces). The outcome of contact procedures is comprised of forces acting between interacting bodies and kinematic contact conditions. In the solution of equilibrium problem, the former are treated as additional external load and the latter as additional support (additional boundary conditions).

In its essence, most of the contact algorithms used today are based on two most principal elements: procedures evaluating the distance between contacting bodies and procedures responsible for calculating contact forces. While there are many variations of the above, their outcome is directly responsible for the results of contact simulation. Detailed descriptions of contact procedures can be found in the literature (69–71).

Although several kinds of contact kinematics procedure are discussed in the literature, all of them rely on the tools provided by differential geometry to ascertain the distance between a point on one body and the projection of this point on an opposite body. In the classical implementation, the user must distinguish two contacting bodies by pointing out the so-called "master body" and "slave body". Then pairs of points on the "slave" and corresponding areas (called segments) on the "master" are found. Once such a pair is found, the distance between the point belonging to the

slave body and its projection on the segment belonging to the master body is found. Schematics of the problem are shown in Fig. 2, where rs denotes a point on the slave body, Γ_m is the segment on the master body and ρ is the perpendicular projection of r_s on Γ_m.
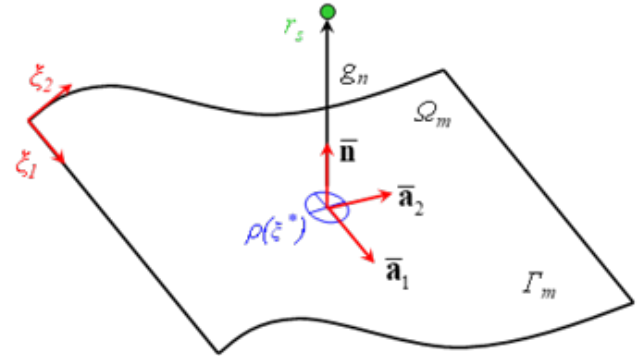
Fig. 2. Scheme of the contact problem in numerical codes

The projection point of the current position of r_s is defined as:

$$\frac{r_s - \rho(\bar{\bar{\xi}}_1, \bar{\bar{\xi}}_2)}{\|r_s - \rho(\bar{\bar{\xi}}_1, \bar{\bar{\xi}}_2)\|} \cdot \bar{\mathbf{a}}_\alpha(\bar{\bar{\xi}}_1, \bar{\bar{\xi}}_2) = 0 \qquad (8)$$

where α = 1,2; $\bar{\mathbf{a}}_\alpha(\bar{\bar{\xi}}_1, \bar{\bar{\xi}}_2)$ are the tangent covariant base vectors at projection point:

$$\bar{\mathbf{a}}_1 = \left. \frac{\partial \rho(\xi^*)}{\partial \xi_1} \right|_{\xi_1 = \xi^*_1, \xi_2 = \xi^*_2}$$

$$\bar{\mathbf{a}}_2 = \left. \frac{\partial \rho(\xi^*)}{\partial \xi_2} \right|_{\xi_1 = \xi^*_1, \xi_2 = \xi^*_2} \qquad (9)$$

Knowing the position of r_s and ρ allows us to define the distance between them and thus the distance between a point on the slave body and the surface of the master body:

$$g_N = [r_s - \rho(\xi^*)] \cdot \bar{\mathbf{n}} \qquad (10)$$

where $\bar{\mathbf{n}}$ refers to the normal to the master face Γ_m at point ρ:

$$\bar{\mathbf{n}} = \frac{\bar{\mathbf{a}}_1 \times \bar{\mathbf{a}}_2}{\|\bar{\mathbf{a}}_1 \times \bar{\mathbf{a}}_2\|} \qquad (11)$$

Knowing the distance g_N contact kinematic procedure allows us to define the kinematic contact conditions, as the following: g_N = 0 denotes contact, g_N > 0 no contact and g_N < 0 penetration.

The above approach can be used in a few different ways. When the contact kinematics procedure follows the above description, it is called a "node to segment" approach, sometimes also denoted as a "one-way contact treatment". The other often-used approach is to apply the above procedure twice, changing slave with master. These kinds of algorithms are called "surface to surface" or "two-way treatment". Finally, in the approach called "segment to segment", areas of potential contact are selected on both contact bodies, and then auxiliary points are created on these segments and the distance between the segments is evaluated using each of these auxiliary points.

In the second stage of the solution of the contact problem, contact forces are determined. This can be done under the assumption that the following conditions are fulfilled on the contact surface:

$$g_N \geq 0; \quad \sigma_N \leq 0; \quad g_N \sigma_N = 0 \qquad (12)$$

where g_N denotes the distance between the contacting bodies, and σN the normal contact stress.

Such conditions define optimality conditions known as Karush-Kuhn-Tucker (KKT) conditions. These are necessary and sufficient conditions for a local minimum in nonlinear programming problems. In case of contact problem, optimisation is used to find contact forces fulfilling Eq. (12). Depending on how σ_N is calculated, several different methods of solving the contact problem are distinguished; among these, one of the most popular is the so-called penalty method, where the value of contact force in the given node is proportional to the value of the penetration of this node.

$$F_N = k_F g_N \qquad (13)$$

where F_N denotes normal contact force, and k_F the penalty coefficient.

Eq. (13) clearly shows the concept of penalty function approach, but real-world implementations are slightly different. To help the procedure to find the optimum of the KKT problem, FEM programs usually calculate preliminary contact stiffness based on local stiffness of the numerical model and the user can adjust this preliminary value using correction coefficients. In the presented paper, the following three approaches of calculation of contact stiffness available in LS-Dyna software package are compared:

Normal stiffness derivation with SOFT = 0 (a representative equation for brick elements):

$$k_F = k_{Fnormal} = \frac{f_s K A^2}{V} \qquad (14)$$

where f_s denotes the scaling factor (SLSFAC) provided by a user (0.1 is a default value), K the bulk modulus of the material of contacting elements, A the area of a segment and V the volume of element containing that segment.

Soft constraint stiffness derivation with SOFT =1.

An alternate way to calculate contact stiffness is to use the stability contact stiffness, k_{sp}, and the same is derived as follows:

$$k_{sp} = 0.5 \cdot f_{sp} \cdot m^* \cdot \left(\frac{1}{\Delta t_c(t)} \right)^2 \qquad (15)$$

where f_{sp} denotes the user-defined scaling factor (SOFSCL) for the SOFT = 1 formulation, m^* the function of the mass of the slave nodes and master nodes and Δt_c the initial time step.

Parameter k_{sp} is calculated based on masses of the nodes in contact and on the Courant's stability criterion of the maximum time step in transient explicit analyses. Then, the maximum value of the contact stiffness calculated using Eqs (14) and (15) is taken as follows:

$$k_{SOFT=1} = \max \left\{ k_{sp}, k_{Fnormal} \right\} \qquad (16)$$

Segment-based stiffness derivation with *SOFT* = 2.

A third option is to apply a segment-based contact, which is similar to the soft constraint option with *SOFT* = 1; however, in this case, segment masses are used rather than nodal masses. Furthermore, when *SOFT* = 2 is activated, the dt is updated only when the solution time step grows by more than 5%. The stiffness in this case is calculated as follows:

$$k_{sp} = 0.5 \cdot f_s \cdot \begin{Bmatrix} SFS \\ \text{or} \\ SFM \end{Bmatrix} \left(\frac{m_1 m_2}{m_1 + m_2} \right) \cdot \left(\frac{1}{\Delta t_c(t)} \right)^2 \qquad (17)$$

where *SFS* and *SFM* denote scale factor on default slave and master penalty stiffness, respectively, and m_1 and m_2 the masses of the segments in contact.

Based on the aforementioned discussion, the application of contact stiffness parameters can be summarised as follows:

- *SFS* and *SFM* are the penalty scale factors of slave and master bodies to modify the contact stiffness.
- *SLSFAC* can scale up or down the contact stiffness, when *SOFT* = 0 or *SOFT* = 2 is used; therefore, the actual scale factor in these cases is the product of SFS or SFM and SLSFAC.
- *SOFSCL*, f_{SP}, the user defined scaling factor influences the contact stiffness only if *SOFT* = 1 is used and *SLS, SFM* and *SLSFAC* have no effect on the penalty contact stiffness.

In Tab. 2, a summary of the contact stiffness calculations using different approaches is shown. Based on these considerations, several cases using the numerical model of the SHPB setup with the FEM and SPH representation of the sandstone specimen were simulated (Section 2.6 can be referred to for more details) to analyse the influence of parameters of contact procedure on the obtained results.

Tab. 2. Summary of contact parameters available in LS-Dyna code

Type of contact	Contact stiffness formulation	SFS/ SFM	SLS FAC	SOF- SCL	Stiffness scaling factor calculation
Nodes to surface	SOFT = 0	+	+	-	SLSFAC*SFS/ SFM
	SOFT = 1	-	-	+	SOFSCL
	SOFT = 2	+	+	-	SLSFAC*SFS/ SFM
Surface to surface	SOFT = 0	+	+	-	SLSFAC*SFS/ SFM
	SOFT = 1	-	-	+	SOFSCL
	SOFT = 2	+	+	-	SLSFAC*SFS/ SFM

2.6. Description of contact parametric study

In the presented study, the influence of different contact kinematics algorithms (nodes to surface (NS), surface to surface (SS)) and different stiffness scaling parameters on the results of simulation of the dynamic compression test is analysed. Combinations of these parameters are summarised in detail in Tab. 3 and Tab. **4**.

For the FEM method, two types of contact were considered: NS and SS, whereas for the SPH method only the NS contact was employed.

In case of the NS contact (FEM and SPH), three main group of tests can be distinguished. In the first group, with the *SOFT* = 1 method of contact stiffness derivation, default values of *SLSFAC, SFS* and *SFM* were used since in this case they do not have any effect on the resultant stiffness. In this group of tests, the *SOFSCL* was modified in each test. Next, the *SOFT* = 0 method was analysed in two steps, in which the *SFS/SFM* were modified firstly, and the other parameters have the same values in each test,

which was then followed by the analysis of different values of *SLSFAC* while *SFS/SFM* = 0.3 and *SOFSCL* = 0 remained unchanged. As shown in Tab. 2, when *SOFT* = 0 is enabled, the actual stiffness scale factor is the product of *SFS/SFM* and *SLSFAC*; thus, different values of these parameters and the resultant stiffness values were studied and discussed.

Tab. 3. Contact stiffness parameters analysed in the SHPB setup using NS method for contact kinematics in FEM and SPH

Test no.	SOFT	SLSFAC	SOFSCL	SFS	SFM
NS_S1_1	1.0	Default 0.1 (no effect)	0.1	Default 1.0	Default 1.0
NS_S1_2			0.3		
NS_S1_3			0.5		
NS_S1_4			0.7		
NS_S1_5			1.0		
NS_S1_6			2.0		
NS_S1_7			5.0		
NS_S1_8			7.0		
NS_S0_1	0.0	Default 0.1	0.0 (no effect)	0.1	0.1
NS_S0_2				0.3	0.3
NS_S0_3				0.5	0.5
NS_S0_4				0.7	0.7
NS_S0_5				1.0	1.0
NS_S0_6				2.0	2.0
NS_S0_7				5.0	5.0
NS_S0_8				7.0	7.0
NS_S0_11	0.0	0.1	0.0 (no effect)	Default 1.0	Default 1.0
NS_S0_12		0.3			
NS_S0_13		0.5			
NS_S0_14		0.7			
NS_S0_15		1.0			
NS_S0_16		2.0			
NS_S0_17		5.0			
NS_S0_18		7.0			

In the case of SS contact, identical contact stiffness factors were used as for the cases presented in Tab. 3. However, two additional stages were also considered to study an effect of the *SOFT* = 2 option, with the same values of stiffness scale factors considered as in the simulations using NS contact. Therefore, with this option the parametric study of *SFS* and *SFM* values with the default *SLSFAC* was conducted, together with consideration of the fact of the study of *SLSFAC* and *SFS/SFM* remaining unchanged.

Tab. 4. Contact stiffness parameters analysed in the SHPB setup using SS method for contact kinematics in FEM

Test no.	SOFT	SLSFAC	SOFSCL	SFS	SFM
SS_S1_1	1.0	Default 0.1 (no effect)	0.1	Default 1.0	Default 1.0
SS_S1_2			0.3		
SS_S1_3			0.5		
SS_S1_4			0.7		
SS_S1_5			1.0		
SS_S1_6			2.0		
SS_S1_7			5.0		
SS_S1_8			7.0		

Test no.	SOFT	SLSFAC	SOFSCL	SFS	SFM
SS_S0_1	0.0	Default 0.1	0.0 (no effect)	0.1	0.1
SS_S0_2				0.3	0.3
SS_S0_3				0.5	0.5
SS_S0_4				0.7	0.7
SS_S0_5				1.0	1.0
SS_S0_6				2.0	2.0
SS_S0_7				5.0	5.0
SS_S0_8				7.0	7.0
SS_S0_11	0.0	0.1	0.0 (no effect)	Default 1.0	Default 1.0
SS_S0_12		0.3			
SS_S0_13		0.5			
SS_S0_14		0.7			
SS_S0_15		1.0			
SS_S0_16		2.0			
SS_S0_17		5.0			
SS_S0_18		7.0			
SS_S2_1	2.0	Default 0.1	0.0 (no effect)	0.1	0.1
SS_S2_2				0.3	0.3
SS_S2_3				0.5	0.5
SS_S2_4				0.7	0.7
SS_S2_5				1.0	1.0
SS_S2_6				2.0	2.0
SS_S2_7				5.0	5.0
SS_S2_8				7.0	7.0
SS_S2_11	2.0	0.1	0.0 (no effect)	Default 1.0	Default 1.0
SS_S2_12		0.3			
SS_S2_13		0.5			
SS_S2_14		0.7			
SS_S2_15		1.0			
SS_S2_16		2.0			
SS_S2_17		5.0			
SS_S2_18		7.0			

3. RESULTS AND DISCUSSION

3.1. Experimental SHPB tests

The representative stress–strain characteristics of the three tests with strain rates of 80 s−1, 110 s−1 and 240 s−1 are shown in Fig. 3a, for which the stress equilibrium in the specimen was achieved (Fig. 3b). For the purpose of the present study, the SHPB test with a middle strain rate of 110 s−1 was selected for studying the contact parameters' influence on the results. Fig. 3c presents waveform data, and Fig. 3d presents an exemplary specimen failure. Notably, these data were further used for analysis of the results in the present study.

The waveform data obtained in the SHPB experiment and numerical simulations were compared to analyse the influence of the contact parameters on the sandstone response. Both the transmitted and reflected characteristics represent a response of the tested material, since ultimately the stress vs. strain curve is directly obtained on their basis. Results are grouped with respect to different contact kinematics approaches (NS, SS). For each kinematics, the influence of the scaling factor of contact force is presented and discussed. The results are represented using waveform data, failure pattern and force values obtained for each case.

Paweł Baranowski, Krzysztof Damaziak
Study of Contact Algorithms Influencing Specimen Response in Numerical Simulation of Dynamic Compression Test

DOI 10.2478/ama-2024-0029
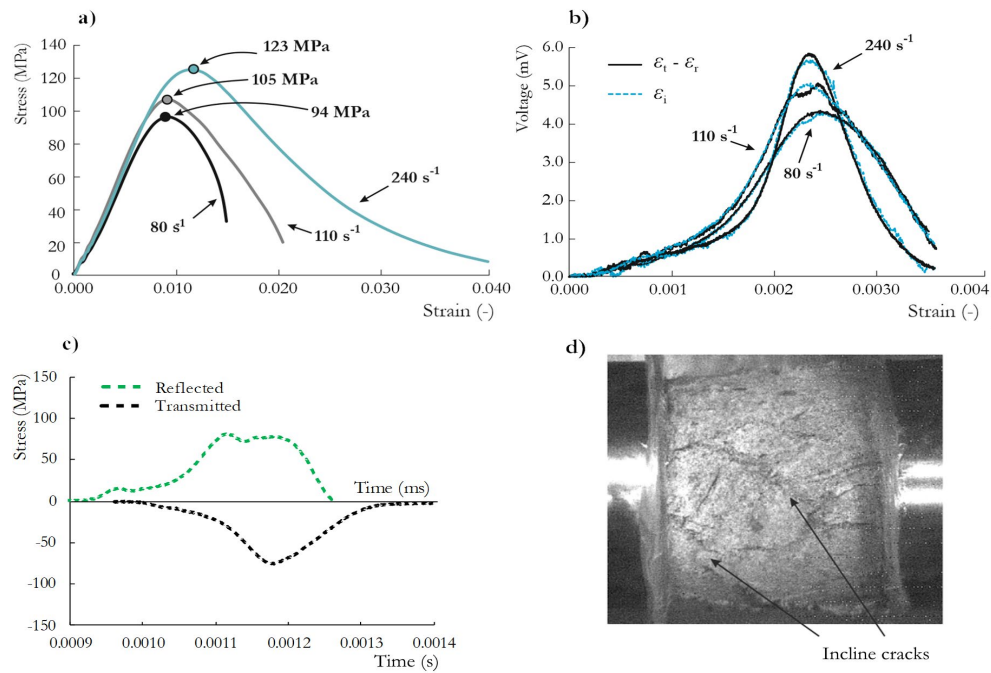
Fig. 3. Dynamic response of the sandstone tested using the SHPB setup; (a) stress vs. strain curves, (b) stress equilibria in three SHPB tests, (c) transmitted and reflected waves from the test at a strain rate of 110 s−1 and (d) representative specimen failure.

3.2. One-way contact (NS)

3.2.1. FEM: NS contact with SOFT = 1

In the first set of tests, the algorithm deriving contact stiffness was set to stabilise contact procedure (*SOFT* = 1). Results of the tests conducted using FEM for different values of the *SOFTSCL* parameter are shown in Fig. 4 and 5, presenting waveform data and specimen failure pattern, respectively. The stress response over time for different *SOFTSCL* values does not change drasti-cally. There are some differences in the shape of transmitted wave, but they are not significant and can be treated as negligible. The very slight differences are noticeable starting from NS_S1_1 and continuing up until NS_S1_5 for *SOFSCL* = 0.1 and 1.0, respectively. The values above 1.0 are inadmissible according to the LS-Dyna manual (54) and they yield the same results as if the *SOFTSCL* was set to 0.1 (or "0", which is a default value; and in fact, it gives 0.1). The same applies to the failure pattern of the specimen, which is nearly identical in all cases.
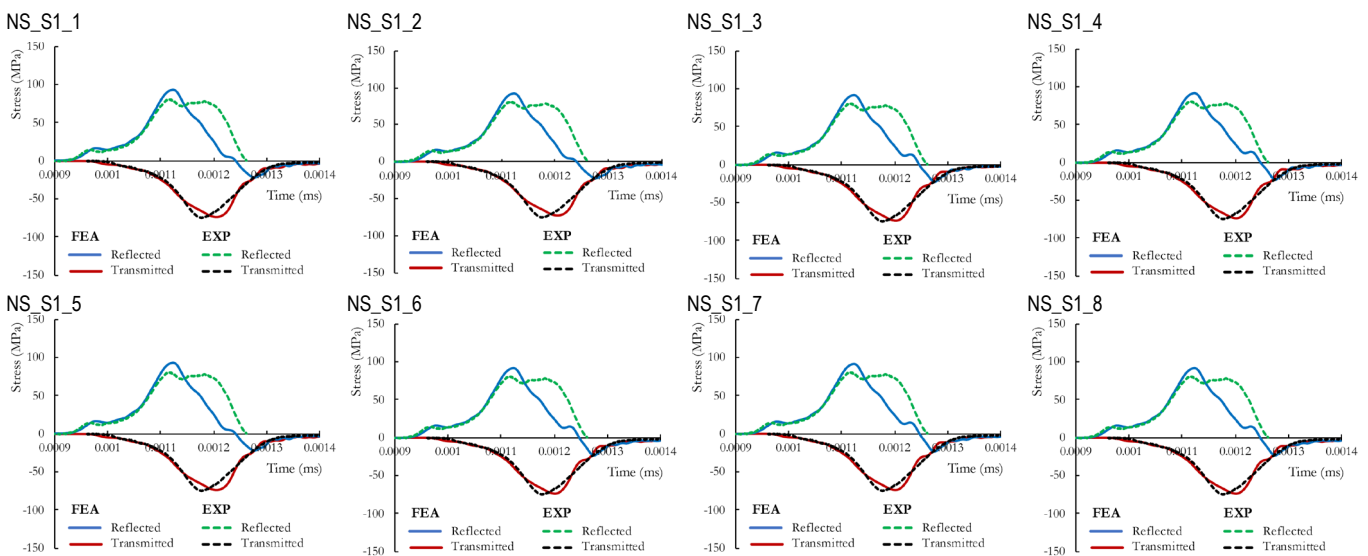
Fig. 4. Waveform data for FEM modelling of the sandstone in the SHPB test: influence of *SOFTSCL* using the *SOFT* = 1 in the NS contact definition
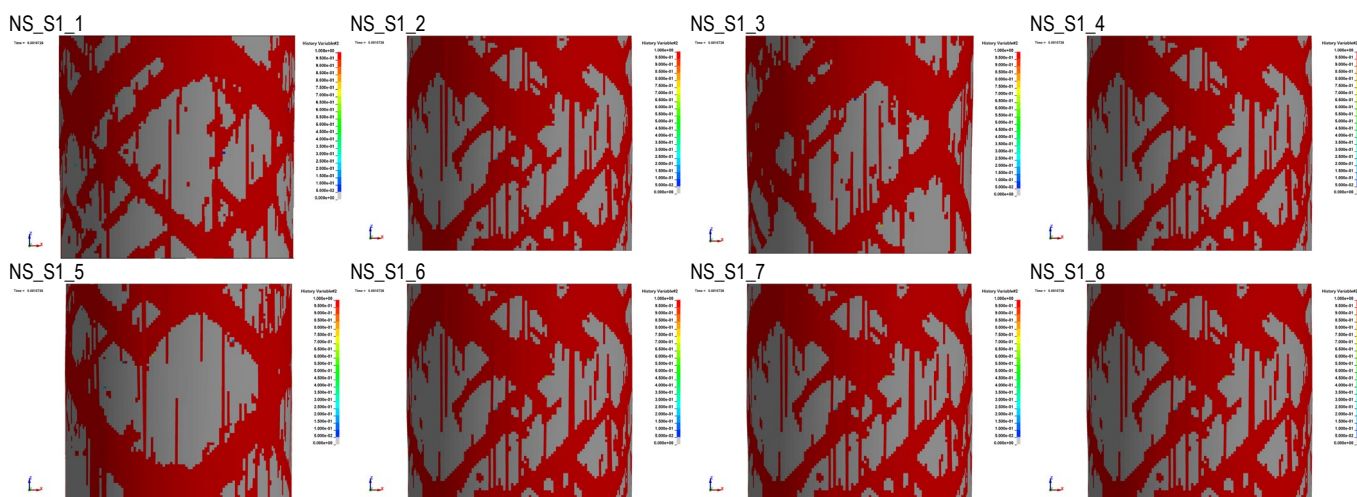
Fig. 5. Specimen failure patterns for FEM modelling of the sandstone in SHPB test: influence of *SOFTSCL* using the *SOFT* =1 in the NS contact definition

3.2.2.   FEM: NS contact with SOFT = 0

In the second set of tests with FEM, the algorithm deriving contact stiffness was set to a default procedure of contact stiffness estimation (*SOFT* = 0). Results showing transmitted and reflected waves and failure pattern of the specimen for different values of *SFM/SFS* parameters are shown in Figs. 6 and 7, respectively. Unlike in the first set of tests, the influence of parameters controlling contact stiffness can be clearly observed. The waveform data of the first two tests can even be described as errors. Increasing the *SFS/SFM* scale factors resulted in a closer correlation between the numerical and experimental curves. However, for the first six cases, pronounced differences prevalent between numerically and experimentally obtained curves are noticeable. An overestimation and underestimation of the reflected and transmitted impulse, respectively, demonstrate that the stress equilibrium in the specimen was not achieved and the elastic wave was not correctly transferred by the specimen material dissipating in the sample. In other words, the impact force was too small due to insufficient contact stiffness between the specimen and the bars. Ultimately, from the series of eight numerical tests, only NS_S0_7 (*SFM/SFS* = 5.0) and NS_S0_8 (*SFM/SFS* = 7.0) show results similar to these obtained in the previous studies. However, in any case a proper reproduction of the real-world measurements was observed, especially in the case of reflected wave and its post-peak behaviour. The transmitted curve differs also from the experimental counterpart as well as numerical results with the *SOFT* = 1 presented in Fig. 5.

The abovementioned observations are reflected also in the incorrect failure patterns of the sandstone specimen (Fig. 7). Insufficient contact stiffness had a pronounced effect on the material failure. Starting from the NS_S0_1 and continuing up until NS_S0_7, an unsymmetrical failure represented by fully damaged elements can be observed within the top and bottom surfaces of the specimen. The first cases with the smallest values of *SFS/SFM* demonstrate the failure patterns that can be considered as numerical instabilities. When the contact stiffness increases, the failure starts to initiate at the boundaries of the specimen near the contact surfaces and for the *SFM/SFS* = 5.0 the cracking distribution starts to have a similar characteristic compared to the experimental outcome (Fig. 3d). Only for the last case are the

results closer to the ones observed in the experiment, but the main drawback of the *SOFT* = 0 manifests in the cracking initiation (damage accumulation) within the specimen boundaries and edges. As a reminder, a lubricant and polyester foil were used between the specimen and the bars to minimise friction in the laboratory tests and consequently to drastically reduce lateral forces within the boundaries that could initiate cracks in the specimen.

The third series of numerical tests with the NS standard contact definition (*SOFT* = 0) involved the worst probable setup of contact parameters that would be used by less experienced users. The study consists of the cases with different values of *SLSFAC* included in the control contact card of the LS-Dyna package. Contrary to the cases with different values of *SFS/SFM* (Figs. 6 and 7), a less pronounced impact on the obtained results was observed here (Fig. 8 – waveform data and Fig. 9 – failure patterns). The worst reproduction of the reflected and transmitted curves was obtained for the first two cases, while the other six have a similar trend and correlation with the laboratory data. Nevertheless, the last four cases provide the best compliance with the experiment, but still the reflected wave with its post-peak behaviour was not correctly captured in any of the cases.

The failure patterns obtained from the simulations with *SOFT* = 0 and various *SLSFAC* are not so disturbed compared to the NS contact with different *SFS/SFM* stiffness values. The worst reproduction of the waveform data shown in Fig. 8 in the first two cases is also reflected in the specimen behaviour. The NS_S0_11 was characterised by a localised failure near the surfaces and edges of the specimen, while the NS_S0_12 demonstrated material failure at boundaries of the specimen and only a few horizontal cracks occurred within its length. A relatively symmetrical response of the specimen was observed with incline and horizontal cracks visible in the specimens starting from the *SLSFAC* = 0.5 (NS_S0_13) and continuing up until the last NS_S0_18 case. Unfortunately, despite well-captured failure patterns in most of the discussed cases (except the first two simulations), cracks started to initiate within the specimen boundaries and its edges, which is an undesirable and unphysical phenomenon, as discussed earlier.
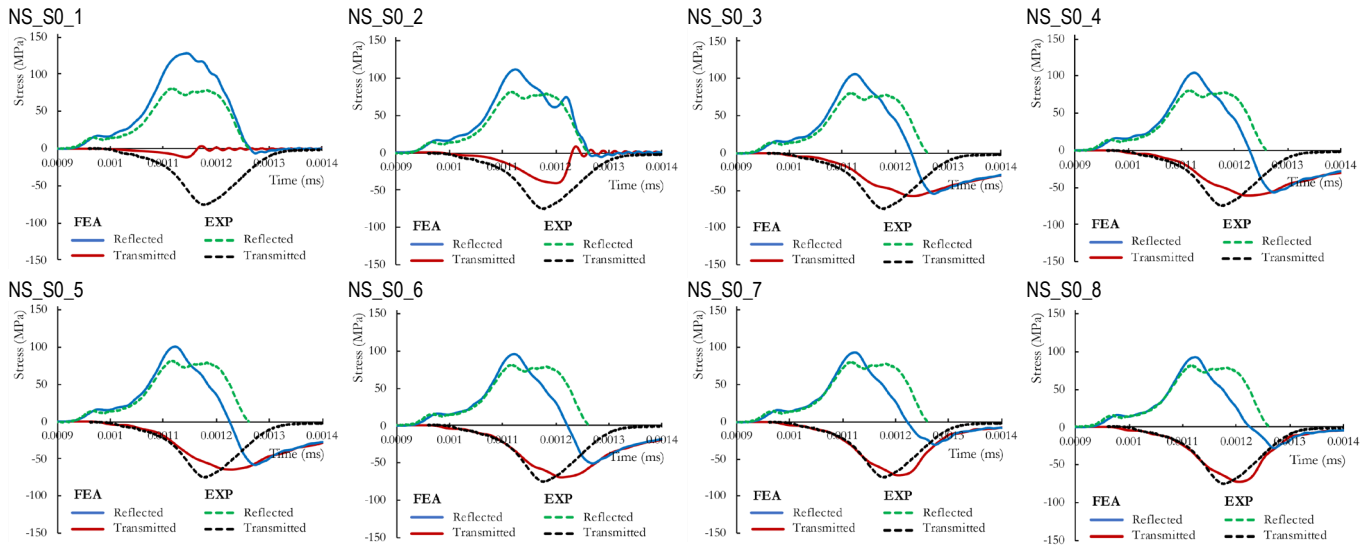
Paweł Baranowski, Krzysztof Damaziak
Study of Contact Algorithms Influencing Specimen Response in Numerical Simulation of Dynamic Compression Test

DOI 10.2478/ama-2024-0029

Fig. 6. Waveform data for FEM modelling of the sandstone in the SHPB test: influence of *SFS/SFM* using the NS standard contact definition (*SOFT* = 0)
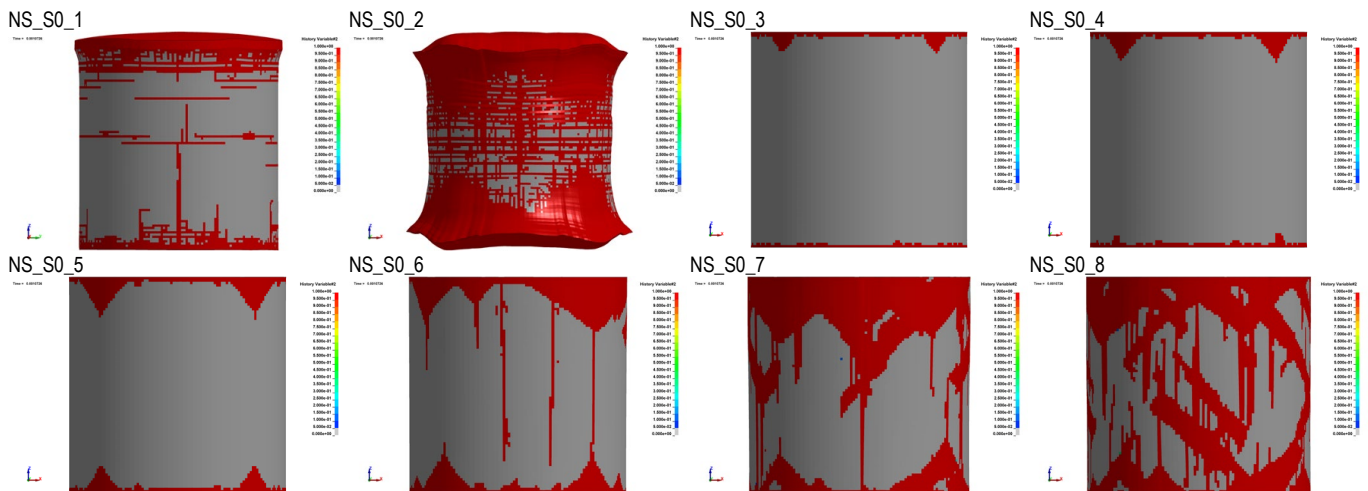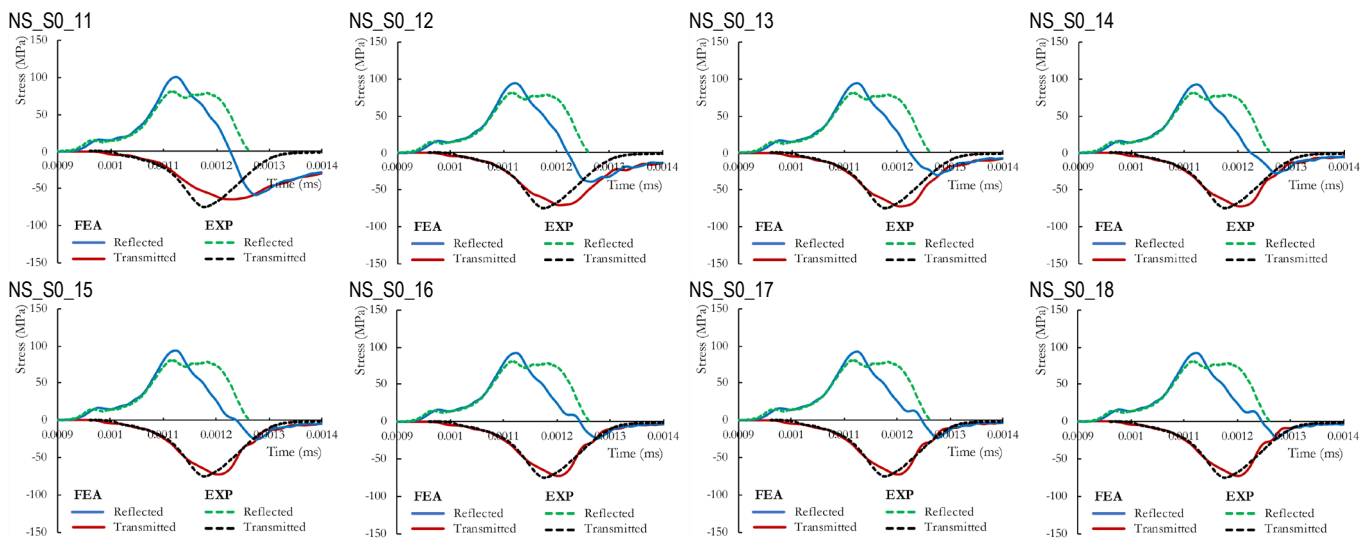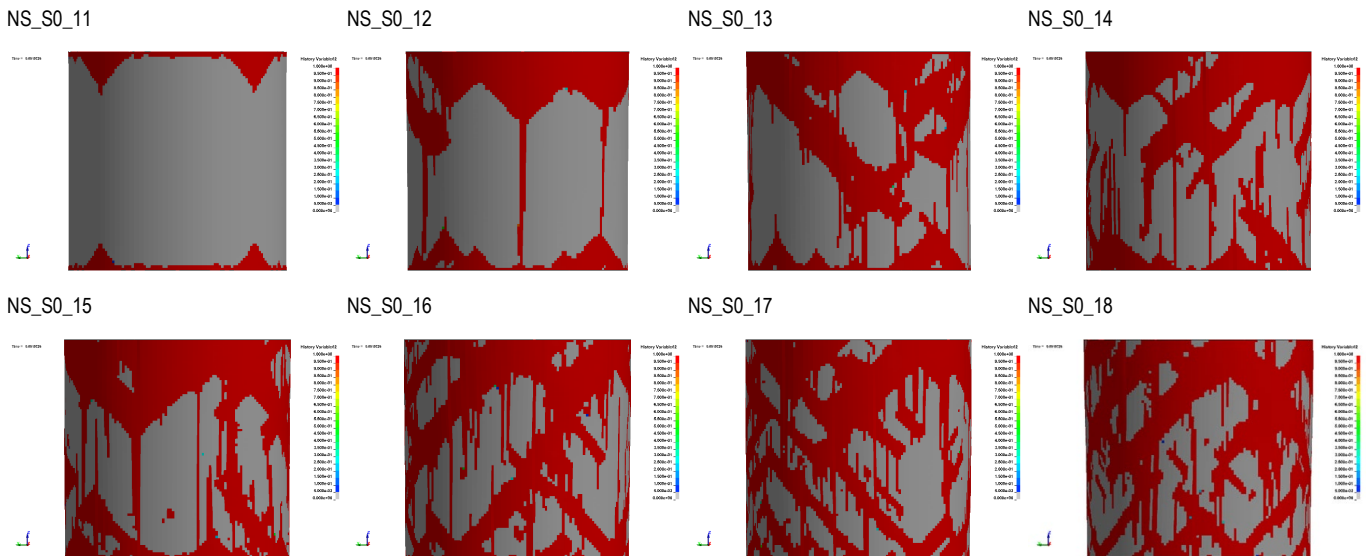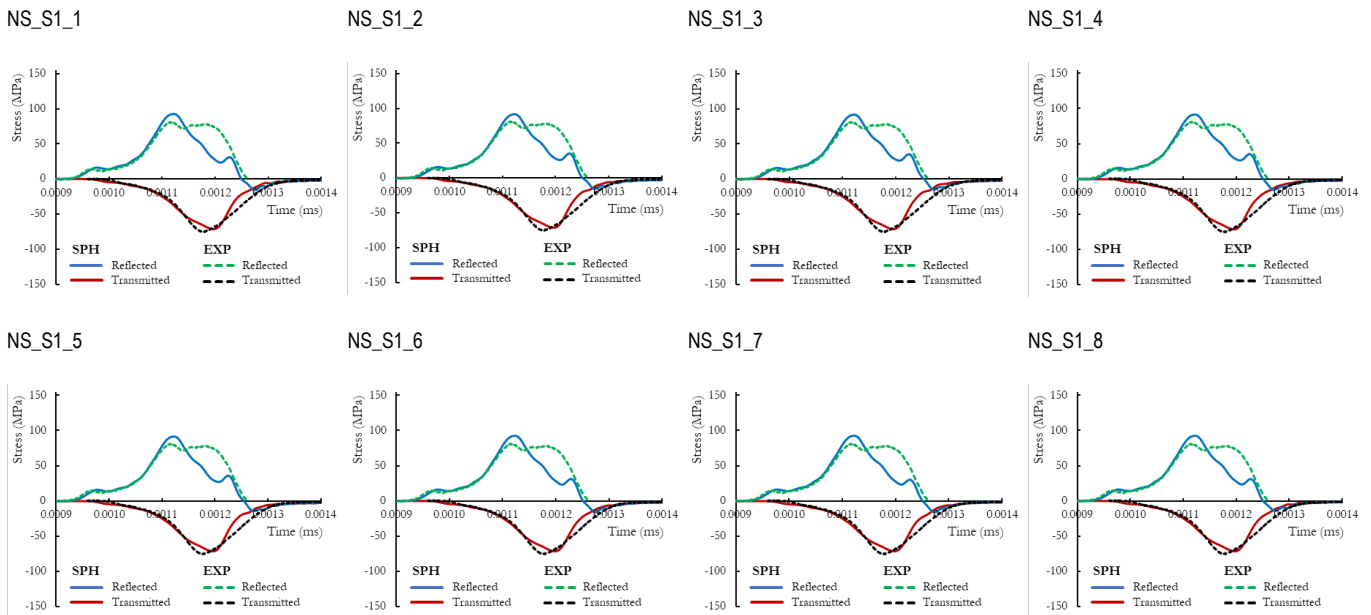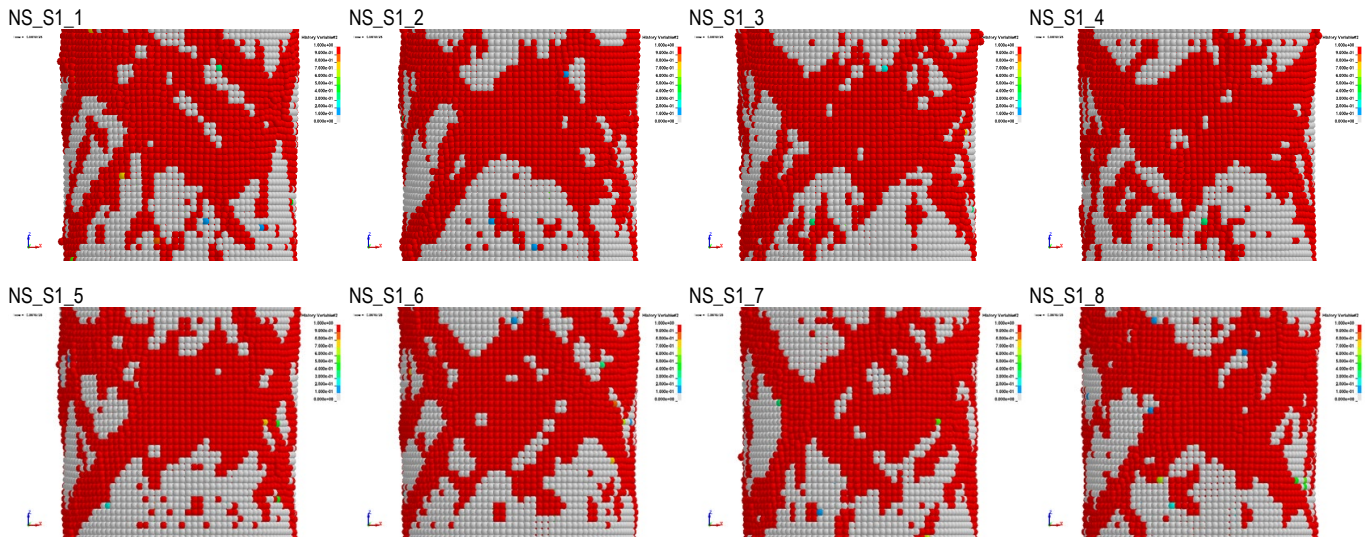

Fig. 7. Specimen failure patterns for FEM modelling of the sandstone in the SHPB test: influence of *SFS/SFM* using the NS standard contact definition (*SOFT* = 0)
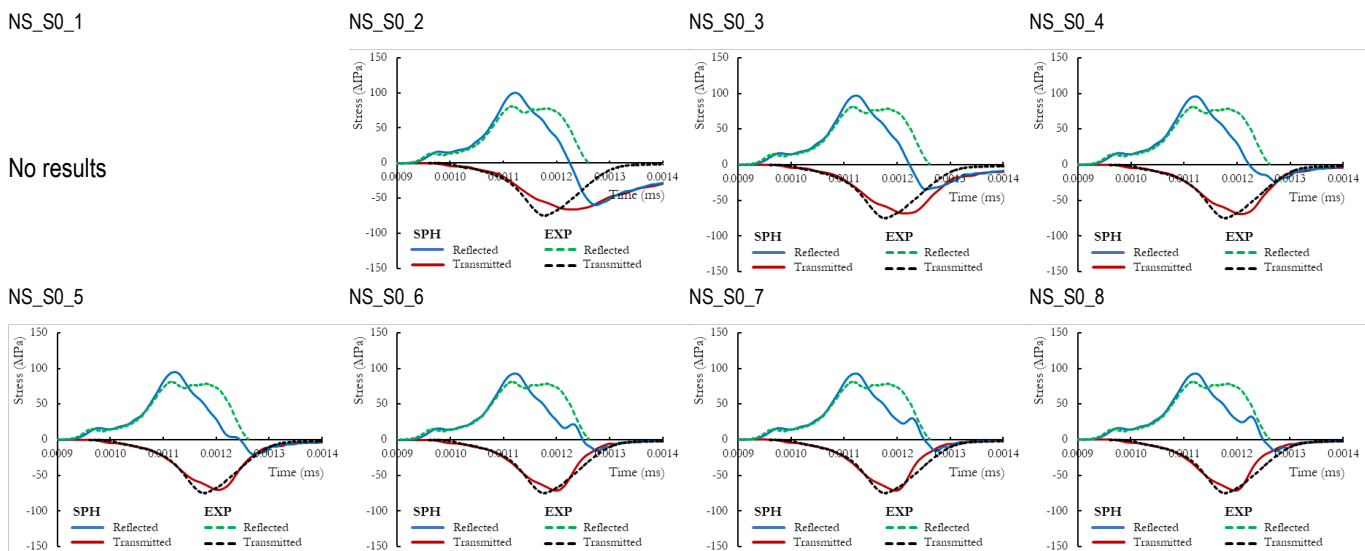

Fig. 8. Waveform data for FEM modelling of the sandstone in the SHPB test: influence of *SLSFAC* using the NS standard contact definition (*SOFT* = 0)

NS_S0_11   NS_S0_12   NS_S0_13   NS_S0_14
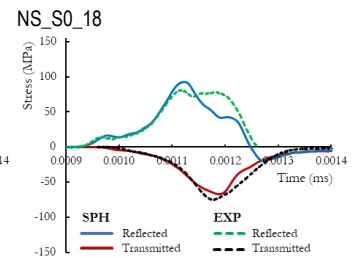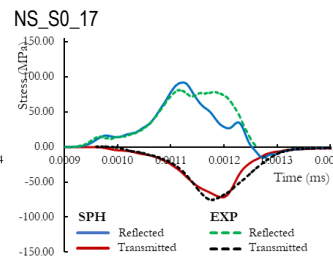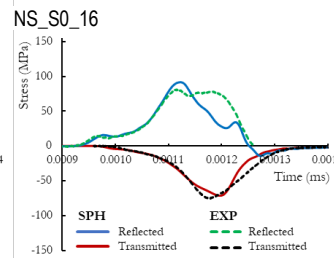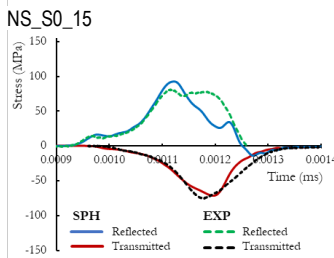

NS_S0_15   NS_S0_16   NS_S0_17   NS_S0_18

Fig. 9. Specimen failure patterns for FEM modelling of the sandstone in the SHPB test: influence of *SLSFAC* using the NS standard contact definition (*SOFT* = 0)

3.2.3. SPH: NS contact with SOFT = 1

Results of the numerical simulation using the meshless technique for different values of the *SOFTSCL* parameter are shown in Fig. 10 and 11, presenting waveform data and specimen failure pattern, respectively. It can be seen that both waveforms and failure patterns are similar to those obtained with FEM. Again, the stress response over time for different *SOFTSCL* values does not change drastically. Differences arise in the shape of transmitted wave, but they are not significant and can be treated as negligible.

The deformation and failure pattern of the specimen are similar to the high-speed camera photos shown in Fig. 3d. The incline and longitudinal cracks were satisfactorily reproduced in the numerical simulations. It must be noted, though, that deformation of the samples is slightly different in comparison with FEM because the sample had already lost cohesion and its fragments had started to move separately. The character of a transmitted wave generated with the use of SPH is comparable with that obtained with FEM, but the shape of the reflected wave is slightly different. It exhibits a raise of stress in the second part. This behaviour is also connected with better representation of decohesion in the SPH domain. In the FEM, damage is represented by erosion parameters and not real loss of material integrity. As was mentioned, this approach causes an artificial energy dampness In SPH, after decohesion, energy can still be transmitted to other parts of the sample via contact between fragments of this sample.

The difference between the highest and the lowest values of maximum contact force is 10.5%.

NS_S1_1   NS_S1_2   NS_S1_3   NS_S1_4

NS_S1_5   NS_S1_6   NS_S1_7   NS_S1_8

Fig. 10. Waveform data for SPH modelling of the sandstone in the SHPB test: influence of *SOFSCL* using the *SOFT* =1 in the NS contact definition

NS_S1_1   NS_S1_2   NS_S1_3   NS_S1_4

NS_S1_5   NS_S1_6   NS_S1_7   NS_S1_8

Fig. 11. Specimen failure patterns for SPH modelling of the sandstone in the SHPB test: influence of *SOFTSCL* using the *SOFT* =1 in the NS contact definition

3.2.4. SPH: NS contact with SOFT = 0

Results of the numerical simulation using the meshless technique for different values of the *SFM/SFS* parameter and stiffness estimation set to *SOFT* = 0 are shown in Fig. 12 and 13. Similar to the case with FEM-based simulations, the influence of *SFM/SFS* parameters controlling contact stiffness is significant. It is seen both in the values of maximum contact forces and in the failure patterns. The contact force varies from 59 kN to 95 kN. For the lowest contact force, the algorithm did not converge. For the next lowest value (see case NS_S0_2) there is no failure of the sample. The impact force was too small due to insufficient contact stiffness between the specimen and the bars.

The following analyses show that failure zone (red areas) is increasing when *SFM/SFS* is increasing. For the value of 2.0 of parameter *SFS/SFM* (case NS_S0_6) and above, failure patterns start to be similar to those observed in the experiment, which indicates that the values of contact forces acting on the sample

are big enough to obtain acceptable results of numerical simulations.

On the waveform charts it can be seen that for low values of contact forces, the difference between numerical solutions and experiments is significant. Starting from the default value of *SFM/SFS* = 1.0, numerically obtained waveforms better reflect experimental stress history. On the reflected side, for lower contact forces values, there is no additional pick on the right side of the chart. This additional pick of stress can be observed for *SFM/SFS* equal to 1.0 or more.

Results of analyses made with SPH for parameter *SOFT* = 0 and different *SLSFAC* values are presented in Fig. 14 and 15. Overall, the influence of *SLSFAC* is similar to the one observed in case of the first set of tests (change of *SOFTSCL* parameter and contact stiffness estimation set to *SOFT* = 1). The pic values of contact force are also similar to the results obtained in first set of tests and vary from 94.1 kN to 95.6 kN; it is thus unsurprising that failure patterns and stress responses over time are also comparable.

NS_S0_1   NS_S0_2   NS_S0_3   NS_S0_4
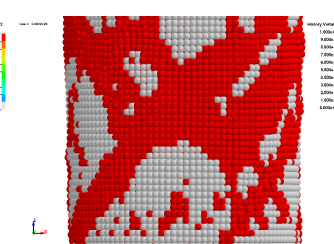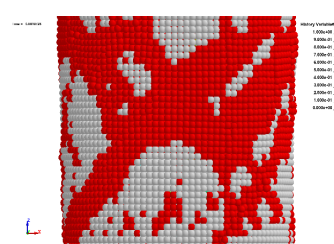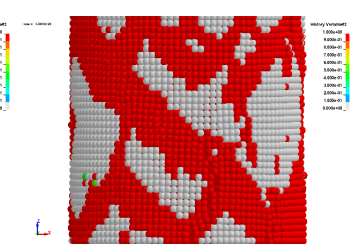
No results

NS_S0_5   NS_S0_6   NS_S0_7   NS_S0_8

Fig. 12. Waveform data for SPH modelling of the sandstone in the SHPB test: influence of *SFS/SFM* using the NS standard contact definition (*SOFT* = 0)

NS_S0_1

No results

NS_S0_2

NS_S0_3

NS_S0_4

NS_S0_5

NS_S0_6

NS_S0_7

NS_S0_8

Fig. 13. Specimen failure patterns for FEM modelling of the sandstone in the SHPB test: influence of *SFS/SFM* using the NS standard contact definition (*SOFT* = 0)

NS_S0_11

NS_S0_12

NS_S0_13

NS_S0_14

NS_S0_15

NS_S0_16
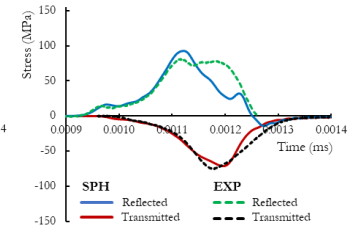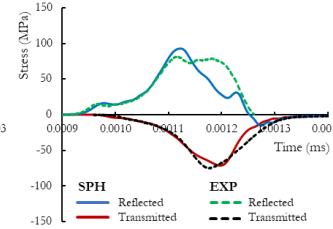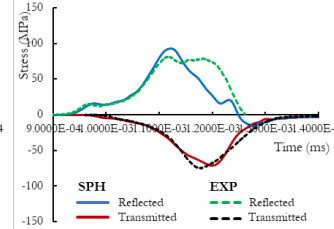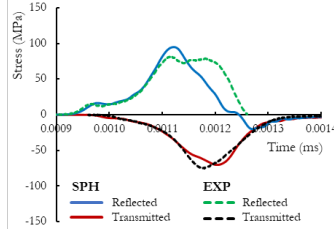
NS_S0_17

NS_S0_18

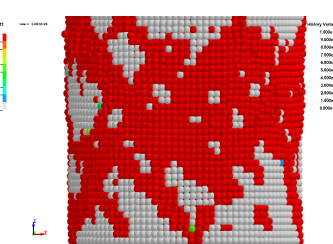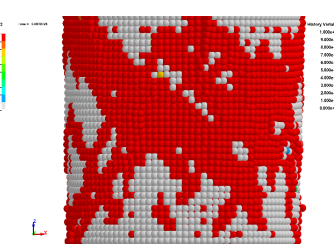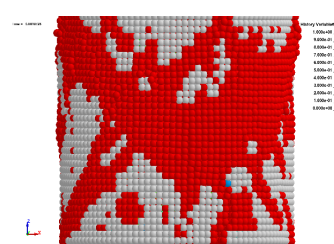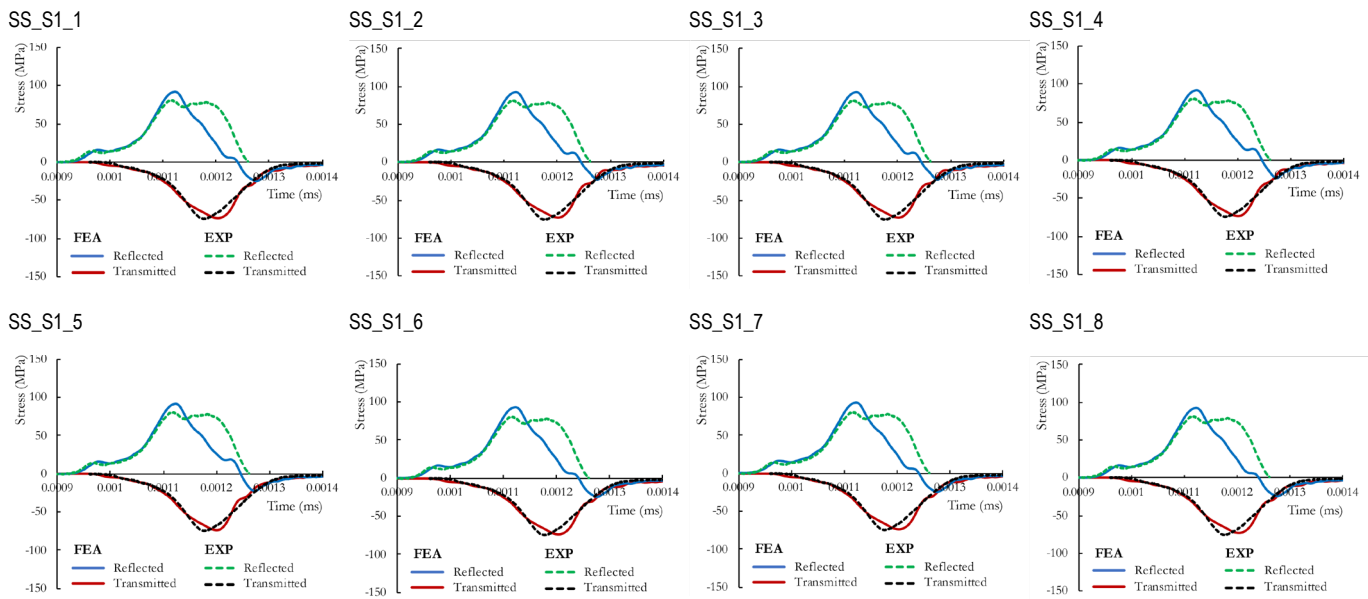**Fig. 14.** Waveform data for SPH modelling of the sandstone in the SHPB test: influence of *SLSFAC* using the NS standard contact definition (*SOFT* = 0)

NS_S0_11

NS_S0_12
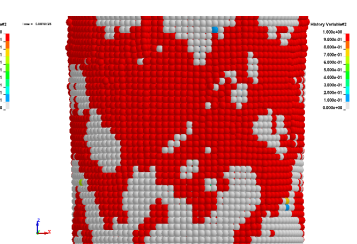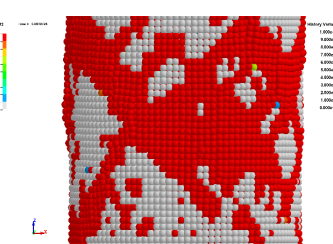
NS_S0_13

NS_S0_14

NS_S0_15

NS_S0_16

NS_S0_17

NS_S0_18

Fig. 15. Specimen failure patterns for SPH modelling of the sandstone in the SHPB test: influence of *SLSFAC* using NS standard contact definition (*SOFT* = 0)

3.3. Two-way contact (SS)

The SS contact was only studied with the specimen modelled using finite elements. For this stage, *SOFT* = 1, *SOFT* = 0 and *SOFT* = 2 with different contact stiffness were considered and have been discussed in the following sections.

3.3.1. FEM: SS contact with SOFT = 1

Changing the contact procedure from NS to SS did not have an influence on the obtained results. The waveform data (Fig. 16) as well as failure patterns (Fig. 17) are nearly identical when both the types of contact were implemented (see **Błąd! Nie można odnaleźć źródła odwołania.** and **Błąd! Nie można odnaleźć źródła odwołania.** with NS for comparison). Insignificant differences in the latter parts of the reflected and transmitted curves were observed between the SS and NS in the corresponding cases. The specimens exhibited very similar failure with two-way contact compared to their counterpart with NS contact definition. Eventually, *SOFT* = 1 provides a practically identical response of the specimen in the SHPB simulation while using one-way and two-way contact treatments.

Fig. 16. Waveform data for FEM modelling of the sandstone in the SHPB test: influence of *SOFTSCL* using the *SOFT* = 1 in the SS contact definition
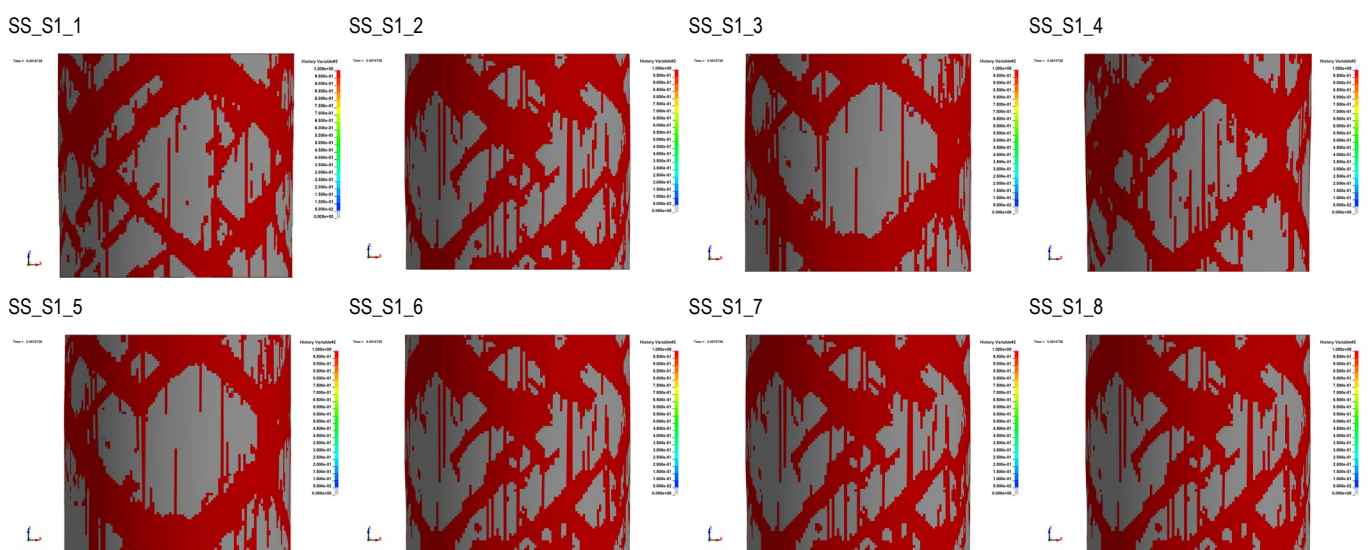
Fig. 17. Specimen failure patterns for FEM modelling of the sandstone in the SHPB test: influence of *SOFTSCL* using the *SOFT* =1 in the SS contact definition

3.3.2. FEM: SS contact with SOFT = 0

When *SOFT* = 0 was adopted for the SS contact, similar observations were also derived compared to the NS contact, with the same algorithm calculating the contact stiffness (see Section 3.2.2). In Fig. 18 and Fig. 19, the transmitted and reflected waves, and failure patterns of the specimen for different values of SFM/SFS with SS and *SOFT* = 0 parameters, respectively, are presented. The influence of parameters controlling contact stiffness can be clearly observed, with significant differences between *FEA* and experiments visible in the first six cases. Especially in the first two tests, the stiffness of contact was too small, resulting in inappropriate transfer of elastic wave in the specimen. From the tested cases, only the last one gave outcomes similar to those associated with the experimental results, but still the reflected wave was not reproduced for its whole length, with an underestimation after the first peak compared to the real-world measurement.

The failure patterns presented in Fig. 19 demonstrate the influence of a different contact stiffness. The incorrect waveform data observed in the first two cases is also demonstrated as an unphysical specimen behaviour with the unsymmetrical failure patterns. The boundary effects near the contact surfaces are noticeable. For the case with *SFS/SFM* = 0.7, longitudinal cracks started to form, and when the contact stiffness increased, additional incline cracks were also observed. By comparison, for the cases using NS contact, cracks were visible only when *SFS/SFM* > 2. Ultimately, the failure pattern was reproduced quite well for the SS_S0_8 case. However, changing the contact from one-way (see

Fig. 7) to two-way did not have an effect on the damage accumulation within the specimen boundaries and edges, which is the unphysical phenomena, especially since the lubricant and polyester foil were used between the specimen and the bars in the experiment.
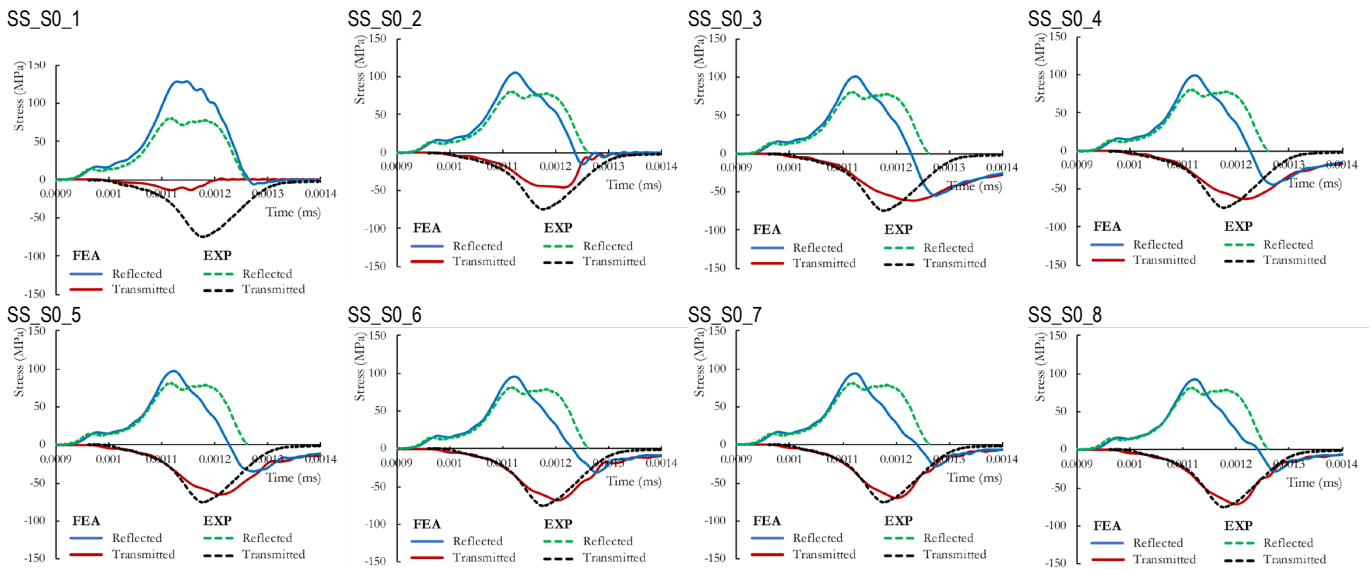

Fig. 18. Waveform data for FEM modelling of the sandstone in the SHPB test: influence of *SFS/SFM* using the *SOFT* = 0 in the SS contact definition
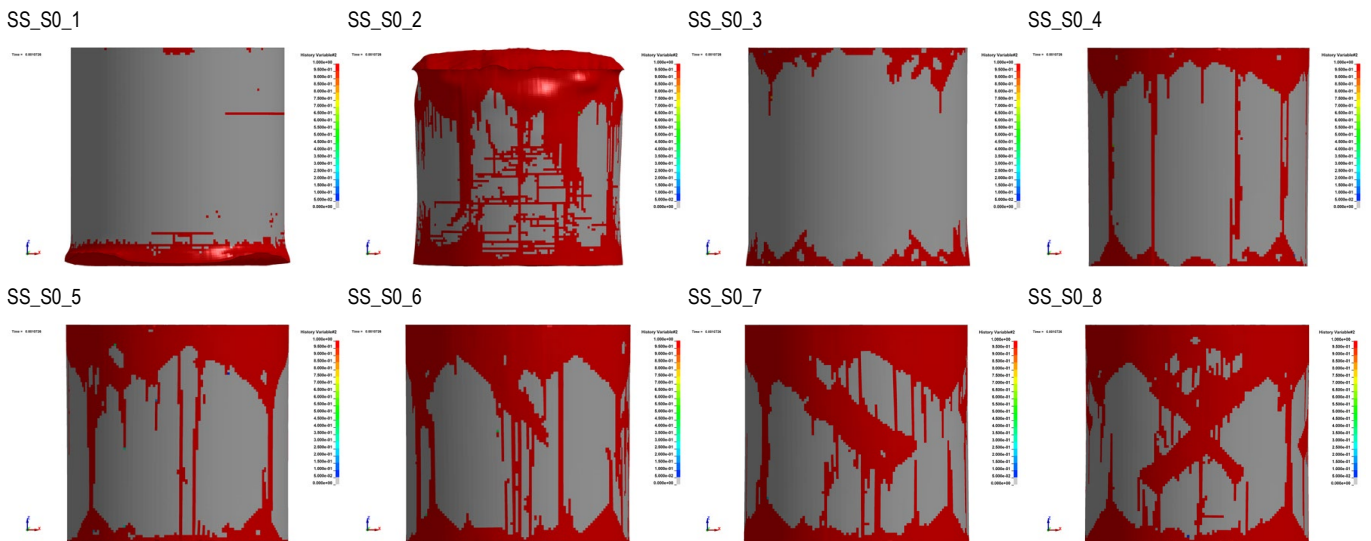

Fig. 19. Specimen failure patterns for FEM modelling of the sandstone in the SHPB test: influence of *SFS/SFM* using the *SOFT* = 0 in the SS contact definition

In the second part of the SS standard contact definition parametric study, different values of *SLSFAC* were changed according to Tab. 4. The waveform data are presented in Fig. 20. For the smallest contact stiffness, the waveform data were not reproduced well by the model, but a general trend is noticeable. Increasing contact stiffness resulted in a better reproduction of the reflected and transmitted curves, and for the SS_S0_16, the best correlation with the experimental outcomes was obtained. Nevertheless, the maximum strength of the material is underestimated (stress peak in the transmitted curve). In the simulations with SLSFAC = 5.0 and SLSFAC = 7.0, the reflected curves were closer to the experimental counterpart, but the material strength was too small. Such phenomenon was not observed for the SFS/SFM study (see Fig. 18), or when the NS contact definition was set in the simulations (see

Fig. 8). The failure patterns are presented in Fig. 21. For the first four cases, only the longitudinal cracks are noticeable, and the boundaries effects had a pronounced effect on the observed

damage accumulation in the specimen material. After exceeding *SLSFAC* = 1.0, the incline cracks were formed, and the best reproduction of the cracking characteristics was observed for the SS_S0_16 with *SLSFAC* = 2.0. The boundary effect was not so pronounced in this case compared to the other simulations when *SOFT* = 0 was used. Further increase of the contact stiffness resulted in the unsymmetrical response (SS_S0_17) and numerical instability (SS_S0_18).

In summary, the SS contact with *SOFT* = 0 ultimately allowed satisfactory results to be obtained, while simulating the *FEM* specimen behaviour in the *SHPB* test. However, in this case, SFS/SFM stiffness parameters should be considerably large enough to obtain accurate results when *SLSFAC* has a default value. On the other hand, caution should be taken when SLSFAC is modified, since too large a value can produce an unpredictable and unphysical specimen response.
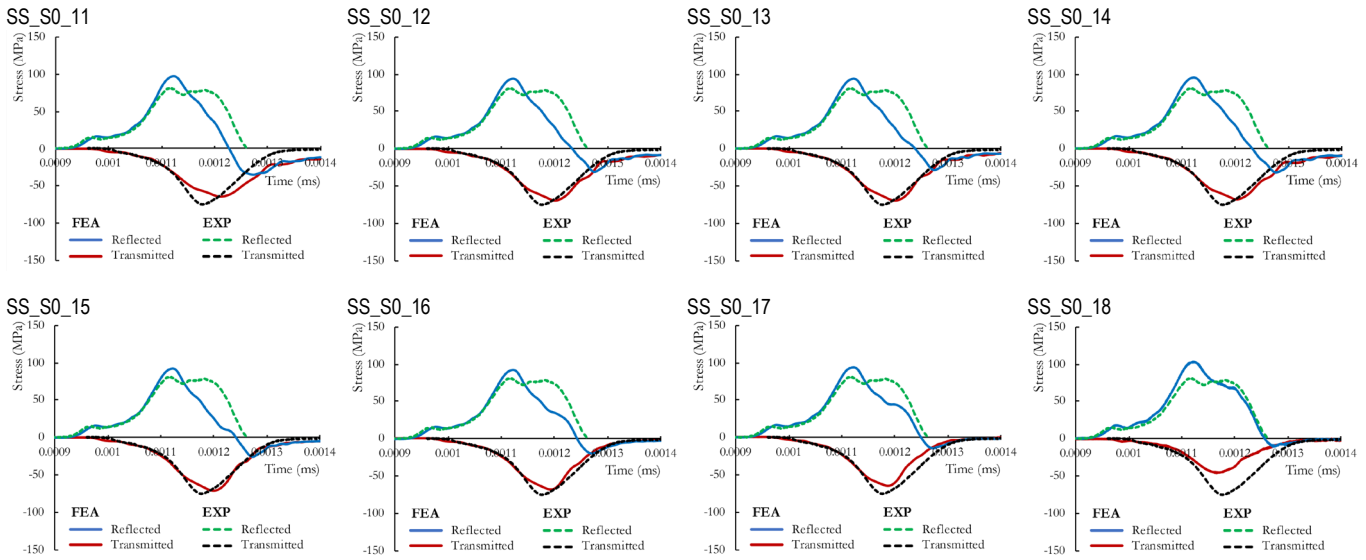

Fig. 20. Waveform data for FEM modelling of the sandstone in the SHPB test: influence of *SLSFAC* using the *SOFT* = 0 in the SS contact definition
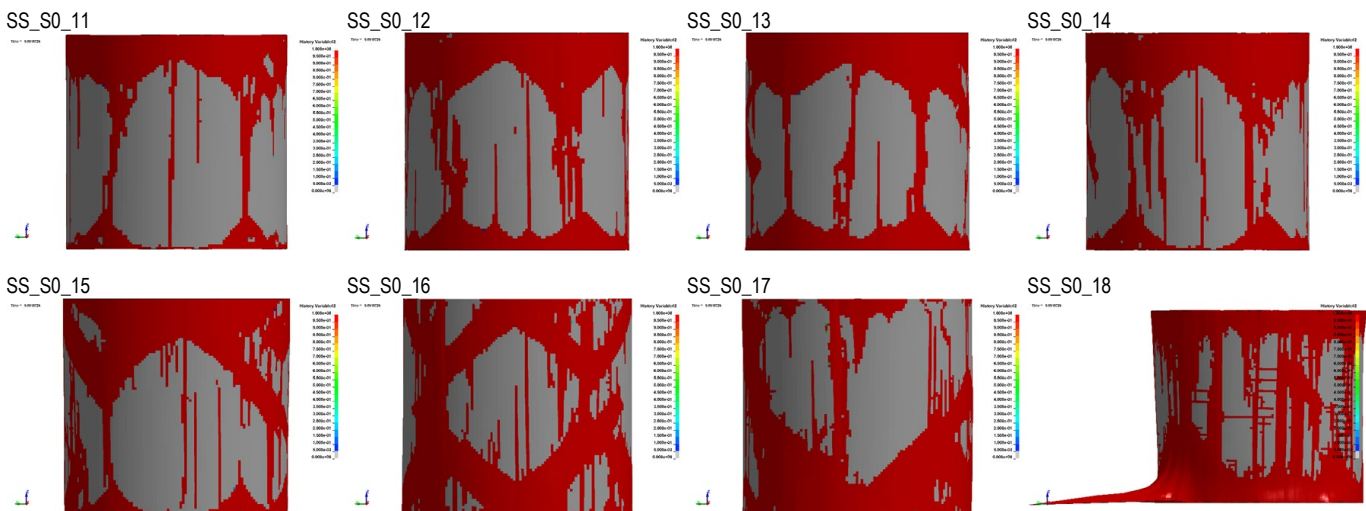

Fig. 21. Specimen failure patterns for FEM modelling of the sandstone in the SHPB test: influence of *SLSFAC* using the *SOFT* = 0 in the SS contact definition

3.3.3. FEM: SS contact with SOFT = 2

In the last stage of the present study, *SOFT* = 2 was used. This option was not adopted in the NS contact since it is only working with a two-way contact procedure, which uses segments of the interacting parts. When *SOFT* = 2 is enabled, *SFS/SFM* and *SLSFAC* parameters influence the contact stiffness.

When different values of *SFS/SFM* were adopted (Fig. 22), considerably better results were obtained compared to the SS contact with *SOFT* = *0*. On the other hand, a larger influence of the *SFS/SFM* parameters was obtained compared to the SS

contact with *SOFT* = *1* and *SOFSCL*. The SS_S2_1 to SS_S2_4 gave the worst reproduction of the waveform data, while the transmitted and reflected curves were closer to the experiments from SS_S2_5 to SS_S2_8. The qualitative analysis of the specimen behaviour and failure patterns corresponds to the qualitative comparison of the measured pulses (Fig. 23). The first three cases differ from the other five, which are nearly identical despite different values of *SFS/SFM.* The worst failure pattern was obtained for the first case, when a value of 0.1 was used for *SFS/SFM*.
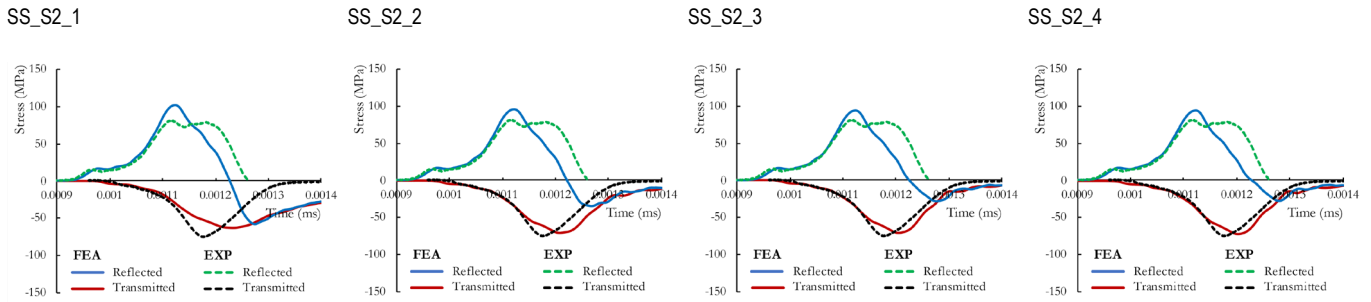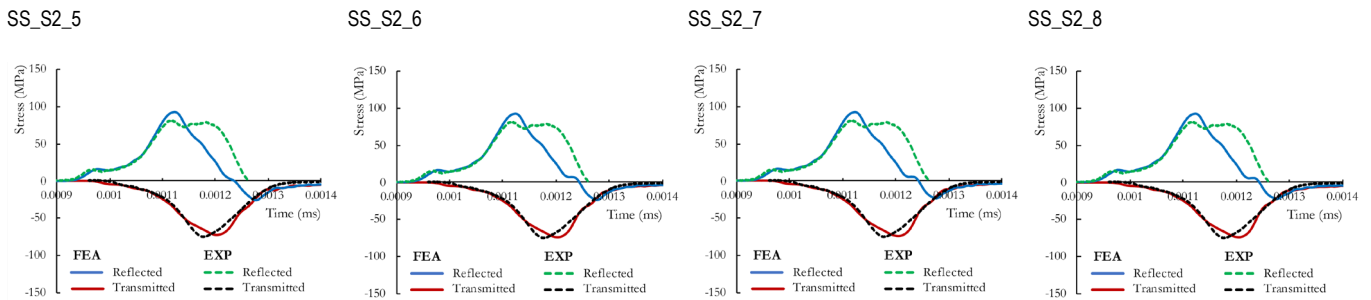

Fig. 22. Waveform data for FEM modelling of the sandstone in the SHPB test: influence of *SFS/SFM* using the *SOFT* = 2 in the SS contact definition
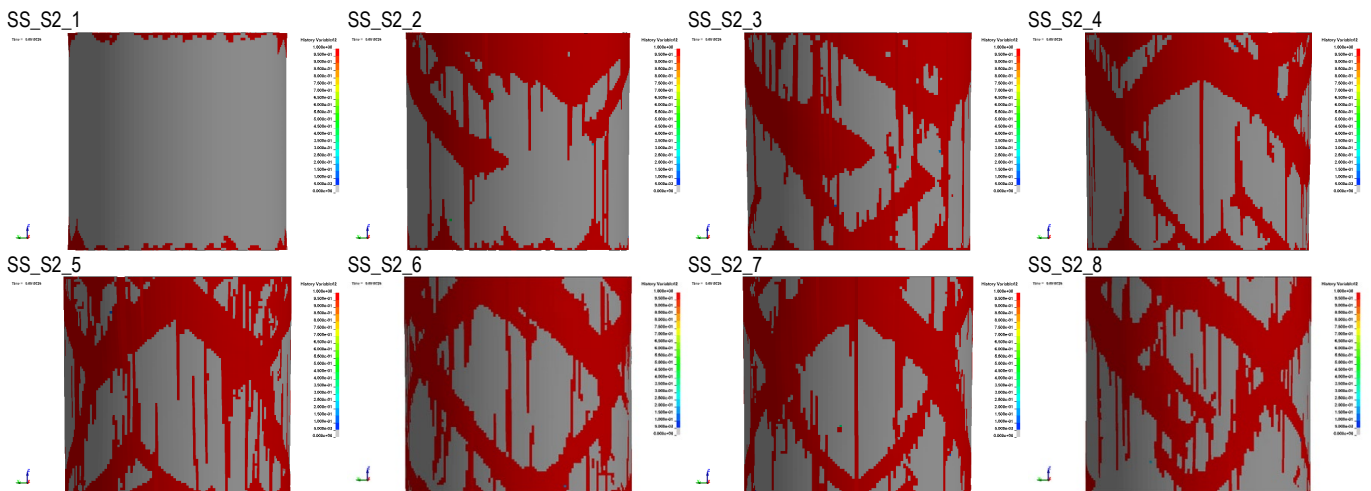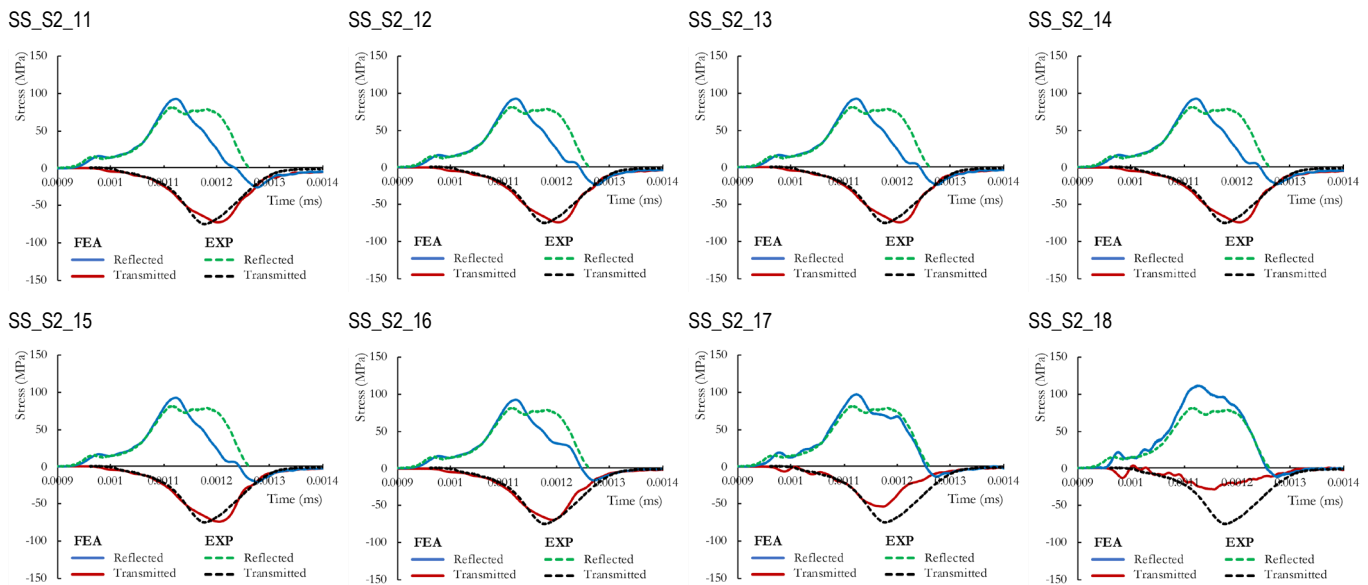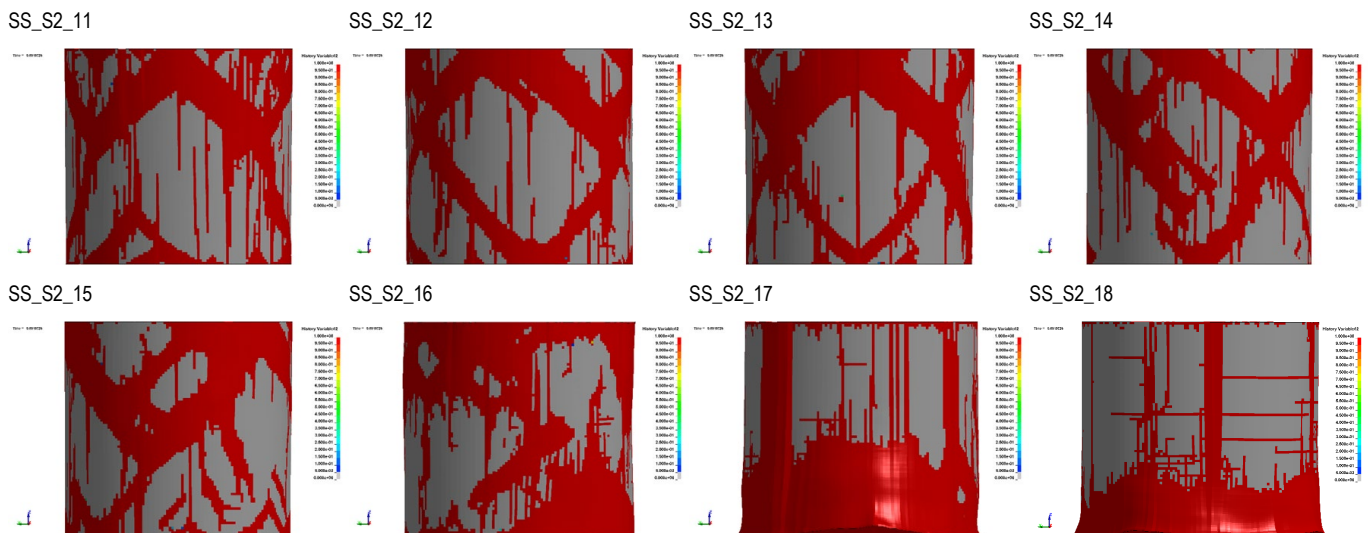

Fig. 22.1. Waveform data for FEM modelling of the sandstone in the SHPB test: influence of *SFS/SFM* using the *SOFT* = 2 in the SS contact definition

Fig. 23.   Specimen failure patterns for FEM modelling of the sandstone in the SHPB test: influence of *SFS/SFM* using the *SOFT* = 2 in the SS contact definition

Fig. 24. Waveform data for FEM modelling of the sandstone in the SHPB test: influence of *SLSFAC* using the *SOFT* = 2 in the SS contact definition

Fig. 25. Specimen failure patterns for FEM modelling of the sandstone in the SHPB test: influence of *SLSFAC* using the *SOFT* = 2 in the SS contact definition

During the last stage of the present study, an analysis of the *SOFT = 2* formulation is performed with the use of various *SLSFAC* values. Starting from the lowest value of *SLSFAC,* better reproduction of the waves is noticeable, and the most similar data were obtained for the SS_S2_16 case (Fig. 24). Compared to the previous six cases, the reflected waves produced in the last two simulations demonstrated the greatest similarity vis-à-vis the experimental counterparts, but on the other hand, the transmitted waves were not quite well-reproduced and unstable results were observed. The discussed results with the parametric studies using *SLSFAC* for *SOFT = 2* are nearly consistent with *SOFT = 0* (see Fig. 20) with very slight differences. The best outcomes were obtained for the SS_S2_16 case. The correspondent failure patterns were relatively close to the real-world observations with inclines and vertical cracks visible in the four first cases (Fig. 25). However, after exceeding the *SLSFAC = 1*, the model was observed to be characterised by unstable behaviour. It is further noteworthy to mention that, despite a relatively good reproduction

of the waveform data for SS_S2_16 case, the failure pattern was not acceptable. The worst reproduction of the specimen behaviour was observed for the last two cases, and this development was also consistent with the corresponding results obtained with the use of *SOFT = 0* (see Fig. 21).

Similarly to the SS contact with *SOFT = 0*, it possible to obtain relatively well-reproduced specimen behaviour and waveform data. However, a user should be cautious since values of *SFS/SFM* stiffness parameters that are too small can produce insufficient contact force, while instability of the model can be observed when too large a value of *SLSFAC* is used.

3.4. General discussion of results

In general, the waveform data are captured well by the FEM, the SPH and the JH-2 constitutive model. For the transmitted curve, both the rise times and peak values are very close to the

laboratory results. However, a slightly more brittle failure can be observed for the numerical simulations compared to the experiment. In the case of reflected waves, the post-peak parts of the curves are not similar. These observations are consistent with previous studies (27, 42, 72) and the main reasons for such discrepancies are: no numerical erosion implementation, homogeneous treatment of the specimen or the mesh being too coarse. Furthermore, fully damaged elements representing the material failure and cracks do not sufficiently reproduce wave effects, and consequently, the reflected wave characteristic is not captured satisfactorily. On the other hand, the deformation and failure pattern of the specimen are similar to the high-speed camera photos shown in Fig. 3d. The incline and longitudinal cracks were satisfactorily reproduced in the numerical simulations.

It can be stated that the NS contact with a default *SOFT* = 0 should be used with caution or should be omitted when interacting materials have significantly different stiffness. Certainly, relatively satisfactory results can be achieved, but the contact stiffness value should be tuned-up in parallel with the constitutive model parameters. This applies both to FEM and SPH.

In the case of both FEM and SPH, NS contact with *SOFT* = 1 provides a relatively good reproduction of the waveform data and failure pattern and is not especially sensitive to the change of the other scaling parameters.

It is possible to obtain satisfactory simulation results using SS kinematics and the *SOFT* = 2 penalty force algorithm, but this would require a careful selection of the scaling parameters. In both investigated scenarios (change of *SFS/SFM* and change of SLSFAC), the results vary from acceptable to the non-physical or even diverging solution.

To better compare numerical results with experimental data, the compressive strength of the sample was verified. This allowed also an evaluation of the contact force values with respect to the quality of the obtained results. Indicative evaluation of failure pattern is also added for better presentation of overall quality of numerical results. Tab. 5–7 contain values for NS contact with FEM, NS contact with SPH and SS contact with FEM, respectively.

For different contact parameters, the pick contact force varies from 57.1 kN to 97.7 kN. It can be noticed that to obtain acceptable results this value must be greater than 95 kN (of course this specific value is connected with the material of sample, and for different materials, the contact force required to produce quality results will be different). Thus, regardless of the other contact options, the *SOFT* = 1 algorithm of deriving contact stiffness gives the highest contact forces and the best correlation with experimental results. Furthermore, this approach is not very sensitive to adjustment of contact stiffness. Therefore, based on the presented studies, it is suggested to use *SOFT* = 1 when simulating the test of rock materials tested on the SHPB apparatus.

Tab. 5. Results from SHPB simulations using FEM and NS contact

Test No.	Exp. compressive strength [MPa]	Num. compressive strength [MPa]	Relative error [%]	FEM contact force [kN]	Failure pattern* [-]
NS_S1_1		73.7	−2.4	97.4	5
NS_S1_2	75.5	73.7	−2.4	97.7	5
NS_S1_3		73.6	−2.5	97.7	5
NS_S1_4		73.7	−2.4	97.7	5

NS_S1_5		73.5	−2.6	97.4	5
NS_S1_6		73.7	−2.4	97.4	5
NS_S1_7		73.7	−2.4	97.3	5
NS_S1_8		73.7	−2.4	97.3	5
NS_S0_1		11.6	−84.6	19.6	1
NS_S0_2		41.2	−45.5	57.1	1
NS_S0_3		57.2	−24.2	75.4	2
NS_S0_4	75.5	60.7	−19.6	79.9	2
NS_S0_5		64.3	−14.8	84.7	2
NS_S0_6		69.3	−8.2	90.9	3
NS_S0_7		71.9	−4.6	94.4	4
NS_S0_8		72.6	−3.7	95.3	5
NS_S0_11		64.3	−14.8	84.7	2
NS_S0_12		70.8	−6.2	92.6	3
NS_S0_13		72.0	−4.6	94.4	3
NS_S0_14		72.6	−3.8	95.4	4
NS_S0_15	75.5	72.8	−3.5	95.9	4
NS_S0_16		73.3	−2.8	96.1	5
NS_S0_17		73.5	−2.6	97.4	5
NS_S0_18		73.6	−2.5	97.5	5

*5 = excellent, 4 = very good, 3 = good, 2 = poor, 1 = instability.

Tab. 6. Results from SHPB simulations using SPH and NS contact

Test no.	Exp. compressive strength [MPa]	Num. compressive strength [MPa]	Relative error [%]	SPH contact force [kN]	Failure pattern* [-]
NS_S1_1		71.4	−5.4	94.8	5
NS_S1_2		71.4	−5.4	94.7	5
NS_S1_3		71.5	−5.2	95.4	5
NS_S1_4	75.5	71.5	−5.2	94.9	5
NS_S1_5		71.5	−5.2	95.4	5
NS_S1_6		71.4	−5.4	94.9	5
NS_S1_7		71.4	−5.4	94.8	5
NS_S1_8		71.4	−5.4	94.9	5
NS_S0_1		12.1	−83.9	58.7	1
NS_S0_2		65.7	−13.0	83.4	2
NS_S0_3		68.4	−9.4	88.1	3
NS_S0_4	75.5	69.7	−7.8	90.7	4
NS_S0_5		70.3	−6.8	92.2	4
NS_S0_6		70.9	−6.1	94.1	5
NS_S0_7		71.4	−5.4	94.3	5
NS_S0_8		71.5	−5.3	95.2	5
NS_S0_11	75.5	70.3	−6.8	92.2	4
NS_S0_12		71.3	−5.5	94.9	5

NS_S0_13		71.4	−5.4	95.1	5
NS_S0_14		71.4	−5.4	95.3	5
NS_S0_15		71.5	−5.2	95.4	5
NS_S0_16		71.6	−5.1	95.6	5
NS_S0_17		71.7	−5.0	90.1	4
NS_S0_18		67.1	−11.1	94.1	5

*5 = excellent, 4 = very good, 3 = good, 2 = poor, 1 = instability.

Tab. 7. Results from SHPB simulations using FEM and SS contact

Test no.	Exp. compressive strength [MPa]	Num. compressive strength [MPa]	Relative error [%]	FEM contact force [kN]	Failure pattern* [-]
SS_S1_1		73.4	−2.6	97.0	5
SS_S1_2		73.6	−2.4	97.6	5
SS_S1_3		73.7	−2.3	97.6	5
SS_S1_4	75.5	73.5	−2.5	97.5	5
SS_S1_5		73.4	−2.6	97.0	5
SS_S1_6		73.3	−2.8	96.9	5
SS_S1_7		73.4	−2.6	97.0	5
SS_S1_8		73.5	−2.5	97.5	5
SS_S0_1		13.9	−81.6	20.5	1
SS_S0_2		45.9	−39.1	60.2	1
SS_S0_3		60.8	−19.4	80.2	1
SS_S0_4	75.5	62.9	−16.7	82.9	2
SS_S0_5		64.8	−14.1	85.2	2
SS_S0_6		67.8	−10.1	89.1	3
SS_S0_7		70.5	−6.6	92.7	4
SS_S0_8		71.3	−5.5	93.8	4
SS_S0_11		64.8	−14.1	85.2	3
SS_S0_12		69.2	−8.3	90.1	3
SS_S0_13		70.5	−6.6	92.7	3
SS_S0_14		68.0	−9.8	89.3	3
SS_S0_15	75.5	71.8	−4.9	94.6	3
SS_S0_16		68.9	−8.6	91.4	4
SS_S0_17		65.0	−13.8	86.5	2
SS_S0_18		45.6	−39.6	59.5	1
SS_S2_1		63.7	−15.5	84.0	2
SS_S2_2	75.5	70.3	−6.9	92.0	3
SS_S2_3		71.3	−5.5	93.5	4
SS_S2_4		71.8	−4.8	94.3	4

SS_S2_5		72.3	−4.2	95.1	5
SS_S2_6		73.6	−2.5	97.2	5
SS_S2_7		74.2	−1.7	97.9	5
SS_S2_8		74.3	−1.5	98.0	5
SS_S2_11		72.3	−4.2	95.1	5
SS_S2_12		73.6	−2.5	97.2	5
SS_S2_13		74.2	−1.7	97.9	5
SS_S2_14	75.5	74.3	−1.5	98.0	5
SS_S2_15		74.3	−1.5	98.0	4
SS_S2_16		69.1	−8.5	91.4	3
SS_S2_17		53.3	−29.3	70.5	1
SS_S2_18		28.7	−61.9	37.7	1

*5 = excellent, 4 = very good, 3 = good, 2 = poor, 1 = instability.

4. CONCLUSIONS

The present study provides numerical simulations of the SHPB dynamic compression test of sandstone sample, aiming to demonstrate the influence of contact procedure parameters on the results with special attention placed on the failure pattern. Based on the obtained results, the following conclusions can be drawn:

− Differences in contact modelling lead to completely different results of the SHPB test simulation, including divergent solutions or unphysical failure patterns. Therefore, the importance attributed to achieving mastery over contact modelling needs to be on a par with that to constitutive modelling, especially in the case of the SHPB test, where the only load acting on the specimens arises from contact/impact, resultant to which verification of the performance of the contact procedure assumes a high degree of importance.

− The nodes to surface (one-way contact) and SS (two-way contact) procedures work well for both FEM and SPH when *SOFT* = 1 is used. In these cases it was possible to obtain results accurately reflecting both data waves and failure patterns.

− With the use of *SOFT* = 0 (default value), generally incorrect results, up to the numerically unstable solutions, were observed despite the added correction of contact stiffness. Utilisation of *SOFT* = 2 requires a number of tests to ascertain the set of parameters that would enable the obtaining of reasonable results.

− Default contact parameters, i.e., those set by the software provider, were also found to give wrong outcomes (see the NS_S0_5 and SS_S0_5 cases), since they resulted in underestimated contact force value.

− Evaluation of waveform data, failure patterns and pick values of stresses is required to efficiently correlate and validate the numerical model, including the constitutive model of a brittle material. Focussing on merely one of these aspects can result in some of the erroneous simulations going unnoticed.

Paweł Baranowski, Krzysztof Damaziak
Study of Contact Algorithms Influencing Specimen Response in Numerical Simulation of Dynamic Compression Test

DOI 10.2478/ama-2024-0029

− Finally, the conducted tests indicate the prevalence of an advantage for SPH over FEM in the modelling of sandstone failure in the SHPB test. This is attributable to the fact that the meshless technique can better represent decohesion of the material and thus does not affect the energy balance in the sample during the dynamic compression test to as great an extent as takes place in FEM.

REFERENCES

1. Y. GH, Scott T, W. SP. Concrete Slab Damage and Hazard from Close-In Detonation of Weaponized Commercial Unmanned Aerial Vehicles. J Struct Eng [Internet]. 2021;147(11):4021190. Available from: https://doi.org/10.1061/(ASCE)ST.1943-541X.0003158

2. Morka A, Kędzierski P, Muzolf P. Optimization of the structure of a ceramic-aluminum alloy composite subjected to the impact of hard steel projectiles. Mech Compos Mater. 2016;52(3):333–46.

3. Kędzierski P, Morka A, Sławiński G, Niezgoda T. Optimization of two-component armour. Bull Polish Acad Sci Tech Sci. 2015;63(1):173–9.

4. Wang J, Yin Y, Esmaieli K. Numerical simulations of rock blasting damage based on laboratory-scale experiments. J Geophys Eng. 2018;15(6):2399–417.

5. Liu K, Wu C, Li X, Li Q, Fang J, Liu J. A modified HJC model for improved dynamic response of brittle materials under blasting loads. Comput Geotech [Internet]. 2020;123(December 2019):103584. Available from: https://doi.org/10.1016/j.compgeo.2020.103584

6. Simons EC, Weerheijm J, Sluys LJ. A viscosity regularized plasticity model for ceramics. Eur J Mech A/Solids. 2018;

7. Johnson GR, Holmquist TJ. Response of boron carbide subjected to large strains, high strain rates, and high pressures. J Appl Phys. 1999;85(12):8060–73.

8. Holmquist TJ, Johnson GR, Cook WH. A computational constitutive model for concrete subjected to large strains, high strain rates, and high pressures. In: The 14th international symposium on ballistic. Quebec: Arlington, VA: American Defense Preparedness Association. 1993; 591–600.

9. Mardalizad A, Caruso M, Manes A, Giglio M. Investigation of mechanical behaviour of a quasi-brittle material using Karagozian and Case concrete (KCC) model. J Rock Mech Geotech Eng. 2019.

10. Pająk M, Janiszewski J, Kruszka L. Laboratory investigation on the influence of high compressive strain rates on the hybrid fibre reinforced self-compacting concrete. Constr Build Mater. 2019;227:116687.

11. Sucharda O, Pajak M, Ponikiewski T, Konecny P. Identification of mechanical and fracture properties of self-compacting concrete beams with different types of steel fibres using inverse analysis. Constr Build Mater [Internet]. 2017;138:263–75. Available from: http://dx.doi.org/10.1016/j.conbuildmat.2017.01.077

12. Máca P, Sovják R, Konvalinka P. Mix design of UHPFRC and its response to projectile impact. Int J Impact Eng. 2014;63:158–63.

13. Sovják R, Vavřiník T, Zatloukal J, Máca P, Mičunek T, Frydrýn M. Resistance of slim UHPFRC targets to projectile impact using in-service bullets. Int J Impact Eng. 2015;76:166–77.

14. Sielicki PW, Łodygowski T. Masonry wall behaviour under explosive loading. Eng Fail Anal. 2019;104:274–91.

15. Wu H, Qin, Zhang YD, Gong ZM, Wu H, Fang Q, et al. Semi-theoretical analyses of the concrete plate perforated by a rigid projectile. Acta Mech Sin. 2012;28(6):1630–43.

16. Wang Z liang L, Li Y chi C, Shen RF. Numerical simulation of tensile damage and blast crater in brittle rock due to underground explosion. Int J Rock Mech Min Sci. 2007;44(5):730–8.

17. Mazurkiewicz Ł, Damaziak K, Małachowski J, Baranowski P. Parametric study of numerically modelled delamination process in a composite structure subjected to dynamic loading. Eng Trans. 2013;61(1):15–31.

18. Mazurkiewicz Ł, Małachowski J, Baranowski P. Optimization of protective panel for critical supporting elements. Compos Struct. 2015;134:493–505.

19. Peng Y, Wu H, Fang Q, Liu JZ, Gong ZM. Flat nosed projectile penetrating into UHP-SFRC target: Experiment and analysis. Int J Impact Eng. 2016;93:88–98.

20. Liang X, Wu C. Meso-scale modelling of steel fibre reinforced concrete with high strength. Constr Build Mater [Internet]. 2018;165:187–98. Available from: https://doi.org/10.1016/j.conbuildmat.2018.01.028

21. Wu H, Li YC, Fang Q, Peng Y. Scaling effect of rigid projectile penetration into concrete target: 3D mesoscopic analyses. Constr Build Mater. 2019;208:506–24.

22. Liu Z, Zhang C, Zhang C, Gao Y, Zhou H, Chang Z. Deformation and failure characteristics and fracture evolution of cryptocrystalline basalt. J Rock Mech Geotech Eng. 2019;11(5):990–1003.

23. Lv TH, Chen XW, Chen G. The 3D meso-scale model and numerical tests of split Hopkinson pressure bar of concrete specimen. Constr Build Mater. 2018;160:744–64.

24. Wang J, Yin Y, Luo C. Johnson–Holmquist-II(JH-2) Constitutive Model for Rock Materials: Parameter Determination and Application in Tunnel Smooth Blasting. Appl Sci. 2018 Sep 16;8(9):1675.

25. Kang HM, Kang MS, Kim MS, Kwak HK, Park LJ, Cho SH. Experimental and numerical study of the dynamic failure behavior of rock materials subjected to various impact loads. In: WIT Transactions on the Built Environment. WITPress; 2014;357–67.

26. Li XB, Hong L, Yin TB, Zhou ZL, Ye ZY. Relationship between diameter of split Hopkinson pressure bar and minimum loading rate under rock failure. J Cent South Univ Technol.2008;15(2):218–23.

27. Pająk M, Baranowski P, Janiszewski J, Kucewicz M, Mazurkiewicz Ł, Łaźniewska-Piekarczyk B. Experimental testing and 3D meso-scale numerical simulations of SCC subjected to high compression strain rates. Constr Build Mater. 2021;302.

28. Zhang J, Wang Z, Yang H, Wang Z, Shu X. 3D meso-scale modeling of reinforcement concrete with high volume fraction of randomly distributed aggregates. Constr Build Mater. 2018;164:350–61.

29. Zhang X, Hao H, Ma G. Dynamic material model of annealed soda-lime glass. Int J Impact Eng. 2015;77:108–19.

30. Ruggiero A, Iannitti G, Bonora N, Ferraro M. Determination of Johnson-holmquist constitutive model parameters for fused silica. EPJ Web Conf. 2012;26:04011.

31. Hao Y, Hao H, Zhang XH. Numerical analysis of concrete material properties at high strain rate under direct tension. Int J Impact Eng. 2012;39(1):51–62.

32. Xiao J, Li W, Corr DJ, Shah SP. Effects of interfacial transition zones on the stress-strain behavior of modeled recycled aggregate concrete. Cem Concr Res. 2013;52:82–99.

33. Kucewicz M, Baranowski P, Małachowski J. Determination and validation of Karagozian-Case Concrete constitutive model parameters for numerical modeling of dolomite rock. Int J Rock Mech Min Sci. 2020;129.

34. Kucewicz Michałand Baranowski PGR, Małachowski J. Investigation of dolomite'rock brittle fracture using fully calibrated Karagozian Case Concrete model. Int J Mech Sci. 2022;107197.

35. Huang Y, Yang Z, Ren W, Liu G, Zhang C. 3D meso-scale fracture modelling and validation of concrete based on in-situ X-ray Computed Tomography images using damage plasticity model. Int J Solids Struct [Internet]. 2015;67–68:340–52. Available from: http://dx.doi.org/10.1016/j.ijsolstr.2015.05.002

36. Pająk M, Baranowski P, Janiszewski J, Kucewicz M, Mazurkiewicz Ł, Łaźniewska-Piekarczyk B. Experimental testing and 3D meso-scale numerical simulations of SCC subjected to high compression strain rates. Constr Build Mater. 2021;302.

37. Zhang R, Li P yu, Zhi X dong, Wang Y hui, Fan F. Johnson–Holmquist-II model of annealed glass and its verification in dynamic compression test. Structures [Internet]. 2023;53(March):396–407. Available from: https://doi.org/10.1016/j.istruc.2023.04.082

38. Li M, Hao H, Cui J, Hao Y fei. Numerical investigation of the failure

mechanism of cubic concrete specimens in SHPB tests. Def Technol [Internet]. 2022;18(1):1–11.
Available from: https://doi.org/10.1016/j.dt.2021.05.003

39. Ren L, Yu X, Guo Z, Xiao L. Numerical investigation of the dynamic increase factor of ultra-high performance concrete based on SHPB technology. Constr Build Mater [Internet]. 2022;325:126756.
Available from: https://doi.org/10.1016/j.conbuildmat.2022.126756

40. Lv Y, Wu H, Dong H, Zhao H, Li M, Huang F. Experimental and numerical simulation study of fiber-reinforced high strength concrete at high strain rates. J Build Eng [Internet]. 2023;65:105812. Available from: https://doi.org/10.1016/j.jobe.2022.105812

41. Deshpande VM, Chakraborty P, Chakraborty T, Tiwari V. Application of copper as a pulse shaper in SHPB tests on brittle materials- experimental study, constitutive parameters identification, and numerical simulations. Mech Mater [Internet]. 2022;171:104336. Available from: https://doi.org/10.1016/j.mechmat.2022.104336

42. Kucewicz M, Baranowski P, Mazurkiewicz Ł, Małachowski J. Comparison of selected blasting constitutive models for reproducing the dynamic fragmentation of rock. Int J Impact Eng. 2023;173.

43. Johnson GR, Holmquist TJ. An improved computational constitutive model for brittle materials. In AIP Publishing; 2008;981–4.

44. Holmquist TJ, Johnson GR, Grady DE, Lopatin CM, Hertel ES. High strain rate properties and constitutive modeling of glass. In: Mayseless M, Bodner S., editors. Proceedings of 15th International Symposium on Ballistics. Jerusalem, Israel; 1995;234–44.

45. Holmquist TJ, Templeton DW, Bishnoi KD. Constitutive modeling of aluminum nitride for large strain, high-strain rate, and high-pressure applications. Int J Impact Eng. 2001;25(3):211–31.

46. Ai HA, Ahrens TJ. Simulation of dynamic response of granite: A numerical approach of shock-induced damage beneath impact craters. Int J Impact Eng. 2006;33(1–12):1–10.

47. Dehghan Banadaki MM, Mohanty B. Numerical simulation of stress wave induced fractures in rock. Int J Impact Eng. 2012;40–41:16–25.

48. Stanislawek S, Morka A, Niezgoda T. Pyramidal ceramic armor ability to defeat projectile threat by changing its trajectory. Bull Polish Acad Sci Tech Sci. 2015;63(4):843–9.

49. Ruggiero A, Iannitti G, Bonora N, Ferraro M. Determination of Johnson-holmquist constitutive model parameters for fused silica. EPJ Web Conf 26. 2012;04011:1–4.

50. Zhang X, Hao H, Ma G. Dynamic material model of annealed soda-lime glass. Int J Impact Eng. 2015;77:108–19.

51. Baranowski P, Kucewicz M, Gieleta R, Stankiewicz M, Konarzewski M, Bogusz P, et al. Fracture and fragmentation of dolomite rock using the JH-2 constitutive model: Parameter determination, experiments and simulations. Int J Impact Eng. 2020;140:103543.

52. Baranowski P, Kucewicz M, Janiszewski J. JH-2 constitutive model of sandstone for dynamic problems. Submitt to J (under Rev Int J Impact Eng. 2023.

53. Pająk M, Baranowski P, Janiszewski J, Kucewicz M, Mazurkiewicz Ł, Łaźniewska-Piekarczyk B. Experimental testing and 3D meso-scale numerical simulations of SCC subjected to high compression strain rates. Constr Build Mater. 2021;302:124379.

54. Hallquist J. LS-DYNA Theory Manual [Internet]. Vol. 19. Livermore Software Technology Corporation (LSTC); 2019. 886 p. Available from:http://ftp.lstc.com/anonymous/outgoing/jday/manuals/DRAFT_Theory.pdf

55. Kurzawa A, Pyka D, Jamroziak K, Bocian M, Kotowski P. Analysis of ballistic resistance of composites based on EN AC-44200 aluminum alloy reinforced with Al 2 O 3 particles. Compos. Struct.2018;201:834 –44.

56. Pach J, Pyka D, Jamroziak K, Mayer P. The experimental and numerical analysis of the ballistic resistance of polymer composites. Compos Part B. 2017;113:24–30.

57. Mazurkiewicz Ł, Małachowski J, Tomaszewski M, Baranowski P, Yukhymets P. Performance of steel pipe reinforced with composite sleeve. Compos Struct. 2018;183:199–211.

58. Zienkiewicz O, Taylor R, Zhu JZ. The Finite Element Method: its Basis and Fundamentals: Seventh Edition. The Finite Element Method: its Basis and Fundamentals: Seventh Edition. 2013. 1–714 p.

59. Bathe K J. Finite Element Procedures [M] [Internet]. 2005; 1037 Available from:
http://books.google.com/books?id=wKRRAAAAMAAJ&pgis=1%5Cnftp://ftp.demec.ufpr.br/disciplinas/EME748/Textos/Bathe, K.-J. - Finite Element Procedures - 1996 - Prentice-Hall - ISBN 0133014584 - 1052s.pdf

60. Logan D.L. A first course in the finite element method. 5th ed. Cengage Learning; 2010.

61. J. R. An Introduction to the Finite Element Method. 3rd ed. McGraw-Hill Education; 2005.

62. Kleiber M, Breitkopf P. Finite Element Methods in Structural Mechanics: With Pascal Programs. Ellis Horwood; 1993.

63. Gander MJ, Wanner G. From euler, ritz, and galerkin to modern computing. SIAM Rev. 2012;54(4):627–66.

64. Gingold RA, Monaghan JJ. Smoothed particle hydrodynamics: theory and application to non-spherical stars. Mon Not R Astron Soc. 1977;181(3):375–89.

65. Liu GR, Gu YT. An introduction to meshfree methods and their programming. An Introd to Meshfree Methods Their Program. 2005;1–479.

66. Liu MB, Liu GR. Smoothed particle hydrodynamics (SPH): An overview and recent developments. Arch Comput Methods Eng. 2010;17(1):25–76.

67. Gasiorek D, Baranowski P, Malachowski J, Mazurkiewicz L, Wiercigroch M. Modelling of guillotine cutting of multi-layered aluminum sheets. J Manuf Process [Internet]. 2018 Aug;34:374–88. Available from: https://linkinghub.elsevier.com/retrieve/pii/S1526612518307059

68. Baranowski Paweł and Janiszewski J, Malachowski J. Study on computational methods applied to modelling of pulse shaper in split-Hopkinson bar. Arch Mech. 2014;66(6):429–52.

69. Wriggers P. Computational contact mechanics. Computational Contact Mechanics. 2006;1–518.

70. Vulović S, Živković M, Grujović N, Slavković R. A comparative study of contact problems solution based on the penalty and Lagrange multiplier approaches. J Serbian Soc Comput Mech. 2007;1(1):174–83.

71. Yastrebov VA. Introduction to Computational Contact. In: Numerical Methods in Contact Mechanics. 2013; 1–14.

72. Kucewicz M, Baranowski P, Małachowski J, Ma J. Determination and validation of Karagozian-Case Concrete constitutive model parameters for numerical modeling of dolomite rock. Int J Rock Mech Min Sci. 2020;129.

Paweł Baranowski: https://orcid.org/0000-0002-5320-9479

Krzysztof Damaziak: https://orcid.org/0000-0002-0439-1606

THERMAL STRESSES IN A MULTI-LAYERED SPHERICAL TANK WITH A SLOWLY GRADED STRUCTURE

Roman KULCHYTSKY-ZHYHAILO*

Bialystok University of Technology, Faculty of Mechanical Engineering, ul. Wiejska 45C, Białystok 15-351, Poland

r.kulczycki@pb.edu.pl

Abstract: The central-symmetrical problem of thermoelasticity for a multi-layered spherical tank is considered. The thermal stresses were caused by a temperature difference between the inner and outer surfaces of the tank. Two approaches to solving this problem have been proposed. In the first approach, the boundary problem defined in the components of a considered inhomogeneous spherical tank was solved. In the second approach, the homogenization method with microlocal parameters was used. Good agreement between the solutions was obtained.

Key words: temperature, displacement, thermal stress, composite material, functionally graded material, multi-layered structure, spherical tank

1. INTRODUCTION

The progress of technology has created a wide range of design possibilities for modern materials combining the positive properties of metals (high tensile strength and good resistance to damage and cracking) and ceramic materials (high hardness, high compressive strength, resistance to surface wear and good thermal insulation). In particular, these materials are used to create protective coatings: thermal barrier coatings and barrier coatings for wear and corrosion protection (Lee et al., 1996; Wang et al., 2000; Schulz et al., 2003; Chen and Tong, 2004). With the possibility of producing complex multilayer structures, the importance of effective mathematical models for predicting the mechanical and thermal properties of these structures is growing.

The multi-layer structures described above are two- or multi-component solids. Classical formulations of a problem based on the theory of thermoelasticity lead to boundary value problems for partial differential equations with discontinuous, strongly oscillating coefficients or considering a large number of elastic components between which certain conditions of mechanical and thermal contact are fulfilled. The solution for these problems can be extremely labour-consuming or sometimes simply impossible to accomplish. For the sake of simplicity, these problems are usually replaced by ones for approximated models, in which the characteristic parameters are calculated on the basis of mechanical and geometrical properties of the components. These models were derived by using some averaging procedures. In the case of the composite that has the properties of an isotropic solid at the macro level, classical averaging methods are still often used: the Voigt estimation (Voigt, 1889) or the Reuss estimation (Reuss, 1929). These estimations are based only on the volume content of the components in a representative cell of the composite. They do not take into account the actual geometry and the distribution of components. This means that these estimations are insufficient to properly describe the composites that have the properties of an anisotropic solid at the macro level (Ganczarski and Skrzypek, 2013), in particular the multi-layer structures.

The configuration, geometry and concentration of the component phases of the composite are taken into account in newer homogenization models. We will list only some of them: asymptotic homogenization (Bensoussan et al., 1978; Sanchez-Palencia, 1989; Jihov et al., 1994; Manevitch et al., 2002), based on the concept applied in the theory of thick plates (Achenbach, 1975), based on the mixture theory (Bedford and Stern, 1971), based on matrix methods (Bufler and Krennerknecht, 1999), the generalized method of cells (Paley and Aboudi, 1992) and the strain compatible method of cells (Gan et al., 2000). Particular attention should be paid to the method of homogenization with microlocal parameters (Woźniak, 1987; Matysiak and Woźniak, 1987), which is used to solve problems for multi-layer media with a periodic structure. This method makes it possible to evaluate not only the mean but also local values of strains and stresses in every layer of the periodicity cell.

It has been shown that the solutions of the theories of heat conduction, elasticity or thermoelasticity for a non-homogenous multi-layer medium with a periodical structure (Kulchytsky-Zhyhailo et al., 2005, 2007) are well compatible with the corresponding solutions of problems in which the medium is replaced by a homogeneous medium whose mechanical and thermal properties are described by the method of homogenization with microlocal parameters. Small deviations were obtained in the calculation of both continuous stresses at the layer-separation boundary and stresses undergoing jumps at the interfaces. This is a strong argument for the use of this homogenization method to describe the mechanical and thermal properties of multi-layer media with a periodic structure.

It is generally accepted that the condition for using the homogenization method is the existence of a representative unit cell that is repeated periodically. The layer that is formed as a result of homogenization of a multi-layer solid with a periodic structure is a homogeneous isotropic or anisotropic layer. If this layer is used as a protective coating, we will obtain a large difference in thermomechanical constants between the layer and the substrate. The difference in constants of the materials often causes cracking of the protective coating and subsequent delamination between the coating and the substrate (Kirchhoff et al., 2004). The solution to this problem is the use of a gradient multilayer structure that causes a gradual change in thermomechanical properties. The protective thermal coating is constructed in such a way that on the surface of the coating we obtain, for example, the properties of a thermal insulator, and at the interface the properties of the substrate. The described structure may have a representative cell, but the configuration, geometry and concentration of the constituent phases of the cell will vary along the thickness of the considered structure. Such a structure is called a slowly graded structure (Szymczyk and Woźniak, 2006). If the coating under consideration contains a significant number of representative cells, the possibility of replacing the multi-layer structure with a gradient coating with a continuous change of thermomechanical properties should be considered. The most reasonable way to do this is to use a homogenization method of choice, for example homogenisation with microlocal parameters.

The ring-multi-layered slowly graded structure has been investigated by Kulchytsky-Zhyhailo et al. (2021). The thermal stresses in the considered long pipe were caused by a temperature difference between its inner and outer surfaces. It has been shown that the homogenization approach with microlocal parameters allows for the correct calculation of radial and circumferential stresses in the ring layer with the slowly graded structure. The effect of material inhomogeneity on the temperature and stress distributions in a multi-layer functionally graded hollow sphere has been analyzed by Kushnir et al. (2022). The numerical solving algorithm was based on the finite difference method.

In this paper, the stress field in the multi-layered spherical tank with the slowly graded structure is investigated. The considered structure contains a certain number of representative cells consisting of two homogeneous isotropic layers. As in the article by Kulchytsky-Zhyhailo et al. (2021), thermal stresses are caused by a temperature difference between its inner and outer surfaces. In the first part of the article, the stress distribution in the tank with the periodical structure is analyzed. The problem based on the homogenization method has a simple analytical solution. Obtaining a good agreement between this solution and the solution to the problem for a heterogeneous multi-layered tank, we can convince ourselves of the reliability of the algorithms used. In the second part of the article, the tested reservoir has the slowly graded structure described above. If the use of constitutive relationships based on the homogenization method with microlocal parameters may raise certain doubts, the created algorithm for solving the problem for a multi-layered spherical tank does not introduce any restrictions on the order and the method of arrangement and the materials and geometrics characteristics of the considered spherical layers. The compatibility of both the solutions will be a clear indication that the chosen homogenization method can also be used effectively for slowly graded structures.

2. FORMULATION OF THE PROBLEM

The state of stress in a spherical nonhomogeneous tank with the internal radius R0 and external radius R1 is investigated. The stress field is caused by a temperature difference T0 between its inner and outer surfaces. The inner and external surfaces of the tank are unloaded. The considerations will be led using the dimensionless spherical coordinates (r, φ, θ) related to the radius R1. The section of the tank with a plane containing its center is shown in Fig. 1.
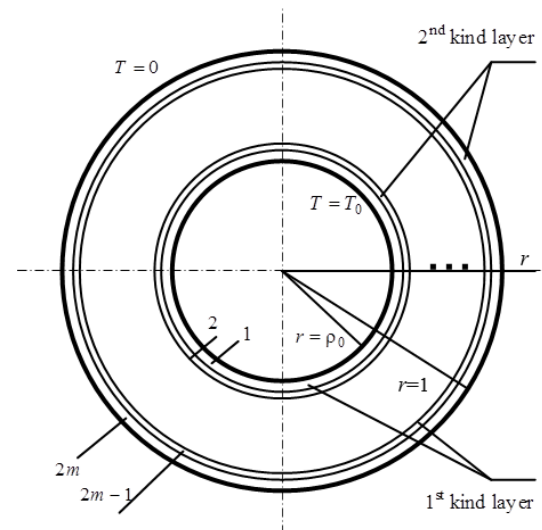

Fig. 1. The scheme of the problem

The cross-section of the investigated tank is composed of n = 2m spherical layers, where m is the number of representative cells. The representative cell contains two homogeneous spherical layers with the thermal conductivity coefficients K1, K2; Young modules E1, E2; Poisson ratios ν1, ν2; the coefficients of linear thermal expansion α1, α2 and dimensionless thickness δ1 = ηδ, δ2 = (1 − η)δ, where δ = (1 − ρ0)/m (ρ0 = R0/R1) is the dimensionless cell thickness. The parameter η ∈ (0, 1) describes the content of the first type of material in a representative cell and can vary along the thickness of the tank. The thermal and mechanical contact between the tank components is ideal.

The considered problem is a central-symmetrical problem. Unknown state functions (the radial displacement u, the radial stress σr, the circumferential stress σθ and the temperature T) can be calculated by solving the following boundary value problem (Timoshenko and Goodier, 1951; Nowacki, 1986) equations:

$$\frac{d}{dr}\left(r^2\frac{dT^{(i)}}{dr}\right) = 0 \, , \ r \in (r_{i-1}, r_i) \, , \ i = 1,2,\dots,n \tag{1a}$$

$$\frac{d}{dr}\left(\frac{1}{r^2}\frac{d}{dr}\left(r^2 u^{(i)}\right) - \frac{1+\nu^{(i)}}{1-\nu^{(i)}}\alpha^{(i)}T^{(i)}\right) = 0 \, , \ r \in (r_{i-1}, r_i) \, , \ i = 1,2,\dots,n \tag{1b}$$

boundary conditions on the internal and external surfaces of the tank:

$$\sigma_r^{(1)}(r_0) = 0, \ \sigma_r^{(n)}(r_n) = 0 \tag{2a}$$

$$T^{(1)}(r_0) = T_0, \ T^{(n)}(r_n) = 0 \tag{2b}$$

interface conditions of the ideal mechanical and thermal contact between the tank components:

$$u^{(i)}(r_i - 0) = u^{(i+1)}(r_i + 0), \quad \sigma_r^{(i)}(r_i - 0) = \sigma_r^{(i+1)}(r_i + 0), \ i = 1,2,\dots,n-1 \tag{3a}$$

$$T^{(i)}(r_i - 0) = T^{(i+1)}(r_i + 0), \quad K^{(i)}\frac{dT^{(i)}}{dr}(r_i - 0) = K^{(i+1)}\frac{dT^{(i+1)}}{dr}(r_i + 0), \ i = 1,2,\dots,n \tag{3b}$$

where the index i corresponds to the number of the spherical layer (see Fig. 1), $\nu^{(2j-1)} = \nu_1$, $\nu^{(2j)} = \nu_2$, $\alpha^{(2j-1)} = \alpha_1$, $\alpha^{(2j)} = \alpha_2$, $K^{(2j-1)} = K_1$, $K^{(2j)} = K_2$, $r_0 = \rho_0$, $r_{2j} = \rho_0 + j\delta$, $r_{2j-1} = r_{2j} - \delta_2$, $j = 1, 2, \dots, m$.

3. CASE 1. MULTI-LAYERED TANK WITH PERIODIC STRUCTURE

The solution of the problem for a multilayered tank with a periodic structure (parameter η = const.) will be compared with the solution of the problem of the tank made of a material with a transversely isotropic homogeneous structure. The thermomechanical properties will be determined by using the method of homogenization with microlocal parameters (Woźniak, 1987; Matysiak and Woźniak, 1987). The received boundary value problem has the form:

– equations:

$$\frac{d}{dr}(r^2 q_{\text{hom}}) = 0, \ r \in (\rho_0, 1) \tag{4a}$$

$$\frac{d\sigma_r^{\text{hom}}}{dr} + \frac{2}{r}(\sigma_r^{\text{hom}} - \sigma_\theta^{\text{hom}}) = 0, \ , \ r \in (\rho_0, 1) \tag{4b}$$

– boundary conditions:

$$\sigma_r^{\text{hom}}(\rho_0) = \sigma_r^{\text{hom}}(1) = 0 \tag{5a}$$

$$T_{\text{hom}}(\rho_0) = T_0, \ T_{\text{hom}}(1) = 0 \tag{5b}$$

The stresses in the transversely isotropic homogeneous tank can be calculated using the following equations (Kaczyński, 2004):

$$\sigma_r^{(1)} = \sigma_r^{(2)} = \sigma_r^{\text{hom}} = A_1 \frac{du_{\text{hom}}}{dr} + 2B\frac{u_{\text{hom}}}{r} - \Lambda_1 T_{\text{hom}} \tag{6a}$$

$$\sigma_\theta^{(j)} = D_j \frac{du_{\text{hom}}}{dr} + \left(E_j + C_j\right)\frac{u_{\text{hom}}}{r} - F_j T_{\text{hom}}, \ j = 1,2 \tag{6b}$$

In the Eqs. (4) - (6), the following notation is introduced: $\sigma_r^{(j)}$ and $\sigma_\theta^{(j)}$, j = 1,2 denote radial and circumferential stress in the j-th layer of the periodicity cell; u_{hom}, σ_r^{hom}, T_{hom}, and q_{hom} are the radial displacement, radial stress, temperature, and heat flux, which are averaged within the periodicity cell;

$$A_1 = \frac{(\lambda_1 + 2\mu_1)(\lambda_2 + 2\mu_2)}{(1-\eta)(\lambda_1 + 2\mu_1) + \eta(\lambda_2 + 2\mu_2)} \tag{7a}$$

$$B = \frac{(1-\eta)\lambda_2(\lambda_1 + 2\mu_1) + \eta\lambda_1(\lambda_2 + 2\mu_2)}{(1-\eta)(\lambda_1 + 2\mu_1) + \eta(\lambda_2 + 2\mu_2)} \tag{7b}$$

$$\Lambda_1 = \frac{(1-\eta)\alpha_2(3\lambda_2 + 2\mu_2)(\lambda_1 + 2\mu_1) + \eta\alpha_1(3\lambda_1 + 2\mu_1)(\lambda_2 + 2\mu_2)}{(1-\eta)(\lambda_1 + 2\mu_1) + \eta(\lambda_2 + 2\mu_2)} \tag{7c}$$

$$C_j = \frac{\lambda_j(B + 2\mu_j)}{\lambda_j + 2\mu_j}, \ D_j = \frac{\lambda_j A_1}{\lambda_j + 2\mu_j}; \ E_j = \frac{4\mu_j(\lambda_j + \mu_j) + \lambda_j B}{\lambda_j + 2\mu_j}, \ j = 1,2 \tag{7d}$$

$$F_j = \frac{2\alpha_j(3\lambda_j + 2\mu_j)\mu_j + \lambda_j\Lambda_1}{\lambda_j + 2\mu_j}, \ j = 1,2 \tag{7e}$$

The constants λ_j, μ_j in Eqs. (7) are Lame constants of the j-th layer of the periodicity cell:

$$\lambda_j = \frac{E_j\nu_j}{(1+\nu_j)(1-2\nu_j)}, \ \mu_j = \frac{E_j}{2(1+\nu_j)}, \ j = 1,2 \tag{8}$$

It should be emphasized that under the proposed homogenization method, we can directly calculate the stresses in each layer of the periodicity cell. The radial stress is continuous at the interfaces: $\sigma_r^{(1)} = \sigma_r^{(2)} = \sigma_r^{\text{hom}}$. The circumferential stress experiences a spike at the interfaces: $\sigma_\theta^{(1)} \neq \sigma_\theta^{(2)}$.

The circumferential stress averaged over the periodicity cell is equal:

$$\sigma_\theta^{\text{hom}} = \eta\sigma_\theta^{(1)} + (1-\eta)\sigma_\theta^{(2)} = B\frac{du_{\text{hom}}}{dr} + (A_2 + C)\frac{u_{\text{hom}}}{r} - \Lambda_2 T_{\text{hom}} \tag{9}$$

where

$$B = \eta D_1 + (1-\eta)D_2, \ A_2 = \eta E_1 + (1-\eta)E_2 \tag{10a}$$

$$C = \eta C_1 + (1-\eta)C_2, \ \Lambda_2 = \eta F_1 + (1-\eta)F_2 \tag{10b}$$

The radial heat flux is continuous at the interfaces:
$$q_r^{(1)} = q_r^{(2)} = q_{\text{hom}} = -K_{\text{hom}}\frac{dT_{\text{hom}}}{dr} \tag{11}$$
where

$$K_{\text{hom}} = \frac{K_1 K_2}{\eta K_2 + (1-\eta)K_1}. \tag{12}$$

Substituting the constitutive relationships (6), (9), and (11) into Eqs. (4), then Eqs. (4) can be regrouped to form:

$$\frac{d}{dr}\left(r^2\frac{dT_{\text{hom}}}{dr}\right) = 0, \ r \in (\rho_0, 1) \tag{13a}$$

$$A_1\frac{d^2 u_{\text{hom}}}{dr^2} + \frac{2A_1}{r}\frac{du_{\text{hom}}}{dr} - 2(A_2 + C - B)\frac{u_{\text{hom}}}{r^2}$$
$$= \Lambda_1\frac{dT_{\text{hom}}}{dr} + \frac{2(\Lambda_1 - \Lambda_2)}{r}T_{\text{hom}}, \ r \in (\rho_0, 1). \tag{13b}$$

4. CASE 2. THE MODELLING OF GRADIENT TANK

In applications, a gradient material is often used to create a smooth transition from the mechanical and thermal properties of the coating to the properties of the substrate. In order to simplify the analysis of modelling, we consider such a gradient spherical layer independently.

Let the thermomechanical properties on the inner surface of the tank be described by parameters $K1$, $E1$, $\nu1$ and $\alpha1$. On the external surface of the tank the properties are specified by parameters $K2$, $E2$, $\nu2$ and $\alpha2$. This means that the parameter η assumes limit values: $\eta(r \to \rho0) \to 1$ and $\eta(r \to 1) \to 0$. Inside the tank, the parameter η changes along its thickness. We assume that the dependence of the parameter η on the coordinate r is described by a linear function:

$$\eta(r) = \frac{1-r}{1-\rho_0}, \ \rho_0 < r < 1 \tag{14}$$

As follows from the dependencies (7) and (12), the material constants are described by the functions of the r coordinate. Substituting the constitutive relationships (6), (9), and (11) into the Eqs. (4), we obtain the differential equations with variable coefficients:

$$\frac{d}{dr}\left(r^2 K_{\text{hom}}(r)\frac{dT_{\text{hom}}}{dr}\right) = 0 \tag{15a}$$

$$A_1 \frac{d^2 u_{\text{hom}}}{dr^2} + \left(\frac{dA_1}{dr} + \frac{2A_1}{r}\right)\frac{du_{\text{hom}}}{dr} - 2\left(A_2 + C - \frac{d(rB)}{dr}\right)\frac{u_{\text{hom}}}{r^2} =$$

$$\frac{d(\Lambda_1 T_{\text{hom}})}{dr} + \frac{(\Lambda_1 - \Lambda_2)}{r}T_{\text{hom}}, \ r \in (\rho_0, 1) \tag{15b}$$

The boundary conditions of the resulting boundary problem are described by dependencies Eqs. (5).

5. METHOD OF SOLUTION

In the first direct approach, we integrate Eqs. (1). The general solutions can be written in the form:

$$T^{(i)}(r)/T_0 = \theta^{(i)}(r) = t_{2i-1} + t_{2i}r^{-1}, \ r_{i-1} \le r \le r_i, \ i = 1,2,\dots,n \tag{16a}$$

$$u^{(i)}(r) = \frac{1-2v^{(i)}}{1+v^{(i)}}s_{2i-1}r - \frac{1}{2}s_{2i}r^{-2} - \frac{1+v^{(i)}}{1-v^{(i)}}\alpha^{(i)}T_0\frac{1}{r^2}\int_r^{r_i}x^2\theta^{(i)}(x)dx, \ r_{i-1} \le r \le r_i, \ i = 1,2,\dots,n \tag{16b}$$

The radial displacement described by formulas generates the stresses:

$$\frac{\sigma_r^{(i)}(r)}{2\mu^{(i)}} = s_{2i-1} + \frac{s_{2i}}{r^3} + \frac{1+v^{(i)}}{1-v^{(i)}}\alpha^{(i)}T_0\frac{2}{r^3}\int_r^{r_i}x^2\theta^{(i)}(x)dx, \ r_{i-1} \le r \le r_i, \ i = 1,2,\dots,n \tag{17a}$$

$$\frac{\sigma_\theta^{(i)}(r)}{2\mu^{(i)}} = s_{2i-1} - \frac{s_{2i}}{2r^3} - \frac{1+v^{(i)}}{1-v^{(i)}}\alpha^{(i)}T_0\frac{1}{r^3}\int_r^{r_i}x^2\theta^{(i)}(x)dx$$

$$-\frac{1+v^{(i)}}{1-v^{(i)}}\alpha^{(i)}T_0\theta^{(i)}(r), \tag{17b}$$
$$r_{i-1} \le r \le r_i, \qquad i = 1,2,\dots,n,$$

where $\mu(2j-1) = \mu 1, \ \mu(2j) = \mu 2, \ j = 1, 2, \dots, m$.

Equation (16a) contains the unknown parameters t_i, $i = 1, 2, \dots, 2n$. Substituting Eqs. (16a) into the boundary conditions (2b) and (3b), we obtain the following system of the linear equations:

$$t_1 + t_2 r_0^{-1} = 1 \tag{18a}$$

$$t_{2i-1} + t_{2i}r_i^{-1} - t_{2i+1} - t_{2i+2}r_i^{-1} = 0, \ i = 1,2,\dots,n-1 \tag{18b}$$

$$K^{(i)}t_{2i} - K^{(i+1)}t_{2i+2} = 0, \ i = 1,2,\dots,n-1 \tag{18c}$$

$$t_{2n-1} + t_{2n} = 0 \tag{18d}$$

The unknown parameters s_i, $i = 1, 2, \dots, 2n$ in the Eqs. (16b) and (17) are calculated using the boundary conditions (2a) and (3a). The system of the linear equations is obtained:

$$s_1 + \frac{s_2}{r_0^3} = -2\tilde{t}_0, \tag{19a}$$

$$\frac{1-2v^{(i)}}{1+v^{(i)}}s_{2i-1}r_i - \frac{s_{2i}}{2r_i^2} - \frac{1-2v^{(i+1)}}{1+v^{(i+1)}}s_{2i+1}r_i + \frac{s_{2i+2}}{2r_i^2} = -\tilde{t}_i r_i, \ i = 1,2,\dots,n-1, \tag{19b}$$

$$\frac{\mu^{(i)}}{\mu^{(i+1)}}s_{2i-1} + \frac{\mu^{(i)}}{\mu^{(i+1)}}\frac{s_{2i}}{r_i^3} - s_{2i+1} - \frac{s_{2i+2}}{r_i^3} = 2\tilde{t}_i, \ i = 1,2,\dots,n-1 \tag{19c}$$

$$s_{2n-1} + s_{2n} = 0 \tag{19d}$$

where

$$\tilde{t}_i = \frac{1+v^{(i+1)}}{1-v^{(i+1)}}\alpha^{(i+1)}T_0\left(t_{2i+1}\frac{r_{i+1}^3 - r_i^3}{3r_i^3} + t_{2i+2}\frac{r_{i+1}^2 - r_i^2}{2r_i^3}\right), \ i = 0,1,\dots,n-1. \tag{20}$$

By first solving the system of Eqs. (18) and next, the system (19), and after substituting the constants t_i, s_i, $i = 1, 2, \dots, 2n$ into Eqs. (16) and (17), the distributions of the temperature, the radial displacement and the thermal stresses in the investigated multi-layered tank will be found.

In the second alternative approach based on the homogenization method, we integrate Eqs. (13) (transversely isotropic homogeneous material) or Eqs. (15) (transversely isotropic gradient material). If the parameter η = const., the obtained Eqs. (13) are the differential equations with constant coefficients. The analytical solution of Eqs. (13), satisfying the boundary conditions Eqs. (5), can be written in form:

$$T_{\text{hom}}(r) = t_{\text{hom}}^{(1)} + t_{\text{hom}}^{(2)}r^{-1}, \ \rho_0 \le r \le 1 \tag{21a}$$

$$u_{\text{hom}}(r) = u_{\text{hom}}^{(e)}(r) + u_{\text{hom}}^{(th)}(r), \ \rho_0 \le r \le 1 \tag{21b}$$

where

$$u_{\text{hom}}^{(e)}(r) = s_{\text{hom}}^{(1e)}r^{\gamma_1} + s_{\text{hom}}^{(2e)}r^{\gamma_2}, \ \rho_0 \le r \le 1 \tag{22a}$$

$$u_{\text{hom}}^{(th)}(r) = s_{\text{hom}}^{(1th)}r + s_{\text{hom}}^{(2th)}, \ \rho_0 \le r \le 1 \tag{22b}$$

$$t_{\text{hom}}^{(1)} = -\frac{T_0\rho_0}{1-\rho_0}, \ t_{\text{hom}}^{(2)} = \frac{T_0\rho_0}{1-\rho_0} \tag{22c}$$

$$2\gamma_{1,2} = -1 \pm \sqrt{1 + 8\gamma_0}, \ \gamma_0 = A_1^{-1}(A_2 + C - B) \tag{22d}$$

$$s_{\text{hom}}^{(1th)} = \frac{\Lambda_1 - \Lambda_2}{A_1 + B - A_2 - C}t_{\text{hom}}^{(1)}, \ s_{\text{hom}}^{(2th)} = -\frac{\Lambda_1 - 2\Lambda_2}{2(A_2 + C - B)}t_{\text{hom}}^{(2)} \tag{22e}$$

$$s_{\text{hom}}^{(1e)} = \frac{\Lambda_1\rho_0 + (A_1 + 2B)s_{\text{hom}}^{(1th)}(\rho_0^{\gamma_2} - \rho_0) + 2Bs_{\text{hom}}^{(2th)}(\rho_0^{\gamma_2} - 1)}{(A_1\gamma_1 + 2B)(\rho_0^{\gamma_1} - \rho_0^{\gamma_2})} \tag{22f}$$

$$s_{\text{hom}}^{(2e)} = \frac{\Lambda_1\rho_0 + (A_1 + 2B)s_{\text{hom}}^{(1th)}(\rho_0^{\gamma_1} - \rho_0) + 2Bs_{\text{hom}}^{(2th)}(\rho_0^{\gamma_1} - 1)}{(A_1\gamma_2 + 2B)(\rho_0^{\gamma_2} - \rho_0^{\gamma_1})} \tag{22g}$$

The radial displacement described by formulas (21b) generates the stresses:

$$\sigma_r^{(1)} = \sigma_r^{(2)} = \sigma_r^{\text{hom}} = (A_1\gamma_1 + 2B)s_{\text{hom}}^{(1e)}r^{\gamma_1-1}$$

$$+(A_1\gamma_2 + B)s_{\text{hom}}^{(2e)}r^{\gamma_2-1} +$$

$$(A_1 + 2B)s_{\text{hom}}^{(1th)} + 2Bs_{\text{hom}}^{(2th)}r^{-1} - \Lambda_1 T_{\text{hom}} \tag{23a}$$

$$\sigma_\theta^{(j)} = (D_j\gamma_1 + E_j + C_j)s_{\text{hom}}^{(1e)}r^{\gamma_1-1} \tag{23b}$$

$$+(D_j\gamma_2 + E_j + C_j)s_{\text{hom}}^{(2e)}r^{\gamma_2-1} +$$

$$+(D_j + E_j + C_j)s_{\text{hom}}^{(1th)} + (E_j + C_j)s_{\text{hom}}^{(2th)} - F_j T_{\text{hom}},$$

$$j = 1,2.$$

If the parameter η changes along the tank thickness, the differential Eqs. (15) are the differential equations with variable coefficients. We can perform analytical integration only in the case of Eq. (15a). The solution of Eq. (15a), which satisfies the boundary conditions (5b), is given in the form:

$$\frac{T_{\text{hom}}(r)}{T_0} = \left(\int_{\rho_0}^1 \frac{dx}{x^2 K_{\text{hom}}(x)}\right)^{-1}\left(\int_r^1 \frac{dx}{x^2 K_{\text{hom}}(x)}\right), \ \rho_0 \le r \le 1$$

Taking into account the relations Eqs. (14), the function $T_{\text{hom}}(r)$, after integration in the Eq. (24), can be written in the form:

$$\frac{T_{\text{hom}}(r)}{T_0} = \frac{(1-r+K_A r \ln(r))\rho_0}{(1-\rho_0+K_A \rho_0 \ln(\rho_0))r}, \ \rho_0 \le r \le 1 \tag{25a}$$

where

$$K_A = \frac{K_2-K_1}{K_2-K_1\rho_0} \tag{25b}$$

Equation (15b) will be solved numerically using the finite difference method. The interval $[\rho 0,1]$ is divided into N equal subintervals. In every internal node the derivatives in Eq. (15b) are replaced with well-known difference equations based on the three nodes. A system containing N – 1 algebraic linear equations was obtained

$$: u_{i-1} - 2u_i + u_{i+1} + 0.5a_i \Delta r(u_{i+1} - u_{i-1}) - b_i(\Delta r)^2 u_i = c_i(\Delta r)^2, i = 1,2,\ldots,N-1 \tag{26}$$

where

$$a_i = \frac{1}{A_1}\left(\frac{dA_1}{dr} + \frac{2A_1}{r}\right), \ r = \rho_i, \ i = 1,2,\ldots,N-1 \tag{27a}$$

$$b_i = \frac{2}{r^2 A_1}\left(A_2 + C - \frac{d(rB)}{dr}\right), \ r = \rho_i, \ i = 1,2,\ldots,N-1 \tag{27b}$$

$$c_i = \frac{1}{A_1}\left(\frac{d(\Lambda_1 T_{\text{hom}})}{dr} + \frac{2(\Lambda_1-\Lambda_2)}{r} T_{\text{hom}}\right), \ r = \rho_i, \ i = 1,2,\ldots,N-1 \tag{27c}$$

Equations (26) contain the unknown parameters u_i, i = 0, 2, ..., N,, describing the values of the radial displacement u in the nodes $\rho i = \rho 0 + i\Delta r$, where $\Delta r = (1-\rho 0)/N$. The obtained system of equations should be supplemented by two equations obtained by substituting constitutive relations (6a) into the boundary conditions (5a). To improve the accuracy of the calculation of the derivative at a point r = $\rho 0$, the well-known five-node difference equations were used:

$$\Delta r \frac{du_{\text{hom}}(\rho_0)}{dr} = -\frac{25}{12}u_0 + 4u_1 - 3u_2 + \frac{4}{3}u_3 - \frac{1}{4}u_4 \tag{28}$$

The equation for the derivative at a point r = 1 is obtained from Eq. (28), substituting parameter Δr by the parameter $-\Delta r$, and index i (i = 0, 1, 2, 3 and 4) replacing by the index N – i.

6. NUMERICAL RESULTS AND DISCUSSION

The analysis of the received relations shows that the stresses in the homogenized model (second alternative approach to solving the problem) depend on the function $\eta(r)$ and the six dimensionless parameters: K1/K2, E1/E2, $\alpha 1/\alpha 2$, $\nu 1$, $\nu 2$ and $\rho 0$. However, if the tank is treated as a multi-layered solid (first approach to solving the problem), one should take into account the number of periodicity cells m.

In order to decrease the number of parameters and decrease the range of their changes, the following assumptions are used:
- the ratio between the internal and external radius of tank is 0.5, so $\rho 0 = 0.5$;
- the function $\eta(r)$ is described by the formula (14) (transversely isotropic gradient material) or the thickness of each spherical layer that is part of the tank is the same, so $\eta = 0.5$ (transversely isotropic homogeneous material);
- Poisson's ratios for both components of the periodicity cell

are the same and $\nu 1 = \nu 2 = 0.3$;
- one of the components of a representative cell is a thermal insulator. The applied insulating materials are often characterized by a greater Young modulus but a smaller coefficient of linear thermal expansion. For this reason, the assumptions, that E2/E1 = $\alpha 1/\alpha 2$ = K1/K2 are taken into account;
- in the aim of an emphasis of possible differences between the solutions obtained by the two presented approaches, some relatively large values of the parameter E1/E2 (or E2/E1) are assumed. We assume that E1/E2 (or E2/E1) = 5 or 10.

Thermal stresses are related to the parameter E*α*T0, where E* = min(E1,E2), α* = max($\alpha 1,\alpha 2$).

Figures 2 and 3 concern the problem, in whit the multi-layered tank with periodic structure is considered. Figure 2 shows the distributions of the radial stress along the tank thickness. Figure 3 presents the distributions of the circumferential stress. The continuous lines in Figs. 2 and 3 and the next figures describe the stresses in the tank obtained within the framework of the homogenization method (second approach to solving the problem). The squares (Fig. 2) or the rhombuses (Fig. 3) mark the numerical results obtained for the non-homogeneous multi-layered tank (first approach to solving the problem). The broken lines in Fig. 2 describe the stress distribution in the homogeneous tank with the parameters E* and α*.
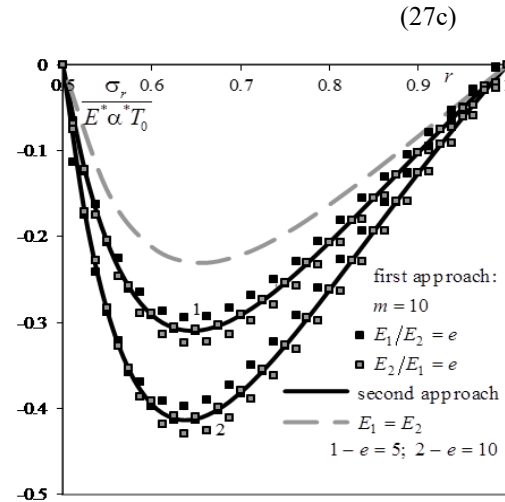
$$\tag{27c}$$

Fig. 2. Distribution of the radial stress along the tank thickness; the black lines are for E = max(E1, E2)/min(E1, E2) = e

The radial stress can be treated as a macro-characteristic, which in the second approach does not depend on the choice of the component of the periodicity cell. The distribution of radial stress in the first approach depends on the sequence of spherical layers. This relation in Fig. 2 is described by using black and grey squares. The black squares present the case, when the first component of the periodicity cell is the thermal insulator, and the grey squares for the first layer with larger thermal conductivity coefficient. From Fig. 2, it follows that the radial stress values for the homogenized model are between the adequate values described by black and grey squares. Calculations show that the difference between the locations of the black and grey squares decreases along with an increase of the number of periodicity cells.

An example of a micro-characteristic is the circumferential stress, the distribution of which along the tank thickness is shown

in Fig. 3. When using the homogenization method, there is no information connected with the kind of spherical layer in the specified point of the tank. At each point we obtain two equations to calculate the circumferential stress. The equation with the index j (see the formula (6b)) allows to determine of the circumferential stress in the j-th (j = 1, 2) layer of the periodicity cell. Two continuous lines in Fig. 3 (black or grey) denoted by numbers 1 or 2 are appropriate for the values of the circumferential stress in layers of the first or second kind. If the circumferential stresses in the multi-layered tank are calculated in odd-numbered layers, the adequate rhombuses are consistent with the continuous line denoted by the number 1. Otherwise, the corresponding rhombuses follow the continuous line marked with the number 2. This means that the proposed homogenization method allows for the calculation with a good accuracy not only of macro-parameters, but also of micro-parameters, whose values depend on the type of the considered component of the periodicity cell.

in Tab. 1. It is the greatest tensile stress. In the column marked "hom" are shown the values calculated using the homogenization method. The first (second) number describes the maximum tensile stress in the layer with the smaller (larger) Young's modulus. In order to compare the difference, which is caused by an application of the two proposed approaches to solving the problem, in the first approach the sequence of the layers in the periodicity cell is chosen in such manner, that the correct (with the smaller or larger Young's modulus) layer of the periodicity cell was located at the point r = 1. In the columns with m = 160, 80, 40 and 20 we present the relative deviations (given in percent's) obtained for the multi-layered tank with the indicated number of periodicity cells. As can be seen from Tab. 1, the double increase in the layer number cause the double decrease in the difference between the analyzed stresses. It means, that for the adequate number of cells, the mathematical model of the problem can be based on the homogenization method.
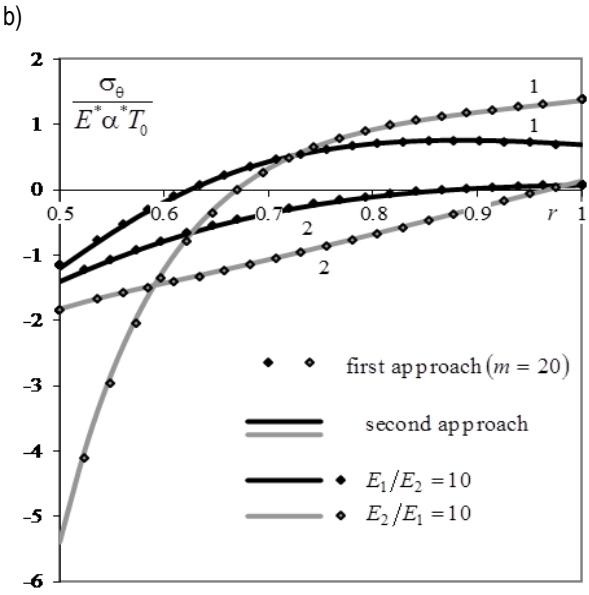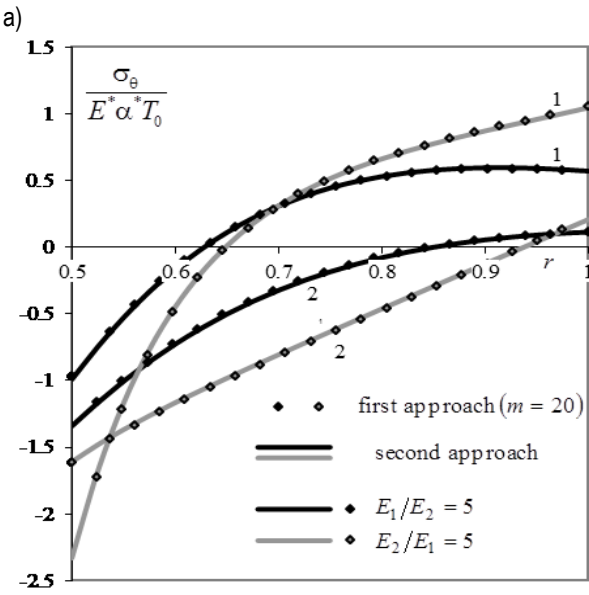
a)

b)

Fig. 3. Distribution of the circumferential stress along the tank thickness; the lines marked number 1 are for circumferential stress in layers with a higher Young modulus; the lines marked number 2 are for circumferential stress in layers with a smaller Young modulus

Tab. 1. Dependence of the circumferential stress on the external surface of the tank with the periodic structure on the dimensionless parameter E = max(E1, E2)/min(E1, E2) and number of representative cells m

	E	"hom"		$m = 160$ (%)	$m = 80$ (%)	$m = 40$ (%)	$m = 20$ (%)
$\frac{\sigma_\theta(1)}{E^*\alpha^*T_0}$	5	0.1624, 0.8119	$E_1/E_2 = 5$	-0.257	-0.515	-1.031	-2.071
			$E_2/E_1 = 5$	0.257	0.513	1.023	2.040
	10	0.1066, 1.0660	$E_1/E_2 = 10$	-0.273	-0.549	-1.104	-2.236
			$E_2/E_1 = 10$	0.272	0.542	1.077	2.128

As follows from Fig. 3, the highest positive value of the circumferential stress is on the external tank surface. The calculated values of the circumferential stress in the point r = 1 are presented

Fig. 4. Distribution of the circumferential stress along the tank thickness; the lines marked number 1 are for circumferential stress in layers with a higher Young modulus; the lines marked number 2 are for circumferential stress in layers with a smaller Young modulus

Tab. 2. Dependence of the circumferential stress on the surfaces of the tank made of the gradient material on the dimensionless parameter E1/E2 and number of representative cells m

			"hom"	$m = 160$ (%)	$m = 80$ (%)	$m = 40$ (%)	$m = 20$ (%)
$\dfrac{\sigma_\theta(\rho_0)}{E^*\alpha^*T_0}$	$E_1 > E_2$	$E_1/E_2 = 5$	-0.9911	-0.267	-0.526	-1.021	-1.921
		$E_1/E_2 = 10$	-1.2029	-0.597	-1.181	-2.296	-4.335
	$E_1 < E_2$	$E_2/E_1 = 5$	-1.6090	0.085	0.168	0.329	0.632
		$E_2/E_1 = 10$	-1.8252	0.144	0.284	0.559	1.079
$\dfrac{\sigma_\theta(1)}{E^*\alpha^*T_0}$	$E_1 > E_2$	$E_1/E_2 = 5$	0.1143	-0.270	-0.536	-1.063	-2.090
		$E_1/E_2 = 10$	0.0691	-0.379	-0.755	-1.501	-2.965
	$E_1 < E_2$	$E_2/E_1 = 5$	1.0471	0.137	0.272	0.538	1.047
		$E_2/E_1 = 10$	1.3679	0.105	0.210	0.413	0.794

Fig. 4 and Tab. 2 describe the distributions of the circumferential stress along the thickness of the tank made of the considered gradient material. It should be emphasized that the stress distributions calculated for parameters E1/E2 and E2/E1 ≠ E1/E2 differ significantly from each other. If E1/E2 > 1 (K1/K2 < 1), the thermal properties of the insulator are on the inner surface of the tank. If E1/E2 < 1 (K1/K2 > 1), they are on the external surface. The black lines and rhombuses in Fig. 4 obtained for the values of the parameter E1/E2 = e > 1, while gray lines and rhombuses describe the distribution of the circumferential stress for the values of the parameter E2/E1 = e > 1. As follows from Fig. 4, the extreme negative and positive values of the circumferential stress are mostly on the surfaces of the tank. These values are presented in Tab. 2. Similar to Tab. 1 in the column marked "hom" are shown the values calculated using the homogenization method. In the columns with m = 160, 80, 40 and 20 are shown the relative deviations (given in percent) obtained using the first approach for the solution of the problem. The results of the comparison of solutions obtained using the two described approaches are similar to those presented above. This means that the proposed homogenization method allows for performing calculations with good accuracy not only for problems concerning solids with a periodic structure, but also for problems concerning solids with a slowly graded structure.

7. CONCLUSIONS

In this paper, the central-symmetrical problem of thermoselasticity for the multi-layered spherical tank with periodical or slowly graded structure was solved. The solution of the boundary problem defined in the components of the considered inhomogeneous tank was compared with the solution of the problem in which the thermomechanical properties of the tank were described by the method of homogenization with microlocal parameters. If the tank has the periodic structure, the solution based on the homogenization method has the form of simple engineering relations. The good agreement between the obtained analytical solution and the solution of the boundary problem for the heterogeneous tank is an irrefutable argument for the reliability of both solutions. The algorithm for solving the boundary problem for the nonhomogeneous tank is the same for different ways of arranging the layers in the tank. This means that obtaining a good correspondence between the solutions in the case of the slowly graded

structure also allows us to conclude that the method of homogenization with microlocal parameters adequately describes the thermomechanical properties of the spherical tank with the considered slowly graded structure. The proposed approach to the homogenization allows to correctly calculate not only the averaged characteristics in the representative cell (the macro-characteristics) but also the characteristics dependent on the choice of the component in the representative cell (the micro-characteristics).

The results obtained allow us to suggest that the proposed approach to the homogenization of a medium with a slowly graded structure will also be effective in other, more complex problems in which the consideration of inhomogeneity of the medium can be extremely laborious or sometimes simply impossible to accomplish.

REFERENCES

1. Achenbach JD. A theory of elasticity with microstructure for directionally reinforces composites. Wien: Springer-Verlag; 1975.
2. Bedford A, Stern M. Toward a diffusing continuum theory of composite materials. J. Appl. Mech. 1971; 38: 8-14.
3. Bensoussan A, Lions JL, Papanicolau AG. Asymptotic methods in periodic structures. Amsterdam: North-Holland 1978.
4. Bufler H, Krennerknecht H. Prestrained elastic laminates: deformations, stability and vibrations, Acta Mechanica. 1999; 48: 1-30.
5. Chen B, Tong L. Sensitivity analysis of heat conduction for functionally graded materials. Materials & Design. 2004; 25(8): 663-672.
6. Gan H, Orozco CE, Herkovich CT. A strain-compatibile method for micromechanical analysis of multi-phase composites, Int. J. Solids Struct. 2000; 37: 5097-5122.
7. Ganczarski A, Skrzypek J. Mechanika nowoczesnych materiałów, Kraków: W-wo Politechniki Krakowskiej 2013.
8. Jihov VV, Kozlov SM, Oleynik OA. Homogenization of differential operators and integral functionals. Berlin: Springer 1994.
9. Kaczyński A. Three-dimensional thermoelastic problems of interface crack in periodic two-layered composites. Engineering Fracture Mechanics. 1994; 62(6): 783-800.
10. Kirchhoff G, Göbel Th, Bahr H-A, Balke H, Wetzig K, Bartsch K. Damage analysis for thermally cycled (Ti, Al)N coatings – estimation of strength and interface fracture toughness. Surface Coat. Tech. 2004; 179: 39-46.
11. Kushnir RM, Yasinskyy AV, Tokovyy YV. Effect of material properties in the direct and inverse thermomechanical analyses of multilayer functionally graded solids. Adv. Eng. Mater. 2022; 24(5): 110-115.
12. Kulchytsky-Zhyhailo R, Matysiak SJ. On heat conduction problem in a semi–infinite periodically laminated layer. Int. Comm. Heat Mass Transfer. 2005; 32: 123-132.
13. Kulchytsky-Zhyhailo R, Matysiak SJ. On some heat conduction problem in a periodically two–layered body. Comparative results. Int. Comm. Heat Mass Transfer. 2005; 32: 332-340.
14. Kulchytsky-Zhyhailo R, Kolodziejczyk W. On the axisymmetric contact problem of pressure of a rigid sphere into a periodically two-layered semi-space. Int. J. Mech. Sci. 2007; 49: 704-711.
15. Kulchytsky-Zhyhailo R, Matysiak SJ, Perkowski DM. On displacements and stresses in a semi-infinite laminated layer: comparative results. Meccanica. 2007; 42: 117-126.
16. Kulchytsky-Zhyhailo R, Matysiak SJ, Perkowski DM. On some thermoelastic problem of a nonhomogeneous long pipe. Int. J. Heat and Technology. 2021; 39(5): 1430-1442.
17. Lee WY, Stinton DP, Berndt CC, Erdogen F, Lee Y–D, Mutasin Z. Concept of functionally graded materials for advanced thermal barrier coating applications. J. Amer. Ceram. Soc. 1996; 79: 3003-3012.
18. Matysiak SJ, Woźniak Cz. Micromorphic effects in a modeling of periodic multilayered elastic composites. Int. J. Engng. Sci. 1987; 25: 549-559.

19. Nowacki W. Thermoelasticity. Warszawa: PWN; 1986.
20. Paley M, Aboudi J. Micromechanical analysis of composites by generalized method of cells. Mechanics and Materials. 1992; 14: 127-139.
21. Reuss A. Berechnung der Flissgrenze von Mischk ristallen auf Grund der Plastizitätsbedingung für Einkristalle. Z. angew. Math. Mech. 1929; 9: 49-58.
22. Sanchez-Palencia E. Non-homogeneous media and vibration theory. Berlin: Springer-Verlag 1989.
23. Schulz U, Bach FW, Tegeder G. Graded coating for thermal, wear and corrosion barriers. Mater. Sci. Eng. Ser. A. 2003; 362(1-2): 61-80.
24. Szymczyk J, Woźniak Cz. Continuum modelling of laminates with a slowly graded microstructure. Arch. Mech. 2006; 58(4-5): 445-458.
25. Timoshenko S, Goodier JN. Theory of elasticity. New York: McGraw-Hill Book Company 1951.
26. Wang BL, Han JC, Du SY. Crack problems for functionally graded materials under transient thermal loading. Journal of Thermal Stresses. 2000; 23(2): 143-168.
27. Voigt W. Über die Beziehungen zwischen beiden Elastizitätskonstanten isotroper Körpär. Wied. Ann. 1889; 38: 573-587.
28. Woźniak Cz. A nonstandard method of modelling of thermoelastic periodic composites. Int. J. Engng. Sci. 1987; 25: 483-499.

Roman Kulchytsky-Zhyhailo: https://orcid.org/0000-0001-6390-2261

PERFORMANCE ESTIMATION OF BLENDED NANO-REFRIGERANTS' THERMODYNAMIC CHARACTERISTICS AND REFRIGERATION EFFICACY

Anirudh KATOCH*◉, Fadil Abdul RAZAK*◉, Arjun SURESH*◉, Baiju S. BIBIN*◉, Adriana R. FARINA◉, Luca CIRILLO**◉,
Arkadiusz MYSTKOWSKI***◉, Kamil ŚMIERCIEW****◉, Adam DUDAR****◉, Edison GUNDABATTINI*****◉**

*School of Mechanical Engineering, Vellore Institute of Technology (VIT), Vellore-632 014, India
**DII, University of Naples Federico II, P.leTecchio 80, 80125, Napoli, Italy
***Department of Automatic Control and Robotics, Faculty of Electrical Engineering, Bialystok University of Technology,
Wiejska 45D, 15-351, Bialystok, Poland
****Department of Thermal Engineering, Faculty of Mechanical Engineering, Bialystok University of Technology,
Wiejska 45C, 15-351, Bialystok, Poland
*****Department of Thermal and Energy Engineering, School of Mechanical Engineering, Vellore Institute of Technology (VIT),
Vellore-632 014, India

anirudhs2102@gmail.com, fadilabdul.razak2017@vitstudent.ac.in, arjun.suresh2017@vitstudent.ac.in,
bibinb.s2019@vitstudent.ac.in, adrianarosaria.farina@unina.it, luca.cirillo2@unina.it,
a.mystkowski@pb.edu.pl, k.smierciew@pb.edu.pl, a.dudar@pb.edu.pl, edison.g@vit.ac.in

Abstract: The use of nanoparticle-infused blended refrigerants is essential for achieving an effective sustainable system. This investigation analyses the efficiency of three nano-refrigerants (CuO-R152a, TiO2-R152a and TiO2-R113a) on the basis of the thermal performance and energy usage of the compressor using MATLAB-Simulink in the vapour compression refrigeration cycle with a two-phase flow domain. Also, nanoparticle volume concentrations of 0.1%–0.5% in the basic refrigerants are investigated. In the Simulink model, the outcomes are calculated mathematically. Using the NIST chemistry webbook, the thermo-physical characteristics of base refrigerants were calculated, and different numerical models were used to compute the characteristics of nano-enhanced refrigerants. MS Excel was used to perform the liquid–vapour interpolation. It was discovered that refrigerants with nanoparticles have superior heat-transfer properties and operate most excellently at an optimal volume fraction of 0.1% for TiO2-R152a and CuO-R152a with a coefficient of performance (COP) as 10.8. However, the other blended nano-refrigerant TiO2-R113a performed the best at 0.5% of nano-particle volume fraction with a COP value of 5.27.

Key words: Coefficient of performance, compressor power, heat-transfer rate, volume percentage, heat extraction, power consumption

1. INTRODUCTION

Scientists from around the world came to the conclusion that air conditioning and refrigeration equipment used far too much energy. As a result, there is a need to use energy-efficient technology to counteract the limited availability of energy [1–5]. In light of the present scenario, to improve the heat transfer in the vapour compression refrigeration systems (VCRSs), it needs new and advanced heat-transfer fluids. Nanoparticles suspended in refrigerants represent a suitable substitute for conventional refrigerants. Various researchers show a higher heat-transfer performance (HTP) of nano-added refrigerants [6–10].

One of the most important issues related to modern refrigeration, air conditioning and heat pump technology is the need to phase out the currently used groups of refrigerants and to replace them with alternative, environmentally safe working fluids, e.g. natural fluids [11]. The fact is that all solutions in refrigeration technology are determined primarily by the thermodynamic properties of refrigerants. In some cases, changing the refrigerant forces the modification of the construction of the device. Replac-

ing the refrigerant may cause the energy efficiency achieved by these devices to significantly reduce. However, manufacturers are taking all measures to ensure that the energy efficiency of the devices is at least at the same level as when working with the withdrawn refrigerants. As a result of this measure, new, synthetic refrigerants are being introduced. Alternatively, the refrigerants are modified with the help of nanoparticles that improve their thermo-physical properties. There are more and more synthetic or modified refrigerants available on the market, the use of which at least minimally eliminates the need to modify the previously used technical solutions. The massive production and consumption of synthetic fluids such as chloro-fluoro-carbons (CFCs) and hydro-chloro-fluoro-carbons (HCFCs) for which negative effects have been demonstrated forced the world community to take steps to radically change this alarming situation. Currently, these refrigerants are classified as the so-called controlled substances.

The Montreal Protocol is the first international agreement on an environmental policy whose primary objective is to prevent the risks related to the emission of these fluids into the atmosphere. The current version of the Protocol deviates from the original one, as the document has been modified many times. The latest

amendments from Kigali came into force on 01 January 2019. For refrigerants belonging to the HCFC group, their use in new refrigeration installations has been banned since 01 January 2004, and a timetable has been set for their complete phase-out. For HCFC refrigerants, the applicable timetable for reducing their consumption by 79% is by 2030 compared to the base year of 2015. In addition, according to the EU regulation [11], the use of refrigerants with a global warming potential (GWP)>150 is prohibited in large centralized refrigeration systems with a capacity above 40 kW and used for commercial applications from 01 January 2020. Also, since 01 January 2022, refrigerants belonging to the HFCs with a GWP > 150 cannot be used in air conditioning units. For single air conditioning split systems with refrigerant chargesof up to 3kg, the use of GWP > 750 refrigerants will be banned from 01 January 2025. As previously mentioned, scholars are making efforts to improve refrigerant properties, e.g. heat transfer coefficients (HTC), viscosity, and so on.

Nanoparticles can be used in refrigerants as additives, aimed at improving the properties such as thermal conductivity, chemical and thermal stability and lubricating properties, which in turn can contribute to increasing the efficiency of the refrigeration system. The use of nanoparticles in refrigerants can increase the production and disposal costs of refrigerants due to higher production costs of nanoparticles and potential difficulties in their disposal. Depending on the desired effect of the base fluid, copper and graphite nanoparticles can be used to improve the thermal conductivity of the refrigerant. Cerium oxide nanoparticles allow for the improvement of the chemical and thermal stability of the refrigerant. Titanium oxide nanoparticles improve the antibacterial properties of intermediate fluids, while carbon nanoparticles are used to improve lubricating properties and reduce friction in intermediate fluids. The stability of the nano-refrigerant is one of the major concerns. The agglomeration of the nanoparticles in the fluid is increased over time by disturbing the viscosity and thermal conductivity of the base fluid. Apart from that, the sustainability of the nano-fluids is not practical because of the cost issues [42–44].

Buonomo et al. [12] used TRNSYS to perform a dynamic simulation of Al_2O_3–water nanofluid in the solar cooling system for volume concentrations of 3% and 6%, and they came to the conclusion that the nanofluid showed higher energy savings for the entire summer season of the year, although the difference between the savings for the two-volume concentrations was small. The same nanofluid was used by the team for a TRNSYS modelling of the automotive cooling circuit, and they discovered that at low engine speeds, the nanofluid performed better in all circumstances and had a substantially higher HTP than the ethylene–glycol coolant [13].The convective HTC increased with a greater concentration of nanoparticles when the Al_2O_3–water nanofluid was through a rectangular micro-channel with uniform and steady heat fluxes on the top wall [14]. The improvement of the HTC that aids in reducing engine overheating was made possible by the use of nanofluids as a cooling system for radiators in automotive vehicles [15]. This results in its utilisation as an engine-coolant substitute [16, 17]. Al_2O_3–mono ethylene glycol (MEG)–water nanofluid's effect on car radiators was examined by Subhedar et al. [18], who also improved the overall HTC and enabled a 36.69% reduction in the radiator surface area. The researchers analyzed the HTP and pressure drop of the new-generation refrigerants such as R1234yf. The investigation shows that the HTC and the pressure drop of the CuO/R1234yf nano-refrigerant are enhanced by 45% and 36%, respectively [45]. Similarly, the HTC

and pressure drop of the TiO_2-doped R1234yf refrigerant is improved by 134.03% and 80.77% [46].

One method to reduce the energy requirement of the VCRS is to use nano-fluid, which is a combination of a specific quantity of nano-sized particles dissolved in a fluid to create a colloidal solution. When these substances are employed for refrigeration, they are referred to as nano-refrigerants. The chemically stable metals like Au and Cu and metal oxides such as Al_2O_3, SiO_2, TiO_2, zirconia, and oxide ceramics are commonly used as nano-sized particles in VCRS [19, 20]. Nano-refrigerants are synthesized by two techniques: (i) the single-stage process and (ii) the double-stage process. The double-stage technique [23] divides the two processes; the single-stage technique [21, 22] combines the creation and mixing of nanoparticles into pure fluid concurrently. Coumaressin and Palaniradja [24] studied the HTP of CuO nano-materials added to an R134a-based refrigerant in VCRs. By increasing the volume fraction of CuO from 0.1% to 0.8%, the HTC of CuO-R134a was increased. Anish et al. [25] studied the effects of adding CuO to the refrigerant R-22 and found that total coefficient of performance (COP) was improved while power consumption was reduced. When 0.05% CuO nanoparticles were introduced, the COP rose from 0.58 to 0.62. According to Bi et al.'s research [26], adding 0.5g/L of TiO_2 to R600a reduced the energy consumption by 9.6%. Kumar et al. [27] demonstrated the influence of the CuO nanometal oxide on liquid petroleum gas–based VCRS, following the efficacious validation of nano-refrigerants in residential VCRs. Figure 1 shows that the system's performance and heat-transfer rate both increased by 36% and 46%, respectively.
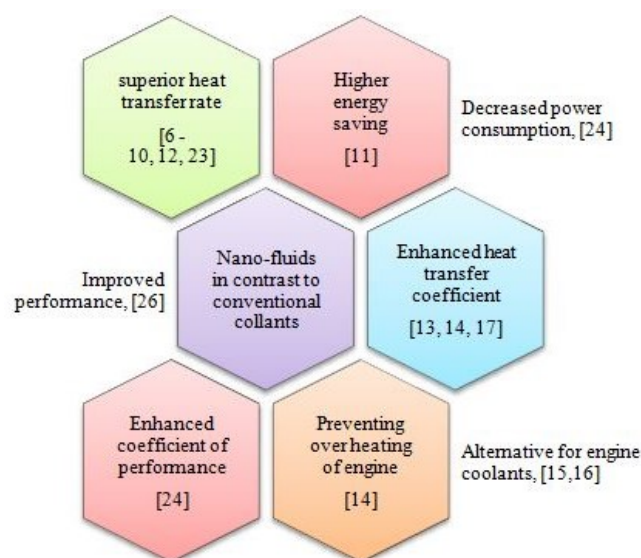

Fig.1. Nano-fluid as a different way to boost the effectiveness of the system

The three nano-added refrigerants, which the MATLAB model simulated, form the primary focus of the study. The main goal of the article is to use nano-enhanced refrigerants to improve system performance and decrease compressor energy usage. Hence, improvising on the performance of the VCR system with nano-refrigerants such as TiO_2-R113, TiO_2-R152a and CuO-R152a forms the crux of this research. Also, in this paper, the thermal properties of these nano-refrigerants are identified, which were crucial for the analysis.

2. METHODOLOGY AND MATERIALS

2.1. Materials

The VCRS is used in this investigation with three nano-enhanced refrigerants, namely, TiO_2-R113a, TiO_2-R152a and CuO-R152a. The pure refrigerant has nanoparticle volume concentrations in the range of 0.1%–0.5%. This range is chosen to obtain a stable nano-refrigerant; beyond this range, there could be the challenge of agglomeration. SRD 69 computed several input parameters for basic refrigerants using the NIST chemistry webbook. Several numerical models were used to determine the thermo-physical parameters of nano-refrigerants.

2.2. Numerical models

There are various ideas and models for determining nano-refrigerant characteristics. Information on the state and type of nanoparticles used must be included in these models. The C_p, k, ρ and size of nano-materials that will be employed in models are given in Tab. 1. These characteristics vary somewhat depending on particle size. It is assumed that the spherical nanoparticles are spread throughout the pure refrigerant.

Tab.1. Nanoparticle properties at environmental temperature

Nano-materials	ρ (kg·m^{-3})	k(W·m^{-1}·K^{-1})	C_p (J·kg^{-1}·K^{-1})	R (nm)
CuO[28]	6,500	20	535.6	20
TiO$_2$[29]	4,230	8.4	692	21

'*k*' is one of the most important aspects of improving nano-refrigerant performance. Several models were evaluated in this work, including Maxwell's [30], Hamilton and Crosser's [31], Yu and Choi's [32] and Koo and Kleinstreuer's [33]. The '*k*' is determined in this study using Maxwell's model. As Simulink software is used here instead of a real setup, the continuous phase with spherical nanoparticles matches Maxwell's model perfectly.

$$\frac{k_{nf}}{k_{ref}} = \frac{k_{np} + 2\,k_{ref} - 2\Phi(k_{ref} - k_{np})}{k_{np} + 2\,k_{ref} - \Phi(k_{ref} - k_{np})} \quad (1)$$

The Gherasim model [34] gave the viscosity of nano-refrigerants with sphere-shaped nanoparticles, which is dependent on the volume concentration and viscosity of the basic refrigerant.

$$\frac{\mu_{nf}}{\mu_{ref}} = 0.904e^{14.8\Phi} \quad (2)$$

The nanoparticle's 'ρ', the 'ρ' of the base refrigerant and the volume fraction all influence the effective 'ρ' of the nano-refrigerant [35].

$$\rho_{nf} = (1 - \Phi)\rho_{ref} + \Phi\rho_{np} \quad (3)$$

This $C_{p,ref}$ value is needed to determine $C_{p,nf}$ using Eq. 4, which is also dependent on base refrigerant densities, nanoparticles, nanoparticle Cp and volume concentration [36]:

$$C_{p,nf}\rho_{nf} = (1 - \Phi)C_{p,ref}\rho_{ref} + \Phi C_{p,np}\rho_{np} \quad (4)$$

The *Pr* is identified by the following correlation, which uses the μ_{nf}, k_{nf}, and $C_{p,nf}$.

$$Pr = \frac{viscous\ diffusion\ rate}{thermal\ diffusion\ rate} = \frac{\mu \times Cp}{k} \quad (5)$$

2.3. Simulation and modelling

The investigations were accomplished with the help of a VCRS model that was created utilizing a unique Simscape two-phase flow domain. The present VCRS cycle is based on the MATLAB–Simulink platform, which is freely accessible on the MathWorks File Exchange [37]. The setup and its characteristics are shown in Figs. 2 and 3. An evaporator, thermostatic expansion valve, condenser, compressor, compartment and controller constitute the VCRS model. The temperature of the compartment is kept at 277K in this analysis by regulating the compressor parameters. The controller is used to turn the compressor on and off. When the temperature of the compartment rises over the set temperature, the compressor is turned on and it cools the compartment below the set temperature.
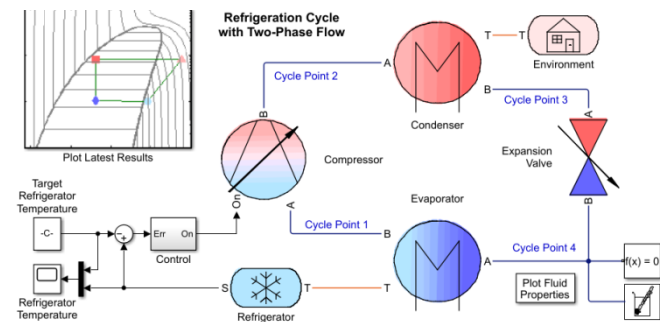

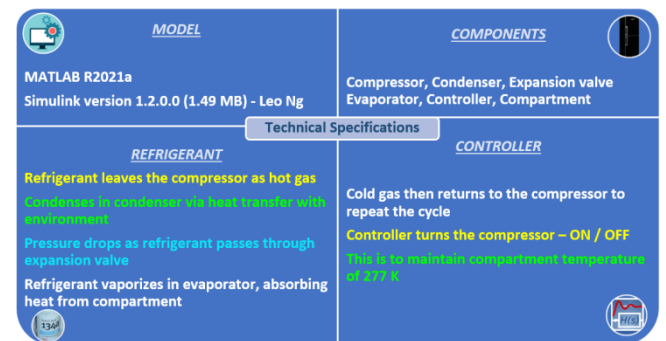**Fig. 2**. Layout of simulation [37]

Fig. 3. Defined specifications

The goal of the simulation is to examine how adding nanoparticles to basic refrigerants affects power usage and COP. There is always an ideal volume fraction when the COP is at its highest. There could be enhancement in the refrigeration effect as the heat-transfer characteristics are improvised with the addition of nanoparticles. As a result, research into that impact might be advantageous.

Many factors, both inside and outside the cycle, influence the compartment heat, extracted compressor power and COP. All these variables are included in all the simulations. Furthermore, using the facility and infrastructure accessible to them, research-

ers have investigated physical setups for different nano-refrigerants. This analysis is using a single platform to run a variety of combinations. The main goal is to detect a broad trend in all of these variables. The cycle conditions are shown in Tab. 2.

Tab. 2. VCRS cycle boundary values

Charge pressure	87 psi
Flow of mass	14.4 kg·h^{-1}
Compressor time constant	20 s
Length of condenser	1,500 mm
Conductivity of Cu	400 W·m^{-1}·K^{-1}
'ρ' of Cu	8,940 kg·m^{-3}
Specific heat of Cu	390 J·kg^{-1}·K^{-1}
Temperature of surrounding	293 K
Length of evaporator	15 m
Surface area of exterior	6 m^2
Area of fin	1 m^2
Fin convention coefficient	150
Conductivity of foam	0.03 W·m^{-1}·K^{-1}
Thickness of foam	0.03 m
Liquid fraction	0.8
Interior area of surface	4.5 m^2
Max area of the throat	2.7 m^2
Max. temperature of throat	230 K
Min. area of the throat	0.1 m^2
Min. temperature of throat	280 K
Coefficient of natural convection	20 W·m^{-2}K^{-1}
Diameter of pipe	15 mm
Thickness of pipe	5 mm

Tab.3. Runtime conditions for a refrigeration cycle

Refrigerant	Nano-concentration (%)	Pressure range (MPa)	Temperature range (K)	Run time (s)
TiO$_2$-R113a	0	0.01–3	240–420.6	509
	0.1			488.5
	0.3			484.5
	0.5			472
TiO$_2$-R152a	0		160–420.4	769
	0.1			854
	0.3			834.5
	0.5			823.5
CuO-R152a	0		160–420.4	769
	0.1			854.5
	0.3			830
	0.5			824

Throughout the refrigeration cycle, the mass flow rate of the refrigerant is kept constant. As a result, the pipe's velocity was not estimated. The phenomenon of sedimentation was not considered. The working conditions used to be similar to the home freezers. Most residential refrigerators have a charge pressure ranging from 0.3 MPa to 1 MPa. Copper is used as the heat exchanger material in the VCRS model, typically with grooves or a tube or coil. Aluminium, brass, stainless steel and other metals are also utilized. Insulation in the refrigerator compartment is provided by polyurethane foam. A compressor on/off mechanism was included in the model. The cycle run times for various combinations of refrigerants are shown in Tab. 3.

It is expected that nano-fluids will behave differently in a real configuration because their stability affects their HTP as well as their flow properties. The kind of nanoparticles employed, the heating surface and the base type are all aspects that will differentiate the simulation research from the real-world arrangement. The boiling HTC decreases when porous deposits form on the heated surface of the nano-materials. The critical flux is significantly impacted by the nano-refrigerant. Because of the high volume fraction of nano-sized materials in the fluid, the critical flux is lowered. The higher viscosity of a base fluid can lessen the influence of the boiling HTP of a nano-refrigerant, resulting in improved HTP since stability is better and nanoparticles exhibit a greater boost in the 'k' value. Higher viscosity also results in less nanoparticle sedimentation on the heated surface [38].

The simulations are based on theoretical discoveries and an idealized design, for the most part. The stability of the nano-refrigerant is not taken into consideration in the formulae. The article's main goal was to evaluate nano-refrigerants to see which one was superior based only on the thermo-physical qualities. In future, laboratory studies may be conducted to confirm these theoretical conclusions. Mechanisms for regulated stability may be devised in the future; at that point, the current research will be useful in determining which combination provides the best performance of the system.

2.4. Simulation model's summary

An experimental configuration is comparable to the Simulink model. If any of the parameters are incorrect, errors are prompted, and various parameters are checked. Only after all mistakes are fixed does the simulation start and then end. Regardless of the pressure differential, the compressor maintains the prescribed mass flow rate. The Fourier law governs heat transfer in condensers and evaporators. It argues that the temperature differential, the area normal to the direction of heat flow, material thermal conductivity and layer thickness are all directly and inversely correlated with the heat transfer. Between the fluid and the pipe wall of both parts, there occurs convective heat transfer. Pressure loss is modelled for the local control restriction elements such as valves and orifices. They are adiabatic devices [39]. Components of the heat exchange use various kinds of friction correlations:

Halland correlation used for identifying the turbulent pipe flow friction factor:

$$f_d = \frac{1}{(-1.8 \, x \log\left(\frac{6.9}{Re} + \left(\frac{eps}{3.7}\right)^{1.11}\right))^2} \tag{6}$$

Laminar regime viscous friction force:

$$F_f = \frac{4 \, f_s \mu V Le}{D_h^2 m} \tag{7}$$

Turbulent regime viscous friction force

$$F_t = \frac{4 \, f_d \, Le}{m \, v} \tag{8}$$

The net power delivered to the fluid flowing from the inlet to the outlet of the compressor is given by

$$W = m \left[\left(u_{out} + (P_{out}V_{out}) + \frac{v_{out}^2}{2}\right) - \left(u_{in} + (P_{in}V_{in}) + \frac{v_{in}^2}{2}\right)\right] \tag{9}$$

Anirudh Katoch, Fadil Abdul Razak, Arjun Suresh, Baiju S. Bibin, Adriana R. Farina, Luca Cirillo, Arkadiusz Mystkowski,   DOI 10.2478/ama-2024-0031
Kamil Śmierciew, Adam Dudar, Edison Gundabattini
Performance Estimation of Blended Nano-Refrigerants' Thermodynamic Characteristics and Refrigeration Efficacy

The heat extracted from the evaporator is determined by:

$$Q_{extract} = h \, S_{sur} \, \Delta T \tag{10}$$

The system performance is expressed by the COP, which is the ratio of the heat extracted from the evaporator to the compressor power input (or net power delivered).

2.5. Model validation

Tsvetok et al.'s [40] experiment is used to determine the thermal conductivity of the R134a refrigerant at low temperatures to validate the Simulink model with base properties. The thermal conductivity was measured at quasi-static isobars at a total of around 54 experimental locations using a coaxial cylinder technique. Figure 4 demonstrates how closely experimental values and simulation results correspond.
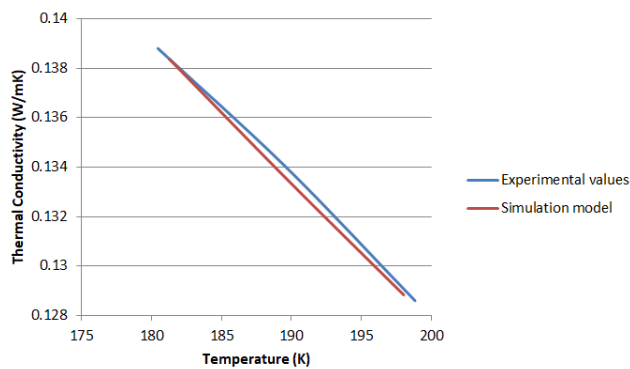
Fig. 4. Validation of simulation model

3. RESULTS AND DISCUSSION

3.1. Nano-enhanced refrigerants' thermodynamic states

As demonstrated in Tab. 4, the 'k' value of the nano-refrigerant enhances as the volume concentration of nanoparticles in the pure fluid increases. The absorbency of the nanofluid is crucial because it enhances the 'k' value of the nano-enhanced refrigerant. Tab. 3 indicates that a 0.1% addition of nanoparticles in CuO-R152a with TiO2-R152a shows only a 0.019% variation in the 'k' value. Meanwhile, the refrigerant is changed with R113a; the 'k' is reduced by 1.33 times.

Tab. 4. The 'k' value of refrigerants at atmospheric conditions

Nano-refrigerant	Volume concentration		
	0.1% (W·m^{-1}·K^{-1})	0.3% (W·m^{-1}·K^{-1})	0.5% (W·m^{-1}·K^{-1})
TiO2-R113a	0.0663	0.0676	0.0687
TiO2-R152a	0.0883	0.0899	0.0915
CuO-R152a	0.0883	0.0900	0.0916

According to the findings of Mahdi et al. [41] and the current study, adding nanoparticles increases the viscosity of the basic refrigerant. When the volume fraction increases as a result of more surface area coming into contact with the refrigerant, the viscosity rises. The presence of nanoparticles is not necessary. At 25°C and 1 atm, Tab. 5 displays the viscosities of the TiO2-R113a, TiO2-R152a, and CuO-R152a refrigerants. The table makes it evident that the viscosity of the nano-refrigerant increases dramatically as the volume percentage of the nano-sized material increases. For instance, TiO2-R113a has a 4.8% increase in viscosity.

Tab.5. Viscosity of combinations at atmospheric condition

Nano-refrigerant	Particle concentration		
	0.1% (10^{-4} kg·m^{-1}s^{-1})	0.3% (10^{-4} kg·m^{-1}s^{-1})	0.5% (10^{-4} kg·m^{-1}s^{-1})
TiO2-R113a	5.209	7.004	9.417
TiO2-R152a	1.281	1.722	2.315
CuO-R152a	1.281	1.722	2.315

Tab. 6. 'ρ' of combination at atmospheric condition

Nano-refrigerant	Nanoparticle loading		
	0.1% (kg·m^{-3})	0.3% (kg·m^{-3})	0.5% (kg·m^{-3})
TiO2-R113a	1,567.66	1,572.99	1,578.32
TiO2-R152a	834.19	840.99	847.79
CuO-R152a	836.47	847.81	859.15

Tab.7. Specific heat of the combinations at atmospheric condition

Nano-refrigerant	Volume fraction		
	0.1% (J·kg^{-1}·K^{-1})	0.3% (J·kg^{-1}·K^{-1})	0.5% (J·kg^{-1}·K^{-1})
TiO2-R113a	911.95	911.84	911.73
TiO2-R152a	1,794.4	1,783.3	1,772.4
CuO-R152a	1,790.2	1,770.9	1,752.2

The specific volume of each nano-refrigerant is determined by its 'ρ'. According to Tab. 6, the 'ρ' of nano-refrigerants is quite high compared to the 'ρ' of its basic refrigerant and gets better as nanoparticles are added. As a result, the specific volume reduces as particle concentration rises. When 0.1% of nanoparticles are introduced into the pure refrigerant, the 'ρ' value of the TiO2-R152a refrigerant is two times greater than that of TiO2-R113a. This is owing to the density variation of the base refrigerants such as R152a and R113a. The percentage increase in 'ρ' of TiO2-

R113a is 0.34% when the nanoparticle concentration changes from 0.3% to 0.5%. However, it is 0.8% in the case of TiO$_2$-R152a.

Table 7 gives the specific heat of all mixtures. The nano-refrigerants' specific heat is shown to increase with volume fraction. At 0.5% nano concentration, TiO$_2$-R152a had the highest specific heat.

3.2. System performance using different nano-enhanced refrigerants

The VCRSs' performance is denoted in terms of the COP. The COP is influenced by compressor power and the heat extracted from the evaporator.

3.2.1. Influence of nanoparticles on heat extraction from the evaporator

For various nano-refrigerants, the heat evacuated from the evaporator is shown in Fig. 5. Fig. 5 clearly shows that the TiO$_2$-R113a nano-refrigerant removes significantly more heat than the R113a refrigerant. In contrast to the pure refrigerant, the heat extraction rose by 170.05% for 0.1% TiO$_2$-R113a nano-refrigerant, while it was only 1.68kW for 0.3% TiO$_2$-R113a, which was somewhat less than 0.1%. The amount of heat extracted for 0.5% TiO$_2$-R113a was the highest at 1.79 kW or nearly three times the amount of heat extracted by the R113a refrigerant. In contrast, the heat extraction for TiO$_2$-R152a and CuO-R152a followed a different pattern. The heat extraction decreased by 9.2% and 9.5% in the cases of 0.1% and 0.5% TiO$_2$-R152a, respectively, but was still higher than that of 0.3% TiO$_2$-R152a, which saw a reduction of 13.13% and reached 0.923 kW. The heat extraction from the evaporator is also reduced with the addition of nanoparticles to the CuO-R152a nano-refrigerant. Heat extraction in nano-refrigerants performed best for 0.1% CuO-R152a and worst for 0.3% CuO-R152a, as 1.03kW and 0.97kW, respectively.
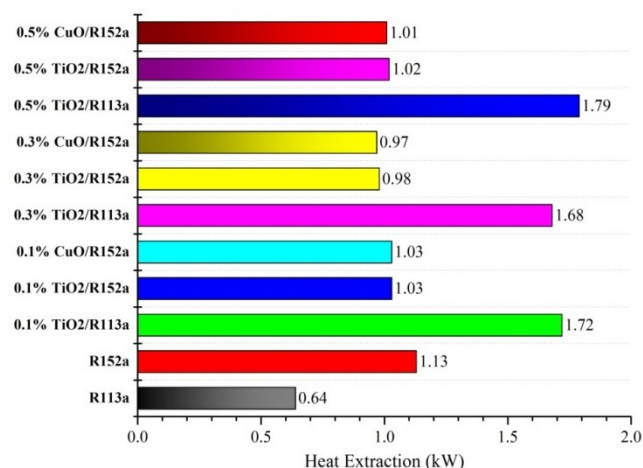
Fig.5. The heat extraction from evaporator

3.2.2. Impact of a nano-sized particle on compressor power usage

Figure 6 illustrates the variation of compressor power usage for TiO$_2$-R113a, TiO$_2$-R152a and CuO-R152a nano-refrigerant.

Figure 6 show the use of nano-refrigerants might reduce compressor energy consumption. For nano-refrigerant containing 0.1% TiO$_2$-R113a, energy consumption decreased by 19.9%. Similarly, at 0.3% of TiO$_2$ in R113a refrigerant, the energy consumption is decreased by 17.7% and it is reduced by 9.91% for 0.5% TiO$_2$-R113a. The power consumption decreased by 35.4% when 0.1% TiO$_2$-R152a was used, but only little when 0.3% and 0.5% of TiO$_2$ in R152a were used. It is decreased by 9.302% and 16.78%, respectively. Likewise, is decreased by about 50% for 0.1% CuO-R152a. However, the drop was 15% and 10%, respectively, for 0.3% and 0.5% CuO-R152a.
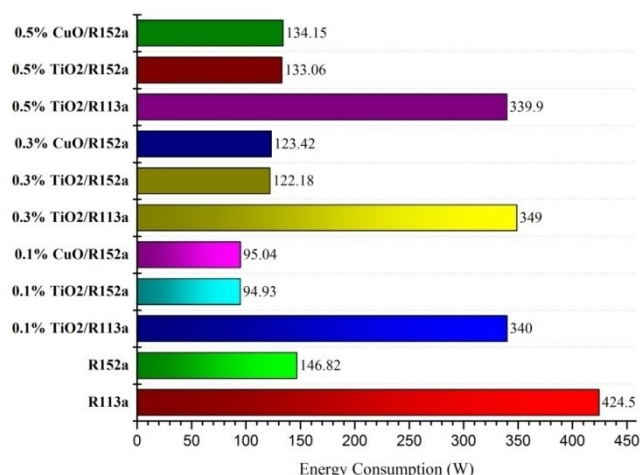
Fig.6. The energy consumption of the compressor

Generally, the power consumption enhances with the nanoparticle addition in the refrigerant. This is due to the viscosity of the fluid increasing with the concentration of the particles. It leads to improving the resistance to flow. This is the reason for the rise in the power consumption of compressors with nano-enhanced refrigerants.
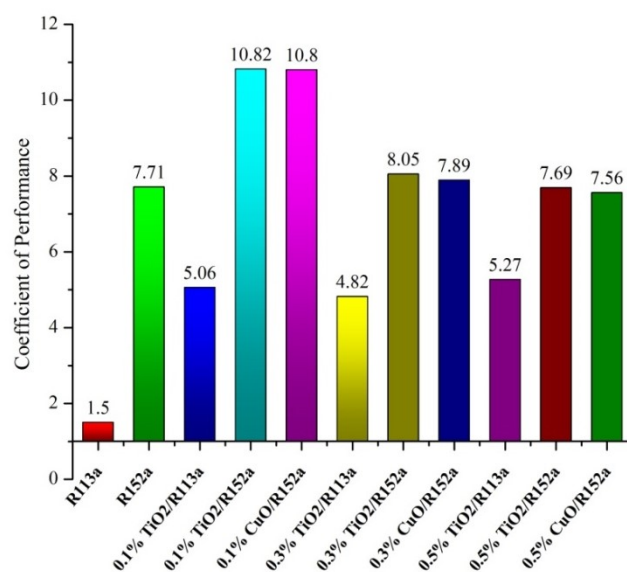
3.2.3. Effect of nanoparticle on COP

Fig. 7. Variation of systems' performance

Anirudh Katoch, Fadil Abdul Razak, Arjun Suresh, Baiju S. Bibin, Adriana R. Farina, Luca Cirillo, Arkadiusz Mystkowski, Kamil Śmierciew, Adam Dudar, Edison Gundabattini
Performance Estimation of Blended Nano-Refrigerants' Thermodynamic Characteristics and Refrigeration Efficacy

DOI 10.2478/ama-2024-0031

Figure 7 demonstrates how the nanoparticles in the refrigerant affect the COP. Figure 7 shows that the COPs for nano-refrigerants are nearly three times more than those for basic refrigerants.

The greatest COP, 5.27, is for 0.5% TiO_2-R113a, whereas 0.1% has a COP of 5.06. Although the COP of 0.3% TiO_2-R113a has grown by 221.193% than base refrigerant R113a, it remains below that for 0.1% and 0.5%. Figure 7 explains that the maximum COP for adding 0.1% TiO_2 nanoparticles to R152a is 10.82, whereas for 0.3%, the improvement in COP over the base refrigerant is just 4.39%. When compared to R152a, the COP is practically the same at 0.5%. Similar to this, R152a's 0.1% addition of CuO nanoparticle results in a 10.8 COP. The COP for base and nano-refrigerants with 0.5% is almost the same. A bit higher than the base refrigerant, the COP for the 0.3% CuO-R152a refrigerant is 7.89.

The difference in the thermo-physical characteristics between nano-refrigerants and base refrigerants can be attributed to this behaviour. As the viscosity increases as the particle concentration, the value of COP declines.

4. FUTURE SCOPE

In the present situation, no software platform exists where a researcher may input nano-refrigerant parameters and obtain results. All of the analyses are carried out theoretically and numerically; therefore, experimental studies are needed in future. The stability of the nano-refrigerant is not taken into consideration in the formulae. The article's main goal was to evaluate nano-refrigerants to see which one was superior based only on thermo-physical qualities. In future, experimental investigations may be conducted to confirm these theoretical conclusions. So, in the near future, there is a possibility of developing a programme for nano research utilizing software such as MATLAB, which may aid in providing different inputs such as nanoparticle diameter, nano-particle type, base refrigerants, charge value and so on. The exergy and environment analysis of the system should become more reliable and the life cycle assessment will provide an idea about the performance of the system. These are the futuristic scope of this work.

Furthermore, it is important to undertake future research regarding theoretical analysis and validation studies of the impact of nanoparticles on the thermal properties of environmentally friendly refrigerants from the HC group such as R600a or R290, as well as other refrigerants with low GWP values such as R1233zd, R1233ze or R1234yf. Additionally, it is extremely important to determine, through research, the impact of lubricating oil in the refrigeration compressor system on the stability of the refrigerant and the uniform concentration of nanoparticles throughout the volume of the refrigerant.

5. CONCLUSION

The addition of the nanoparticles to the refrigerant improves the COP of the refrigeration system and reduces the power consumption by the compressor than the base refrigerants. Except for TiO_2-R113a, it can be inferred that the 0.1% concentration of nano-sized materials in the pure refrigerant has the greatest COP. The efficiency was lowered by 0.3% and 0.5% owing to an im-provement in viscosity. The maximum COP obtained for adding 0.1% TiO_2 nanoparticles to R152a is 10.82. Meanwhile, the power consumption decreased by 35.4% when 0.1% TiO_2-R152a was used, but only to a lesser extent when 0.3% and 0.5% TiO_2-R152a were used. Two of the features of blended nano-refrigerants, including viscosity and thermal conductivity, were also examined in the study that is presented. According to sources, the use of nanoparticles increases viscosity, improving the compressor's tribology. The system's performance thus declines to some extent as a result of the system's increased viscosity and the ensuing decrease in pressure. Additionally, a mixed nano-refrigerant with low viscosity and excellent heat conductivity maximizes the efficacy of nano-refrigeration systems. An investigation implies that blended nano-refrigerant systems could be one of the sustainable energy solutions. Hence, energy-efficient nano-refrigeration systems with compressors consuming less power and systems giving more COP could curtail the global warming. Also, one could optimize the efficacy of the refrigeration system by choosing the appropriate percentage of volume concentration of the nanoparticles.

Nomenclature:

Abbreviation:

CFC	Chloro-fluoro-carbon
COP	Coefficient of performance
EU	European Union
GWP	Global warming potential
HCFC	Hydro-chloro-fluoro-carbon
HTC	Heat-transfer coefficient, $W \cdot m^{-2} K^{-1}$
HTP	Heat-transfer performance
NIST	National institute of standard and technology
VCRS	Vapour compression refrigeration system

Symbols:

Cp	Specific heat, $J\ kg^{-1} K^{-1}$
D_h	Hydraulic diameter, m
eps	Internal surface absolute
f_d	Flow fraction factor
f_s	Shape factor
k	Thermal conductivity, W
m	Mass flow rate, $kg\ s^{-1}$
v	Specific volume, $m^3 \cdot kg^-$
F_f	Laminar flow friction for
F_t	Turbulent flow friction fo

L_e	Effective length, m
P	Pressure, MPa
Pr	Prandtl number
R	Radius of nanoparticle, nm
Re	Reynolds number
S_{sur}	Surface area of evaporator, m^2
T	Temperature, K
U	Internal energy, $kJ\ kg^{-1}$
V	Velocity, ms^{-1}

Subscripts:

ref	Base refrigerant
nf	Nano-refrigerant
sat	Saturation
np	Nanoparticle

Greek Symbols:

ρ	Density, $kg\ m^{-3}$
ϕ	Concentration
μ	Viscosity, $kg \cdot m^{-1} s^{-1}$

REFERENCES

1. Yılmaz AC. Performance evaluation of a refrigeration system using nanolubricant. Applied Nanoscience [Internet]. 2020 Jan 20;10(5):1667–78. Available from: https://doi.org/10.1007/s13204-020-01258-5

2. Barbato M, Cirillo L, Menditto L, Moretti R, Nardini S. Geothermal energy application in Campi Flegrei Area: The case study of a swimming pool building. International Journal of Heat and Technology [Internet]. 2017 Sep 20;35(Special Issue1):S102–7. Available from: https://doi.org/10.18280/ijht.35sp0114

3. Cascetta F, Di Lorenzo R, Nardini S, Cirillo L. A Trnsys Simulation of a Solar-Driven Air Refrigerating System for a Low-Temperature Room of an Agro-Industry site in the Southern part of Italy. Energy Procedia [Internet]. 2017 Sep 1;126:329–36. Available from: https://doi.org/10.1016/j.egypro.2017.08.259

4. Cascetta F, Cirillo L, Della Corte A, Nardini S. Comparison between different solar cooling thermally driven system solutions for an office building in Mediterranean Area. International Journal of Heat and Technology [Internet]. 2017 Mar 30;35(1):130–8. Available from: https://doi.org/10.18280/ijht.350118

5. Cirillo L, Della Corte A, Nardini S. Feasibility study of solar cooling thermally driven system configurations for an office building in Mediterranean area. International Journal of Heat and Technology [Internet]. 2016 Oct 31;34(S2):S472–80.
Available from: https://doi.org/10.18280/ijht.34s240

6. Leong KY, Saidur R, Kazi SN, Mamun A. Performance investigation of an automotive car radiator operated with nanofluid-based coolants (nanofluid as a coolant in a radiator). Applied Thermal Engineering [Internet]. 2010 Dec 1;30(17–18):2685–92. Available from: https://doi.org/10.1016/j.applthermaleng.2010.07.019

7. Hussein A, Bakar RA, Kadirgama K, Sharma KV. Heat transfer enhancement using nanofluids in an automotive cooling system. International Communications in Heat and Mass Transfer [Internet]. 2014 Apr 1;53:195–202. Available from:
https://doi.org/10.1016/j.icheatmasstransfer.2014.01.003

8. Subhedar D, Ramani BM, Gupta AK. Experimental investigation of overall heat transfer coefficient of AL2O3/Water-Mono ethylene glycol nanofluids in an automotive radiator. Heat Transfer [Internet]. 2016 Oct 4;46(7):863–77. Available from:
https://doi.org/10.1002/htj.21247

9. Contreras EMC, Oliveira GA, Filho ÊPB. Experimental analysis of the thermohydraulic performance of graphene and silver nanofluids in automotive cooling systems. International Journal of Heat and Mass Transfer [Internet]. 2019 Apr 1;132:375–87. Available from: https://doi.org/10.1016/j.ijheatmasstransfer.2018.12.014

10. Naiman II, Ramasamy D, Kadirgama K. Experimental and one dimensional investigation on nanocellulose and aluminium oxide hybrid nanofluid as a new coolant for radiator. IOP Conference Series: Materials Science and Engineering [Internet]. 2019 Jan 16;469:012096. Available from: https://doi.org/10.1088/1757-899x/469/1/012096

11. Regulation (EU) No 517/2014 of the European Parliament and of the Council on fluorinated greenhouse gases and repealing Regulation (EC) No 842/2006

12. Buonomo B, Cascetta F, Cirillo L, Nardini S. Application of nanofluids in solar cooling system: Dynamic simulation by means of TRNSYS software. Modelling, Measurement & Control [Internet]. 2018 Sep 30;87(3):143–50. Available from:
https://doi.org/10.18280/mmc_b.870305

13. Buonomo B, Cirillo L, Manca O, Nardini S. Effect of nanofluids on heat transfer enhancement in automotive cooling circuits. AIP Conference Proceedings [Internet]. 2019 Jan 1; Available from: https://doi.org/10.1063/1.5138764

14. Buonomo B, Cirillo L, Ercole D, Manca O, Nardini S. Numerical Investigation on Viscous Dissipation Effect in Forced Convection in Rectangular Microchannels With Nanofluids. ASME International Mechanical Engineering Congress and Exposition, Proceedings (IMECE) [Internet]. 2016 Nov 11; Available from:
https://doi.org/10.1115/imece2016-66189

15. Vasu V, Krishna KR, Kumar A. Thermal design analysis of compact heat exchanger using nanofluids. International Journal of Nanomanufacturing [Internet]. 2008 Jan 1;2(3):271. Available from: https://doi.org/10.1504/ijnm.2008.018949

16. Bianco V, Manca O, Nardini S, Vafai K. Heat Transfer Enhancement with Nanofluids [Internet]. CRC Press eBooks. 2015. Available from: https://doi.org/10.1201/b18324

17. Sidik NAC, Yazid MNAWM, Mamat R. Recent advancement of nanofluids in engine cooling system. Renewable & Sustainable Energy Reviews [Internet]. 2017 Aug 1;75:137–44. Available from: https://doi.org/10.1016/j.rser.2016.10.057

18. Subhedar D, Ramani BM, Gupta AK. Experimental investigation of overall heat transfer coefficient of Al_2O_3/Water-Mono ethylene glycol nanofluids in an automotive radiator. Heat Transfer [Internet]. 2016 Oct 4;46(7):863–77. Available from: https://doi.org/10.1002/htj.21247

19. Saidur R, Leong KY, Mohammad H. A review on applications and challenges of nanofluids. Renewable & Sustainable Energy Reviews [Internet]. 2011 Apr 1;15(3):1646–68.
Available from: https://doi.org/10.1016/j.rser.2010.11.035

20. Alawi OA, Sidik NAC, Beriache M. Applications of nanorefrigerant and nanolubricants in refrigeration, air-conditioning and heat pump systems: A review. International Communications in Heat and Mass Transfer [Internet]. 2015 Nov 1;68:91–7. Available from: https://doi.org/10.1016/j.icheatmasstransfer.2015.08.014

21. Nair V, Parekh AD, Tailor PR. Water-based Al2O3, CuO and TiO2 nanofluids as secondary fluids for refrigeration systems: a thermal conductivity study. Journal of the Brazilian Society of Mechanical Sciences and Engineering [Internet]. 2018 Apr 25;40(5). Available from: https://doi.org/10.1007/s40430-018-1177-6

22. Yang L, Du K. An optimizing method for preparing natural refrigerant: ammonia-water nanofluids. Integrated Ferroelectrics [Internet]. 2013 Jan 1;147(1):24–33. Available from:
https://doi.org/10.1080/10584587.2013.790278

23. Li Z, Renault FL, Gómez AOC, Sarafraz MM, Khan HMU, Safaei MR, et al. Nanofluids as secondary fluid in the refrigeration system: Experimental data, regression, ANFIS, and NN modeling. International Journal of Heat and Mass Transfer [Internet]. 2019 Dec 1;144:118635. Available from:
https://doi.org/10.1016/j.ijheatmasstransfer.2019.118635

24. Coumaressin T, Palaniradja K. Performance analysis of a refrigeration system using nano fluid. *International Journal of Advanced Mechanical Engineering*. 2014;4(4):459-70.

25. Anish M, Senthilkumar G, Beemkumar N, Kanimozhi S, Arunkumar T. Performance study of a domestic refrigerator using CuO/AL2O3-R22 nanorefrigerant as a working fluid. International Journal of Ambient Energy [Internet]. 2018 Apr 7;41(2):152–6. Available from: https://doi.org/10.1080/01430750.2018.1451376

26. Bi S, Guo K, Liu Z, Wu J. Performance of a domestic refrigerator using TiO2-R600a nano-refrigerant as working fluid. Energy Conversion and Management [Internet]. 2011 Jan 1;52(1):733–7. Available from: https://doi.org/10.1016/j.enconman.2010.07.052

27. Kumar R, Singh J, Kundal P. Effect of CuO nanolubricant on compressor characteristics and performance of LPG based refrigeration cycle: experimental investigation. Heat and Mass Transfer [Internet]. 2017 Nov 29;54(5):1405–13.
Available from: https://doi.org/10.1007/s00231-017-2231-0

28. Alawi OA, Sidik NAC. Influence of particle concentration and temperature on the thermophysical properties of CuO/R134a nanorefrigerant. International Communications in Heat and Mass Transfer [Internet]. 2014 Nov 1;58:79–84. Available from:
https://doi.org/10.1016/j.icheatmasstransfer.2014.08.038

29. Said Z, Saidur R, Hepbaşlı A, Rahim NA. New thermophysical properties of water based TiO2 nanofluid—The hysteresis phenomenon revisited. International Communications in Heat and Mass Transfer [Internet]. 2014 Nov 1;58:85–95. Available from:
https://doi.org/10.1016/j.icheatmasstransfer.2014.08.034

30. James Clark Maxwell, A Treatise on Electricity and Magnetism, Unabridged, Dover,1954.

31. Hamilton R, Crosser OK. Thermal conductivity of heterogeneous Two-Component systems. Industrial & Engineering Chemistry Fundamentals [Internet]. 1962 Aug 1;1(3):187–91. Available from: https://doi.org/10.1021/i160003a005

Anirudh Katoch, Fadil Abdul Razak, Arjun Suresh, Baiju S. Bibin, Adriana R. Farina, Luca Cirillo, Arkadiusz Mystkowski, Kamil Śmierciew, Adam Dudar, Edison Gundabattini

Performance Estimation of Blended Nano-Refrigerants' Thermodynamic Characteristics and Refrigeration Efficacy

DOI 10.2478/ama-2024-0031

32. Yu W, Choi SJ. The role of interfacial layers in the enhanced thermal conductivity of nanofluids: a renovated Maxwell model. Journal of Nanoparticle Research [Internet]. 2003 Apr 1;5(1/2):167–71. Available from: https://doi.org/10.1023/a:1024438603801

33. Koo J, Kleinstreuer C. A new thermal conductivity model for nanofluids. Journal of Nanoparticle Research [Internet]. 2004 Dec 1;6(6):577–88. Available from: https://doi.org/10.1007/s11051-004-3170-5

34. Gherasim I, Roy G, Nguyen CT, Vo-Ngoc D. Experimental investigation of nanofluids in confined laminar radial flows. International Journal of Thermal Sciences [Internet]. 2009 Aug 1;48(8):1486–93. Available from: https://doi.org/10.1016/j.ijthermalsci.2009.01.008

35. Ghasemi B, Aminossadati SM. Brownian motion of nanoparticles in a triangular enclosure with natural convection. International Journal of Thermal Sciences [Internet]. 2010 Jun 1;49(6):931–40. Available from: https://doi.org/10.1016/j.ijthermalsci.2009.12.017

36. Zhang M, Wang RX, Lou JF. Actuality and Application foreground of nanofluids in refrigeration system. Materials Science Forum [Internet]. 2011 Jul 1;694:261–5. Available from:
https://doi.org/10.4028/www.scientific.net/msf.694.261

37. Leo Ng (2021). Refrigeration Cycle in Simscape (https://www.mathworks.com/matlabcentral /fileexchange /46448-refrigeration-cycle-in-simscape), MATLAB Central File Exchange. Retrieved April 18, 2021.

38. Yao S, Teng Z. Effect of nanofluids on boiling heat transfer performance. Applied Sciences [Internet]. 2019 Jul 15;9(14):2818. Available from: https://doi.org/10.3390/app9142818

39. Leo Ng (2021). Refrigeration Cycle in Simscape (https://www.mathworks.com/matlabcentral /fileexchange /46448-refrigeration-cycle-in-simscape), MATLAB Central File Exchange.Retrieved April 18, 2021.

40. Tsvetkov OB, Laptev YuA, Asambaev AG. Thermal conductivity of refrigerants R123, R134a, and R125 at low temperatures. International Journal of Thermophysics [Internet]. 1994 Mar 1;15(2):203–14. Available from: https://doi.org/10.1007/bf01441582

41. Mahdi QS, Theeb MA, Saed H. Enhancement on the performance of refrigeration system using the Nano-Refrigerant. Journal of Energy and Power Engineering [Internet]. 2017 Apr 28;11(4). Available from: https://doi.org/10.17265/1934-8975/2017.04.004

42. Anderson A, Brindhadevi K, Salmen SH, Alahmadi TA, Maroušková A, Sangeetha M, et al. Effects of nanofluids on the photovoltaic thermal system for hydrogen production via electrolysis process. International Journal of Hydrogen Energy [Internet]. 2022 Oct 1; 47(88):37183–91.
Available from: https://doi.org/10.1016/j.ijhydene.2021.12.218

43. Shen T, Xie H, Gavurová B, Sangeetha M, Karthikeyan C, Praveenkumar TR, et al. Experimental analysis of photovoltaic thermal system assisted with nanofluids for efficient electrical performance and hydrogen production through electrolysis. International Journal of Hydrogen Energy [Internet]. 2023 Jun 1;48(55):21029–37. Available from: https://doi.org/10.1016/j.ijhydene.2022.12.079

44. Senthilkumar A, Sahaluddeen PAM, Noushad MN, Musthafa EKM. Experimental investigation of ZnO / Sio2 hybrid nano-lubricant in R600a vapour compression refrigeration system. Materials Today: Proceedings [Internet]. 2021 Jan 1;45:6087–93. Available from: https://doi.org/10.1016/j.matpr.2020.10.180

45. Bibin BS, Gundabattini E. Investigation on transport properties, heat transfer characteristics and pressure drop of CuO enhanced R1234yf based refrigerant. Case Studies in Thermal Engineering [Internet]. 2023 Sep 1;49:103229.
Available from: https://doi.org/10.1016/j.csite.2023.103229

46. Bibin BS, Gundabattini E. Pressure drop and heat transfer Characteristics of TIO2/R1234YF Nanorefrigerant: A Numerical approach. Sustainability [Internet]. 2023 Aug 20;15(16):12605. Available from: https://doi.org/10.3390/su151612605

Anirudh Katoch: https://orcid.org/0009-0006-9706-6322

Fadil Abdul Razak: https://orcid.org/0009-0009-9718-5753

Arjun Suresh: https://orcid.org/0000-0002-5321-5799

Baiju S. Bibin: https://orcid.org/0000-0002-9142-5068

Adriana R. Farina: https://orcid.org/0000-0001-8951-4267

Luca Cirillo: https://orcid.org/0000-0002-8705-8912

Arkadiusz Mystkowski: https://orcid.org/0000-0002-5742-7609

Kamil Śmierciew: https://orcid.org/0000-0001-6482-770X

Adam Dudar: https://orcid.org/0000-0001-6585-1795

Edison Gundabattini: https://orcid.org/0000-0003-4217-2321

LABORATORY TESTING AND MODELLING
OF MAGNETORHEOLOGICAL ELASTOMERS IN TENSION MODE

Denys GUTENKO[*] , **Paweł ORKISZ**[**] , **Bogdan SAPIŃSKI**[**]

[*] Faculty of Electrical and Computer Engineering, Department of Automatics and Computer Science,
Cracow University of Technology, Warszawska 24, 31-155, Krakow, Poland
[**] Faculty of Mechanical Engineering and Robotics, Department of Process Control,
AGH University of Krakow, Mickiewicza 30 av., 30-059 Krakow, Poland

denys.gutenko@doktorant.pk.edu.pl, orkisz@agh.edu.pl, deep@agh.edu.pl

Abstract: The study deals with experimental testing and estimating the modified Dahl model parameters of magnetorheological elastomers (MREs) differing in volumetric concentrations of carbonyl iron particles (CIP). The authors present briefly an overview of scientific reports relating to MREs research. Next, they describe the structure and magnetic properties of two fabricated MREs, which were investigated using a scanning electron microscope, a magnetometer and a gaussmeter. Then, they reveal the structure of a specially engineered test rig for materials sample examination and present a scenario of experiments. Next, the test results of the material's mechanical properties conducted in the absence and presence of a magnetic field were discussed. Then, they describe a modified Dahl model of the material followed by parameters estimation and validation procedure. Finally, the authors summarise the test results and outline further research steps.

Key words: magnetorheological elastomer, modified Dahl model, magnetic field, force, displacement, stiffness, estimation, parameter

1. INTRODUCTION

Among the so-called smart materials, one special place is occupied by magnetorheological materials such as fluids, elastomers and foams. Magnetorheological elastomers (MREs) possess field-dependent characteristics that allow them to be used in various application areas, including vibration isolators [1,2], soft robots [3], sensors [4], and so on. That is why, in recent years, research interests in MREs have grown rapidly. The studies have been focused on the material structure of the MREs, their field-dependent characteristics, operating modes and applications. By principle, the MREs are composed of magnetic particles in a non-magnetic elastic matrix. In addition to that, MRE formulations feature additives to affect their properties. For example, the addition of graphene oxide decreases their compressive modulus [5], and silane coupling agents lead to a more uniform distribution of magnetic particles in the matrix [6]. Another problem refers to the influence of particles' parameters, such as the shape [7,8], volume fraction [9] and particle size [10]. Moreover, MREs exhibit either isotropic or anisotropic structures depending on the manufacturing method. With the isotropic MREs, magnetic particles are arranged randomly. For comparison, the anisotropic MRE samples are seasoned in the presence of a magnetic field which leads to the formation of chains of magnetic particles aligned in the direction of the field. After the material hardens, the position of the particles is fixed, which causes these chains to remain in place. As such, anisotropic MREs exhibit different behaviours depending on the direction of the acting forces. Therefore, the influence of anisotropy remains a challenge [11]. The studies of MRE properties refer mainly to the influence of the magnetic field level on various mate-

rial parameters, for example, permeability [12,13], stick-slip effect [14] and durability [15].

MREs can be operated in at least one of the following modes: shear, squeeze (stretch) and active field. The mentioned modes are described in detail in Li et al. [16]. A number of studies involve the shear mode [17–22]; however, less attention has been paid to the field active mode [23] and the squeeze mode [24]. An important part of the research studies is modelling the MREs behaviour when exposed to magnetic fields. Such studies have been carried out using microscale models [7,22,25,26], phenomenological models [27] or hybrid models [20]. Most research workers use the following models: Kelvin–Voigt [24], Bouc–Wen [18,19,28], Dahl [27], LuGre [2], the four-parameter model [29] and their modifications.

The present study addresses the experimental tests of MREs and a new estimation procedure of the modified Dahl model parameters of the materials. The proposed procedure can be useful in the simulation of mechatronic systems considering MREs. To achieve that, two MREs with different volumetric concentrations of carbonyl iron particles (CIP) were fabricated, an original test rig was assembled and an assumed scenario of experiments was implemented.

The paper is structured as follows. In Section 2 the authors reveal the structure of the MRE samples and characterise their magnetic properties. Section 3 highlights the preparation of the MRE samples, describes the test rig experiment and discusses the materials' test results. Section 4 describes the modified Dahl model for representing the behaviour of MREs in the presence of magnetic fields and reveals the model parameter estimation procedure. Finally, conclusions are provided in Section 5.

2. STRUCTURE AND MAGNETIC PROPERTIES OF MATERIALS

To fabricate the two MRE samples, two basic components, CIP and Ecoflex 00-10 silicone rubber (platinum-catalysed silicon), were mixed thoroughly. Next, an attempt was made to remove the air bubbles using an ultrasonic homogeniser mixer. The degassed material was cured without a magnetic field at ambient temperature. The concentration of CIP by volume in the materials is appr. 26% (sample S1) and 30% (sample S2), respectively, similar to that suggested in Bastola and Hossain [17]. Both fabricated materials are isotropic.

The samples S1 and S2 were examined under the Versa 3D scanning electron microscope [30]. Particle morphology observations were recorded using a secondary electron detector. Since the samples are non-conductive materials, the measurements were made in the low vacuum mode, and steam was used as the gas. The operating parameters of the microscope were as follows: level of voltage for accelerating the electron beam at $17\,\mathrm{kV}$, electron beam diameter (spot size) at 4.5 nm and water vapour pressure of 90 Pa. The microscope images showing the structures of the samples S1 and S2 are revealed in Fig. 1. It can be seen that in both cases, the magnetic particles are evenly distributed inside the elastic matrix, sometimes grouped into small clusters. Note that the structure of the samples contains a small air bubble not removed by the degassing procedure; see the detail marked in Fig. 1.
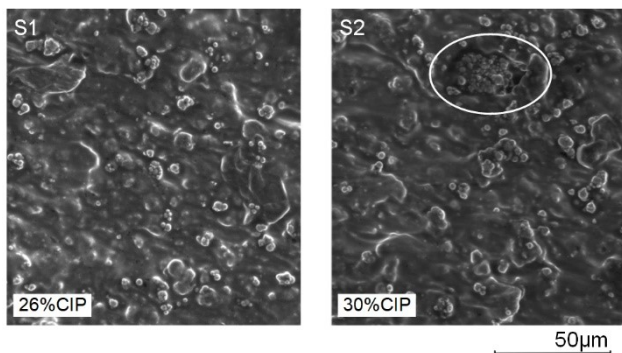
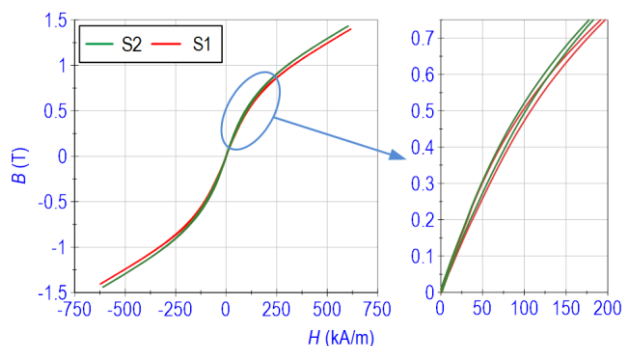**Fig. 1.** Microscope images of samples: S1 and S2

Fig. 2. Magnetic flux density B vs magnetic field strength H

Next, the magnetic tests of the samples, S1 and S2 ($3\,\mathrm{mm}\times 3\,\mathrm{mm}$), were carried out using a LakeShore 7400 series vibrating sample magnetometer (VSM) [31] at two temperature levels: $0°C$ and $25°C$. The temperature has no effect on the magnetisation

curves (within the examined range). Fig. 2 shows the obtained magnetisation curves $B(H)$ for both samples. The hysteresis width is equal for both samples but the curves differ slightly (see the zoomed-in section in Fig. 2).

3. TESTING OF MATERIALS

The purpose of the material tests was to determine the relationship between their mechanical properties and the external stimuli affecting them. The tests of the MRE samples were carried out according to the diagram in Fig. 3a. Similar to the material in Section 2, we use the designations S1 and S2 to distinguish the MREs with differing concentrations of CIP by volume. The samples S1/S2 were placed between the movable platform and the force sensor (FS) to measure the displacement z and the resulting force F_m. Fig. 3b presents the sketch of the tested sample (4) with purpose-designed handles. It can be seen that the opposing surfaces of the sample were fixed to the handles using the cyanoacrylate glue layer (3). The handle consists of the plastic base (2), the nut (5) and the retaining screw (1). Fig. 3b also shows the dimensions of the fabricated sample and those of the handles.
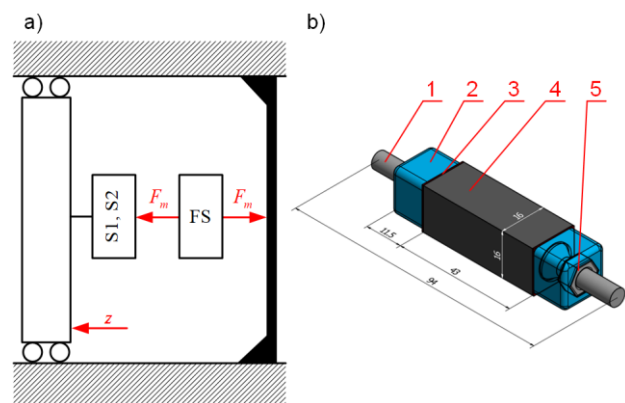

Fig. 3. MRE testing concept: (a) schematic diagram of the test rig concept, (b) MRE sample with handles

3.1. Preparation of samples

The samples were tested in the absence and presence of a magnetic field induced by NdFeB N38 neodymium magnets. Due to the installation of the permanent magnets, the plastic housing was designed and 3D printed. The housing was attached to the upper plastic base (see component 2 in Fig. 3b) using four screws. Fig. 4a,b shows the magnet housing view and its dimensions, respectively. The size of the housing (1) allows for an air gap of 0.5 mm between the sample (3) and the housing. Additionally, the housing ensures that the two magnets (2) can be placed symmetrically on the sample's opposite surfaces. Both magnets were of cylindrical shape and axially magnetised. The dimensions of the magnets are provided in Fig. 4b.

The testing of the samples (S1 and S2) was preceded by determining the magnetic flux density distribution in their surrounding using the Finite Element Method Magnetics package (FEMM) [32]. The simulations were conducted in a cartesian coordinate system, taking into account the measured non-linear magnetisation curves shown in Fig. 2. The magnet housing (1) (see Fig. 4a) and the

plastic base (2) (see Fig. 3b) were made using non-magnetic PLA filament, and their magnetisation characteristics were those of air. The retaining screw (1) (see Fig. 3b) was modelled using the stainless steel 316 material characteristics, while the magnets (2) (see Fig. 4a) were modelled by means of the N30 material B-H curve, assuming a coercivity of 686.4 kA/m. The planar model depth was equal to 15 mm.
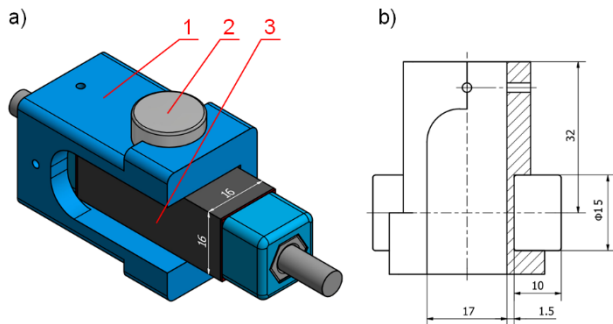

Fig. 4. Magnet housing: (a) view, (b) cross-section

Taking into account the designations B_x and B_y of the magnetic flux density components, the resultant magnetic flux density B can be expressed as:

$$B = \sqrt{B_x{}^2 + B_y{}^2} \qquad (1)$$

The distribution of magnetic flux density B in the sample S1 is illustrated in Fig. 5. It can be seen that the lines of magnetic flux density were deformed to a small extent by the MRE sample.
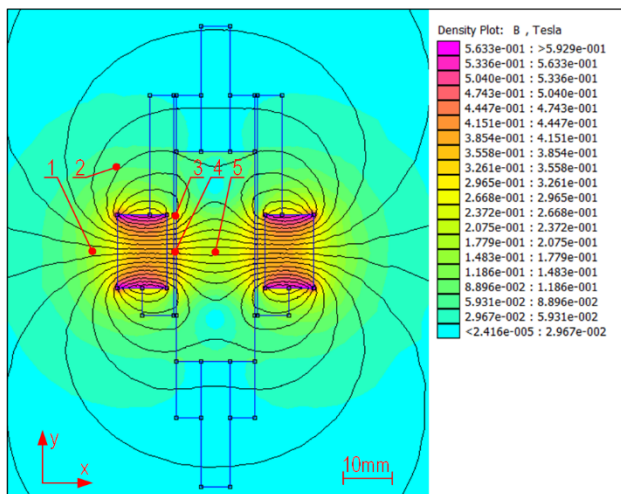
Fig. 5. Distribution of magnetic flux density B: sample S1

The values of B_x and B_y were interpreted at five points marked in Fig. 5 by the numbers 1, 2, 3, 4 and 5 and are provided in Tab. 1 for the samples S1 and S2 in columns 2 and 3. Accordingly, the numbers in column 4 were obtained by measuring the sample S1 using the gaussmeter GM2 [33] with a standard Hall probe.

Points 1 and 2 were selected only for verification purposes, whereas points 3 and 4 can be used for interpreting the values of magnetic flux density near the left magnet's housing wall. Point 5

is located in the sample's centre. The test results provided in Tab. 1 for the samples S1 and S2 are similar. Considering the values in the blue cells, the authors drew the following conclusions. Due to the limitations of the FEMM package and the cylindrical shape of the employed magnets, the best correlation between the simulation results and the test data was achieved at points 1,4 and 5. In the worst cases, the differences occurring at points 2 and 3 do not exceed 48 mT.

Tab. 1. Components B_x and B_y at the selected measurement points

Point no.	FEMM, S1 mT		FEMM, S2 mT		GM2, S1 mT	
	B_x	B_y	B_x	B_y	B_x	B_y
1	175	−2	176	−2	175	-
2	−53	−63	−54	−64	-	−32
3	136	125	138	120	185	-
4	361	0	366	0	370	-
5	219	0	220	0	183	-

"-" no space available for measurements

3.2. Test rig

For further examinations of the samples, a special test rig was assembled (see Fig. 6). In the rig, two main modules can be distinguished: the mechanical rig and the electrical module (actuation). The mechanical rig consists of an aluminium frame (10) and linear guides along which three movable platforms move. The vibration shaker platform (3) was used for generating the excitation (displacement) z using the electrodynamic linear LA30 motor (2) [34]. The middle platform (9) was fixed and was used only to eliminate the clearance directly upon the assembly of the tested sample. Platform (11) was not utilised in the test program.
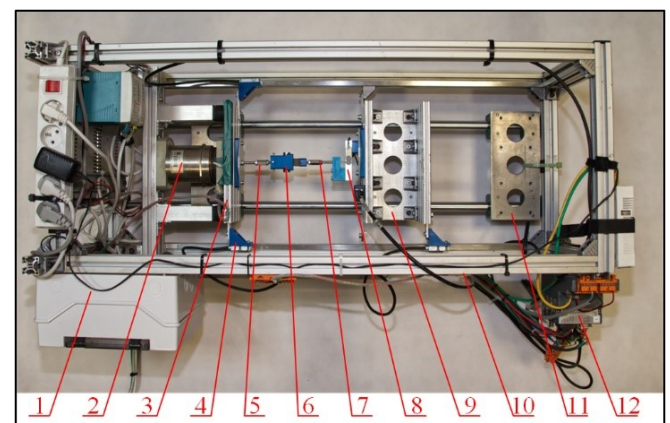

Fig. 6. View of the test rig

The electrical module of the rig was composed of the power supply unit (1), the cRIO 9063 controller (12) [35], the personal computer and the three dedicated measurement boards connected with the following components:
- NI-9505 motor drive module to generate the displacement z;
- NI 9237 strain full bridge input module to measure the force F_m using the NA27 strain gauge beam (8) calibrated within the range of ± 10N and attached to the fixed platform;

− NI-9215 analogue input module to measure the displacement z using the linear encoder (4) [36].

The architecture of the control software developed in the LabVIEW environment is described in Snamina and Orkisz [37]. The tested sample with the magnet handle (see Fig. 4a and component 6 in Fig. 6) was equipped with the fixtures (5) and (7), and mounted between the shaker platform and the strain gauge beam.

3.3. Scenario of tests

The tests were split into two stages. In the first stage, the authors measured the response of the samples subjected to static excitations. First, the samples were excited sinusoidally using an amplitude of $A_z = 3$ mm and at a frequency of $f = 0.1$ Hz. Next, the authors measured the response of the samples to dynamic excitations. The samples were excited sinusoidally at three different amplitude levels: A_z 0.4 mm, 0.6 mm and 0.8 mm, and the frequency of the sinewave was slowly increased from 0.3 Hz to 10 Hz. The tests were carried out at a temperature of 25°C. The sampling frequency was $f_p = 4$ kHz..

Due to the high sampling frequency, the test results were filtered using a moving average filter (the window width was 20 samples). The precision of the displacement measurements expressed with the standard deviation value of the displacement z was $2.88 \cdot 10^{-4}$ mm and the standard deviation value of the measured force F_m was $1.85 \cdot 10^{-3}$ N. The tests were implemented several times for each sample, taking into account the influence of the magnetic field and the input displacement amplitude A_z.

To simplify the interpretation of the test results, the authors introduced the following designation $SX_{A_z}^{MY}$ where X refers to the sample number, A_z denotes the displacement amplitude and MY refers to the level of magnetic field; $Y = 0$ – no magnetic field and $Y = 1$ – magnetic field applied.

3.4. Results and discussion

The results of the static tests were obtained by recording the behaviour of the samples during five 10-second excitation cycles. Fig. 7 shows exemplary time patterns of the displacement z and the force F_m for the sample S1 in the cases M0 and M1. Next, the recorded results were used to determine the force–displacement loops $F_m(z)$ shown for the sample S1 in Fig. 8 and for the sample S2 in Fig. 9.
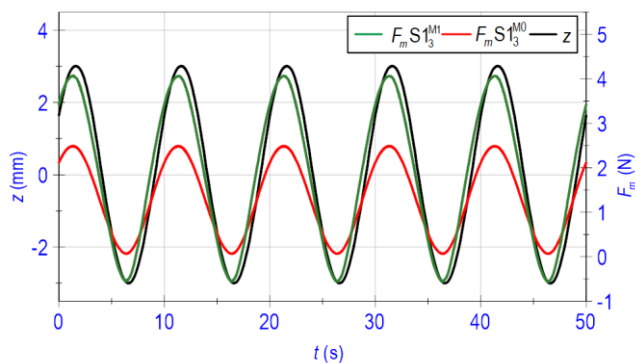

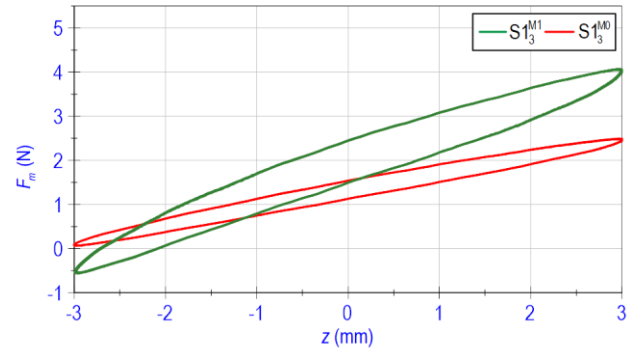**Fig. 7.** Time histories of displacement z and force F_m: sample S1

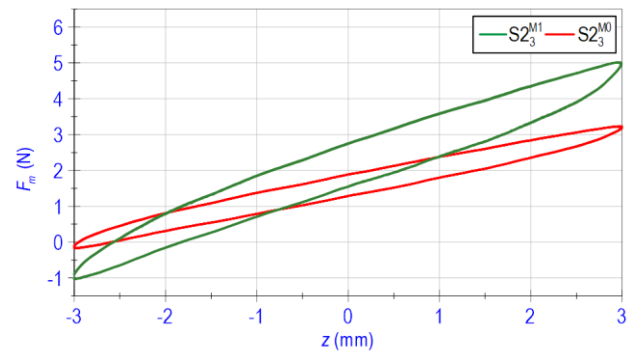**Fig. 8.** Force F_m vs displacement z: sample S1

Fig. 9. Force F_m vs displacement z: sample S2

Taking into account the plots in Figs. 8 and 9, the length of the sample $d = 43$ mm and the cross-sectional area of the sample $a_s = 256$ mm^2, the sample deformation ε_s expressed in percents was calculated as follows:

$$\varepsilon_s = \frac{z + max(z)}{d} \cdot 100 \qquad (2)$$

while the tensile stress σ_s was computed according to the following formula:

$$\sigma_s = \frac{F_m}{a_s} \qquad (3)$$

The equivalent stiffness coefficient k_s was then calculated as:

$$k_s = \frac{A_{Fm}}{A_z} \qquad (4)$$

where A_{F_m} is the force amplitude and A_z is the displacement amplitude. Similarly, the equivalent damping coefficient c_s was calculated as follows:

$$c_s = \frac{A_{Fm}}{A_{\dot{z}}} \qquad (5)$$

where $A_{\dot{z}}$ refers to the velocity amplitude. The value of the hysteresis coefficient h_s was calculated using the formula:

$$h_s = 0.5 \cdot \left[F_m\left(z_0^\uparrow\right) - F_m\left(z_0^\downarrow\right) \right] \qquad (6)$$

where $F_m\left(z_0^\uparrow\right)$ is the force registered for the increasing displacement z at the value of 0 mm and $F_m\left(z_0^\downarrow\right)$ refers to force registered for the decreasing displacement z at the same value.

Tab. 2. Test results

Sample no.	Range of ε_s %	Range of σ_s kPa	k_s N/mm	c_s N·s/mm	h_s N
$S1_3^{M0}$	0, 13.95	0.27, 9.70	0.40	0.64	0.205
$S1_3^{M1}$	0, 13.95	−2.10, 15.87	0.77	1.23	0.475
$S2_3^{M0}$	0, 13.95	−0.64, 12.65	0.57	0.91	0.300
$S2_3^{M1}$	0, 13.95	−4.00, 19.58	1.01	1.61	0.600

The results obtained using the assumed excitations are provided in Tab. 2. In each case, the values of the sample deformations ε vary within the range from 0% to 13.95%. The value of the tensile stress σ_s does not exceed 20 kPa. The equivalent stiffness coefficient k_s, the equivalent damping coefficient c_s and the hysteresis coefficient h_s depend on the magnetic flux density level and the CIP volume. The higher CIP content sample is characterised by a greater increase of the equivalent stiffness coefficient, the equivalent damping coefficient as well as the higher value of the hysteresis coefficient h_s.

The results also revealed the effect of long-term exposure of the samples to the magnetic field (residual magnetism). For the sample subjected to magnetic field for at least 6 h, regardless of the displacement z, a constant increase in the force F_m of 0.15 N was observed. The data provided in Tab. 2 relate to the behaviour of the samples subjected to constant amplitude and constant frequency excitations. Considering the non-linear nature of the MREs, dynamic tests were conducted under sinusoidal excitations of the amplitudes A_z of 0.4 mm, 0.6 mm and 0.8 mm. The plot of the equivalent stiffness coefficient k_s versus the frequency f was adopted, following formula (3) and taking into account that the ratio of A_{F_m} to A_z was dependent on the excitation frequency. Fig. 10 shows the test results for the sample S1 and Fig. 11 reveals the data obtained for the sample S2.
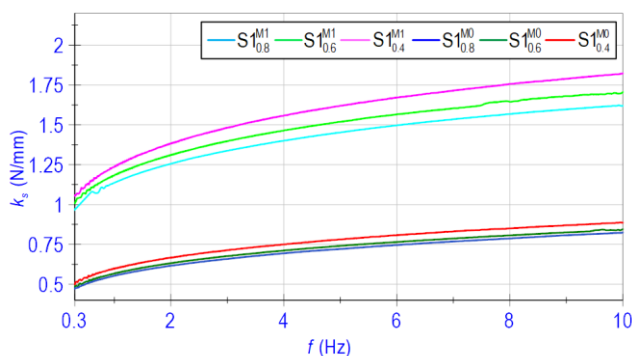

Fig. 10. Equivalent stiffness coefficient k_s versus frequency f: sample S1

The results reveal, on one hand, that an increase in the frequency f results in an increase in the equivalent stiffness coefficient k_s. On the other hand, the increase in amplitude A_z causes a decrease in the coefficient k_s. Next, Tab. 3 provides the impact of the concentrations of CIP by volume on the coefficient k_s, and Fig. 12 shows the comparison between the coefficient k_s values obtained for both samples. The parameter k_d^{M0} in Tab. 3 designates the differences between the values of k_s in the case of $S2_{0.4}^{M0}$ and $S1_{0.4}^{M0}$, while the k_d^{M1} designates the differences between

the values of k_s in the case of $S2_{0.4}^{M1}$ and $S1_{0.4}^{M1}$. It is apparent that the values of k_d^{M0} and k_d^{M1} were nearly equal at frequencies above 3 Hz. Therefore, the differences between the values of the stiffness coefficient k_s for the samples S1 and S2 depend mostly on the magnetic field level and to a slight extent on the volume of CIP particles.
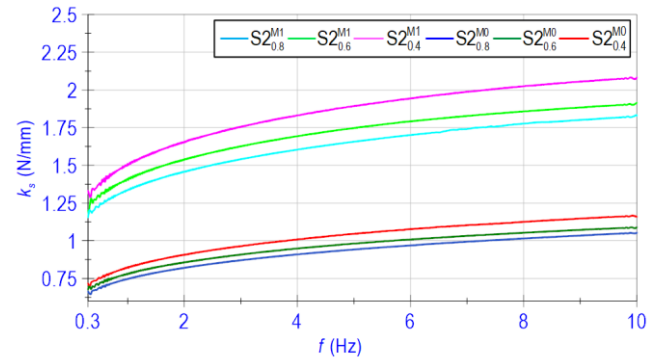

Fig. 11. Equivalent stiffness coefficient k_s versus frequency f: sample S2

Tab. 3. Equivalent stiffness coefficient versus frequency

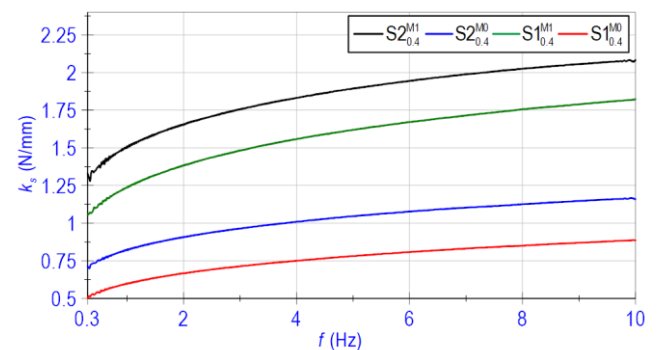| Freq. f Hz	$k_s S1_{0.}^{M}$ N/mm	$k_s S2_{0.4}^{M0}$ N/mm	k_d^{M0} N/mm	$k_s S1_{0.4}^{M1}$ N/mm	$k_s S2_{0.4}^{M1}$ N/mm	k_d^{M1} N/mm
1	0.60	0.83	0.23	1.24	1.50	0.26
3	0.71	0.96	0.25	1.48	1.76	0.28
5	0.78	1.05	0.27	1.62	1.89	0.27
7	0.83	1.11	0.28	1.71	1.99	0.28
9	0.87	1.15	0.28	1.79	2.06	0.27

Fig. 12. Equivalent stiffness coefficient k_s versus frequency f: samples S1, S2

4. MODIFIED DAHL MODEL OF MATERIALS

Most parametric models in field-dependent behaviour of MREs are based on Kelvin–Voigt, Bouc–Wen, Dahl, LuGre and four-parameter viscoelastic models. Among the models that concern the description of the hysteresis phenomenon, the Dahl model considers fewer parameters whose values must be estimated, making it computationally more efficient. In this work, the authors select for analysis the modified Dahl model with the structure shown in Fig. 13.
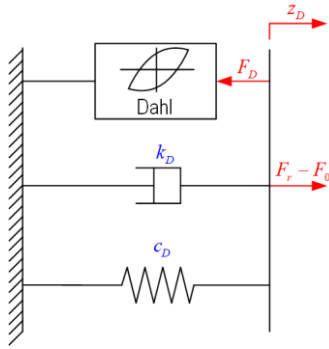
Fig. 13. Structure of the modified Dahl model

The model can be described as follows:

$$F_r = F_D + c_D \dot{z}_D + k_D z_D + F_0 \qquad (7)$$

where z_D is the displacement, c_D denotes the damping coefficient and k_D refers to the stiffness coefficient. As it can be seen, the force F_r incorporates four components, namely the Dahl model friction force F_D, the viscous force $c_D \dot{z}$, the spring force $k_D z$ and offset in the force F_0. The component F_D is expressed using the following formula:

$$\frac{\partial F_D}{\partial z_D} = \sigma \left[1 - \frac{F_D}{h_D} sgn\left(\frac{dz_D}{dt}\right) \right]^b \qquad (8)$$

where σ represents the Dahl's model stiffness coefficient, b describes the shape of the stress–strain curve and h_D is the Coulomb friction force. Assuming that $\rho = \frac{\sigma}{h_D}$, $r = F_D/h_D$ and $b = 1$ [38], equation (8) can be rewritten as:

$$\dot{r} = \rho(\dot{z}_D - r|\dot{z}_D|) \qquad (9)$$

Let us consider that displacement z_D varies sinusoidally with the amplitude A_{zD} and frequency f_{zD} in one cycle:

$$z_D(t) = -A_{zD} \cdot cos(2\pi f_{zD} t) \qquad (10)$$

Then, in the first half of the displacement cycle period, the value of z_D increases from $-A_{zD}$ to A_{zD}, whereas in the second half of the period this value decreases. Following Eq. (10), the velocity takes the form:

$$v_D(t) = 2\pi f_{zD} A_{zD} sin(2\pi f_{zD} t) \qquad (11)$$

Combining Eqs (7, 9–11), the modified Dahl model can be written as:

$$\begin{cases} F_r(t) = h_D r + c_D v_D(t) + k_D z_D(t) + F_0 \\ \dot{r}(t) = \rho(v_D(t) - r|v_D(t)|) \end{cases} \qquad (12)$$

It is evident then that the model contains seven parameters $(k_D, c_D, h_D, \rho, A_{zD}, f_{zD}, F_0)$. Three of them, A_{zD}, f_{zD} and F_0, may be determined directly from the test results, whereas the remaining parameters have to be estimated. Designating the sampling time by t_{pr}, the number of samples can be calculated according to:

$$n = \frac{1}{f_{zD} t_{pr}} \qquad (13)$$

Using Eq. (12) in the simulations, the authors assumed the constant sampling time t_{pr}, and the initial condition $r(0) = -1$. The initial condition estimate was set to avoid initial errors and improve the calculations' accuracy.

Considering the differences in the phase time pattern of the displacements $z(t)$ and $z_D(t)$, the authors proposed to correct the time shift of the displacement z and force F_m by the value of Δt_m. Introducing displacement $z_\Delta(t) = z(t - \Delta t_m)$ and force $F_{m\Delta}(t) = F_m(t - \Delta t_m)$ the accuracy of the modified Dahl model can be evaluated by the following quality factor:

$$J_e = \sqrt{\frac{1}{nt_{pr}} \int_0^{nt_{pr}} (F_r(t) - F_{m\Delta}(t))^2 dt} \qquad (14)$$

To achieve a better accuracy of the factor J_e, the scaling factor $s_c = 0.5(|\sin(2\pi f_{zD} t)| + 1)$ was used and then, the modified quality factor could be expressed as follows:

$$J_{es} = \sqrt{\frac{\int_0^{nt_{pr}} \left(0.5(|\sin(2\pi f_{zD} t)| + 1) \cdot (F_r(t) - F_{m\Delta}(t))^2\right) dt}{nt_{pr}}} \qquad (15)$$

Taking into account the shape of the relationship $F_{m\Delta}(z_\Delta)$, the benefit of the quality factor J_{es} is in reducing the weight factor for the samples located at the maximum and minimum values of the displacement z_Δ, respectively. Such modification yields an improved projection of the model on the test results.

4.1. Estimation procedure of model parameters

The proposed procedure for the estimation of the modified Dahl model parameters (see Fig. 14) consists of the following four stages:

Stage 1. Data import and estimation of parameters A_{zD}, f_{zD}, F_0, Δt_m. The stage consists of two steps.
− Step 1. Test results are imported considering the displacement z and the force F_m.
− Step 2. The A_{zD} is determined as $0.5 \cdot (max(z) - min(z))$, the f_{zD} is calculated using the autocorrelation function, Δt_m is estimated using the cross-correlation function taking into consideration the displacements $z(t)$ and $z_D(t)$, F_0 is computed by averaging $F_m(t)$ over one cycle.

Stage 2. Initial estimation of parameters k_D, c_D, h_D, ρ. The stage consists of three steps.
− Step 1. Parameter initialisation. The one hundred sets of the parameters k_D, c_D, h_D, ρ were randomly selected within the corresponding ranges: $k_D \in [0,1.2]$ N/mm , $c_D \in [0,1.8]$ N·s/mm , $h_D \in [0,0.7]$ N , $\rho \in [1,2]$ s/mm . The ranges of k_D, c_D and h_D are selected based on Tab. 2, whereas the range of the parameter ρ is selected in order to preserve the shape of $r(z_D)$.
− Step 2. Calculation of the force $F_r(t)$ and the quality factor J_{es} using previously generated sets of parameters.
− Step 3. Selection of the set of parameters for which the smallest value of the J_{es} factor was obtained. For further calculations, the selected set is referred to as S_b.

Stage 3. Improvement of parameter estimation. The stage consists of four steps.
− Step. 1 The parameter modification. Taking into account the set S_b, one to three of the parameters are randomly selected for modification. The modification considers random changes of the parameter value varying from 0 to twice its obtained value.
− Step 2. Calculation of the force $F_r(t)$ and the quality factor J_{es}

based on the formerly modified parameters.

− Step 3. Selection of the best-fitted set of parameters. If the value of J_{es} calculated for the set of modified parameters is less than the factor J_{es} calculated for the set S_b, then the modified set of parameters is considered as the new set S_b.

− Step 4. Steps 1–3 are repeated 10^5 times.

Stage 4. Non-linear least-squares method application. The stage consists of two steps.

− Step 1. The parameter set S_b is used as an initial condition in the lsqcurvefit function in MATLAB to calculate the modified set of parameters.

− Step 2 If the value of the quality factor J_{es} determined for the set of parameters in Step 1 is smaller than the value obtained for the set S_b, then Stage 4 should be skipped.
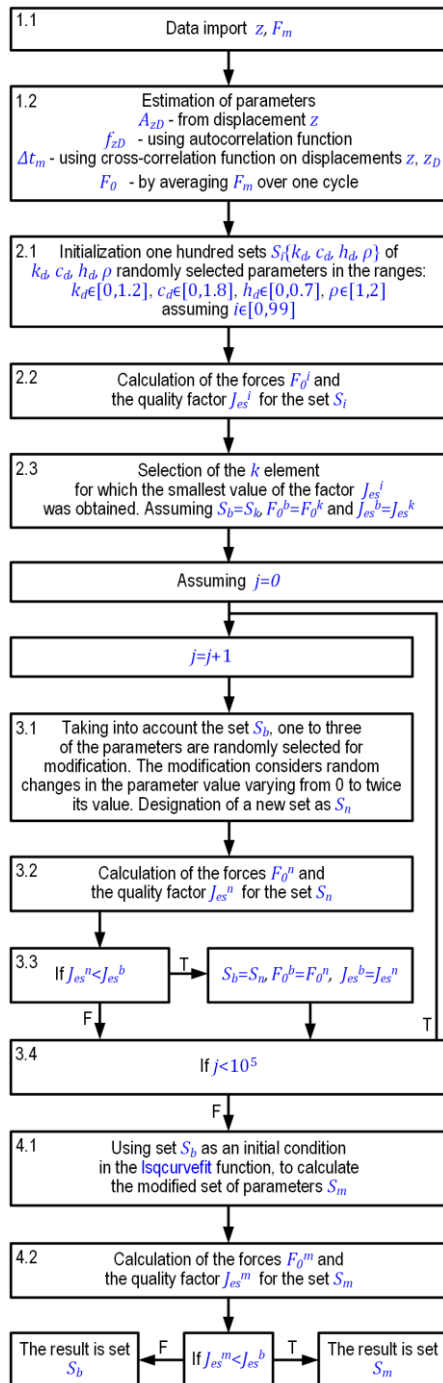

Fig. 14. Block diagram of the estimation procedure

4.2. Validation of procedure

The procedure elaborated in Subsection 4.1 was validated by comparing the simulation data obtained with the model against the test results.

The input to the procedure was the time patterns of the displacement z and force F_m registered for the sample $S1_3$ (see Fig. 7). Two cases were considered, M0 and M1, which refer to both the absence and presence of the magnetic field. The procedure was repeated 10 times for both cases.

The validation results are shown in the form of force–displacement loops (see Figs. 15,16). In addition to that, in Tab. 4 the authors provide the calculated values (averaged over the set of realisations) to summarise each stage of the procedure.
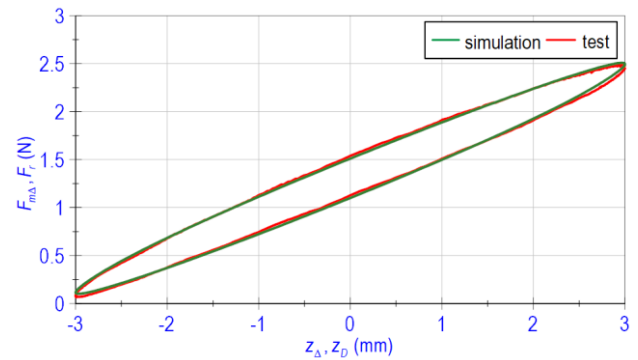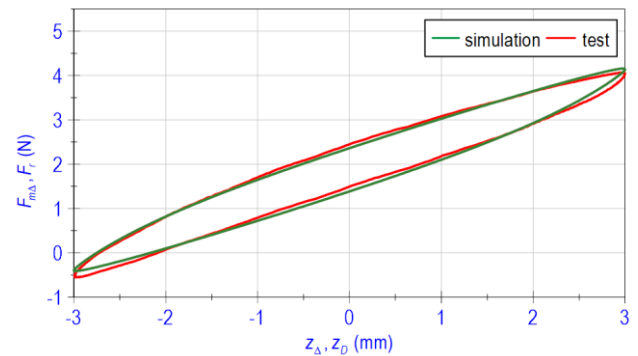

Fig. 15. Validation of the model: $S1_3^{M0}$

Fig. 16. Validation of the model: $S1_3^{M1}$

Tab. 4. Parameter estimates: sample $S1_3$

Stage no.	Model parameters	Quality factors
	Case M0	
1	$A_{zD} = 3.01$ mm, $f_{zD} = 0.099$ Hz, $F_0 = 1.3$ N, $\Delta t_m = 6.63$ s.	-
2	$k_D = 0.3494$ N/mm, $c_D = 0.0811$ N·s/mm, $h_D = 0.1972$ N, $\rho = 1.59$ s/mm.	$J_e = 0.20002$ N, $J_{es} = 0.16608$ N.
3	$k_D = 0.3819$ N/mm, $c_D = 0.0886$ N·s/mm, $h_D = 0.0409$ N, $\rho = 1.46$ s/mm.	$J_e = 0.01673$ N, $J_{es} = 0.01351$ N.

Denys Gutenko, Paweł Orkisz, Bogdan Sapiński
Laboratory Testing and Modelling of Magnetorheological Elastomers in Tension Mode

DOI 10.2478/ama-2024-0032

4	$k_D = 0.3834$ N/mm, $c_D = 0.0912$ N·s/mm, $h_D = 0.0353$ N, $\rho = 1.46$ s/mm.	$J_e = 0.01666$ N, $J_{es} = 0.01345$ N.
Case M1		
1	$A_{zD} = 2.99$ mm, $f_{zD} = 0.1$ Hz, $F_0 = 1.85$ N, $\Delta t_m = 6.64$ s.	-
2	$k_D = 0.6602$ N/mm, $c_D = 0.1130$ N·s/mm, $h_D = 0.2906$ N, $\rho = 1.41$ s/mm.	$J_e = 0.14802$ N, $J_{es} = 0.11682$ N.
3	$k_D = 0.6784$ N/mm, $c_D = 0.1343$ N·s/mm, $h_D = 0.2372$ N, $\rho = 1.46$ s/mm.	$J_e = 0.06506$ N, $J_{es} = 0.05300$ N.
4	$k_D = 0.6797$ N/mm, $c_D = 0.1374$ N·s/mm, $h_D = 0.2309$ N, $\rho = 1.44$ s/mm.	$J_e = 0.06511$ N, $J_{es} = 0.05296$ N.

The comparison of the plots in Figs. 15,16 shows that a good agreement was achieved between the simulation data and the test results. Some insignificant inaccuracies could be observed only for the values of the force F_r which relate to the maximal and minimal values of the displacement z_D. The best-fitted parameter set of the model is marked in blue in Tab. 4. It is apparent that the values of the quality factors J_e and J_{es} took a less and less value at each stage, which confirms the accuracy of the estimation procedure. Moreover, the values of the parameters A_{zD} and f_{zD}, correspond to the values of A_z and f obtained from the tests. It can be seen that when comparing the case M1 against the case M0, the values of the stiffness coefficient k_D and the damping coefficient c_D increase by 0.3 N/mm and 0.046 N·s/mm . Furthermore, the parameter h_D assumes a small value, and, effectively, the developed models may resemble the Kelvin–Voigt model. The determined values of the parameter ρ vary mostly within the assumed range of $[1,2]$ s/mm in the case of M0 and M1. Keeping in mind that $\sigma = h_D\rho$, a small value of the parameter h_D has an adverse effect on the estimation of the parameter ρ. The minimal and maximal values of parameters k_D, c_D, h_D, ρ based on the set of realisations estimated at Stage 4 are provided in Tab. 5.

Tab. 5. Min/max values of the parameters obtained at Stage 4

Parameters	Case M0	Case M1
$\text{Min}(k_D)$	0.3800 N/mm	0.6689 N/mm
$\text{Max}(k_D)$	0.3856 N/mm	0.6899 N/mm
$\text{Min}(c_D)$	0.0892 N·s/mm	0.1285 N·s/mm
$\text{Max}(c_D)$	0.0937 N·s/mm	0.1492 N·s/mm
$\text{Min}(h_D)$	0.0286 N	0.1993 N
$\text{Max}(h_D)$	0.0442 N	0.2598 N
$\text{Min}(\rho)$	0.99 s/mm	1.18 s/mm
$\text{Max}(\rho)$	1.85 s/mm	1.68 /mm

5. CONCLUSION

This study deals with experimental tests and modelling of two fabricated MRE samples with different concentrations of CIP by volume. The work presents the microscopic examination of the material samples, discusses the influence of the magnetic field on the MRE samples' behaviour and proposes the estimation procedure of the modified Dahl model parameters.

The outcome of the research leads the authors to the following conclusions:

- The CIP inside the fabricated samples is regularly distributed in the silicon matrix, but the matrix contains inclusions of small air bubbles.
- The difference between the magnetisation curves of the examined samples results from different CIP contents.
- The equivalent stiffness and damping coefficients of the samples depend on the magnetic field level and the concentration of CIP by volume.
- The modified quality factor J_{es} increases the accuracy of the model parameters' determination in the zones close to the zero value of the displacement z_D.
- The estimated parameters of the modified Dahl model guarantee the reproduction of the real behaviour of the investigated sample.
- The multi-stage estimation procedure was proposed by the authors due to the potential application of more complex models such as Bouc–Wen or LuGre model.

The ongoing research will be focused on the extended test conditions to develop an inverse model of the manufactured MREs. The authors intend to investigate the influence of the magnetic flux density, amplitude and excitation frequency on the material behaviour.

REFERENCES

1. Brancati R, Di Massa G, Pagano S, Santini S. A magneto-rheological elastomer vibration isolator for lightweight structures. Meccanica 2019;54:333–49. https://doi.org/10.1007/s11012-019-00951-2
2. Yu Y, Li Y, Li J. Parameter identification and sensitivity analysis of an improved LuGre friction model for magnetorheological elastomer base isolator. Meccanica 2015;50:2691–707. https://doi.org/10.1007/s11012-015-0179-z
3. [Gutenko D. State of the art of soft robotic applications based on magneto-rheological materials. MATEC Web Conf 2020;322:01050. https://doi.org/10.1051/matecconf/202032201050
4. Hu T, Xuan S, Ding L, Gong X. Stretchable and magneto-sensitive strain sensor based on silver nanowire-polyurethane sponge enhanced magnetorheological elastomer. Mater Des 2018;156:528–37. https://doi.org/10.1016/j.matdes.2018.07.024
5. Zhang G, Zhang J, Guo X, Zhang M, Liu M, Qiao Y, et al. Effects of graphene oxide on microstructure and mechanical properties of isotropic polydimethylsiloxane-based magnetorheological elastomers. Rheol Acta 2022;61:215–28. https://doi.org/10.1007/s00397-022-01329-0
6. Kashima S, Miyasaka F, Hirata K. Novel Soft Actuator Using Magnetorheological Elastomer. IEEE Trans Magn 2012;48:1649–52. https://doi.org/10.1109/TMAG.2011.2173669
7. Keip M-A, Rambausek M. Computational and analytical investigations of shape effects in the experimental characterization of magnetorheological elastomers. Int J Solids Struct 2017;121:1–20. https://doi.org/10.1016/j.ijsolstr.2017.04.012

8. Samal S, Blanco I. Investigation of Dispersion, Interfacial Adhesion of Isotropic and Anisotropic Filler in Polymer Composite. Appl Sci 2021;11:8561. https://doi.org/10.3390/app11188561

9. Vatandoost H, Rakheja S, Sedaghati R. Effects of iron particles' volume fraction on compression mode properties of magnetorheological elastomers. J Magn Magn Mater 2021;522:167552. https://doi.org/10.1016/j.jmmm.2020.167552

10. Winger J, Schümann M, Kupka A, Odenbach S. Influence of the particle size on the magnetorheological effect of magnetorheological elastomers. J Magn Magn Mater 2019;481:176–82. https://doi.org/10.1016/j.jmmm.2019.03.027

11. Kaleta J, Królewicz M, Lewandowski D. Magnetomechanical properties of anisotropic and isotropic magnetorheological composites with thermoplastic elastomer matrices. Smart Mater Struct 2011;20:085006. https://doi.org/10.1088/0964-1726/20/8/085006

12. Schubert G, Harrison P. Magnetic induction measurements and identification of the permeability of Magneto-Rheological Elastomers using finite element simulations. J Magn Magn Mater 2016;404:205–14. https://doi.org/10.1016/j.jmmm.2015.12.003

13. Vatandoost H, Sedaghati R, Rakheja S. A novel methodology for accurate estimation of magnetic permeability of magnetorheological elastomers. J Magn Magn Mater 2022;560:169669. https://doi.org/10.1016/j.jmmm.2022.169669

14. Lian C, Lee K, An J, Lee C. Effect of stick-slip on magnetorheological elastomer with a magnetic field. Friction 2017;5:383–91. https://doi.org/10.1007/s40544-017-0150-1

15. Johari MAF, Mazlan SA, Nasef MM, Ubaidillah U, Nordin NA, Aziz SAA, et al. Microstructural behavior of magnetorheological elastomer undergoing durability evaluation by stress relaxation. Sci Rep 2021;11:10936. https://doi.org/10.1038/s41598-021-90484-0

16. Li Y, Li J, Li W, Du H. A state-of-the-art review on magnetorheological elastomer devices. Smart Mater Struct 2014;23:123001. https://doi.org/10.1088/0964-1726/23/12/123001

17. Bastola AK, Hossain M. A review on magneto-mechanical characterizations of magnetorheological elastomers. Compos Part B Eng 2020;200:108348.https://doi.org/10.1016/j.compositesb.2020.108348

18. Nguyen XB, Komatsuzaki T, Truong HT. Adaptive parameter identification of Bouc-wen hysteresis model for a vibration system using magnetorheological elastomer. Int J Mech Sci 2022;213:106848. https://doi.org/10.1016/j.ijmecsci.2021.106848

19. Wang P, Yang S, Liu Y, Zhao Y. Experimental Study and Fractional Derivative Model Prediction for Dynamic Viscoelasticity of Magnetorheological Elastomers. J Vib Eng Technol 2022;10:1865–81. https://doi.org/10.1007/s42417-022-00488-x

20. Nguyen XB, Komatsuzaki T, Zhang N. A nonlinear magnetorheological elastomer model based on fractional viscoelasticity, magnetic dipole interactions, and adaptive smooth Coulomb friction. Mech Syst Signal Process 2020;141:106438. https://doi.org/10.1016/j.ymssp.2019.106438

21. Nedjar A, Aguib S, Djedid T, Nour A, Settet A, Tourab M. Analysis of the Dynamic Behavior of Magnetorheological Elastomer Composite: Elaboration and Identification of Rheological Properties. Silicon 2019;11:1287–93. https://doi.org/10.1007/s12633-018-9921-1

22. Wang B, Bustamante R, Kari L, Pang H, Gong X. Modelling the influence of magnetic fields to the viscoelastic behaviour of soft magnetorheological elastomers under finite strains. Int J Plast 2023;164:103578. https://doi.org/10.1016/j.ijplas.2023.103578

23. Metsch P, Kalina KA, Spieler C, Kästner M. A numerical study on magnetostrictive phenomena in magnetorheological elastomers. Comput Mater Sci 2016;124:364–74. https://doi.org/10.1016/j.commatsci.2016.08.012.

24. Kukla M, Górecki J, Malujda I, Talaśka K, Tarkowski P. The Determination of Mechanical Properties of Magnetorheological Elastomers (MREs). Procedia Eng 2017;177:324–30. https://doi.org/10.1016/j.proeng.2017.02.233

25. Janbaz M, Saeidi Googarchin H. Experimental and numerical analysis on magneto-hyper-viscoelastic constitutive responses of magnetorheological elastomers: A characterization procedure. Mech Mater 2021;154:103712. https://doi.org/10.1016/j.mechmat.2020.103712

26. Asadi Khanouki M, Sedaghati R, Hemmatian M. Adaptive dynamic moduli of magnetorheological elastomers: From experimental identification to microstructure-based modeling. Mater Sci Eng B Solid-State Mater Adv Technol 2021;267. https://doi.org/10.1016/j.mseb.2021.115083

27. Yu Y, Li J, Li Y, Li S, Li H, Wang W. Comparative Investigation of Phenomenological Modeling for Hysteresis Responses of Magnetorheological Elastomer Devices. Int J Mol Sci 2019;20:3216. https://doi.org/10.3390/ijms20133216

28. Yu Y, Hoshyar AN, Li H, Zhang G, Wang W. Nonlinear characterization of magnetorheological elastomer-based smart device for structural seismic mitigation. Int J Smart Nano Mater 2021;12:390–428. https://doi.org/10.1080/19475411.2021.1981477

29. Li W, Zhou Y, Tian T, Alici G. Creep and recovery behaviors of magnetorheological elastomers. Front Mech Eng China 2010;5:341–6. https://doi.org/10.1007/s11465-010-0096-8

30. Versa 3D scanning electron microscope, Technical documentation 2023. https://www.microscop.ru/uploads/VERSA3D.pdf (accessed April 17, 2023)

31. Magnetometer LakeShore 7400 series, Technical documentation 2023. https://www.lakeshore.com/products/categories/overview/discontinued-products/discontinued-products/7400-series-vsm (accessed April 17, 2023)

32. FEMM 4.2, Technical documentation. 2023. https://www.femm.info/wiki/Documentation/ (accessed April 17, 2023)

33. Gaussmeter GM2, Technical documentation 2023. https://www.alphalabinc.com/product/gm2/ (accessed April 17, 2023).

34. Linear actuator, LA30-43-000A, Technical documentation 2023. https://www.sensata.com/sites/default/files/a/sensata-voice-coil-actuator-linear-frameless-la30-43-000a-drawing.pdf (accessed April 17, 2023)

35. 9063 CompactRIO Controller, Technical documentation 2023. https://www.ni.com/pl-pl/support/model.crio-9063.html (accessed April 17, 2023).

36. Linear encoder with sinus/cosinus output, LIKA SMS12, Technical documentation 2023. http://www.lika.pl/pliki_do_pobrania/CAT%20SMS12%20E.pdf (accessed April 17, 2023)

37. Snamina J, Orkisz P. Active vibration reduction system with mass damper tuned using the sliding mode control algorithm. J Low Freq Noise Vib Act Control 2021;40:540–54. https://doi.org/10.1177/1461348420904257

38. Wang DH, Liao WH. Magnetorheological fluid dampers: a review of parametric modelling. Smart Mater Struct 2011;20:023001. https://doi.org/10.1088/0964-1726/20/2/023001

Denys Gutenko: iD https://orcid.org/0000-0003-4160-724X

Paweł Orkisz: iD https://orcid.org/0000-0002-8928-8455

Bogdan Sapiński: iD https://orcid.org/0000-0001-6952-8303

MODIFIED SEMI-ANALYTICAL APPROACH FOR DUFFING EQUATION

Um E AMARA*⬤**, Shahida REHMAN****⬤**, Mujahid ABBAS*/****⬤**, Jamshaid Ul REHMAN**** ⬤

*Department of Mathematics, Government College University, Lahore-54600, Pakistan
**Abdus Salam School of Mathematical Sciences, Government College University, Lahore-54600, Pakistan

uamara95@gmail.com, shahidarehman21@sms.edu.pk, abbas.mujahid@gcu.edu.pk, jamshaidrahman@gmail.com

Abstract: This research endeavour-investigates the enhanced adaptation of the Laplace-based variational iteration method (VIM) tailored specifically for tackling the Duffing Equation. This is accomplished by incorporating the Lagrange multiplier as a strategic tool to effectively address the inherent natural frequency within the Duffing Equation. Using a meticulous comparative analysis, here are juxtapose the analytical outcomes generated by the modified VIM approach with the numerical solution obtained through the application of the renowned Runge-Kutta Fehlberg method (RKF45), implemented by using the powerful mathematical software, MAPLE. Furthermore, by exploring the profound influence of diverse initial conditions on the resulting solution, a diverse array of distinct graphical representations is presented.

Keywords: nonlinear dynamics, modified variational iterative method, Simulink model, mechanical vibration.

1. INTRODUCTION

In the 1990s, many mathematicians work to solve the dribbled flow in fractional derivatives and nonlinear differential equations [1-3] and they introduced a method that is known as the variational iterative method (VIM) and now in recent times VIM has been applied immensely as an important mathematical tool for solving nonlinear differential equations in various field of sciences (for instance, visit [4-10]). For linear problems, the Lagrange multiplier is identified and used to obtain the exact solution with single iteration.

This method is very desired in the directory of techniques for nonlinear models and high summons record articles that are concerned with the "Variational iterative method" which has been into account. Also, this method is more reliable and effective than other existing strategies, for example, the Adomian decomposition and perturbation method etc. The other benefits of VIM are that we can reduce the measurements of computation and still maintain the precision of the numerical solution. However, the strength of this technique is the ability to handle a large group of analytical applications as well as numerical applications in real-life problems. The Integral Transform-based VIM (ITVIM) is a mathematical technique that combines the variational iteration method (VIM) with integral transforms, such as the Laplace transform, to solve differential equations. This hybrid approach leverages the advantages of both methods, allowing for the efficient solution of a wide range of differential equations, including ordinary differential equations (ODEs) and partial differential equations (PDEs). The Laplace transform-based VIM offers a robust approach for solving a wide array of differential equations, providing researchers and engineers with a valuable tool for understanding and analysing dynamic systems in different fields.

The main concern of this method is about nonlinear oscillators like Fangzhu Oscillators [11], lowfrequency property of fractal

vibration model [12], microelectro mechanical system oscillators [13, 14] time-fractional problems [15, 16] etc. The VIM was modified with the help of Laplace transformation by Rehman et al. [17]. In this work the nonlinear differential equation is solved by using the method, known as the Modified VIM (MVIM) and periodic solution is obtained. The MVIM retains an approximate solution for each time level. The tactics MVIM identify incontestable use and the Lagrange multiplier is so easy to handle than that of Variational principle [18-22]. We assume a nonlinear oscillator that is expressed by equation:

$$y''(t) + f(y) = 0, \qquad (1)$$

with following initial conditions

$$y(0) = A, \qquad y'(0) = 0.$$

We can write Eq. (1) as

$$y'' + \omega^2(y) + r(y) = 0, \qquad (2)$$

where ω is unknown frequency,

$$r(y) = f(y) - \omega^2 y, \qquad (3)$$

and inVIM, for the Eq. (2) the convolution is given by [23] and known as the correction functional which is

$$v_{n+1}(t) = v_n(t) + \int_0^t \eta(t,\xi)[v''_n(\xi) + \omega^2 v_n(\xi) + \tilde{r}(v_n)]d\xi, n = 0,1,2,3, \dots \qquad (4)$$

In the above expression the general Lagrange multiplier is η, and by using VIM [24-27] with respect to v_n, it can be alternatively calculated by stabilizing the conditions of Eq. (4). The symbol n represents the nth approximation of the solution and $\tilde{r}$ denotes the restricted variation. By assembling stabilised $v_n(t)$, the convolution will give the value of η . Now we obtain a relationship between amplitude and angular frequency and we incorporate

Laplace transform in the well-known VIM. Then we will apply this method on the equations arising from Duffing equation. Applying MVIM to the Duffing equation offers valuable insights into the behaviour of nonlinear systems, including understanding complex dynamics, resonance phenomena, bifurcation analysis; and sensitivity to system parameters. These implications are not only important for theoretical understanding but also have practical applications in engineering and related fields. The Duffing equation is a nonlinear second-order differential equation frequently used to model the behaviour of various physical systems, including mechanical, electrical, and biological systems. It was named after the German engineer and physicist Georg Duffing, who extensively studied this equation in the early 20th century. In mechanical engineering, it describes the behaviour of certain mechanical systems, such as a nonlinear oscillator with cubic stiffness. In electrical engineering, it represents the response of certain electronic circuits to external inputs. Moreover, it has been applied in biology to model the dynamics of biological systems, such as the motion of the human heart under certain conditions. Studying the Duffing equation and its solutions provides valuable insights into the behavior of nonlinear systems and help to use them in various scientific and engineering disciplines.

The generalized Duffing Equation is defined by Petrova [28] and given as:

$$s''(t) + \delta s'(t) + \alpha s(t) + \beta s^3(t) = \varphi(t), \tag{5}$$

where α, β and δ are positive constants and $\varphi(t)$ is a well-known function.

The above equation is a nonlinear second-order differential equation. If β = 0, then this equation will reduce to linear equation. The Duffing equation shows the chaotic nonlinear behaviour of dynamical system. If β > 0 the equation denotes a rigid springs and if β < 0, the equation denotes the smooth springs and, in this case the phase portrait will be closed [29]. The many terms from the qualitative theory of ODE can be easily illustrated by using the Eq.(5) i.e. limit cycle [30] and chaotic behaviour. Tao et al. [31] introduced a promising method for solving fractional differential equations by combining the homotopy perturbation method with the Aboodh transform. This innovative hybrid technique offers a straightforward way to obtain an approximate solution, which converges rapidly to the exact solution, requiring minimal computational effort.

Anjum and He [32] proposed a simplified method utilising the Laplace transform to calculate the multiplier, thereby making this approach accessible to researchers dealing with diverse nonlinear problems. Anjum et al. [33] explored the Elzaki transform, a modified version of the Laplace transform known for its effectiveness in dealing with nonlinear oscillators. The study demonstrated that a single iteration using this transform results in a highly accurate solution, highlighting its practical utility for researchers. In this paper we will solve by taking a special case of Duffing equation and applying the MVIM on this equation.

2. APPLICATIONS OF MVIM TO DUFFING EQUATION

Problem 1: Firstly, we take δ = 0, α = 0 and $\varphi(t) = 0$ in Eq. (5) of Duffing equation,

$$s'' + s^3 = 0, \quad when \quad s(0) = A, s'(0) = 0. \tag{6}$$

This equation represents the Duffing oscillator. In order to solve the Duffing equation, with the help of Laplace transform

inVIM, we will consider the nonlinear oscillator form

$$s'' + \omega^2 s^3 + g(s) = 0, \tag{7}$$

where $\quad g(s) = (1 - \omega^2)s^3$.

Consider the correctional formula for VIM

$$\mathcal{L}[v_{n+1}(t)] = \mathcal{L}[v_n(t)] - \mathcal{L}\int_0^t \frac{1}{\omega}\sin\omega(t-\xi)\left(v_n''(\xi) + \omega^2 v^3_n(\xi) + g(v_n)\right)d\xi, \tag{8}$$

and now by using convolution for the Laplace transformation, we get

$$\mathcal{L}[s_{n+1}(t)] = \mathcal{L}[s_n(t)] - \frac{1}{\omega}\mathcal{L}[\sin\omega t]\mathcal{L}[s''_n + \omega^2 s^3_n + g(s_n)]. \tag{9}$$

By substituting the value of $g(s_n)$, we have

$$\mathcal{L}[s_{n+1}(t)] = \mathcal{L}[s_n(t)] - \frac{1}{\omega}\mathcal{L}[\sin\omega t]\mathcal{L}[s_n'' + \omega^2 s^3_n + (1 - \omega^2)s_n^3, \tag{10}$$

$$\mathcal{L}[s_{n+1}(t)] = \mathcal{L}[s_n(t)] - \frac{1}{\omega}\mathcal{L}[\sin\omega t]\mathcal{L}[s_n'' + s_n^3]. \tag{11}$$

Use trail function $s_0(t) = A\cos wt$, then the Eq. (11) becomes, when n = 0,

$$\mathcal{L}[s_1(t)] = \mathcal{L}[s_0(t)] - \frac{1}{\omega}\mathcal{L}[\sin\omega t]\mathcal{L}[s_0'' + s_0^3]. \tag{12}$$

By substituting the value of $s_0(t) = A\cos\omega t$, and $s_0''(t) = -A\omega^2\cos\omega t$, we get,

$$\mathcal{L}[s_1(t)] = \mathcal{L}[A\cos\omega t] - \frac{1}{\omega}\mathcal{L}[\sin\omega t]\mathcal{L}[-A\omega^2\cos\omega t + A^3\cos\omega t^3], \tag{13}$$

$$\mathcal{L}[s_1(t)] = \mathcal{L}[A\cos\omega t] - \frac{1}{\omega}\mathcal{L}[\sin\omega t]\mathcal{L}[-A\omega^2\cos\omega t + \frac{A^3}{4}(\cos 3\omega t + 3\cos\omega t)]. \tag{14}$$

By solving the above, we have following equation

$$\mathcal{L}[s_1(t)] = \mathcal{L}[A\cos\omega t] + \left[A\omega - \frac{3A^3}{4\omega}\right]\mathcal{L}[\sin\omega t]\mathcal{L}[\cos\omega t] - \frac{A^3}{4\omega}\mathcal{L}[\sin\omega t]\mathcal{L}[\cos 3\omega t]. \tag{15}$$

Now apply the inverse Laplace transform, the first order approximate solution is of the form

$$s_1(t) = [A\cos\omega t] + \left[A\omega - \frac{3A^3}{4\omega}\right]\left[\frac{1}{2}t\sin\omega t\right] - \frac{A^3}{4\omega}\left[\frac{1}{8\omega}(\cos\omega t - \cos 3\omega t)\right], \tag{16}$$

$$s_1(t) = A\cos\omega t + \left[A\omega - \frac{3A^3}{4\omega}\right]\left[\frac{1}{2}t\sin\omega t\right] - \frac{A^3}{4\omega}\left[\frac{1}{8\omega}(\cos\omega t - \cos 3\omega t)\right]. \tag{17}$$

In the above, the second term is a secular term because it increases in amplitude with time, so avoiding the secular term in approximate solution requires that

$$A\omega - \frac{3A^3}{4\omega} = 0,$$

$$\omega^2 = \frac{3}{4}A^2,$$

$$\omega = \sqrt{\frac{3}{4}}A. \tag{18}$$

The above expression of angular frequency is same as is obtained by the first-order Hamiltonian approach, second-order Hamiltonian approach and third-order Hamiltonian approach in Eq.(2) by Yildirim et al. [34]. So periodic solution in this case becomes same as that of first-order Hamiltonian approach, second-order Hamiltonian approach and third-order Hamiltonian approach while approximate solution is

$$s_1(t) = A\cos - \frac{A^3}{4\omega}\left[\frac{1}{8\omega}(\cos\omega t - \cos 3\omega t)\right]. \tag{19}$$

Problem 2: We will take $\varphi(t) = f_0 \cos\omega t$ in Eq. (5). This leads to a new case of Duffing equation,

$$s''(t) + \delta s'(t) + \alpha s(t) + \beta s^3(t) = f_0 \cos\omega t, \quad when \quad s(0) = A,\ s'(0) = 0. \tag{20}$$

This equation represents the Duffing oscillator. In order to solve Duffing equation, by making Laplace transform in VIM, we will consider the nonlinear oscillator form

$$s'' + \omega^2 s + g(s) = 0, \tag{21}$$

where

$$g(s) = \delta s'(t) + \alpha s(t) + \beta s^3(t) - f_0 \cos\omega t - \omega^2 s.$$

Consider the correctional formula for VIM

$$\mathcal{L}[v_{n+1}(t)] = \mathcal{L}[v_n(t)] - \mathcal{L}\int_0^t \frac{1}{\omega}\sin\omega(t-\xi)\left(v_n''(\xi) + \omega^2 v_n(\xi) + g(v_n)\right)d\xi. \tag{22}$$

Now by using convolution for the Laplace transformation, we get

$$\mathcal{L}[s_{n+1}(t)] = \mathcal{L}[s_n(t)] - \frac{1}{\omega}\mathcal{L}[\sin\omega t]\mathcal{L}[s_n''(t) + \omega^2 s_n + g(s_n)]. \tag{23}$$

By substituting the value of $g(s_n)$, we have

$$\mathcal{L}[s_{n+1}(t)] =$$

$$\mathcal{L}[s_n(t)] - \frac{1}{\omega}\mathcal{L}[\sin\omega t]\mathcal{L}[s_n''(t) + \omega^2 s_n + \delta s'(t) + \alpha s(t) + \beta s^3(t) - f_0 \cos\omega t] \tag{24}$$

$$\mathcal{L}[s_{n+1}(t)] = \mathcal{L}[s_n(t)] - \frac{1}{\omega}\mathcal{L}[\sin\omega t]\mathcal{L}[s_n''(t) + \delta s_n'(t) + \alpha s_n(t) + \beta s_n^3(t) - f_0 \cos\omega t]. \tag{25}$$

Using the trail function $s_0(t) = A\cos\omega t$, and when n = 0, the above equation becomes

$$\mathcal{L}[s_1(t)] = \mathcal{L}[s_0(t)] - \frac{1}{\omega}\mathcal{L}[\sin\omega t]\mathcal{L}[s_0''(t) + \beta s_0^3(t) + \delta s_0'(t) + \alpha s_0(t) - f_0 \cos\omega t]. \tag{26}$$

By substituting the value of $s_0(t) = A\cos\omega t$, $s_0'(t) = -A\omega\sin\omega t$, and $s_0''(t) = -A\omega^2\cos\omega t$, we get,

$$\mathcal{L}[s_1(t)] = \mathcal{L}[A\cos\omega t] - \frac{1}{\omega}\mathcal{L}[\sin\omega t]\mathcal{L}[-A\omega^2\cos\omega t + \alpha A\cos\omega t - \delta A\omega\sin\omega t + \beta A^3\cos\omega t^3 - f_0\cos\omega t], \tag{27}$$

$$\mathcal{L}[s_1(t)] = \mathcal{L}[A\cos\omega t] - \frac{1}{\omega}\mathcal{L}[\sin\omega t]\mathcal{L}[-A\omega^2\cos\omega t + \alpha A\cos\omega t - \delta A\omega\sin\omega t + \frac{\beta A^3}{4}\cos 3\omega t + \frac{3\beta A^3}{4}\cos\omega t - f_0\cos\omega t], \tag{28}$$

$$\mathcal{L}[s_1(t)] = \mathcal{L}[A\cos\omega t] - \frac{1}{\omega}\mathcal{L}[\sin\omega t]\mathcal{L}[(-A\omega^2 + \alpha A + \frac{3\beta A^3}{4} - f_0)\cos\omega t - \delta A\omega\sin\omega t + \frac{\beta A^3}{4}\cos 3\omega t], \tag{29}$$

and by solving these, obtain following equation

$$\mathcal{L}[s_1(t)] = \mathcal{L}[A\cos\omega t] - \frac{1}{\omega}\left(-A\omega^2 + \alpha A + \frac{3\beta A^3}{4} - f_0\right)\mathcal{L}[\sin\omega t]\mathcal{L}[\cos\omega t] - \delta A\mathcal{L}[\sin\omega t]\mathcal{L}[\sin\omega t] - \frac{\beta A^3}{4\omega}\mathcal{L}[\sin\omega t]\mathcal{L}[\cos 3\omega t]. \tag{30}$$

Applying the inverse Laplace transform, the formulation for the first order approximate solution is

$$s_1(t) = A\cos\omega t - \frac{1}{\omega}\left(-A\omega^2 + \alpha A + \frac{3\beta A^3}{4} - f_0\right)\left(\frac{1}{2}t\sin\omega t\right) - \frac{\delta A}{2\omega}(\sin\omega t - t\omega\cos 3\omega t) - \frac{\beta A^3}{4\omega}\left(\frac{1}{8\omega}(\cos\omega t - \cos 3\omega t)\right), \tag{31}$$

$$s_1(t) = A\cos\omega t - \frac{1}{\omega}\left(-A\omega^2 + \alpha A + \frac{3\beta A^3}{4} - f_0\right)\left(\frac{1}{2}t\sin\omega t\right) - \frac{\delta A}{2\omega}\sin\omega t + \frac{\delta A}{2\omega}t\omega\cos 3\omega t - \frac{\beta A^3}{4\omega}\left(\frac{1}{8\omega}(\cos\omega t - \cos 3\omega t)\right). \tag{32}$$

In this, the second term is a secular term because it increases in amplitude with time, and so avoiding the secular term in approximate solution requires that

$$-\frac{1}{\omega}\left(-A\omega^2 + \alpha A + \frac{3\beta A^3}{4} - f_0\right) = 0,$$

$$A\omega^2 - \alpha A - \frac{3\beta A^3}{4} + f_0 = 0,$$

$$A\omega^2 = \alpha A + \frac{3\beta A^3}{4} - f_0,$$

$$\omega^2 = \alpha + \frac{3\beta A^2}{4} - \frac{f_0}{A},$$

$$\omega = \sqrt{\alpha + \frac{3\beta A^2}{4} - \frac{f_0}{A}}. \tag{33}$$

The above expression shows the angular frequency of the system using the periodic solution approach while approximate solution is

$$s_1(t) = A\cos\omega t - \frac{\delta A}{2\omega}\sin\omega t - \frac{\beta A^3}{4\omega}\left[\frac{1}{8\omega}(\cos\omega t - \cos 3\omega t)\right]. \tag{34}$$

3. RESULT AND DISCUSSION OF PROBLEM 1

In this problem, we take a Duffing Equation with a special case to obtain analytical solution by modified VIM and now we will compare our results with the numerical method that is Runge-Kutta Fehlberg method (RKF45). The Figs. 1, 2 and 3 show the comparison between analytical solutions obtained by MVIM and numerical solutions by RKF45 whichconforms the validity of MVIM:
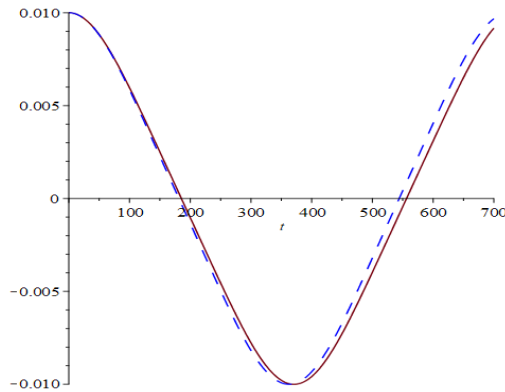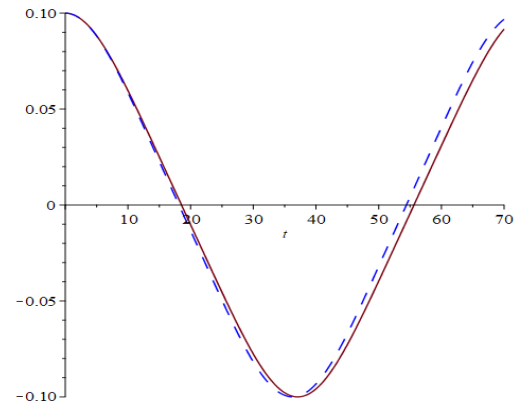

Fig. 1. Comparison between VIM with Laplace and RKF45 for A = 0.01. RKF45, Runge-KuttaFehlberg method: VIM, Variational iteration method.

In this session, we have characterised the error analysis of the analytical solution by MVIM and numerical solution by RKF45. In Tab. 1, error term E1 conforms the validity of the solution by MVIM.

Tab. 1. Error analysis for problem

Time steps	RKF45	MVIM	E_1
1.	0.00999999500495420	0.009999996250	0.000000000622523
2.	0.009999998001985614	0.009999985000	0.00000000249007
3.	0.009999995504478561	0.009999966250	0.00000000560261
4.	0.009999992007985009	0.009999940000	0.00000000996007
5.	0.00999987512518472	0.009999906250	0.0000000155624
6.	0.00999982018095232	0.009999865000	0.0000000224095
7.	0.00999975524734341	0.009999816251	0.0000000305018
8.	0.00999968032457617	0.009999760001	0.0000000398382
9.	0.00999959541289647	0.009999696252	0.0000000504196
10.	0.00999950051257784	0.009999625002	0.0000000622447

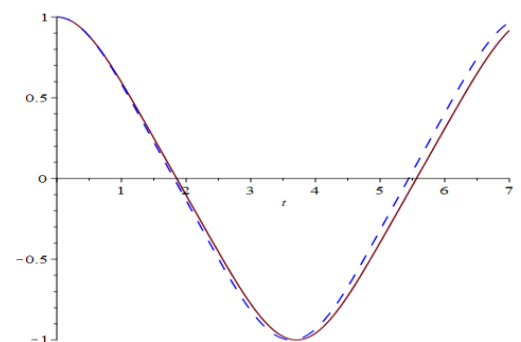MVIM, modified Variational iteration method; RKF45, Runge-Kutta Fehlberg method.

Fig. 2. Comparison between VIM with Laplace and RKF45 for A = 0.1. RKF45, Runge-Kutta Fehlberg method; VIM, Variational iteration method.

In this session, we have characterised the error analysis of the analytical solution by MVIM and numerical solution by RKF45. In Tab. 2, error term Error E2 again conforms the validity of the solution by MVIM.

Tab. 2. Error analysis for problem

Time steps	RKF45	MVIM	E_2
1.	0.0999950010279834	0.09999625002	0.000000624496
2.	0.0999800056260519	0.09998500037	0.00000249737
3.	0.0999550182421241	0.09996625190	0.00000561683
4.	0.0999200462264396	0.09994000600	0.00000997989
5.	0.0998750998315593	0.09990626465	0.0000155824
6.	0.0998201922123647	0.09986503037	0.0000224191
7.	0.0997553394260590	0.09981630627	0.0000304834
8.	0.0996805604321661	0.09976009598	0.0000397678
9.	0.0995958770925311	0.09969640374	0.0000502633
10.	0.0995013141713202	0.09962523432	0.0000619601

MVIM, modified Variational iteration method; RKF45, Runge-Kutta Fehlberg method.

Fig. 3. Comparison between, VIM with Laplace and RKF45 for A = 1. RKF45, Runge-Kutta Fehlberg method; VIM, Variational iterative method.

In this session, we have characterised the error analysis of the analytical solution by MVIM and numerical solution by RKF45. In Tab. 3, error term E3 again conforms the validity of the solution by MVIM.

Tab. 3. Error analysis for problem

Time steps	RKF45	MVIM	E₃
1.	0.995012463963846	0.9962523432	0.00061994
2.	0.980197633634482	0.9850374625	0.002419914
3.	0.955985874143270	0.9664394171	0.005226771
4.	0.923053269838254	0.9405976051	0.008772168
5.	0.882266426229066	0.9077057190	0.012719646
6.	0.834616758953844	0.8680102938	0.016696767
7.	0.781152682325995	0.8218088592	0.020328088
8.	0.722917072594592	0.7694477095	0.023265318
9.	0.660895283270746	0.7113193077	0.025212012
10.	0.595976638587752	0.6478593447	0.025941353

MVIM, modified Variational iteration method; RKF45, Runge-Kutta Fehlberg method.

4. RESULT AND DISCUSSION OF PROLEM 2

In this problem, we consider a Duffing Equation with a special case to obtain analytical solution by MVIM and the results are compared with the numerical method that is RKF45.
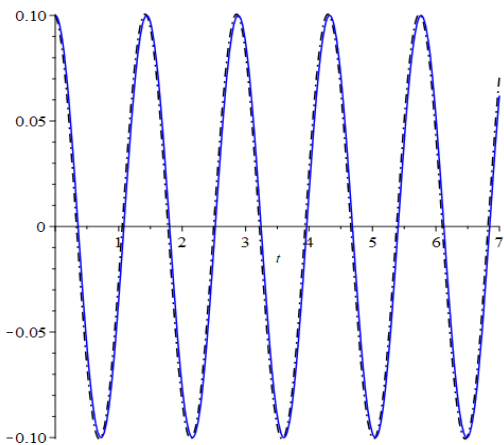

Fig. 4. Comparison between, VIM with Laplace and RKF45 for A = 0.1. RKF45, Runge-Kutta Fehlberg method; VIM, Variational iterative method.

The Figs. 4, 5 and 6 show the comparison between analytical solutions obtained by MVIM and numerical solution by RKF45 which conforms the validity of MVIM. MVIMs, including the Laplace-based variant, offer a flexible and powerful approach to solving a wide range of differential equations. However, users

should be aware of its limitations and the specific characteristics of the problems they intend to solve. Additionally, it's important to stay updated with the latest research in this field, as ongoing developments might address some of the current limitations [35-37].

Note that we have characterised the error analysis of the analytical solution by MVIM and numerical solution by RKF45 in this session. In Tab. 4, error term E4 conforms the validity of the solution by MVIM.

Tab. 4. Error analysis for problem

Time steps	RKF45	MVIM	E4
1.	0.090647789	0.090647651	0.000000068965
2.	0.064339347	0.064339933	0.00000002931
3.	0.025999877	0.025997625	0.000000112601
4.	-0.01720434	-0.017207461	0.00000156036
5.	-0.05719678	-0.057193943	0.00000141875
6.	-0.086484702	-0.08648247	0.00000111599
7.	-0.099596785	-0.099594713	0.00000103591
8.	-0.094045679	-0.094078066	0.0000161936
9.	-0.070989376	-0.070964401	0.0000124876
10.	-0.034789867	-0.034577059	0.000106404

MVIM, modified Variational iteration method; RKF45, Runge-Kutta Fehlberg method.
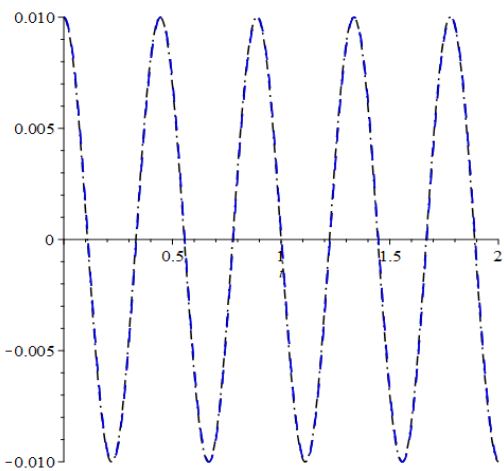

Fig. 5. Comparison between, VIM with Laplace and RKF45 for A = 0.01. RKF45, Runge-Kutta Fehlberg method; VIM, Variational iterative method.

In this part, we have characterised the error analysis of the analytical solution by MVIM and numerical solution by RKF45. In Tab. 5, error term Error E5 again conforms the validity of the solution by MVIM.

Tab. 5. Error analysis for problem

Time steps	RKF45	MVIM	E5
1.	0.001594365	0.001594392	0.0000000136765
2.	-0.009491547	-0.009491583	0.0000000179675
3.	-0.004621835	-0.004621054	0.000000390476
4.	0.008017644	0.008018028	0.000000192285
5.	0.007178921	0.00717783	0.000000545386
6.	-0.005726789	-0.005729173	0.00000119161
7.	-0.009006871	-0.00900474	0.00000106561
8.	0.002859876	0.002857755	0.0000010607
9.	0.009919876	0.009916016	0.00000192992
10.	0.000398376	0.000304249	0.00000470636

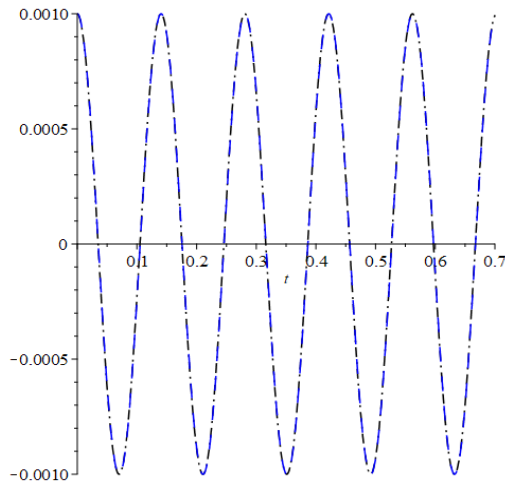MVIM, modified Variational iteration method; RKF45, Runge-Kutta Fehlberg method.

Fig. 6. Comparison between, VIM with Laplace and RKF45 for A = 0.001. RKF45, Runge-Kutta Fehlberg method; VIM, Variational iterative method

In this section, we have characterised the error analysis of the analytical solution by MVIM and numerical solution by RKF45. In Tab. 6, error term E6 again conforms the validity of the solution by MVIM.

Tab. 6. Error analysis for problem

Time steps	RKF45	MVIM	E6
1.	-0.000239068	-0.000239034	0.0000000167992
2.	-0.0008857	-0.000885725	0.0000000126032
3.	0.000662679	0.000662472	0.000000103627
4.	0.000569568	0.000569018	0.000000274801
5.	-0.00093679	-0.000934501	0.0000011442

6.	-0.000126891	-0.000122262	0.0000023141
7.	0.000996544	0.000992951	0.00000179618
8.	-0.000308648	-0.000352436	0.0000218943
9.	-0.000875433	-0.000824463	0.0000254851
10.	0.000905437	0.000746586	0.0000794254

MVIM, modified Variational iteration method; RKF45, Runge-Kutta Fehlberg method.

5. CONCLUSIONS

The Modified Laplace-Based variational Iteration Method VIM (MLVIM) has been applied to the Duffing equation and has yielded numerical results that are in good agreement with numerical solution.

Numerical simulations using the MLVIM have shown that the method is capable of capturing the nonlinear behavior exhibited by the Duffing equation. The approximate solutions obtained through the MLVIM approach closely match the expected trends and characteristics of the Duffing equation, including nonlinear oscillations, bifurcations, and chaos.

Comparisons between the MLVIM results and RKF45 have demonstrated a high degree of accuracy. The MLVIM has been successful in reproducing key features of the Duffing equation, such as the amplitude-frequency response, phase portraits, and frequency response curves.

Additionally, the MVIM has proven to be a versatile method for studying different variations of the Duffing equation, including those with additional nonlinear terms or external forcing. By appropriately modifying the iterative scheme and incorporating the necessary terms, the MLVIM has been able to handle these extensions and produce satisfactory numerical results.

It is worth noting that the accuracy of the MLVIM solutions depends on the number of iterations performed and the convergence behaviour of the method. In cases where the Duffing equation exhibits strong nonlinearity or complex dynamics, a higher number of iterations may be required to achieve desired accuracy.

We can conclde that the MLVIM has provided numerical results which are in good agreement with RKF45 for the Duffing equation. This method demonstrates its effectiveness in capturing the nonlinear behavior and complex dynamics exhibited by the Duffing equation, making it a valuable tool for analysing and understanding such systems.

REFERENCES

1. He JH. Variational iteration method–a kind of non-linear analytical technique: some examples. International journal of non-linear mechanics. 1999 Jul 1;34(4):699-708.
2. He JH. A short remark on fractional variational iteration method. Physics Letters A. 2011 Sep 5;375(38):3362-4.
3. Suleman M, Lu D, Yue C, Ul Rahman J, Anjum N. He–Laplace method for general nonlinear periodic solitary solution of vibration equations. Journal of Low Frequency Noise, Vibration and Active Control. 2019 Dec;38(3-4):1297-304.

4. He JH. Variational principles for some nonlinear partial differential equations with variable coefficients. Chaos, Solitons & Fractals. 2004 Mar 1;19(4):847-51.

5. He JH. Variational approach to (2+1)-dimensional dispersive long water equations. Physics Letters A. 2005 Feb 7;335(2-3):182-4.

6. Ul Rahman J, Mohyuddin MR, Anjum N, Zahoor S. Mathematical modelling & simulation of mixing of salt in 3-interconnected tanks. Journal of Advances in Civil Engineering. 2015;1(1):1-6.

7. Anjum N, He JH. Analysis of nonlinear vibration of nano/microelectromechanical system switch induced by electromagnetic force under zero initial conditions. Alexandria Engineering Journal. 2020 Dec 1;59(6):4343-52.

8. Ain QT, Anjum N, He CH. An analysis of time-fractional heat transfer problem using two-scale approach. GEM-International Journal on Geomathematics. 2021 Dec;12:1-0.

9. He, J. H., & El-Dib, Y. O. (2020). Homotopy perturbation method for Fangzhu oscillator. Journal of Mathematical Chemistry, 58, 2245-2253.

10. Ul Rahman J, Lu D, Suleman M, He JH, Ramzan M. He–Elzaki method for spatial diffusion of biological population. Fractals. 2019 Aug 13;27(05):1950069.

11. Suleman M, Lu D, He JH, Farooq U, Hui YS, Rahman JU. Numerical investigation of fractional HIV model using Elzaki projected differential transform method. Fractals. 2018 Oct 5;26(05):1850062.

12. He CH, Liu C, He JH, Gepreel KA. Low frequency property of a fractal vibration model for a concrete beam. Fractals. 2021 Aug 25;29(05):2150117.

13. Anjum N, He JH. Higher-order homotopy perturbation method for conservative nonlinear oscillators generally and microelectromechanical systems' oscillators particularly. International Journal of Modern Physics B. 2020 Dec 30;34(32):2050313.

14. Tian D, Ain QT, Anjum N, He CH, Cheng B. Fractal N/MEMS: from pull-in instability to pull-in stability. Fractals. 2021 Mar 10;29(02):2150030.

15. Ain QT, Anjum N, He CH. An analysis of time-fractional heat transfer problem using two-scale approach. GEM-International Journal on Geomathematics. 2021 Dec;12:1-0.

16. Ain QT, He JH, Anjum N, Ali M. The fractional complex transform: A novel approach to the time-fractional Schrödinger equation. Fractals. 2020 Nov 2;28(07):2050141.

17. Rehman S, Hussain A, Rahman JU, Anjum N, Munir T. Modified Laplace based variational iteration method for the mechanical vibrations and its applications. acta mechanica et automatica. 2022;16(2):98-102.

18. He JH. Some asymptotic methods for strongly nonlinear equations. International journal of Modern physics B. 2006 Apr 20;20(10): 1141-99.

19. Noor MA, Mohyud-Din ST. Variational iteration method for solving higher-order nonlinear boundary value problems using He's polynomials. International Journal of Nonlinear Sciences and Numerical Simulation. 2008 Jun;9(2):141-56.

20. He JH. Generalized equilibrium equations for shell derived from a generalized variational principle. Applied Mathematics Letters. 2017 Feb 1;64:94-100.

21. He JH. An alternative approach to establishment of a variational principle for the torsional problem of piezoelastic beams. Applied Mathematics Letters. 2016 Feb 1;52:1-3.

22. Wu Y, He JH. A remark on Samuelson's variational principle in economics. Applied Mathematics Letters. 2018 Oct 1;84:143-7.

23. He JH. Variational iteration method—some recent results and new interpretations. Journal of computational and applied mathematics. 2007 Oct 1;207(1):3-17.

24. He JH, Wu XH. Variational iteration method: new development and applications. Computers & Mathematics with Applications. 2007 Oct 1;54(7-8):881-94.

25. He JH. Variational iteration method for autonomous ordinary differential systems. Applied mathematics and computation. 2000 Sep 11;114(2-3):115-23.

26. He JH. Variational theory for linear magneto-electro-elasticity. International Journal of Nonlinear Sciences and Numerical Simulation. 2001 Dec;2(4):309-16.

27. He J. Variational iteration method for delay differential equations. Communications in Nonlinear Science and Numerical Simulation. 1997 Dec 1;2(4):235-6.

28. Petrova Z, Puleva T. Mathematical modeling of the equation of Duffing with applications for master degree students—Part I. InAIP Conference Proceedings 2018 Dec 10 (Vol. 2048, No. 1). AIP Publishing.

29. Kanamaru T. Duffing oscillator. Scholarpedia. 2008 Mar 25; 3(3):6327.

30. Savov VN, Georgiev ZD, Todorov TG. Analysis and synthesis of perturbed Duffing oscillators. International journal of circuit theory and applications. 2006 May;34(3):281-306.

31. Tao H, Anjum N, Yang YJ. The Aboodh transformation-based homotopy perturbation method: new hope for fractional calculus. Frontiers in Physics. 2023 Apr 27;11:1168795.

32. Anjum N, He JH. Laplace transform: making the variational iteration method easier. Applied Mathematics Letters. 2019 Jun 1;92:134-8.

33. Anjum N, Suleman M, Lu D, He JH, Ramzan M. Numerical iteration for nonlinear oscillators by Elzaki transform. Journal of Low Frequency Noise, Vibration and Active Control. 2020 Dec;39(4):879-84.

34. Yildirim A, Saadatnia Z, Askari H, Khan Y, KalamiYazdi M. Higher order approximate periodic solutions for nonlinear oscillators with the Hamiltonian approach. Applied Mathematics Letters. 2011 Dec 1;24(12):2042-51.

35. Rehman S, Muhammad N. Mathematical analysis of nonlinear models and their role in dynamics. Modern Physics Letters B. 2023 Oct 31:2450097.

36. Shah NA, Rehman S, Vieru D, Yook SJ. Unsteady flows of micropolar fluids parallel to the axis of an annular domain with a porous layer. Alexandria Engineering Journal. 2023 Aug 1;76:275-87.

37. Rehman S, Muhammad N, Alshehri M, Alkarni S, Eldin SM, Shah NA. Analysis of a viscoelastic fluid flow with Cattaneo–Christov heat flux and Soret–Dufour effects. Case Studies in Thermal Engineering. 2023 Sep 1;49:103223.

Um E Amara: https://orcid.org/0009-0009-0572-7368

Shahida Rehman: https://orcid.org/0000-0001-7137-9079

Mujahid Abbas: https://orcid.org/0000-0001-5528-1207

Jamshaid Ul Rehman: https://orcid.org/0000-0001-8642-0660

EXPERIMENTAL DETERMINATION OF SPRINGBACK CHARACTERISTICS
IN A THREE-POINT BENDING TEST
OF THE ALUMINIUM ALLOY SHEET WITH ALUMINIUM CLADDING

Stanisław KUT*, Grzegorz PASOWICZ**, Feliks STACHOWICZ*

*Faculty of Mechanical Engineering and Aeronautics, Rzeszow University of Technology,
al. Powstańców Warszawy 8, 35-959 Rzeszów, Poland
**Doctoral School of the Rzeszow University of Technology, al. Powstańców Warszawy 12 35-959 Rzeszów, Poland

stan_kut@prz.edu.pl, grzegorz.j.pasowicz@lmco.com, stafel@prz.edu.pl

Abstract: The springback phenomenon that occurs during cold forming is the main problem that affects the dimensional accuracy of bent products. This article presents the results of the analysis of the springback phenomenon occurring during a three-point air bending of 0.5 mm, 0.8 mm, 1.0 mm and 2.0 mm thick AW-2024 aluminium alloy sheet, AW-1050A aluminium clad. For sheets with a thickness of 1.0 mm and 2.0 mm, the influence of heat treatment and natural ageing time of sheets on the value of the springback coefficient was also tested. The springback characteristics were determined by defining the dependence of the springback coefficient on the bending deflection of the band. The experimental results obtained indicate a linear dependence of the value of the springback coefficient on the relative deflection w/fg index (w – distance between supports, fg – deflection under load), both in the case of the influence of the sheet thickness and the ageing time of the sheets.

Key words: AW-2024 sheet, three-point bending, springback, clad sheet metal, natural ageing

1. INTRODUCTION

One of the main criteria in the selection of material for the production of parts, especially in aviation and automotive production, is the index determining the ratio of its density to the strength limit [1]. Therefore, aluminium alloys, due to their properties and the well-developed ability to produce them, are widely used in aviation and other areas of the transport industry [2, 3]. Currently, apart from composite materials, their percentage share is the largest in aircraft production.

In the aerospace industry, the materials used to make aircraft skins are mainly high-strength aluminium alloys; however, the disadvantage of these materials is usually their low resistance to corrosion. Corrosion damage arising during operation is a serious threat, especially for many years of operation of aluminium aircraft structures [4, 5]. To improve the corrosion resistance of the case of high-strength sheets made of aluminium alloys, technically pure aluminium is used as the coating material, applied on both sides in the rolling process to the parent material [6].

An example of an alloy widely used in aviation production is the AW-2024 aluminium alloy, whose precipitation hardening ability is very often used to obtain the required mechanical properties [7]. After thermal treatment (heat treatment and ageing), it obtains relatively high strength and good fracture toughness [8–10]. The ageing process can be carried out naturally or accelerated (artificial ageing) [11]. Natural ageing generally gives better results in the form of increasing the strength of the material than accelerated ageing, but it takes a long time, even 4–5 days, while the use of higher temperatures during artificial ageing shortens the time of this process [12, 13].

Stampings made of aluminium sheets capable of precipitation hardening are most often shaped from the sheet in the delivery condition, i.e. after soft annealing, and then subjected to heat treatment and ageing. In engineering practice, due to a number of advantages, heat-treated sheets are also subjected to shaping in the initial stage of natural ageing [14]. For this reason, when designing processes for the forming of drawpieces from these sheets, it is important to know the value of the springback coefficient K, both for the sheets as delivered and after the heat treatment during the forming operation. It should be emphasised that shaping operations should be performed as soon as possible after heat treatment due to the deteriorating technological properties of the sheet during natural ageing.

The shaping of various types of parts and sheet metal coatings is carried out by bending processes. In the bending process, three basic stages can be distinguished in this process, i.e. elastic bending, plastic bending and springing. The distribution of longitudinal strains and stresses on the cross-section of the bent strip (Fig. 1) shows that during loading, the outer and inner layers of the material are plastically deformed, while the material in the middle layer remains under the influence of elastic stresses. As a result, after removing the load, the phenomenon of return elastic deformation is observed, i.e. the curvature of the bend decreases. The decisive coefficient for the quality of bent elements is their dimensional and shape accuracy; therefore, during the analysis and design of this process, it is very important to determine the springback effect after removing the bending load.

Quantitative assessment of the springback is carried out by means of experimental research, analytical calculations, numerical modelling and others. The amount of springback is most often

Stanisław Kut, Grzegorz Pasowicz, Feliks Stachowicz
Experimental Determination of Springback Characteristics in a Three-Point Bending Test of the Aluminium Alloy Sheet with Aluminium Cladding

DOI 10.2478/ama-2024-0034

determined by the dimensionless springback coefficient K. This coefficient is calculated from formula (1) as the quotient of the bending radius under load ρ_g and the bending radius after unloading ρ_s or as the quotient of the bending angle after unloading γ_s and the bending angle under load γ_g (Fig. 2).

$$K = \frac{\gamma_s}{\gamma_g} = \frac{\rho_g}{\rho_s} \qquad (1)$$

where γ_g, γ_s – band deflection angle under load and after springback, respectively, ρ_g, ρ_s – band radius under load and after springback, respectively.
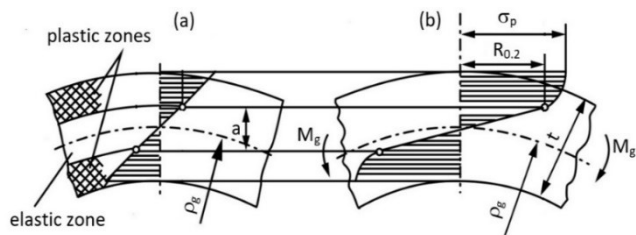

Fig. 1. Distribution of longitudinal strains (a) and stresses (b) on the cross-section of the bent strip
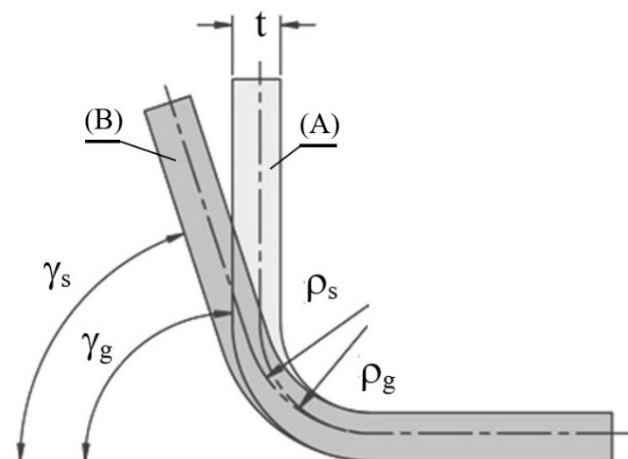

Fig. 2. The shape of a bent sample: (A) under load and (B) after unloading [15]

When designing the technological process and the bending tools, it is necessary to determine to what angle (radius) the input material should be bent to obtain the final product required after springing. Knowing the value of the springback coefficient for specific cases of bending, we can determine the radius or angle that should be used during bending in order to obtain a product with the desired shape after bending. This gives an opportunity to minimise the effects of springing after bending in the design stage of technological processes and technological devices.

In engineering practise, the correction of the shape of the prototype bending tools specified in the design is often done by trial and error. The number of these tests can be significantly reduced by increasing the accuracy of calculations that consider a wide range of coefficients affecting the amount of springback. Therefore, it is important to take into account as many coefficients as possible that influence the parameters of the analysed process when determining the value of the springback coefficient.

Various research works have been devoted to the analysis

and study of the springback phenomenon of sheets after bending and for various materials, using various approaches to solving the issues under consideration – analytical [16-18], numerical [19-21] as well as the use of neural networks [22]. However, there is a lack of knowledge on the impact of cladding layers on forecasting springback of clad aluminium alloy sheets; only studies on bending aluminium-clad steel sheets can be found [23].

Knowledge about the amount of springback of materials after bending is practically useful. The lack of data from the literature on the influence of thickness, as well as the influence of heat treatment and natural ageing time of the clad sheets made of the AW-2024 alloy on the value of the springback coefficient K as a function of relative deflection (w/f_g) was the motivation to undertake this research. The prepared characteristics of the springback coefficient of the tested sheets, in addition to cognitive aspects, have practical application in the analysis of the bending process and in the design of equipment for bending these sheets, both in the delivered condition and after heat treatment and during natural ageing.

The paper presents the results of experimental investigations of the three-point air bending process of AW-2024 aluminium alloy, with rolled AW-1050A cladding for anti-corrosion protection, which, among others, are used to make the outer plating of aircraft structures. The tests were carried out for four sheet thicknesses under delivery conditions, i.e. after soft annealing, for which the dependence on the value of the springback coefficient K as a function of sheet thickness t and relative band deflection (w/f_g) was determined. In addition, for two thicknesses of the tested sheets, the effect of the natural ageing time after heat treatment on the value of the springback coefficient as a function of relative band deflection (w/f_g) was determined.

2. MATERIAL AND EXPERIMENTAL PROCEDURE

The tests were carried out using AW-2024 aluminium alloy sheets with thicknesses of 0.5 mm, 0.8 mm, 1.0 mm and 2.0 mm – and the thickness of the AW_1050A clad layers (Fig. 3) applied on both sides was 12.1%, 10.4%, 10.0% and 5.5% of the sheet thickness, respectively. Observations of the microstructure in the cross-section of the sheets (Fig. 3) showed good cohesion of the clad material with the base material. During the bending tests, no loss of cohesion was observed. The microstructure shown corresponds to the softened state of the material, with coagulation of precipitates present, without a granular structure. No significant differences in structure were observed depending on the direction of sample collection. Experimental studies, both determining the mechanical parameters of the sheet material and bending tests, were carried out for two variants:

− all sheets are tested for material as supplied, i.e. for annealed materials,

− for sheets with a thickness of 1.0 mm and 2.0 mm, heat treatment was carried out.

In the heat-treatment process, the samples were successively heated in the furnace to a temperature of 493°C and kept at this temperature for 40 min and 45 min for thicknesses of 1 mm and 2 mm, respectively [24], and then rapidly cooled in cold water. Uniaxial tensile and bending tests were carried out using sheet samples of material delivered as delivered, immediately after heat treatment and after natural ageing for 20 min, 45 min, 90 min and 120 min. The ageing time range covered by the tests was determined based on an analysis of the assortment of produced

stamps and engineering practise, taking into account the AMS2770 standard [24].
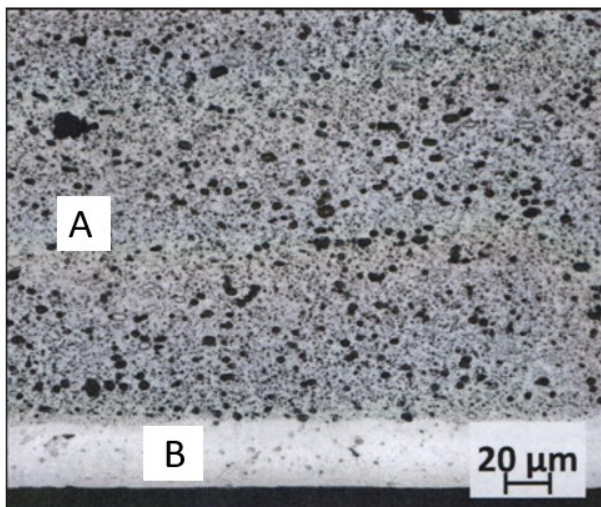

Fig. 3. An exemplary microstructure of a clad sheet in delivery condition: A – base material, B – cladding layer

From the supplied sheets, samples were taken for uniaxial stretching in the 0°, 45° and 90° according to the rolling direction of the sheets. The shape and dimensions of the samples for testing according to ISO 6892-1 are shown in Fig. 4. Static uniaxial tensile tests of individual samples were carried out on the Zwick/Roell Z030 test machine. The tensile speed of the samples was 30 mm/min. During the tensile test, the values of selected material parameters were determined:

- yield stress $R_{0.2}$,
- ultimate strength R_m,
- parameters of the strain hardening curve according to Hollomon $\sigma = C \cdot \varepsilon^n$, where C and n are the hardening coefficient and the hardening curve exponent, respectively.

Bending samples that were 40 mm wide and 100 mm long were taken in parallel with the rolling direction. Experimental bending tests were carried out on the Zwick/Roell Z030 testing machine in a three-point tool system with the same radii $r = 5$ mm (Fig. 5). For samples of each of the sheets tested, the deflection under load was set in eight cycles, successively with the value of 2 mm, 4 mm, 6 mm, 8 mm, 11 mm, 14 mm, 17 mm and 20 mm. The samples were then unloaded and the value of deflection springback was measured.

Then, on the basis of the experimental data, the numerical values of the sample deflection arrow after unloading in subsequent bending cycles were determined. The bending angle and springback angle values were calculated in subsequent cycles, together with the numerical values of the springback coefficient corresponding to these cycles. Based on the measured deflection values, the values of the deflection angles under load γg and after unloading γs were calculated.

As observed above [15], the position of the contact point of the sample with the surface of the shaping tools changes with the increase of the deflection arrow, which has a decisive impact on the value of the calculated bending angle. Therefore, to calculate the angle of bend, formula (2) was used, considering the observed phenomenon and also considering the effect of the band thickness:

$$\gamma = \mathrm{arctg}\left(\frac{2f}{w - Af}\right) \tag{2}$$

where f – band deflection arrow, w – distance between the outer bending rollers, A – dimensionless coefficient depending on the thinness coefficient t/r, and the size of the distance between the outer bending rolls w, determined on the basis of geometrical relationships, using the least squares method with the use of the Logger Pro programme.

The author's Eq. (2) was presented in detail together with the method of determining the coefficient A in the work [15].
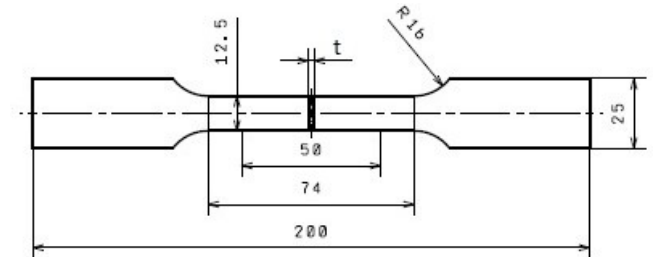

Fig. 4. Dimensions of the samples for the uniaxial tensile test in mm [15]
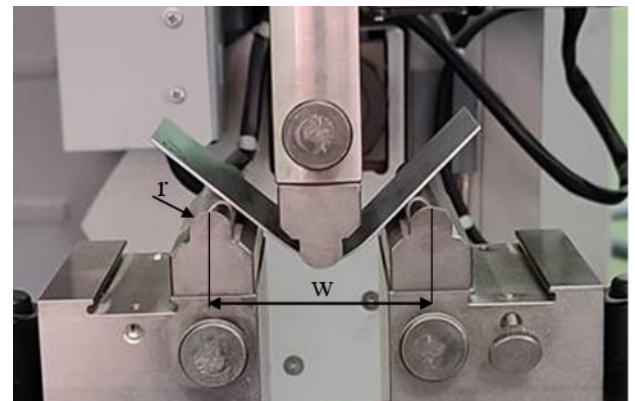

Fig. 5. A photograph of a bent sample [15]

3. RESULTS AND DISCUSSION

Based on the results of the tensile test, it can be seen that both the yield stress values and the strength limit for all thicknesses of the sheets tested under delivery conditions are more than two times higher than the values of these parameters for the clad material (Tab. 1). Heat treatment of the sheet material resulted in a very significant increase in the value of both the yield point (respectively by 110% for 1.0 mm thick sheet and 86% for 2.0 mm thick sheet), the strength limit (respectively by 99% for 1.0 mm thick sheet and 93% for 2.0 mm thick sheet) as well as for the value of the strain hardening exponent (respectively by 24% for 1.0 mm thick sheet and 44% for 2.0 mm thick sheet). With increasing ageing time, further increases in the values of both the yield point and the strength limit were observed. The values of the strain hardening exponent decrease with increasing ageing time (Tab. 2). Therefore, the observation arises that taking into account the course and effect of forming the stamps, as well as the mechanical parameters of the finished product, the conditions of heat treatment of the sheet material should be taken into account.

Stanisław Kut, Grzegorz Pasowicz, Feliks Stachowicz
Experimental Determination of Springback Characteristics in a Three-Point Bending Test of the Aluminium Alloy Sheet with Aluminium Cladding

DOI 10.2478/ama-2024-0034

Tab. 1. Selected mechanical parameters of the tested sheet material under delivery condition

Sheet thickness	Mean values of the three orientations relative to the rolling direction (0°, 45° and 90°)			
t	$R_{0.2}$	R_m	C	n
mm	MPa	MPa	MPa	
0.5	73.33	171.66	337.42	0.260
0.8	70.25	166.45	319.67	0.256
1.0	64.62	166.43	325.78	0.268
2.0	73.01	178.05	352.99	0.256
Cladding	30.07	74.50	114.60	0.225

Tab. 2. Selected mechanical parameters of the sheet material after heat treatment and ageing

Sheet thickness	Aging time	Mean values of the three orientations relative to the rolling direction (0°, 45° and 90°)			
t	Min	$R_{0.2}$	R_m	C	n
mm		MPa	MPa	MPa	
1.0	0	135.994	331.806	669.104	0.3169
	20	143.779	336.116	663.629	0.3046
	45	155.888	343.384	659.387	0.2872
	90	175.573	356.754	661.054	0.2658
	120	189.493	366.459	665.233	0.2498
2.0	0	135.853	344.660	710.125	0.3236
	20	144.999	350.551	706.208	0.3143
	45	157.429	360.241	705.092	0.2994
	90	179.438	377.486	710.667	0.2720
	120	194.363	389.288	715.725	0.2587

The springback characteristics were presented as a dependence of the springback coefficient on the value of the w/fg index because, as shown earlier [15], it allows one to obtain a linear relationship between these parameters described by a linear equation of the form:

$$K = -A\left(\frac{w}{f_g}\right) + B \qquad (3)$$

where A and B – material coefficients determined experimentally.

This is confirmed by the results of the experimental investigations presented in this study, as evidenced by the high values of the correlation coefficients R2 (Fig. 6). The data presented in the graph (Fig. 6) show that the springback coefficient K also depends on the thickness of the sheet t; so, in this case, it is a function of two variables:

$$K = f\left(\frac{w}{f_g}, t\right) \qquad (4)$$

In order to take into account the influence of the second variable, i.e. the thickness of the sheet t, the values of coefficients A and B in Eq. (3) should be determined as a function of the thickness of the sheet. Taking into account the determined values of these coefficients for the thicknesses tested (see equations in Fig. 6), the approximation method determined the relationship be-
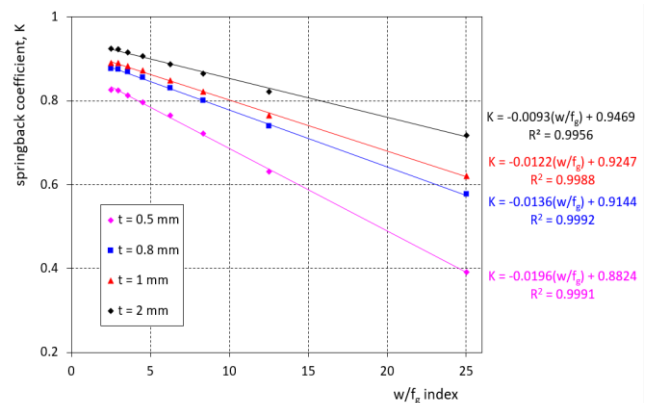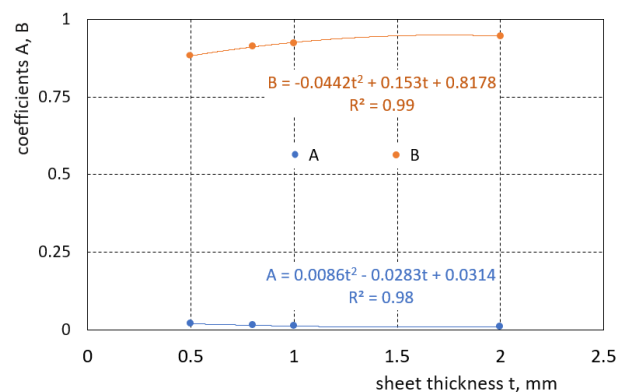
tween the sheet thickness and the value of coefficients A and B, which is presented in the graph (Fig. 7). After substituting the coefficients A and B determined as functions of thickness into formula (3), we obtain the relationship:

$$K = -(0{,}086t^2 - 0{,}0283t + 0{,}0314)\left(\frac{w}{f_g}\right)$$
$$+ (0{,}8178 + 0{,}153t - 0{,}0442t^2) \qquad (5)$$

allowing us to calculate the numerical value of the spring coefficient K as a function of the w/f_g index and the thickness of the sheet t in the range of thickness $t = (0.5\text{-}2.0)$ mm and the quotient $(w/f_g) = (2.5–25)$.

The above equation can be used for quick and estimated selection of the shape of the bending tools in order to obtain the required geometry of the final stamps.
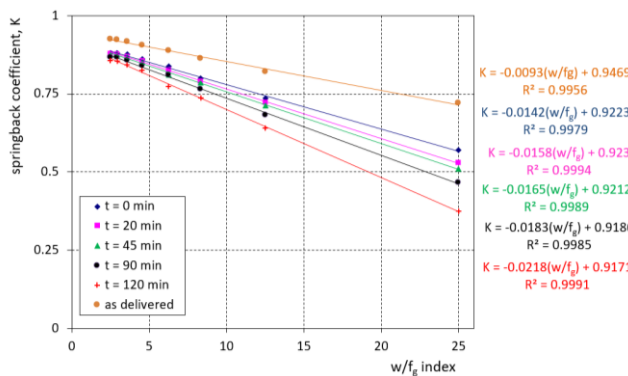
As expected, the value of the springback coefficient clearly depends on the thickness of the sheet. For the sheet with a thickness of 0.5 mm, the values of the springback coefficient are clearly lower than for the other sheets (Fig. 6). This is due to the fact that for the curvatures used in bending tests, for the thinnest sheet, the share of the elastic stress layer a (Fig. 1) is the largest. In addition, for this sheet, the percentage share of the clad thickness in relation to the sheet thickness is the highest; therefore, the more easily deformable material in the outer layers of the sheets results in a greater value of springback after removing the bending load.

Fig. 6. Dependence of the springback coefficient on the value of the w/f_g index for sheets of different thickness

Fig. 7. The influence of sheet thickness on the value of coefficients A and B in Eq. (3)

The heat treatment of the material also resulted in a significant increase in the springback susceptibility of the sheets, especially for small bending curvatures (high values of the w/fg ratio) (Figs. 8 and 9). The values of the springback coefficient for the material delivered, especially for sheets 1.0 mm thick, are clearly higher than the values of the K coefficient for sheets after heat treatment. The values of the K coefficient decrease (increase springback) as the annealing time increases. Taking into account the practical use of these relationships, it is recommended to shape products in bending processes using sheets in the delivered condition, and then heat treat the finished parts in order to increase the mechanical parameters of the material [14].
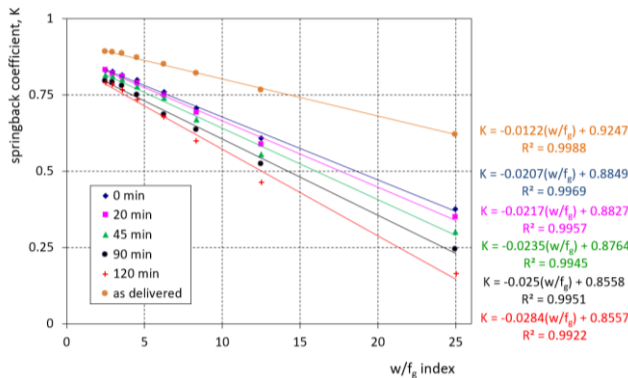
Fig. 8. Dependence of the springback coefficient on the value of the w/f_g index for sheets for different ageing times for 1.0 mm thick sheets (compared to the springback characteristics for sheet with mechanical parameters as delivered)
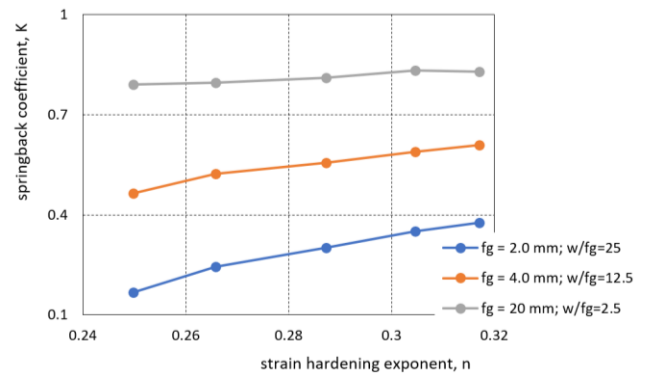

Fig. 9. Dependence of the springback coefficient on the value of the w/f_g index for sheets for different ageing times for 2.0 mm thick sheets (compared to the springback characteristics for sheet with mechanical parameters as delivered)
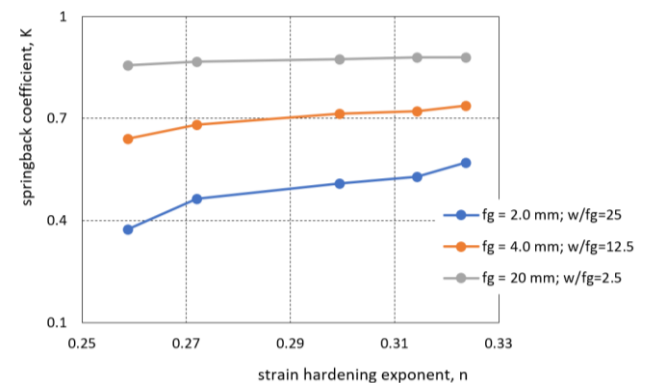
The value of the springback coefficient of sheets 1.0 mm and 2.0 mm thick after different ageing times showed a dependence on the tendency of the material to strain hardening (Figs. 10 and 11). An increase in the value of the strain hardening exponent results in an increase in the value of the springback coefficient. This relationship is more pronounced as the bending curvature (greater deflection of the samples).

During natural ageing of the tested sheets in the time range of 0–120 min, an increase of almost 40% and 43% in yield stress was observed for sheets with a thickness of 1.0 mm and 2.0 mm, respectively. At the same time, a much less intense increase in ultimate strength was recorded, which was 10% and 13% for sheets with a thickness of 1.0 mm and 2.0 mm, respectively (Tab. 2). The influence of these parameters, specifically the ratio
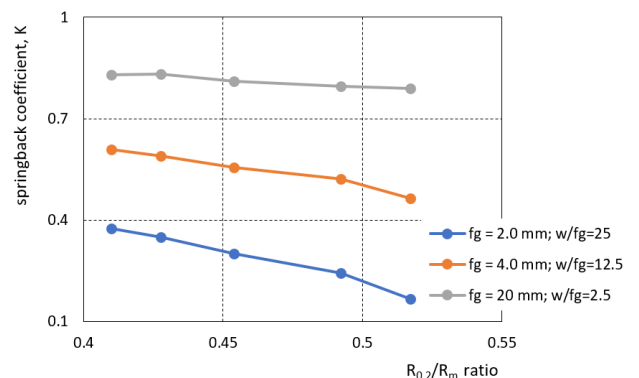
$R_{0.2}/R_m$, on the springback coefficient for three values of w/f_g, is shown in Figs. 12 and 13 for sheet metal with a thickness of 1.0 mm and 2.0 mm, respectively. Both in the case of a 1.0 mm thick sheet (Fig. 12) and a 2.0 mm thick sheet (Fig. 13), the value of the springback coefficient K decreases with the increase in the $R_{0.2}/R_m$ ratio. The intensity of the decrease in the value of the springback coefficient K with an increase in the $R_{0.2}/R_m$ ratio depends on the relative deflection w/f_g and is greater with the lower value of w/f_g. In other words, the smaller the radius of the bending curvature, the greater the springback after the bending. The amount of this springback increases additionally with the increase in the $R_{0.2}/R_m$ ratio, and this increase is more intense with a smaller bending radius.

Fig. 10. Dependence of the springback coefficient on the value of the strain hardening exponent for sheets for different deflection for sheets 1.0 mm thick

Fig. 11. Dependence of the springback coefficient on the value of the strain hardening exponent for sheets for different deflection for 2.0 mm thick sheets

Fig. 12. Dependence of the springback coefficient on the value of the $R_{0.2}/R_m$ ratio for sheets for different deflection for 1.0 mm thick sheets

Stanisław Kut, Grzegorz Pasowicz, Feliks Stachowicz

Experimental Determination of Springback Characteristics in a Three-Point Bending Test of the Aluminium Alloy Sheet with Aluminium Cladding

DOI 10.2478/ama-2024-0034

Fig. 13. Dependence of the springback coefficient on the value of the $R_{0.2}/R_m$ ratio for sheets for different deflection for 2.0 mm thick sheets
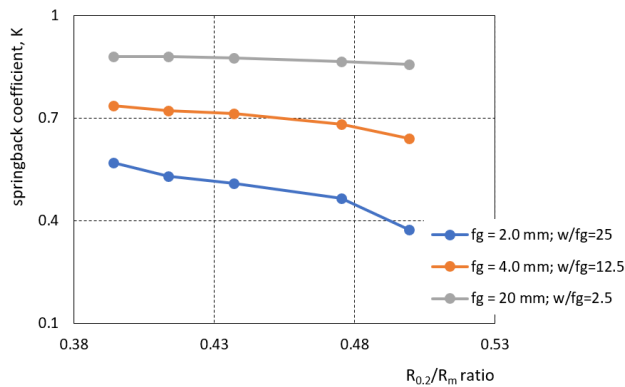
4. CONCLUSIONS

This work presents the results of the analysis of the springback phenomenon observed during elastic–plastic cold bending of 0.5 mm, 0.8 mm, 1.0 mm and 2.0 mm thick of the AW-2024 aluminium alloy with AW-1050A aluminium clad. For the sheet material in the delivery condition and after heat treatment and various ageing times, the value of the selected mechanical parameters and the springback characteristics were determined. The main conclusions of this work can be summarised as follows:

− Heat treatment of the material in the as-deliver resulted in an average approximately two-fold increase in the values of both the yield stress and the ultimate strength, and an approximately 20% increase in the hardening deformation exponent. Compared to the parameters of the heat-treated material, the increase in the yield stress and the ultimate strength after an ageing time of 120 min was on average approximately 40% and 11%, respectively. In the tested ageing time range, the strain hardening exponent values decrease with increasing ageing time, up to a value close to the value of this parameter for the material in the delivery condition.

− For all the tested sheets, a linear dependence of the value of the springback coefficient on the value on the relative deflection w/fg index was observed – with increasing bending curvature (decreasing w/fg index), the value of the springback coefficient increases. In the entire tested w/fg range, for example, for the sheet as delivered with a thickness of 2 mm, this increase was 1.28 times, while for the same sheet immediately after heat treatment, it was 1.54 times and 2.21 times after 120 min of natural ageing. It was observed that, regardless of heat treatment and ageing time, this increase was greater with the smaller the thickness of the tested sheet.

− The values of the springback coefficient for the material in the delivery state are clearly higher than the value of this index for sheets after heat treatment. Extending the ageing time of the material results in a decrease in the value of the springback coefficient.

− For heat-treated sheets, an increase in the Re/Rm ratio was observed with the increase in natural ageing time. In the tested ageing time range of up to 120 min, the value of the springback coefficient decreases as the Re/Rm ratio increases. The intensity of this decrease increases with the deflection of the sample.

− An increase in the value of the strain hardening exponent results in an increase in the value of the springback coefficient.

REFERENCES

1. Himagireesh Ch, Ramji K, Durga Prasad KG, Hari Kiran V. Multi-criteria decision model for selection of a material suitable to lightning strike protection in aerospace applications. Materials Today Proc. 2022;59: 725-733.
2. Polmear I. Light Alloy - From traditional Alloys to Nanocrystals. Butterworth-Heinemann: Oxford 2006.
3. Davies G. Materials for Automobile Bodies. Butterworth-Heinemann: Oxford 2003.
4. Atluri SN, Sampath SG, Tong P. Structural Integrity of Aging Airplanes. Springer Verlag: Berlin/Heidelberg 1991.
5. Pantelakis SpG, Chamos AN, Setsika D. Tolerable corrosion damage on aircraft aluminium structures: Local cladding patterns. Theor. Appl. Fracture Mech. 2012;58:55-64.
6. Zinonga T, Binga Z, Junb J, Zhiqianga L, Jianguob L. A study on the hot roll bonding of aluminium alloys. Procedia Manufacturing. 2020; 50:56-62.
7. Kučera V, Vojtěch D. Influence of the Heat Treatment on Corrosion Behavior and Mechanical properties of the AA 7075 Alloy. Manufacturing Technology. 2017;17:747-752.
8. Miller WS, Zhuang L, Bottema J, Wittebrood AJ, Smet PD, Haszler A, et al. Recent development in aluminium alloys for the automotive industry. Compos Sci. Technol. 2000;280:37-49.
9. May A, Belouchrani MA, Taharboucht S,Boudras A. Influence of heat treatment on the fatigue behaviour of two aluminium alloys 2024 and 2024 plated. Procedia Engineering. 2010; 2:1795-1804.
10. Sun S, Fang Y, Zhang L, Li C, Hu S. Effects of aging treatment and peripheral coarse grain on the exfoliation corrosion behaviour of 2024 aluminium alloy using SR-CT. J. Mater. Res. Technol. 2020;9:3219-3229.
11. ASM Handbook, Volume 4. Heat Treating ASM Handbook Committee, p. 841-879. DOI: 10.1361/asmhba0001205
12. Sobotka J, Solfronk P, Kolnerova M, Korecek D. Influence of technological parameters on ageing of aluminium alloy AW-2024. Manufacturing Technology. 2018;18:1023-1028.
13. Fallah Tafti M, Sedighi M, Hashemi R. Effects of natural ageing treatment on mechanical, microstructural and forming properties of Al 2024 aluminum alloy sheets. Iranian J. Mater. Sci. Engng. 2018;15:1-10. doi: 10.22068/ijmse.15.4.1
14. Kut S, Pasowicz G, Stachowicz F. The influence of natural aging of the AlCu4Mg1 aluminum sheet alloy on the constitutive parameters of selected models of flow stress. Adv. Sci. Technol. Res. J. 2022;16: 216-229. doi.org/10.12913/22998624/154792
15. Kut S, Pasowicz G, Stachowicz F. On the springback and load in three-point air bending of the AW-2024 aluminium alloy sheet with AW-1050A aluminium cladding. Materials. 2023;16:2945. doi. 10.3390/ma16082945.
16. Sharma PK, Gautam V, Agrawal AK. Analytical and numerical prediction of Springback of SS/Al-alloy cladded sheet in V-Bending. J. Manuf. Sci. Eng. 2021;143(3):031011.
17. https://doi.org/10.1115/1.4048953
18. Zhu YX, Liu YL, Yang H, Li HP. Development and application of the material constitutive model in springback prediction of cold bending. Materials Designe. 2012;42:245-258.
19. Wu Z, Gong J, Chen Y, Wang J, Wei Y, Gao J. Springback prediction of dieless forming of AZM120 sheet metal based on constitutive model. Metals. 2020;10:780. doi:10.3390/met10060780.
20. Vorkov V, Aerens R, Vandepitte D, Duflou JR. Springback prediction of high-strength steels in large radius air bending using finite element modeling approach. Procedia Eng. 2014;81:1005-1010. doi:10.1016/j.proeng.2014.10.132

21. Lin J, Hou Y, Min J, Tang H, Carsley JE, Stoughton TB. Effect of constitutive model on springback prediction of MP980 and AA6022-T4. Int. J. Material Forming. 2020;13:1-13. doi.org/10.1007/s12289-018-01468-x

22. Sharma PK, Gautam V, Agrawal AK. Experimental and numerical investigations of springback and residual stresses in bending of a three-ply clad sheet. Proc IMechE Part L: J. Materials: Design Applications. 2021;235,2823-2838
https://doi.org/10.1177/14644207211037006

23. Trzepieciński T, Lemu HG. Improving prediction of springback in sheet metal forming using multilayer perceptron-based genetic algorithm. Materials. 2020;13:3129. doi.org/10.3390/ma13143129.

24. Yilamua K, Hino R, Hamasaki H, Yoshida F. Air bending and springback of stainless steel clad aluminium sheet. J. Mater. Proc. Technol. 2010;210:272-278. doi.org/10.1016/j.jmatprotec.2009.09.010.

25. AMS2770. Heat Treatment of Wrought Aluminum Alloy Parts. Rev. 2015-09.

Stanisław Kut: https://orcid.org/0000-0003-0870-7548

Grzegorz Pasowicz: https://orcid.org/0000-0002-7932-0044

Feliks Stachowicz: https://orcid.org/0000-0003-2756-0414

Maciej Obst, Dariusz Kurpisz, Michał Jakubowski
Experimental and Analytical Approaches on Air Spring Absorbers Made of LDPE Polymer

DOI 10.2478/ama-2024-0035

EXPERIMENTAL AND ANALYTICAL APPROACHES ON AIR SPRING ABSORBERS MADE OF LDPE POLYMER

Maciej OBST[*], **Dariusz KURPISZ**[*], **Michał JAKUBOWSKI**[**]

*Institute of Applied Mechanics, Poznań University of Technology, ul. Jana Pawła II 24, 60-965 Poznań, Poland
**Faculty of Mechanical Engineering, Poznań University of Technology, ul. Jana Pawła II 24, 60-965 Poznań, Poland

maciej.obst@put.poznan.pl, dariusz.kurpisz@put.poznan.pl, michal.g.jakubowski@student.put.poznan.pl

Abstract: Damping and energy-consuming elements can be found in many technical applications. This means these component types can prevent fractures or injuries in the case of products or people, respectively. In the last time, many modern applications and inventions associated with the reduction of the effects of an impact are observed especially in the mode of transportation safety area. The significant development of the automotive industry, increasing popularity of motorbikes, electric bikes and scooters, sports field, etc., require new solutions for personal safety protection. Human head and neck protection, and other body parts protection are typical groups of solutions from biomechanics and mechanical engineering. Authors have investigated LDPE-made pneumatic absorbers under axial impact force. Based on the experimental approach and analytical model, mechanical characteristics are presented. Impact force value, deceleration and damping for different loading conditions are shown. Because safety systems' impact protective features can be matched to impact conditions, results indicated that absorber damping could possibly be a good solution for them, shaping the impact characteristics according to safety requirements.

Key words: LDPE absorbers, reaction on impact, analytical approach, mechanical parameters, impact test, LDPE bellows impact, protective

1. INTRODUCTION

Materials, components or structures are very often subjected to complex loading covering a dynamic one. This means the stress state is represented by a few components, and deformation can occur at more complicated features than it can be noticed at a one-axial loading type (1,2). Research on the dynamics behaviour of materials and structures can be divided into experimental researches (3–8), simulation ones and hybrid methods (9–12). Modern materials and rapid development of engineering materials create new opportunities for scientists and engineers dealing with the protection of human health and life. Dynamic tests concerning the loading impulse are the basis for all activities aimed at developing more and more effective protection systems against the effects of accidents. The review paper (13) contains a list of currently designed layered structures acting as impact and explosion energy absorbers. Attention was drawn to the enormity of works related to the dynamic study of layered structures, which makes the topic up-to-date due to the attempt to unify the issue. The structures of the cores are interesting because they are designed based on origami inspiration. Structures with auxetic properties are also geometrically complex and give possibilities of impact energy-absorbing applications. Interest in auxetics as cores of layered energy-absorbing structures is a very interesting direction. In this paper, a layered structure was also specified, where the core is made of pipes arranged parallel to each other, perpendicular to the linings. Attention is paid to the material from which pipe cores are currently made. They are metals or polymers. Tubes filled with foam are characterised by very good energy consump-

tion. Structures of this type are used in protection against the effects of impacts at relatively low speeds, where structure performance may occur. In paper (3), the method of dynamic testing of polypropylene obtained uniaxial effects, determining the strain rate values at the following levels: 100 s^{-1}, 200 s^{-1}, 300 s^{-1}, 400 s^{-1} and 500 s^{-1} was presented. During the experiment, the authors have used a split-Hopkinson pressure bar giving constant strain rates. The obtained results of dynamic tests were compared with the quasi-static test ones. Lower values of strain at destruction at dynamic loading were observed. In the analysis of the results, the wave phenomenon was taken into account, based on the one-dimensional wave theory. Jordan et al. (4) also used the split-Hopkinson pressure bar and the relationship between strain rate and grain size and mechanical properties of OFHC copper was investigated. The measurement of the radial and longitudinal deformation was carried out using the laser technique together with the registration of images with a high-speed camera. It was pointed out that the Poisson ratio in dynamic tests assumes a constant (14). The results of tension dynamic tests of X20MnAlSi16-3-3 steel are presented. A rotary hammer was used, which allows setting the strain velocity in the range 5–40 m/s. Based on the obtained results, it was found that the tested high-grade steel strengthens with increasing strain velocity values. An increase in the hardness of the tested steel was observed (5). Experimental and analytical results for a radially loaded ring during an explosion are presented. Ring deformations were measured using the X-ray method. Ring specimens, placed on a cylindrical explosive charge, made it possible to measure changes in radius and deformation rate. In theoretical investigations, the

specimen ring was treated as a thin-walled structure, assuming: symmetry during sample deformation, plane strain state occurrence, ring outer side pressure equal to zero, isotropic properties, no compressible, ideal plastic material and the instantaneous value of the ring sample radius is determined experimentally. Analytical model of investigated ring was based on the Tresca condition. Stankiewicz et al. (15) presented the results of energy consumption tests of the following elastomers: Asmathane (65 ShA), Asmaprene BE (55 ShA), Asmaprene Q (55 ShA), Easyprene FPS (30 ShA), Biresin U1303 (hardener Biresin U1402), Biresin U1305 (hardener Biresin U1305) and Biresin U1419 (hardener Biresin U1419). Properties of these materials are resistance to large deformations and thermal dissipation of impact energy. A drop tower was used as a test stand, where piezoelectric force sensor and laser displacement sensor was applied. In the study, a high-speed camera was used to record successive cycles of dynamic specimen deformations. The authors based on the obtained experimental characteristics, build constitutive models of dynamic mechanical material properties. Then, models were applied to numerical investigations and design impact protection cover. In paper (11), Raponi and Fiumarella presented experimental and numerical analysis of attenuator made of thermoplastic composite material parameter identification under axial impact loading. Composite materials have light weight and good energy dissipation. Investigated truncated-cone shape bumper with a rectangular cross-section was crushed in a quasi-static experimental test. Kathiresan et al. (12) described results of the experimental and simulation of quasi-static compression test of thin-walled cone made of glass fibre and epoxy resin reinforced composite. Conical specimens had different forming angles. Loading deformation characteristics were compared with those obtained by Abaqus simulation. In paper (16), new proposition of glass or carbon fibre sandwich panel with foam core was presented. Prepared panels was tested for impact load under different energy. Authors used Instron Dynatup 9250HV drop weight impact testing machine and did tests according to the ASTM norm. Applied impact head speed was equal to 2 mm/min. Avalle Belingardi (17) presented a model of the foam material, the purpose and application of it which is to give possibilities to select the appropriate foam due to the absorption of impact energy. The presented model of the foam material includes, among others, the influence of the strain rate on its mechanical properties. Proposed foam one-dimensional material model is fitted to experimental data based on past experimental data of the authors. The aluminium foam model studies included quasi-static, dynamic, and impact tests at different loading speeds and impact energy. It was pointed out that foams are materials commonly used in devices protecting the safety of people and in the transport of delicate goods. In paper (9), Koohbor et al. presented the results of mechanical energy absorption tests under low-velocity impact loading for elastomeric hybrid structure polyurethane foam. The authors pointed out on the measure stress and strain in foam structure, energy indicators and evolution of the Poisson ratio. Optical systems were used during experimental tests. The examined foam behaviour was characterised by an increase of strength value when strain rate increased. Reyes and Børvik (8) presented the continuation of their research on the energy dissipation properties of layered structures. Various foams acting as the core were tested. Thin aluminium plates were used as covers. Dynamic loading was used by means of the drop tower, where a constant mass of 15 kg impacted the tested specimens with different velocities between 5 m/s and 10 m/s. During the research, high-

speed cameras were used to record the movement. In conclusion, it was found that the best energy dissipation effects can be obtained by using low-density foam cores. In paper (18), foam-filled, thin-walled structures were presented as mechanical energy absorbers. The interesting fact is that foam density varies throughout the foam depth. The authors noted that variable foam density has a significant influence on the energy dissipation process during impact. Investigated structures were prepared as square, thin-walled aluminium-made pipes filled by aluminium foam, where foam density varies on the specimen length in accordance with impact direction. Research was made by the FEM simulation software. Robinson et al. (19) investigated the interaction between head and protective football helmet under impact load. Influence factors that lead to mild traumatic brain injury (MTBI) were the main revealing goal of the researchers. The authors pointed out that the reduction of the coefficient of friction between the head and the helmet liner results in a reduction of overloads acting on the head. In paper (20), Maw et al. investigated skater's helmets under impact loading, where helmet size and shape were decision-making parameters. During the experimental tests, the helmet fell on the special pad. The authors used four levels of the drop. As a conclusion, it was found that the size and the helmets' radius of curvature have an important influence on the linear decelerations during the helmet impact. Research on the energy consumption of helmets is also presented by Clough et al. (6). Modern elastomeric lattice properties, applied as helmet shock absorber padding are investigated. The researchers have paid attention to two types of materials used as helmet linings: single-hit material and self-recovering. Resistance to multiple impacts undoubtedly increases the usefulness of the helmet. Additive manufacturing of cellular architecture is giving new possibilities to design more effective cellular structure where we can design more precisely the safety properties. The problem of head overloads was studied by Lewis et al. (21), where they experimentally investigated the problem of head acceleration, which was protected by football helmets. Volunteers between the age of 16 years and 30 years, with football helmet worn, had accelerometers inside their mouths. They also applied accelerometers installed inside the lining layer. Human cadaver heads were used with and without protective helmets for a more intense impact during tests. In the case of a corpse, blunt impact force was realised by pendulum device. The recorded results were compared with each other, paying attention to the acceleration peak values. The test results showed the advantages of safety helmets. Attention was focussed on the differences between the results of the measured accelerations for the sensors placed in the mouth and the helmet lining. The results of research on the chin part of the full-face helmet were presented by Whyte et al. (22). The finite element method was used for dynamic simulation of the helmet behaviour. The author applied two composite layers to increase the stiffness of the chin part of the helmet. This modification resulted in a reduction of peak acceleration of the head. It was noted that the stiffness of the foam lining the helmet should be selected in correlation with the properties of the helmet shell. The lowest acceleration values were obtained when the stiffness of the helmet shell was increased and the stiffness of the foam lining inside the helmet was reduced. Trzaskalska and Chwastek (7) conducted studies on the effect of the density of ski helmet liners made of expanded polystyrene (EPS) in order to assess the energy dissipation properties. It was found that increasing the EPS density increases the damping properties while reducing flexibility and increasing the hardness and brittleness of the ski helmet

Maciej Obst, Dariusz Kurpisz, Michał Jakubowski
Experimental and Analytical Approaches on Air Spring Absorbers Made of LDPE Polymer

DOI 10.2478/ama-2024-0035

liners. Mizuno et al. (10) used FEM simulations for the investigation of cyclist helmet properties protection during the impact of vehicle A-pillar. Due to the high stiffness of the A-pillar, a head impact results in serious injuries. It was noted that, in the case under study, the helmet liner had little effect on the HIC parameter but by reducing the stiffness of the A-pillar, the HIC parameter can be reduced. It should be noted that the authors used a simplified FEM simulation model. Considerations led by Ghajari et al. (23) made it possible to notice that the tests of protective helmets are carried out using standard heads, ignoring the rest of the body. Using the finite element method, a full-face helmet study was conducted taking into account the interaction of the whole body during impacts. The authors pointed out that even during 10 m/s impact, the whole body causes the helmet liner to be crushed. The results described by Wu et al. (24) present the resistance to the secondary impacts of construction helmets. It was found that the protective performance of these helmets can be improved by using polyethylene air-bubble cushions. During the experimental tests, a drop tower was used. Multiple strokes were performed at different times by dropping the impactor with an accelerometer from different heights. The authors found that the use of air-bubble cushions significantly improves the protective qualities of construction helmets. Mazurek and Szyguła (25) performed a numerical FEM analysis of the impact on a thin-walled aluminium-made column. Columns with circular, square and triangular cross-sections were tested at the impact velocity of 30 km/h. The influence of notches on the crushing process of the columns was also examined. Based on the research, interesting conclusions were drawn. During axial impact, the cross-sectional shape of the column affects the dissipated energy capacity. The columns with notches or embossing results in increase of the amount of dissipated energy and a more favourable deceleration curve. Research results are presented in Böhm et al. (26) for conducted tests on the front bumper bracket of a passenger car. Bumper bracket was made from carbon fibre epoxy bumper brackets reinforced with 2D biaxial and 2D triaxial braids. Experimental studies were conducted on a dedicated drop tower equipped with fast cameras. Simultaneously, numerical research was carried out in the Abaqus software. The usefulness of new phenomenological textile-reinforced composites models of all damages were also demonstrated. Raponi and Fiumarella (11) presented the results of experimental and simulation tests of a bumper made of thermoplastic composite. Material parameters were identified on the basis of the experimental study. The crushing test of the component was performed and compared with the results of the computer simulation. Optimisation of the simulation model was carried out by adapting it to the characteristics of the load-displacement based on the experimental crushing test.

In the current paper, the results of selected experimental and analytical approaches for the air LDPE absorbers system will be presented. The attention follows not only the influence of impact velocity on mechanical characteristics, but is focussed on analytical description of the relation between dynamic characteristics for open and closed LDPE absorbers system.

2. EXPERIMENTAL IMPACT TESTS

Laboratory tests were carried out using a drop tower stand with a steel 0.2-kg mass impactor. The free fall of the impactor took place from several levels relative to the base of the test

stand, namely: 200 mm, 400 mm, 600 mm and 900 mm. During the impact test, the impactor hit the aluminium plate bumper shown in Fig. 1, equipped with very low friction coefficient ball bearings, one in each corner. The aluminium plate bumper moved along the corner bar guides, where the resistance to movement was negligible. Pneumatic LDPE absorbers have been impact loaded, where at the same time, four spring LDPE absorbers were tested and placed parallel.
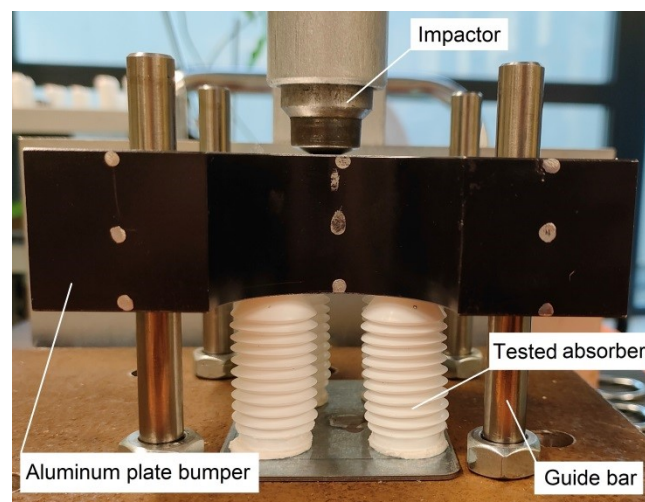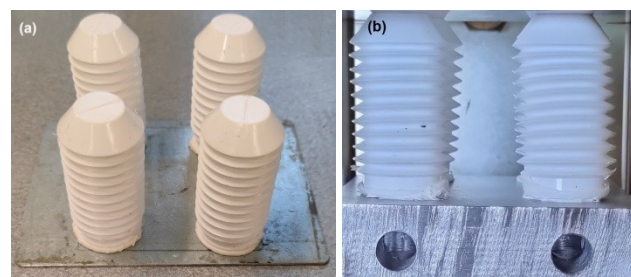

Fig. 1. Impact test stand

Fig. 2. Pneumatic LDPE absorbers: (a) sealed absorbers, (b) free airflow absorbers

Tested LDPE absorbers were examined as sealed space—Fig. 1, where the air was compressed under impact loading, and in another case, when free airflow was released through a passage channel in the steel base of the absorber—Fig. 2b. In the second case, only the dynamic stiffness of the LDPE absorber was followed. The results of the experimental research were dynamic characteristics for the air-compressing absorber and the absorber with the resistance posed only by its shell.

3. LDPE FOIL TENSION TEST RESULTS

LDPE polymer used to produce the tested absorbers was delivered in a sheet of foil form. A specimen was subjected to a static tensile test at room temperature. Based on results from the tensile test, fundamental LDPE mechanical characteristics were elaborated—Fig. 3.2.

Fig. 3.1. Specimen of LDPE foil used in the tensile test

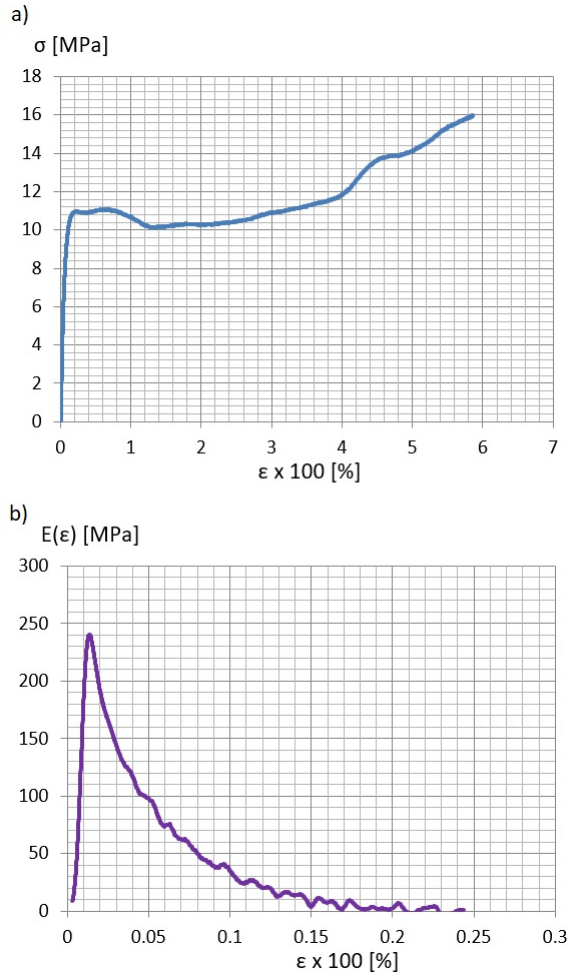The thickness of the foil sheet wasn't constant and it oscillated from 0.36 mm to 0.39 mm.

Fig. 3.2. Stress–strain relations (a) for tangential modulus E(ε)
(b) for LDPE

4. ANALYTICAL MODEL OF PNEUMATIC ABSORBER

Based on the experimental dynamic results of the LDPE absorbers, a phenomenological analytical description was proposed. The purpose of the analytical research was focussed on the description of the impact phenomenon.

For the clarity of the investigations, the following assumptions were taken:

− The geometry and the static characteristics of the absorber are well-known.
− The absorber's deflection was connected only with the reaction of its harmonic part.

− The absorber was filled with the medium (air) about the initial pressure, p_o [MPa] and the temperature compatible with the ambient temperature.
− The connection between the absorber and the base is perfectly tight.
− Impact time is so short that every exchange of the thermal energy with the ambient does not exist.

Due to the complete tightness of the discussed absorber and its volume change as a consequence of dynamic compression, the relation between current values of pressure, p, and volume, ϑ [mm³], is the same, like in the case of adiabatic transformation. In consequence, we can write:

$$p\vartheta^\kappa = const. \tag{4.1}$$

where κ is the Poisson's coefficient, depending on the medium fitting the absorber.

Therefore, for the increase of pressure, Δp, caused by the volume change, $\Delta\vartheta$, the following relationship is true:

$$p_o\vartheta_o^\kappa = (p_o + \Delta p)(\vartheta_o + \Delta\vartheta)^\kappa, \tag{4.2}$$

and hence:

$$\Delta p = p_o \cdot \left[\left(\frac{\vartheta_o}{\vartheta_o + \Delta\vartheta}\right)^\kappa - 1\right], \tag{4.3}$$

or equivalently:

$$\Delta p = p_o \cdot \left[\left(1 + \frac{\Delta\vartheta}{\vartheta_o}\right)^{-\kappa} - 1\right], \tag{4.4}$$
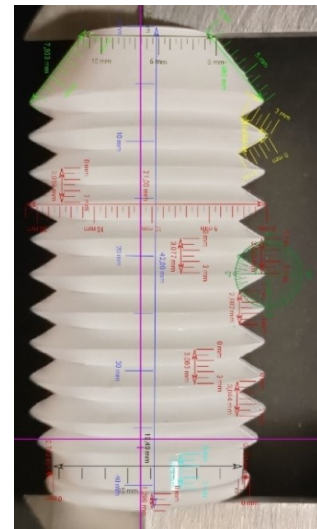
where p_o and ϑ_o are respectively the initial values of pressure and absorber's volume.

According to Pascal's law, because the pressure propagates independently in the direction, it can be considered that it is the quotient of the force increment, ΔF_1 [N], (of the gas pressure) and the cross-surface area, A_o [mm²], of the absorber, which in effect gives:

$$\Delta F_1 = A_o p_o \cdot \left[\left(1 + \frac{\Delta\vartheta}{\vartheta_o}\right)^{-\kappa} - 1\right], \tag{4.5}$$

where $A_o = \frac{1}{4}\pi D^2$ and D are absorber's cross-section diameter.

In order to determine the initial volume, ϑ_o, and its change, $\Delta\vartheta$, let's consider the absorber geometry, based on Fig. 4.1.

Fig. 4.1. Detail dimensions of the discussed absorber

Maciej Obst, Dariusz Kurpisz, Michał Jakubowski
Experimental and Analytical Approaches on Air Spring Absorbers Made of LDPE Polymer

DOI 10.2478/ama-2024-0035

Based on the measurements, the work of the spring absorber can be illustrated, just like in the following figures.
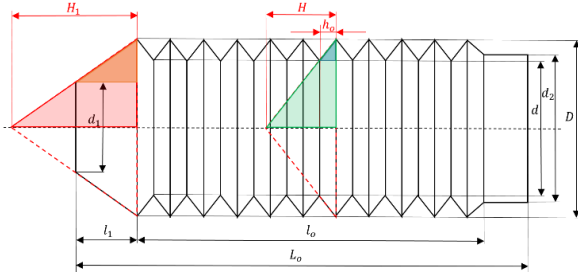

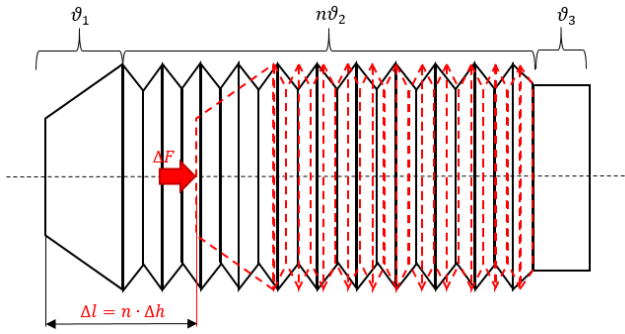**Fig. 4.2.** Absorber geometry parameters in the initial state

Fig. 4.3. Deflection of the absorber

Assuming the acceptable simplification of the shape, geometry can be assumed that the initial volume of the absorber is:

$$\vartheta_o = \vartheta_1 + n\vartheta_2 + \vartheta_3, \tag{4.6}$$

where ϑ_1, ϑ_2 and ϑ_3 denote the volume of the top, working and base parts of the absorber, respectively.

The similarity between two pairs of triangles: orange and red, blue and green implies:

$$H_1 = \frac{D}{D-d_1} \cdot l_1, \tag{4.7}$$

and

$$H = \frac{D}{D-d} \cdot h_o, \tag{4.8}$$

which gives:

$$\vartheta_1 = \frac{1}{12}\pi D^2 H_1 - \frac{1}{12}\pi d_1^2(H_1 - l_1) = \frac{1}{12}\pi[(D^2 - d_1^2)H_1 + d_1^2 l_1] = \frac{1}{12}\pi(D^2 + Dd_1 + d_1^2)l_1, \tag{4.9}$$

$$\vartheta_2 = \frac{1}{12}\pi D^2 H - \frac{1}{12}\pi d^2(H - h_o) = \frac{1}{12}\pi[(D^2 - d^2)H + d^2 h_o] = \frac{1}{12}\pi(D^2 + Dd + d^2)h_o. \tag{4.10}$$

Using Eq. (4.6), we get:

$$\vartheta_o = \frac{1}{12}\pi(D^2 + Dd_1 + d_1^2)l_1 + \frac{1}{12}\pi n(D^2 + Dd + d^2)h_o + \frac{1}{4}\pi d_2^2(L_o - l_o - l_1). \tag{4.11}$$

According to the interpretation illustrated in Fig. 4.3, the absorber volume change, $\Delta\vartheta$, can be expressed as:

$$\Delta\vartheta = \vartheta - \vartheta_o \tag{4.12}$$

where,

$$\vartheta = \frac{1}{12}\pi(D^2 + Dd_1 + d_1^2)l_1 + \frac{1}{12}\pi n(D^2 + Dd + d^2)(h_o + \Delta h) + \frac{1}{4}\pi d_2^2(L_o - l_o - l_1), \tag{4.13}$$

which gives:

$$\Delta\vartheta = \frac{1}{12}\pi n(D^2 + Dd + d^2)\Delta h. \tag{4.14}$$
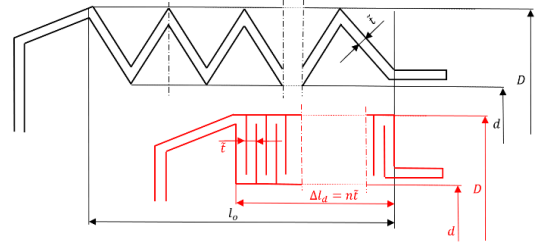

Fig. 4.4. Absorber reaction on compression force

Due to the thickness, $\tilde{t}$, of the absorber surface, elastic compression ends; when its value equals the limit value, $\Delta l_d = n\tilde{t}$ (see Fig. 4.4), which implies the real change of the volume:

$$\Delta\vartheta_r = \frac{1}{12}\pi n(D^2 + Dd + d^2)h_o - \frac{1}{4}\pi d^2(l_o - \Delta l_d). \tag{4.15}$$

On the other hand, based on Eq. (4.14), this reaction implies the volume decrease:

$$\Delta\vartheta_d = \frac{1}{12}\pi(D^2 + Dd + d^2)\Delta l_d. \tag{4.16}$$

During the compensation, the absorber thickness changes its volume, therefore, we introduce the correction coefficient:

$$k = \frac{\Delta\vartheta_r}{\Delta\vartheta_d} = \frac{l_o}{\Delta l_d} - 3 \cdot \frac{d^2}{D^2 + Dd + d^2} \cdot \frac{l_o - \Delta l_d}{\Delta l_d}. \tag{4.17}$$

hence:

$$\Delta\tilde{\vartheta} = k \cdot \Delta\vartheta = \frac{1}{12}\pi kn(D^2 + Dd + d^2)\Delta h, \tag{4.18}$$

and next, after substituting into Eq. (4.5), we get:

$$\Delta F_1 = A_o p_o \cdot \left[\left(1 + \frac{nk(D^2 + Dd + d^2)\Delta h}{(D^2 + Dd_1 + d_1^2)l_1 + n(D^2 + Dd + d^2)h_o + 3d_2^2(L_o - l_o - l_1)}\right)^{-\kappa} - 1\right]. \tag{4.19}$$

Due to the fact that the complete change of the absorber height, $\Delta l = n\Delta h$ (where, $n\Delta h \leq \Delta l_d$), we can write:

$$\Delta F_1 = A_o p_o \cdot \left[\left(1 + \frac{k(D^2 + Dd + d^2)\Delta l}{(D^2 + Dd_1 + d_1^2)l_1 + n(D^2 + Dd + d^2)h_o + 3d_2^2(L_o - l_o - l_1)}\right)^{-\kappa} - 1\right] \tag{4.20}$$

and taking into account the experimental dynamic absorber axial stiffness, C_m (which is known from the experimental results for open LDPE absorbers system), we have:

$$\Delta F_2 = C_m \cdot \Delta l, \tag{4.21}$$

which finally gives:

$$\Delta F(\Delta l) = \Delta F_1 + \Delta F_2. \tag{4.22}$$

The received pattern is an analytical description of the theoretical characteristic of the ideal sealed absorber.

Replacing the absorber height change, Δl, with the displacement, x, along its axis, the equation of motion for a package consisting of N absorber (in our case, $N = 4$) can be written as:

$$m\frac{d^2x}{dt^2} = -N\Delta F(x), \tag{4.23}$$

where m is the running mass.
Because:

$$\frac{d^2x}{dt^2} = V\frac{dV}{dx}, \tag{4.24}$$

so:

$$mV\frac{dV}{dx} = -NA_o p_o \cdot [(1 - Bx)^{-\kappa} - 1] - NC_m x, \tag{4.25}$$

where:

$$B = \frac{k(D^2 + Dd + d^2)}{(D^2 + Dd_1 + d_1^2)l_1 + n(D^2 + Dd + d^2)h_o + 3d_2^2(L_o - l_o - l_1)}. \tag{4.26}$$

Finally, using of condition, $V(0) = V_o$, it can be written that:

$$V = $$
$$\sqrt{V_o^2 + 2N\frac{A_o p_o}{Bm} \cdot \left\{\frac{1}{1-\kappa}[(1 - Bx)^{-\kappa+1} - 1] + Bx\right\} - N \cdot \frac{1}{m}C_m x^2}. \tag{4.27}$$

Returning to the substitution, $V = \frac{dx}{dt}$, the relation between compression, x, and time, t, can be expressed as:

$$t = \int_0^x \frac{dx}{\sqrt{V_o^2 + 2N\frac{A_o p_o}{Bm}\left\{\frac{1}{1-\kappa}[(1-Bx)^{-\kappa+1}-1]+Bx\right\} - N\cdot\frac{1}{m}C_m x^2}}. \tag{4.28}$$

Based on the above equation, it is possible to determine the relation between the dynamic absorbers deflection and time in the case of an ideal sealed system of absorbers, on the base of the same characteristic but in the free flow of air state. The determined characteristics are presented and discussed in the next part of the current paper.

5. APPROXIMATION OF EXPERIMENTAL RESULTS AND APPLICATION OF THEORETICAL INVESTIGATIONS

The basic experimental characteristic was the relation between deflection, x, of the LDPE absorbers system, and the time, t, (see blue lines in Fig. 5.1). The necessity of the achievement of the calculated values of velocity $V(t)$, acceleration $a(t)$ and force $F(t)$ implies that the approximation $x(t)$ should be three times differentiable and equal zero at zero point ($x(0) = 0$).

To achieve the above assumptions, the approximation function was taken in the form:

$$x(t) = a \cdot \sin(bt) \quad \text{for } t \langle 0; \frac{\pi}{2b}\rangle, \tag{5.1}$$

and in consequence:

$$V(t) = \dot{x}(t) = ab\cos(bt) \text{ for } t \langle 0; \frac{\pi}{2b}\rangle, \tag{5.2}$$

$$a(t) = \dot{V}(t) = -ab^2\sin(bt) = -b^2 x(t) \text{ for } t\langle 0; \frac{\pi}{2b}\rangle, \tag{5.3}$$

$$F(t) = m_P \cdot a(t) = -m_P \cdot b^2 x(t) \text{ for } t\langle 0; \frac{\pi}{2b}\rangle, \tag{5.4}$$

and finally:

$$\dot{F}(t) = -m_P \cdot b^2 \dot{x}(t) = -m_P \cdot ab^3\cos(bt), \tag{5.5}$$

where a and b are experimental coefficients and m_P is the mass of the palte.

It is easy to see that:

$$F(t) = -m_P \cdot b^2 x(t) = -C_p x(t), \tag{5.6}$$

where $C_p = m_P \cdot b^2$ is the experimental dynamic stiffness, and

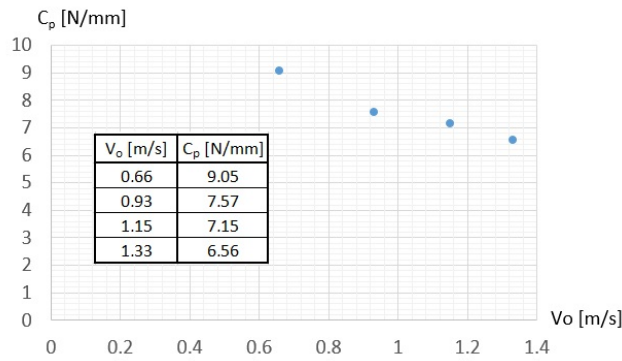$$C_m = \frac{1}{N} \cdot C_p, \tag{5.7}$$

is the dynamic stiffness of a single absorber.

The approximations of experimental characteristics is illustrated. Based on the results of the experiments, the initial velocities of the bumper, corresponding to the falls of the impactor from the heights of 200 mm, 400 mm, 600 mm and 900 mm, were assumed to be equal to: 0.66 m/s, 0.93 m/s, 1.15 m/s and 1.33 m/s.
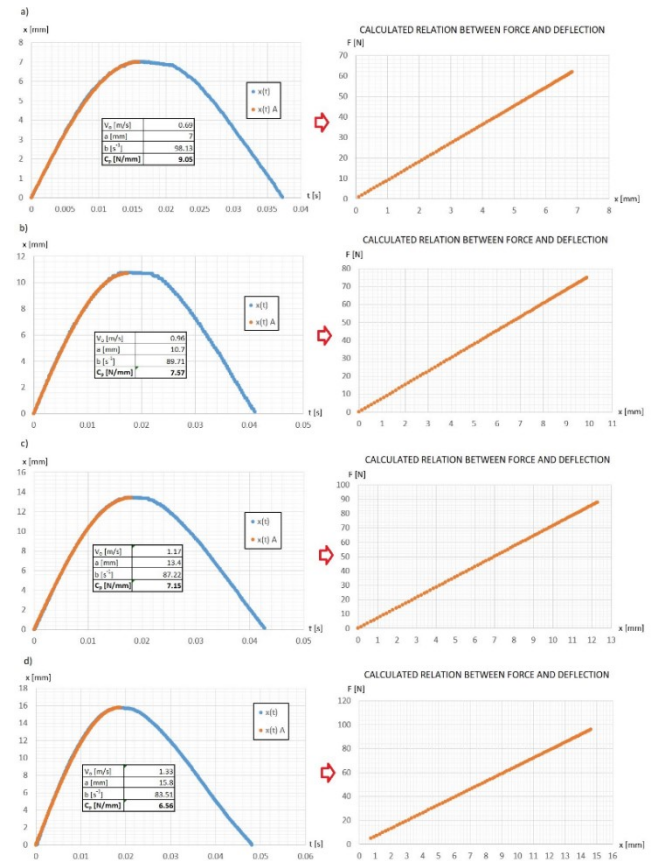

Fig. 5.1. The approximation (orange line) of experimental characteristics (blue line) for open absorbers system in case of initial velocity: (a) $V_o = 0.69$ $[\frac{m}{s}]$, (b) $V_o = 0.96$ $[\frac{m}{s}]$, (c) $V_o = 1.17$ $[\frac{m}{s}]$, (d) $V_o = 1.33$ $[\frac{m}{s}]$

Dynamic stiffness of the free flow of the air LDPE absorbers system, determined on the basis of experimental characteristics approximation, at different values of the initial deflection velocity, is presented on the graph (Fig. 5.2).

Maciej Obst, Dariusz Kurpisz, Michał Jakubowski
Experimental and Analytical Approaches on Air Spring Absorbers Made of LDPE Polymer

DOI 10.2478/ama-2024-0035

Fig. 5.2. Dynamic stiffness of free flow of air LDPE absorbers system at different values of initial impact velocity

V_o [m/s]	C_p [N/mm]
0.66	9.05
0.93	7.57
1.15	7.15
1.33	6.56

Using the above experimental dynamic stiffness of a free flow of air LDPE absorbers system, one can determine the theoretical characteristic $x(t)$ for a closed system (see Eq. 4.28). With respect to the possibility of validation of the results of theoretical approaches, the experimental characteristics of the closed system were introduced (see Fig. 5.3), while theoretical and experimental characteristics are presented in Fig. 5.4.
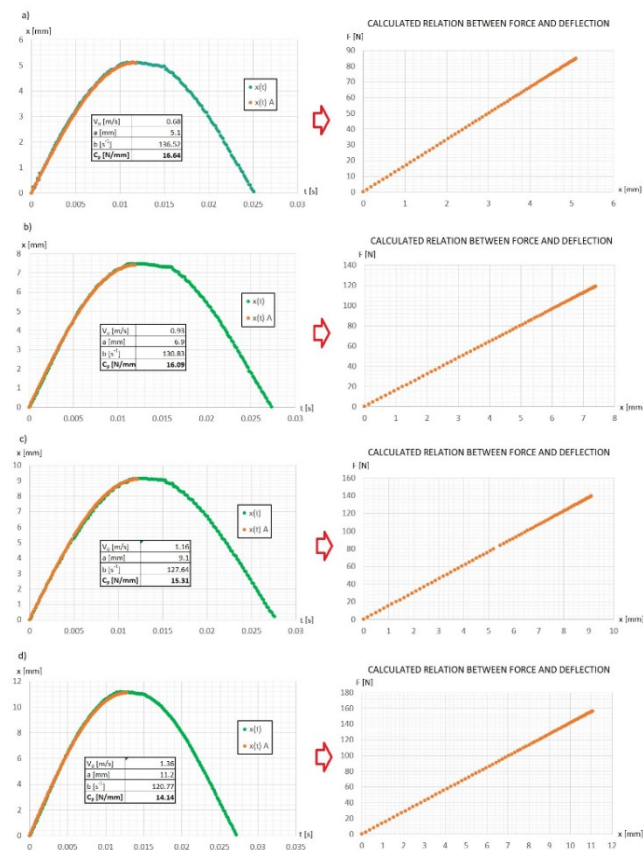
Fig. 5.3. Dynamic stiffness of sealed absorbers system for different value of initial deflection velocity
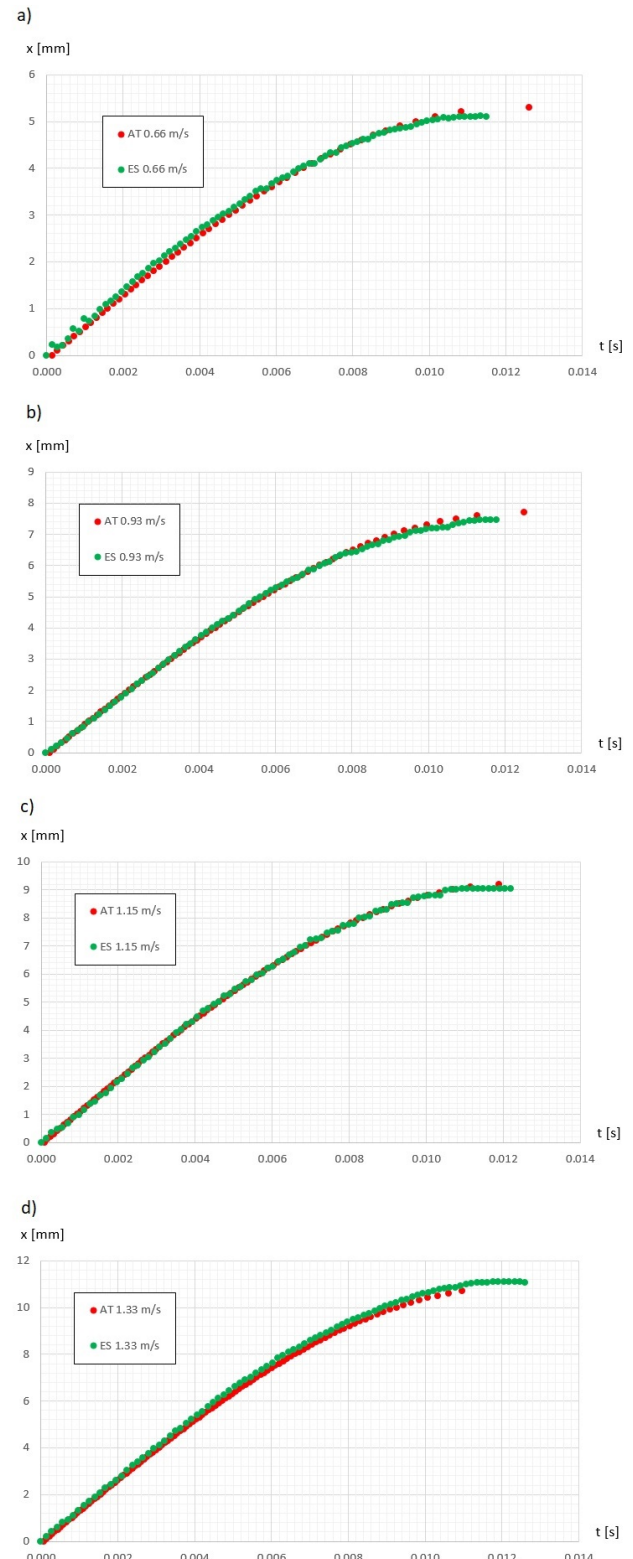
Fig. 5.4. The comparison of the theoretical curve x(t) (red line) on experimental (green line) by initial absorber compression velocity: (a) 0.66 m/s, (b) 0.93 m/s, (c) 1.15 m/s and (d) 1.33 m/s

Using experimental characteristics (see Fig. 5.1), one can define the damping parameter as:

$$T = \left(1 - \frac{E_{k2}}{E_{k1}}\right) \cdot 100\%, \tag{5.8}$$

where E_{k1} and E_{k1} denote, respectively, the kinetic energy of the absorbers system at the beginning and end of the impact test.

Because the energy is a function of mass and current velocity, this can be written in the following form:

$$T = \left(1 - \frac{V_2^2}{V_1^2}\right) \cdot 100\%,\qquad(5.9)$$

where V_1 and V_2 are, respectively, the velocity at the beginning and end of the impact process.

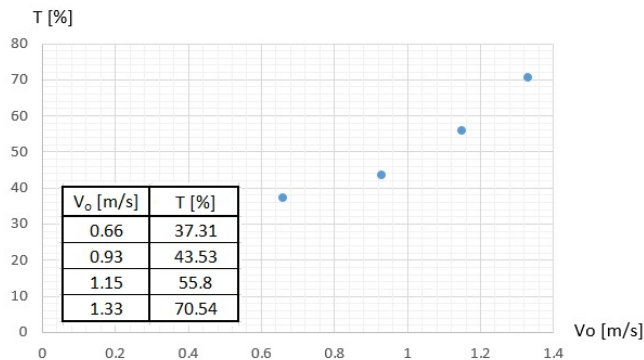The experimental values of damping have been presented in Fig. 5.5.

V_o [m/s]	T [%]
0.66	37.31
0.93	43.53
1.15	55.8
1.33	70.54

Fig. 5.5. The values of damping for free flow of air absorbers system

Based on the Eq. (5.5), the intensity of force change can be determined.
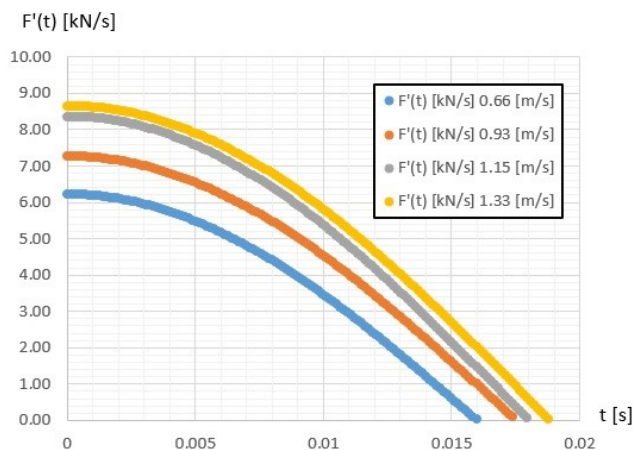

Fig. 5.6. The intensity of change reaction force for the free flow of air absorbers system

6. RESULTS AND DISCUSSIONS

The obtained results of experimental and analytical approaches enabled to notice several interesting aspects of functioning of the LDPE absorbers system. At the beginning, it was easy to observe that the dynamic deflection–time relation is strictly connected with the initial value of deformation velocity. The contraction maximum value of the open absorbers system increases due to the value of initial velocity (see Fig. 5.1), but the stiffness, C_p, decreases (see Figs 5.1 and 5.2).

At bigger numbers of absorbers, the stiffness palte increases while compression decreases their stiffness and decreases the total deflection arrows for the individual initial velocities (see Fig. 5.3). On the ground of adiabatic transformation it is possible to describe the compression–time relation for sealed absorbers system, based only on the same relation for open air LDPE absorbers system (see Eq. 4.28). The agreement between the analytical solution and experimental results is satisfactory (see Fig. 5.4).

The relationship between the damping of the free flow absorbers system and the initial value of deformation velocity is still interesting. The results obtained on the basis of the analysis of experimental characteristics allow us to conclude that the attenuation increases with the increase of the initial strain rate (see Fig. 5.5), that can be connected among others with the mechanical properties of the absorbers construction materials and motion of the air. The air pressure influence of the tight absorbers system stiffness is still an open question, and it will be one of the future aims for the authors' investigations.

7. CONCLUSIONS

Tested, sealed and free airflow absorbers made of polymer LDPE are primarily characterised by usability in the energy-intensive sense. The possibility of estimating the damping values for sealed absorbers compressing air during impact was demonstrated. The characteristics of dynamic properties of the sealed LDPE absorbers at extreme loading conditions were analytically modelled, showing the perfect agreement of the approximation with the results obtained experimentally. It is advisable to conduct further research on the presented absorbers whose dynamic characteristics will be between the extreme cases presented in this paper, i.e. obtained for a sealed absorber and a free airflow absorber.

REFERENCES

1. Kurpisz D, Obst M. The energetic and experimental based approach to description of basic material characteristics and mechanical properties of selected polymers. Journal of Theoretical and Applied Mechanics. 2020;58:183–93.
2. Wegner T, Kurpisz D. An energy-based method in phenomenological description of me-chanical properties of nonlinear material under plane stress. Journal of Theoretical and Applied Mechanics. 2017;55:129–39.
3. Khlif M, Masmoudi N, Bradai C. Polypropylene tensile test under dynamic loading. Journal of KONES Powertrain and Transport. 2014 Dec 28;21(1):131–8.
4. Jordan JL, Siviour CR, Sunny G, Bramlette C, Spowart JE. Strain rate-dependant mechanical properties of OFHC copper. J Mater Sci. 2013 Oct;48(20):7134–41.
5. Włodarczyk E, Janiszewski J. Dynamiczne stany naprężenia i skończonego odkształcenia w metalowym cienkim pierścieniu rozszerzanym wybuchowo. Biuletyn Wojskowej Akademii Technicznej. 2007;Vol. 56(nr 1):126–42.
6. Clough EC, Plaisted TA, Eckel ZC, Cante K, Hundley JM, Schaedler TA. Elastomeric Microlattice Impact Attenuators. Matter. 2019 Dec;1(6):1519–31.
7. Trzaskalska M, Chwastek R. Damping Properties and Density of Helmet Liners Made of Expanded Polystyrene (EPS). Archives of Metallurgy and Materials. 2021;66(1):339–44.

Maciej Obst, Dariusz Kurpisz, Michał Jakubowski
Experimental and Analytical Approaches on Air Spring Absorbers Made of LDPE Polymer

DOI 10.2478/ama-2024-0035

8. Reyes A, Børvik T. Low velocity impact on crash components with steel skins and polymer foam cores. International Journal of Impact Engineering. 2019 Oct;132:103297.

9. Koohbor B, Blourchian A, Uddin KZ, Youssef G. Characterization of Energy Absorption and Strain Rate Sensitivity of a Novel Elastomeric Polyurea Foam. Adv Eng Mater. 2021 Jan;23(1):2000797.

10. Mizuno K, Ito D, Oida K, Kobayashi G, Han Y. Head protection with cyclist helmet in impact against vehicle A-pillar. International Journal of Crashworthiness. 2017 May 4;22(3):322–31.

11. Raponi E, Fiumarella D. Experimental analysis and numerical optimization of a thermoplastic composite in crashworthiness. IOP Conf Ser: Mater Sci Eng. 2021 Feb 1;1038(1):012030.

12. Kathiresan M, Manisekar K, Manikandan V. Crashworthiness analysis of glass fibre/epoxy laminated thin walled composite conical frusta under axial compression. Composite Structures. 2014 Feb;108:584–99.

13. Tarlochan F. Sandwich Structures for Energy Absorption Applications: A Review. Materials. 2021 Aug 22;14(16):4731.

14. Jabłońska MB, Śmiglewicz A, Niewielski G. The Effect Of Strain Rate On The Mechanical Properties And Microstructure Of The High-Mn Steel After Dynamic Deformation Tests. Archives of Metallurgy and Materials. 2015 Jun 1;60(2):577–80.

15. Stankiewicz M, Popławski A, Bogusz P, Gieleta R, Sławiński G. Experimental Evaluation Of Energy Absorbing Properties Of Selected Elastomer Materials. Journal of KONES Powertrain and Transport. 2015 Jan 1;22(3):241–8.

16. Liang W, Bonsu AO, Tang X, Lei Z, Yang B. Impact and CAI behavior of SGF mat filled sandwich panels made from foam core and FRP facesheet. Composites Communications. 2022 Jan;29:101000.

17. Avalle M, Belingardi G. A Mechanical Model of Cellular Solids for Energy Absorption. Adv Eng Mater. 2019 Apr;21(4):1800457.

18. Sun G, Li G, Hou S, Zhou S, Li W, Li Q. Crashworthiness design for functionally graded foam-filled thin-walled structures. Materials Science and Engineering: A. 2010 Mar;527(7–8):1911–9.

19. Robinson MB, Stousland T, Baqui M, Karami G, Ziejewski M. Reducing effect of softball-to-head impact by incorporating slip-surface in helmet. Procedia Engineering. 2011;13:415–21.

20. Maw S, Lun V, Clarke A. The influence of helmet size and shape on peak linear decelerations when impacting crash pads. Procedia Engineering. 2012;34:819–24.

21. Lewis LM, Naunheim R, Standeven J, Lauryssen C, Richter C, Jeffords B. Do Football Helmets Reduce Acceleration of Impact in Blunt Head Injuries? Acad Emergency Med. 2001 Jun;8(6):604–9.

22. Whyte T, Gibson T, Eager D, Milthorpe B. Response of a full-face motorcycle helmet FE model to the UNECE 22.05 chin bar impact test. International Journal of Crashworthiness. 2016 Nov;21(6):555–65.

23. Ghajari M, Peldschus S, Galvanetto U, Iannucci L. Evaluation of the effective mass of the body for helmet impacts. International Journal of Crashworthiness. 2011 Dec;16(6):621–31.

24. Wu JZ, Pan CS, Ronaghi M, Wimer BM, Reischl U. Application of polyethylene air-bubble cushions to improve the shock absorption performance of Type I construction helmets for repeated impacts. BME. 2021 Jan 21;32(1):1–14.

25. Mazurek K, Szyguła M. Dynamic analysis of thin-walled structures as energy absorbers. MM. 2020 Jul 6;(162):2–12.

26. Böhm R, Hornig A, Weber T, Grüber B, Gude M. Experimental and Numerical Impact Analysis of Automotive Bumper Brackets Made of 2D Triaxially Braided CFRP Composites. Materials. 2020 Aug 12;13(16):3554.

Maciej Obst: https://orcid.org/0000-0001-6555-6198

Dariusz Kurpisz: https://orcid.org/0000-0003-2233-8638

Michał Jakubowski: https://orcid.org/0009-0000-7888-1520

BIOMECHANICAL ASSESSMENT OF CRITICAL FACTORS DURING PATIENT LIFTING: SHOULDER GIRDLE AND CUMULATIVE MOMENT ERGONOMIC EVALUATION

Karolis SENVAITIS*, **Kristina DAUNORAVIČIENĖ***, **Aušra ADOMAVIČIENĖ****

*Vilnius Tech (Department of Biomechanical Engineering), Lithuania
**Vilnius University (Department of Rehabilitation, Physical and Sports Medicine), Lithuania

karolis.senvaitis@vilniustech.lt, kristina.daunoraviciene@vilniustech.lt, ausra.adomaviciene@mf.vu.lt

Abstract: This study examines the ergonomics of the patient lifting motion often used by healthcare professionals, focusing on the shoulder area, as manual weight management is still an important part of daily work. Data acquisition was made with the 17 IMU sensors, Movella Xsens system. A total of 25 quality measurements were acquired for further data processing. A mathematical model with the defined assumptions is presented in this research calculating shoulder moment-kinematics. The load engagement profile was determined based on the hip extension as a variable size for different test subjects and trials. Shoulder flexion-extension range of motion (ROM) variance was estimated, determining each test subject's technique, together with shoulder moment and cumulative shoulder moment. Cumulative shoulder load varied from -31.46% to 27.78% from the mean shoulder moment value. During the estimated accumulation of a 5-year work span, the difference in worst to best techniques accumulated to 1.86 times. Recommendations on how the technique and the further scope of the research could be improved were given.

Key words: shoulder girdle, range of motion, cumulation, lift motion

1. INTRODUCTION

Manual weight handling is still a significant part of everyday work in today's rapidly evolving healthcare segment. The working nature of healthcare specialists impacts them which is becoming a concern. The demanding nature of their work often requires them to engage in physically intensive tasks, such as patient lifting or transferring. While these activities are essential for providing healthcare, they also pose potential risks. It has a significant impact on various musculoskeletal disorders [1].

Scientific evidence shows that ergonomic intervention can effectively lower the physical demands of manual labour tasks [2]. As different industry manual weight handling tasks are being changed with the machinery, it is relatively hard to impact patient handling in the healthcare sector. Although there are various equipment that might help to lift and transport patients, lifting procedures done manually by nursing staff specialists are not yet extinct. Different rooms, procedures and surfaces make it hard and costly to implement automated solutions. Not only the circumstances, but the patients themselves are different; not to mention that patient lifting and nursing might be required at patient homes.

Rapid injuries can often be defined and predicted by the force applied to different muscle skeletal segments and to the strain of different types of tissues [3]. Chronic musculoskeletal diseases are harder to predict and define as not only it take time but it is hard to replicate. Although this is true, chronic traumas of musculoskeletal apparatus can be reduced if we limit the accumulation of non-ergonomic positions, high-strain movements and loads in general to a different segment of the body [4]. Measuring and evaluating the motions involved in patient lifting is a critical step in identifying potential stress points and areas of strain on the human musculoskeletal system. This involves the utilisation of advanced motion capture technologies that allow for precise tracking and quantification of joint angles, range of motion (ROM), and forces exerted during lifting activities. By collecting and analysing such data, researchers can gain insights into the biomechanical dynamics of various patient lift techniques. This would enable the identification of problematic movement patterns that may lead to overexertion and subsequent injuries. ROM is relatively easy to calculate and requires input in many calculations and estimations. This makes ROM one of the most impactful factors and highly associated with ergonomics since it is crucial for force moment evaluation. ROM amplitude can magnify moment by at least a few times. If we count its possible accumulation, the impact of correct posture of movement might be drastic.

There are a lot of advancement in lower back and leg research and studies, while shoulder, neck and arms are relatively unresearched and problematic areas. Research done in 2021 shows that 53% of the 233 test population experienced shoulder pains, related to work-related activities [5]. Patient lifting motions, involving repetitive movements of the shoulders, neck and arms, have been observed to lead to discomfort, pain and even chronic musculoskeletal issues among healthcare professionals. At the same time, shoulders were the body part that experienced work-related muscle skeletal disorders most frequently in Hong Kong [6] and Norway [7]. The choice to analyse shoulder segments can be further supported by consulting healthcare sector specialists. The significance of maintaining a healthy workforce within the healthcare sector cannot be understated, as their ability to provide

optimal patient care is directly linked to their physical well-being. Addressing the ergonomic aspects of patient lifting has the potential to alleviate the physical burden on healthcare specialists and also enhance their overall job performance and satisfaction. Furthermore, mitigating the risks associated with repetitive stress injuries and chronic pain can lead to a healthier and more resilient healthcare workforce, resulting in improved patient outcomes and reduced healthcare costs.

Evaluating the forces exerted on the body and the ROM limitations during patient lifting serves as a crucial aspect of biomechanical analysis [8–10]. By quantifying forces, researchers can identify thresholds beyond which tissues and structures may become compromised, leading to discomfort or injuries. Similarly, assessing the ROM limitations helps pinpoint potential constraints that might hinder proper lifting techniques and contribute to musculoskeletal strain. Such evaluations provide valuable insights into the critical parameters that must be considered when designing ergonomically sound patient lift protocols. This research delves into the intricacies of healthcare specialists' everyday patient lift motions. It places a significant emphasis on the biomechanics of shoulders – the area most commonly reported to experience discomfort and pain. By understanding the underlying ergonomic factors contributing to these issues, effective interventions and strategies can be developed to optimise patient lifting techniques. Consequently, this research seeks to bridge the gap between the demands of patient care and the well-being of healthcare specialists, fostering an environment where both patient safety and provider health are equally prioritised.

In the following sections of this research article, patient lift motion is analysed with the evaluation of the cumulative load's impact, progressing to recommendations and discussions on the following topic. Methodology on how to calculate shoulder moment with accumulated load is presented. The initial goal of this study was to find quantitative assessment methods that would allow accurate assessment of shoulder girdle injury risk in medical staff during patient transfer. This research aims to contribute to the ongoing efforts to create a safer, healthier and more sustainable healthcare environment for both practitioners and patients alike.

2. MATERIALS AND METHODS

2.1. Test subjects and analysed motion

For the test subjects, various body type scholars were chosen. This research includes five participants doing at least five quality repetitions. This makes in total 25 quality measurements. Test subjects' anthropometry data needed for the scope of this research is listed in Tab. 1.

The test environment was represented by two chairs each 0.5 m tall and 0.5 m apart from the starting position of the test subject (**Fig. 1**) One indicates the surface from which the patient is being lifted while the other represents the surface at which the patient has to be put down. Same height surfaces were chosen to emphasise the motion and its ergonomics and not the environment itself. A weight of 5 kg was given to have better representable lift motion. It was chosen not to use representation of the patient to avoid possible injuries as this was not professionally trained personnel and multiple measurements were taken in a short period.

Tab. 1. Test subjects anthropometry data

	Subject 1	Subject 2	Subject 3	Subject 4	Subject 5
Sex	Female	Female	Female	Male	Male
Full body height (cm)	168.00	164.00	170.00	184.00	187.00
Upper arm length, cm (l_{ua})	30.35	29.63	30.72	38.79	39.42
Lower arm length, cm* (l_{la})	35.61	34.76	36.04	42.68	43.37
Full body weight (kg)	80.00	82.00	68.00	84.00	83.00
Upper arm weight (kg)	2.32	2.38	1.97	2.72	2.69
Lowe arm weight (kg)	1.89	1.94	1.60	2.23	2.21

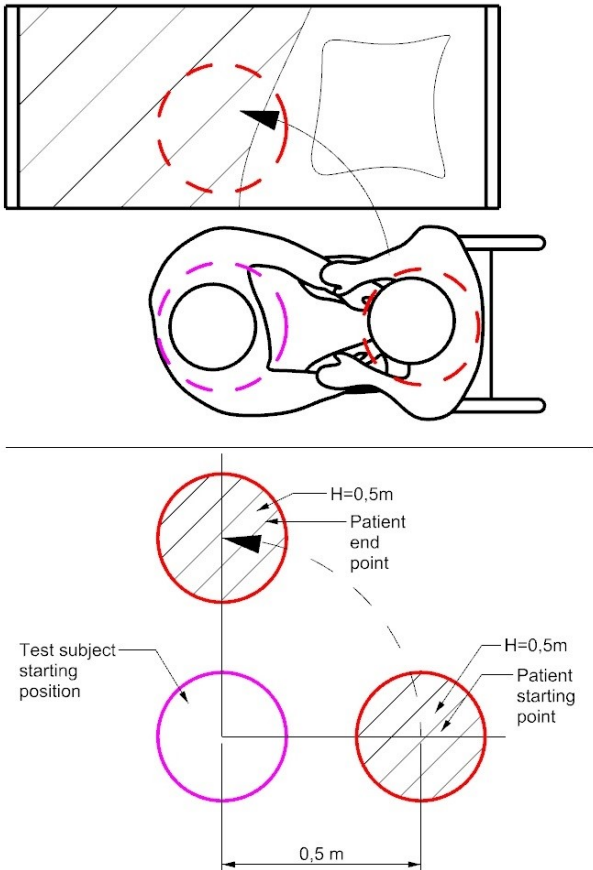*Elbow to the middle of the hand, where grip of the load is expected.

Fig. 1. Simplified researched motion scene schematics

For this research, imitated patient lift motion was chosen. It is based on the physiotherapists' ergonomic lift techniques and safe lifting recommendations. Techniques were practiced by the test subjects before conducting a recorded movement. The correct technique was not enforced to have a broader spectrum of movements and their impact on the research. The movement sequence combines three basic motions – lifting the patient up,

pivoting while transferring body weight and putting the patient down. The test subject approaches the patient so they have their waist at their reach and hugs the patient. After stabilising their posture and securing the grip, they stand up, by lifting a patient's weight. Afterwards, left leg is being transferred to align body weight and position to the destination of the lift. Left leg repositioning is followed by the right leg, keeping a steady posture and firm stance. After both legs are repositioned and pivoting is done, the patient is being put down by gradually squatting. Subsequently, the grip is released and the patient is secured on the new surface [11, 12].

Analysed motion definition starts when the test subject is present in from of the patient (has both feet firm on the ground) and starts bending motion to hug the patient preparing for transfer. Motion end is recorded when patient is transferred to the end surface and test subject releases patients body weight and stands in neutral standing position with hands to his sides.

2.2. Equipment and research procedure

In this research, measurement of the whole body is made. From there, upper body limbs can be analysed while having full body movement as a context. Researched movement was recorded with the Movella Xsens inertia measurement units (IMU) costume. This costume has custom marker layout for the main body segments. In total, 17 IMU sensors were used. Finger movements are not measured in this research. Sensors are placed in approximate centre of gravity (COG) positions on each segment. Movement noise is removed with the high-definition post processing of the Xsens MVN 2023.2.0 software version. Recording was done with a 60 Hz data acquisition frequency.

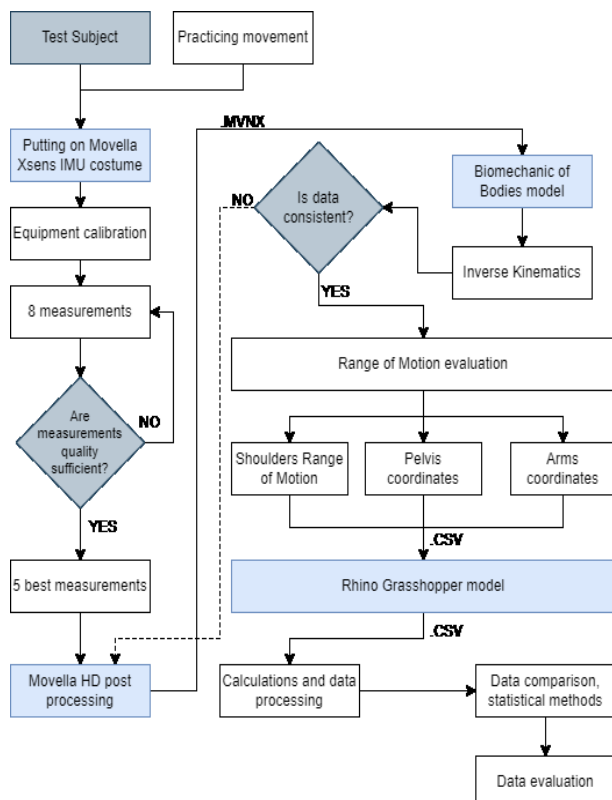The study was performed in the sequence shown in the Fig. 2.

First, as aforementioned, test subjects were instructed and practiced given motion. Then, IMU costumes were equipped and calibrated. Eight measurements were taken to have broader volume, so five with the most consistent data would be taken. As a rule of thumb, first measurement of every test subject was excluded from the measurement as additional practice, while performing movement under-recording. In total 43 data recordings were made with 25 chosen to progress.

All 25 measurements were then batch HD post-processed. This helped to remove noise, and motion inconsistencies, interpolate any gaps, etc. Afterwards, data was exported in MVNX format file. This data then was imported to biomechanics of bodies software 10.5 and after inverse kinematics, ROM data were taken. Data was compared with the original Xsens ROM data to make sure that it is consistent and does not show any significant visual differences. For further analysis, these main input points were needed: Shoulders ROM, pelvis sensor coordinates and arms sensors' coordinates (shoulders, arms, hands). These coordinates were imported into Rhino Grasshopper version 7-SR26 for further analysis since neither Movella, nor biomechanics of bodies models exports needed angles. In Rhino Grasshopper, model was made to find spine angle, which is necessary for shoulder moment calculation, the same as sagittal arm angle. Since arm angle can be impacted by various ROMs, it was decided to take sensor coordinate systems and project them on the created sagittal plane. After this, data were taken out from the model, so further calculations and data processing could be made. It was chosen to calculate shoulder moment, with cumulative moment evaluation, that would contribute to data comparison and final results evaluation [13]. Grasshopper is an algorithmic modelling plugin that is a power tool widely used by various engineers and designers. It is flexible that is able to read, write, process or manipulate various data with pre-integrated tools [14].

2.3. Tools and mathematical methods for kinematics and shoulder moment evaluation

Shoulder moments were calculated as quasi-static, without taking the acceleration of individual segments into account. The quasi-static analysis assumes that the system or segment remains similar or in equilibrium with negligible dynamic effects such as inertia and time-dependent behaviour.
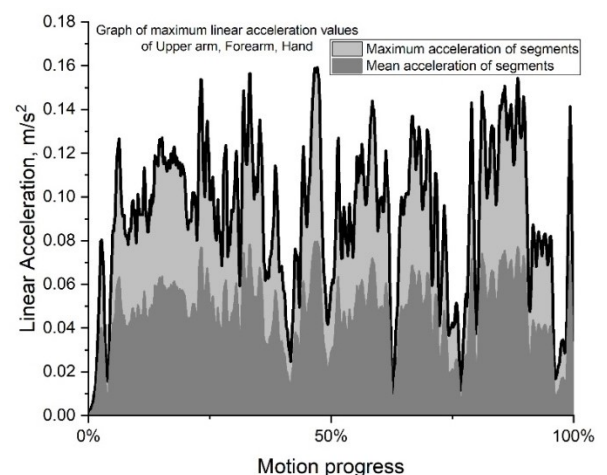

Fig. 2. Research sequence. IMU, inertia measurement units

Fig. 3. Maximum linear acceleration of Upper arm, Forearm and Hand evaluated altogether

sciendo

Karolis Senvaitis, Kristina Daunoravičienė, Aušra Adomavičienė   DOI 10.2478/ama-2024-0036
Biomechanical Assessment of Critical Factors during Patient Lifting: Shoulder Gridle and Cumulative Moment Ergonomic Evaluation

Based on the linear acceleration values of the analysed segments, shown in **Fig. 3**, the maximum acceleration is 0.159 m/s². As this is only 1.62% of gravity constant, the dynamic load is being accounted as negligible effect to further calculations and therefore, further analysis is quasi-static.

Since the average pelvis width is 20 cm, load COG was taken 10 cm from the grip and directed to the test subject's body.

Shoulder moments were calculated from equations as follows [15]:

$$SM = sm_{ua} + sm_{la} + sm_{load}$$

$$sm_{ua} = F_{ua} \cdot D_{sua} = m_{ua} \cdot g \cdot D_{sua}$$

$$sm_{la} = F_{la} \cdot D_{sla} = m_{la} \cdot g \cdot D_{sla}$$

$$sm_{load} = F_{load} \cdot D_{sl} = m_l \cdot g \cdot D_{sl}$$

Shoulder moment consists of three key components: shoulder moment of upper arm (sm_{ua}), moment of lower arm (sm_{la}) and moment of load (sm_{load}). Note that g is a gravity constant, taken as a 9.81 m/s² and m represents the mass of a specific segment or load: upper arm, lower arm and load respectively – is a projected distance from shoulder acting as moment arm. Each of these components is a multiplication of its gravity force and projected distance between the shoulder and COG. **Fig. 4** illustrates the main forces impacting shoulder moment.
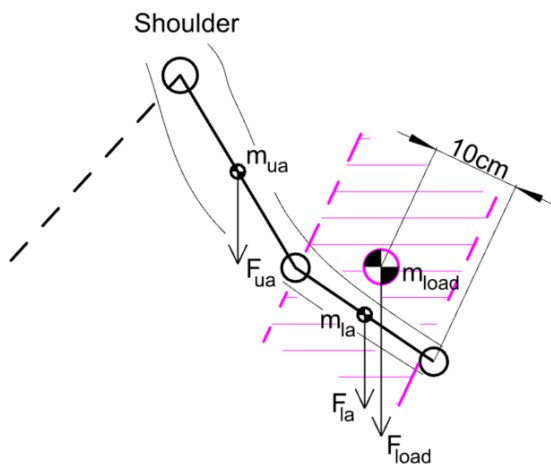

Fig. 4. Diagram of forces impacting shoulder moment

In this calculation, the hand is accounted as a part of the forearm and is being evaluated together as a lower arm. Since the wrists are mostly acting in a locked position relative to the forearm during the motion, it was decided to treat them in conjunction. The weight and length were recalculated to fit the segment as if the hand would have fingers bent 90° as this is the closest pose of hand participants had during recorded motion. Generalised human body parameters were used, the centre of mass for the upper arm being 0.436 of its length ratio, located closer to the shoulder. After recalculating lower arm parameters, including forearm and hand centre of mass is located at 0.496 of segment length ratio, located closer to the elbow.

Loads are relatively static, but distances are constantly changing depending on body posture. That's why the emphasis is on

posture and its overall impact on the shoulder moment and its accumulation. Moment arm distances were calculated as follows:

$$D_{sua} = 0.436 l_{ua} \cdot \sin(\alpha - \beta)$$

$$D_{sla} = 2 \cdot D_{sua} + 0.496 l_{la} \cdot \cos(\delta)$$

$$D_{sl} = 2 \cdot D_{sua} + (l_{la} - 0.1) \cdot \cos(\delta)$$

$$\cos(\delta) = \cos(180° - (90° - \beta) - \beta - \gamma = \cos(90° - \gamma)$$

Schematics of calculation inputs can be found in **Fig. 5**. α represents shoulder flexion-extension joint angle. β is a spine angle in a reference to vertical line, calculated from the parametric model. γ is arm angle projected to the ground plane, calculated as a derivative size from elbow joint angle in a parametric model. Hand anthropometric data were taken from the Tab. 1.
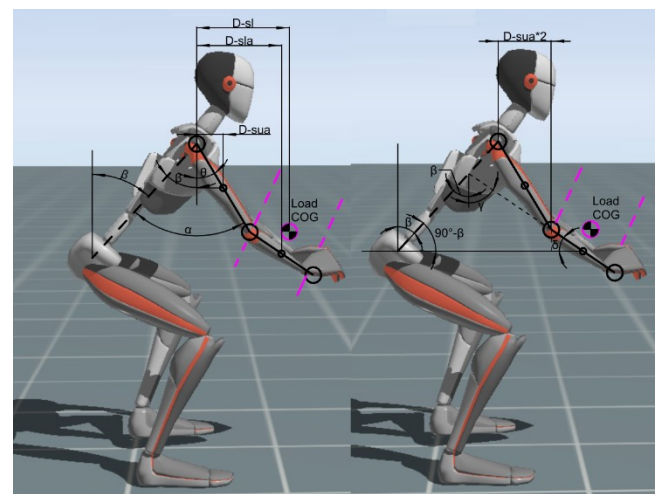

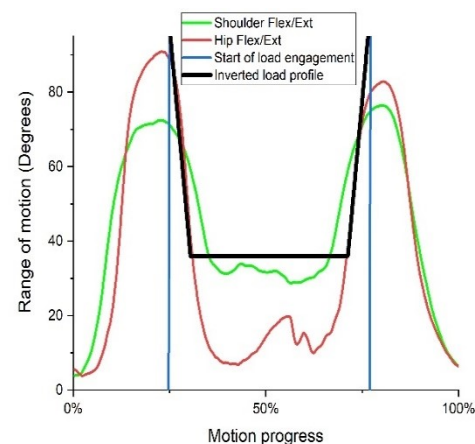**Fig. 5.** Mathematical scheme of project shoulder distance calculations

Fig. 6. Load engagement step configuration graph

During lift motion, the load is engaged gradually and is not present during the whole motion. This is important to define as the load size of this particular study is set to be 36 kg. Patient whose weight is 60 kg was taken as a baseline for patient load with the assumption that the patient can still carry 40% of its body weight on his own, during transportation motion. During motion, the load of a patient to the test subject is applied when the test subject is standing up, it has been decided to replicate the slope of hip ex-

tension joint angle. It is understood, that load is being engaged after the grip is initiated and the hip starts to extend. illustrates the relation between hip and shoulder flexure-extension joint angles. It can be observed that hip starts to extend at first and only afterwards shoulders follow. As hips are extending, more and more weight is being lifted until the whole load is engaged on the subject arms. The assumption is made that the load is fully engaged on the subject when shoulder extension stops. The black line () indicates inverted load profile from the start of load engagement to its full capacity.

In this research, it has been found that a spine angle with reference to a vertical line is needed for shoulder moment calculation. This is required to calculate moment arms as shoulder flexion and extension joint angle can yield different shoulder moment arm results depending on the body posture. Furthermore, a projected arm angle is needed so the moment arm of load can be determined more accurately. For this purpose, the parametric model was designed in Rhino Grasshopper so the whole motion can be evaluated at once [13].

The spine angle to the vertical line (β in **Fig. 5**) was identified as an angle between the vertical line and line, constructed between the pelvis marker and midpoint of an imaginary line between shoulder points. The vertical line was created from the pelvis marker to act as a measurement baseline for β angle calculation. Baseline vertical line always belongs to the sagittal plane constrained as a middle plane between shoulder points, with pelvis marker set as origin point. This acts as a reference plane for angle measurements. Evaluating main parameters is crucial, to lower the approximation level, as different components can transform the final shoulder moment calculation. Especially for such complex motions, involving different bending, squatting and rotating motions. The parametric model was defined with the geometrical constraint in **Fig. 5**.

2.4. Evaluating and representing results

Statistical methods were used to process and represent the results of this research. Origin 2018 SR1 software was used for processing of final result and presentation. Data comparison was done by calculating mean values of the different lift motions, together with the range, in which repetitive motions happen. Peak and cumulation evaluation was conducted to understand the critical limits of the motion and aggregate effects of the loads. Graphs were compared by overlaying them for visual estimation, together with statistical difference calculation and evaluating deviation from mean values.

To have a comparable data, normalisation of shoulder moments in relation to individuals' body weight and height ratios was conducted. This normalisation process enabled us to establish a common baseline for evaluating shoulder moments across participants, irrespective of their physical attributes. By doing so, more comparable data is gained so more insightful assessments could be made. Together with physiology data, time normalisation was conducted so motion could be overlaid in the same progress of the movement axis [16, 17].

Furthermore, for data to be comparable, shoulder moments were normalised in time and expressed as 100% of the motion completion. The motion of average duration was taken as a set-point to shrink and extend the remaining data sets. Afterwards,

results were normalised in the ratio of body weight to height [18, 19].

The root mean square error (RMSE) serves as a statistical metric in this study, providing a quantitative measure of the accuracy of biomechanical measurements. By calculating RMSE, the disparity between observed and predicted values is being assessed, such as joint angles and ROM, providing a clear indication of the fidelity of the data [20].

Utilising the standard deviation in the scope of this research aids in comprehending the variability and consistency within the data. It serves as a base statistical measure, allowing one to gauge how individual data points deviate from the mean or average. A low standard deviation implies that the data points tend to cluster closely around the mean, indicating a high degree of consistency in presented biomechanical measurements. Conversely, a higher standard deviation suggests greater variability, prompting the investigation of potential sources of variation or error [21].

3. RESULTS

Shoulder ergonomics during lift motion were evaluated throughout temporal values and ROMs intervals. Initial motion kinematics determination yielded results as shown in Tab. 2. Total average duration of performed lift motion is 9.61 s out of 25 calculated trials. Time data shows that most of the motions are consistent, having less than second of variance between different mean values and different repetitions.

Tab. 2. Motion duration characteristics

| Test subject	Mean motion duration (s)	RMSE
Subject 1	10.29 ± 0.81	0.73
Subject 2	8.70 ± 0.40	0.35
Subject 3	10.70 ± 1.02	0.91
Subject 4	8.75 ± 0.34	0.31
Subject 5	9.59 ± 0.44	0.39

RMSE, root mean square error.

By time normalising each of the subject's trials and overlaying them, variance ROMs can be seen (**Fig. 7**). Subject 1 data was not included as it shows a similar trend as test subject 2 results. These ROMs identify the highest and lowest boundaries of performed motion. This allows to judge the consistency of the motion and general trend. From this shoulder flexion extension graphs, different techniques can be identified. Test subjects 1 and 2 show consistent shoulder engagement during whole motion. This indicates potentially bigger loads in the shoulder area, without resting arms and putting additional strain. Test subject 3 releases the shoulder after lifting the patient but not as much as test subjects 4 and 5. During test subjects 4 and 5 motions, a few key aspects of the motion can be identified: first peak represents squat to hug and lift the patient, while second peak identifies squat to put down and release the patient. Furthermore, less variance can be seen on test subjects 4 and 5 technique as the range areas from lowest to highest ROM values are visually smaller.

From recorded motions, none of the test subjects reached 90° ROM, which is identified as risky by ISO or Rapid Upper Limb Assessment (RULA) standards. To be able to further evaluate data, the risky joint angle was set to 70°. Medium risk is treated

sciendo

Karolis Senvaitis, Kristina Daunoravičienė, Aušra Adomavičienė
Biomechanical Assessment of Critical Factors during Patient Lifting: Shoulder Gridle and Cumulative Moment Ergonomic Evaluation

DOI 10.2478/ama-2024-0036

when shoulders are >45˚. These values are taken lower than the aforementioned standard since the handled load is bigger too. Values were adapted to the analysed motion, so estimation would yield insights on the ergonomics and motion parameters. Exposure evaluated in percentage of motion duration is shown in Tab. 3:
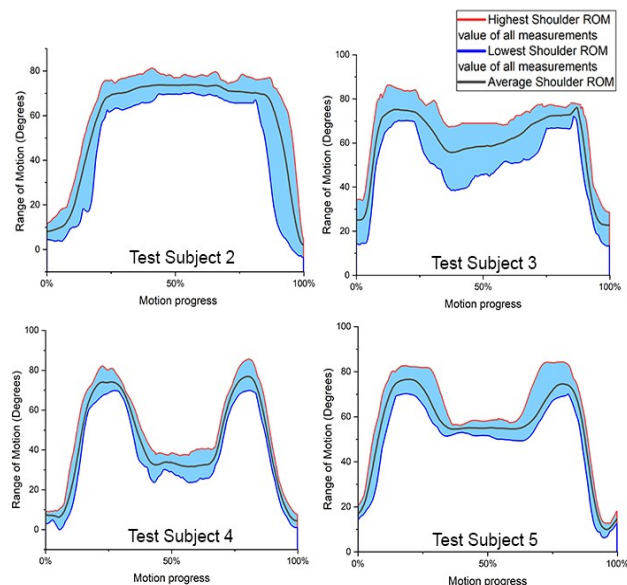
Fig. 7. Test subjects' shoulder flexion-extension ROM. ROM, range of motion

Tab. 3. Shoulder flexion exposure to different joint angles

| Test subject	Mean time portion of movement >45˚	Mean time portion of movement >70˚
Subject 1	81.68%	38.61%
Subject 2	76.08%	54.61%
Subject 3	85.47%	33.69%
Subject 4	43.13%	20.90%
Subject 5	81.25%	24.11%

Shoulder flexion that is >45˚ can be seen as dominant for most of the test subjects' movements. 3 out of 5 test subjects have >80% of their motion >45˚. 3 out of 5 test subjects have their movements with >30% exposure time >70˚ with subject 2 having the most exposure – 54.61%.

Fig. 8 shows different ROMs and angle components. Motion characteristics can be identified – lift, pivot and put down motions. Furthermore, it can be seen that these angles translate to same motion pattern.

Projected distances are shown in **Fig. 9**. As they are calculated from the anthropometric data and ROM angle, similarities can be seen with the appropriate **Fig. 8** angles. Projected load distance is a sum of both, shoulder and forearm distances.

Normalised total shoulder moment is shown in **Fig. 10**. On average, shoulder moment contributed from the body weight ranges at $10.70 \pm 2.67\%$. Subjects 1, 2, 3 and 5 overlap for at least part of the motion, while subject 4 has the lowest shoulder moment through the whole motion when load is engaged. This acts as a baseline to further evaluate the technique of subject 4 determining benefits of the posture and recommendations for the rest of the test subjects' techniques. An observation has been made that by shifting the grip position lower towards the patient's waist, it is possible to reduce the required shoulder range to execute the motion. Furthermore, this brings the patient's body weight into closer proximity to the lifting individual. This approach, involving relaxing the shoulders and trying to tie the patient to the lifting person closer, can serve as an additional prompt for minimising shoulder strain.
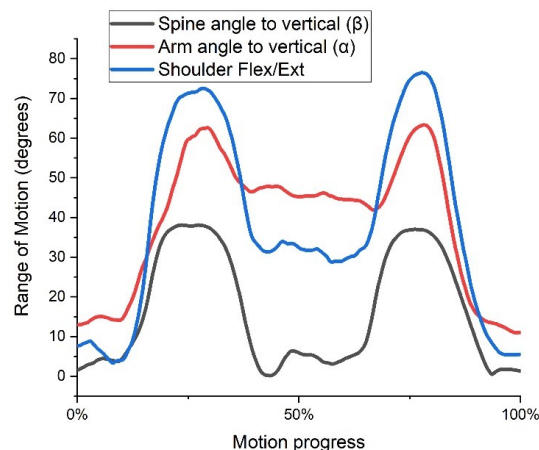
Fig. 8. Test subject 4 ROM components for shoulder moment calculation. ROM, range of motion
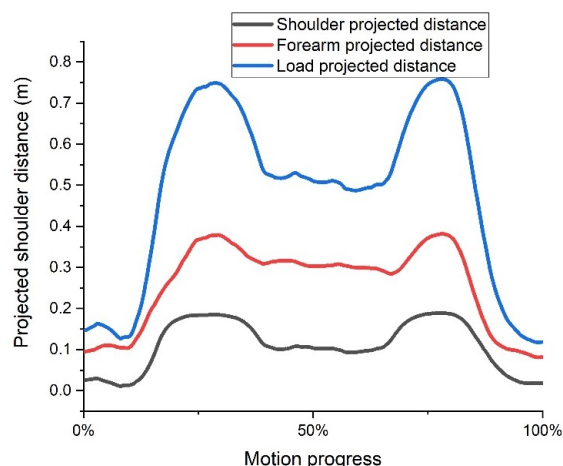
Fig. 9 Test subject 4 projected distance components for shoulder moment calculation. Forearm distance is shown as a component from elbow, instead of shoulder as for other components.
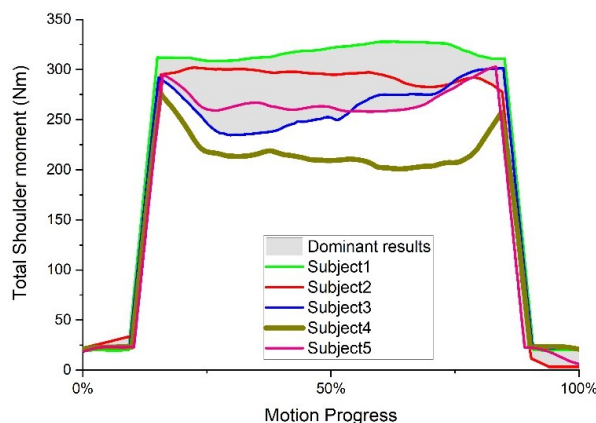
Fig. 10 Time and Body height/weight ratio normalised total shoulder moment data. Grey area covers dominant trend of the results
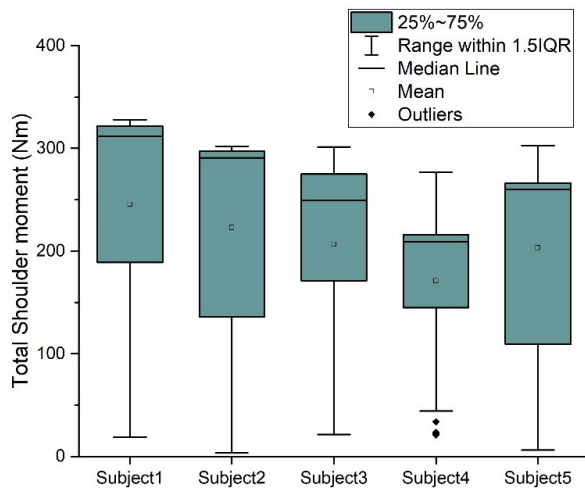
Fig. 11. Box plot of total shoulder moments

Fig. 12. Cumulative shoulder moment trend during years of repetitive manual labour

The box plot shown in the **Fig. 11** shows that subjects 3 and 4 have least distribution throughout the results. All of the results' mean values are below median and only few outliers observed in the results. Based on this consistency, results can be considered reliable.

Cumulative shoulder moment was calculated as Nm, seconds considered as dt and they are shown in Tab. 4. Mean values of cumulative shoulder load per single repetition range from 791 Nm to 1,475 Nm. The mean value of the cumulative moment is 1,154 Nm with the standard deviation of ±225 Nm. By evaluating each subject's cumulative shoulder moment difference from the mean value, a final assessment of their technique can be observed. Subject 1 has the least effective ergonomics of lift motion with 27.78% above the mean value, while subject 4 has the most efficient ergonomics with cumulative shoulder moment 31.46% below the mean value.

Tab. 4. Cumulative shoulder moment results

Test subject	Mean cumulative load per single repetition (Nm)	Mean Cumulative load per second of repetition (Nm/s)	Mean value (Nm)	Mean difference (%)
Subject 1	1,475 ± 134	151		+27.78
Subject 2	1,103 ± 101	142		−4.46
Subject 3	1,279 ± 97	131	1,154 ± 225	+10.86
Subject 4	791 ± 92	98		−31.46
Subject 5	1,123 ± 112	139		−2.72

In order to estimate the possible long term effects and thus, possible chronic traumas, assumptions for further calculations were made. Assumptions were made together with the ergotherapy specialists and nurses, to have approximated, but representative values:

- Every lift within the trend estimation is taken as a mean value of 5 measurements from the test subject.
- 5 patient lifts per day as calculated in this research is estimated.
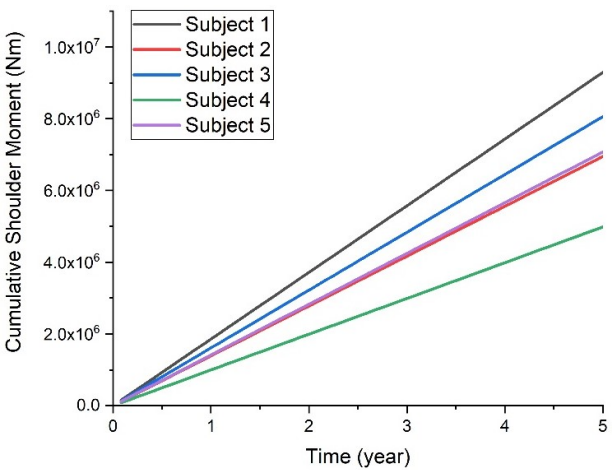- 21 work days per month, 252 work days per year is estimated.

The cumulative shoulder moment shown in **Fig. 12** is an estimation of the different technique impacts through the multiple years of work. If we were to compare the lowest and highest shoulder moments, the difference would be 46.37%. By taking the best ergonomics posture with the lowest cumulative shoulder moment as a baseline, we can estimate how many extra lifts are being done with worse techniques within the defined time. By comparing lowest and highest shoulder moment accumulations within 5 years, we are getting 6,300 repetitions versus 11,748 repetitions. That is 1.86 times more strain on the shoulders of what it could have been if best technique within this scope of research had been performed.

4. DISCUSSION

In this study, ergonomics of shoulder movement during patient lift was assessed. The methodology for cumulative load evaluation was presented. In the context of temporal kinematics within the scope of this research, the initial estimate of motion duration revealed an average duration of 9.61 s across all 25 trials, with relatively minimal variance observed between different repetitions. This consistent timing suggests that the lift technique can be performed at a relatively stable pace during patient lift task without extensive experience. Pace can be essential for both, execution of the motion and settings for easier recommendations for improvement and research applications [22]. To project long-term effects of these observed techniques, cumulative shoulder moments over multiple years of work were estimated. The higher the cumulative shoulder moment was calculated, the higher was contribution of own body weight to the sum moment. This can be explained by the general posture and shoulder ROM of the test subjects. During calculation arm, forearm and hand weight impose bigger moment force the bigger amplitudes are. The results demonstrate that utilising the preferred ergonomic posture could potentially reduce shoulder strain drastically over 5 years. That means an even bigger difference in senior healthcare specialists' work experience. This emphasises the significance of promoting and implementing optimal lifting techniques to mitigate the risk of chronic traumas and musculoskeletal disorders among healthcare specialists [23].

Although temporal parameters are analysed, this research focused on spatial parameters. ROM and joint angles were evaluat-

ed, with the addition of hip ROM and further extension of parameters such as spine angle to the vertical. This research was based on well-known ergonomic recommendations, putting effort into analysing constraints and determining what would be the risk factors of analysed movement. The analysis of ROM helps to identify distinct techniques employed by the test subjects during patient lifts. Some of the analysed test subjects exhibited continuous shoulder engagements throughout the entire motion, potentially indicating higher loads on the shoulder area. This could have happened due to reduced opportunities for testing the arms. In contrast, some of the test subjects displayed variation in their technique with discernible peaks corresponding to different phases of the lift. Putting even bigger emphasis not to only analysing motion with quantifiable sizes, but with exact motions and movements that determines those metrics, can improve analysis and prognosis of the ergonomics and whole research. The calculation of shoulder moment considered both time and body weight to height ratio normalisation. Furthermore, it required some additional inputs that were not default export parameters of the data processing software like spine angle to vertical or projected arm angle. In the scope of this research, it has been shown how hip extension is related to the shoulder flexion during lift motion. This implies the importance of understanding whole body motions even when single segment of the body is being targeted for the analysis [24]. Especially, when technique is being analysed to determine the best motion solutions and patterns. Hand joint angles' relations in the mathematical model explain the coherence between different body segments and how one segment load can be increased or decreased by the motion of the other one.

Ergonomic recommendations from recognised standards such as the RULA or ISO 11228-1-2021 emphasise the importance of shoulder flexion in patient lifting tasks. Shoulder flexion >45˚ is identified as risky ROM that might require changes and >90˚ poses a significant risk. From recorded motions, none of the test subjects reached 90˚ ROM, although they were close to the aforementioned boundary – 80˚.

During this research, a few limitations were identified:

– Ergonomic standards that were used to evaluate researched motion define ROMs where the risk of musculoskeletal strain increases. However, during the scope of this research, it was foreseen that limitations given in the RULA or ISO 11228-1-2021 standards are very generalised and simplified, possible in order to have them more applicable. Due to this generalisation, it lacked some biomechanical constraints that might ease the evaluation of risk zones, ROMs, exposure times, etc.

– Although it has its variance, techniques and motions were not analysed very deeply, leaving a gap in understanding what are the specifics that determined one of the other analysed motion ergonomics.

– Additional limitation to the uncertainty and constraint of this calculation was the load engagement profile that was not evaluated in the scope of this research due to the lack of equipment and the additional margin of complexity that this would add. Furthermore, the load that has been used suggests that with the real patient overall kinematics of the motion would change. Since only dummy weights were used for recalculating as it would be part of the patient's body weight, no exact ergonomic recommendations or technique advice could be drawn from the research.

– One additional limitation of conducted research is the assumption that lift motion is static, without taking acceleration into account. Including acceleration in calculation could possibly yield different accumulated load results as the technique might not be only defined by the posture, but by how fast motions should be made. Further evaluation of accelerations of the motion might shed some further light on how the shoulders and whole body react to the given load [25].

– Population of the research is not as large as it could be. 25 trials pose statistical significance for methodological purposes but would require a bigger sample to make more certain conclusions.

– To have a more in-depth understanding of the motion and its long-term effect, more of a body should be taken into account, as it was shown in this research how different body segments can impact load and changes on overall posture.

– The well-known limitation of similar research is biomechanical simplifications. In this study, it was sought to grasp the implications needed to fill the gaps in the calculations and their analysis. This implies the necessity for formulating fundamental or supplementary assumptions upon which further calculations were based on. By formulating assumptions, an estimation of the cumulative load and its cumulation trend could be formed, to better illustrate how ergonomic choices during manual handling tasks translate into disparities of data [26].

– Although models are getting better and mostly kinematics were evaluated for this research, only 17 sensors were used for the recording of body motion. Further simplification assumptions were made during mathematical model and parametric model evaluation. These models, while informative, may not fully capture the individual variations in musculoskeletal structures and neuromuscular control among healthcare specialists. This research is a low-volume evaluation of different body types and technique effects on the same lifting task in the most similar conditions. It was assumed that if the lift conditions are relatively similar between different test subjects, we will see impact on their motion ergonomics allowing us to do make first assumptions that would be later on backed up by a larger volume measurement.

– Shoulder moment calculation does not include body and tendon structures, so the load calculated on shoulders is not directly associated with the tissue that might be at risk of damage [27]. However, these simplifications and assumptions might be critical in order to evaluate a bigger population. Increasing the count of participants or measurements limits the amount of data that can be processed, observed and concluded.

The goal of this research was to deepen the knowledge and methodologies to calculate shoulder moment and understand the strain that occurs during lift motion, although this research has limitations, it is thought that this might still pose some valuable insights and methodologies.

5. RECOMMENDATIONS

It is recommended to broaden the spectrum of this research with increased availability of concerned persons/factors to solve mentioned limitations. To better understand the impact and vari-

ance of different techniques, professional healthcare specialists are recommended to participate. This way, the scope of the research will have more practical and experience-based techniques. A bigger population sample is highly recommended, as that might yield better results possibly introducing new and different trends and insights.

From the ergonomics that were observed during this research, it is recommended to invest in lifting techniques if there is no availability of additional equipment. Furthermore, it has been noticed that lowering the grip, to the waist of the patient lowers the shoulder ROM and allows to have patient body weight closer to the lifting person. Releasing the shoulders and trying to drag the patient that is being lifted might work as an additional reminder on how to focus on lowering the strain of the shoulders.

6. CONCLUSION

In conclusion, the results of this study offer valuable insights and techniques into the biomechanics and ergonomics of general analysis of the lift motion, particularly with the healthcare specialists' patient lift technique. The results of the conducted research showed that a relatively small variance in technique can yield a significant cumulative load during the year. In a 5-year span, it was estimated that the difference between the worst techniques in the scope of this research, compared to best, would induce 1.86 times more strain on the shoulders.

Moreover, the implications of these findings extend beyond the immediate scope of the research. They underscore the critical need to broaden methodologies of evaluating more of a critical muscle-skeletal segments. The substantial disparity in cumulative shoulder loads between suboptimal and optimal techniques identifies the possible cause of chronic musculoskeletal disorders. Thus, it is important not to only broaden research but implement evidence-based interventions and training programs to mitigate risks.

REFERENCES

1. Tariah HA, Nafai S, Alajmi M, Almutairi F, Alanazi B. Work-related musculoskeletal disorders in nurses working in the Kingdom of Saudi Arabia. Work. 2020;65(2):421-428. https://doi.org/10.3233/WOR-203094

2. Wurzelbacher SJ, Lampl MP, Bertke SJ, Tseng CY. The effectiveness of ergonomic interventions in material handling operations. Appl Ergon. 2020;87:103139. https://doi.org/10.1016/j.apergo.2020.103139

3. Bani Hani D, Huangfu R, Sesek R, Schall MC Jr, Davis GA, Gallagher S. Development and validation of a cumulative exposure shoulder risk assessment tool based on fatigue failure theory. Ergonomics 2021; 64(1): 39-54. https://doi.org/10.1080/00140139.2020.1811399

4. Canadian Centre for Occupational Health and Safety. Health and Safety Programs. https://www.ccohs.ca/oshanswers/hsprograms/patient_handling.html #section-1-hdr Accessed: 2023-06-23

5. Cheung K, Ma KY, Cheung HH, Lee CH, Chan IMM, Cheung ST, Chung WY, Yeung SS, Lo WC. Predictors of work-related musculoskeletal symptoms in shoulders among nursing assistants working in nursing homes. PeerJ. 2021;9:11152. https://doi.org/10.7717/peerj.11152

6. Cheung K, Szeto G, Lai GKB, Ching SSY. Prevalence of and Factors Associated with Work-Related Musculoskeletal Symptoms in Nursing Assistants Working in Nursing Homes. Int J Environ Res Public Health. 2018;15(2):265. https://doi.org/10.3390/ijerph15020265

7. Eriksen W, Bruusgaard D, Knardahl S. Work factors as predictors of sickness absence: a three month prospective study of nurses' aides. Occupational and Environmental Medicine. 2003;60:271–278. https://doi.org/10.1136/oem.60.4.271

8. Hignett S, McAtamney L. Rapid entire body assessment (REBA). Appl Ergon. 2000 Apr;31(2):201-5. 10.1016/s0003-6870(99)00039-3

9. David GC. Ergonomic methods for assessing exposure to risk factors for work-related musculoskeletal disorders. Occup Med (Lond). 2005;55(3):190-9. https://doi.org/10.1093/occmed/kqi082

10. Buchholz B, Paquet V, Punnett L, Lee D, Moir S. PATH: a work sampling-based approach to ergonomic job analysis for construction and other non-repetitive work. Appl Ergon. 1996 Jun;27(3):177-87. https://doi.org/10.1016/0003-6870(95)00078-x

11. Occupational Health Clinics for Ontario Workers Inc. "Patient Handling For Healthcare Workers" http://www.ohcow.on.ca/edit/files/general_handouts/Healthcare%20 Workers%20Patient%20Handling.pdf

12. National Institute for Occupation Safety and Health (NIOSH) "Safe patient Handling and Mobility" https://www.cdc.gov/niosh/topics/safepatient/default.html

13. Senvaitis K, Daunoravičienė K. Skeletal Modeling in Rhino Grasshopper—A Confirmed Kinematic Model. Machines 2023; 11: 556. https://doi.org/10.3390/machines11050556

14. Farid M, Gang Z, Khuong TL, Sun ZZ, Ur Rehman N. Grasshopper Knee Joint – Inverse Kinematic Modeling and Simulation of Ionic Polymer Metal Composites (IPMC) Actuators. JBBTE 2014;19:1–11. https://doi.org/10.4028/www.scientific.net/jbbte.19.1

15. Greenland KO, Merryweather AS, Bloswick DS. The effect of lifting speed on cumulative and peak biomechanical loading for symmetric lifting tasks. Saf Health Work. 2013;4(2):105-10. https://doi.org/10.1016/j.shaw.2013.04.001

16. Kaufman KR, Hughes C, Morrey BF, Morrey M, Kai-Nan An. Gait characteristics of patients with knee osteoarthritis, Journal of Biomechanics. 2001; 34(7): 907-915. https://doi.org/10.1016/S0021-9290(01)00036-7

17. Mündermann A, Dyrby CO, Andriacchi TP.Secondary gait changes in patients with medial compartment knee osteoarthritis: Increased load at the ankle, knee, and hip during walking. Arthritis & Rheumatism. 2005; 52: 2835-2844.https://doi.org/10.1002/art.21262

18. Wannop JW, Worobets JT, Stefanyshyn DJ. Normalization of ground reaction forces, joint moments, and free moments in human locomotion. J Appl Biomech. 2012;28(6):665-76. https://doi.org/10.1123/jab.28.6.665.

19. Baellow A, Glaviano NR, Hertel J, Saliba SA. Lower Extremity Biomechanics During a Drop-Vertical Jump and Muscle Strength in Women With Patellofemoral Pain. J Athl Train 1 June 2020; 55(6): 615–622. https://doi.org/10.4085/1062-6050-476-18

20. Halawi L, Clarke A, George K. Evaluating Predictive Performance. In Harnessing the Power of Analytics; Springer International Publishing: Cham. Switzerland 2022; 51–59.

21. El Omda S, Sergent SR. Standard Deviation. [Updated 2023 Aug 14]. In: StatPearls [Internet]. Treasure Island (FL): StatPearls Publishing 2023. https://www.ncbi.nlm.nih.gov/books/NBK574574/

22. Ferdinands RE, Singh U. Investigating the biomechanical validity of the V-spine angle technique in cricket fast bowling. International Journal of Sports Science & Coaching. 2023; 18(4): 1091–1101. https://doi.org/10.1177/17479541221108252

23. Edwards N, Dickin C, Wang H. Low back pain and golf: A review of biomechanical risk factors. Sports Med Health Sci. 2020 9;2(1):10-18. https://doi.org/10.1016/j.smhs.2020.03.002

24. Vera-Jiménez JC, Meléndez-Sánchez FL, Álvarez JA, Ayuso J. An Analysis of Biomechanical Parameters in OTP Police Physical Intervention Techniques for Occupational Risk Prevention. Int. J. Environ. Res. Public Health 2022; 19: 6615. https://doi.org/10.3390/ijerph19116615

25. Greenland KO, Merryweather AS, Bloswick DS. The effect of lifting speed on cumulative and peak biomechanical loading for symmetric lifting tasks. Saf Health Work. 2013;4(2):105-10. https://doi.org/10.1016/j.shaw.2013.04.001
26. Patrick G. Dempsey. A critical review of biomechanical, epidemiological, physiological and psychophysical criteria for designing manual materials handling tasks. Ergonomics. 1998; 41(1): 73-88. https://doi.org/10.1080/001401398187332
27. Bani Hani D, Huangfu R, Sesek R, Schall MC Jr, Davis GA, Gallagher S. Development and validation of a cumulative exposure shoulder risk assessment tool based on fatigue failure theory. Ergonomics 2021; 64(1): 39-54. https://doi.org/10.1080/00140139.2020.1811399

Karolis Senvaitis: https://orcid.org/0009-0003-2703-0517

Kristina Daunoravičienė: https://orcid.org/0000-0003-0898-4860

Aušra Adomavičienė: https://orcid.org/0000-0002-5946-6265

DEVELOPMENT OF A BIOMECHANICAL HUMAN MODEL
FOR SAFETY ANALYSIS OF THE OPERATORS OF SELF-PROPELLED MINING MACHINES

Paulina DZIAŁAK*, **Jacek KARLIŃSKI***, **Paweł MAŚLAK***

**Wrocław University of Science and Technology, Faculty of Mechanical Engineering
Department of Machine and Vehicle Design and Research, Wrocław, Poland*

paulina.dzialak@pwr.edu.pl, jacek.karlinski@pwr.edu.pl, pawel.maslak@pwr.edu.pl

Abstract: In the paper, the authors presented an elaboration of the biomechanical model of a human in a sitting position for the dynamic tests related to the impact loads acting on operators of self-propelled mining machines. Here, the human body was replaced with a one-dimensional multi-mass model (in the form of concentrated masses connected with elastic and damping elements). The models of this type are currently used to study ergonomics in vehicles. However, their use is limited because they are adapted to much lower dynamic loads than those acting on the operator in accident situations in mines. Many models of this type, in which the stiffness and damping characteristics of the elements are constant, have been described in the literature. Due to the specificity of the analysed loads acting on the operator, the literature studies were mainly focused on models for vertical forces analysis. By developing non-linear stiffness characteristics, in the currently used car seat ergonomics linear biomechanical models, it was possible to use simple multi-mass models with several degrees of freedom to analyse the effects of dynamic excitation characterised by large displacements. The validation of the developed characteristics was performed using a full-size dummy in a sitting position positioned in the cabin, on the operator's seat.

Key words: passive safety, mining safety, biomechanics, numerical simulation.

1. INTRODUCTION

The requirements for structures protecting mining machine operators are limited to assessing the effects of machine roll-over (Roll-Over Protective Structure [ROPS]) and assessing the effects of events related to falling objects (Falling Object Protective Structure (FOPS)] [1]. These studies do not take into consideration any injuries the operators may sustain. They only describe the deformation of the cabin's load-bearing structure and analyse if the protected space inside the cabin remains intact. However, the analysis of accident situations shows that it is insufficient to assess the operators' safety [2]. It is necessary to define and evaluate biomechanical criteria, as well as to take into account other factors causing accidents that threaten the health and life of operators.

The analysis of accident situations over the last few decades confirms that the current standards do not provide sufficient protection for the operators while significant vertical loads acting on the machine. The authors considered injuries of the operators caused by the machine being thrown upwards as one of the greatest threats. In underground mines, this is due to the dynamic uplift of the floor or burying of the loader buckets by the material, resulting in throwing the machine in a vertical direction. This often results in permanent injury or even death to the operator, due to the limited space above the head in self-propelled mining machines with low transport heights.

The authors conducted a numerical analysis of such a phenomenon using a full-size, anthropometric model of a human being, considering its biomechanics (Fig. 1). A coupled analysis was carried out using two software for numerical simulations: MADYMO (a multibody biomechanical human model) and LS-Dyna (a discrete model of the operator's cabin load-bearing structure with the seat). The human model used during the analysis is based on a dummy used to test the safety of passengers during accidents and emergencies in aircraft, where the vertical forces affect the human body the most.

The construction of the dummy is adapted to transfer such loads, and the obtained results are similar to the response of the human body and repeatable, which was the main reason for the selection of this type of model. This is a 50th-percentile male dummy from the Hybrid III family. It is marked with the abbreviation FAA meaning the Federal Aviation Administration, a transportation agency of the U.S. Government that regulates all aspects of civil aviation [3]. The described dummy was created for the purpose of testing the safety of passengers and airline seats.

As a result of the performed analyses, the injuries that the operator may suffer depending on the velocity at which the machine is thrown upwards were determined [4]. These studies have enabled the operator's safety to be assessed in a wide variety of accident situations. However, this method is not free from disadvantages. Calculations of a full human model with a seat and cabin are complicated and time-consuming, and the software used for numerical simulation is expensive and requires specific knowledge in this area. Therefore, the authors developed a simplified (one-dimensional with four degrees of freedom) biomechanical human model (SBHM) that allows determining the dynamic response to dynamic loads with a large amplitude of kinematic excitations. The authors assumed that the developed research method could be used more widely for testing the safety

Paulina Działak, Jacek Karliński, Paweł Maślak
Development of a Biomechanical Human Model for Safety Analysis of the Operators of Self-Propelled Mining Machines

DOI 10.2478/ama-2024-0037

of operators and did not force the use of dedicated commercial software.
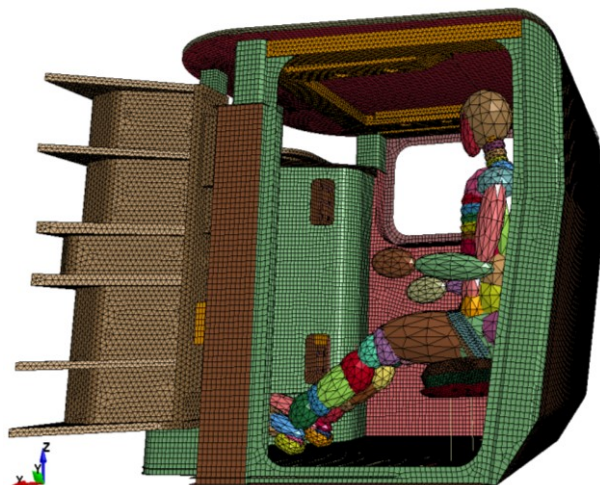

Fig.1. Full-size dummy model with the cab and operators seat

2. BIOMECHANICAL HUMAN MODEL USED IN THE LITERATURE

In the literature, there are many simple dynamic models currently used to study the ergonomics of machine operators and vehicle passengers. However, they are adapted to the analysis of vibrations (with accelerations up to 5 m/s2 and small amplitudes excitations), which do not threaten the lives of operators [5]. In some literature, scientists attempt to modify models of this type to adjust them to much larger loads. Unfortunately, the introduced modifications adapt them only to the one type and value of loads [6]. The introduction of any modifications of the initial boundary conditions in the analyses using models of this type causes the results obtained with their use to differ significantly from the dynamic response obtained using full-size models of the human body. The authors decided to elaborate on such a one-dimensional model in which the applied characteristics defining stiffness and damping will allow to obtain a dynamic response similar to those obtained using a full-size dummy model for a wider range of initial boundary conditions.

In the first stage of the model development, the level of detail of the model was established. It should have enough elements in order to determine the key injuries for the health and life of the operator while maintaining a simple structure with a relatively simple description of the characteristics. While analysing accidents involving machine operators, the authors determined that the effects of spinal injuries, especially in the cervical and lumbar section, as well as head injuries, are most tragic. For this reason, a model with four degrees of freedom was chosen, in which the following elements of the human body can be distinguished: head with neck, body divided into thoracic and lumbar parts, as well as thighs with a sacral part of the spinal cord. More degrees of freedom would significantly complicate the elaboration of the model by introducing too many variables, while a smaller number would make it impossible to obtain the most important information about injuries due to insufficient accuracy.

Due to the above-mentioned aspects, the further analysis included two models with four degrees of freedom available in the literature, which have been proven for years in the study of operator ergonomics [7]. These are models developed by Boileau et al. [8] and Wan and Schimmels [9]. In the literature, you can find many similar models of the human body with four degrees of freedom as those of Abbas [10], Zhang [11], Liu [12], Singh and Wereley [13] or Srdjevic and Cveticanin [14], but all of them are only extensions and modifications of previously mentioned models, which is why the authors focused only on the two basic ones.

Boileau and Rakheja proposed a human model with constant and linear characteristics (Fig. 2). It is a model of a human sitting on a seat with his feet supported and his hands held in a car driving position. It is supposed to enable proper distribution of loads from the vehicle and the seat to the head. It was established that the four degrees of freedom of the model are enough to obtain the data necessary to determine the impact on the behaviour of key parts of the human body. The parameters of the model were selected based on published results of studies on people subjected to low-frequency loads [15], with the limitations identified based on the analysis of anthropometric and biomechanical data available for the human body. The model was tested and, on this basis, it was found that its dynamic response is comparable to the response of the human body under dynamic excitations with acceleration values not exceeding 4 m/s2. The proposed driver model consists of four elements with a mass, connected by elastic elements with linear stiffness and damping characteristics. This assumption is consistent with the generally accepted idea that in the first approximation, the non-linearity of the human body can be neglected when the vibration load is not excessive. The four weights represent the following four parts of the body: head and neck (m_1), chest with upper torso (m_2), lower torso (m_3) and thighs and pelvis with seat (m_4). The weight of the lower legs with feet is not included in the model, because its share in the dynamic response is negligible and does not affect the results in terms of loads and displacements of the upper part of the biomechanical model of the human body. This is due to the support of the feet and the fact that the mentioned elements of the model are outside the seat and do not constitute a load for it. This assumption is also justified by Fairley [16], who proved that the share of the legs in transferring the vertical forces of the cushioned seat is relatively insignificant, as both the legs and the seat are subjected to the same kinematic inputs. Hands and further arms are supported on the steering wheel and are also not included in the model, assuming that their mass has a negligible contribution to the obtained dynamic response of the whole body. The inertia of the four main body segments in the model is determined based on anthropometric data identified by Pheasant [17]. On this basis, the proportion of total body weight estimated for different body segments is 8.4% for the head and neck, 36.6% for the chest and upper body, 13.4% for the lower body and 20% for the thighs and pelvis. For a seated driver with an average body weight of 75.4 kg, it is assumed that 73.6% of the weight is supported by the seat, so it is approximately 55.5 kg of total body weight. The following segments are connected by elements with the following stiffness and damping coefficients: pelvis and thighs are represented by k_1 and c_1, lumbar region by k_2, c_2, thoracic region by k_3, c_3, and cervical spine by k_4, c_4. The development of a human body model involves the identification of these parameters. The biomechanical properties of the spine, thorax, and upper body are relatively unknown and vary widely. In a study conducted on corpses, Kazarian [18] determined the stiffness for

the lumbar spine in the range of 100–300 kN/m and for the thoracic spine in the range of 150–200 kN/m. Mertens [19] proposed a model of the human body using damping coefficients in the range of 500–4000 Ns/m. Although the reported data represents high variability, the identified ranges can be used as effective limit values for optimising the models.
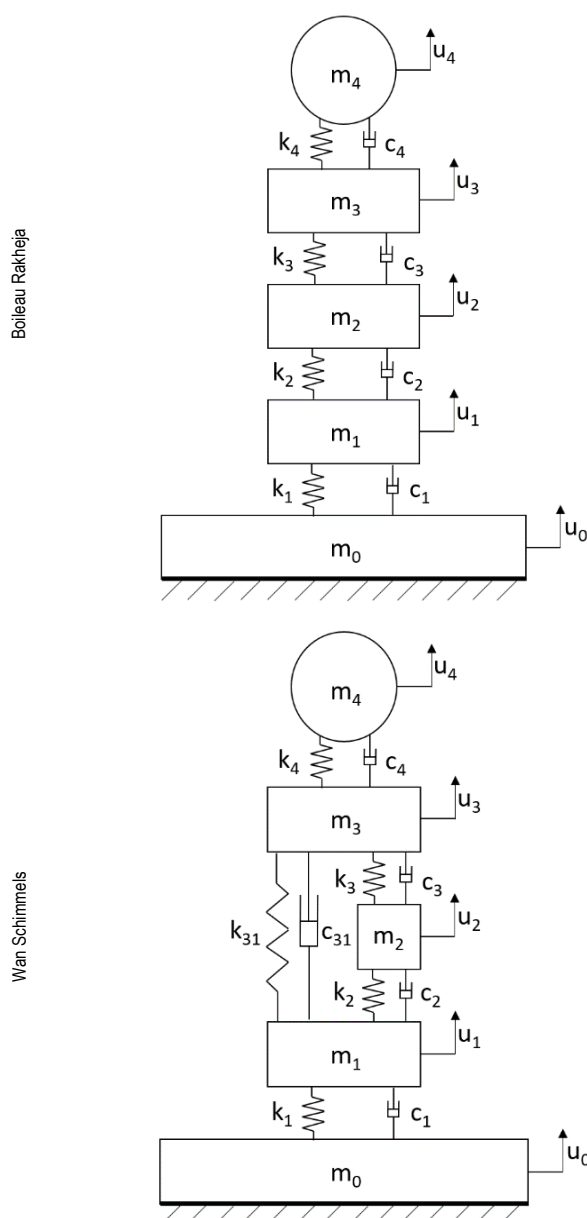

Boileau Rakheja

Wan Schimmels

Fig.2. BR and WS models. BR, Boileau-Rakheja; WS, Wan-Schimmels

Finally, for the elements of the analysed model, the following characteristics were adopted by Boileau and Rakheja [20]:

m_1 = 12.78 kg,	k_1 = 90 kN/m,	c_1 = 2,064 Ns/m.
m_2 = 8.62 kg,	k_2 = 162.8 kN/m,	c_2 = 4,585 Ns/m,
m_3 = 28.49 kg,	k_3 = 183 kN/m,	c_3 = 4,750 Ns/m,
m_4 = 5.31 kg,	k_4 = 310 kN/m,	c_4 = 400 Ns/m.

This approach made it possible to develop a generalised and unique model of the seated vehicle drivers, based on which the dynamic behaviour of the human body can be estimated.

The Wan-Schimmels (WS) model, similar to the Boileau-Rakheja (BR) model discussed above, is composed of four separate mass segments. The difference is the number of connections – the segments are connected with each other by five pairs of springs and dampers, and the total weight of the model is 60.67 kg. The stiffness and damping properties of the thighs and pelvis are ($k1$) and ($c1$), the lower torso is ($k2$) and ($c2$), the upper torso is ($k3$, $k31$) and ($c3$, $c31$), and the head is ($k4$) and ($c4$). The values of masses, stiffnesses and dampings determined in this model are as follows:

m_1 = 36 kg,	k_1 = 49.34 kN/m,	c_1 = 2,475 Ns/m.
m_2 = 5.5 kg,	k_2 = 20 kN/m,	c_2 = 330 Ns/m,
m_3 = 15 kg,	k_3 = 10 kN/m,	c_3 = 200 Ns/m,
	k_{31} = 192 kN/m,	c_{31} = 909,1 Ns/m
m_4 = 4.17 kg,	k_4 = 134.4 kN/m,	c_4 = 250 Ns/m.

The four weights represent the following body segments: head and neck (m4), upper torso (m3), lower torso (m2) and thighs and pelvis (m1). The arms and legs are connected to the upper torso and thigh respectively.
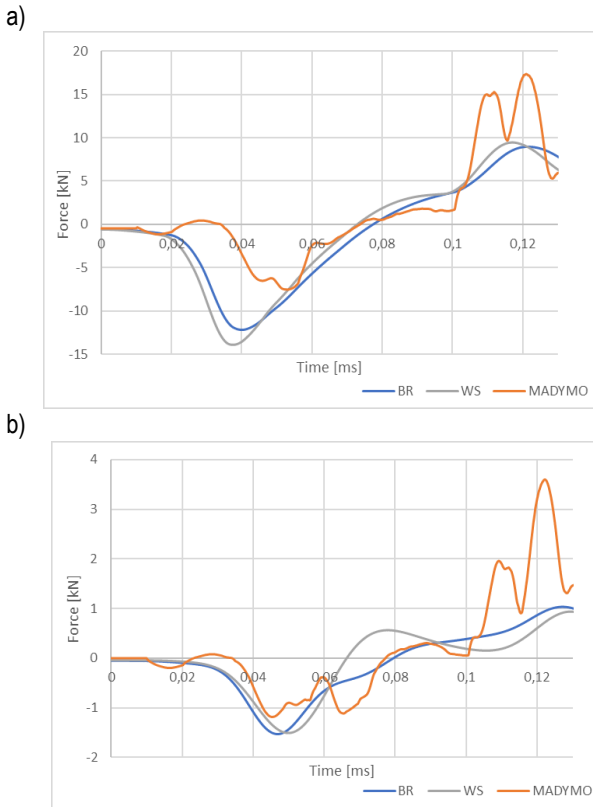
The WS model is also limited to acceleration in the range around 4 to 5 m/s2.

2.1. Literature models comparison

The models discussed above have been subjected to loads that may be experienced by machine operators during accidents in mines related to the uplift of the floor. These results were then compared with the results obtained after analysing a full-size human model in the MADYMO program (Hybrid III). All models were analysed with the velocity of the upthrow of 10 m/s and then suddenly stopped, which was followed by a rebound and free fall [21]. This simulates the event of throwing the machine up and then impacting the roof of mine gallery [22]. An additional degree of freedom has been added to the biomechanical models in the form of the operator's seat, along with the stiffness and damping of its base. A comparison of the dynamic response for the dummy from MADYMO and the models presented in Fig. 2 for velocities 5 m/s and 10 m/s are shown on charts in Figs. 3 and 4.

The results obtained from both one-dimensional models described in the literature were similar and at the same time, both significantly differed from the results obtained using a full-size human body dummy. This confirms the authors' assumption of these models regarding the limitation of kinematic excitation to which they may be subjected. In the performed analysis, the loads significantly exceeded the limit, and permissible accelerations were specified in the range of up to 5 m/s2. This means that none of these models can be used directly to study this phenomenon causing accidents in mines without introducing the necessary modifications to them.

Finally, the Boileau-Rakhej model was adopted for further analysis due to the smaller number of parameters and thus characterized by a greater simplicity of description, which in turn facilitates the process of adapting the model to the given boundary conditions.

Paulina Działak, Jacek Karliński, Paweł Maślak
Development of a Biomechanical Human Model for Safety Analysis of the Operators of Self-Propelled Mining Machines

DOI 10.2478/ama-2024-0037

a)

b)

Fig. 3. Comparison of forces acting on a lumbar spine of the human model; BR model, WS model, MADYMO – MADYMO Hybrid III dummy (a – lumbar spine, b – cervical spine; velocity 5 m/s). BR, Boileau-Rakheja; WS, Wan-Schimmels

a)

b)
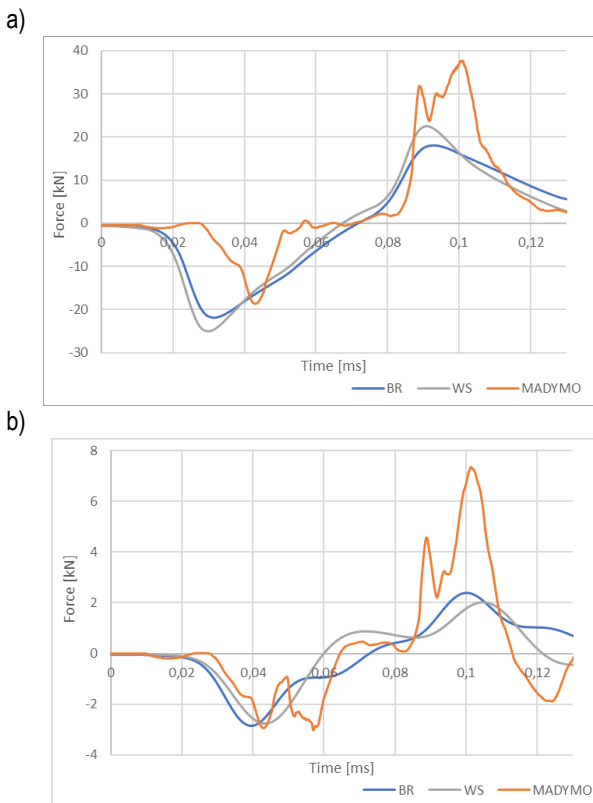
Fig. 4. Comparison of forces acting on a cervical spine of the human model; BR model, WS model, MADYMO – MADYMO Hybrid III dummy (a – lumbar spine, b – cervical spine; velocity 10 m/s). BR, Boileau-Rakheja; WS, Wan-Schimmels

3. SIMPLIFIED BIOMECHANICAL HUMAN MODEL

The one-dimensional model of a seated human was developed, whose dynamic response to the imposed excitation is similar to a full-size dummy seated on the operator's seat (Fig. 5).
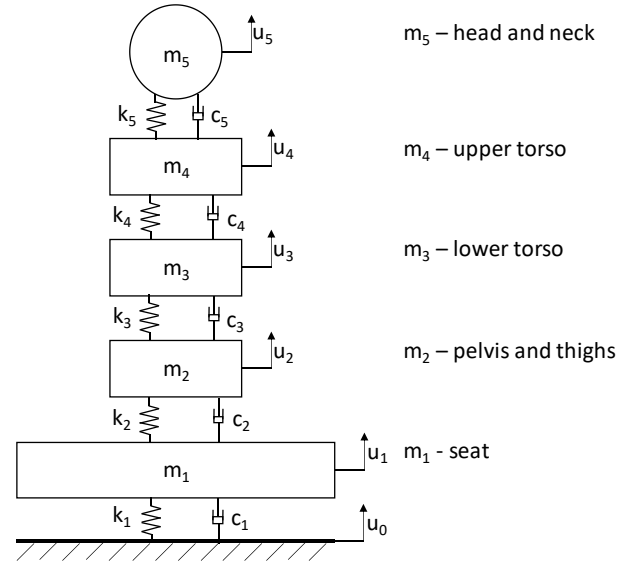
Fig. 5. Applied, SBHM of the operator positioned on the seat, with 5 degrees of freedom SBHM, simplified biomechanical human model

It is a 5-degree-of-freedom model that can be analysed with any software capable of solving inhomogeneous non-linear second-order differential equations. The model is described by the differential equations of motion shown below:

$$m_1\ddot{u}_1 + c_1(\dot{u}_1 - \dot{u}_0) + k_1(u_1 - u_0) - c_2(\dot{u}_2 - \dot{u}_1) - k_2(u_2 - u_1) = 0$$

$$m_2\ddot{u}_2 + c_2(\dot{u}_2 - \dot{u}_1) + k_2(u_2 - u_1) - c_3(\dot{u}_3 - \dot{u}_2) - k_3(u_3 - u_2) = 0$$

$$m_3\ddot{u}_3 + c_3(\dot{u}_3 - \dot{u}_2) + k_3(u_3 - u_2) - c_4(\dot{u}_4 - \dot{u}_3) - k_4(u_4 - u_3) = 0$$

$$m_4\ddot{u}_4 + c_4(\dot{u}_4 - \dot{u}_3) + k_4(u_4 - u_3) - c_5(\dot{u}_5 - \dot{u}_4) - k_5(u_5 - u_4) = 0$$

$$m_5\ddot{u}_5 + c_5(\dot{u}_5 - \dot{u}_4) + k_5(u_5 - u_4) = 0 \qquad (1)$$

where: m_n – mass of following segments; u_n – time-variable displacements; k_n – stiffness as a non-linear deflection function; c_n – damping.

The dynamic model was built in Matlab Simulnk R2022b. The model is shown in Fig. 6. As part of the tests performed, the dynamic responses of the system to the given excitation were analysed. In the model, elements of the integrator type were used twice to integrate the acceleration signal of a given term, to the velocity and, in the second step, to the displacement. These blocks are marked in yellow on the model. The blocks marked in orange describe the dependence of the segment stiffness on the

value of the displacement difference between individual segments (deflection). The Ki(Ui) relationship diagrams are shown in Figs. 6–10. Damping values adopted following literature data [8] are marked in green, and mass elements used in the model are marked in light blue. The model uses blocks from groups: Math Operations, Continuous, Lookup Tables, Sources and Sinks.
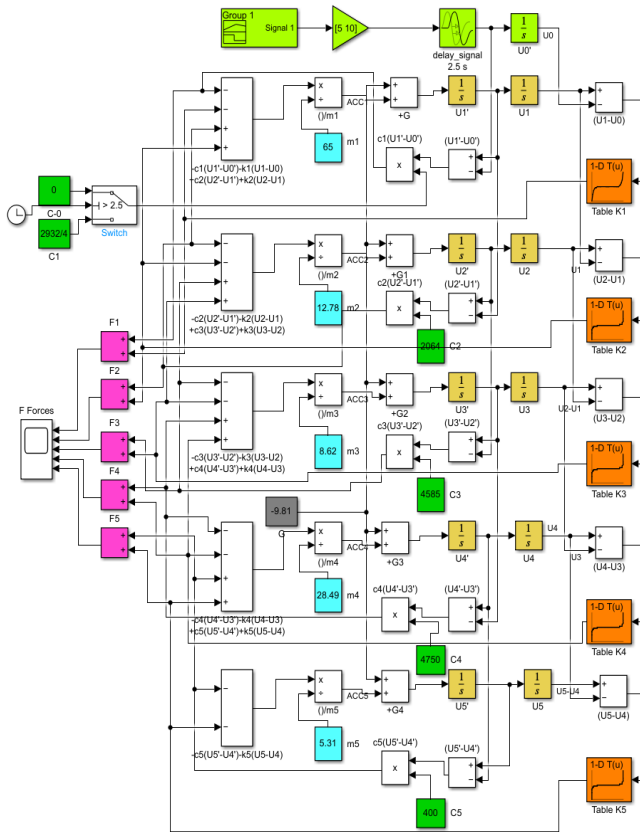
comparing and matching the results with the results obtained using a full-size numerical model of a human placed in the operator's seat (there was also a condition that in a certain range of deflections, the deviation checked by the least squares method from the linear model should meet the condition R > 0.9998).

Fig. 5. Diagram of the developed SBHM in MATLAB Simulink. SBHM, simplified biomechanical human model

Fig. 6. Stiffness k1 of the seat base segment

Fig. 7. Stiffness k2 of the thighs and sacral part of the spine with seat cushion segment

The simulation was carried out for a period of 3.5 s. For the first 3 s, the only load acting is gravity, which helped to stabilize the system. Then, an excitation in the form of a time-varying displacement is introduced into the system. Kinematic excitation in the form of variability of displacements over time was obtained by integrating the course of velocity changes (excitation U0 – the excitation signal was marked with light green in the diagram). The dynamic response was analysed for two maximum values of the excitation velocity 5 m/s and 10 m/s (maximum value of the course), respectively. In the proposed model, the values of forces acting on individual elements in the model were determined (marked in magenta). The values obtained from the Matlab Simulink R2022b model were compared with the values obtained from analyses in the Abaqus and Madymo software.

The configuration parameters set in the simulation are as follows: simulations were performed with a constant integration step of 1.0 e−5/s. The method of direct integration of equations (solver based on Euler's equations) was used, i.e. the Euler integration method is used to compute the model state at the next time step as an explicit function of the current value of the state and the state derivatives. This solver requires fewer computations than a higher-order solver [23].

The stiffness parameters were selected empirically, by

Fig. 8. Stiffness k3 of the lower torso segment

Paulina Działak, Jacek Karliński, Paweł Maślak
Development of a Biomechanical Human Model for Safety Analysis of the Operators of Self-Propelled Mining Machines

DOI 10.2478/ama-2024-0037

Fig. 9. Stiffness k4 of the upper torso segment

Fig.10. Stiffness k5 of the cervical spine segment

4. MODEL COMPARISON

To develop a one-dimensional biomechanical model of a seated operator, the authors used a model with four degrees of freedom developed to assess the ergonomics of machines and vehicles [8]. The linear models used so far in ergonomics studies have been developed based on experimental studies involving people, subjected to dynamic inputs, with small ranges of displacement (vibrations) safe for the health of the subjects. The existing models, due to linear characteristics, do not allow obtaining the correct result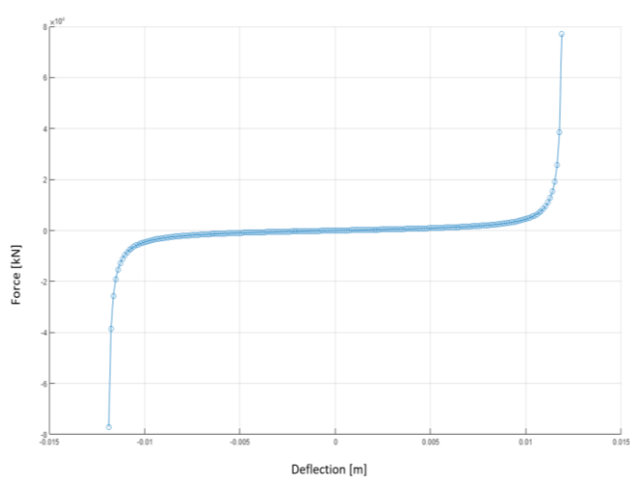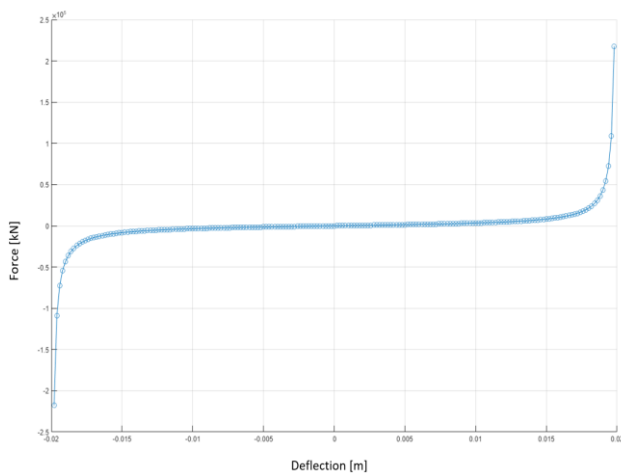s for excitations with large displacement amplitudes occurring simultaneously with high velocities, which occur in accident situations involving mining machine operators [21,22].

The authors introduced significant changes to the existing models consisting of describing the characteristics with non-linear functions and thus obtained a dynamic response in a one-dimensional model, similar to the results obtained in analyses using commercial solutions based on full-size dummies. Satisfactory results were obtained primarily for high velocities of the occurring phenomena. Characteristics that allowed the use of simple one-dimensional biomechanical models with four degrees of freedom to analyse impact dynamic loads were developed. To verify the correctness of the developed model, the obtained results (forces acting in individual segments) for various excitation

velocities were compared with the results obtained for the Hybrid III (MADYMO) dummy. The developed biomechanical model allows us to determine the values of loads acting in several individual parts of the spine and to analyse the effects of the accident situation. It also allows for the deliberate development of structural elements to reduce the loads acting on the operator without the need to use commercial solutions in the form of, for example, the Hybrid III dummy. Requirements for structures protecting operators in terms of assessment of work ergonomics with loads related to vibrations arising during normal operation of machines can also be successfully analysed using the developed biomechanical model. In the linear part (at small ranges of deflection changes), the characteristics describing the stiffness of individual model elements were developed based on experimental studies on people, subjected to low dynamic excitations (vibrations safe for the health of the subjects). The authors showed that in the case of large deflections, the results obtained from the models described in section 2 of the paper are not correct, especially for the loads to which machine operators are subjected during an accident situation.

The modification of the linear characteristics in the models, introduced by the authors, allowed us to obtain quantitatively and qualitatively similar results to those obtained with the use of full-size dummies, as well as for large kinematic excitation. A method for determining the characteristics was developed, which allows the model to be adapted to the analysis of different loads in terms of duration and intensity. The results for different excitation velocities for SBHM, Hybrid III and Boileu-Rakheja original models were compared to verify the correctness of the developed characteristics, (Figs. 11 and 12).
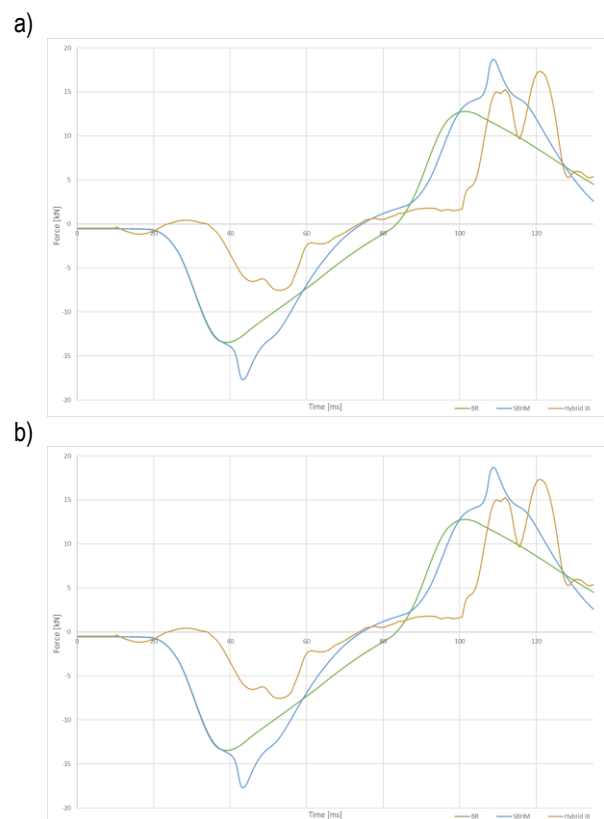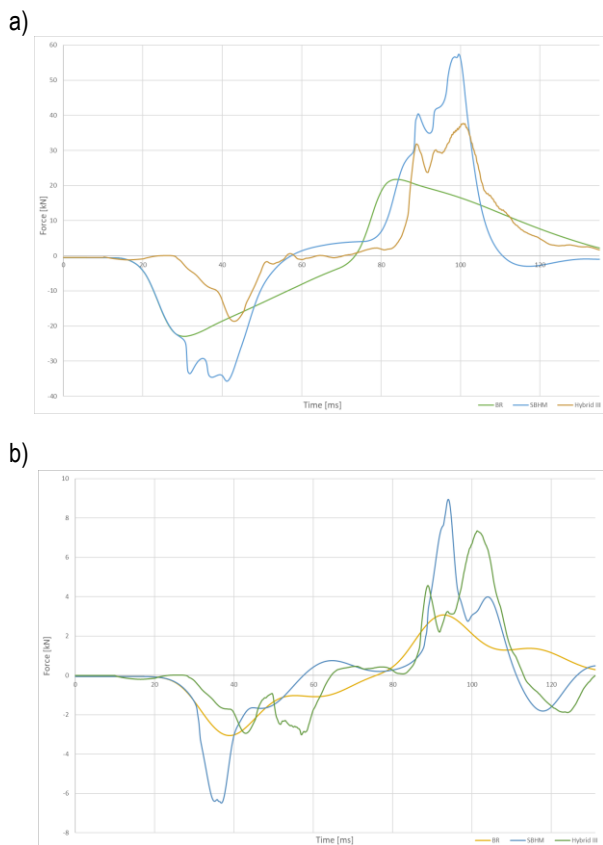
a)

b)

Fig. 11. Results comparison of full-size dummy (Hybrid III) and elaborated model SBHM; a – lumbar spine, b – cervical spine; velocity 5 m/s. SBHM, simplified biomechanical human model

a)

b)

Fig. 12. Results comparison of full-size dummy (Hybrid III) and
elaborated model SBHM; a – lumbar spine, b – cervical spine;
velocity 10 m/s. SBHM, simplified biomechanical human model

5. CONCLUSIONS

The authors performed a comparison of the results obtained from two models, for the analysis of which the same initial boundary conditions were adopted. One of them is a full-size model of the operator with the seat and cabin, while the other is a proprietary one-dimensional model (the 5th degree of freedom is related to the movement of the seat).

1. A model has been developed in a way that allows the analysis of accident situations in mines, which have not been taken into account in safety studies so far.
2. A one-dimensional model of the human body (SBHM) based on the BR model was introduced, enabling a relatively simple and quick analysis of the loads acting on the human body, which can replace the full-size model in the initial analysis.
3. The characteristics that allow the multi-mass model with 5 degrees of freedom to be used for this analysis of impact phenomena were developed based on the author's method.

The developed characteristics implemented in a simple human model can also be used to analyse other phenomena related to the everyday operation, not only to assess the safety of mining machine operators. Safety assessment methods, so far limited to assessing the effects of rollover of the machine ROPS and assessing the effects of events related to falling objects FOPS [1] (these studies do not determine operator injuries, describe only the deformations of the cabin load-bearing structure and analyse the protected space) can now be supplemented with additional test methods and assessment criteria based on the

biomechanics of the human body.

The direction for further research is the implementation of the model in studies on energy-absorbing elements, which will mitigate injuries resulting from accidents caused by vertical loads.

REFERENCES

1. Kalita M. Konstrukcja ochronna operatora ładowarki górniczej w świetle przepisów i badań niszczących Maszyny Górnicze 2013; 20-4: 322-34.
2. Karliński J, Ptak M, Działak P, Kułakowski K. Analiza zagrożeń działających na operatorów samojezdnych maszyn górniczych podczas tąpań, Górnictwo Odkrywkowe 2014;55-4/5:155-59. https://www.faa.gov/10.11.2021
3. Działak P, Karliński J, Rusiński E. Method of operator safety assessment for underground mobile mining equipment. E3S Web of Conferences 2018;29: 1-9.
4. Liang CC, Chiang CF. A study on biodynamic models of seated human subjects exposed to vertical vibration. International Journal of Industrial Ergonomics 2006;36-10:869-90.
5. Singh HJ, Wereley NM. Biodynamic Model of a Seated Occupant Exposed to Intense Impacts. AIAA Journal 2015;53-2:426-35.
6. Bai XX, Xu S, Cheng W, Qian LJ. On 4-degree-of-freedom biodynamic models of seated occupants: Lumped-parameter modeling. Journal of Sound and Vibration 2017;402:122-41.
7. Boileau PÉ, Wu X, Rakheja S. Definition of a range of idealized values to characterize seated body biodynamic response under vertical vibration. J. Sound Vib. 1998;215:841-62.
8. Wan Y, Schimmels JM. A simple model that captures the essential dynamics of a seated human exposed to whole body vibration. ASME-PublicationsBED 1995:333-34.
9. Abbas W, Abouelatta OB, El-Azab M, Elsaidy M, Megahed AA. Optimization of biodynamic seated human models using genetic algorithms. Engineering 2010;2:710-19.
10. Zhang E, Xu LA, Liu ZH, Li XL. Dynamic modeling and vibration characteristics of multi-DOF upper part system of seated human body. Chin. J. Eng. Des. 2008;15:244-49.
11. Liu XX, Shi J, Li GH, Le X, Zhao B, Yue M, Ke W. Biodynamic response and injury estimation of ship personnel to ship shock motion induced by underwater explosion, in: Proceeding of 69th Shock and Vibration Symposium 1998;18:1-18.
12. Singh HJ, Wereley NM. Biodynamic model of a seated occupant exposed to intense impacts. AIAA Journal 2014;53:426-35.
13. Srdjevic Z, Cveticanin L. Entropy compromise programming method for parameter identification in the seated driver biomechanical model. Int. J. Ind. Ergon. 2004;34:307-18.
14. Coermann RR. The mechanical impedance of the human body in sitting and standing position at low frequencies. Human Factors. 1962;227-53.
15. Fairley TE. Predicting seat transmissibilities: The effect of the legs. U.K. and French Joint Meeting on Human Response to Vibration. INRS. Vandoeuvre. France 1988.
16. Pheasant S. 1986. Bodyspace - Anthropometry, Ergonomics and Design. Taylor & Francis. London.
17. Kazarian L. Dynamic response characteristics of the human vertebral column: an experimental study on human autopsy specimens. Acta Orthop. Scand. 1972;43:1-188.
18. Mertens H. Nonlinear behavior of sitting humans under increasing gravity. Aviat. Space Environ. Med. 1978;49:287-98.
19. Boileau PÉ, Rakheja S. Whole-body vertical biodynamic response characteristics of the seated vehicle driver: measurement and model development. Int. J. Ind. Ergon. 1998;22:449-72.
20. Działak P, Rusiński E, Karliński J. Ptak M., Analiza obciążeń działających na operatorów samojezdnych maszyn górniczych podczas tąpań. Górnictwo Odkrywkowe 2014;55-4/5:191-96.

21. Działak P, Ptak M, Karliński J, Iluk A. Injury biomechanics of a mining machine operator. W: 2014 International Research Council on the Biomechanics of Injury: IRCOBI 2014: conference proceedings. Berlin Germany. 10th-12th September 2014. Zurich: International Research Council on the Biomechanics of Injury. 2014; 495-505.
22. Matworks documentation - Matlab Simulink. https://www.mathworks.com/help/simulink/gui/solver.html

Paulina Działak: https://orcid.org/0000-0002-5905-1270

Jacek Karliński: https://orcid.org/0000-0001-6928-5970

Paweł Maślak: https://orcid.org/0000-0001-8796-6155

NUMERICAL MODELLING AND SIMULATION
OF THE SHEAR-SLITTING PROCESS OF ELECTRICAL STEELS

Łukasz BOHDAL* , **Agnieszka KUŁAKOWSKA*** , **Marcin KUŁAKOWSKI***

*Faculty of Mechanical Engineering, Koszalin University of Technology, ul. Racławicka 15-17, 75-620 Koszalin, Poland

lukasz.bohdal@tu.koszalin.pl, agnieszka.kulakowska@tu.koszalin.pl, marcinkulakowski@wp.pl

Abstract: Despite the development of laser processing, the mechanical cutting process is still widely used in the formation of electric steels that are very sensitive to thermal phenomena. However, proper process control is difficult due to the large number of factors determining the quality of the products. As a result, the quality of the cut edge is characterised by the presence of burrs, the removal of which increases the production costs. Due to their magnetic properties, these materials should not be exposed to excessive stresses and deformations. The article presents the possibilities of predicting the characteristic features of the cut edge as well as stress distributions in this area. Original shear-slitting finite element method (FEM) models were developed, the results of which were verified experimentally. The proposed method based on stress triaxiality analysis enables precise analysis of stress states in the cutting zone and the boundaries of the slip fracture transition in the separating fracture, as well as determining the method of material cracking. Variable control factors such as cutting clearance, rake angle of the upper knife, and cutting speed were taken into account in the models. Parametric analysis of the process was carried out and it was determined how the process parameters should be selected in order to obtain the appropriate quality of the product. The developed analysis results can be useful on production lines for proper process control.

Key words: shear-slitting, electrical steels, residual stress, triaxiality, sheared-edge

1. INTRODUCTION

In the process of cutting metal materials, it is very important to properly control the process in order to obtain the optimal technological quality of the product. It depends on both the characteristics of the cut surface and the dimensional and shape accuracy of the formed elements. In the processes of cutting thin materials such as electrical steel sheets or amorphous tapes in industrial conditions, there is a problem with the formation of burrs on the cut edge. Burrs are hard, sharp and raised edges created on the cut surface of the material during the process. They often have an irregular height along the cut line. The presence of burrs must be removed by further processing, such as machining or deburring, further increasing the cost of production [1]. The intensity of the increase in the height of the burrs increases with the wear of the cutting tool blades [2]. In the case of cutting thin sheets, it is also important to select the appropriate cutting clearance, so that the width of the deformed zone along the cut edge is as small as possible [3]. As research by the authors of papers [4–7] has shown, the clearance value should be selected depending on the cutting speed. Since the cutting process generates plastic strains and residual stresses that concentrate near the cutting edge of the sheet, it is necessary to have knowledge about the distribution of plastic strains and stresses in the cutting zone. According to many authors, the reason for the deterioration of the magnetic properties is the change in the flux density distribution due to material stresses and deformations [8–10]. In the works [8, 11], it was shown that the residual stresses after punching and blanking go further into the material than the strain-hardened area. According

to studies, the zone of plastic deformation after mechanical cutting is at least 0.1 mm and grows rapidly with the increase in the wear of cutting tools [8, 12, 13]. Deformations along the cutting line may be the reason for the formation of an elastic stress zone in the depth of the material, adjacent to the plastically deformed area. As a result, both zones strongly influence the magnetic properties. In the case of aluminium sheets, the burr adversely affects the processes of joining sheets, while in the case of electrical steel sheets, on the packing in the magnetic cores. In the literature, there are known techniques for measuring the hardness of the sheet in the vicinity of the cut edge, aimed at determining the plastic state and the width of the deformation zone into the material. These are invasive methods that cause local changes in the magnetic properties in the measurement zone. The degree of degradation of magnetic properties also depends on factors such as chemical composition, type of material, type of cutting technique, technological parameters of the process, etc. Moreover, in the case of thin sheets, the measurement is subject to error [14–16].

In the available literature, many works focus on the analysis of the negative impact of punching and blanking processes on the magnetic properties of grain-oriented and non-grain oriented silicon electrical steel sheets [17, 18]. The impact of the blanking process, depending on the thickness of the non-grain oriented electrical steel and the deterioration of core losses was studied in Toda et al. [19] and Omura et al. [20]. It was found that the distribution of the hardness increase near the shear edge was almost half of the plate thickness for all the tested steels. The use of thinner steel sheets for the magnetic core could reduce the iron losses in the punching process. In works [21] and [22] it was

Łukasz Bohdal, Agnieszka Kułakowska, Marcin Kułakowski
Numerical Modelling and Simulation of The Shear-Slitting Process of Electrical Steels

DOI 10.2478/ama-2024-0038

shown that electrotechnical steels with a high content of silicon and characterised by large grains are more sensitive to the deterioration of magnetic properties in the punching process. Subramonian et al. [23] determined the effect of the punching process parameters on various 0.25 mm and 0.8 mm thick steel sheets by means of experimental studies. The authors showed that blanking clearance is the most important factor influencing the quality of the cut edge. Its values must be selected depending on the thickness of the cut sheet and the type of material. An increase in clearance above a critical value causes a significant increase in burr on the cut surface. In work [24], the effect of grain size and banking clearance on selected magnetic characteristics was experimentally analysed. As a result of process optimisation, guidelines were proposed to reduce core losses by 5.8%. In the work [8], the impact of material grain size on iron losses after the blanking process and on the course of the blanking forces was assessed. In Wang et al. [14], the impact of the blanking process on the magnetic properties of non-oriented electrical steel sheets was analysed, focussing on the assessment of the degree of changes in magnetic properties depending on the increase in stress in the cutting zone. Variable geometry tools were used. With the help of appropriate tool geometries and clearance values, it was possible to limit the negative changes in magnetic properties.

Recent literature provides information on the characteristics of the width of the cut edge and new methods used to quantify its length. Problems with obtaining high-quality cut edges are indicated because deformations of the material domain walls occur and, as a consequence, the domain magnetisation flux decreases and the shift between the magnetisation flux and the total flux increases. Monitoring techniques are used to determine the characteristic features of the cut edge [25–28]. In paper [29], the relations between the relevant material parameters, i.e., sheet thickness, alloying and grain size and non-linear magnetic properties, are studied, with a focus on cut surface features and iron losses. Paper [30] presents an approach for image-based blanking tool wear monitoring and workpiece shape. The workpiece images offer the possibility to apply computer vision algorithms for handcrafted feature extraction in order to capture the cut surface formation and product properties as time-efficiently as possible. The work [31] analysed the causes of burr formation on the cut edge of blanked details. The authors indicated that the main cause of this is the wear of the cutting edges of the punch and die. The correct determination of the width of individual zones on the cut surface, and thus the prediction of the occurrence of areas with variable fracture mechanisms, is currently one of the main difficulties encountered in the literature related to mechanical cutting processes. According to the works [4, 9, 32, 33], the local state of stress in the shear zone is important for the formation of shear bands and significantly affects the topography of the cut surface. Higher local compressive stresses inhibit cracking and allow the material to flow plastically for longer periods.

The finite element method (FEM) is increasingly used in many industries as a powerful numerical tool to analyse physical phenomena occurring in various processes and to shorten the cycle time of introducing new solutions. FEM provides the ability to effectively track and analyse the deformation process, which may be difficult to observe in experimental studies. Simulation of the finite element cutting process can enable the analysis of the influence of various technological input parameters, such as cutting clearance, tool edge radius, cutting speed and sheet thickness, etc. on burr height, deformed zone width, stress and strain values

in the cutting zone compared to experimental methods. In the available literature, there are many papers devoted to modelling the process of cutting construction materials and light metal alloys. There is a lack of numerical simulations of the process of cutting electrical steels, especially of small thicknesses [4, 14, 23]. This is especially true of the shear-slitting process in which the tools perform a rotary motion.

This paper proposes an approach to modelling the process of cutting electrical steel sheets under real process conditions. The correct determination of the width of individual zones on the cut surface, and thus also the prediction of the occurrence of areas with variable fracture mechanisms using numerical modelling techniques, is currently one of the main difficulties encountered in the literature related to mechanical cutting processes. The new method proposed in the manuscript, based on the analysis of stress triaxiality, enables precise analysis of stress states in the cutting zone and the boundaries of the slipping fracture in the separating fracture, as well as determining the manner of material cracking. The developed models allow for the prediction of stress values and areas of their occurrence depending on the adopted processing parameters.

2. MATERIALS AND METHODS

2.1. Experimental setup

In order to carry out the experiment, a special test stand was designed, shown in Figure 1a. The stand is equipped with a cutting device consisting of rotary knives, a motor, special guides and holders for fixing metal sheets. It allows you to cut sheets in a straight line and cut out rings or circles. A special roller made of polyurethane allows the sheet to be moved horizontally during cutting (Fig. 1b). It is possible to precisely set the value of cutting clearance hc, knife overlap cv and cutting speed v (Fig. 1a, c). The upper knife can be replaced depending on the preferred value of the rake angle α. Before starting the experiments, trial tests of the device were carried out to verify the correct operation. Input, output, disturbing and constant factors were specified. The tests were carried out as follows: prepared electrical steel sheets were mounted in the device and fixed with a special needle. Due to the rotation of the knives and the clamping roll, the cut element was moved along the z-axis, resulting in its separation (Fig. 1b). At the final stage of the process, the attached part remained in place due to the action of the needle, while the cut part fell off. Due to the high complexity and speed of the course of physical phenomena, an advanced vision method (digital image correlation) was used in the cutting process in the form of a specially designed monitoring system, which consisted of a high-speed camera i-SPEED TR, zoom lens, light sources and the GOM Correlate and i-SPEED Suite software. A resolution of 1,280 × 1,024 pixels, and a speed of 2,000 fr/s. were used in images registration. The test stand also includes intermediate rings, LED rings and LED lamps with different diode power. During the experiment, synchronous tracking of points in the recorded sequences of images was carried out. A correlation algorithm was used to create the object model, which may be the first frame of the recorded sequence of test images. The ranges of the variability of the studied factors are summarised in Tab. 1.

Tab. 1. The ranges of the variability of the studied factors

Horizontal clearance, h_c	0.02−0.1 mm
Vertical clearance, c_v	0.1 mm
Slitting velocity, v_2	3−24 m/min
Rake angle, α	5°−40°

(a)

(b)

(c)
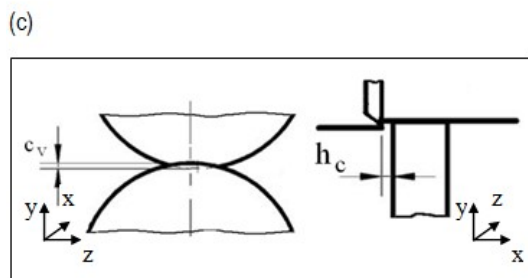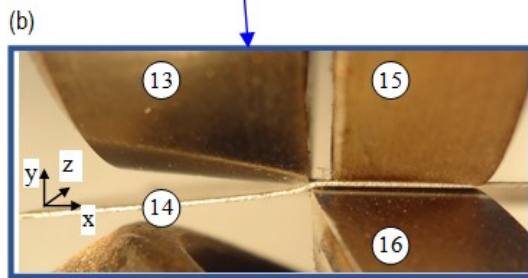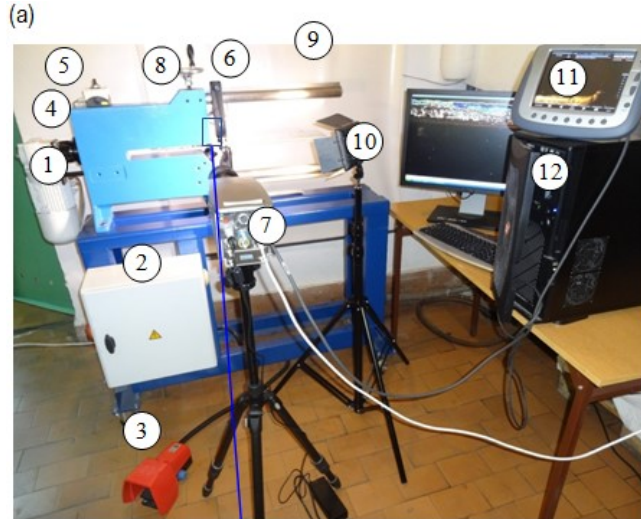
Fig. 1. Experimental test stand: a) 1 – engine, 2 – electrical system, 3 – drive pedal, 4 – threaded socket with a scale for adjusting the cutting clearance, 5 – cutting speed regulator, 6 – sheet stabilizer (needle), 7 – high-speed camera, 8 – knife overlap regulator, 9 – scale for determining the diameter of cut discs for curvilinear outlines, 10 – LED lamp, 11 – auxiliary screen for recording and analysis, 12 – computer workstation for archiving measurement data, b) zoom of contact zone: 13 – upper knife, 14 – sheet, 15 – clamping roll and 16 – lower knife, c) characteristic parameters of the process
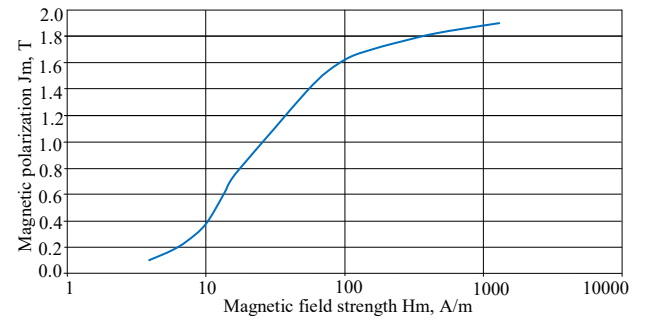
2.2. Material characteristics

ET 110-30LS with thickness t = 0.3 mm electrical steel was used in research. Mechanical properties are presented in table 2.

Tab. 2. Mechanical properties of ET 110-30LS steel [34]

Density [kg/dm³]	Yield point [MPa]	Elongation [%]	Hardness [HV₅]
7.8	310 ± 5	14 ± 1.5	170 ± 6

A thickness of t = 0.3 mm was chosen due to this thickness having the greatest applicability for the construction of electrical devices. The mechanical and magnetic properties are presented in Tab. 1 and Fig. 2.

Fig. 2. Magnetisation characteristic J_m=f(H_m) for ET 110-30LS [34].

3. FE MODELLING OF THE SHEAR-SLITTING PROCESS

A mathematical model of the shear-slitting process is incrementally formulated containing the following: a material model, a contact model, an equation of both the motion and deformation, and both the initial and boundary conditions.

3.1. Material modelling

3.1.1. The incremental model of the yield stress

For a typical step time, $t \rightarrow \tau = t + \Delta t,$ a model $\Delta\sigma_Y$ was defined as [35]:

$$\Delta\sigma_Y = E_T \cdot \Delta\varepsilon_e^{(VP)} + \dot{E}_T \cdot \Delta\dot{\varepsilon}_e^{(VP)}, \qquad (1)$$

where $\Delta\varepsilon_e^{(VP)}$ and $\Delta\dot{\varepsilon}_e^{(VP)}$ are the increments of the effective viscoplastic strain and rate, respectively, $E_T \cdot \Delta\varepsilon_e^{(VP)}$ represents the change in the temporary yield stress $\Delta\sigma_Y$ with changing viscoplastic strain, where $E_T = \partial\sigma_Y(\cdot)/\partial\varepsilon_e^{(VP)}$ is the temporary hardening parameter assuming a constant accumulated effective viscoplastic strain rate at time t ($\Delta\dot{\varepsilon}_e^{(VP)} = $ const) and $\dot{E}_T \cdot \Delta\dot{\varepsilon}_e^{(VP)}$ represents the change in the temporary yield stress, σ_Y, with changing viscoplastic strain rate, where $\dot{E}_T = \partial\sigma_Y(\cdot)/\partial\dot{\varepsilon}_e^{(VP)}$ is the temporary hardening parameter assuming a constant accumulated effective viscoplastic strain at time t ($\Delta\varepsilon_e^{(VP)} = $ const).

3.1.2. Elastic/viscoplastic material model

A new mixed hardening model for isotropic materials, which includes the combined effects of elasticity (reversible domain), and viscoplasticity (non-reversible domain) (E/VP), is used. This

Łukasz Bohdal, Agnieszka Kułakowska, Marcin Kułakowski
Numerical Modelling and Simulation of The Shear-Slitting Process of Electrical Steels

DOI 10.2478/ama-2024-0038

model accounts for the mechanic history of the material. The constitutive equation for the incremented components in a total Green–Lagrange strain tensor takes the following form [35, 36]:

$$\Delta\varepsilon_{ij} = \frac{1}{1-\tilde{S}^{**}} \cdot \left(D_{ijkl}^{(E)} \cdot \Delta\sigma_{kl} - \frac{\frac{2}{3} \cdot [\sigma_Y(\cdot)] \cdot \dot{E}_T \cdot \Delta\dot{\varepsilon}_e \cdot \tilde{S}_{ij}}{\tilde{S}_{ij} \cdot C_{ijkl}^{(E)} \cdot \tilde{S}_{kl} + \frac{2}{3}\sigma_Y^2(\cdot) \cdot \left(\tilde{C}(\cdot) + \frac{2}{3}E_T\right)} \right) \quad (2)$$

Whereas the incremented components for the total second symmetric Pioli–Kirchhoff's stress tensor are as follows [36]:

$$\Delta\sigma_{ij} = C_{ijkl}^{(E)} \cdot \left(\Delta\varepsilon_{kl} - \psi \frac{\tilde{S}_{kl} \cdot \left\{ \tilde{S}_{ij} \cdot C_{ijkl}^{(E)} \cdot \Delta\varepsilon_{kl} - \frac{2}{3}\sigma_Y(\cdot) \cdot \dot{E}_T^{(VP)} \cdot \Delta\dot{\varepsilon}_Z^{(VP)} \right\}}{\tilde{S}_{ij} \cdot C_{ijkl}^{(E)} \cdot \tilde{S}_{kl} + \frac{2}{3}\sigma_Y^2(\cdot) \cdot \left(\tilde{C}(\cdot) + \frac{2}{3}E_T\right)} \right) \quad (3)$$

where Δ – increment, ε_{ij} – strain tensor component, σ_{ij}- – stress tensor component, $\tilde{S}^{**} = \tilde{S}_{ij}^* \cdot C_{ijmn}^{(E)} \cdot \tilde{S}_{mn}$ is a positive scalar variable, $\tilde{S}_{ij} = S_{ij} - \alpha_{ij}$ $(i,j = 1-3)$ is the stress deviator component, $\widetilde{D}_\sigma$ and $D_{ijkl}^{(E)}$ is the component for the tensor $D^{(E)} = C^{(E)-1}$ in time t, $C_{ijkl}^{(E)}$ are the elastic constitutive tensor components $C^{(E)}$, $\widetilde{C}(\cdot) = \widetilde{C}(\varepsilon_e^{(VP)}, \dot{\varepsilon}_e^{(VP)})$,is the temporary translation hardening parameter in time t, $\sigma_Y(\cdot) = \sigma_Y(\varepsilon_e^{(VP)}, \dot{\varepsilon}_e^{(VP)})$ is the accumulated material yield stress, which depends on the history of the viscoplastic strain and strain rate, and $\varepsilon_e^{(VP)}$ and $\dot{\varepsilon}_e^{(VP)}$ are the cumulative effective viscoplastic strain and strain rate, respectively. It is assumed that the relationship of $\sigma_Y(\cdot)$ and $\widetilde{C}(\cdot)$ to $\varepsilon_e^{(VP)}$ and $\dot{\varepsilon}_e^{(VP)}$ can be derived from data obtained during a series of tensile tests at different strain rates using virgin material specimens [37, 38]. The instantaneous value of the yield stress σY was calculated from Johnson-Cook material law [39]:

$$\sigma_Y = [A + B(\bar{\varepsilon}^p)^n][1 + Cln\dot{\varepsilon}^*][1 - (T^*)^m], \quad (4)$$

where: $A, B,$ and n are strain hardening constants, C is the strain rate hardening constant, σ_Y is the equivalent flow stress, $\bar{\varepsilon}^p$ is the equivalent plastic strain, m is the thermal softening constant and T^* is the homologous temperature term, where $T^* = \frac{T - T_r}{T_m - T_r}$, T is the temperature of the material, T_r is a reference temperature, and T_m is the melt temperature of the material, $\dot{\varepsilon}^*$ is the normalised strain rate of the material or $\dot{\varepsilon}^* = \frac{\dot{\bar{\varepsilon}}^p}{\dot{\varepsilon}_0}$, where $\dot{\varepsilon}_0 = 1.0s^{-1}$. The model parameters are presented in Tab. 3.

Tab. 3. The Johnson-Cook constitutive model constants for ET 110-30LS steel [34]

| A [MPa]	B [MPa]	C	n	m
110.4	456	0.049	0.41	0.51

3.2. Simulation model

For the purpose of the work, FEM models were developed in the LS-DYNA solver for the spatial state of stress and the plane (2D) or spatial state of strain (3D) (Figs. 3 and 4). 2D models were used to predict the course of the plastic flow and cracking process in very small cross-sectional areas of the sheet. On the other hand, 3D models, after taking into account the length of the cut line, make it possible to predict deformation and stress states

along the cut line and model sheet defects, e.g. bends and corrugations. The models take into account variable rake angle values (α), the value of the radius of the knives, the length of the cutting line and the variable cutting speed. It is also possible to control the setting of overlap c_v.
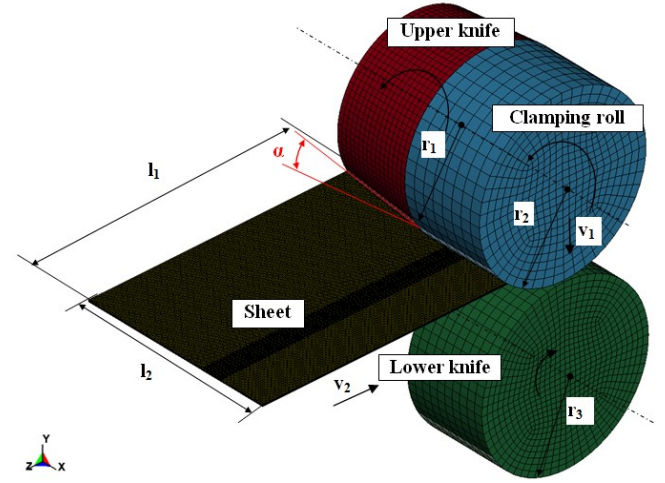
Fig. 3. 3D FE model with boundary conditions

The numerical simulations were carried out for the process control variables in the range of α = 5°–40°, v_2 = 3–32 m/min and h_c = 0.02–0.1 mm. A constant value of tools overlap c_v = 0.1 mm was assumed. The following geometric parameters of the test stand were applied: $r_1 = r_2$ = 15 mm, r_3 = 20 mm, l_1 = 80 mm, l_2 = 40 mm.
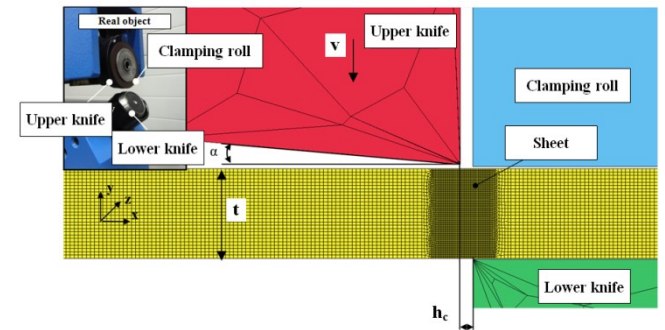
Fig. 4. 2D FE model with boundary conditions

Constant coefficients of static $\mu_s = 0.15$ and dynamic $\mu_d = 0.1$ friction were assumed. A 4-node element of the PLANE 162 type for 2D models and 3D SOLID 164 for 3D models was used to discretise the object.

4. FE MODELLING RESULTS

4.1. Shear-slitting phases and model validation

Since the concentration of maximum deformations and displacements in cutting processes occurs in a small area, advanced vision methods can be used to observe many physical phenomena. Currently, image registration is an important issue in the su-

pervision of manufacturing processes in real time. In this way, it is possible to fully observe the formation of possible product defects. The proposed research methodology uses an advanced vision system for measuring displacements and deformations in the cutting zone, crack propagation moment, trajectory analysis, cracking speed measurement and product quality assessment, depending on the adopted machining parameters at any time during the process.

The proposed method using an advanced vision system was used to analyse deformation states in the cutting zone, crack propagation and crack trajectory. The deformation values and the width of the deformation zone in the material after cutting were also determined. The obtained results were used to validate the simulation results obtained using FEM models.

Fig. 5 shows the plastic flow phase transitioning to the cracking phase of the process. Both in the 2D model and the 3D model, local cracks are visible in the areas of the cutting edges of the knives. Due to the minimal clearance hc used, cracking occurs in the cutting zone and proceeds stably without causing transverse cracking and burr formation, which is consistent with the results obtained experimentally. Particular attention was paid during the comparative analysis to the correct representation of the flow mechanics of the material, the formation of individual zones on the cut surface, among others edge roundness and burrs, the degree of material deformation and the formation of sheared-burnished and fracture zones.
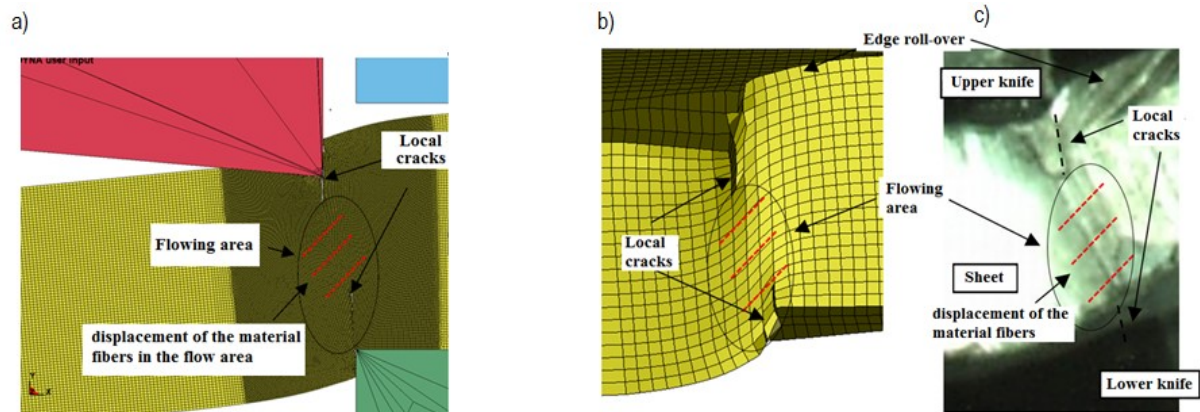

Fig. 5. Numerical representation and visual recording of the transition from plastic flow to cracking: (a) 2D FEM model, (b) 3D FEM, model, (c) camera image (h_c = 0.04 mm, α = 7°, v = 7 m/min).
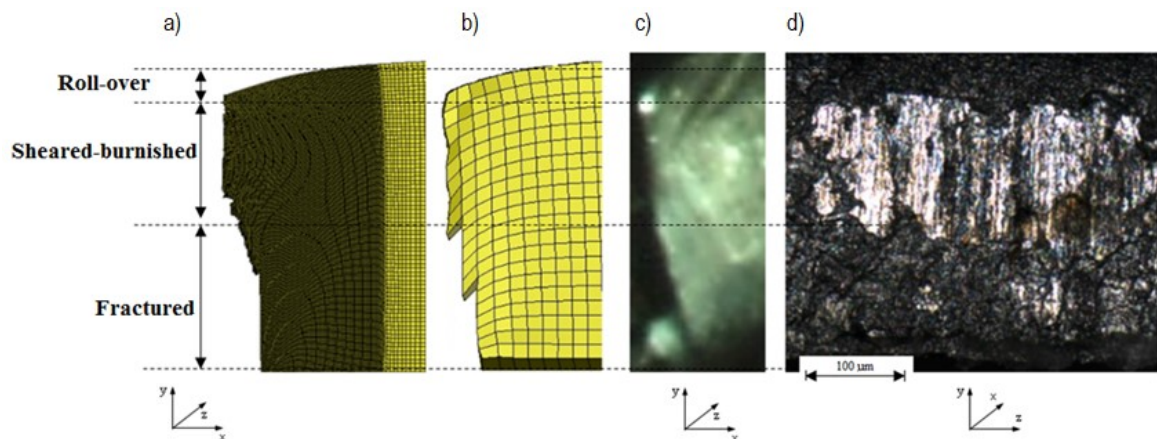

Fig. 6. Analysis of selected features of the cut edge: (a) appearance of the cut edge for the 2D model, (b) appearance of the cut edge for the 3D model, (c) appearance of the cut edge obtained experimentally, (d) image of the surface of the cut edge

Fig. 6 shows the appearance of the cut edge after the cutting process for the configuration of the parameters hc = 0.04 mm, α = 7° and v = 10 m/min. Shaping materials with small thicknesses often causes problems on production lines because (even small deviations from the optimal settings of processing parameters and disturbances cause product defects) they are very sensitive to changes in processing parameters, which causes the formation of burrs and excessive roll-over of the edges. The analyses of the cut edge for the validation of FEM models were made using images recorded with a high-speed camera in the cross-section of the sheet and images of the geometric structure of the cut surface recorded along the cutting line with a LEXT OLS4000 laser confo-

cal microscope from OLYMPUS. The presented example is characterised by a clear transition boundary of the sheared-burnished in the fractured area, which is characterised by the perpendicularity deviation within 40 µm both in simulation models and in the experiment. The rollover zone is acceptable from a technological point of view and is about 30–40 µm. The simulation models correctly reflect the boundaries of the fractures and the size of the roll-over. In the presented case, there is a negligible burr, which was shown in FEM models and confirmed experimentally.

Fig. 7 shows the selected results with clearance hc = 0.08 mm, α = 7° and v = 7 m/min. The effect of the increased clearance on the course of the plastic flow and cracking phases is

Łukasz Bohdal, Agnieszka Kułakowska, Marcin Kułakowski
Numerical Modelling and Simulation of The Shear-Slitting Process of Electrical Steels

DOI 10.2478/ama-2024-0038

particularly visible. In the selected stage of the process phase, the first cracks appear in the contact area of the knife blades with the material. In the 2D model, micro-gaps can be observed near the cutting edges of the knives. In the 3D model, the initial phase of material cracking can be observed. The deformed zone is wider than in the case of reduced clearance cutting and the flow area is non-symmetrical. The fibre arrangement of the material is significantly curved. The asymmetry of the concentration of maximum plastic strains causes uneven and unstable cracking of the material, which does not run in a straight line. Crack propagation proceeds at different speeds. Initially, in the contact zone of the lower knife with the material, the crack propagates faster than in the

area under the upper knife, but at a certain stage it stabilises, and due to the movement of the upper knife, cracking accelerates in the area of its contact with the edge of the sheet. The fracture line is far from the knife's cutting edge, resulting in burr formation. Due to the increased bending moment, an increased roll-over of the sheet edges can be observed. The results obtained using FEM models are consistent with the results obtained experimentally, and the characteristic phenomena occurring in the process are correctly predicted. Experimental measurements confirmed the formation of a burr on the lower surface of the sheet edge and a characteristic depression just behind the burr line, which may indicate the area of local micro-cracks.
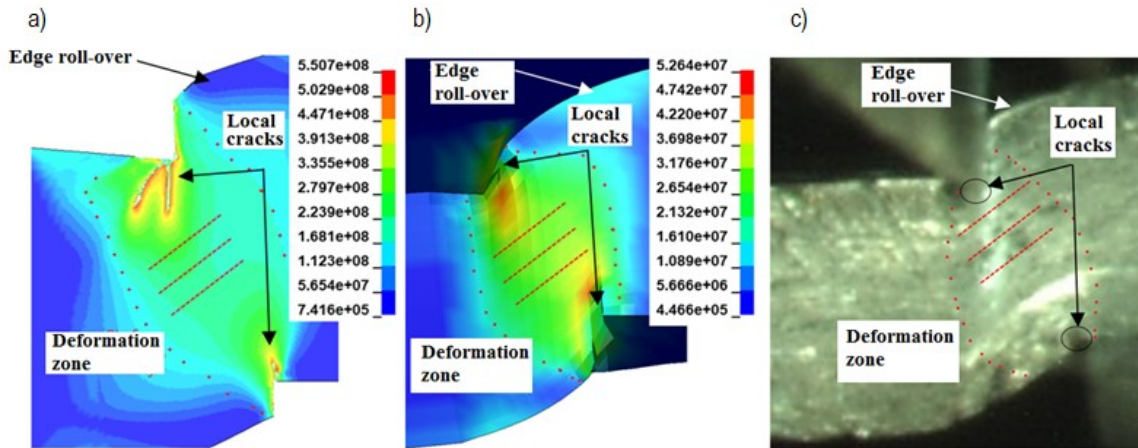
Fig. 7. The course of the plastic flow phase with the beginning of the cracking phase for $h_c = 0.08$ mm, $\alpha = 7°$, $v = 7$ m/min: (a) 2D model, (b) 3D model, (c) camera image
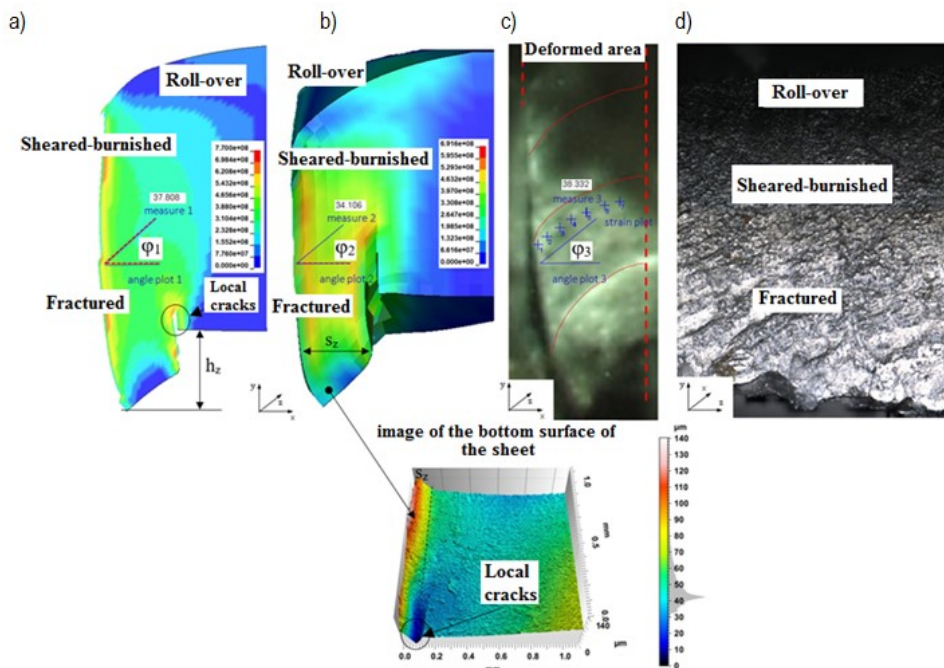
Fig. 8. View of the cut edge after the cutting process for: $h_c = 0.08$ mm, $\alpha = 7°$, $v = 7$ m/min: (a) 2D FEM model, (b) 3D FEM model, (c) camera image, (d) image of the surface of the cut edge, and geometric structure of the lower surface of the sheet in the area of the cut edge

After the cutting process, the following measurements were made: the height of the burr and its width, which are in the range of about $h_z = 110–130$ µm, $s_z = 70–80$ µm for both simulation and experiment (Figs. 8a and 8b). It was possible to accurately meas-

ure thanks to the option of tracking the displacements of the nodes of the FEM model and the analysis of images of the geometric structure of the bottom surface of the metal sheet registered with a confocal microscope. The flow angle was measured

using specialised ImageJ and GOM Correlate software. The results of the measurements of the flow angle φ are consistent with the experiment (φ_1 = 37.8°, φ_2 = 34.1°, $\varphi_3$ = 38.3°) and do not differ significantly at the assumed significance level (Fig. 8c). The sample is characterised by the lack of a clear transition boundary of the sheared-burnished in the fractured (Fig 8d). In order to predict the area of occurrence of this boundary on the cut edge, a new approach based on the analysis of distributions of the stress triaxiality coefficient was proposed.

4.2. Residual stress analysis

4.2.1. Stress triaxiality distribution

A method, based on stress triaxiality, enables precise analysis of stress states in the cutting area and the boundaries of the zones as well as determining the manner of material cracking. The location of the transition points of individual zones on the cut edge can be determined on the basis of the study of the distribution of the stress triaxiality coefficient η defined as the ratio of hydrostatic stress (hydrostatic pressure) and the equivalent stress (usually calculated using von Mises criterion) [40]. With the use of particular ranges of the triaxiality coefficient developed in the

literature, it is possible to predict, using FEM models, characteristic areas of fracture boundaries, even for samples with no clear division boundary. This makes it possible to design tools and select process conditions so as to extend the shearing and plastic flow phase, which causes the formation of a sheared-burnished zone on the cut edge with a minimum share of tensile stresses, causing significant deterioration of magnetic properties.

Figs. 9 and 10 show selected phases of the cutting process with the distribution of the stress triaxiality factor for two values of the cutting clearance hc. In the initial stages, the cutting edges of the tools cause elastic deformation of the material. It is strongly compressed – stresses and elastic strains concentrate near the cutting edges as a result of the elastic bending of the cut material. With a further increase in the load near the cutting edges, plastic deformations occur (Figs. 9a, 10a). Shear areas where the triaxiality coefficient oscillates within the range of η = 0.0 ± 0.16 in the initial phase of the process are close to each other for the two analysed clearance values. Outside the shear area states of uniaxial compression occur in the cross-section of the sheet. In the vicinity of the cutting edges of the tools, there is biaxial compression with significantly negative values of the triaxiality coefficient.

Fig. 9. Triaxiality coefficient values: (a) plastic flow phase, (b) plastic flow phase with a transition to cracking, (c) cracking phase: h_c = 0.02 mm, α = 7°, *v* = 7 m/min)
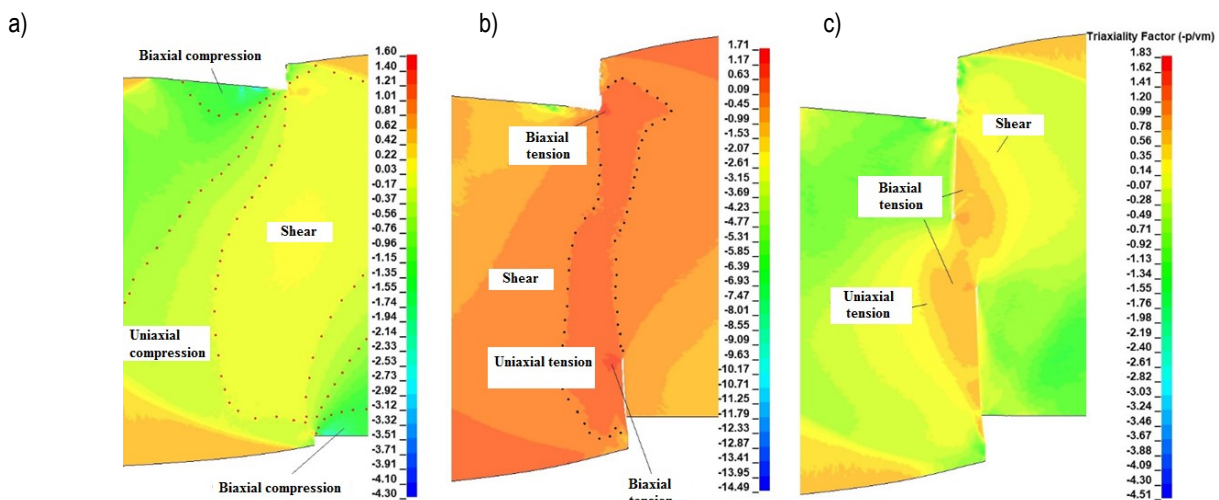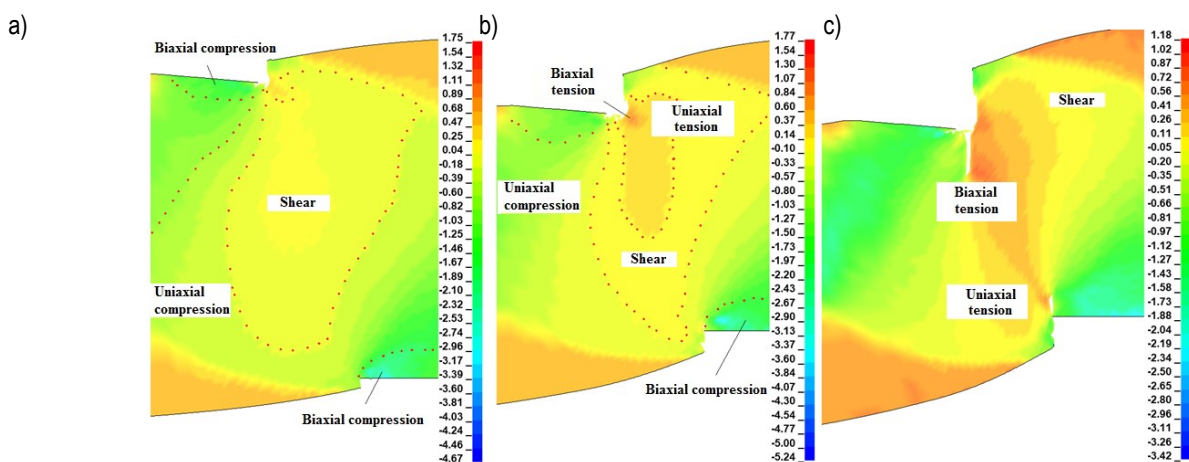

Fig. 10. Triaxiality coefficient values: (a) plastic flow phase, (b) plastic flow phase with a transition to cracking, (c) cracking phase: h_c = 0.08 mm, α = 7°, *v* = 7 m/min)

Łukasz Bohdal, Agnieszka Kułakowska, Marcin Kułakowski
Numerical Modelling and Simulation of The Shear-Slitting Process of Electrical Steels

DOI 10.2478/ama-2024-0038

In the next stage of the process, the reduced clearance accelerated the cracking process and the formation of a uniaxial stretching zone dominated by the above positive values of the triaxiality coefficient (Fig. 9b). Small areas of biaxial tension are also visible, which can cause micro-cracks in the vicinity of the blades, which was confirmed by experimental studies. For the increased clearance, the shear area occurs at this stage in the lower areas of the sheet thickness (Fig. 10b). Under the upper knife, however, the state of uniaxial tension begins and the transition from the phase of plastic flow to cracking begins. Biaxial tension fields are also visible. In the cracking phase, characteristic distributions of the triaxiality coefficient fields can be observed. For the reduced clearance, the distributions are symmetrical with the separation of areas of biaxial and uniaxial tension of small width along the fracture line (Fig. 9c). For increased clearance, the zone of increased coefficients is wider than for reduced clearance (Fig. 10c). In the fracture line there are states of uniaxial and biaxial tension, and the area of ideal shear is distant from the cut line. When the clearance between the cutting edges of tools is greater than the allowable, as a result of the edge spreading, the bending moment increases, causing excessive bending of the edges of the cut material. As a result, with shearing, there is excessive tension of the material in the gap between the cutting edges, which causes a thick bent burr.
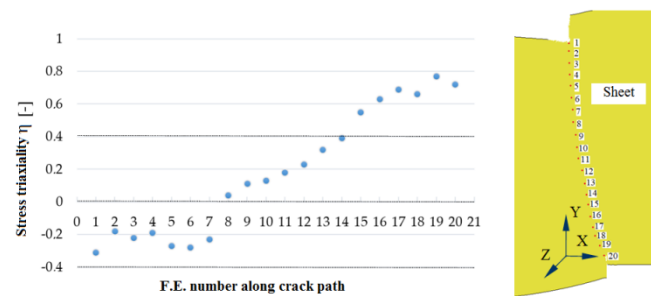

Fig. 11. Triaxiality factor values recorded before removing the finite elements from the mesh in the cracking line: h_c = 0.02 mm, α = 7°, v = 15 m/min

Fig. 11 shows the values of the stress triaxiality factor determined in the finite elements located along the crack path. A sample without a clear fracture separation boundary was selected for the study. Finite elements in the section analysed and lying on the fracture path are marked in Fig. 11. The chart highlights three main areas. The first contains finite elements with negative values of the stress triaxiality coefficient. The second shows the values of the stress triaxiality coefficient in the range from η = 0 to η = 0.4. The third area is the triaxiality of stresses above η = 0.4. The obtained results can be discussed on the basis of analyses of Bao and Wierzbicki's research [41]. The finite elements located in the upper part of the sheet cross-section (elements No. 1–7) were subjected to a shear fracture mechanism and a smooth zone was formed. The features numbered 8–14 were generated by a combination of shear and fracture growth modes. The predicted fracture zone was probably formed by the removal of finite elements from 15 to 20 and was mainly subjected to a mode of fracture formation and growth.

4.2.2. Influence of the process parameters on the residual stresses in the area of the cut edge

Figs. 12–14 show the influence of process parameters on equivalent stresses in the area of the cut edge. The magnetic domain structure is characterised by domains with dimensions similar to the thickness of the sheet and the walls separating them pass through the entire thickness of the sheet and are parallel to the direction of rolling. The plastic deformation of the cut edges causes local displacements of the material, which effectively hinders the movement of the domain walls and domain rotation. As a consequence, this leads to lower permeability, higher coercivity and higher hysteresis losses. In addition, stresses in electrical steel affect the magnetic properties due to the inverse magnetostrictive effect. Fig. 12 shows the influence of the cutting clearance value on the stress values in the cutting zone. The measurement was made in the zone of greatest strengthening in the middle of the cross-section of the sheet. The obtained results confirmed the significant influence of the analysed process parameters on the stress values in the area of the cut surface. In some cases, it can be seen that the maximum stress concentration occurs at a certain distance from the cut surface and not at its edge. In the case of cutting clearances in the h_c = 0.02–0.04 mm range, the concentration of maximum stress values occurs in the area of the cut surface, and their values decrease away from the cut edge. In the case of cutting clearance h_c = 0.06 mm, the maximum stress concentration occurs at a distance of about x_1 = 100 μm from the cut edge. Their values, however, decrease rapidly as they move away from the cut edge. The largest zone of stress concentration occurred for cutting clearances above h_c = 0.08 mm.
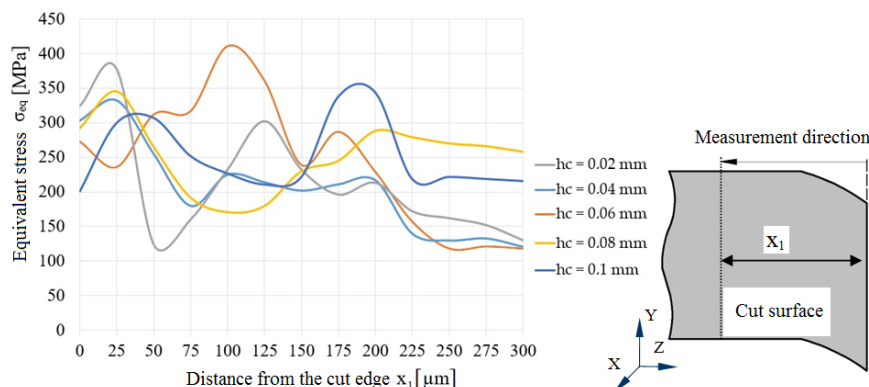
Fig. 12. Influence of cutting clearance h_c on the value of equivalent stresses in the area of the cut edge

The influence of the rake angle of the upper knife cutting edge α on the stress values in the cutting zone is shown in Fig. 13. The value of the angle α has a significant impact on the values of maximum stresses in the cutting zone. The high value of α causes the concentration of maximum stresses directly on the cut edge and their increase compared to α = 7°. For the angle α = 7°, the width of the stress zone is greater than when α = 20° and α = 40°, but their maximum values are smaller.
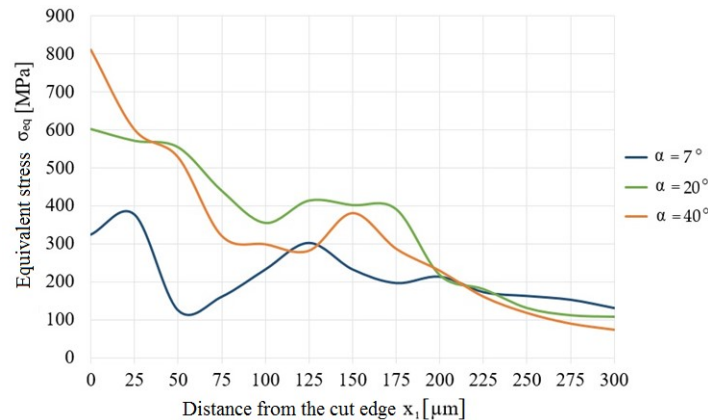
Fig. 13. Influence of rake angle α on the value of equivalent stresses in the area of the cut edge

The influence of cutting speed on the values of equivalent stresses in the cut edge is shown in Fig. 14. In the analysed cases, a significant impact of cutting speed on the values of maximum stresses in the vicinity of the cutting edge can be observed. In the case of cutting with speed v = 32 m/min, the maximum stress values cover a larger area of the material than when cutting speeds are lower. For v = 3 m/min and v = 17 m/min the maximum stress values are lower, which may indicate a reduced width of the plastically hardened zone in the area of the cutting edge.
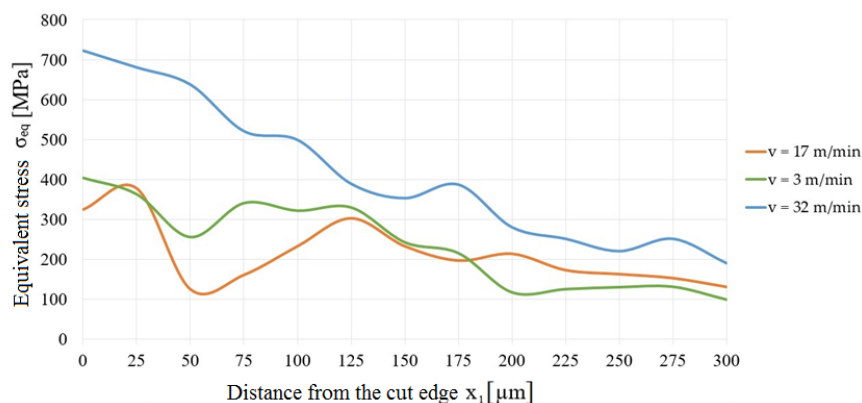
Fig. 14. Influence of cutting speed v on the value of equivalent stresses in the area of the cut edge

4.3. Burr formation

The concentration of high stresses and strains in the cutting zone may result in deformation of the cut edge in the form of burrs [42, 43]. The occurrence of burrs on the cut surface is one of the main problems in industrial lines. Parametric analyses of the process were carried out to show which of the machining parameters are crucial and have the greatest impact on burr formation.

The research results indicate that the use of clearances above hc = 0.06 mm causes a significant increase in burr height, regardless of the cutting speed (Fig. 15). This may be due to the fact that the stability of the flow and cracking process decreases, which causes a decrease in the width of the sliding fracture and an increase in the width of the separation fracture and the height of the burr. An increase in clearance above the allowable one causes excessive concentration of the bending moment in the cutting zone.

Fig. 15. Influence of cutting speed v and clearance h_c on burr height

Łukasz Bohdal, Agnieszka Kułakowska, Marcin Kułakowski
Numerical Modelling and Simulation of The Shear-Slitting Process of Electrical Steels

DOI 10.2478/ama-2024-0038

Fig. 16. Influence of cutting speed *v* and rake angle α on burr height

For clearances above h_c = 0.08 mm, the burr height is too large and can be a problem on the production line for each analysed cutting speed. The increase in the burr also contributes to the increase in the rounding and rollover of the edges. Reducing the clearance value to h_c = 0.04 mm makes it possible to increase the cutting speed even to *v* = 24 m/min and obtain an acceptable burr value. For this cutting speed value, the rake angle should be within the range α = 30°–40° (Fig. 16). If the clearance value is less than h_c = 0.04 mm, small angle values α = 5°–18° should be used. In the case of using clearance above h_c = 0.06, it is more advantageous to increase the rake angle. This reduces the bending moment in the cutting area because the contact zone of the knives with the material is smaller and the material cracks earlier.

5. CONCLUSIONS

The process of cutting soft electrical steels is complicated due to the large number of factors affecting the quality of the product. From an industrial point of view, the appropriate quality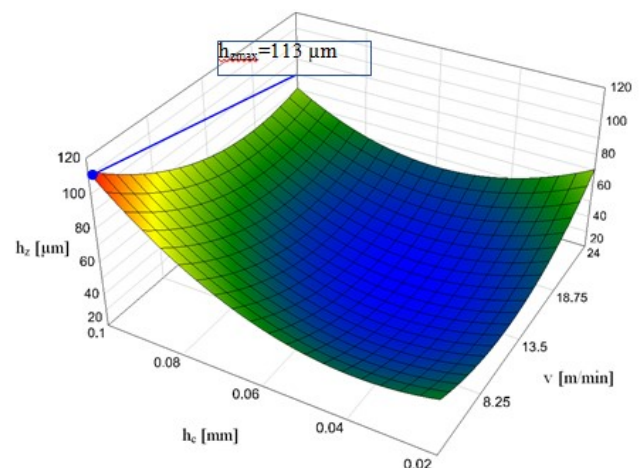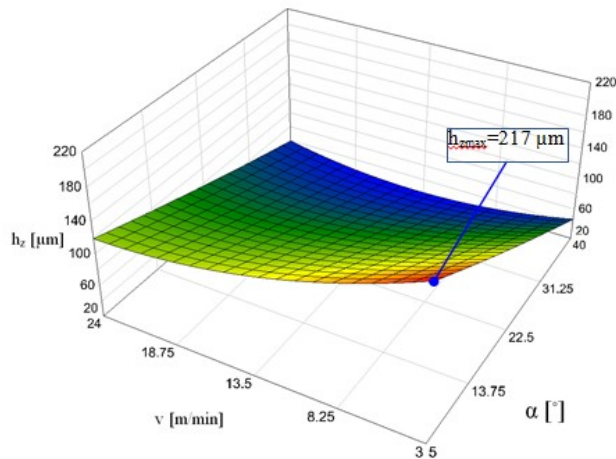 of the product can be achieved by appropriate control of the process. At the same time, it is important to ensure high process efficiency and reduce the negative impact of process conditions on tool wear and energy consumption. The specificity of electrotechnical materials and their small thickness require very precise settings of machining parameters and process stability. Due to the lack of knowledge on how to control the process, in many cases the amount of waste increases. The paper proposes an approach enabling forecasting the influence of process conditions on product quality. Numerical modelling with the use of finite element analysis was used to analyse the values of stresses, deformations and the quality of the cut edge. As a result, it was determined which conditions can ensure high quality and repeatability of products on production lines and which should be avoided. After the research, the following detailed conclusions can be drawn:

- The obtained research results indicate that there is a limit value of the cutting clearance, after which the stress concentration in the area of the cut edge and the burr increases significantly. This value is for sheet thickness *t* = 0.3 mm, h_c = 0.06 mm.
- It is unfavourable to use a cutting clearance of h_c = 0.08 mm. This causes excessive bending torque and burr formation that can damage the cut edge.
- The correct selection of the cutting clearance is particularly

important in the case of high cutting speeds, where with excessive clearance, the stability of the process decreases and the stresses cover the area away from the cut edge by up to 300 μm.
- The value of the tool rake angle should be selected depending on the cutting clearance. With clearances smaller than h_c = 0.04 mm, angle values α = 5°–18° should be used. In the case of using clearance above h_c = 0.06 mm, it is more advantageous to increase the rake angle.
- The results of simulations and experimental tests can be used for the correct selection of machining parameters depending on the adopted criteria.

REFERENCES

1. Jin SY, Pramanik A, Basak AK *et al*. Burr formation and its treatments—a review. International J of Adv Man Tech. 2020; 107: 2189–2210. https://doi.org/10.1007/s00170-020-05203-2
2. Ghadbeigi H, Al-Rubaye A, Robinson FCJ *et al*. Blanking induced damage in thin 3.2% silicon steel sheets. Prod Eng. 2020; 14: 53–64. https://doi.org/10.1007/s11740-019-00931-1
3. Arslan Y, Özdemir A. Punch structure, punch wear and cut profiles of AISI304 stainless steel sheet blanks manufactured using cryogenically treated AISI D3 tool steel punches. Int J of Adv Man Tech. 2016; 87: 587–599. https://doi.org/10.1007/s00170-016-8515-6
4. Falconnet E, Makich H, Chambert J, Monteil G, Picart P. Numerical and experimental analyses of punch wear in the blanking of copper alloy thin sheet. Wear. 2012; 296: 598-606. https://doi.org/10.1016/j.wear.2012.07.031
5. Kurosaki Y, Mogi H, Fujii H. Importance of punching and workability in non-oriented electrical steel sheets. J of Mag and Magn Mat. 2008; 320: 2474–2480. https://doi.org/10.1016/j.jmmm.2008.04.073
6. Lewis N, Anderson P, Hall J, Gao Y. Power loss models in punched non-oriented electrical steel rings. IEEE Trans on Mag. 2016; 52 (5): 1-4. https://doi.org/10.1109/TMAG.2016.2530304
7. Liu Y, Wang Ch, Han H, Shan D, Guo B. Investigation on effect of ultrasonic vibration on micro-blanking process of copper foil. Int J of Adv Man Tech. 2017; 93: 2243-2249. https://doi.org/10.1007/s00170-017-0684-4
8. Boehm L, Hartmann C, Gilch I, Stoecker A, Kawalla R, Wei X, Hirt G, Heller M, Korte-Kerzel S, Leuning N *et al*. Grain size influence on the magnetic property deterioration of blanked non-oriented electrical steels. Materials. 2021; 14: 7055. https://doi.org/10.3390/ma14227055
9. Wilczyński W. Wpływ technologii na właściwości magnetyczne rdzeni maszyn elektrycznych. IEI Warszawa 2003 (in Polish).
10. Miyagi D, Miki K, Nakano M, Takahashi N. Influence of compressive stress on magnetic properties of laminated electrical steel sheets. IEEE Trans of Mag. 2010; 46: 318-321. https://doi.org/10.1109/TMAG.2009.2033550.
11. Naumoski H, Riedmüller B, Minkow A. Herr U. Investigation of the influence of different cutting procedures on the global and local magnetic properties of non-oriented electrical steel. J of Mag and Magn Mat. 2015; 392: 126–133.https://doi.org/10.1016/j.jmmm.2015.05.031
12. Xiong X, Hu S, Hu K, Zeng S. Texture and magnetic property evolution of non-oriented Fe-Si steel due to mechanical cutting, Jof Magn and Magn Mat. 2016; 401: 982-990. https://doi.org/10.1016/j.jmmm.2015.10.023
13. Leuning N, Steentjes S, Schulte M, Bleck W, Hameyer K. Effect of elastic and plastic tensile mechanical loading on the magnetic properties of NGO electrical steel. J of Magn and Magn Mat. 2016; 417: 42-48. https://doi.org/10.1016/j.jmmm.2016.05.049
14. Wang X, Wang Z, Cui R, Li Sh. Influence of blanking process on the magnetic properties of non-oriented electrical steel lamination. J of Shan Jiao Tong Univ. 2019; 53(9): 1115-1121. https://doi.org/10.1109/TMAG.2018.2799839

15. Wang N, Golovashchenko S.F. Mechanism of fracture of aluminum blanks subjected to stretching along the sheared edge. J of Mat Proc Tech. 2016; 233: 142–160.
https://doi.org/10.1016/j.jmatprotec.2016.02.022

16. Falconnet E, Chambert J, Makich H, Monteil G, Winter S, Nestler M, Galiev E, Hartmann F, Psyk V, Kräusel V, Dix M. Adiabatic blanking: Influence of clearance, impact energy, and velocity on the blanked surface. J of Man and Mat Proc. 2021; 5: 35.

17. Molitor D.A, Kubik C, Hetfleisch R.H, Groche P. Workpiece image-based tool wear classification in blanking processes using deep convolutional neural networks. Prod Eng. 2022; 1-12.
https://doi.org/10.1007/s11740-022-01113-2

18. Mucha J, Jaworski J. The quality issue of the parts blanked from thin silicon sheets. JMEPEG. 2017; 26: 1865–1877.
https://doi.org/10.1007/s11665-017-2589-7

19. Toda H, Zaizen Y, Namikawa M, Shiga N, Oda Y, Morimoto S. Iron loss deterioration by shearing process in non-oriented electrical steel with different thicknesses and its influence on estimation of motor iron loss. IEEJ J of Ind Appl. 2014; 3 (1): 55-61.
https://doi.org/10.1541/ieejjia.3.55

20. Omura T, Zaizen Y, Fukumura M, Senda K, Toda H. Effect of hardness and thickness of nonoriented electrical steel sheets on iron loss deterioration by shearing process. IEEE Trans on Magn. 2015; 51 (11). https://doi.org/10.1109/TMAG.2015.2443176

21. Schoppa A, Schneider J, Roth J.O. Influence of the cutting process on the magnetic properties of non-oriented electrical steels. J of Magn and Magn Mat. 2000; 215-216: 100-102.
https://doi.org/10.1016/S0304-8853(00)00077-9

22. Rygal R, Moses A. J, Derebasi N, Schneider J, Schoppa A. Influence of cutting stress on magnetic field and flux density distribution in non-oriented electrical steels. J of Magn and Mag Mat. 2000; 215–216: 687–689. https://doi.org/10.1016/S0304-8853(00)00259-6

23. Subramonian S, Altan T, Campbell C, Ciocirlan B. Determination of forces in high speed blanking using FEM and experiments. J of Mat Proc Tech. 2013; 213: 2184-2190.
https://doi.org/10.1016/j.jmatprotec.2013.06.014

24. Wang Z, Li S, Cui R, Wang X, Wang B. Influence of grain size and blanking clearance on magnetic properties deterioration of non-oriented electrical steel. IEEE Trans on Magn. 2018; 54 (5): 1–7.
https://doi.org/10.1109/TMAG.2018.2799839

25. Winter K, Liao Z, Ramanathan R, Axinte D, Vakil G, Gerada C. How non-conventional machining affects the surface integrity and magnetic properties of non-oriented electrical steel. Mat and Des. 210. 2021.
https://doi.org/10.1016/j.matdes.2021.110051

26. Smudde CM, D'Elia CR, San Marchi CW, Hill MR, Gibeling JC. Effects of residual stress on orientation dependent fatigue crack growth rates in additively manufactured stainless steel. Int J of Fat. 2023; 169: 107489. https://doi.org/10.1016/j.ijfatigue.2022.107489

27. Khatri N, Barkachary BM, Muneeswaran B, Al-Sayegh R, Luo X, Goel S. Surface defects incorporated diamond machining of silicon. Int J of Extr Man. 2020; 2(4): 045102. https://doi.org/10.1088/2631-7990/abab4a

28. Zhao Y, Wang S, Yu W, Long P, Zhang J, Tian W, Gao F, Jin Z, Zheng H, Wang C et al. Simulation and Experimental Study of Laser Processing NdFeB Microarray Structure. Micromachines 2023; 14: 808. https://doi.org/10.3390/mi14040808

29. Leuning N, Jaeger N, Schauerte M, Stöcker B, Kawalla A et al. Material design for low loss non-oriented electrical steel for energy efficient drives. Materials 2021; 14: 6588.
https://doi.org/10.3390/ma14216588

30. Molitor DA, Kubik C, Hetfleisch RH, Groche P. Workpiece image-based tool wear classification in blanking processes using deep convolutional neural networks. Prod Eng. 2022; 1-12.
https://doi.org/10.1007/s11740-022-01113-2

31. Kamarul Adnan AA, Azinee SN, Norsilawati N, Izzul KAM. Analysis of the influence of the blanking clearance size to the burr development on the sheet of mild steel, brass and aluminium in blanking process. J of Ach in Mat and ManEng 2022;111(1):26-32.
https://doi.org/10.5604/01.3001.0015.9093.

32. Dzidowski ES. Mechanizm pękania poślizgowego w aspekcie dekohezji sterowanej metali. Wydawnictwo Politechniki Wrocławskiej. Wrocław 1990 (in Polish).

33. Gutknecht F, Steinbach F, Hammer T, Clausmeyer T, Volk W, Tekkaya AE. Analysis of shear cutting dual phase steel by application of an advanced damage model, 21st European Conference on Fracture ECF21. 20-24 June 201. Catania Italy. Procedia Structural Integrity. 2016; 2:1700-1707.
https://doi.org/10.1016/j.prostr.2016.06.215

34. Kułakowski M. Badania wpływu parametrów i warunków procesu cięcia mechanicznego na lokalne zmiany właściwości laserowanych blach elektrotechnicznych. Rozprawa doktorska. Politechnika Koszalińska. Koszalin 2023 (in Polish).

35. Kukielka L, Kulakowska A, Patyk R. Numerical modeling and simulation of the movable contact tool-worpiece and application in technological processes. J of Syst. Cyb and Inf. 2010; 8(3): 36-41.

36. Kukielka L. Nonlinear modeling for elasto/visco – plastic contact problem in technological processes, International Scientific IFNA – ANS Journal, Problems of non – linear Analysis in Engineering Systems 2004;2:39-53.

37. Kałduński P, Kukiełka L. The numerical analysis of the influence of the blankholder force and the friction coefficient on the value of the drawing force. PAMM 2007; 7 (1): 4010045-4010046.
https://doi.org/10.1002/pamm.200701059

38. Kałduński P, Kukiełka L. The sensitivity analysis of the drawpiece response on the finite element shape parameter. PAMM. 2008; 8 (1): 10725-10726. https://doi.org/10.1002/pamm.200810725

39. Johnson GR, Cook WH. Fracture characteristics of three metals subjected to various strains, strain rates, temperatures and pressures. Eng Frac Mech. 1985; 21 (1): 31-48.
https://doi.org/10.1016/0013-7944(85)90052-9

40. Rickhey F, Hong S. Stress triaxiality in anisotropic metal sheets—definition and experimental acquisition for numerical damage prediction. Materials. 2022; 15(11):3738.
https://doi.org/10.3390/ma15113738

41. Bao Y, Wierzbicki T. On fracture locus in the equivalent strain and stress triaxiality space. Int J of Mech Sci. 2004; 46: 81-98.
https://doi.org/10.1016/j.ijmecsci.2004.02.006

42. Kuo SK, Lee WC, Lin SY, Lu CY. The influence of cutting edge deformations on magnetic performance degradation of electrical steel. 2014 17th International Conference on Electrical Machines and Systems (ICEMS) 2014; 3041-3046.
https://doi.org/10.1109/ICEMS.2014.7014017

43. Cao H, Hao L, Yi J, Zhang X, Luo Z, Chen Sh et al. The influence of punching process on residual stress and magnetic domain structure of non-oriented silicon steel. J of Mag and Magnetic Materials. 2016; 406: 42–47. https://doi.org/10.1016/j.jmmm.2015.12.098

Łukasz Bohdal: https://orcid.org/0000-0002-8085-9530

Agnieszka Kułakowska: https://orcid.org/0000-0001-5506-5440

Sankar E, Duraivelu K
Evaluation of some Thermophysical Properties of SN500 Lubrication Oil Blended with SiO2, Al2O3 And TiO2 Nano-Additives, using Fuzzy Logic

DOI 10.2478/ama-2024-0039

EVALUATION OF SOME THERMOPHYSICAL PROPERTIES
OF SN500 LUBRICATION OIL BLENDED
WITH SiO2, Al2O3 AND TiO2 NANO-ADDITIVES, USING FUZZY LOGIC

Sankar E *, Duraivelu K *

*Department of Mechanical Engineering, SRM Institute of Science and Technology, Kattankulathur, Tamilnadu 603 203, India

sankare1@srmist.edu.in, duraivek1@srmist.edu.in

Abstract: Nano-additives are generally blended with the base lubricant oil, to enhance the lubricant characteristics such as wear, coefficient of friction (CoF), thermal conductivity, density, and flash and fire points of the lubricant. In this research, nano-additives of SiO2, Al2O3 and TiO2 are blended with the base SN500 oil with different proportions of mixture. When these three nanoparticles are used together in base oil, they enhance most of the desirable properties of a lubricant; 27 samples with three different levels of a mixture of nano-additives are identified using factorial design of experiments. The experimental outcomes for the selected three characteristics of interest of density, flash point and fire point are determined. Conducting experiments for 'n' number of samples with different proportions of mixture of nano-additives is a cumbersome, expensive and time-consuming process, in order to determine the optimum mix of nano-additives for the desirable level of characteristics of interest. In this research, attempt has been made to apply fuzzy logic to simulate a greater number of samples with different proportions of a mixture of three nano-additives with the respective outcomes of characteristics of three thermophysical properties. Out of the numerous samples simulated using fuzzy logic, the sample with the optimum mix of three nano-additives of SiO2, Al2O3 and TiO2 blended with the base oil is identified for the desirable level of characteristics of interest of density, flash point and fire point. The values of the identified sample are found to be at the desirable level of 0.9008 gm/ml, 231°C and 252°C, respectively.

Key words: nano-additives, density, flash and fire points, fuzzy logic.

1. INTRODUCTION

Nano-additives have captured the attention of researchers as a newly emerged and evolved technology for use due to their special thermophysical characteristics, in lubrication and heat transfer systems. Classified as a new category of fluids, the stability of nano-additives and their performance in various scenarios, including extreme temperatures, are vital focal points in expanding our knowledge of lubrication and heating systems and creating a useful nano lubricant [1-2]. Recent literature recommends using base oil blended with nano-additives for enhancing lubricating properties. Studies have examined the impact of SiO2, Al2O3 and TiO2 nano-additives on the wear rate and coefficient of friction (CoF). The best combination of SiO2, Al2O3 and TiO2 nano-additives in SN500 base oil was examined by Sankar et al [3]. When polyolester oil is combined with SiO2 nano-additive by up to 0.15%, this leads to improved rheological characteristics. The maximum increase in flash point and fire point is observed at 7% and 5.9%, respectively, for the 0.2% SiO2/POE nanolubricant [4]. Flash and fire points are found to be increasing due to the addition of SiO2 nanoparticles in the base oil [5]. By adding SiO2 nano-additives, in a step by step manner at 0.3 wt.% in SAE20W40 engine oil, the flash and fire points become minimum at 0.6 wt.%, and by increasing further from 0.6 wt.% to 1.5 wt.%, the flash and fire points increase [6]. Flashpoint enhancement percentages of 5.042%, 6.612%, 8.502% and

10.67% are achieved for SiO2 nano-additive concentrations of 0.25%, 0.5%, 0.75% and 1 wt.%, respectively. Similarly, Al2O3 nano-additives result in enhancement of 4.237%, 5.04%, 7% and 9.63% for the respective concentrations [7]. In concentrations of 0.2% and 1%, SiO2 has a higher flash and fire point than Al2O3. So it is recommended to add SiO2 in a higher proportion than Al2O3, since it notably increases the operating temperatures [8]. In the case of Al2O3 nanoparticle, which was introduced into two base lubricants, Marula oil and Mineral oil, within the range of 0–2 wt.%, the trend is consistent in both lubricants, where the flash and fire points increase with the addition of Al2O3 nanoparticles, peaking at 0.75 wt.%. Beyond this concentration, these points gradually decrease. Consequently, the optimal Al2O3 amount exhibits an increase in both flash and fire points [9]. The addition of 100 ppm of Al2O3 to diesel significantly raises the flash point from 66°C to 69°C. Even slight increments in the nano-additives content contribute to this enhancement [10]. The addition of Al2O3 nanoparticles in N10, P20 and T30 has shown an increase in their respective flash points than pure base oils [11]. Adding Al2O3 nanoparticles in Servo SAE 20W-40 flash point increases slightly till the value of 0.02% concentration and then decreases with respect to further increase in nanoparticles [12]. The addition of Al2O3 nano-additive at 0.25 wt.%, 0.65 wt.%, 1.05 wt.%, 1.45 wt.% and 1.85 wt.% drastically increased the flash point by 1.33%, 3.54%, 5.75%, 7.52% and 9.73% respectively, which increased the flashpoint from 228°C to 249°C in the lube oil stock-60 [13]. Addition of Al2O3 nano-additive shows

an increase in flash and fire points with the base local Iraqi lubricant oil of 20W-50 [14]. Conversely, the flash point decreases with inclusion of TiO2 nanoparticles, with no further variation observed beyond a concentration of 0.6% [15]. The flashpoint rate increases by adding TiO2 nano-additives at different concentrations: 0.1 wt.%, 0.2 wt.%, 0.5 wt.% and 1 wt.%, resulting in flash point increases of 4.54%, 9.45%, 11.81% and 13.63%, respectively, relative to the base fluid. Notably, changes in higher concentrations are less pronounced compared with those in lower concentrations [16]. By the addition of TiO2 nano-additive, there is an enhancement of flash and fire points of castor oil [17]. Kumar [15] investigated the physicochemical and tribological properties of TiO2 nano lubricant oil at different concentrations; 0.2% of TiO2 in SAE 20 W40 exhibits the higher value of flash and fire points while compared with base oil SAE 20 W40. Both flash and fire points are directly proportional to the size of the nanoparticle and the base engine oils the surface modifying behaviour [18]. In the case of nano-lubricating oil made of TiO2 nanoparticles, the flashpoint increased by 9.3% [19].

It has been found that titanium oxide and aluminium oxide nanoparticles are the most effective thermal enhancers [20]. Based on the statistical performance indicators acquired, designing the model and estimate using the ANFIS technique can be done with a high degree of dependability [21]. The accuracy of prediction is determined by calculating statistical data from the values of experimental and predicted models [22]. The model's performance in the experiment is assessed using R2 and RMSE values [23]. These observations suggest that the ANFIS model demonstrates greater resilience in predicting values when compared with the RSM model [24]. Based on the statistical performance indicators acquired, designing the model and estimate using the ANFIS technique can be done with a high degree of dependability [25].

John Shelton et al. [26] recently examined the rheological properties of Al2O3-TiO2/MO hybrid nanofluids, focusing on temperature, particle concentration, ratio and composition. The results show more Newtonian flow behaviour compared with conventional nanofluids, with higher TiO2 ratios affecting the properties. Kia et al. [27] also examined the heat transfer and pressure drop characteristics of Al2O3 and SiO2/base oil nanofluid flow in a helical tube, revealing that nanofluid enhances heat transfer factor and pressure drop, with the highest rate at 0.5% mass concentrations.

Every nanoparticle blending with the base oil enhances the property of a lubricant in a distinct manner [28]. From the literature, it is found that mixing of SiO2 with base oil induces the ball bearing effect and hence reduces the friction between rubbing surfaces. Similarly, Al2O3 improves the thermal conductivity of a lubricant and hence disseminates the heat considerably away from the rubbing surfaces and thus improves the lubricant action. TiO2 reduces the wear rate considerably. In this research, attempt has been made to blend optimally all these three nanoparticles together with the base oil SN500, in order to enhance the selected properties of the lubricant to its respective desirable level.

2. METHODOLOGY

The chosen three additives, SiO2, Al2O3 and TiO2, are blended with the SN500 base oil in three distinct ratios of 0.05%, 0.5% and 1% during the nanofluid preparation process. The three nano-additives of SiO2, Al2O3 and TiO2 are chosen with particle size of 35.9 nm, 32.9 nm and 50.56 nm respectively. The specifications of the nanoparticles used in this research are given in Tab. 1.

Tab. 1. Specifications of nanoparticles used

Molecular formula	TiO$_2$	SiO$_2$	Al$_2$O$_3$
Purity (%)	99	99	99
Average particle size (nm)	<100	<100	<100
Molecular weight (g/mol)	79.8658	231.533	101.96
Colour	White	White	White
Surface area (m^2/g)	150	220	110
Bulk density (g/cm^3)	0.9	0.3	0.6

Courtesy: Ad Nano Technologies, India.

Recycled base oil SN500-distilled is suitable for use in high-temperature applications due to its low volatility, or its inability to evaporate quickly. This product is less likely to ignite or catch fire because of its high flash point. Tab. 2 describes the properties of the base lubricant oil SN500 used in the experimental work.

Tab. 2. Specifications of SN500 base oil

Property	Test method	Typical result of SN500 base oil
Density @15°C, kg/m^3	ASTM D 1298	880
Viscosity @100˚C,cSt	ASTM D 445	9.4
Viscosity index	ASTM D 2270	92
Flash point °C	ASTM D 92	225
Pour point °C	ASTM D 97	−3
Colour	ASTM D 150	2

https://tnzoil.com/wp-content/uploads/2020/11/Base-Oil-SN500

The optimal settings for the independent variables may be estimated using a full factorial design of experiments which also determines the main effects and the effects of interactions on the response variable. A three-level factorial design is used in this research. This means that k factors are considered, each at three levels which are also referred to as low, intermediate and high levels. In this research, 27 samples (treatments) are created for the complete factorial design of experiments with three different additives selected at three distinct levels. The experimental values of density, flash and fire points are determined for all the selected 27 samples. Using a proper weight proportion of three nano-additives along with Span 80 surfactant are blended with the SN500 base oil. Using the magnetic capsule, the mixture is stirred for 30 min at 300 RPM at 100°C using a hot plate magnetic stirrer. In order to ensure that the nanoparticles settle uniformly in the oil, the mixture is further treated in an ultrasonic cleaner for 30 min at 60°C.

Cleveland open cup tester is used to measure the flash and fire points in accordance with ASTM D92 standards. The experimental values are obtained for the 27 samples which are used as inputs in the fuzzy logic program later to determine the optimum mix of three nano-additives for all the three characteristics of interest of density, flash and fire points of lubricant at their desirable levels.

sciendo

Sankar E, Duraivelu K

Evaluation of some Thermophysical Properties of SN500 Lubrication Oil Blended with SiO2, Al2O3 And TiO2 Nano-Additives, using Fuzzy Logic

DOI 10.2478/ama-2024-0039

Tab. 3. Density (gm/ml), Flash point and Fire point (°C)

Sample number	Nano-additives concentration (wt.%)			Density (gm/ml)	Flash point (°C)	Fire point (°C)
	SiO$_2$	TiO$_2$	Al$_2$O$_3$			
1	0.05	0.05	0.05	0.88	230	261
2	0.5	0.5	0.5	0.8906	220	226
3	1	1	1	0.9008	231	252
4	0.05	0.05	0.5	0.8929	224	240
5	0.05	0.05	1	0.8927	228	242
6	0.5	0.05	0.05	0.8904	215	232
7	0.5	0.05	0.5	0.8916	224	251
8	0.5	0.05	1	0.8911	220	250
9	1	0.05	0.05	0.8909	232	252
10	1	0.05	0.5	0.8911	230	260
11	1	0.05	1	0.8934	210	241
12	0.05	0.5	0.05	0.8884	192	218
13	0.05	0.5	0.5	0.8905	183	221
14	0.05	0.5	1	0.8924	197	225
15	0.5	0.5	0.05	0.8944	180	206
16	0.5	0.5	1	0.8913	189	223
17	1	0.5	0.05	0.8928	141	162
18	1	0.5	0.5	0.8886	194	228
19	1	0.5	1	0.8924	212	236
20	0.05	1	0.05	0.8872	185	215
21	0.05	1	0.5	0.8933	190	210
22	0.05	1	1	0.8968	196	227
23	0.5	1	0.05	0.8913	180	210
24	0.5	1	0.5	0.894	191	229
25	0.5	1	1	0.8905	195	220
26	1	1	0.05	0.8924	205	235
27	1	1	0.5	0.891	210	240

From Tab. 3, it is observed that the three different samples of 1, 3 and 9 possess the desirable high values of density, flash and fire points, respectively. However, it is required to determine a single sample that possesses the closely desirable level of characteristics of density, flash and fire points. In this study, attempt has been made to apply fuzzy logic to find a sample with an optimum mix of three nano-additives of SiO2, Al2O3 and TiO2, which possess the desirable characteristics of density, flash and fire points.

3. FUZZY LOGIC APPROACH

A fuzzy system describes the inputs and outputs using fuzzy sets and membership functions. The surface response graph is a three-dimensional graph that visually represents the output varying with changes in input variables. It is determined by the fuzzy rules and inference mechanisms used. Higher regions indicate stronger output responses, while lower regions indicate weaker responses. The surface response graph can help optimise the system by identifying suboptimal output regions and adjusting fuzzy rules or membership functions accordingly. It can also be used for system validation by comparing the predicted output with the actual responses and refining and validating the model. The surface response graph's shape indicates how the fuzzy system responds to different input values. The rules are developed using the relationships between the measured parameters of density, flash point and fire point, with different nano lubrication concentration of SiO2, TiO2 and Al2O3 nano-additives. Three membership functions are employed for the input (nano lubrication concentration of SiO2, TiO2 and Al2O3 nanoparticles) and output variables (density, flash point and fire point) to categorise them in different response levels as Low, Medium and High, used for the input variables to categorise them in different set-up levels, as shown in Tab. 4.

Tab. 4. Fuzzy linguistic variables used for each parameter

Input parameter	Linguistic variables	Range of parameter
SiO$_2$	L, M, H	0.05 wt.%, 0.5 wt.% and 1 wt.%
TiO$_2$	L, M, H	0.05 wt.%, 0.5 wt.% and 1 wt.%
Al$_2$O$_3$	L, M, H	0.05 wt.%, 0.5 wt.% and 1 wt.%
Output parameter	Linguistic variables	Range of parameters
Density (gm/ml)	L, M, H	0.88–0.8909, 0.891–0.8924 and 0.8927–0.9008
Flash point °C	L, M, H	141–192°C, 194–215°C and 220–232°C
Fire point °C	L, M, H	162–223°C, 225–240°C and 241–261°C

where L = Low, M = Medium, H = High.

Tab. 3 is rewritten with the above linguistic variables, as shown in Tab.5.

The fuzzy linguistic variables are high for density, flash point and fire point in Samples 3 and 5. High-density lubricants typically have higher viscosity and better load-carrying capacity. They can provide better film strength and protection against surface wear and contact fatigue in high-load applications. So, it leads to better thermal stability, which means they can withstand higher operating temperatures without breaking down. High-density lubricants are generally more resistant to oxidation, preventing the formation of harmful deposits and sludge. However, in order to get an optimum mix of the three nano-additives even with concentrations other than 0.05 wt.%, 0.5 wt.% and 1 wt.%, a fuzzy logic approach is used in this study.

Tab. 5. Fuzzy linguistic variables used for experimental values

S. No.	SiO$_2$	TiO$_2$	Al$_2$O$_3$	Density (gm/ml)	Flash point (°C)	FIRE point (°C)
1	L	L	L	L	H	H
2	M	M	M	L	H	M
3	H	H	H	H	H	H
4	L	L	M	H	H	M
-	-	-	-	-	-	-
-	-	-	-	-	-	-
26	H	H	L	M	M	M
27	H	H	M	M	M	M

The proposed model demonstrates that the type of membership function utilised during fuzzification relies on the relevant event. Fig. 1 illustrates the properties of the FIS. In this specific scenario, the input variables are partitioned based on the range of experimental parameters.
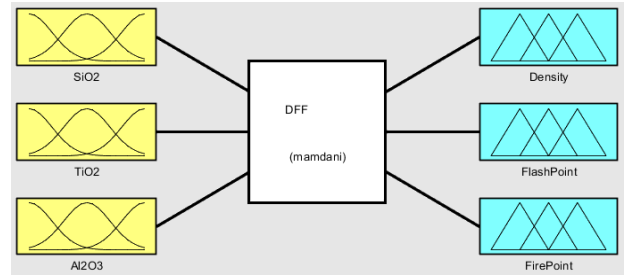
Fig. 1. FIS properties
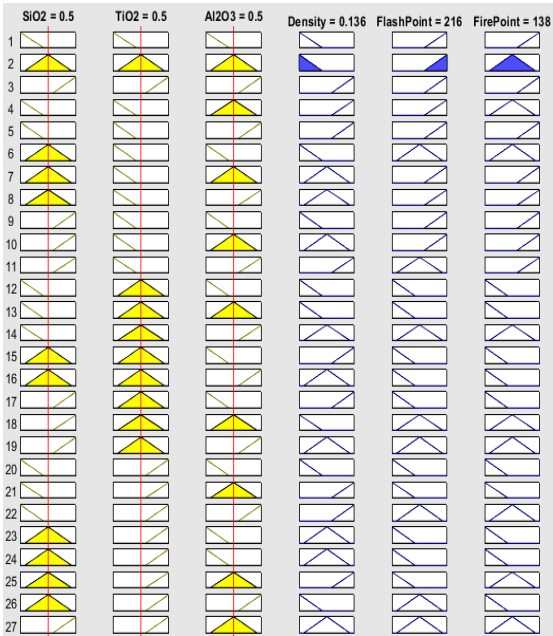
Fig. 2. Rules used in fuzzy logic approach

The surface response is determined by system-defined fuzzy rules and an inference mechanism, with each point on the surface associated with input values and output values determined by fuzzy inference.

Using SiO2, TiO2 and Al2O3 nanosuspension lubricant, a total of 27 rules for density, flash point and fire point are developed using the experimental data, as shown in Fig. 2. The experiment's findings are then examined utilising Mamdani Fuzzy Logic through the MATLAB software.

A fuzzy system describes the inputs and outputs using fuzzy sets and membership functions, which represent the degree to which a particular input or output belongs to a fuzzy set.

(a) Input variable "SiO$_2$"

(b) Input variable "TiO$_2$"

(c) Input variable "Al$_2$O$_3$"
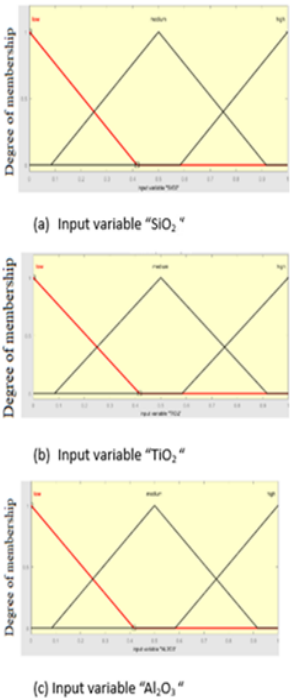
Fig. 3. Input variables in the membership function (a) SiO2 (b) TiO2 (c) Al2O3

(a) Output variable "Density (gm/ml)"

(b) Output variable "Flash Point(°C)"

(c) Output variable "Fire Point (°C)"
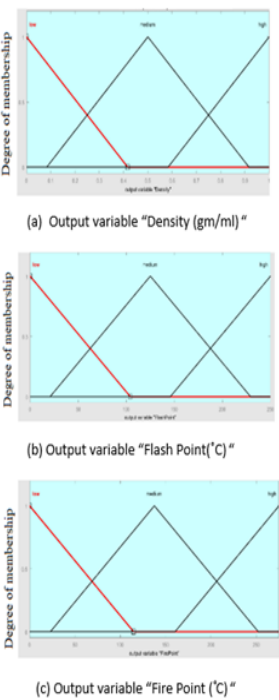
Fig. 4. Output variables in the membership function (a) density (b) flash point (c) fire point

Sankar E, Duraivelu K

Evaluation of some Thermophysical Properties of SN500 Lubrication Oil Blended with SiO2, Al2O3 And TiO2 Nano-Additives, using Fuzzy Logic

DOI 10.2478/ama-2024-0039

4. RESULTS AND DISCUSSION

The surface response graph is a three-dimensional visualisation that shows how the output of a fuzzy system changes with changes in multiple input variables, illustrating the smooth variation of the output as input variables change. The relationship between the amount of nanoparticles added and the changes in the properties are represented here using the surface graphs. In the surface graph, with increase in the altitude of the surface and property of the nano-additives combination, the colour of the surface changes from blue to yellow, where the blue represents lower values and yellow represents the higher values. Also, in between the blue and yellow there is a transition of middle values represented from conversion of blue into yellow colour.
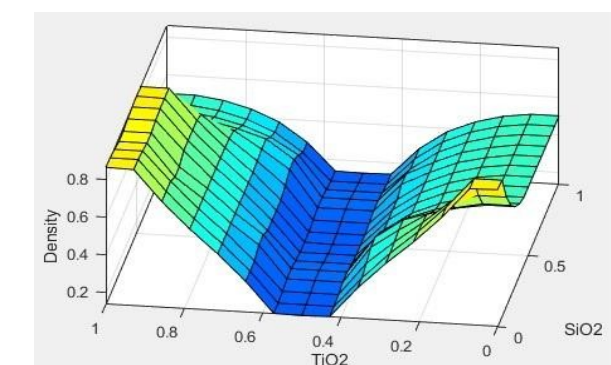
a.
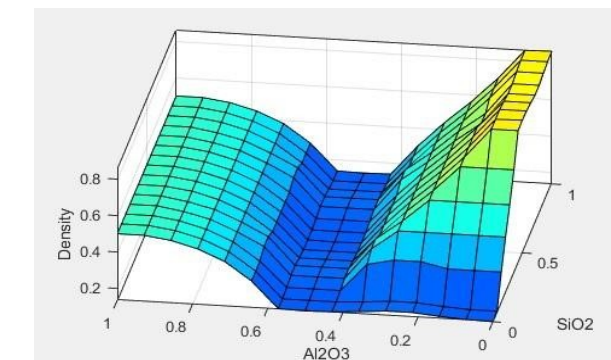
b.
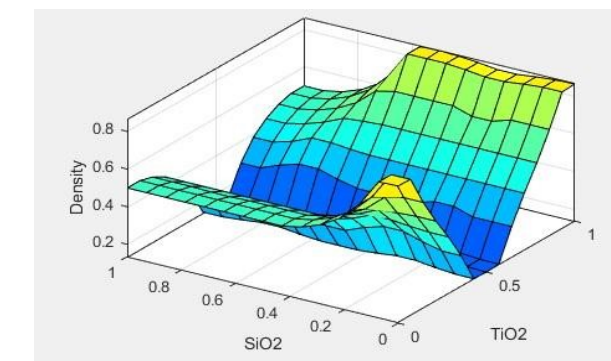
c.

d.

e.

f.

**Fig. 5.** Predicted density by fuzzy logic in relation to SiO2, TiO2 and Al2O3. (a) Density in relation to concentration of SiO2 and TiO2. (b) Density in relation to concentration of SiO2 and Al2O3. (c) Density in relation to concentration of SiO2 and TiO2. (d) Density in relation to concentration of TiO2 and Al2O3.(e) Density in relation to concentration of Al2O3 and SiO2. (f) Density in relation to concentration of Al2O3 and TiO2.

Fig. 5 shows the predicted density using the fuzzy logic for the SiO2, Al2O3 and TiO2 nano-additives as pairs of two nano-additives, in six possible combinations. It is represented as the surface graph where the relation between the nano-additives concentration and density can be clearly observed.

Fig. 5 shows the relationship between three input parameters, that is, 0 wt.% to 1 wt.% of SiO2, TiO2 and Al2O3 nanoparticles and their density as the output parameter in a 3-D input–output space. Fig. 5a, c, d and f, shows an increase in the level of wt.% of TiO2 to obtain maximum density, and Fig. 5b and

e, shows an increase in the level of wt.% of SiO2 to obtain the maximum density. The influence of the Al2O3 nanoparticle is less than that of the other two nanoparticles.

Fig. 6 shows the predicted flash point (°C) the fuzzy logic for the SiO2, Al2O3 and TiO2 nano-additives as pairs of two nano-additives, in six possible combinations. It is represented as the surface graph where the relation between the nano-additives concentration and flash point (°C) can be clearly observed.

Fig. 6 shows the relationship between three input parameters, that is, 0 wt.% to 1 wt.% of SiO2, TiO2 and Al2O3 and their flash point temperature in °C as the output parameter in a 3-D input–output space. Fig. 6a, c, d and f, shows minimum levels of the wt.% of TiO2 to obtain maximum flash point temperature, and Fig. 5b and e shows an increase in the level of 0.4 wt.% to 0.6 wt.% of SiO2 and Al2O3 to obtain the maximum flash point temperature. The influence of the TiO2 nanoparticle is less than that of the other two nanoparticles.
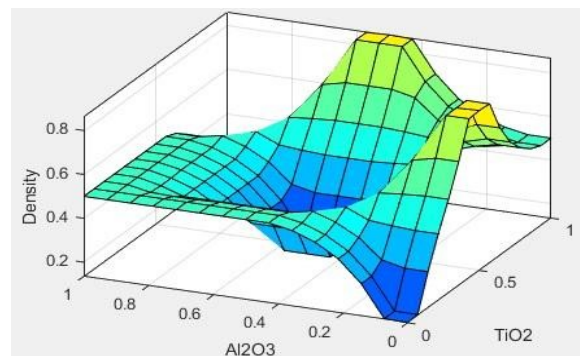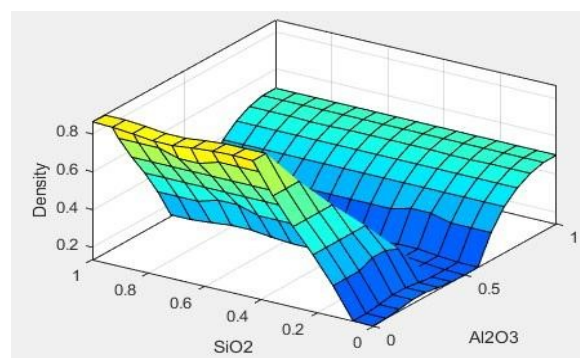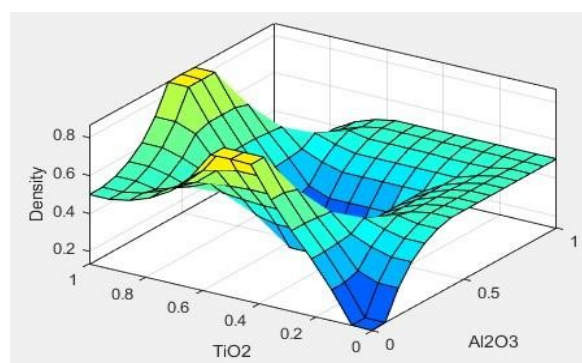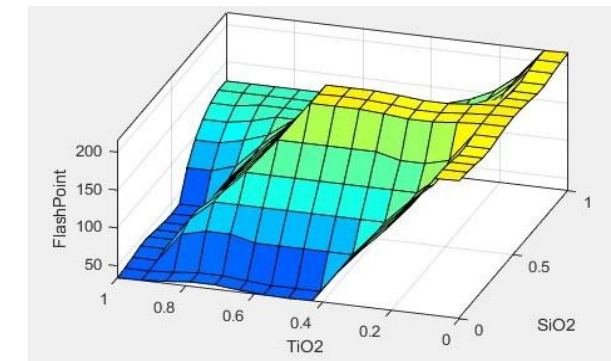

a.
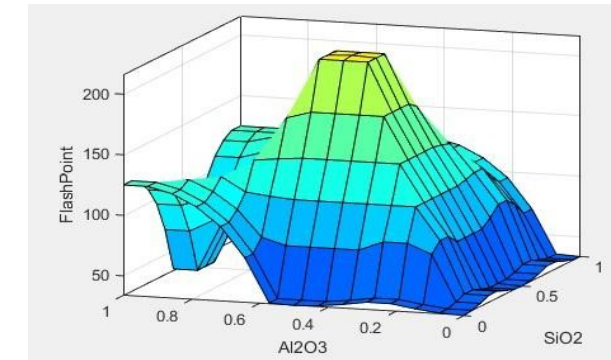
b.
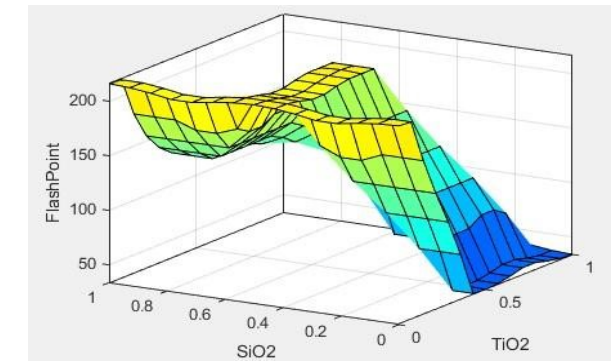
c.
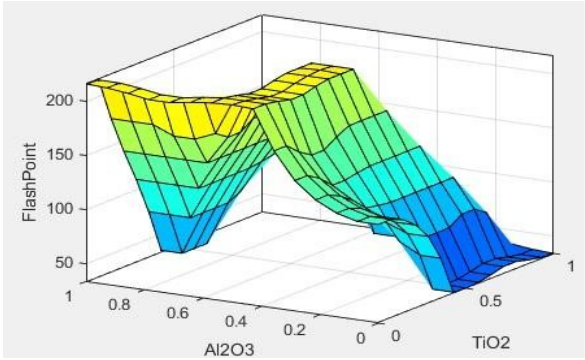
d.
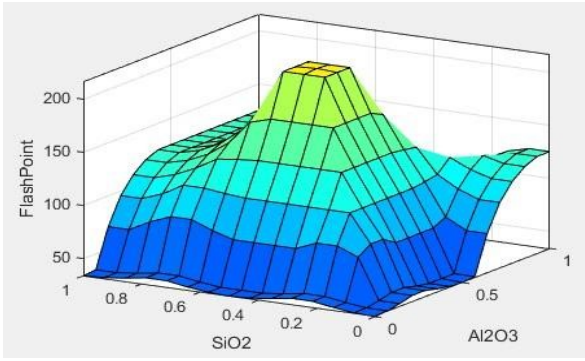
e.
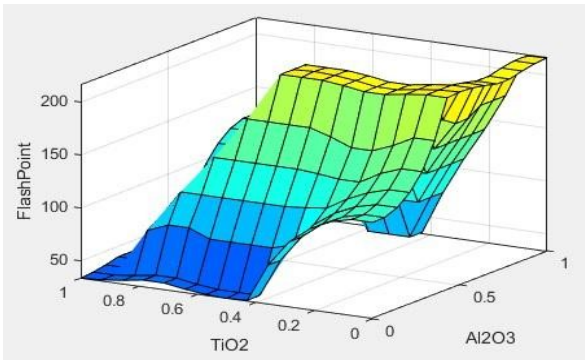
f.

Fig. 6. Predicted flash point by fuzzy logic in relation to SiO2, TiO2 and Al2O3. (a) Flash point (°C) in relation to concentration of SiO2 and TiO2. (b) Flash point (°C) in relation to concentration of SiO2 and Al2O3. (c) Flash point (°C) in relation to concentration of TiO2 and SiO2. (d) Flash point (°C) in relation to concentration of TiO2 and Al2O3. (e) Flash point (°C) in relation to concentration of Al2O3 and SiO2. (f) Flash point (°C) in relation to concentration of Al2O3 and TiO2.

Fig. 7 shows the predicted fire point (°C) using the fuzzy logic for the SiO2, Al2O3 and TiO2 nano-additives as pairs of two nano-additives, in six possible combinations. It is represented as the surface graph where the relation between the nano-additives concentration and fire point (°C) can be clearly observed.

Fig. 7 shows the relationship between three input parameters, that is, 0 wt.% to 1 wt.% of SiO2, TiO2 and Al2O3 and their fire point temperature in °C as the output parameter in a 3-D input–output space. Fig. 6a, c, d and f, shows the minimum level of the wt.% of TiO2 to obtain the maximum fire point temperature, and Fig. 5b and e, shows an increase in the level of

Sankar E, Duraivelu K
Evaluation of some Thermophysical Properties of SN500 Lubrication Oil Blended with SiO2, Al2O3 And TiO2 Nano-Additives, using Fuzzy Logic

DOI 10.2478/ama-2024-0039

0.4 wt.% to 0.6 wt.% of Al2O3, and 0.6 wt.% to 1 wt.% of SiO2 to obtain the maximum fire point temperature. The influence of the TiO2 nanoparticle is less than that of the other two nanoparticles.
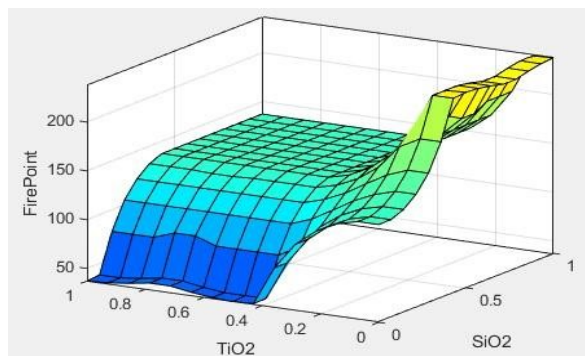
a.
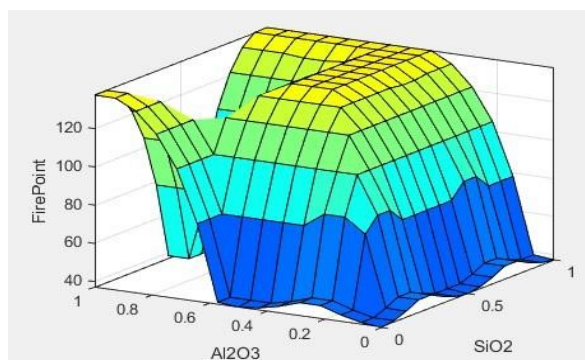
b.
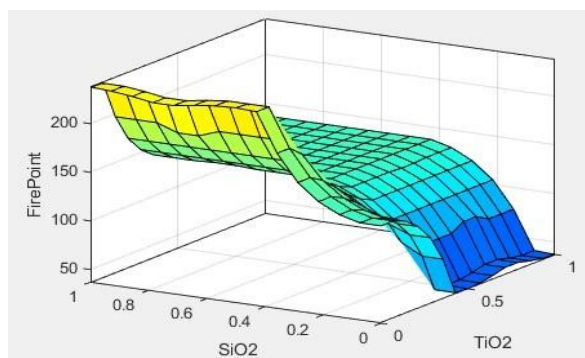
c.
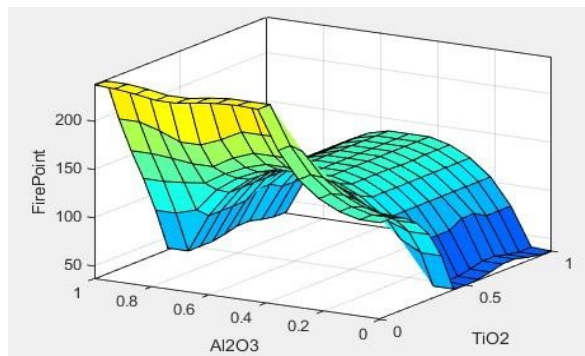
d.
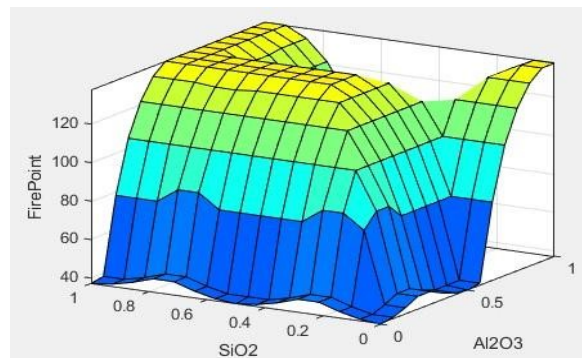
e.

f.

Fig. 7. Predicted fire point by fuzzy logic in relation to SiO2, TiO2 and Al2O3. (a) Fire point (°C) in relation to concentration of SiO2 and TiO2. (b) Fire point (°C) in relation to concentration of SiO2 and Al2O3. (c) Fire point (°C) in relation to concentration of TiO2 and SiO2. (d) Fire point (°C) in relation to concentration TiO2 and Al2O3. (e) Fire point (°C) in relation to concentration of Al2O3 and SiO2. (f) Fire point (°C) in relation to concentration of Al2O3 and TiO2.

Fig. 7 shows the relationship between three input parameters, that is, 0 wt.% to 1 wt.% of SiO2, TiO2 and Al2O3 and their fire point temperature in °C as the output parameter in a 3-D input–output space. Fig. 6a, c, d and f, shows the minimum level of the wt.% of TiO2 to obtain the maximum fire point temperature, and Fig. 5b and e, shows an increase in the level of 0.4 wt.% to 0.6 wt.% of Al2O3, and 0.6 wt.% to 1 wt.% of SiO2 to obtain the maximum fire point temperature. The influence of the TiO2 nanoparticle is less than that of the other two nanoparticles.

In this study, the desired values for fuzzy logic are assumed to be HIGH for the selected applications for all the outputs. Using fuzzy logic 8,000 samples are generated taking 27 input samples. Of these 8,000 samples, the maximum flash point from fuzzy logic is found to be 232°C when the lubricant contains 1% of SiO2, 0.05% of TiO2 and 0.05% Al2O3. Similarly, the maximum fire point obtained in fuzzy logic is found to be 261°C when the lubricant contains 0.05% of SiO2, 0.05% of TiO2 and 0.05% Al2O3. The sample containing 0.95% of SiO2, 0.05% of TiO2 and 0.5% Al2O3 shows the best optimum values of both flash and fire points of 229.39°C and 259.16°C, respectively.

Although the unique sample identified from the 8,000 samples simulated using fuzzy logic, exhibits the optimum values for both flash and fire points, it is observed that they are not the best desirable values compared with the other researches carried out with one of any three nano-additives of Al2O3, TiO2

and SiO2 blended with other base oils as indicated in Tab. 6. However, the mix of these three nano-additives is observed to be enhancing the other tribological properties of wear rate, CoF and shear rate of the base oil SN 500 compared with the other researches carried out in this domain. Hence, the research carried out for enhancing most of the tribological properties of a lubricant oil using the mix of these three nano-additives is found to be more promising and adding useful knowledge to this domain [29].

Tab. 6. Comparison of various research findings on enhancing flash point of a lubricant

Researcher	Base oil investigated	Nanoparticle blended	Attained flash point °C	% increase / decrease
Awad et al.	Stock-60	1.85 wt.% of Al_2O_3	248	+9.373
Deepak et al.	SAE20W40	0.2 wt.% of TiO_2	246.2	+12.73
Desai et al.	SAE20W40	0.6% of mass fraction of SiO_2	200	−9.7%
Gumus et al.	Nano diesel-2	50 ppm of Al_2O_3	68	+13.33%
Koppula et al.	SAE 0W20	1.2 wt.% of Al_2O_3	243	+21.5%
Sajith et al.	SAE20W40	0.02 % volume fraction of Al_2O_3	228	+2.2%
Authors of this manuscript	SN500	1 wt.% of each SiO_2, TiO_2 and Al_2O_3	232	+2.66%

5. CONCLUSION

An attempt has been made in this research to determine the optimum mix of three nano-additives of SiO2, Al2O3 and TiO2 blended with the base SN500 lubricant oil, for enhancing the level of the thermophysical properties of density, flash and fire points using fuzzy logic approach. The experimental analysis of 27 samples resulted in three different samples of 1, 3 and 9 for higher (desirable) values of fire point, density and flash points, respectively. However, it is required to determine one sample with a desirable value for all three thermoplastic properties of density, flash and fire point. The fuzzy logic approach used in this research facilitates to determine such unique samples beyond 27 experimental samples. From the fuzzy logic analysis, the sample number 3 possesses the desirable values of 0.9008 gm/ml, 231°C and 252°C for density, flash and fire points, respectively.

This approach can be extended further to determine a sample of lubricant with the optimum mix of any number of nano-additives along with the enhancement of various lubricant properties at their desirable levels. The scope of further work includes enhancing other thermophysical properties such as viscosity, thermal conductivity and shear rate. The other promising optimisation techniques such as RSM, ANN and SVM may also be attempted by researchers in this field for determining the optimum mix of various nano-additives with the base oil to attain the desirable level for all the characteristics of interest simultaneously.

REFERENCES

1. Wang B, Wang X, Lou W, Hao J. Thermal conductivity and rheological properties of graphite/oil nanofluids. Colloids and Surfaces A: Physicochemical and Engineering Aspects. 2012;414:125-131. https://doi.org/10.1016/j.colsurfa.2012.08.008
2. Pico D F M, da Silva L R R, Mendoza O S H, Bandarra Filho E P. Experimental study on thermal and tribological performance of diamond nano-lubricants applied to a refrigeration system using R32. International Journal of Heat and Mass Transfer. 2020;152: 119493. https://doi.org/10.1016/j.ijheatmasstransfer.2020.119493
3. Sankar E, Duraivelu K. The effect of SiO2-Al2O3-TiO2 nanoparticle additives on lubrication performance: Evaluation of wear and coefficient of friction. Materials Today: Proceedings. 2022;68:2387-2392. https://doi.org/10.1016/j.matpr.2022.09.107
4. Narayanasarma S, Kuzhiveli B T. Evaluation of the properties of POE/SiO2 nanolubricant for an energy-efficient refrigeration system–An experimental assessment. Powder Technology. 2019;356:1029-1044. https://doi.org/10.1016/j.powtec.2019.09.024
5. Narayanasarma S, Kuzhiveli BT. The effect of silica nanoparticle on thermal, chemical, corrosive, and the nature-friendly properties of refrigerant compressor lubricants - A comparative study. Asia-Pacific Journal of Chemical Engineering. 2020;15(5):2551. https://doi.org/10.1002/apj.2551
6. Desai N, Nagaraj A M, Sabnis N. Analysis of thermo-physical properties of SAE20W40 engine oil by the addition of SiO2 nanoparticles. Materials Today: Proceedings. 2021;47:5646-5651. https://doi.org/10.1016/j.matpr.2021.03.688
7. Awad A M, Sukkar K A, Jaed D M. Development of an extremely efficient Iraqi nano-lubricating oil (Base-60) employing SiO2 and Al2O3 nanoparticles. In AIP Conference Proceedings. 2022;2443(1). https://doi.org/10.1063/5.0091951
8. Koppula S B, Sudheer N V V S. Experimental Studies and Comparison of Various Mechanical and Thermal Properties of Lubricants by Adding Nano Additives of Al2O3 and SiO2. In IOP Conference Series: Materials Science and Engineering. 2018;455(1):012056.
9. https://doi.org/10.1088/1757-899X/455/1/012056
10. Raj R A, Samikannu R, Yahya A, Mosalaosi M. Investigation of survival/hazard rate of natural ester treated with Al2O3 nanoparticle for power transformer liquid dielectric. Energies. 2021;14(5):1510. https://doi.org/10.3390/en14051510
11. Gumus S, Ozcan H, Ozbey M, Topaloglu B. Aluminum oxide and copper oxide nanodiesel fuel properties and usage in a compression ignition engine. Fuel. 2016;163:80-87. https://doi.org/10.1016/j.fuel.2015.09.048
12. Muthurathinama S G, Perumalb A V. Experimental study on effect of nano Al2O3 in physiochemical and tribological properties of vegetable oil sourced biolubricant blends. Digest journal of nanomaterials and biostructures. 2022;17(1):47-58. https://doi.org/10.15251/DJNB.2022.171.47
13. Sajith V, Mohiddeen M D, Sajanish M B, Sobhan C B. An investigation of the effect of addition of nanoparticles on the properties of lubricating oil. In Heat Transfer Summer Conference. 2007;42754:329-335. https://doi.org/10.1115/HT2007-32772
14. Awad A M, Sukkar K A, Jaed D M. Deep Understanding of the Mechanism and Thermophysical Properties of Prepared Nanofluids Lube Oil Stock-60 with Al2O3 NPs. Journal of Applied Sciences and Nanotechnology. 2022;2(3):37-51. http://doi.org/ 10.53293/jasn.2022.4394.1107
15. Hadi N J, Abd Al-Hussain R K. Physical properties improvement of the diesel engine lubricant oil reinforced nanomaterials. Journal of Mechanical and Energy Engineering. 2018;2(3):233-244. https://doi.org/10.30464/jmee.2018.2.3.233
16. Sukkar K A, Karamalluh A A, Jaber T N. Rheological and thermal properties of lubricating oil enhanced by the effect of CuO and TiO2 nano-additives. Al-Khwarizmi Engineering Journal. 2019;15(2):24-33. https://doi.org/10.22153/kej.2019.12.002

Sankar E, Duraivelu K

DOI 10.2478/ama-2024-0039

Evaluation of some Thermophysical Properties of SN500 Lubrication Oil Blended with SiO2, Al2O3 And TiO2 Nano-Additives, using Fuzzy Logic

17. Kumar M, Afzal A, Ramis M K. Investigation of physicochemical and tribological properties of TiO2 nano-lubricant oil of different concentrations. TRIBOLOGIA-Finnish Journal of Tribology. 2017;35(3):6-15. https://journal.fi/tribologia/article/view/60703

18. Singh Y, Chaudhary V, Pal V. Friction and wear characteristics of the castor oil with TiO2 as an additive. Materials Today: Proceedings. 2020;26:2972-2976.
https://doi.org/10.1016/j.matpr.2020.02.612

19. Deepak S N, Ram C N. Physio-chemical study of traditional lubricant SAE 20 W40 and virgin coconut oil using TiO2 nano-additives. Materials Today: Proceedings. 2021;42:1024-1029.
https://doi.org/10.1016/j.matpr.2020.12.046

20. Ahmadi H, Rashidi A, Nouralishahi A, Mohtasebi S S. Preparation and thermal properties of oil-based nanofluid from multi-walled carbon nanotubes and engine oil as nano-lubricant. International Communications in Heat and Mass Transfer. 2013;46:142-147.
https://doi.org/10.1016/j.icheatmasstransfer.2013.05.003

21. Hafeez M, Krawczuk M, Shahzad H. An Overview of Heat Transfer Enhancement Based Upon Nanoparticles Influenced By Induced Magnetic Field with Slip Condition Via Finite Element Strategy. Acta Mechanica et Automatica. 2022;16(3):200-206.
https://doi.org/10.2478/ama-2022-0024

22. Bouhamatou Z, Abedssemed F. Fuzzy Synergetic Control for Dynamic Car-Like Mobile Robot. Acta Mechanica et Automatica. 2022;16(1):48-57. https://doi.org/10.2478/ama-2022-0007

23. Kumar S, Jain S, Kumar H. Application of adaptive neuro-fuzzy inference system and response surface methodology in biodiesel synthesis from jatropha–algae oil and its performance and emission analysis on diesel engine coupled with generator. Energy. 2021;226:120428. https://doi.org/10.1016/j.energy.2021.120428

24. Kumar S, Jain S, Kumar H. Performance evaluation of adaptive neuro-fuzzy inference system and response surface methodology in modeling biodiesel synthesis from jatropha–algae oil. Energy Sources, Part A: Recovery, Utilization, and Environmental Effects. 2018;40(24):3000-3008.

25. Kumar S, Bansal S. Performance evaluation of ANFIS and RSM in modeling biodiesel synthesis from soybean oil. Biosensors and Bioelectronics: X. 2023;15:100408.
https://doi.org/10.1016/j.biosx.2023.100408

26. Kumar S. Estimation capabilities of biodiesel production from algae oil blend using adaptive neuro-fuzzy inference system (ANFIS). Energy Sources, Part A: Recovery, Utilization, and Environmental Effects. 2020;42(7):909-917.
https://doi.org/10.1080/15567036.2019.1602203

27. Shelton J, Saini N K, Hasan S M. Experimental study of the rheological behavior of TiO2- Al2O3/mineral oil hybrid nanofluids. Journal of Molecular Liquids. 2023;380:121688.
https://doi.org/10.1016/j.molliq.2023.121688

28. Kia S, Khanmohammadi S, Jahangiri A. Experimental and numerical investigation on heat transfer and pressure drop of SiO2 and Al2O3 oil-based nanofluid characteristics through the different helical tubes under constant heat fluxes. International Journal of Thermal Sciences. 2023;185:108082.
https://doi.org/10.1016/j.ijthermalsci.2022.108082

29. Sankar E, Duraivelu K. Simulation of optimal mix of SiO2-TiO2-Al2O3 nano additives for the minimal wear and coefficient of friction of lubricant using fuzzy logic. Jurnal Teknologi. 2023;86(1):125-133. https://doi.org/10.11113/jurnalteknologi.v86.20402

30. Duraivelu K. Digital transformation in manufacturing industry – a comprehensive insight. Journal of Materials Today : Proceedings. 2022;68(6):1825-1829. https://doi.org/10.1016/j.matpr.2022.07.409

Sankar E: [iD] https://orcid.org/0000-0001-5253-7529

Duraivelu K: [iD] https://orcid.org/0000-0003-1853-6965

RECOGNITION OF HUMAN GAIT BASED ON GROUND REACTION FORCES
AND COMBINED DATA FROM TWO GAIT LABORATORIES

Marcin DERLATKA*, Maria SKUBLEWSKA-PASZKOWSKA**, Paweł POWROŹNIK**, Jakub SMOŁKA**,
Edyta ŁUKASIK**, Agnieszka BORYSIEWICZ***, Piotr BORKOWSKI*, Dariusz CZERWIŃSKI****

*Institute of Biomedical Engineering, Faculty of Mechanical Engineering, Bialystok University of Technology,
Wiejska 45C, 15-351 Bialystok, Poland
** Department of Computer Science, Faculty of Electrical Engineering and Computer Science Lublin University of Technology,
Nadbystrzycka 36B, 20-618 Lublin, Poland
*** Department of Emergency Medicine, Faculty of Health Sciences, Medical University of Białystok,
Szpitalna 37, 15-295 Bialystok, Poland
**** Department of Applied Computer Science, Faculty of Mathematics and Information Technology, Lublin University of Technology,
Nadbystrzycka 38B, 20-618 Lublin, Poland

m.derlatka@pb.edu.pl, maria.paszkowska@pollub.pl, p.powroznik@pollub.pl, jakub.smolka@pollub.pl,
e.lukasik@pollub.pl, agnieszka.borysiewicz@umb.edu.pl, p.borkowski@pb.edu.pl, d.czerwinski@pollub.pl

Abstract: In a world in which biometric systems are used more and more often within our surroundings while the number of publications related to this topic grows, the issue of access to databases containing information that can be used by creators of such systems becomes important. These types of databases, compiled as a result of research conducted by leading centres, are made available to people who are interested in them. However, the potential combination of data from different centres may be problematic. The aim of the present work is the verification of whether the utilisation of the same research procedure in studies carried out on research groups having similar characteristics but at two different centres will result in databases that may be used to recognise a person based on Ground Reaction Forces (GRF). Studies conducted for the needs of this paper were performed at the Bialystok University of Technology (BUT) and Lublin University of Technology (LUT). In all, the study sample consisted of 366 people allowing the recording of 6,198 human gait cycles. Based on obtained GRF data, a set of features describing human gait was compiled which was then used to test a system's ability to identify a person on its basis. The obtained percentage of correct identifications, 99.46% for BUT, 100% for LUT and 99.5% for a mixed set of data demonstrates a very high quality of features and algorithms utilised for classification. A more detailed analysis of erroneous classifications has shown that mistakes occur most often between people who were tested at the same laboratory. Completed statistical analysis of select attributes revealed that there are statistically significant differences between values attained at different laboratories.

Key words: human gait recognition, biometrics, ground reaction forces, databases.

1. BACKGROUND

Nowadays, in a world that has become more and more digital, the fast, correct identification of a user, granting him access to his resources including documents, photos, films, or even money, becomes quite significant. At the same time, various biometric features such as fingerprints [1], eye movement [2], voice [3], keystroke [4], face [5], gait [6] or a combination of two or more of such features [7, 8] are more frequently utilised as a tool of such recognition.

Among the biometrics mentioned, human gait is drawing increasing attention [9, 10]. This is caused by its unique characteristics. The human gait is the most complex activity performed subconsciously by a person. It is accepted that after maturity, the way a human being walks remains unchanging and is characteristic of that particular person. What is more, its measurement is possible without any type of unnatural interaction between the considered person and the measuring device.

It should be noted that reliable identifications require statistical accuracy including data of sufficient quantity and quality. It is for this reason that numerous laboratories all around the world concerned with the biomechanics of human gait have compiled many databases containing biometric samples [11–13]. These databases were then made available to researchers to support their efforts related to the search for the optimal human recognition algorithms. Such databases also include values of attributes concerning human gait, with the number of people from whom the data was obtained ranging from few to several thousand (OULP-Age). Unfortunately, these databases are rarely compatible. This is mainly caused by differing measurement values describing human gait. These indexes most often contain data that:

- has been recorded by video cameras [14],
- is accelerometer and gyroscope data collected from inertial measurement units or mobile devices [15],
- describes ground reaction forces (GRF) registered by force plates [12].

Additionally, some databases contain data that illustrates situations that are problematic for human gait recognition algorithms such as people walking while doing different activities [16], in the

wild [17], at different speeds and wearing varying clothing [13], with or without a bag [18], seen from various viewing angles [19], on different surfaces [20] or in various shoe types [12].

Another potential problem concerns the utilisation of measuring systems for gathering data having varying characteristics including differing sampling frequency or performing measurements under diverse conditions resulting in the acquisition of data that differs significantly. Differences in force plate levelling are also a source of slight differences in results. Smith and Ditroilo [21] analysed ground reaction force values under conditions when the force plates were either bare or covered by three varying materials including vinyl, sportflex and astroturf. Statistical analysis showed that covering material had a significant impact on peak force and rate of force development measurements during a testing procedure.

As mentioned earlier, the databases are primarily used to build biometric systems characterised by the highest possible quality, understood as the accuracy of human recognition. The main part of every biometric system is a module that assigns a particular biometric signature to one of the people represented within the database. This assignment is realised using classifiers. Thus, the search for classification algorithms and features that describe a person's physical characteristics or behaviour is a large part of work in the biometrics field.

Horst et al. [22] make human gait recognition based on GRF and three publicly available datasets. For the experiments, they utilised subsets of the AIST Gait Database, the GaitRec dataset, and the Gutenberg Gait Database. It should be emphasised that the main aim of their work was demonstrating the uniqueness of gait signatures and highlighting the gait characteristics that are most distinctive of each person. The problem of the integrity of the data contained in different databases and its impact on the quality of classification of the combined sets was not analysed in this work.

According to the author's knowledge within the literature there are no works that could indicate whether the combination of data gathered by various gait laboratories allows a relatively problem-free expansion of a database. The present work aims to verify if adherence to the same research procedure in a study carried out on a similar sample group at two different research centres will result in the compilation of databases that can be used for human recognition based on GRFs.

2. MATERIAL AND METHODS

Research was carried out at two human gait biomechanics laboratories: the Institute of Biomedical Engineering of the Bialystok University of Technology (BUT) and the Department of Computer Science of the Lublin University of Technology (LUT). Testing paths at both labs were of similar length with measurements made at BUT performed using two Kistler-made, 60 cm × 40 cm force plates registering data with a frequency of 960 Hz. GRF registration at LUT occurred through the utilisation of two 60 cm × 40 cm force plates manufactured by AMTI, model no. BP400600-4000, which recorded data with a frequency of 1,000 Hz (Fig. 1). To eliminate the largest number of factors that may have an impact on the results of performed measurements, the tests were carried out in accordance with the same procedure and under the supervision of the same person, the first author of the present work.

Fig. 1. Image of the LUT testing path with two AMTI-manufactured force plates indicated in the foreground. LUT, Lublin University of Technology

2.1. The study group

The study conducted at BUT was carried out with the participation of 322 people including 139 women and 183 men while that realised at LUT involved 14 people including 4 women and 10 men. Data concerning both groups has been presented in Tab. 1.

Tab. 1. Characteristics of people comprising groups of study participants

	Age (years ± SD)	Body height (cm ± SD)	Body weight (kg ± SD)
BUT	21.54 ± 1.17	175.01 ± 9.59	74.59 ± 16.74
LUT	22.36 ± 1.01	175.07 ± 9.59	70.02 ± 13.86

BUT, Bialystok University of Technology; LUT, Lublin University of Technology.

Prior to the initiation of measurements, every person taking part in the study, regardless of whether they were tested at BUT or LUT, was informed about the aim and course of the testing and signed appropriate authorisations. Next, the participants were asked to walk at their own pace through the testing path containing two hidden force plates. The test was initiated by the person conducting the research. In cases where the participant did not clearly hit into both platforms, their starting point was slightly corrected. Every person walked through the testing path numerous times wearing their own sports shoes. To prevent fatigue, 1–2 min rest was conducted after every 10 passes through the path. In total, during the study, 5,980 gait cycles were recorded at BUT and 218 at LUT. The study was conducted in accordance with the Declaration of Helsinki, and approved by the Bioethics Committee of Regional Medical Chamber in Bialystok (no 18/2006, 8 November 2006) and the Bioethics Committee of Medical University of Bialystok (no. APK.002.192.2022, 28 April 2022, and no. APK.002.251.2023, 20 April 2023).

2.2. Calculating of features

GRFs gained by individual force plates consisted of three components: vertical, medial/lateral and anterior/posterior. The values of the vertical component of GRF attained at LUT, in com-

parison to those gathered at BUT, were negative, therefore, to standardise measurement data, Fy values from LUT were negated (Fig. 2). Registered GRFs were presented using time series x1, x2, …, xN, where N is the number of samples. Generally, the duration time of the support phase of a person's gait depends on several factors and varies so N is variable. To minimise the impact of the duration of the support phase and facilitate the comparison of two distinct gait cycles, parameter values were calculated using formulas (1)–(7).

The features describing gait were selected on the results reported in the work [23]:

− Mean of the signal:

$$\bar{x} = \frac{1}{N}\sum_{i=1}^{N} x_i = \frac{x_1 + x_2 + \cdots + x_N}{N} \tag{1}$$

− Variance of the signal:

$$var = \frac{1}{N}\sum_{i=1}^{N}|x_i - \bar{x}|^2 \tag{2}$$

− Standard deviation of the signal:

$$SD = \sqrt{\frac{1}{N}\sum_{i=1}^{N}(x_i - \bar{x})^2} \tag{3}$$

− Peak-to-peak (ptp) amplitude of the signal:

$$ptp = (\max(x) - \min(x)) \tag{4}$$

where x is the signal-set containing the values of time series x1, x2, …, xN, of a given lower limb and a given GRF component.

− Skewness of the signal is computed as the Fisher-Pearson coefficient of skewness:

$$skew = \frac{m_3}{m_2^{3/2}} \tag{5}$$

where $m_i = \frac{1}{n}\sum_{i=1}^{n}(x_i - \bar{x})^k$ the biased kth sample central moment

− Kurtosis of the signal:

$$kurtosis = \frac{m_4}{var^2} \tag{6}$$

− Hurst exponent of the signal is calculated from the rescaled range and averaged over all the partial time series of length N:

$$\left(\frac{R}{SD}\right)_t = \frac{R_t}{SD_t} \tag{7}$$

where R/SD is averaged over the regions *[x₁,xₜ],[xₜ₊₁,x₂ₜ]* until *[x₍ₗ₋₁₎ₜ₊₁,xₗₜ]* where *l=floor(N/t)*, *t* = 1,2,...,N, *R* is the range of series, *SD* standard deviation of series. Hurst exponent is defined as the slope of the least-squares regression line going through a cloud of partial time series [16].

It is also necessary to specify that signal features were calculated independently for each component of GRF and separately for each lower limb. Thus, created input space consisted of a total of 42 parameters. Since the values of obtained parameters vary significantly from one another it becomes necessary to standardize them before classification using the following equation:

$$x_{std} = \frac{x_{old} - \overline{x_{old}}}{SD} \tag{8}$$

where:

$\overline{x_{old}}$ - mean of the *j*-th feature value before standardisation;

x_{old} - single value of the *j*-th feature value before standardisation.

It should be stressed that the standardisation of data was carried out separately for every utilised data set (only BUT, only LUT, BUT + LUT).
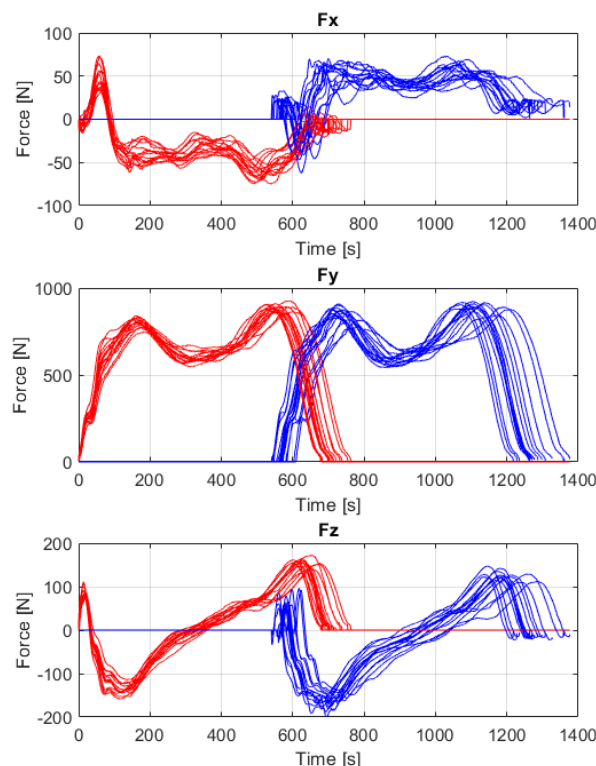
Fig. 2. Components of GRF in: medial/lateral—Fx; vertical—Fy (negated); anterior/posterior—Fz direction of the left lower limb (blue line) and of the right one (red line) in sports shoes. The graph shows a dozen steps of a man aged 23 years with a weight of 82.2 kg and height of 178 cm recorded on the LUT. GRF, ground reaction forces; LUT, Lublin University of Technology

2.3. Classification algorithms

Within the presented solution, it had been decided to test several well-known algorithms. Among them were: k nearest neighbors (kNN) classifier, naive Bayes (NB), feedforward neural network with no more than two hidden layers (MLP), Classification and Regression Tree (CART), support vector machines (svm), regularised linear discriminant analysis (rLDA) and Adam Deep Learning Optimization Algorithm (deep ANN). The feedforward neural network consisted of one or two hidden layers with relu or tanh activation functions. The output (classification) layer used the softmax activation function. The number of inputs was always equal to 42 and the number of outputs was equal to the number of classes. MLP used Broyden–Fletcher–Goldfarb–Shanno quasi-Newton algorithm for learning.

The employed deep neural network consisted of the following seven layers:

− feature input layer (42 inputs);
− dense layer with 400 neurons;
− batch normalisation layer;
− relu layer;

− dense layer with the number of neurons equal to the number of classes;
− softmax layer;
− classification layer.

A more detailed description of the working of individual algorithms may be found in literature including, for example, [23–25].

Every classifier was trained for a group of features listed in subsection 2.2 using 10 folds of cross-validation. Each time, the same division of data into folds was utilised, thanks to which results obtained by different classifiers were comparable. The quality of every classifier was determined by its accuracy. This represents the proportion of true positive results (both true positive as well as true negative) in the selected population.

$$Accuracy = \frac{TruePositive+TrueNegative}{Number\ of\ classified\ data} \qquad (9)$$

The number of classes equalled the number of people being recognised and, of course, differed depending on the data set being utilised. All data processing and analysis were performed using MATLAB 2023a software.

3. RESULTS AND DISCUSSION

Tab. 2 presents the accuracy results for individual classifiers. It must be stressed that these results are the product of having conducted several learning cycles allowing the optimisation of parameters specific to particular classification algorithms. Tab. 2 contains the best-obtained results.

Tab. 2. Results of person identification depending on the utilised classifier and data set

	BUT	LUT	BUT + LUT
kNN	96.76%	99.08%	96.90%
NB	96.07%	97.52%	96.11%
MLP	93.14%	98.62%	92.80%
CART	72.66%	83.94%	72.81%
SVM	89.85%	98.62%	90.03%
rLDA	99.46%	100%	99.52%
deep ANN	96.79%	98.18%	96.93%

BUT, Bialystok University of Technology; CART, classification and regression tree; kNN, k nearest neighbors; naïve Bayes (NB); feedforward neural network (MLP); support vector machines (svm); deep artificial neural network (deep ANN); LUT, Lublin University of Technology; rLDA, regularised linear discriminant analysis.

The results displayed in Tab. 2 indicate that all classifiers except for decision tree (CART), cope well or very well with the task of identifying a particular person. The highest values, reaching >99.45%, were obtained with the rLDA algorithm and are reflected in the study results [23]. In the paper [22], the worst result of classification, as here, was obtained using CART. In contrast to our results in the paper [22], SVM classifier did the best job, allowing a correct recognition in >99.3% of cases. This result is only slightly lower than the best score presented in Tab. 2, however it was obtained for a larger group of people.

It is easy to see that the best results were attained with relation to the LUT data set while the worst were seen for the BUT data set. Undoubtedly, this is connected with the number of study

participants and, as has been shown, for example, in paper [26], a rise in the number of identified people causes a gradual yet unavoidable fall in the percentage of correct identifications. Therefore, to be able to directly compare recognition results for both the BUT and LUT sets, 14 people were randomly drawn 10 times from the BUT set and the table presents the average classifier accuracy results for both BUT and LUT with 10-fold cross-validation also being used in this case (Tab. 3). The direct comparison shows that in case of human gait recognition based on samples consisting of 14 people the accuracy for the BUT database is only slightly higher than the for LUT database. The biggest differences are for NB and CART classifiers. It should be noted that in all other classifiers, the accuracy of recognising individuals from the LUT database is within the range for the BUT database given in Tab. 3.

Tab. 3. Person identification results depending on the classifier used for the database containing 14 people from the BUT data set

	BUT (14 person)	Standard deviation	Range <min-max>
kNN	99.70%	0.377	98.94%–100%
NB	99.43%	0.491	98.45%–100%
MLP	98.70%	0.614	97.89%–99.62%
CART	93.08%	2.905	87.21%–96.88%
SVM	99.24%	0.573	98.45%–100%
rLDA	99.93%	0.154	99.63%–100%
deep ANN	98.94%	0.550	97.73%–99.64%

BUT, Bialystok University of Technology; CART, classification and regres-sion tree; kNN, k nearest neighbors; naïve Bayes (NB); feedforward neural network (MLP); support vector machines (svm); deep artificial neural network (deep ANN); rLDA, regular-ised linear discriminant analysis.

Looking at Tab. 2, it was noted that the results for all classifiers except MLP for the combined set (BUT + LUT) are slightly higher than just for BUT. Since, according to the previous statement, they should be rather slightly worse, this could mean that features established for the LUT data set assume different values than for the BUT data set. In that case, there will be no increase in the number of classes in the same place of the feature space, since the data from the two labs is far enough apart. Therefore, the classification of data from the LUT set will provide very good results (see Tab. 2), and since for both BUT + LUT sets, there will be more correctly classified instances then accuracy will slightly increase.

Tab. 4. Number (and percentage) of errors in the identification of people with relation to the laboratory at which, in reality, those people were tested occurring in classifications using deep ANN

		Predicted research centre	
		BUT	LUT
Actual research centre	**BUT**	182 (3.04%)	1 (0.02%)
	LUT	1 (0.46%)	5 (2.29%)

BUT, Bialystok University of Technology; LUT, Lublin University of Technology.

For this reason, the tables below present a specific form of a confusion matrix that shows whether incorrect identifications

concern people who were tested at the same or at different laboratories. Incorrect recognitions made by the most accurate classifier rLDA (Tab. 5) and, to better illustrate the phenomenon, a somewhat less precise, in this case, deep ANN classifier (Tab 4), were chosen for the tables. Even a cursory analysis of values presented in the tables allows the conclusion that the errors are mostly made with respect to people who were tested at the same laboratory. Erroneous identifications for people who were tested at different centres, on the other hand, are, literally, singular occurrences.

Tab. 5. Number (and percentage) of errors in the identification of people with relation to the laboratory at which, in reality, those people were tested occurring in classifications using rLDA

		Predicted research centre	
		BUT	**LUT**
Actual research centre	**BUT**	29 (0.48%)	0 (0.00%)
	LUT	0 (0.00%)	1 (0.02%)

BUT, Bialystok University of Technology; LUT, Lublin University of Technology.

Tab. 6. The average and standard deviation for the mean of the signal as well as the amplitude peak-to-peak features attained for both lower extremities as well as for both laboratories

	Feature	Average (N/(kg·m/s²))	SD
BUT	Mean_Left_Fy	0.4301	0.0101
	Mean_Right_Fy	0.4435	0.0101
	P2p_Left_Fy	1.1415	0.0665
	P2p_Right_Fy	1.1652	0.0641
	Mean_Left_Fz	0.0002	0.0047
	Mean_Right_Fz	0.0008	0.0042
	P2p_Left_Fz	0.3811	0.0702
	P2p_Right_Fz	0.4171	0.0613
LUT	Mean_Left_Fy	0.4414	0.0142
	Mean_Right_Fy	0.4444	0.0160
	P2p_Left_Fy	1.1291	0.0574
	P2p_Right_Fy	1.1377	0.0643
	Mean_Left_Fz	0.0089	0.0044
	Mean_Right_Fz	−0.0151	0.0069
	P2p_Left_Fz	0.3834	0.0558
	P2p_Right_Fz	0.3886	0.0573

BUT, Bialystok University of Technology; LUT, Lublin University of Technology.

To further verify differences between data statistical tests were performed with four characteristics from every data set being selected. These were mean and p2p values of anterior-posterior and vertical components of GRF for both lower limbs calculated according to formulas (1) and (4), respectively. In contrast to values of features utilised to train classifiers, this time these values were normalised for the body mass of the person, a standard procedure used in human gait biomechanics allowing the comparison of GRFs gathered from people whose body weight differs. Parameters calculated on the basis of Fy and Fz were selected since it has been shown that the medial-lateral component has the smallest impact on human recognition [27]. The mean and stand-ard deviation values of these features have been presented in Tab. 6.

The verification of the hypothesis that appropriate parameters measured at different laboratories vary from one another was carried out using the Statistica software. Based on the Central Limit Theorem and sample cardinality obtained in both labs, it was accepted that the attributes described by the present work exhibit normal distribution. Since the number of samples gathered at individual laboratories differed significantly the Welch test was utilised to demonstrate a statistically significant difference between the values recorded at BUT in relation to those calculated on the basis of measurements performed at LUT. The values of these tests attained during the verification of the hypotheses as to a lack of statistically significant differences have been presented in Tab. 7. Statistically significant values have been marked in red.

Tab. 7. Welch test *p*-level values

Feature	Welch test *p*-level	Feature	Welch test *p*-level
Mean_Left_Fy	<0.001	Mean_Right_Fy	0.409
P2p_Left_Fy	0.002	P2p_Right_Fy	<0.001
Mean_Left_Fz	<0.001	Mean_Right_Fz	<0.001
P2p_Left_Fz	0.002	P2p_Right_Fz	<0.001

Results of statistical tests indicate that statistically significant differences at levels of $p < 0.05$ do not occur solely with the mean value of the right leg vertical component. Through this, the results presented in Tabs 4 and 5 are verified and confirm the existence of significant differences between measurements done at the two research centres. It is worth mentioning that the cause of these differences may be found in the fact that the force plates were manufactured by different companies as well as in the level of force inhibition of the material used to cover them [21]. Another, although less likely, possible cause for differing results is that the samples consisted of different people, each with a characteristic manner of gait. Thus, an interesting question arises, one unanswered by the present work, whether the results would be different if the tests were conducted on the same group of people at both research centres. The answer would ultimately confirm the thesis concerning the differences between laboratories.

5. CONCLUSION

The paper presents the working of a biometric system for the recognition of a person based on their gait. Test data was recorded at two biomechanics human gait laboratories. Generally, the obtained human identification results were very good and confirmed the great potential of human gait as a biometric measure. An analysis of errors, enriched with statistical analysis, showed that the specific character of a given laboratory may significantly impact the results of measurements. It turned out that even with the utilisation of the same procedure and with the same personnel conducting the tests the final results may differ, with the conclusion being that the combining of databases compiled by different sources does not have to result in better data allowing the creation of a biometric system that is, for example, more resistant to external factors.

REFERENCES

1. Yang W, Wang S, Hu J, Zheng G, Valli C. Security and accuracy of fingerprint-based biometrics: A review. Symmetry (Basel). 2019; 11(2): 141. https://doi.org/10.3390/sym11020141
2. Lohr D, Komogortsev OV. Eye Know You Too: Toward Viable End-to-End Eye Movement Biometrics for User Authentication. IEEE Transactions on Information Forensics and Security. 2022;17:3151–64. https://doi.org/10.1109/TIFS.2022.3201369
3. Chen X, Li Z, Setlur S, Xu W. Exploring racial and gender disparities in voice biometrics. Scientific Reports. 2022; 12(1), 3723. https://doi.org/10.1038/s41598-022-06673-y
4. Stragapede G, Delgado-Santos P, Tolosana R, Vera-Rodriguez R, Guest R, Morales A. Mobile keystroke biometrics using transformers. In 2023 IEEE 17th International Conference on Automatic Face and Gesture Recognition (FG). IEEE. Waikoloa Beach, HI, USA 2023. 1-6. https://doi.org/10.1109/FG57933.2023.10042710
5. Taskiran M, Kahraman N, Erdem CE. Face recognition: Past, present and future (a review). Digital Signal Processing. 2020; 106: 102809. https://doi.org/10.1016/j.dsp.2020.102809
6. Parashar A, Parashar A, Ding W, Shekhawat RS, Rida I. Deep learning pipelines for recognition of gait biometrics with covariates: A comprehensive review. Artificial Intelligence Review. 2023; 1-65. https://doi.org/10.1007/s10462-022-10365-4
7. Szczuko P, Harasimiuk A, Czyżewski A. Evaluation of decision fusion methods for multimodal biometrics in the banking application. Sensors. 2022; 22(6): 2356. https://doi.org/10.3390/s22062356
8. Ren H, Sun L, Guo J, Han C. A dataset and benchmark for multimodal biometric recognition based on fingerprint and finger vein. IEEE Transactions on Information Forensics and Security. 2022; 17: 2030-2043. https://doi.org/10.1109/TIFS.2022.3175599
9. Delgado-Santos P, Tolosana R, Guest R, Deravi F, Vera-Rodriguez R. Exploring transformers for behavioural biometrics: A case study in gait recognition. Pattern Recognition. 2023; 143: 109798. https://doi.org/10.1016/j.patcog.2023.109798
10. Rani V, Kumar M. Human gait recognition: A systematic review. Multimedia Tools and Applications. 2023; 1-35. https://doi.org/10.1007/s11042-023-15079-5
11. Horst F, Slijepcevic D, Simak M, Schöllhorn WI. Gutenberg Gait Database, a ground reaction force database of level overground walking in healthy individuals. Scientific data. 2021; 8(1): 232. https://doi.org/10.1038/s41597-021-01014-6
12. Derlatka M, Parfieniuk M. Real-world measurements of ground reaction forces of normal gait of young adults wearing various footwear. Scientific data. 2023; 10(1): 60. https://doi.org/10.1038/s41597-023-01964-z
13. Makihara Y, Nixon MS, Yagi Y. Gait recognition: Databases, representations, and applications. Computer Vision: A Reference Guide. 2020; 1-13. https://doi.org/10.1007/978-3-030-03243-2_883-1
14. Song C, Huang Y, Wang W, Wang L. CASIA-E: a large comprehensive dataset for gait recognition. IEEE Transactions on Pattern Analysis and Machine Intelligence. 2022; 45(3): 2801-2815. https://doi.org/10.1109/TPAMI.2022.3183288
15. Ngo TT, Ahad MAR, Antar AD, Ahmed M, Muramatsu D, Makihara Y, et al. OU-ISIR wearable sensor-based gait challenge: Age and gender. In 2019 International Conference on Biometrics (ICB). 2019; 1-6. IEEE. https://doi.org/10.1109/ICB45273.2019.8987235
16. Malekzadeh M, Clegg RG, Cavallaro A, Haddadi H. Protecting sensory data against sensitive inferences. In Proceedings of the 1st Workshop on Privacy by Design in Distributed Systems. 2018; 1-6. https://doi.org/10.1145/3195258.3195260
17. Zou Q, Wang Y, Wang Q, Zhao Y, Li Q. Deep learning-based gait recognition using smartphones in the wild. IEEE Transactions on Information Forensics and Security. 2020; 15: 3197-3212. https://doi.org/ 10.1109/TIFS.2020.2985628
18. Tan D, Huang K, Yu S, Tan T. (2006, August). Efficient night gait recognition based on template matching. In 18th International Conference on Pattern Recognition (ICPR'06). IEEE. 2006; 3: 1000-1003. https://doi.org/10.1109/ICPR.2006.478
19. Yu S, Tan D, Tan T. A framework for evaluating the effect of view angle, clothing and carrying condition on gait recognition. In 18th International Conference on Pattern Recognition (ICPR'06). 2006; 4: 441-444. IEEE. https://doi.org/10.1109/ICPR.2006.67
20. Sarkar S, Phillips PJ, Liu Z, Vega IR, Grother P, Bowyer KW. The humanID gait challenge problem: Data sets, performance, and analysis. IEEE Transactions on Pattern Analysis and Machine Intelligence. 2005; 27(2): 162-177. https://doi.org/10.1109/TPAMI.2005.39
21. Smith T, Ditroilo M. Force plate coverings significantly affect measurement of ground reaction forces. Plos one. 2023; 18(11): e0293959. https://doi.org/10.1371/journal.pone.0293959
22. Horst F, Slijepcevic D, Simak M, Horsak B, Schöllhorn WI, Zeppelzauer M. Modeling Biological Individuality Using Machine Learning: A Study on Human Gait. Computational and Structural Biotechnology Journal. 2023; 21:3414-3423 https://doi.org/10.1016/j.csbj.2023.06.009
23. Derlatka M, Borowska M. Ensemble of heterogeneous base classifiers for human gait recognition. Sensors, 2023; 23(1): 508. https://doi.org/10.3390/s23010508
24. Guo Y, Hastie T, Tibshirani R. Regularized linear discriminant analysis and its application in microarrays. Biostatistics. 2007; 8:86–100. https://doi.org/10.1093/biostatistics/kxj035.
25. Kingma DP, Ba J. Adam: A method for stochastic optimization. arXiv preprint arXiv:1412.6980. 2014. doi:10.48550/arXiv.1412.6980
26. Derlatka M, Bogdan M. Recognition of a person wearing sport shoes or high heels through gait using two types of sensors. Sensors. 2018; 18(5): 1639. https://doi.org/10.3390/s18051639
27. Duncanson K, Thwaites S, Booth D, Abbasnejad E, Robertson WS, Thewlis D. The most discriminant components of force platform data for gait based person re-identification. 2021. https://doi.org/10.36227/techrxiv, 16683229, v1

Marcin Derlatka: https://orcid.org/0000-0002-6736-5106

Maria Skublewska-Paszkowska: https://orcid.org/0000-0002-0760-7126

Paweł Powroźnik: https://orcid.org/0000-0002-5705-4785

Jakub Smołka: https://orcid.org/0000-0002-8350-2537

Edyta Łukasik: https://orcid.org/0000-0003-3644-9769

Agnieszka Borysiewicz: https://orcid.org/0000-0001-7740-7800

Piotr Borkowski: https://orcid.org/0000-0001-9038-2601

Dariusz Czerwiński https://orcid.org/0000-0002-3642-1929